frontiers | Research Topics

Editors' showcase insights in molecular and cellular reproduction

2022

Edited by
Rafael A. Fissore and Shao-Chen Sun

Published in
Frontiers in Cell and Developmental Biology

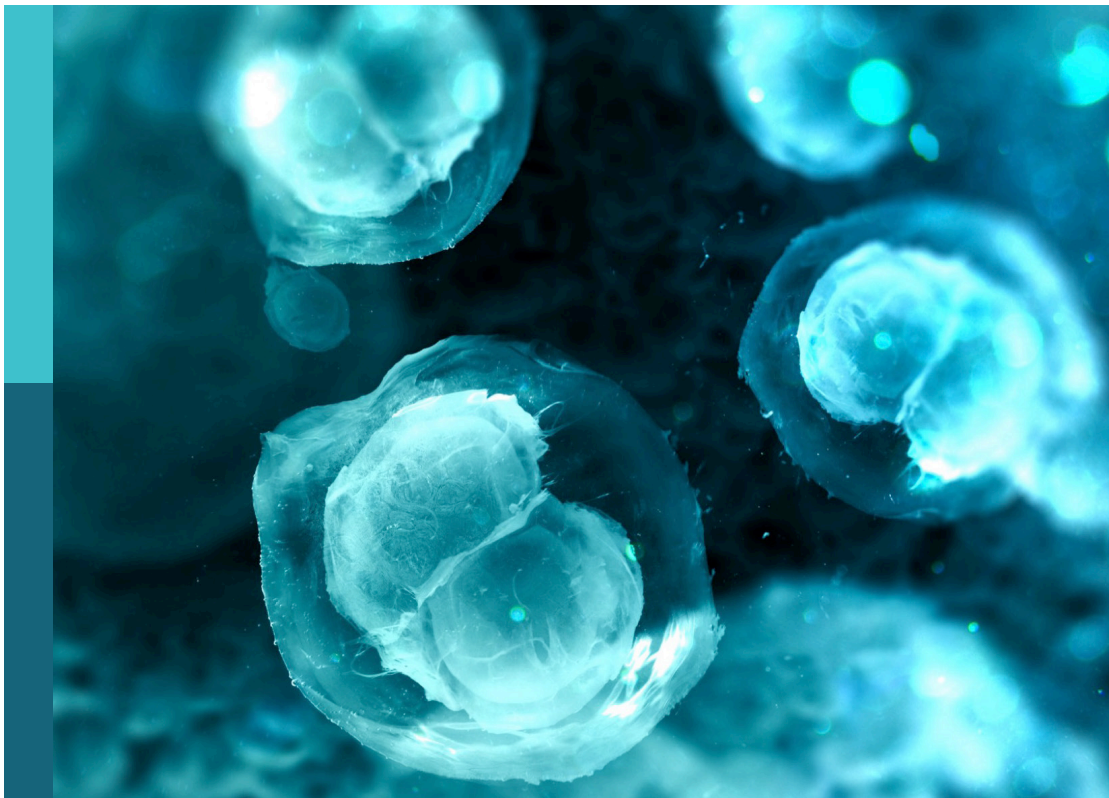

ISSN 1664-8714
ISBN 978-2-8325-4010-7
DOI 10.3389/978-2-8325-4010-7

About Frontiers

Frontiers is more than just an open access publisher of scholarly articles: it is a pioneering approach to the world of academia, radically improving the way scholarly research is managed. The grand vision of Frontiers is a world where all people have an equal opportunity to seek, share and generate knowledge. Frontiers provides immediate and permanent online open access to all its publications, but this alone is not enough to realize our grand goals.

Frontiers journal series

The Frontiers journal series is a multi-tier and interdisciplinary set of open-access, online journals, promising a paradigm shift from the current review, selection and dissemination processes in academic publishing. All Frontiers journals are driven by researchers for researchers; therefore, they constitute a service to the scholarly community. At the same time, the *Frontiers journal series* operates on a revolutionary invention, the tiered publishing system, initially addressing specific communities of scholars, and gradually climbing up to broader public understanding, thus serving the interests of the lay society, too.

Dedication to quality

Each Frontiers article is a landmark of the highest quality, thanks to genuinely collaborative interactions between authors and review editors, who include some of the world's best academicians. Research must be certified by peers before entering a stream of knowledge that may eventually reach the public - and shape society; therefore, Frontiers only applies the most rigorous and unbiased reviews. Frontiers revolutionizes research publishing by freely delivering the most outstanding research, evaluated with no bias from both the academic and social point of view. By applying the most advanced information technologies, Frontiers is catapulting scholarly publishing into a new generation.

What are Frontiers Research Topics?

Frontiers Research Topics are very popular trademarks of the *Frontiers journals series*: they are collections of at least ten articles, all centered on a particular subject. With their unique mix of varied contributions from Original Research to Review Articles, Frontiers Research Topics unify the most influential researchers, the latest key findings and historical advances in a hot research area.

Find out more on how to host your own Frontiers Research Topic or contribute to one as an author by contacting the Frontiers editorial office: frontiersin.org/about/contact

Editors' showcase 2022: Insights in molecular and cellular reproduction

Topic editors

Rafael A. Fissore — University of Massachusetts Amherst, United States

Shao-Chen Sun — Nanjing Agricultural University, China

Citation

Fissore, R. A., Sun, S.-C., eds. (2023). *Editors' showcase 2022: Insights in molecular and cellular reproduction*. Lausanne: Frontiers Media SA.

doi: 10.3389/978-2-8325-4010-7

Table of contents

frontiers | Frontiers in Cell and Developmental Biology

TYPE Editorial
PUBLISHED 13 November 2023
DOI 10.3389/fcell.2023.1321358

OPEN ACCESS

EDITED AND REVIEWED BY
Ken-Ichi Sato,
Kyoto Sangyo University, Japan

*CORRESPONDENCE
Shao-Chen Sun,
sunsc@njau.edu.cn
Rafael A. Fissore,
rfissore@umass.edu

RECEIVED 13 October 2023
ACCEPTED 03 November 2023
PUBLISHED 13 November 2023

CITATION
Ju J-Q, Fissore RA and Sun S-C (2023), Editorial: Editors' showcase 2022: insights in molecular and cellular reproduction.
Front. Cell Dev. Biol. 11:1321358.
doi: 10.3389/fcell.2023.1321358

Editorial: Editors' showcase 2022: insights in molecular and cellular reproduction

Jia-Qian Ju[1], Rafael A. Fissore[2]* and Shao-Chen Sun[1]*

[1]College of Animal Science and Technology, Nanjing Agricultural University, Nanjing, China, [2]Department of Veterinary and Animal Sciences, University of Massachusetts Amherst, Amherst, MA, United States

KEYWORDS

folliculogenesis, oocyte, spermatogenesis, fertilization, embryo, placenta

Editorial on the Research Topic
Editors' showcase 2022: insights in molecular and cellular reproduction

Introduction

Germ cells, which give rise to sperm and eggs, undergo meiosis during their differentiation process. Meiosis is a specialized form of cell division that results in the production of haploid cells from diploid cells. In this process, the chromosomes in the germ cells are duplicated only once, followed by two rounds of cell division. This leads to the formation of haploid cells, each containing half the number of chromosomes compared to the original diploid cell. However, after the haploid sperm and egg are formed, they come together through fertilization, wherein they fuse to create a diploid zygote. The zygote then develops into a new organism, initiating the next cycle of life.

Meiosis is also essential for sexual reproduction and the generation of genetic diversity, as crossing over between different-origin chromosomes takes places during the early stages of this process. Therefore, both molecular and cellular reproduction are fundamental processes that ensure the continuity of life and the transmission of genetic information from one generation to the next and whose underlying mechanism(s) must be understood.

This Research Topic includes 1 method, 2 reviews, and 11 original research articles, providing critical and novel insights into cell and developmental biology. Specifically, it sheds light on folliculogenesis, oocyte maturation, embryo development, spermatogenesis, sperm maturation, sperm capacitation, and fertilization.

Folliculogenesis and oocyte maturation

Female fertility female is closely associated with several processes, including folliculogenesis and oogenesis (the development of follicles, oocytes and eggs, respectively) and oocyte maturation. Here, 4 articles introduce and discuss aspects of female fertility.

The initiation of estrous cycles in female mammals, which marks the initiation of the fertile period, is prompted by an increase in the circulating levels of gonadotropins, including the pre-ovulatory luteinizing hormone (LH). The LH surge serves as the stimulant for the

onset of oocyte maturation, follicle cell luteinization, increased follicular vascularity, and breakdown of the follicle wall that leads to ovulation (Robker et al., 2018). According to Hessock et al., the LH surge results in an increased availability of amino acids and metabolites for cumulus and granulosa cells, which are utilized for energy production and also transferred to the oocyte to support meiotic maturation. Furthermore, at a later stage, these metabolites may also be utilized by the ovulatory follicle for protein production.

Oogenesis is the complex process of female gamete (oocyte) growth and maturation that occurs in a regulated fashion and in waves in the ovaries and continues throughout their reproductive lifespan. PGs (prostaglandins) have been reported to regulate almost every aspect of female reproduction. For example, loss of PG synthesis blocks mammalian follicle maturation and ovulation (Tootle, 2013). According to Talbot et al., PGs play a crucial role during oogenesis in carefully regulating the level and forms of nuclear actin. This regulation is necessary to control nucleolar activity required for the production of fertilization-competent oocytes. In addition, microtubule movement plays an important role in mRNA localization and modeling in *Drosophila* oocytes (Goldman and Gonsalvez, 2017). Neiswender et al. recently identified the *Drosophila* ortholog of TTC1 (dTtc1) as an interacting partner of Egalitarian, an RNA adaptor of the Dynein motor, and showed that the depletion of dTtc1 leads to defective oogenesis in *Drosophila* (fruit flies), resulting in the absence of mature eggs. Further examination revealed that the egg chambers without dTtc1 displayed a distinct phenotype, characterized by severely swollen mitochondria. Furthermore, Oocyte quality and its genetic integrity play a crucial role in fertility. Environmental toxins can negatively affect oocyte quality and fertility, and have recently become a cause for concern, which also threatens food safety. There is growing evidence that Azoxystrobin (AZO) is widespread in the environment and has the potential to induce developmental toxicity in animals. For example, AZO has been reported to impair neuronal migration by inducing mitochondrial deactivation and induction of apoptosis increasing (Kang et al., 2021). Gao et al. suggested that AZO is one of the most widely used fungicides in agriculture, and female exposure to AZO impairs oocyte maturation by negatively influencing a variety of cellular functions such as increasing oxidative stress and mitochondrial dysfunction, decreasing MTOC integrity and the subsequent spindle formation and chromosome alignment.

Spermatogenesis, sperm capacitation and fertilization

Spermatogenesis is the process of sperm cell development in the testes of male organisms. It involves the production and maturation of sperm cells, also known as spermatozoa. Spermatogenesis is an extraordinarily complex process. The differentiation of spermatogonia into spermatocytes, spermatid and finally in mature spermatozoa requires the participation of non-spermatogenic cell types, hormones, paracrine factors, genes, and epigenetic regulators. Here, a total of 8 articles introduced the effects of the fertility of male.

Efficient sperm production requires the translocation of protamines from the cytoplasm to the nucleus. The Sperm-associated antigen 17 (SPAG17) is found to be expressed in testicular germ cells during the late stages of sperm development and is shown to localize to the manchette, contributing to protein trafficking (Kazarian et al., 2018). Here, Agudo et al. discovered for the first time that Spag17 was essential for normal manchette structure, protein transport, and formation of the sperm head and flagellum, in addition to its role in sperm motility. During sperm maturation, significant changes occur, including the loss of most membrane organelles and a substantial accumulation of ether glycerolipids, that is a well-conserved phenomenon across different species. These specific lipid molecules contribute to the unique composition and properties of sperm cells (Teves and Roldan, 2022). Remedios et al. reviewed the existing knowledge on the relevance of the different types of ether lipids involved in sperm production, maturation, and function, and provided a comprehensive metabolic map associated with ether-lipids and peroxisomal-related functions in sperm.

After ejaculation, sperm cells undergo a process called capacitation, which is necessary for them to become fully capable of fertilizing an egg. Targeted disruption of the soluble adenylyl cyclase (ADCY10; sAC) gene results in male-specific sterility without affecting spermatogenesis, mating behavior, or spermatozoa morphology and count; however, it dramatically impairs sperm motility and prevents capacitation (Akbari et al., 2019). Research by Ritagliati et al. demonstrate that sAC KO male mice are infertile because their sperm do not penetrate beyond the UTJ suggests that human's sAC KO men are infertile because their sperm will not cross the cervix to enter the uterus to be able to ever reach the oviduct and the fertilization site. Because the vagina reacidifies following intercourse, in the absence of sAC, human sperm are not likely to survive long after sex. Additionally, Balbach et al. compared the metabolic changes that occur during capacitation in mouse sperm obtained from the epididymis versus ejaculated sperm. They also related these changes to human ejaculated sperm. The study revealed that capacitation induced metabolic changes in pathways that support the motility of both epididymal and ejaculated sperm. During capacitation, sperm experience a change in their motility pattern to a more vigorous, this process requires the uptake of calcium ions through the sperm-specific CatSper channel complex. This channel represents a promising target for contraception research. Recent advances have reported that the rise in intracellular Ca^{2+} concentration after exposure to an alkaline-high K^{+} solution was evaluated as an indirect measure of CatSper function in a high-throughput drug screening (Carlson et al., 2022). Here, Luque et al. proposed an alternative method to specifically evaluate CatSper opening. Their approach involves removing external free divalent cations through chelation, which then allows CatSper to efficiently conduct monovalent cations. By using this method, researchers can test various compounds to determine their ability to inhibit CatSper function in sperm. This screening process is valuable for identifying potential drugs or compounds that could target CatSper as a means of contraception or fertility control.

Fertilization occurs when a sperm cell successfully negotiates the outer protective layers of the egg and fuses with the egg's plasma membrane. Sperm contain a single, large dense-core secretory granule (the acrosome) whose contents are released by regulated exocytosis (acrosomal exocytosis, AE) prior to fertilization. α-Synuclein, a small cytosolic protein, has emerged as an important

regulator for membrane fusion (Khounlo et al., 2021). Here, Buzzatto et al. have discovered that α-Synuclein is necessary for sperm exocytosis in a post-fusion stage for expanding the fusion pores in the acrosome. In oocytes, the glycophosphatidylinositol (GPI) anchored protein Juno (Bianchi et al., 2014) and a member of the tetraspanin family, CD9 (Kaji et al., 2000), have been identified as critical for mammalian fertilization. Frolikova et al. propose the existence of Juno-CD9 complexes in specific spatially defined compartments within the microvillar regions of the mouse oolemma. This complex is believed to play a distinct functional role in sperm binding sperm to the oocyte. This research provides insights into the molecular mechanisms involved in sperm-oocyte interactions and adds to our understanding of the fertilization process. Understanding the genetic underpinnings of fertilization is essential for developing infertility treatments, contraceptive targets, understanding speciation, and mechanisms of cell-cell interactions. Maniates and Singson discussed potential experimental biases and intrinsic biological factors that hinder the discovery of genes related to fertilization. They also shed light on current strategies aimed at identifying these genes, which may lead to further advancements in understanding this complex process.

Embryo and placenta

The embryo and placenta are two crucial components of mammalian reproduction. The embryo is the early stage of development of a multicellular organism. Fertilization results in the formation of a zygote, which undergoes a series of cell divisions called cleavage. As the cells continue to divide and differentiate, the embryo gradually forms. The placenta is an organ that develops during pregnancy in mammals and plays a critical role in supporting the growth and development of the fetus during pregnancy. It facilitates the exchange of nutrients, gases, and waste products between the mother and the developing baby, while also producing hormones and providing immune protection. Here, a total of 2 articles introduced the embryo and placenta.

Previous reports have shown that the pig extraembryonic endoderm (pXEN) cells contribute both to extraembryonic tissues including visceral yolk sac as well as embryonic gut when injected into host blastocysts, and generate live offspring when used as a nuclear donor in somatic cell nuclear transfer (SCNT) (Park et al., 2021). Based on this, Park et al. developed a method for generating primary fibroblast-like cells from pluripotent cells from embryonic outgrowths and tested the hypothesis that these fibroblast-like cells derived from the embryo serve as an ideal nuclear donor for embryo transfer procedures. They showed that embryo-derived fibroblasts (EFs) share many characteristics with fetal fibroblasts (FFs), including the spindle-shaped morphology and expression of key fibroblast-specific molecular markers. In addition, transcriptomic analysis via RNA sequencing (RNA-seq) confirmed the similarity of EFs to FFs. The EFs used as nuclear donors for SCNT resulted in enhanced *in vivo* developmental competence.

The placenta integrates an array of signals from both the mother and fetus to maintain fetal homeostasis. It performs numerous functions critical for normal fetal growth and development, including mediating nutrient and waste transfer, secreting hormones, serving as an immunological barrier, and performing xenobiotic detoxification (Díaz et al., 2014). Kelly et al. perform RNA-seq analysis at embryonic day 18.5 to identify genes differentially expressed in the placentas of obese and normal-weight dams (controls) using a mouse model of diet-induced obesity with fetal overgrowth. The data shows that maternal obesity with fetal overgrowth differentially regulates the transcriptome in male and female placentas, including genes involved in oxidative phosphorylation. They also provide evidence that the findings in mice have clinical relevance because the expression of the placental mitochondrial complex in humans was downregulated and negatively correlated with maternal pre-pregnancy BMI and birth weight in male infants.

Overall, the findings in this Research Topic provide new insights into the molecular and cellular aspects of many reproductive processes, including aspects of germ cell specification, folliculogenesis, spermatogenesis, oocyte maturation, sperm capacitation, and embryo development. The new information has broad implications for understanding fundamental biological processes, disease mechanisms, and implementing potential therapies.

Author contributions

J-QJ: Data curation, Formal Analysis, Investigation, Software, Writing–original draft. RF: Conceptualization, Supervision, Validation, Writing–review and editing. S-CS: Conceptualization, Funding acquisition, Supervision, Validation, Writing–review and editing.

Funding

The authors declare financial support was received for the research, authorship, and/or publication of this article. Natural Science Foundation of Guangxi in China (2021GXNSFDA220001); Fundamental Research Funds for the Central Universities of China (KYT2023002).

Conflict of interest

The authors declare that the research was conducted in the absence of any commercial or financial relationships that could be construed as a potential conflict of interest.

The authors declared that they were an editorial board member of Frontiers, at the time of submission. This had no impact on the peer review process and the final decision.

Publisher's note

References

Akbari, A., Pipitone, G. B., Anvar, Z., Jaafarinia, M., Ferrari, M., Carrera, P., et al. (2019). ADCY10 frameshift variant leading to severe recessive asthenozoospermia and segregating with absorptive hypercalciuria. *Hum. Reprod.* 34, 1155–1164. doi:10.1093/humrep/dez048

Bianchi, E., Doe, B., Goulding, D., and Wright, G. J. (2014). Juno is the egg Izumo receptor and is essential for mammalian fertilization. *Nature* 508, 483–487. doi:10.1038/nature13203

Carlson, E. J., Francis, R., Liu, Y., Li, P., Lyon, M., Santi, C. M., et al. (2022). Discovery and characterization of multiple classes of human CatSper blockers. *ChemMedChem* 17, e202000499. doi:10.1002/cmdc.202000499

Díaz, P., Powell, T. L., and Jansson, T. (2014). The role of placental nutrient sensing in maternal-fetal resource allocation. *Biol. Reprod.* 91, 82. doi:10.1095/biolreprod.114.121798

Goldman, C. H., and Gonsalvez, G. B. (2017). The role of microtubule motors in mRNA localization and patterning within the Drosophila oocyte. *Results Probl. Cell. Differ.* 63, 149–168. doi:10.1007/978-3-319-60855-6_7

Kaji, K., Oda, S., Shikano, T., Ohnuki, T., Uematsu, Y., Sakagami, J., et al. (2000). The gamete fusion process is defective in eggs of Cd9-deficient mice. *Nat. Genet.* 24, 279–282. doi:10.1038/73502

Kang, J., Bishayee, K., and Huh, S.-O. (2021). Azoxystrobin impairs neuronal migration and induces ROS dependent apoptosis in cortical neurons. *Int. J. Mol. Sci.* 22, 12495. doi:10.3390/ijms222212495

Kazarian, E., Son, H., Sapao, P., Li, W., Zhang, Z., Strauss, J. F., et al. (2018). SPAG17 is required for male germ cell differentiation and fertility. *Int. J. Mol. Sci.* 19, 1252. doi:10.3390/ijms19041252

Khounlo, R., Hawk, B. J. D., Khu, T.-M., Yoo, G., Lee, N. K., Pierson, J., et al. (2021). Membrane binding of α-synuclein stimulates expansion of SNARE-dependent fusion pore. *Front. Cell. Dev. Biol.* 9, 663431. doi:10.3389/fcell.2021.663431

Park, C.-H., Jeoung, Y.-H., Uh, K.-J., Park, K.-E., Bridge, J., Powell, A., et al. (2021). Extraembryonic endoderm (XEN) cells capable of contributing to embryonic chimeras established from pig embryos. *Stem Cell. Rep.* 16, 212–223. doi:10.1016/j.stemcr.2020.11.011

Robker, R. L., Hennebold, J. D., and Russell, D. L. (2018). Coordination of ovulation and oocyte maturation: a good egg at the right time. *Endocrinology* 159, 3209–3218. doi:10.1210/en.2018-00485

Teves, M. E., and Roldan, E. R. S. (2022). Sperm bauplan and function and underlying processes of sperm formation and selection. *Physiol. Rev.* 102, 7–60. doi:10.1152/physrev.00009.2020

Tootle, T. L. (2013). Genetic insights into the *in vivo* functions of prostaglandin signaling. *Int. J. Biochem. Cell. Biol.* 45, 1629–1632. doi:10.1016/j.biocel.2013.05.008

frontiers | Frontiers in Cell and Developmental Biology

TYPE Original Research
PUBLISHED 10 November 2022
DOI 10.3389/fcell.2022.1059710

OPEN ACCESS

EDITED BY
Il-Keun Kong,
Gyeongsang National University, South Korea

REVIEWED BY
Kenneth White,
Utah State University, United States
Talluri Thirumala Rao,
Indian Council of Agricultural Research (ICAR), India

*CORRESPONDENCE
Bhanu P. Telugu,
telugub@umsystem.edu

SPECIALTY SECTION
This article was submitted to Molecular and Cellular Reproduction, a section of the journal Frontiers in Cell and Developmental Biology

RECEIVED 01 October 2022
ACCEPTED 27 October 2022
PUBLISHED 10 November 2022

CITATION
Park C-H, Jeoung Y-H, Zhang L, Yeddula SGR, Park K-E, Waters J and Telugu BP (2022), Establishment, characterization, and validation of novel porcine embryonic fibroblasts as a potential source for genetic modification.
Front. Cell Dev. Biol. 10:1059710.
doi: 10.3389/fcell.2022.1059710

Establishment, characterization, and validation of novel porcine embryonic fibroblasts as a potential source for genetic modification

Chi-Hun Park[1,2], Young-Hee Jeoung[1,2], Luhui Zhang[1], Sai Goutham Reddy Yeddula[1], Ki-Eun Park[2], Jerel Waters[2] and Bhanu P. Telugu[1,2]*

[1]Division of Animal Sciences, University of Missouri, Columbia, MO, United States, [2]RenOVAte Biosciences Inc., Reisterstown, MD, United States

Fibroblasts are the common cell type in the connective tissue-the most abundant tissue type in the body. Fibroblasts are widely used for cell culture, for the generation of induced pluripotent stem cells (iPSCs), and as nuclear donors for somatic cell nuclear transfer (SCNT). We report for the first time, the derivation of embryonic fibroblasts (EFs) from porcine embryonic outgrowths, which share similarities in morphology, culture characteristics, molecular markers, and transcriptional profile to fetal fibroblasts (FFs). We demonstrated the efficient use of EFs as nuclear donors in SCNT, for enhanced post-blastocyst development, implantation, and pregnancy outcomes. We further validated EFs as a source for CRISPR/Cas genome editing with overall editing frequencies comparable to that of FFs. Taken together, we established an alternative and efficient pipeline for genome editing and for the generation of genetically engineered animals.

KEYWORDS

embryonic fibroblast, livestock, somatic cell nuclear transfer (SCNT), genome editing and engineering, embryo development

Introduction

The recent discovery and successful deployment of CRISPR/Cas -based genome editing represents a significant milestone for the large animal transgenesis field (Whitelaw et al., 2016; Perisse et al., 2020; Whitworth et al., 2022), ever since the successful generation of "dolly" by somatic cell nuclear transfer (SCNT) over 2 decades ago (Campbell et al., 1996). The CRISPR reagents can be delivered directly into the zygotes (zygotic injection) or into somatic cells followed by SCNT for the generation of genome-edited (GE) piglets (Whitelaw et al., 2016; Whitworth et al., 2022). The key advantages of zygote injection approach are the high efficiency of introducing targeted genetic mutations, high pregnancy, and litter rates. However, the editing outcomes in the

resulting offspring are often unpredictable, with mosaicism and off-targeting being primary concerns (Tanihara et al., 2019; Rubinstein et al., 2021). This often precludes the use of G0 founders in the phenotypic analysis, necessitating outcrossing of the founders to parse out the alleles and subsequent breeding of the offspring to homozygosity, which takes nearly 3 years in pigs. Needless to say, this strategy puts a huge strain on resources (physical space, labor, feed costs, *etc.*) to generate GE models. An alternative to zygotic injections is SCNT, which is widely used for generating GE pigs. The key advantage of SCNT is the generation of a cohort of animals with pre-determined modifications following a round of embryo transfer, and therefore a more conducive timeline for experiments. The main cell type used for genetic modification and for SCNT are the fibroblasts, which represent the most abundant cell type in the connective tissue of the body and are involved in the maintenance of structural integrity and architecture of tissues and organs. Fibroblasts can be easily isolated from diverse tissue sources and maintained under standard culture conditions, and hence are used extensively for cell culture and cellular reprogramming (e.g., SCNT and iPSCs). Even though adult tissue-derived fibroblasts represent an easily accessible cell source, they have a limited life span in culture and can present a significant challenge for long-term culture to screen for targeted mutations in clonal lines (Park et al., 2021). Thus, researchers prefer using fibroblasts of fetal origin with a relatively extended proliferative capacity.

Despite significant efforts for improving the SCNT process, including the choice of somatic cell source (Inoue et al., 2003; Wang et al., 2020), success in generating normal viable offspring by SCNT remains a formidable challenge with efficiencies ranging from 1 to 5%, and in desperate need of improvement (Keefer, 2015; Matoba and Zhang, 2018). The process of SCNT can be impacted by numerous factors, which makes it extremely difficult to correlate the developmental defects in cloned embryos (Inoue et al., 2003; Gouveia et al., 2020). Adding to this difficulty is the poor viability of fibroblasts following cell-mediated transgenesis, which can adversely impact embryonic development (Matoba and Zhang, 2018). Based on the evidence that the tissue-specific cells can be derived by directed differentiation of human and mouse pluripotent stem/precursor cells (Torres et al., 2012; Bao et al., 2016; D'Angelo et al., 2018; Wang et al., 2020), we sought to develop a method for generating primary fibroblast-like cells from pluripotent cells of embryonic outgrowths, and test the hypothesis that the primary cells derived from the embryo serve as an ideal nuclear donor, and result in high SCNT efficiencies. The rationale is based on previously reported finding that genetically modified FFs that hitherto failed to generate a viable offspring by SCNT were able to give rise to embryo-derived extraembryonic endoderm stem cells (XEN), and the use of rederived embryonic cells resulted in viable cloned offspring with high SCNT efficiencies (Park et al., 2021).

In this report, we demonstrate the successful and efficient derivation of embryo-derived fibroblasts (EFs), which share many characteristics with fetal fibroblasts (FFs), including the spindle-shaped morphology and expression of key fibroblast-specific molecular markers. In addition, transcriptomic analysis *via* RNA sequencing (RNA-seq) further confirmed the close similarity of EF to FF. The EFs used as nuclear donors for SCNT resulted in enhanced *in vivo* developmental competence. Finally, we demonstrated the feasibility of establishing EFs from edited embryos and the feasibility of genetic modification directly in the EFs. The ability to pre-screen the clonal EF lines without the need for performing embryo transfers to establish FF lines is expected to overcome the current limitation of SCNT (poor reprogramming efficiency with the use of FF lines) and zygotic microinjection (unpredictability of edited outcomes and mosaicism). The established EFs may, therefore, represent an important cell resource for gene-editing and for generating genetically modified animals.

Materials and methods

All chemicals were purchased from Sigma-Aldrich (St. Louis, MO) unless stated otherwise. All experiments involving live animals were performed as per the approved guidelines of the University of Missouri, Institutional Animal Care and Use Committee protocol# 14400.

Generation of *in vitro*, *in vivo,* and SCNT pig embryos

Porcine *in vitro*, *in vivo,* and *SCNT* embryos were produced as described in our previous studies (Park et al., 2021). Briefly, cumulus-oocyte-complexes (COC) were purchased from a commercial supplier (De Soto Biosciences, Seymour, TN, United States). After *in vitro* maturation, the cumulus cells were removed from oocytes by gentle pipetting in a 0.1% (w/v) hyaluronidase solution. For *in vitro* fertilization (IVF), pre-diluted fresh semen (commercially sourced from PIC) was centrifuged twice at 200 g for 3 min in DPBS containing 0.2% BSA. The sperm pellet was adjusted to a concentration of 2×10^5 sperm per mL and co-incubated with matured oocytes in a modified Tris-buffered medium containing 0.4% BSA for 5 h in a humidified atmosphere (5% CO_2 in air). For SCNT, embryonic or fetal fibroblasts were synchronized to the G1/G0-phase by serum deprivation (DMEM with 0.1% FBS) for 96 h. The oocytes are enucleated by aspirating the polar body and the MII metaphase plates by a micropipette (Humagen, Charlottesville, VA, United States) in 0.1% DPBS supplemented with 5 μg/ml of cytochalasin B. After enucleation, a donor cell was placed into the perivitelline

space of an enucleated oocyte. The cell–oocyte couplets were fused by applying two direct current (DC) pulses (1-s interval) of 2.0 kV/cm for 30 μs using an ECM 2001 Electroporation System (BTX, Holliston, MA). After fusion, the reconstructed oocytes were activated by a DC pulse of 1.0 kV/cm for 60 μs, followed by post-activation in 2 mM 6-dimethylaminopurine for 3 h. After overnight culture in PZM3 with a histone deacetylase inhibitor Scriptaid (0.5 μM), the cloned embryos were cultured and maintained in PZM3 medium in a low oxygen environment (5% O_2, 5% CO_2 and 90% N_2). Embryos were transferred into synchronized recipients on the first day of standing estrus. Pregnancies were confirmed by ultrasound on day 25–27 following embryo transfer and fetuses were retrieved around day 40 of pregnancy.

Establishment and culture of adult, fetal and embryonic fibroblasts

Adult fibroblast (AF) cells were obtained from ear skin biopsies, and fetal fibroblast (FF) cells were obtained from fetuses from artificially inseminated embryos on day 28 of pregnancy. The tissue samples were cut into small pieces (~1 mm^3). Dissected tissues were then cultured in Dulbecco's modified Eagle's medium (DMEM; Gibco-BRL) supplemented with 10% fetal bovine serum (FBS; Atlanta biologicals), 1 mM sodium pyruvate, 2 mM L-glutamine, penicillin-streptomycin, 0.1 mM 2-β-mercaptoethanol, 1% non-essential amino acids (NEAA), 100 units/mL antibiotics and antimycotics until reaching confluency at 38.5°C in 5% CO_2 and air. For establishing EFs, primary outgrowths from d7 embryos were established as previously described (Park et al., 2021). Briefly, expanded blastocysts either fully hatched or zona denuded by brief exposure to Acid Tyrode's solution (pH 2.5), were seeded onto a feeder layer of CF-1 mouse embryonic fibroblast (MEF) cells mitotically inactivated by mitomycin-C treatment (3 h, 10 μg/ml) at passage 3. The MEF medium was replaced with 'outgrowth medium' which included DMEM/Nutrient Mixture Ham's F12 (DMEM/F-12, Gibco) supplemented with 15% fetal calf serum (HyClone), 1 mM sodium pyruvate, 2 mM L-glutamine, 100 units/ml penicillin-streptomycin, 0.1 mM 2-β-mercaptoethanol, 1% non-essential amino acids (NEAA) (all from Gibco), and the factors; 10 ng/ml human recombinant leukemia inhibitory factor (hrLIF; Peprotech) and 10 ng/ml human recombinant basic fibroblast growth factor (hrbFGF; Peprotech). Primary outgrowths began to emerge after approximately 5 days, based on the embryo quality and conditions. Following the emergence of outgrowths, the medium was switched to the outgrowth medium without hrLIF to initiate differentiation. After incubation in the medium for 4–5 days, the medium was subsequently changed to inductive fibroblast medium (IFM; DMEM/F12 medium, supplemented with 10% FBS, the cytokines, 20 ng/ml Activin A, and 10 μg/ml insulin). After 5–7 days of culture in the IFM, the differentiated cell clumps formed within the outgrowths were dissociated with TrypLE Express (Gibco) and plated onto a cell culture dish without MEFs. Each derivative was frozen in FBS based medium supplemented with 8% (v/v) DMSO and recovered with high viability.

Cell size measurement and growth curves

Countess® Automated Cell Counter and Countess® cell counting chamber slides were purchased from Invitrogen (Carlsbad, CA). A cell count was performed by mixing 20 μl of a sample with 10 μl of 0.8% trypan blue solution, afterwards, the mixture was loaded into the chamber slide to count the cells.

RNA-seq library preparation and transcriptomic analysis

The RNA from FF and EF cells was extracted using RNeasy Mini Kit (Invitrogen). Libraries for sequencing were prepared using the QIAseq FX Single Cell RNA Library Kit following the manufacturer's protocol (Qiagen). Triplicate biological replicates were performed for each group. An Illumina Hiseq 4,000 sequencer was used for paired-end sequencing with read length at 150 bp. On average, 25 million reads were obtained for each library. Quality of the RNA-Seq reads was evaluated by FastQC (Babraham Bioinformatics). Low quality reads and adapter contaminations were trimmed using Trimmomatic (Bolger et al., 2014). RNA-seq data were then aligned to the porcine reference genome (Sscrofa11.1) by using STAR (Dobin et al., 2013). The identification of differentially expressed genes (DEGs) was performed by using EdgeR (Robinson et al., 2010). KEGG pathway analysis was performed using clusterProfiler (Wu et al., 2021).

Gene targeting in EFs

To validate the feasibility of genome editing in EFs, *NANOS3* was chosen for targeting. Candidate high-ranking guide RNAs (sgRNA) were designed using CRISPR design tools (http://chopchop.cbu.uib.no/). The sgRNAs (Integrated DNA Technologies, Coralville, IA) were incubated with SpCas9 Nuclease 3NLS protein (Synthego, Redwood City, CA) at a molar ratio of 1:3 (20 pmol Cas9/60 pmol sgRNA) at room temperature (RT) for 10 min. Single-stranded oligodeoxynucleotides (ssODNs; 100 μM) containing the in-frame 3X-flag tag and translational stop codon were nucleofected alongside Cas9 ribonucleoproteins (RNPs) into 2×10^5 cells using a P3 Primary Cell 4D-Nucleofector X Kit and Nucleofector™ 4D (Lonza, Basel, Switzerland) according to

the manufacturer's recommendation. The experiments were performed using at least three biological replicates (n = 3) and two independent experiments. Following nucleofection, the cells were allowed to recover for 5 days and then plated at a low density onto a 10-cm dish to establish isolated colonies. Ten days later, individual colonies were picked based on morphology and replated into individual wells of 48-well plates. When cells reached near confluency (80%–90%), half of the cells were used for genomic DNA (gDNA) isolation for genotyping analysis, and the other half were cryopreserved. For zygotic injection, the RNPs were pre-complexed by incubating for 10 min at 37°C and diluted to a final concentration of 25 ng/μl for microinjection. Microinjection was performed 4 h after electrical parthenogenetic activation.

Genotyping analysis

The gDNA from each colony was isolated by using DNA Isolation micro Kit (Norgen) according to the manufacturer's instructions. PCR was performed by using KOD Hot start mastermix (Novagen) by using the following conditions: denaturation and polymerase activation step of 95°C/3 min, 35 cycles of 95°C/20 s, 60°C/10 s, 70°C/10 s, and the final extension step of 70°C/5 min. The primer sequence and information are provided in Supplementary Table S1. The PCR products were purified using NucleoSpin gel and PCR clean-up kit (Machery Nagel, Bethlehem, PA), and they were subjected to Sanger sequencing (using the forward PCR primer; Table 1). For genotyping analysis in blastocysts and primary outgrowths, each sample was lysed in lysis buffer (20 mM Tris-Cl (pH 8.0), 1% Tween 20, 1% Nonidet P-40 and 100 μg/ml proteinase K) at 56°C for 50 min and boiled at 95°C for 10 min and used as a template for PCR as above. The Sanger trace data was analyzed by using inference of CRISPR edits (ICE, https://ice.synthego.com/) algorithm to measure the extent of mosaicism in individual blastocysts and outgrowths. The PCR amplicons produced for next-generation sequencing (NGS) were purified using a GFX PCR DNA and Gel band purification kit (GE healthcare). NGS library preparations and paired-end (250 bp) sequencing on an Illumina iSeq™ platform was performed by Genewiz, Inc. Amplicon sequencing data were analyzed with CRISPResso v2 with HDR mode.

Immunocytochemistry

For immunofluorescence staining, cells were fixed with 4% formaldehyde for 5 min at room temperature (RT). After washing once in PBS with 0.1% BSA, cells were permeabilized in PBS with 0.3% Triton X-100 for 15 min and blocked with SuperBlock™ blocking buffer superblock (Thermo Fisher Scientific Inc.) for 30 min prior to antibody incubation. Primary and secondary antibodies were diluted in the blocking solution. Incubation with the primary antibodies was performed at 4°C overnight and secondary antibody at RT for 1 h. The following primary antibodies were used: mouse anti-Vimentin, 1:100 (Santa Cruz sc-6260), rabbit anti-PCNA,1:100 (Abcam ab15580), rabbit, anti-a-SMA, 1:100 (Abcam ab5694). Secondary antibodies were Alexa goat-anti-mouse-647, 1:1,000 (LifeTech A-21121) and Alexa goat-anti-rabbit-488, 1:1,000 (LifeTech A-11034). The nuclei were counterstained with 5 mg/L DAPI (Thermo Fisher Scientific Inc.) for 5 min.

Statistical analysis

The statistical analysis was performed using GraphPad Prism software. The data was expressed as mean ± SD. For normally distributed data, *t*-test was used for comparison between two independent samples, and one-way analysis of variance (ANOVA) was used for comparisons of multi-samples. A *p*-value of <0.05 was considered as statistically significant. The number of replicates in each experimental setting and statistical significance were shown in each figure legend.

Results

Generation of primary fibroblast-like cells from blastocyst outgrowths

In the conceptus, primary fibroblasts arise from the primary mesenchyme as the epiblast (Epi) cells undergo an epithelial-to-mesenchymal transition (EMT) during gastrulation (Popovic et al., 2019; LeBleu and Neilson, 2020). Several lines of evidence show that primary fibroblasts can be obtained from the embryonic outgrowths during the embryonic stem cell (ESC) derivation process (D'Angelo et al., 2018). Porcine blastocysts on day 7 of culture that were either hatched or zona denuded were seeded onto mitotically inactivated MEF cultures in the outgrowth medium supplemented with recombinant hbFGF and hLIF. Primary outgrowths begin to emerge after 5 days in culture. Based on a spontaneous differentiation protocol involving LIF withdrawal, we assessed the efficiency of mesenchymal differentiation by analyzing the expression of mesenchymal marker Brachyury (T) and epithelial cytokeratin (KRT)18 in the primary blastocyst outgrowths. Four days after switching to the hLIF withdrawal medium, a tight cluster of T-positive (+) and KRT18-negative (-) cells were identified in the blastocyst outgrowths, which is a key characteristic of mesenchymal cells, while the other extraembryonic cell types (trophoblast and primitive endoderm) show an opposing trend (T- and KRT18+) [Figures 1A,B]. However, the emergence of primary mesenchyme in primary blastocyst outgrowths was observed sporadically and occasionally, so the approach based

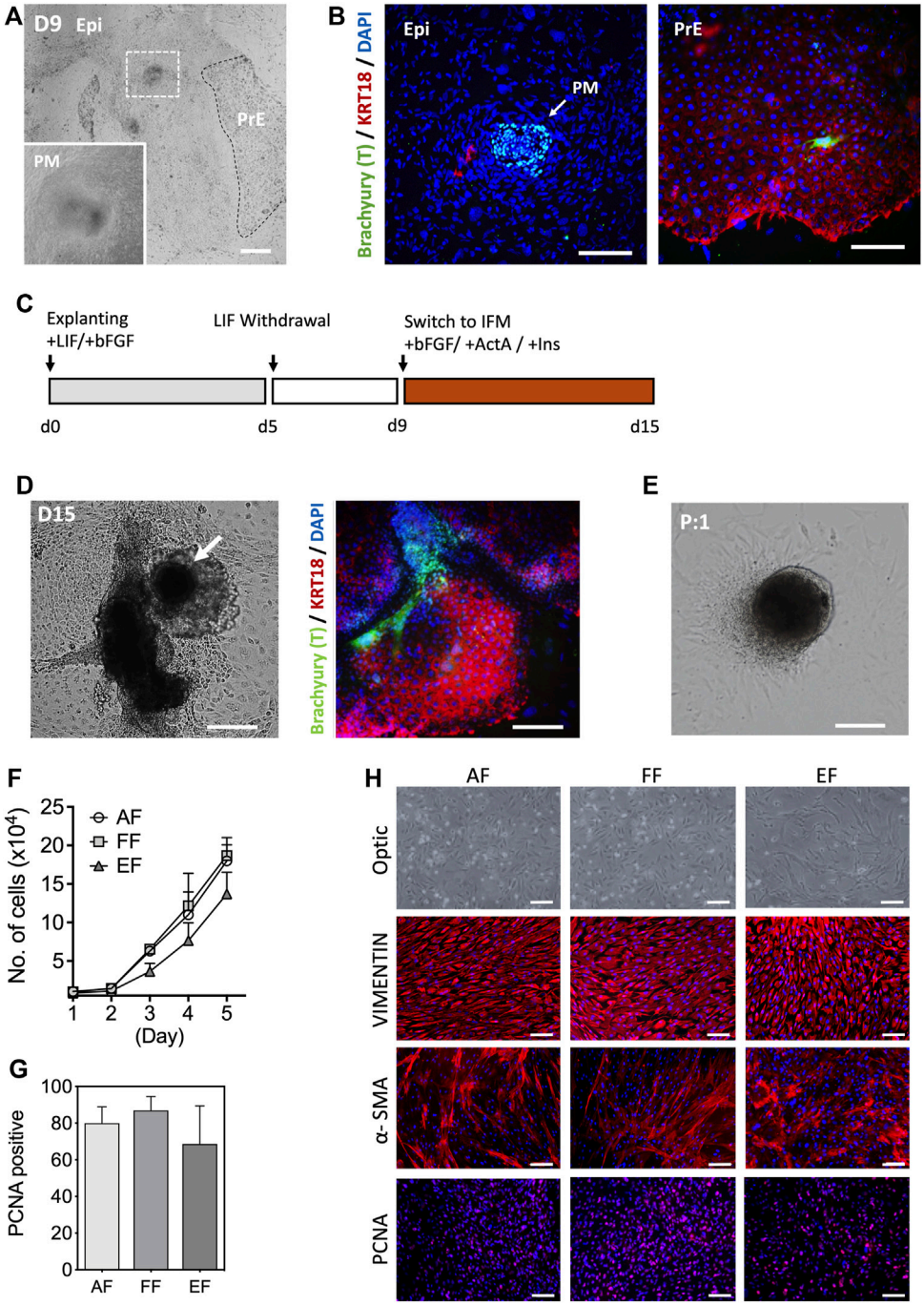

FIGURE 1
Characterization of embryonic fibroblasts (EF) derived from blastocyst outgrowths. **(A)** Representative images of d9 primary blastocyst outgrowth. Differentiated cell aggregates appear in outgrowths following explanting blastocysts in culture (white dotted, inlet). **(B)** Immunofluorescence staining indicated that the differentiated cell clusters were positive for a mesenchymal marker Brachyury (T; arrow), but negative for epithelial KRT18 after 9 days of differentiation in the hLIF withdrawal medium. **(C)** Schematic of the differentiation protocol. **(D)** Morphological appearance of differentiated cells and immunofluorescence staining of T and KRT18 in d15 primary blastocyst outgrowths. **(E)** The population of spindle-shaped cells grew from the edges of explants following subculture. **(F)** Cell growth curves for the three fibroblast groups: five AFs from a neonatal ear biopsy, five FFs from day 28–50 fetuses, and six EFs from day 7 blastocysts fertilized *in vitro*. Ten thousand cells (passage 3) were used for the experiment (n = 3). **(G)** The mean number of PCNA positive nuclei. In this study, the fetal fibroblast cells displayed higher PCNA positivity than the adult and embryonic fibroblasts, but there were no statistical differences in the number of PCNA positive cells (ANOVA, $p < 0.05$). **(H)** Representative immunostaining images of VIMENTIN, α-SMA, and PCNA marker expression in three fibroblasts. EPI, epiblast, PM, primary mesenchyme, PrE, primitive endoderm. Data is presented as the mean ± SD. Bar, 100 μm.

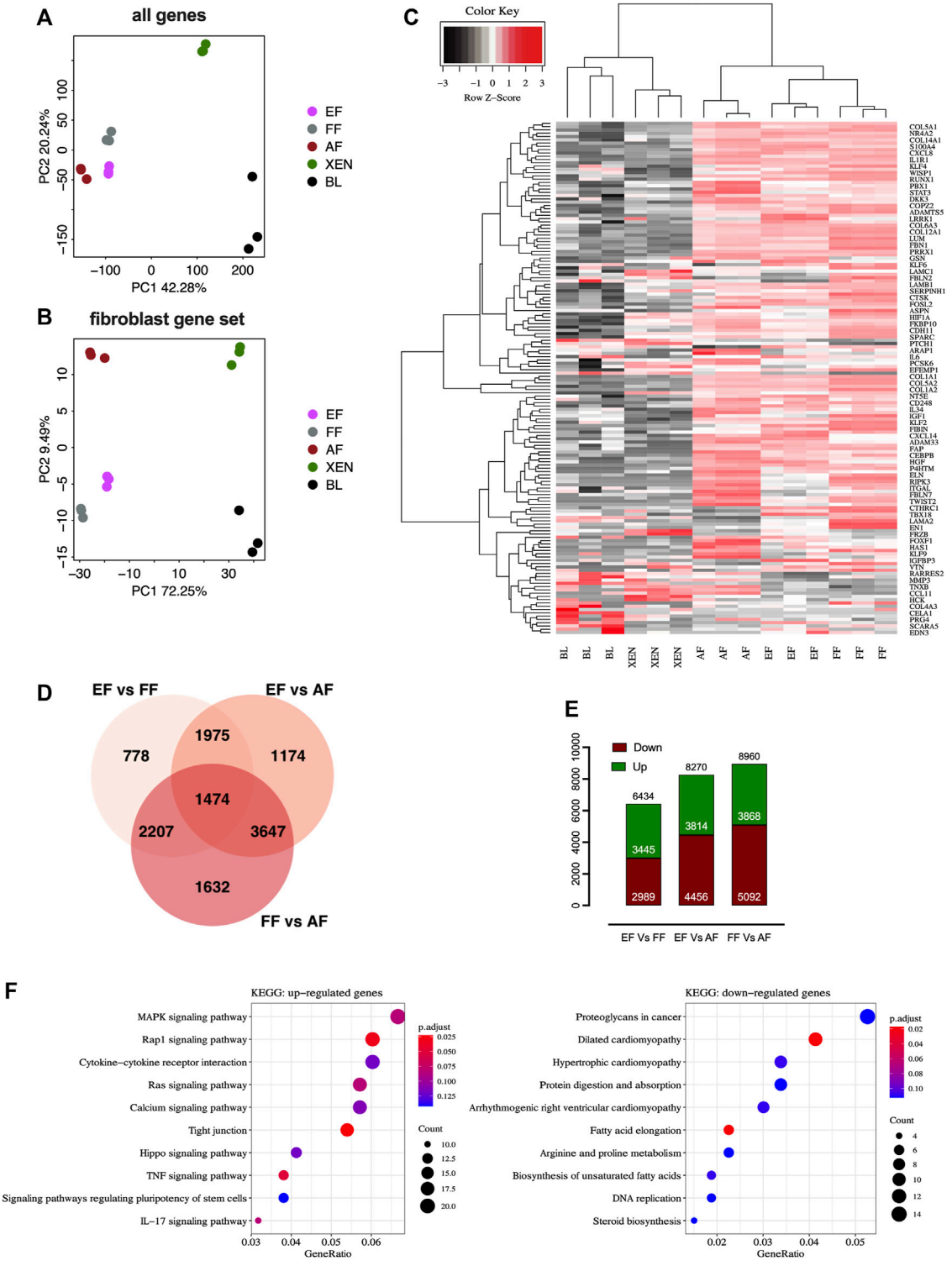

FIGURE 2
RNAseq analysis of fibroblasts from different origins. Principal component analysis (PCA) plots of RNA-seq data based on **(A)** global gene expression or a candidate list of **(B)** fibroblast marker genes. The two axes PC1 and PC2 represent the first two principal components identified by the analysis. Each color code denotes different cell types in the scheme in the middle of the plots. **(C)** Gene expression heatmap of 156 genes in the fibroblast gene-set. **(D)** Venn diagram showing that numbers in each segment represent differentially expressed genes (DEGs) that are not shared, and in overlapping segments-the shared DEGs among the fibroblasts. **(E)** Bar plot of the number of differentially expressed genes (DEGs). Downregulated genes are depicted in red, and upregulated genes are depicted in green. **(F)** KEGG pathway enrichment analysis of DEGs. Bubble
(*Continued*)

FIGURE 2 (Continued)
plots showing the significant pathways for up-and downregulated DEGs, in which the –log10 of the adjusted *p*-value are represented by colors. The number of DEGs in the pathway is indicated by the circle area, and the circle color represents the range of the adjusted q values (FDR). We display the top 10 pathway terms enriched by KEGG database. AF, adult fibroblast; EF, embryonic fibroblast; FF, fetal fibroblast; XEN, extraembryonic endodermal stem cells; BL, blastocyst.

on spontaneous differentiation was not consistent. In an effort to improve efficiency, d9 blastocyst outgrowths were switched to IFM differentiation medium supplemented with Activin A and insulin from 9 to 15 days, and compared to the outgrowths cultured without supplements [Figure 1C]. Combined induction with Activin A and insulin rendered 33.2% of the outgrowths positive for T, compared to 12.5% without ($p < 0.05$, n = 5) supplementation, indicating that IFM containing Activin A and Insulin promote primary mesenchyme (T+) development after continued culture for 2 weeks in the medium without passaging [Figure 1D]. Following the first passage, the tight clusters of cells remained intact, from which fibroblast-like cells grew out and serially propagated in culture in a manner similar to the cells from fetal tissues [Figure 1E]. The growth rate of the blastocyst-derived embryonic fibroblasts (EF) cells was comparable to that of fibroblasts from adult (AF) and fetal (FF) origins, although EFs had a slightly lower growth rate (not significant) than AF and FF cells [Figure 1F]. As shown in Figures 1G,H, the EFs displayed typical spindle-shaped morphology and expression of the fibroblast molecular markers, vimentin (VIM) and α-smooth muscle actin (α-SMA), and the proliferating cell nuclear antigen (PCNA). The expression of α-SMA was lower in AFs and FFs than EFs, whereas VIM was consistently expressed in fibroblast cells regardless of origins. In particular, the early-passage EFs were a mixed population (e.g., shape, cell size, growth rate, or marker expression) of large and small cells with varied expression of α-SMA and PCNA [Supplementary Figures S1A,B]. As illustrated in Figure 1C, our results suggest that blastocyst outgrowths could differentiate into cells with characteristics typical of fibroblast phenotype.

Comparison of global expression profiles of fibroblasts from different origins

We performed comparative RNA-seq transcriptomic analysis of EF cells. Three cell lines from each group, EFs from *in vitro* d7 blastocysts, and FFs from d28 fetuses were analyzed alongside publicly available datasets for AFs (NCBI GSE146494), XEN cells (NCBI GSE128149), Blastocysts (BL; NCBI GSE128149). The principal component analysis (PCA) plots based on the global expression profile clustered the fibroblasts of embryonic, fetal, or adult origin together confirming fibroblastic profile of EF cells [Figure 2A]. The PCA plot based on the candidate fibroblast-marker gene-set [Supplementary Table S2] showed that EFs and FFs were grouped closely compared to AFs [Figure 2B]. Hierarchical clustering using fibroblast marker genes (156) also showed a pattern consistent with principal clustering analysis results [Figure 2C]. Venn diagram comparing differentially expressed genes (DEGs) revealed that AFs transcriptome is different from EFs and FFs, with 8,270 DEGs compared to EFs and 8,960 DEGs compared to FFs, whereas there are 6,434 DEGs between EFs and FFs [Figure 2D]. The smaller number of up-and down-regulated genes in the EFs *versus* FFs indicated that they are more comparable to each other than to AFs [Figure 2E]. Functionally, as revealed by KEGG-pathway analysis of the clusters (EF + FF vs. AF), many genes down-regulated in AFs were related to ribosome biogenesis, RNA degradation, protein digestion, and absorption/ECM-receptor interaction, suggesting down-regulation specifically of post-transcriptional regulation [Supplementary Figures S2A,B]. Furthermore, the enrichment analysis of EFs vs. FFs showed that the DEGs in EFs were primarily enriched for fibroblast growth factor (FGF) signaling including MAPK, Ras, Rap1, and TNF kinase pathways [Figure 2F]. This result indicates that growth factor and cytokines (bFGF and LIF) used for the cell derivation may lead to constitutive activation of relevant pathways that in turn changes gene expression patterns. With regard to the biological relevance of these findings, the observed changes in the presence of signaling molecules, and their importance for phenotypic characteristics remain to be seen.

In vivo developmental potential of cloned embryos generated from embryonic fibroblasts

As has been proven previously, the derivation of XEN cells from genetically modified porcine FFs deemed 'unfit' for SCNT, and subsequent generation of cloned animals from the newly established XEN cells with enhanced cloning efficiencies, highlighted novel opportunities to generate cloned animals from desirable, yet cells not clonable by SCNT (Park et al., 2021). To determine whether a similar effect on SCNT could be achieved with EFs, we have generated the cloned blastocysts from previously reported transgenic fibroblast cells FF $^{UBC:GFP}$ [labeled "UBC:eGFP"; Figure 3A]. Consistent with the process for derivation of EFs from *in vivo* or *in vitro* fertilized embryos, outgrowths from the cloned embryos in culture with a tight cluster of mesenchymal-like cells (Brachyury +/KRT18 -) were observed by day 9 [Figure 3B], and following the first subculture,

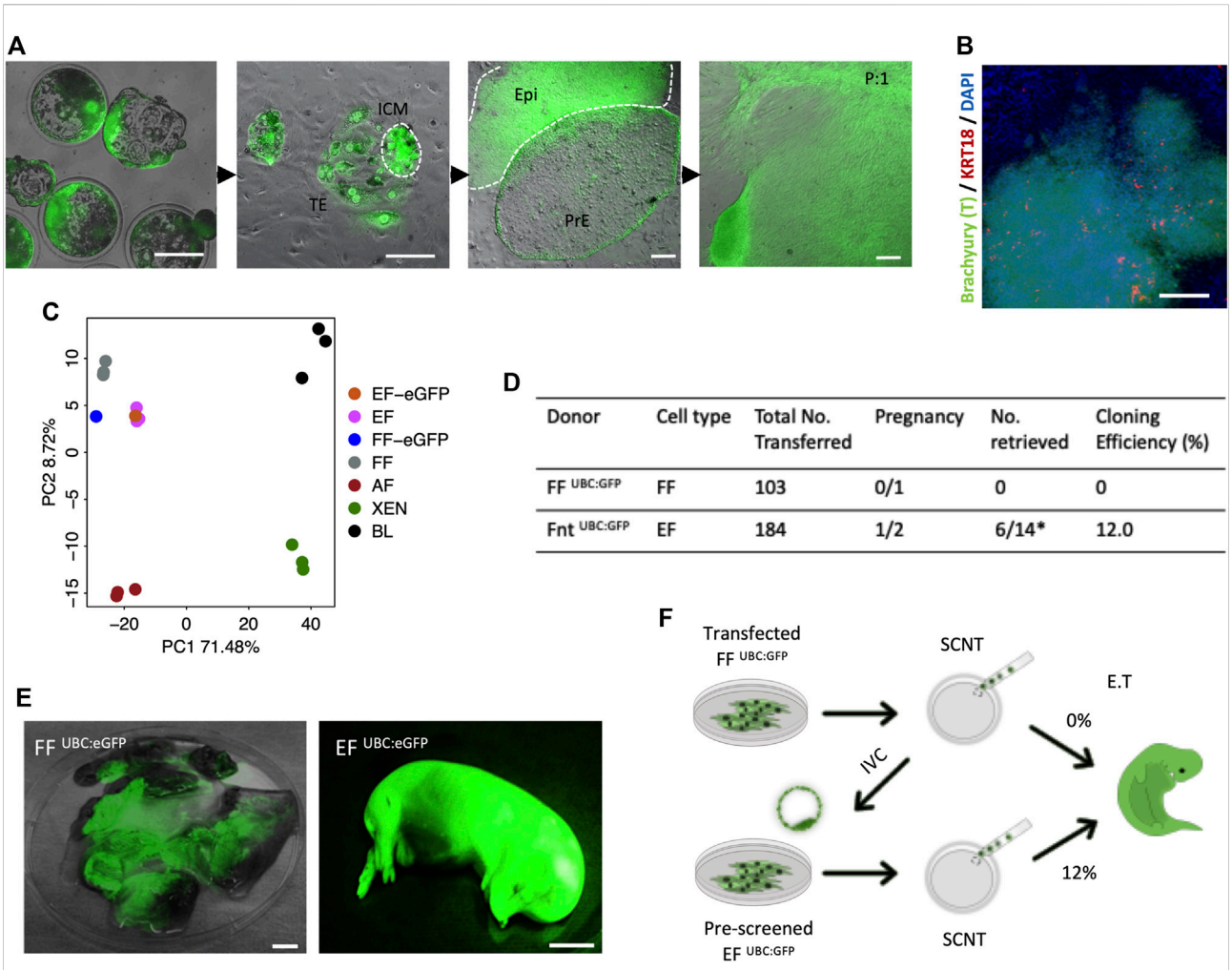

Donor	Cell type	Total No. Transferred	Pregnancy	No. retrieved	Cloning Efficiency (%)
FF $^{UBC:GFP}$	FF	103	0/1	0	0
Fnt $^{UBC:GFP}$	EF	184	1/2	6/14*	12.0

FIGURE 3
In vivo development of 40-day fetuses following SCNT. **(A)** Representative images of the blastocyst outgrowths and the derivation of EF and PRE cells. The constitutive hUBC promoter-driven GFP transgenic FF (FF $^{UBC:eGFP}$) were used for generating SCNT. The establishment of primary outgrowths from SCNT embryonic explants on day 2 of culture and the emergence of PrE and Epi in d9 primary outgrowths. After the first passage, fibroblast-like cells grew from the differentiated cell clump (EF $^{UBC:eGFP}$). **(B)** Immunofluorescence staining confirmed that the differentiated cell clusters were Brachyury positive but KRT18 negative after 15 days of differentiation in the IFM medium. **(C)** PCA plot of FF $^{UBC:eGFP}$ and EF $^{UBC:eGFP}$. **(D)** Pregnancy and cloning efficiency rate of pig embryos generated from FF $^{UBC:eGFP}$ and EF $^{UBC:eGFP}$ both on the same genetic background. **(E)** Representative images of mummified fetuses from FF $^{UBC:eGFP}$ (left) and normal developmentally competent fetuses from EF $^{UBC:eGFP}$ cloned embryos (right) expressing ubiquitous eGFP on day 40 of pregnancy. **(F)** Schematic summary of the genome-edited experiments highlighting improved SCNT efficiencies with the use of EF as nuclear donor cells in SCNT. Bar, 1 mm.

large cell clusters migrated out onto the plate surface [Figure 3A]. From individual embryonic outgrowths, we induced EF and XEN cells, and the transcriptomic analysis was performed on the established EF cells. As expected, the PCA plot confirmed that the EFs clustered closely with FFs and that the EFs closely resemble FFs [Figure 3C]. To examine the *in vitro* developmental competence of EFs, we performed SCNT using EF $^{UBC:eGFP}$ and FF $^{UBC:eGFP}$, showing that there were no significant differences in the cleavage (74%) and blastocyst formation percentages (36%) compared to the percentages with FFs used for generating the UBC:GFP reporter transgenic cells (Data not shown). A total of 184 reconstituted embryos from EF $^{UBC:GFP}$ were transferred into two surrogate gilts, and one pregnancy was established, while 103 cloned from FF $^{UBC:GFP}$ failed to establish a pregnancy. Of the 14 cloned fetuses retrieved at day 40 of pregnancy, six fetuses developed normally and their size is compatible with their embryonic stage, while the remainder were developmentally delayed (8/14) [Figure 3D]. All of them exhibited a strong GFP expression [Figure 3E]. Taken together, these results confirm that the EFs could potentially improve SCNT efficiencies and are in line with the improved SCNT efficiencies observed with the use of rederived embryonic cells as nuclear donors [previously observed (Park et al., 2021)] [Figure 3F].

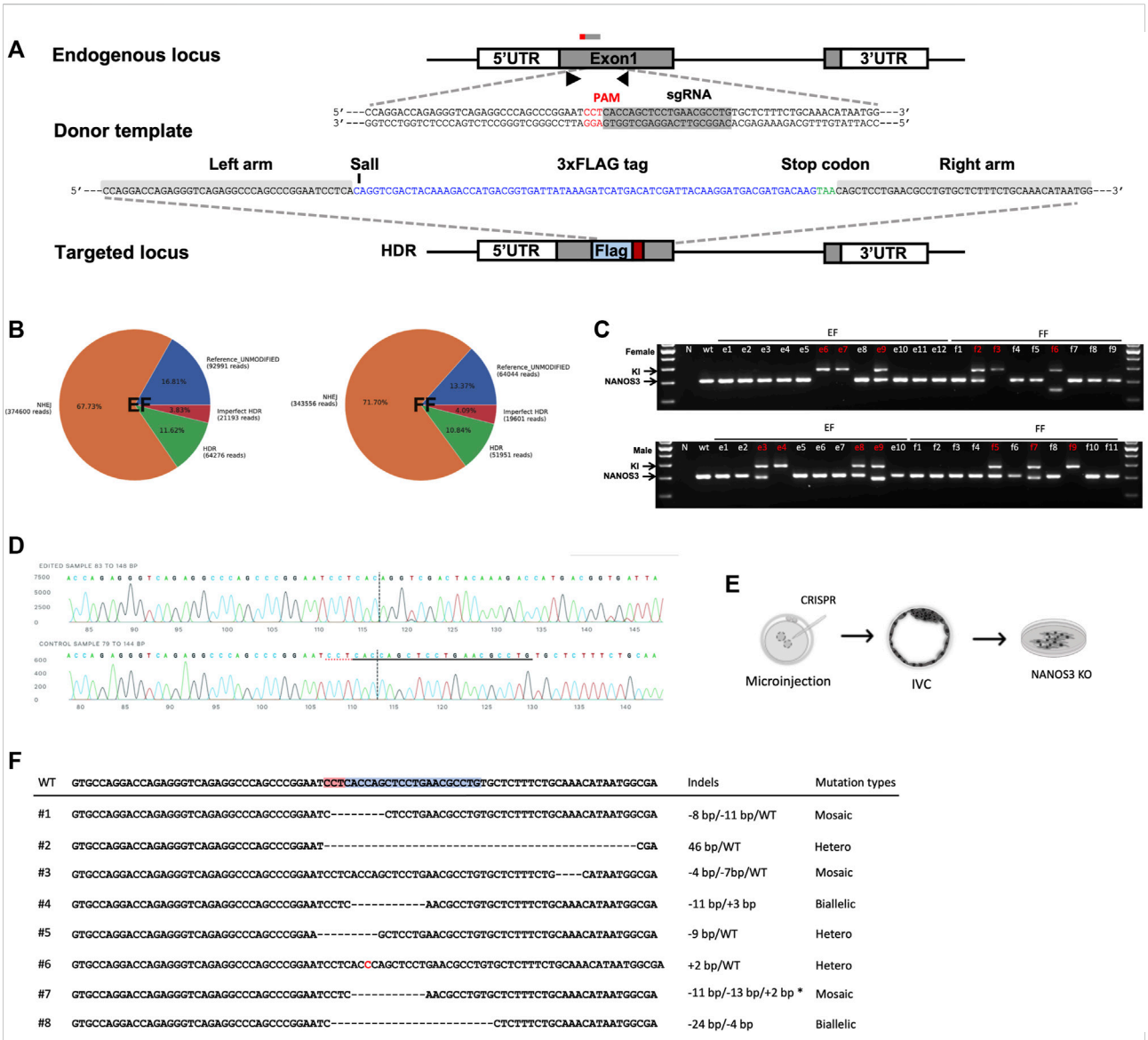

FIGURE 4
CRISPR/Cas9-mediated modification of *NANOS3* in embryonic fibroblasts. **(A)** Strategy for disruption of *NANOS3* with insertion of a premature translational-stop codon (PTC). A candidate ssODN was designed containing a 3xFLAG epitope tag and a PTC (TAA) flanked by 40 nt homology arms corresponding to the region to be edited. The cassette contains restriction enzyme cut sites (SalI) to assist in RFLP-based assay. **(B)** Quantification and visualization of the outcomes of genome editing. Pie charts summarizing the frequencies of events in the *NANOS3* loci from targeted amplicon sequencing in EF and FF cells. When an expected HDR amplicon is provided, CRISPResso classifies sequence reads as blue, unmodified alleles; orange, NHEJ mutations; red, imperfect HDR; green, HDR alleles as distinct outcomes. **(C)** Genomic sequencing showing homozygous/heterozygous mutant DNA carrying the intended edit. Using the primers indicated by the arrows, the amplicons from genomic DNA were resolved on a gel revealing HDR (374 bp) and wild-type (Wt, 300bp) and/or NHEJ (<300bp) fragments. **(D)** Sanger sequencing of clonal EFs showing precise gene knockin at the target site. **(E)** Schematic outline for the direct generation of knockout *NANOS3* $^{-/-}$ embryonic fibroblasts from outgrowths. **(F)** Sanger sequencing of established EFs *via* zygotic injection shows a range of mutations at the target site.

Embryonic fibroblasts as a source for gene targeting

Based on the observation that EFs constitute an improved cell source for SCNT, and to harness the true potential of EFs as a tool for generating genetically modified offspring, we tested two distinct approaches: 1) targeted modification directly in the EFs, and 2) generating EFs from genome edited embryos. As a candidate for genetic manipulation, we chose *NANOS3* to test the feasibility of this approach. The candidate gene- *NANOS3* belongs to the NANOS family of proteins, which have an essential role in germ cell development. Mutations in

NANOS2 cause germ cell loss in male pigs but not in females, as reported in our prior publication (Park et al., 2017). *NANOS3* was shown to have an essential role in both male and female germ cells throughout spermatogenesis and oogenesis (Tsuda et al., 2003; Ideta et al., 2016). First, we transiently transfected cells with a control plasmid (pmaxGFP) to assess the feasibility and patency of transfection of nucleic acids into EFs. Fluorescence-activated cell sorting (FACS) analysis showed that the EFs are compatible and tolerate nucleofection, with 72.0% of EFs showing GFP expression compared to 83.4% for FFs [Supplementary Figures S4A,B]. Next, to evaluate the delivery and efficient activity of SpCas9 at the target site, we designed two candidate sgRNAs targeting *NANOS3*, precomplexed with SpCa9 protein, and the resulting ribonucleoprotein complexes (RNPs) nucleofected into EFs. Following a period of recovery (2–3 days) the efficiencies of targeting were assessed by targeted amplicon sequencing (Illumina). We identified successful delivery and high efficiency of on-site editing with candidate guide#1 (indel rate; 82.32% for guide1 and 47.62% for guide 2). The high activity, Guide#1 was selected for subsequent experiments [Supplementary Figure S4C]. To evaluate CRISPR-mediated, homology-directed repair (HDR) based knock-in at the target site, ssODNs containing an in-frame three Flag epitopes in tandem (3xFlag), and a translational stop codon to prematurely truncate the protein before its zinc finger domain consisting of two consecutive C2HC-type zinc finger motifs, and a novel SalI restriction site for a restriction fragment polymorphism (RFLP) assay was designed for HDR mediated knock-in into and subsequent knockout of the *NANOS3* allele [Figure 4A]. We delivered RNPs alongside ssODNs into candidate female EF and FF cells. Following transfection, and screening *via* RFLP and Sanger sequencing, we identified 11.6% of HDR and 67.7% of non-homologous end joining (NHEJ) events within the EFs; and 10.8% HDR and 71.7% NHEJ events within the FFs, respectively. The overall editing rates in EFs were similar to that of FFs ($n = 3$, $p < 0.01$) [Figure 4B and Supplementary Figure S4D]. Following confirmation of editing, the transfected EFs were plated at a low density to establish clonal lines. Among the established lines, a total of 3 colonies (2 homozygous and 1 biallelic) from female and 4 colonies (1 homozygous and 3 biallelic) male EFs were identified to have precise HDR targeting events as confirmed by RFLP and Sanger sequencing [Figures 4C,D]. Furthermore, a similar strategy was employed with female and male FFs. The results showed that 3 colonies (1 homozygous and 2 biallelic) from female and 3 colonies (1 homozygous and 2 biallelic) from male FFs were precisely corrected [Supplementary Figure S4E]. These colonies were cryopreserved for future studies.

Secondly, we investigated the feasibility of gene targeting directly in the embryos (zygotic injection) and establishing clonal EFs from the edited embryos [Figure 4E]. As above, the guide#1 which exhibited a high editing efficiency was used, and the RNPs targeting the *NANOS3* were injected into parthenogenetic zygotes ($n = 65$), a total of 58 embryos developed to the blastocyst stage and 20 blastocysts were utilized to screen for mutation frequencies. Most of the screened embryos (17/20) displayed on-site activity and displayed a range of mutations, including either sgRNA site–spanning insertions/deletions or deletion distantly from the sgRNA target site, with a high mosaicism frequency (11 of 20 were mosaic) [Supplementary Figure S4F]. Following confirmation of editing, the remaining expanded d7 blastocysts ($n = 38$) were used for EF derivation through blastocyst outgrowth. We obtained a total of 8 EF lines from these outgrowths, with 1 candidate line showing biallelic mutations [Figure 4F]. Taken together, we showed the feasibility of establishing edited EF lines, with implications for generating gene-edited animals.

Discussion

The recent development of GE technologies, principally the CRISPR/Cas system has now afforded facile genetic modification in pigs and other livestock species. The GE piglets can be generated by the delivery of CRISPR reagents into somatic cells, typically FF followed by SCNT. Although infrequent, there is a concern of reduced cell viability in clonally derived modified cells following transfection, which can have an adverse impact on SCNT efficiency (Keefer, 2015; Matoba and Zhang, 2018; Gouveia et al., 2020). While GE methods have significantly improved in recent years, the selection of prospective donor cells suitable for SCNT among the potential multitude of clonal lines with the correct targeting events remains difficult. Our previous study demonstrated that embryo-derived primary cells can serve as an alternative source of donor cells with an enhanced efficiency (Park et al., 2021). However, there is a drawback due to the intrinsic properties of such cells, including the relatively higher costs for derivation, and difficulty in isolating clonal populations for GE. Relying on fibroblasts directly obtained from blastocyst outgrowths is highly advantageous for the following reasons: 1) in contrast to culturing stem cells, fibroblasts are easily cultured and maintained *in vitro*, allowing their use as their equivalents from fetuses; 2) preselect donor cells carrying the targeted modifications for a successful outcome following SCNT; and 3) serial editing followed by SCNT and stacking of multiple genetic engineering events, bypassing the need to establish FF by embryo transfer between each targeting round.

The primary mesenchyme is detectable in spontaneously differentiating blastocyst outgrowths and pluripotent stem cells (D'Angelo et al., 2018). Based on the conditions shown to differentiate ESC to fibroblasts *in vitro* (Wang et al., 2014; Bao et al., 2016), we have also observed that the reported differentiation conditions including a combination of bFGF, Activin A, and Insulin have resulted in similar differentiation

to primary fibroblasts from primary embryonic outgrowths. By comparing transcriptome signatures of fibroblasts that were established from different developmental stages, the newly established EFs exhibited marked similarities to FFs as compared to AFs, reflecting the developmental proximity to the fetal developmental stage, even though the cultured fibroblasts from different origins had similarities in morphology, marker expression, and proliferation. Our efforts to derive the EF cells have been met with reliable but modest success (33.2%) due to high heterogeneity among the established embryos and the resulting embryonic outgrowths. Further optimization is needed to directly differentiate the outgrowths into specific cell types including fibroblasts. The proposed approach in this report is expected to serve as a baseline for improving our understanding of the developmental signaling mechanisms that are crucial for specifying EF cell formation and help fuel further technical refinements and validation efforts.

Culturing of the embryos beyond the blastocyst stage, assessing outgrowth development, and an *in vitro* implantation assay are used as useful experimental models to investigate the predictive capacity of embryo quality for successful implantation following embryo transfer (Popovic et al., 2019). Although genome modification with precise modification *via* HDR for introducing point mutations (or knocking-in transgenes) is desirable over the error-prone NHEJ, it is often associated with an increase in cytotoxicity that could negatively impact the generation of GE animals using SCNT. In this context, pre-selection of developmental competence of the edited embryos, and their subsequent ability to generate explants and allow clonal selection of EFs may serve as a positive predictor of their eventual developmental competence and a high potential for successful implantation and pregnancy. As shown in this report, rederivation of a genetically modified EF cell line has resulted in high cloning efficiency (12%). Second trimester (day 40) was chosen as an endpoint because, 1) healthy fetuses at this stage (six in this study) are relatively a good predictor of a successful pregnancy outcome, and 2) the fetuses at this stage do not initiate breathing and will not need to be euthanized. Going forward, these results will need to be validated further by allowing the pregnancies progress to term and the birth of live offspring.

Extensive reports on the high rates of generating genotypic mosaicism induced in CRISPR/Cas9 mediated gene-edited animals generated by zygote injection have already been published (Park et al., 2016; Zhou et al., 2016; Burkard et al., 2017; Hennig et al., 2022). From a technical perspective, previous reports of generating GE animals by zygotic injections among various species with the goal of reducing mosaicism have met with limited success (Hashimoto et al., 2016; Ma et al., 2017; Vilarino et al., 2017; Li et al., 2020). Despite the high targeting efficiency in the zygotes and relative simplicity of the procedure, a great deal of work remains to be performed on this issue of mosaicism and inheritance of intact alleles, confounding the phenotype of resulting mutations and alleles among the G0 founders. Taking the variable editing outcomes into consideration from zygotic or cellular engineering, and the low predictability of edited cells in generating robust embryos *via* SCNT for a successful pregnancy, the proposed method in this report can be leveraged for rapid and efficient generation of GE donor EFs from *in vitro* cultured embryos followed by zygotic injection for efficient generation of GE cloned pigs. Overall, the proposed methodology is expected to decrease time and costs, bypass the need for surgical procedures, animal suffering, and sacrificing the surrogates for establishing FFs, culminating in the overall improved efficiency of the process for generating genetically modified pigs, and other livestock animals.

Conclusion

This study demonstrated that blastocyst outgrowths can differentiate directly into primary EFs, which are similar to fetal derived fibroblasts in morphology, marker expression, and transcriptomic signature, but further studies are warranted to further standardize the fibroblast derivation protocol from blastocyst outgrowths. Importantly, EFs provide the ability to isolate developmentally competent SCNT donor cells from genome edited zygotes, and also as a source for somatic genome-editing, potentially facilitating serial and limitless genome editing capability without a loss of proliferative ability.

Data availability statement

The datasets presented in this study can be found in online repositories. The names of the repository/repositories and accession number(s) can be found below: SRA database accession number: PRJNA885580.

Ethics statement

All experiments involving live animals were performed as per the approved guidelines of the University of Missouri, Institutional Animal Care and Use Committee protocol# 14400.

Author contributions

C-HP and BT conceived the project and designed the experiments; C-HP, Y-HJ, LZ, and SY established and performed characterization of embryonic outgrowths and fibroblasts; Y-HJ performed the knockin and generated the NANOS3 cells; C-HP and LZ generated the libraries for transcriptomic analysis; K-EP and JW performed embryo transfer. C-HP wrote the initial draft; BT revised the manuscript based on the input from all authors. All authors approved the final draft for submission.

Funding

This study received funding from Genus plc.

Conflict of interest

K-EP, JW, and BT serve as consultants at RenOVAte Biosciences Inc (RBI). BT and K-EP are founding members of RBI. JW is employed by RBI.

The remaining authors declare that the research was conducted in the absence of any commercial or financial relationships that could be construed as a potential conflict of interest.

Publisher's note

Supplementary material

The Supplementary Material for this article can be found online at: https://www.frontiersin.org/articles/10.3389/fcell.2022.1059710/full#supplementary-material

References

Bao, X., Lian, X., Hacker, T. A., Schmuck, E. G., Qian, T., Bhute, V. J., et al. (2016). Long-term self-renewing human epicardial cells generated from pluripotent stem cells under defined xeno-free conditions. *Nat. Biomed. Eng.* 1, 0003. doi:10.1038/s41551-016-0003

Bolger, A. M., Lohse, M., and Usadel, B. (2014). Trimmomatic: A flexible trimmer for Illumina sequence data. *Bioinformatics* 30, 2114–2120. doi:10.1093/bioinformatics/btu170

Burkard, C., Lillico, S. G., Reid, E., Jackson, B., Mileham, A. J., Ait-Ali, T., et al. (2017). Precision engineering for PRRSV resistance in pigs: Macrophages from genome edited pigs lacking CD163 SRCR5 domain are fully resistant to both PRRSV genotypes while maintaining biological function. *PLoS Pathog.* 13, e1006206. doi:10.1371/journal.ppat.1006206

Campbell, K. H., Mcwhir, J., Ritchie, W. A., and Wilmut, I. (1996). Sheep cloned by nuclear transfer from a cultured cell line. *Nature* 380, 64–66. doi:10.1038/380064a0

D'angelo, W., Chen, B., Gurung, C., and Guo, Y. L. (2018). Characterization of embryonic stem cell-differentiated fibroblasts as mesenchymal stem cells with robust expansion capacity and attenuated innate immunity. *Stem Cell Res. Ther.* 9, 278. doi:10.1186/s13287-018-1033-8

Dobin, A., Davis, C. A., Schlesinger, F., Drenkow, J., Zaleski, C., Jha, S., et al. (2013). Star: Ultrafast universal RNA-seq aligner. *Bioinformatics* 29, 15–21. doi:10.1093/bioinformatics/bts635

Gouveia, C., Huyser, C., Egli, D., and Pepper, M. S. (2020). Lessons learned from somatic cell nuclear transfer. *Int. J. Mol. Sci.* 21, E2314. doi:10.3390/ijms21072314

Hashimoto, M., Yamashita, Y., and Takemoto, T. (2016). Electroporation of Cas9 protein/sgRNA into early pronuclear zygotes generates non-mosaic mutants in the mouse. *Dev. Biol.* 418, 1–9. doi:10.1016/j.ydbio.2016.07.017

Hennig, S. L., Owen, J. R., Lin, J. C., Mcnabb, B. R., Van Eenennaam, A. L., and Murray, J. D. (2022). LincRNA#1 knockout alone does not affect polled phenotype in cattle heterozygous for the celtic POLLED allele. *Sci. Rep.* 12, 7627. doi:10.1038/s41598-022-11669-9

Ideta, A., Yamashita, S., Seki-Soma, M., Yamaguchi, R., Chiba, S., Komaki, H., et al. (2016). Generation of exogenous germ cells in the ovaries of sterile NANOS3-null beef cattle. *Sci. Rep.* 6, 24983. doi:10.1038/srep24983

Inoue, K., Ogonuki, N., Mochida, K., Yamamoto, Y., Takano, K., Kohda, T., et al. (2003). Effects of donor cell type and genotype on the efficiency of mouse somatic cell cloning. *Biol. Reprod.* 69, 1394–1400. doi:10.1095/biolreprod.103.017731

Keefer, C. L. (2015). Artificial cloning of domestic animals. *Proc. Natl. Acad. Sci. U. S. A.* 112, 8874–8878. doi:10.1073/pnas.1501718112

Lebleu, V. S., and Neilson, E. G. (2020). Origin and functional heterogeneity of fibroblasts. *FASEB J.* 34, 3519–3536. doi:10.1096/fj.201903188R

Li, Y., Weng, Y., Bai, D., Jia, Y., Liu, Y., Zhang, Y., et al. (2020). Precise allele-specific genome editing by spatiotemporal control of CRISPR-Cas9 via pronuclear transplantation. *Nat. Commun.* 11, 4593. doi:10.1038/s41467-020-18391-y

Ma, H., Marti-Gutierrez, N., Park, S. W., Wu, J., Lee, Y., Suzuki, K., et al. (2017). Correction of a pathogenic gene mutation in human embryos. *Nature* 548, 413–419. doi:10.1038/nature23305

Matoba, S., and Zhang, Y. (2018). Somatic cell nuclear transfer reprogramming: Mechanisms and applications. *Cell Stem Cell* 23, 471–485. doi:10.1016/j.stem.2018.06.018

Park, C. H., Jeoung, Y. H., Uh, K. J., Park, K. E., Bridge, J., Powell, A., et al. (2021). Extraembryonic endoderm (XEN) cells capable of contributing to embryonic chimeras established from pig embryos. *Stem Cell Rep.* 16, 212–223. doi:10.1016/j.stemcr.2020.11.011

Park, K. E., Kaucher, A. V., Powell, A., Waqas, M. S., Sandmaier, S. E., Oatley, M. J., et al. (2017). Generation of germline ablated male pigs by CRISPR/Cas9 editing of the NANOS2 gene. *Sci. Rep.* 7, 40176. doi:10.1038/srep40176

Park, K. E., Park, C. H., Powell, A., Martin, J., Donovan, D. M., and Telugu, B. P. (2016). Targeted gene knockin in porcine somatic cells using CRISPR/Cas ribonucleoproteins. *Int. J. Mol. Sci.* 17, E810. doi:10.3390/ijms17060810

Perisse, I. V., Fan, Z., Singina, G. N., White, K. L., and Polejaeva, I. A. (2020). Improvements in gene editing technology boost its applications in livestock. *Front. Genet.* 11, 614688. doi:10.3389/fgene.2020.614688

Popovic, M., Bialecka, M., Gomes Fernandes, M., Taelman, J., Van Der Jeught, M., De Sutter, P., et al. (2019). Human blastocyst outgrowths recapitulate primordial germ cell specification events. *Mol. Hum. Reprod.* 25, 519–526. doi:10.1093/molehr/gaz035

Robinson, M. D., Mccarthy, D. J., and Smyth, G. K. (2010). edgeR: a Bioconductor package for differential expression analysis of digital gene expression data. *Bioinformatics* 26, 139–140. doi:10.1093/bioinformatics/btp616

Rubinstein, C. D., Mclean, D. T., Lehman, B. P., Meudt, J. J., Schomberg, D. T., Krentz, K. J., et al. (2021). Assessment of mosaicism and detection of cryptic alleles in CRISPR/Cas9-Engineered neurofibromatosis type 1 and TP53 mutant porcine models reveals overlooked challenges in precision modeling of human diseases. *Front. Genet.* 12, 721045. doi:10.3389/fgene.2021.721045

Tanihara, F., Hirata, M., Nguyen, N. T., Le, Q. A., Hirano, T., and Otoi, T. (2019). Effects of concentration of CRISPR/Cas9 components on genetic mosaicism in cytoplasmic microinjected porcine embryos. *J. Reprod. Dev.* 65, 209–214. doi:10.1262/jrd.2018-116

Torres, J., Prieto, J., Durupt, F. C., Broad, S., and Watt, F. M. (2012). Efficient differentiation of embryonic stem cells into mesodermal precursors by BMP, retinoic acid and Notch signalling. *PLoS One* 7, e36405. doi:10.1371/journal.pone.0036405

Tsuda, M., Sasaoka, Y., Kiso, M., Abe, K., Haraguchi, S., Kobayashi, S., et al. (2003). Conserved role of nanos proteins in germ cell development. *Science* 301, 1239–1241. doi:10.1126/science.1085222

Vilarino, M., Rashid, S. T., Suchy, F. P., Mcnabb, B. R., Van Der Meulen, T., Fine, E. J., et al. (2017). Author correction: CRISPR/Cas9 microinjection in oocytes disables pancreas development in sheep. *Sci. Rep.* 7, 7500. doi:10.1038/s41598-020-64443-0

Wang, R., Wang, J., Acharya, D., Paul, A. M., Bai, F., Huang, F., et al. (2014). Antiviral responses in mouse embryonic stem cells: Differential development of cellular mechanisms in type I interferon production and response. *J. Biol. Chem.* 289, 25186–25198. doi:10.1074/jbc.M113.537746

Wang, X., Qu, J., Li, J., He, H., Liu, Z., and Huan, Y. (2020). Epigenetic reprogramming during somatic cell nuclear transfer: Recent progress and future directions. *Front. Genet.* 11, 205. doi:10.3389/fgene.2020.00205

Whitelaw, C. B., Sheets, T. P., Lillico, S. G., and Telugu, B. P. (2016). Engineering large animal models of human disease. *J. Pathol.* 238, 247–256. doi:10.1002/path.4648

Whitworth, K. M., Green, J. A., Redel, B. K., Geisert, R. D., Lee, K., Telugu, B. P., et al. (2022). Improvements in pig agriculture through gene editing. *CABI Agric. Biosci.* 3, 41. doi:10.1186/s43170-022-00111-9

Wu, T., Hu, E., Xu, S., Chen, M., Guo, P., Dai, Z., et al. (2021). clusterProfiler 4.0: A universal enrichment tool for interpreting omics data. *Innovation.* 2, 100141. doi:10.1016/j.xinn.2021.100141

Zhou, X., Wang, L., Du, Y., Xie, F., Li, L., Liu, Y., et al. (2016). Efficient generation of gene-modified pigs harboring precise orthologous human mutation via CRISPR/Cas9-Induced homology-directed repair in zygotes. *Hum. Mutat.* 37, 110–118. doi:10.1002/humu.22913

frontiers | Frontiers in Cell and Developmental Biology

TYPE Original Research
PUBLISHED 02 December 2022
DOI 10.3389/fcell.2022.1053654

OPEN ACCESS

EDITED BY
Shao-Chen Sun,
Nanjing Agricultural University, China

REVIEWED BY
Ana Peropadre,
Autonomous University of Madrid, Spain
Xiang-Shun Cui,
Chungbuk National University, South Korea

*CORRESPONDENCE
Jeong Su Oh,
ohjs@skku.edu

†These authors have contributed equally to this work

SPECIALTY SECTION
This article was submitted to Molecular and Cellular Reproduction, a section of the journal Frontiers in Cell and Developmental Biology

RECEIVED 26 September 2022
ACCEPTED 21 November 2022
PUBLISHED 02 December 2022

CITATION
Gao W, Zhang C, Li B and Oh JS (2022), Azoxystrobin exposure impairs meiotic maturation by disturbing spindle formation in mouse oocytes. *Front. Cell Dev. Biol.* 10:1053654. doi: 10.3389/fcell.2022.1053654

Azoxystrobin exposure impairs meiotic maturation by disturbing spindle formation in mouse oocytes

Wen Gao[1,2†], Chen Zhang[1,3†], Bichun Li[2] and Jeong Su Oh[1,4*]

[1]Department of Integrative Biotechnology, Sungkyunkwan University, Suwon, South Korea, [2]College of Animal Science and Technology, Yangzhou University, Yangzhou, China, [3]RNA Medicine Center, International Institutes of Medicine, Zhejiang University, Hangzhou, Zhejiang, China, [4]Biomedical Institute for Convergence at SKKU (BICS), Sungkyunkwan University, Suwon, South Korea

Fungicides are a type of pesticide used to protect plants and crops from pathogenic fungi. Azoxystrobin (AZO), a natural methoxyacrylate derived from strobilurin, is one of the most widely used fungicides in agriculture. AZO exerts its fungicidal activity by inhibiting mitochondrial respiration, but its cytotoxicity to mammalian oocytes has not been studied. In this study, we investigated the effect of AZO exposure on mouse oocyte maturation to elucidate the underlying mechanisms of its possible reproductive toxicity. We found that AZO exposure disturbed meiotic maturation by impairing spindle formation and chromosome alignment, which was associated with decreased microtubule organizing center (MTOC) integrity. Moreover, AZO exposure induced abnormal mitochondrial distribution and increased oxidative stress. The AZO-induced toxicity to oocytes was relieved by melatonin supplementation during meiotic maturation. Therefore, our results suggest that AZO exposure impairs oocyte maturation not only by increasing oxidative stress and mitochondrial dysfunction, but also by decreasing MTOC integrity and subsequent spindle formation and chromosome alignment.

KEYWORDS

azoxystrobin, oocyte maturation, spindle formation, MTOC, melatonin

Introduction

Azoxystrobin (AZO), a natural methoxyacrylate derived from strobilurin, has been one of the most commonly used fungicides in agriculture since 1996, owing to its efficiency and broad-spectrum characteristics in protecting crops (Rodrigues et al., 2013; Abdelraheem et al., 2015). Mechanistically, AZO acts as a specific inhibitor of the ubiquinol oxidizing site (Qo) of mitochondrial respiratory complex III to block electron transfer between cytochrome b and cytochrome c1 in fungal cells. This results in cellular oxidative stress and ATP synthesis failure (Kim et al., 2007). In 2018, the amount of AZO usage was approximately 1,130 tons in the United States (USGS, 2018), and about 10,000 tons were applied to crops in China (Kumar et al., 2020). Since its widespread use, AZO has been prioritized as one of the major chemicals for

biomonitoring in many countries due, in large part, to AZO residues in foodstuffs and environmental matrices, including soil, water, and air (Pellizzari et al., 2019; Wang et al., 2021a). In addition to functioning as a pesticide in agriculture, AZO has recently been detected in mold-resistant wallboards at a concentration of 88.5 μg/g, leading to potential pollution in the indoor environment (Cooper et al., 2020).

Given the extensive presence in the environment, studies on AZO exposure effects are numerous. Accumulating evidence suggests that AZO has the potential to induce developmental toxicity in animals. For instance, AZO has been reported to impair cortical migration by increasing reactive oxygen species (ROS) levels and inducing mitochondrial deactivation in mouse embryos (Kang et al., 2021). Also, parental exposure to AZO in zebrafish may cause mortality and developmental malformations in their F1 offspring (Cao et al., 2019). Furthermore, reproductive toxicity of AZO results in reductions in sex hormone production and testis damage in a dose- and time-dependent manner in rats (El-Hak et al., 2022). In addition, a recent study reported that AZO transfers efficiently through the placenta from exposed prenatal mice to offspring (Hu et al., 2022). AZO has been reported to effectively induce esophageal cancer cell apoptosis *via* the mitochondrial pathway and is a potential candidate for drug therapy of esophageal cancer (Shi et al., 2017). Likewise, a positive correlation between AZO exposure and oral cancer suppression *via* inhibition of the mitochondrial respiratory pathway has been well documented (Chen et al., 2020). However, to date, the effects of AZO exposure on oocyte maturation have not been fully elucidated.

Mammalian oocyte maturation is a complex cellular process that is of paramount importance for fertilization and embryo development. After prolonged arrest at the prophase of the first meiosis (MI) which is morphologically identified by a large nucleus called germinal vesicle (GV), oocytes resume meiosis and undergo two consecutive meiotic divisions. After meiotic resumption, spindle microtubules are assembled from microtubule organizing centers (MTOCs) and form a barrel-shaped bipolar spindle with highly organized bundles of microtubules (Mogessie et al., 2018). When spindle microtubules emanated from opposite pole correctly attach to the kinetochores of homologous chromosomes and thereby chromosomes align at the middle of spindle, oocytes enter anaphase and eventually extrude the first polar body (Radford et al., 2017). Oocytes then become arrested again at the metaphase II (MII), awaiting for fertilization. Although many cellular organelles are involved in this process, mitochondria function is of great importance to ensure meiotic maturation and to preserve oocyte quality. Dysfunction of mitochondria could induce the ROS production and eventually led to apoptosis (Kirillova et al., 2021). Moreover, mitochondria have been known to be sensitive to environmental toxicants (Meyer et al., 2013).

Due to the prolonged dormancy, oocytes are susceptible to adverse internal or external factors. Indeed, females exposed to toxic environmental chemicals, such as those found in pesticides, metals, plastics, and food additives, are more vulnerable to reproductive health compromise (Ge et al., 2019). However, the underlying mechanisms of reproductive toxicity have not been thoroughly investigated. In this study, we assessed the effect of AZO on mouse oocyte maturation with the aim of uncovering the underlying mechanisms of its reproductive toxicity.

Materials and methods

Animals and reagents

Three- to four-week-old female ICR mice (Koatech, Korea) were used in all experiments. All procedures for mouse care and use were conducted in accordance with the guidelines and approval of the Institutional Animal Care and Use Committee of Sungkyunkwan University (approval ID: SKKUIACUC 2021-09-69-1). Azoxystrobin (131860-33-8, Sigma) and melatonin (73-31-4, Sigma) were dissolved in dimethyl sulfoxide (DMSO) to create stock solutions to be used at dilutions of 0.1% or below.

Oocyte collection and culture

Ovaries were isolated from mice 46 h–48 h after injection of five international units (IU) of pregnant mare serum gonadotropin (PMSG; HOR-272, Prospec). Mice were humanely euthanized by exposure to CO_2 and cervical dislocation, and ovaries were placed in M2 medium containing 0.4% bovine serum albumin (BSA; A7906, Sigma) and 100 μM of 3-isobutyl-1-methylxanthine (IBMX) to prevent meiotic maturation. After puncturing antral follicles with a fine needle under a dissecting microscope, fully grown oocytes at the germinal vesicle (GV) stage were collected. For *in vitro* maturation, GV oocytes were cultured for 8 h to allow MI stage progression and 16 h for MII stage progression, during which time oocytes were in IBMX-free M2 medium and covered with mineral oil at 37°C in an atmosphere containing 5% CO_2.

Azoxystrobin and melatonin treatment

Azoxystrobin (AZO; 131860-33-8, Sigma) were dissolved in dimethyl sulfoxide (DMSO) to create 10 mM stock solutions. The stock was diluted in the M2 medium to obtain a series of working solutions of 1, 5, 8, and 10 μM AZO. The final concentration of DMSO in the medium is 0.1% or below. For ROS scavenging experiment in Figures 5–7, melatonin (73-31-4, Sigma) was dissolved in DMSO to make 10 mM stock solutions and stocks were diluted to 10 μM in the M2 medium.

Immunofluorescence

After washing three times with PVS (3 mg polyvinyl pyrrolidone/1 mL phosphate-buffered saline), oocytes were fixed in 4% paraformaldehyde at room temperature for 10 min, permeabilized with PVS containing 0.1% Triton X-100 and 0.01% Tween 20 at room temperature for 20 min, and incubated in PVS containing 1.0% BSA at 37°C for 2 h. Oocytes were then incubated overnight at 4°C with anti-α-tubulin (1:1,000; T7451, Sigma), anti-CEP192 (1:200; AR07-PA0001, Young In Frontier), anti-PCNT (1:100; ab4448, Abcam), and anti-p-Aurora A (1:250; 3079, Cell Signaling) antibodies diluted in blocking solution. After washing three times with PVS, oocytes were incubated with Alexa Fluor 488 AffiniPure goat anti-mouse IgG (H + L) (1:500; 115-545-146, Jackson ImmunoResearch) or Alexa Fluor 594 AffiniPure goat anti-rabbit IgG (H + L) (1:500; 111-585-144, Jackson ImmunoResearch) for 2 h at room temperature. Oocytes were then mounted on glass slides, counterstained with DAPI, and examined under a Nikon Eclipse Ti inverted microscope (Nikon).

Reactive oxygen species detection

DHR123 (D1054, Sigma) was diluted to create a 20 mM stock solution and used at dilutions of 0.1% in M2 medium. Oocytes treated with AZO, MT, or AZO with MT were cultured for 8 h to allow MI progression or for 16 h to allow progression through MII. After washing with M2 medium three times, oocytes were incubated with 20 μM dihydrohodamine-123 (DHR123, D1054, Sigma Aldrich) in M2 medium for 30 min at 37°C in a 5% CO_2 atmosphere. After washing three times, oocytes were counterstained with DAPI and mounted on glass slides. Oocytes were then observed under a Nikon Eclipse Ti inverted microscope, (Nikon), and the fluorescence was quantified using ImageJ software (National Institutes of Health, NIH).

Mitochondria detection

Working solution was prepared by diluting 1 μl MitoGreen Indicator with 500 μl Live Cell Staining Buffer (ab112143, Abcam) and 500 μl of M2 medium. Oocytes were incubated with working solution for 30 min at 37°C in a 5% CO_2 atmosphere. After washing three times with PBS/PVS, fluorescence signals were acquired from live oocytes under a Nikon Eclipse Ti inverted microscope (Nikon). Oocytes were then mounted on glass slides, counterstained with DAPI, and imaged again at large magnification. Images were processed using a Nikon Eclipse Ti inverted microscope and mitochondrial fluorescence was quantified using ImageJ software.

Expression analysis by reverse transcription-PCR

Total RNAs were extracted from 50 oocytes using the RNeasy Micro Kit (QIAGEN) followed by reverse transcription (RT) using a Sensiscript RT Kit (QIAGEN), according to the manufacturer's instruction. PCR was performed using the following primers: superoxide dismutase (SOD), 5′-GCAGGG AACCATCCACTT-3′ and 5′- TGCCCAGGTCTCCAACAT -3′; glutathione peroxidase (GPX), 5′-GTGCGAAGTGAA TGGTGAGA-3′ and 5′-CTGGGACAGCAGGGTTTCTA-3′; cytochrome b (CYTB), 5′-AATCCACTAAACACCCCACCC-3′ and 5′-GCTTCGTTGCTTTGAGGTATGA-3′; β-Actin, 5′-GGGAAATCGTGCGTGAC-3′ and 5′-AGGCTGGAAAAG AGCCT-3′. The PCR conditions consisted of an initial denaturation at 95°C for 5 min, followed by 40 cycles at 95°C for 30 s, 55°C for 30 s, and 72°C for 30 s and final extension at 72°C for 5 min. The levels of mRNA were normalized to those of β-Actin.

Statistical analysis

All experiments were performed three times. Each experimental group included at least 15 oocytes. The results are expressed as the mean ± SEM from at least three independent experiments unless otherwise stated. One-way ANOVA with Tukey's post-hoc test was used to analyze the significance of differences between groups (*$p < 0.05$ = significant difference and **$p < 0.01$ = extremely significant difference). GraphPad Prism 9 software (GraphPad Software, San Diego, CA, United States) was used for statistical analysis.

Results

Azoxystrobin exposure impairs mouse oocyte maturation

To determine the potential effect of AZO on oocyte maturation, oocytes at the GV stage were cultured in M2 medium containing different concentrations (0, 1, 5, 8, 10 μM) of AZO for 16 h, and germinal vesicle breakdown (GVBD) and first polar body extrusion (PBE) were examined. As shown in Figure 1A, though a slight delay was observed in GVBD, oocytes treated with 1 μM AZO underwent GVBD. However, 5 μM AZO treatment significantly reduced the GVBD rate, and only about 60% of oocytes underwent GVBD after culturing for 4 h (60.65 ± 5.08). Oocytes exposed to 8–10 μM AZO failed to undergo GVBD from 0 to 4 h. Similarly, in comparison with the control group, 1 μM AZO treatment had no significant effect on polar body extrusion (control, 86.68 ± 2.98; 1 μM AZO, 83.68 ± 5.07). However,

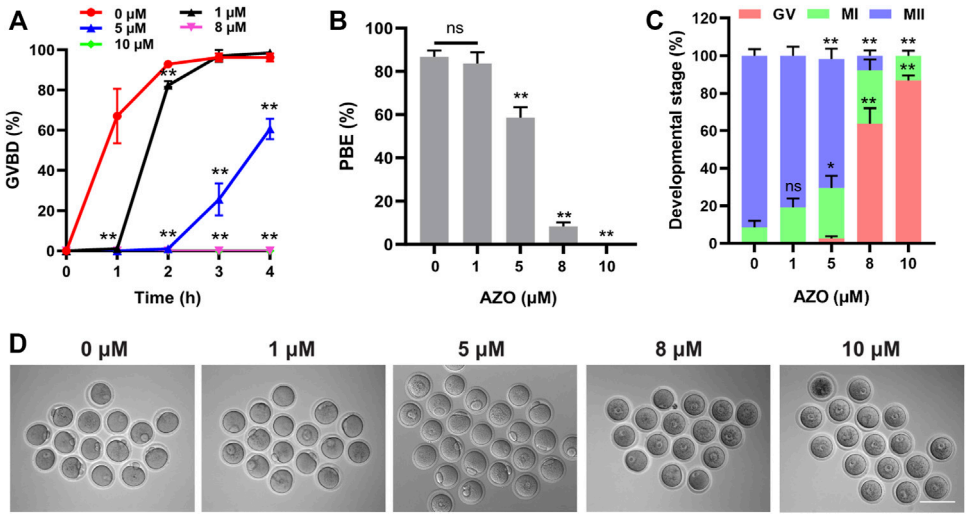

FIGURE 1
The effect of AZO on oocyte meiotic maturation is dose-dependent. **(A)** Oocytes were treated with different doses of AZO following IBMX release. The percentage of GVBD is expressed as mean ± SEM from three independent experiments. **(B)** After 16 h of culture with AZO treatments using different doses, the percentage of polar body extrusion is expressed as mean ± SEM from three independent experiments. **(C)** Percentage of AZO-treated oocytes at GV, MI, and MII stages. **(D)** Representative images of oocytes at 16 h of culture with different dose-treatments of AZO following IBMX release. Scale bar, 100 μm $*p < 0.05$, $**p < 0.01$, ns, not significant.

8–10 μM AZO exposure resulted in a sharp decline in PBE rate (8 μM, 8.26 ± 1.87; 10 μM, 0.00 ± 0.00), and most of the oocytes were arrested at the GV stage (8 μM, 63.83 ± 8.13; 10 μM, 86.82 ± 2.57). Notably, 5 μM AZO exposure led to a considerable reduction in PBE rate (58.65 ± 4.81), and about 68.5% oocytes underwent meiosis II (MII) (68.5 ± 5.51) progression (Figures 1B–D). These results suggest that AZO exposure negatively impacts meiotic maturation in mouse oocytes in a dose-dependent manner. Accordingly, we used 5 μM AZO as the working concentration for subsequent experiments.

Azoxystrobin exposure impairs spindle assembly and chromosome alignment at the MI stage

Meiotic arrest is usually associated with disorganized cytoskeletal structures (Zhang et al., 2020; Leem et al., 2022). Therefore, we examined the spindle phenotype and chromosome alignment in AZO-exposed oocytes at meiosis I (MI) by immunofluorescence staining. While a typical barrel-shaped spindle and well-aligned chromosomes on the equatorial plate were observed in the control group, the percentages of aberrant spindles (13.16 ± 2.20 vs. 70.86 ± 6.17) and misaligned chromosomes (15.08 ± 2.24 vs. 67.54 ± 7.56) were significantly increased in oocytes after AZO exposure (Figures 2A–C). Moreover, AZO exposure significantly reduced the fluorescence intensity of spindles (1.00 ± 0.03 vs. 0.55 ± 0.02) (Figure 2D). Therefore, these results suggest that AZO exposure impairs proper spindle assembly and chromosome alignment during meiotic maturation in mouse oocytes.

Azoxystrobin exposure impairs microtubule organizing center assembly during meiotic maturation

In many species, the timely migration and accurate positioning of spindles in oocytes proceed through self-organization of multiple acentriolar microtubule organizing centers (MTOCs) (Londoño-Vásquez et al., 2022). To address whether AZO exposure impedes MTOC assembly in the same manner as spindle organization during meiotic maturation, we detected the subcellular localization and intensity of CEP192 as a MTOC marker after AZO exposure (Lee et al., 2018). Compared with the state of CEP192 in control oocytes, AZO-treated oocytes exhibited a disrupted localization and a significant decrease in fluorescence intensity (1.00 ± 0.02 vs. 0.77 ± 0.03) (Figures 3A,B). Moreover, the number of MTOCs was significantly increased in oocytes treated with AZO (16.71 ± 1.45 vs. 37.26 ± 1.12) (Figure 3C). In addition to CEP192, pericentrin (PCNT) and Aurora A play essential roles in accurate spindle assembly and chromosome-microtubule interactions (Baumann et al., 2017; Wang et al., 2021b). Therefore, we examined PCNT and

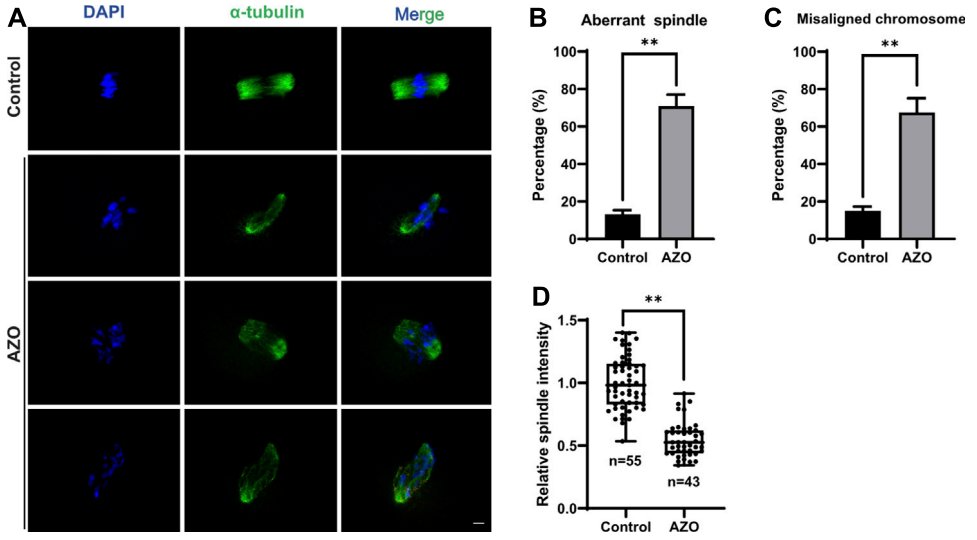

FIGURE 2
AZO treatment impairs alignment of chromosomes and organization of spindles in oocytes. **(A)** Representative images showing spindle morphologies and chromosome alignment in AZO-treated oocytes and control oocytes. The MI stage oocytes were stained with α-Tubulin antibody and DAPI to visualize spindle and chromosomes, respectively. Scale bar, 10 μm. **(B)** The aberrant spindle rate was evident in the control and AZO-treated oocytes at MI stage. **(C)** The aberrant misaligned chromosome was evident in control and AZO-treated oocytes at MI stage. **(D)** Quantification of spindle intensity in control and AZO-treated oocytes at MI stage. Data are expressed as mean ± SEM. $^{**}p < 0.01$.

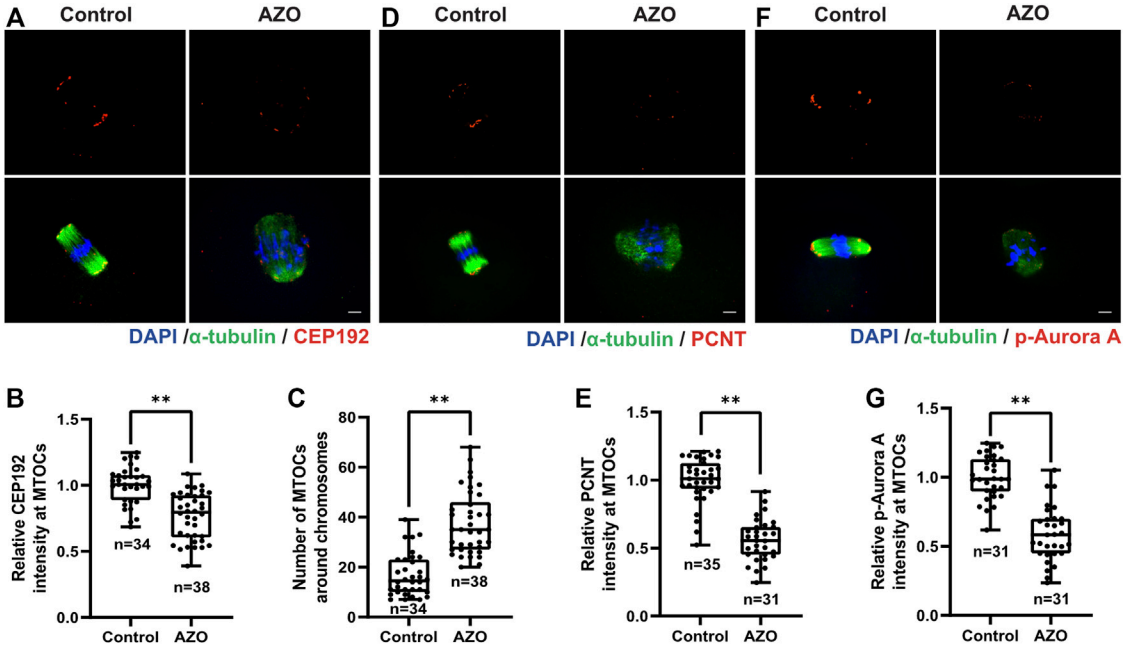

FIGURE 3
AZO exposure impairs acentriolar MTOC assembly during meiotic maturation. Oocytes were cultured with 5 μM AZO for 8 h and stained with the indicated antibodies and DAPI. **(A,D,F)** Representative images of oocytes labeled with α-Tubulin, CEP192, PCNT, and p-Aurora antibodies. **(A)**. Scale bar, 10 μm. **(B,E,G)** The intensities of CEP192, PCNT, and p-Aurora A around MTOCs are quantified. **(C)** The number of MTOCs around chromosomes is quantified using CEP192 fluorescent foci. All data are expressed as mean ± SEM. $^{**}p < 0.01$.

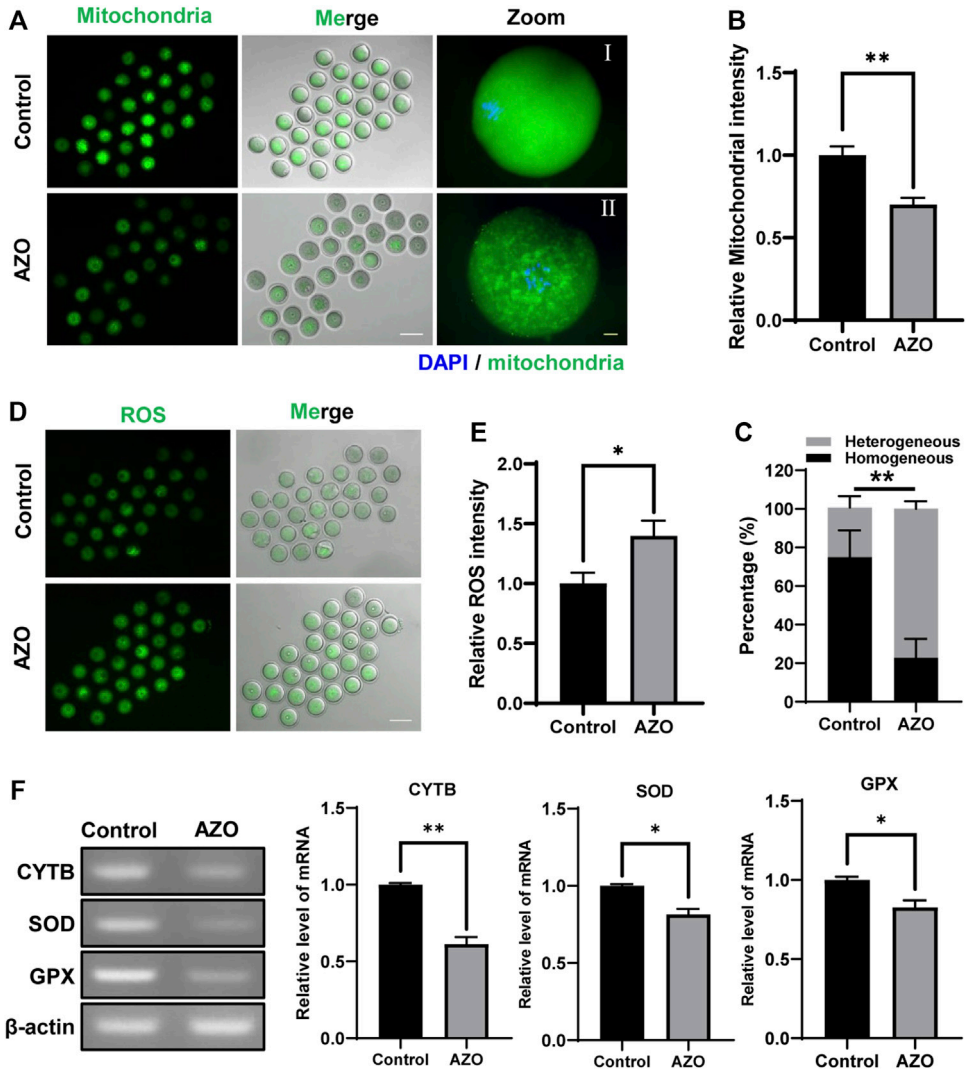

FIGURE 4
AZO impairs mitochondrial distribution and increases ROS levels. Mitochondria were stained with Mitotracker after 8 h of culture with DMSO (Control) or AZO. **(A)** Representative images of live oocytes stained with Mitotracker. Scale bar, 100 μm (white). Enlarged images of oocyte with homogeneous distribution in the control group and oocyte with heterogeneous distribution in the AZO group. Scale bar, 10 μm (yellow). **(B)** Mitochondrial intensity of oocytes in control and AZO groups is determined. **(C)** Percentage of oocytes with homogeneous or heterogeneous mitochondrial distribution. **(D)** Representative images of live oocytes stained with DHR-123. Scale bar, 100 μm. **(E)** The fluorescent intensity of ROS in control and AZO-treated oocytes. **(F)** Relative mRNA expression of CYTB, SOD, and GPX in control and AZO-treated oocytes. Data are expressed as mean ± SEM from five independent experiments except panel **(F)**. Data in panel **(F)** derived from two independent experiments. *$p < 0.05$, **$p < 0.01$.

p-Aurora A localization and expression after AZO exposure by immunofluorescence staining. Similar to CEP192, the signal intensity levels of PCNT and p-Aurora A were significantly reduced after AZO treatment (PCNT, 1.00 ± 0.03 vs. 0.56 ± 0.03; p-Aurora A, 1.00 ± 0.03 vs. 0.59 ± 0.03) (Figures 3D–G). These results collectively indicated that the abnormality in spindle organization and chromosome alignment after AZO exposure was related to disruption of the MTOC assembly during meiotic maturation in mouse oocytes.

Azoxystrobin exposure compromises mitochondrial distribution

Since AZO was found to impair mitochondrial function by blocking the electron transfer chain in the inner mitochondrial membrane of microorganisms (Inoue et al., 2012), we determined the effects of AZO on mitochondria in MI-stage oocytes. Our results showed that mitochondria were homogeneously distributed in the cytoplasm in control oocytes (74.93 ± 5.68). However, about 77% of AZO-exposed

oocytes exhibited heterogeneous distribution in mitochondria (77.13 ± 2.11) (Figures 4A,C). Moreover, we found that AZO exposure significantly reduced the signal intensity of mitochondria (1.00 ± 0.05 vs. 0.70 ± 0.04) (Figure 4B). Considering that abnormal mitochondrial functioning leads to an increase in reactive oxygen species (ROS), thereby disrupting oocyte maturation through oxidative stress (Kirillova et al., 2021), we next determined the ROS level in MI-stage oocytes exposed to AZO. As expected, AZO exposure significantly increased the ROS levels compared to control oocytes (1.00 ± 0.09 vs. 1.40 ± 0.13) (Figures 4D,E).

To further investigate the effect of AZO on ROS production, we examined the expression of mitochondrial cytochrome b (CYTB) and antioxidant enzymes including superoxide dismutase (SOD) and glutathione peroxidase (GPX) after AZO treatment. We found that AZO treatment significantly decreased mRNA expression of CYTB, SOD, and GPX (Figure 4F). Therefore, our results demonstrated that mitochondrial function was impaired after AZO treatment; and, as a result, oocyte ROS levels were elevated during meiotic maturation.

Melatonin rescues azoxystrobin-induced meiotic maturation of mouse oocytes

Given the mitochondrial dysfunction and increased ROS levels in AZO-exposed oocytes, we tested a method designed to reduce ROS levels to determine if oocyte maturation could be rescued. Melatonin (N-acetyl-5-methoxytryptamine) is synthesized and released from the pineal gland and modulates various physiological processes, including female reproduction. It is a strong natural antioxidant and free radical scavenger and has been reported to promote oocyte maturation and embryo development through its antioxidant effects (Galano et al., 2011; Tamura et al., 2012). Therefore, we chose melatonin to test the effect of ROS scavenging on AZO-induced oocyte maturation suppression. GV oocytes were randomly assigned to four groups: the control group (Control), AZO-treated group (AZO), melatonin-exposed group (MT), and AZO-MT-exposed group (AZO + MT). Melatonin was diluted in 5 μM AZO medium to a final concentration of 10 μM. Compared to the exclusive treatment with AZO, addition of melatonin significantly increased the GVBD rate and PBE rate in oocytes cultured for 4 and 16 h, respectively (GVBD, 66.40 ± 4.29 vs. 83.15 ± 1.69; PBE, 54.17 ± 3.73 vs. 79.12 ± 8.43) (Figures 5A–D). Moreover, the intensity of spindle microtubules (0.57 ± 0.03 vs. 0.81 ± 0.03) and CEP192 (0.77 ± 0.02 vs. 0.84 ± 0.03) at MTOCs and the number of MTOCs (34.70 ± 2.29 vs. 27.38 ± 2.11) were restored after melatonin treatment for AZO exposure (Figures 6A–D). Similarly, the abnormalities of spindle assembly and chromosome alignment induced by AZO exposure were rescued by melatonin treatment (aberrant spindle, 65.58 ± 1.73 vs. 36.25 ± 6.70; chromosome misalignment, 78.08 ± 4.31 vs. 48.32 ± 3.59) (Figures 6E,F). In addition, our data showed that melatonin supplementation eliminated the excessive ROS and reversed mitochondrial dysfunction induced by AZO (1.39 ± 0.03 vs. 1.06 ± 0.049 for ROS intensity; 0.64 ± 0.03 vs. 0.78 ± 0.03 for mitochondrial intensity) (Figures 7A–E). Taken together, our data suggest that AZO induces mitochondrial dysfunction and excessive accumulation of ROS, while melatonin treatment effectively rescues oocytes from these impairments.

Discussion

In recent years, there has been considerable interest in the effects of pesticides on human health. Azoxystrobin (AZO), a typical broad-spectrum fungicide, is one of the most frequently detected pesticide residues due to its widespread use (Park et al., 2022). The European Food Safety Authority (EFSA) has classified AZO as highly toxic to a majority of aquatic organisms (EFSA, 2010). For instance, AZO has been reported to have high reproductive toxicity in adult zebrafish (Cao et al., 2019). A recent study revealed that AZO exhibited reproductive toxicity in a dose- and time-dependent manner in male rats (El-Hak et al., 2022). However, the effect of AZO on mammalian oocyte maturation has not been well characterized. In this study, we found that AZO exposure impaired oocyte maturation not only by inducing mitochondrial dysfunction and oxidative stress, but also by decreasing MTOC integrity and subsequent spindle formation and chromosome alignment.

During oocyte maturation, GVBD and PBE are two critical markers of meiotic progression. Therefore, the effect of AZO on oocyte maturation was first examined by evaluating the GVBD and PBE rates. Previous studies have shown that AZO at 1 μM was sufficient to induce changes in transcriptional activity, while 5–10 μM could result in reactive oxygen species accumulation in primary neuronal cells (Pearson et al., 2016; Simon et al., 2019; Kang et al., 2021). Moreover, AZO at micromolar concentrations (1–3 μM) has been shown to modify membrane ion permeability in thymocytes (Imura et al., 2019). Accordingly, we chose a concentration range of 1–10 μM to test the effect of AZO on oocyte maturation. Our results showed that 5–10 μM AZO supplementation significantly reduced the GVBD and PBE rates, and 5 μM was an appropriate dose for further detection since this dose led to a considerable reduction in PBE rate. To further confirm the toxic effects of AZO on oocyte maturation, we examined spindle assembly and chromosome alignment, which are critical for meiotic progression. Aberrant spindle formation and lower intensity and irregular arrangement of chromosomes were frequently observed in AZO-exposed oocytes. Therefore, our results suggest that abnormalities in spindle assembly and chromosome alignment are the main contributors to impaired meiotic maturation after AZO

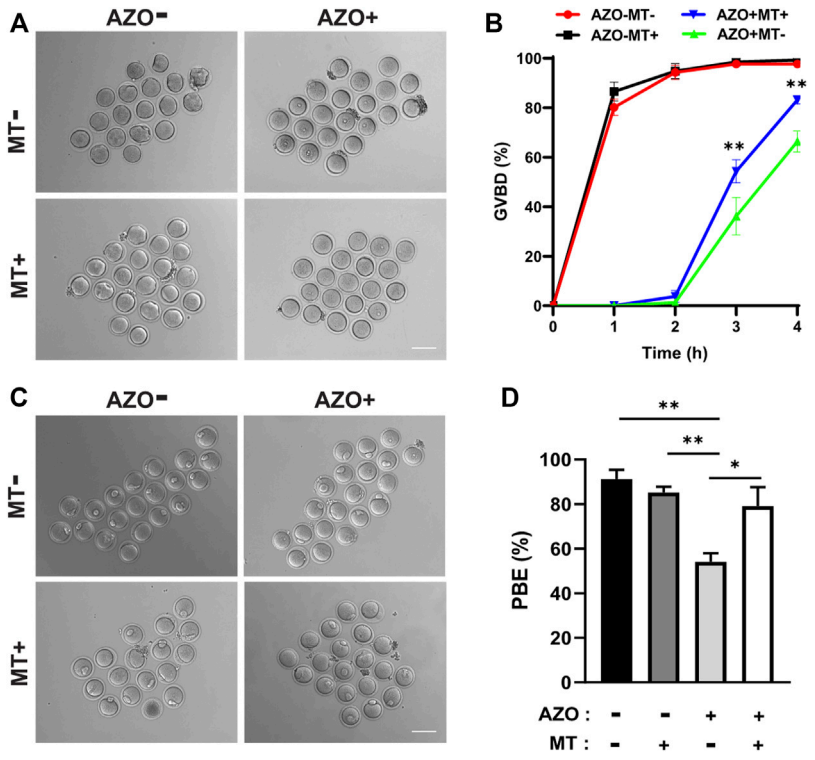

FIGURE 5
Melatonin rescues PBE impaired by AZO exposure. Oocytes were matured in the absence (–) or presence (+) of AZO and melatonin (MT) during meiotic maturation. **(A)** Representative images of oocytes at 4 h of culture with different treatments following IBMX release. Scale bar, 100 μm. **(B)** The percentage of GVBD is expressed as mean ± SEM from two independent experiments. **(C)** Representative images of oocytes at 16 h of culture with different treatments following IBMX release. Scale bar, 100 μm. **(D)** After 16 h of culture with different treatments, the percentage of polar body extrusion was expressed as mean ± SEM from three independent experiments. *$p < 0.05$, **$p < 0.01$.

treatment. However, despite the high incidence of spindle abnormalities, the PBE rate did not decrease proportionally. While the kinetochore microtubules directly attach to chromosomes and regulate chromosome segregation and, when impaired, activate spindle assembly checkpoint (SAC) and cause MI arrest, the polar microtubules do not interact with chromosomes but instead interdigitate with polar microtubules from the opposite pole, and thus are important to maintain spindle bipolarity and morphology (Wittmann et al., 2001). In this respect, we are tempting to speculate that the polar microtubules are more susceptible to AZO exposure than kinetochore microtubules. Thus, after AZO treatment, oocytes with aberrant spindle morphology may override SAC arrest and eventually undergo PBE. Given that spindle microtubules are emanated from MTOCs in mouse oocytes, it is also possible that decreased MTOC integrity may partially decrease spindle stability, which displays abnormal spindle morphology. Indeed, we observed that MTOC integrity was reduced after AZO treatment. Similar to our observation, it has been reported that a partial decrease in MTOC integrity caused severe spindle abnormalities, but partly disturbed PBE (Wang et al., 2017; Yin et al., 2021).

In contrast to somatic cells, mammalian oocytes lack canonical centrosomes because centrioles are lost during early oogenesis (Manandhar et al., 2005). Instead, multiple acentriolar microtubule organizing centers (MTOCs) functionally replace centrosomes and play a key role in oocyte microtubule nucleation (Schuh and Ellenberg, 2007; Clift and Schuh, 2015). Previous studies revealed that disruption of MTOC function in mouse oocytes could result in spindle instability, chromosome misalignment, and error-prone meiotic division that lead to female subfertility (Ou et al., 2010; Namgoong and Kim, 2018). Thus, we tested MTOC function by examining the levels of the MTOC markers CEP192, PCNT, and p-Aurora A (Lee et al., 2018). Our data showed that AZO treatment significantly decreased the number of MTOCs around chromosomes, as well as the intensity of CEP192, PCNT, and p-Aurora A, suggesting that impairments of spindle organization and chromosome alignment induced by AZO may be related to defects in MTOC assembly.

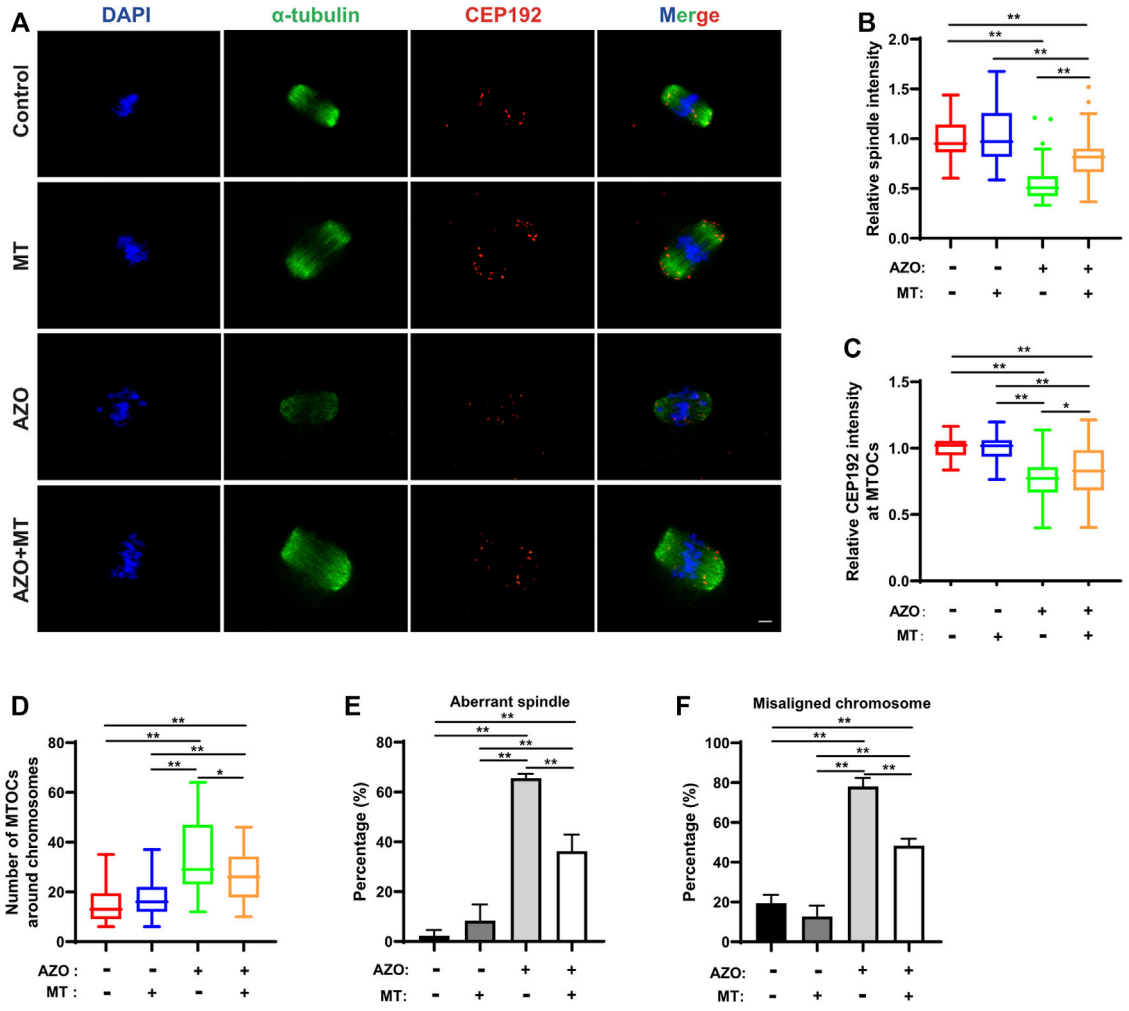

FIGURE 6
Melatonin rescues AZO-induced impairment of spindle assembly. Oocytes were cultured for 8 h in the absence (–) or presence (+) of AZO and melatonin (MT) during meiotic maturation. **(A)** Representative images of oocytes labeled with α-Tubulin and CEP192. Scale bar, 10 μm. **(B,C)** The intensities of spindle and CEP192 around MTOCs are quantified. **(D)** The number of MTOCs around chromosomes is quantified using CEP192 fluorescent foci. **(E)** The aberrant spindle rate was evident in the control and AZO-treated oocytes at MI stage. **(F)** The aberrant misaligned chromosome was evident in control and AZO-treated oocytes at MI stage. All data are expressed as mean ± SEM. $*p < 0.05$, $**p < 0.01$.

One basic mechanism of AZO cellular toxicity is its association with inhibition of the electron transfer chain in the oxidative phosphorylation process, impairing mitochondrial function (Shi et al., 2017). Mitochondria play an essential role in mammalian oocyte maturation by providing the ATP for meiotic division through oxidative phosphorylation. Notably, mitochondria surrounding the spindle periphery supply sufficient energy for spindle migration and chromosome segregation (Yu et al., 2010). Excessive clustering of mitochondria around the spindle, however, may lead to arrest of mouse oocytes at the metaphase I stage (Wang et al., 2020). Consistent with previous findings, our data showed that most mitochondria dispersed homogenously in the control oocyte cytoplasm, with enrichment around the spindle (Sathananthan and Trounson, 2000; Dalton and Carroll, 2013). However, the mitochondria in AZO-treated oocytes were heterogeneous and could not form a regular mitochondrial ring around the spindle, suggesting that AZO supplementation disrupted the distribution of cytoplasmic mitochondria. Indeed, accumulation of mitochondria around the spindle was associated with migrating cytoplasmic MTOCs, driven by dynein, during the first mitotic division in mouse oocytes (Dalton and Carroll, 2013). Our data showed that AZO treatment significantly compromised the integrity of MTOCs. Therefore, we propose that the mitochondrial dysfunction induced by AZO contributed to the failure of spindle assembly and migration, leading to PBE failure during meiotic maturation in mouse oocytes.

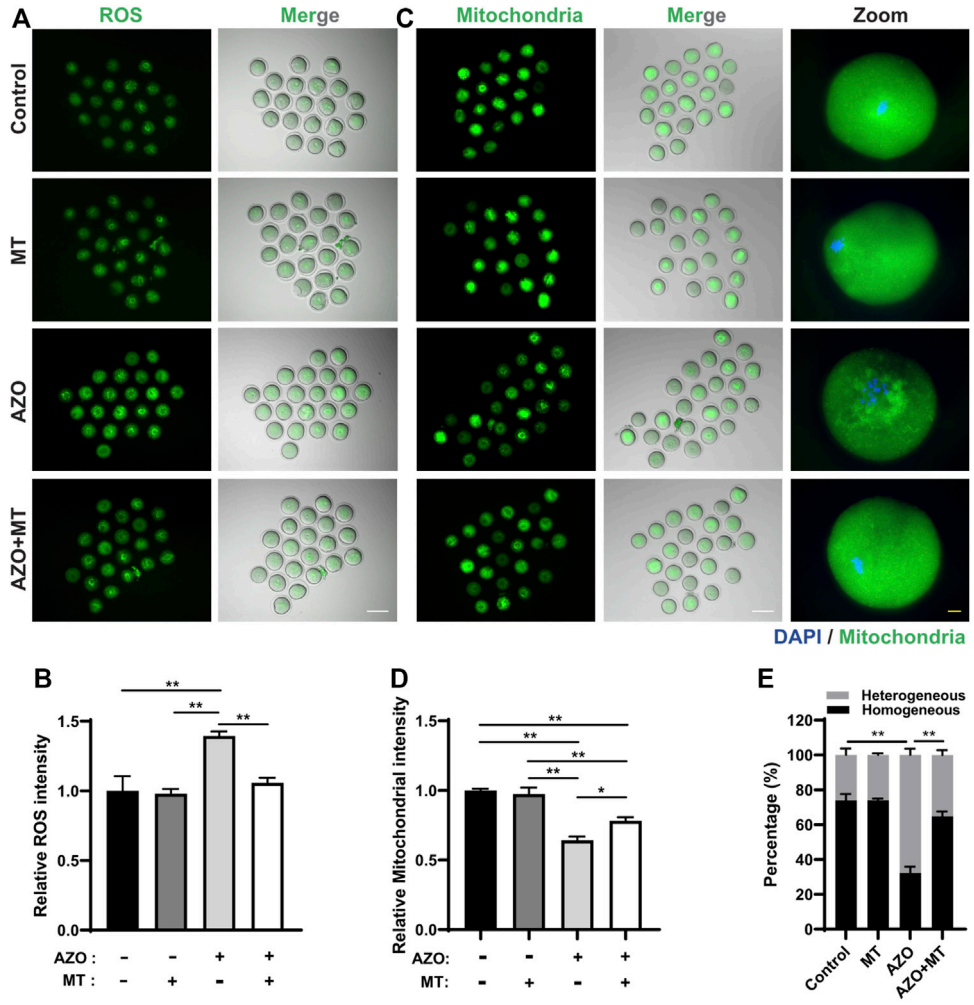

FIGURE 7
Melatonin protects against oxidative stress and mitochondrial dysfunction induced by azoxystrobin (AZO). Oocytes were cultured for 8 h in the absence (–) or presence (+) of AZO and melatonin (MT) during meiotic maturation. **(A)** Representative images of live oocytes stained with DHR-123. Scale bar, 100 μm. **(B)** ROS intensity of oocytes in control, MT, AZO, and AZO + MT groups are determined. **(C)** Representative images of live oocytes stained with Mitotracker. Scale bar, 100 μm (white). Enlarged images of oocyte with homogeneous distribution in the control, MT, and AZO + MT groups and oocyte with heterogeneous distribution in the AZO group. Scale bar, 10 μm (yellow). **(D)** Mitochondrial intensity of oocytes in control, MT, AZO, and AZO + MT groups are determined. **(E)** Percentage of oocytes with homogeneous or heterogeneous mitochondrial distribution. Data are expressed as mean ± SEM from five independent experiments. *$p < 0.05$, **$p < 0.01$.

Typically, dysfunctional mitochondria are less able to counteract ROS production, which contributes to oxidative stress. We therefore examined the ROS levels in oocytes exposed to AZO. As expected, AZO addition caused excessive accumulation of ROS. Previous studies suggested that oxidative stress had negative impacts on oocyte maturation and embryo development, while the application of antioxidants could be effective in rescuing the defects of oocyte maturation (Cajas et al., 2020; Cao et al., 2021). Melatonin, a hormone produced by many organs including the pineal gland, has strong free radical scavenging and antioxidant properties and has been found to protect oocytes from oxidative damage (Pang et al., 2016; Xing et al., 2021). Mechanistically, melatonin protects against oxidative stress mainly through inducing the expression of antioxidant enzymes, inactivating pro-oxidants, and maintaining mitochondrial homeostasis (Zhang and Zhang, 2014). Accordingly, we used melatonin to determine whether defects in oocyte maturation could be eliminated during AZO exposure. Our data showed that defects in chromosome organization, spindle and MTOC assembly, and first PBE after AZO treatment were remarkably restored by melatonin during mouse oocyte maturation. Moreover, excessive ROS production and heterogeneous mitochondrial distribution induced by AZO were significantly reduced by melatonin addition. Given that the

expression of antioxidant enzymes decreased after AZO exposure, it is likely that melatonin may restore the expression of these enzymes and thereby improve ROS scavenging capacity of oocytes. Consistent with our results, melatonin has been reported to improve oocyte quality by decreasing ROS levels (Jiang et al., 2021). However, the precise mechanisms of melatonin in protecting oocytes against AZO-induced toxicity need to be determined.

In conclusion, our results demonstrate that AZO exposure results in meiotic arrest by disrupting MTOC-mediated spindle assembly and chromosome alignment, mainly due to dysfunctional mitochondria and excessive ROS accumulation induced by AZO. Moreover, melatonin, due to its antioxidant properties, is likely to be a promising compound to rescue oocyte maturation from AZO-induced cytotoxicity. Given that *in vitro* assay may not replicate the precise cellular conditions of an organisms, we could not entirely exclude that AZO could react with biological components after entering into circulation system in the body and generate secondary metabolites, which in turn indirectly affects cellular system including oocyte maturation. It is also considerable the compensatory effects from surrounding environment such as follicular fluids and granulosa and cumulus cells in the ovary. Therefore, further verification of cytotoxicity of AZO on oocyte maturation is required using *in vivo* model system.

Data availability statement

The original contributions presented in the study are included in the article/supplementary material, further inquiries can be directed to the corresponding author.

Ethics statement

The animal study was reviewed and approved by the International Animal Care and Use Committees of Sungkyunkwan University (Approval ID: SKKUIACUC 2021-09-69-1).

Author contributions

JO conceived the study. WG and CZ performed experiments and data analysis. BL provided intellectual advice. JO supervised the project. JO and WG wrote the manuscript.

Funding

This work was supported by the Basic Science Research Program through the National Research Foundation of Korea (NRF) funded by the Ministry of Education (NRF-2017R1A6A1A03015642 and NRF-2019R1I1A2A01041413).

Acknowledgments

WG thanks Yangzhou University for the international academic exchange funding and the support of the Postgraduate Research Innovation Program of Jiangsu Province (KYCX21_3259).

Conflict of interest

The authors declare that the research was conducted in the absence of any commercial or financial relationships that could be construed as a potential conflict of interest.

Publisher's note

References

Abdelraheem, E. M., Hassan, S. M., Arief, M. M., and Mohammad, S. G. (2015). Validation of quantitative method for azoxystrobin residues in green beans and peas. *Food Chem.* 182, 246–250. doi:10.1016/j.foodchem.2015.02.106

Baumann, C., Wang, X., Yang, L., and Viveiros, M. M. (2017). Error-prone meiotic division and subfertility in mice with oocyte-conditional knockdown of pericentrin. *J. Cell. Sci.* 130, 1251–1262. doi:10.1242/jcs.196188

Cajas, Y. N., Cañón-Beltrán, K., Ladrón De Guevara, M., Millán De La Blanca, M. G., Ramos-Ibeas, P., Gutiérrez-Adán, A., et al. (2020). Antioxidant nobiletin enhances oocyte maturation and subsequent embryo development and quality. *Int. J. Mol. Sci.* 21, E5340. doi:10.3390/ijms21155340

Cao, F., Li, H., Zhao, F., Wu, P., Qian, L., Huang, L., et al. (2019). Parental exposure to azoxystrobin causes developmental effects and disrupts gene expression in F1 embryonic zebrafish (*Danio rerio*). *Sci. Total Environ.* 646, 595–605. doi:10.1016/j.scitotenv.2018.07.331

Cao, M., Wang, Y., Yang, F., Li, J., and Qin, X. (2021). Melatonin rescues the reproductive toxicity of low-dose glyphosate-based herbicide during mouse oocyte maturation via the GPER signaling pathway. *J. Pineal Res.* 70, e12718. doi:10.1111/jpi.12718

Chen, H., Li, L., Lu, Y., Shen, Y., Zhang, M., Ge, L., et al. (2020). Azoxystrobin reduces oral carcinogenesis by suppressing mitochondrial complex III activity and inducing apoptosis. *Cancer Manag. Res.* 12, 11573–11583. doi:10.2147/CMAR.S280285

Clift, D., and Schuh, M. (2015). A three-step MTOC fragmentation mechanism facilitates bipolar spindle assembly in mouse oocytes. *Nat. Commun.* 6, 7217. doi:10.1038/ncomms8217

Cooper, E. M., Rushing, R., Hoffman, K., Phillips, A. L., Hammel, S. C., Zylka, M. J., et al. (2020). Strobilurin fungicides in house dust: Is wallboard a source? *J. Expo. Sci. Environ. Epidemiol.* 30, 247–252. doi:10.1038/s41370-019-0180-z

Dalton, C. M., and Carroll, J. (2013). Biased inheritance of mitochondria during asymmetric cell division in the mouse oocyte. *J. Cell. Sci.* 126, 2955–2964. doi:10.1242/jcs.128744

Efsa (2010). Peer review report to the conclusion regarding the peer review of the pesticide risk assessment of the active substance azoxystrobin. *EFSA J.* 8, 1542.

El-Hak, H. N. G., Al-Eisa, R. A., Ryad, L., Halawa, E., and El-Shenawy, N. S. (2022). Mechanisms and histopathological impacts of acetamiprid and azoxystrobin in male rats. *Environ. Sci. Pollut. Res. Int.* 29, 43114–43125. doi:10.1007/s11356-021-18331-3

Galano, A., Tan, D. X., and Reiter, R. J. (2011). Melatonin as a natural ally against oxidative stress: A physicochemical examination. *J. Pineal Res.* 51, 1–16. doi:10.1111/j.1600-079X.2011.00916.x

Ge, W., Li, L., Dyce, P. W., De Felici, M., and Shen, W. (2019). Establishment and depletion of the ovarian reserve: Physiology and impact of environmental chemicals. *Cell. Mol. Life Sci.* 76, 1729–1746. doi:10.1007/s00018-019-03028-1

Hu, W., Liu, C. W., Jiménez, J. A., Mccoy, E. S., Hsiao, Y. C., Lin, W., et al. (2022). Detection of azoxystrobin fungicide and metabolite azoxystrobin-acid in pregnant women and children, estimation of daily intake, and evaluation of placental and lactational transfer in mice. *Environ. Health Perspect.* 130, 27013. doi:10.1289/EHP9808

Imura, N., Ae, M., Hoshino, R., Abe, M., Yamamuro, T., Oyama, K., et al. (2019). Membrane hyperpolarization and depolarization of rat thymocytes by azoxystrobin, a post harvest fungicide. *Chem. Biol. Interact.* 300, 35–39. doi:10.1016/j.cbi.2019.01.006

Inoue, K., Tsurumi, T., Ishii, H., Park, P., and Ikeda, K. (2012). Cytological evaluation of the effect of azoxystrobin and alternative oxidase inhibitors in Botrytis cinerea. *FEMS Microbiol. Lett.* 326, 83–90. doi:10.1111/j.1574-6968.2011.02438.x

Jiang, Y., Shi, H., Liu, Y., Zhao, S., Zhao, H., Wang, Y., et al. (2021). Preparation of gold nanoparticles and its effect on autophagy and oxidative stress in chronic kidney disease cell model. *J. Nanosci. Nanotechnol.* 2021, 1266–1271. doi:10.1166/jnn.2021.18655

Kang, J., Bishayee, K., and Huh, S. O. (2021). Azoxystrobin impairs neuronal migration and induces ROS dependent apoptosis in cortical neurons. *Int. J. Mol. Sci.* 22, 12495. doi:10.3390/ijms222212495

Kim, J. H., Campbell, B. C., Mahoney, N., Chan, K. L., Molyneux, R. J., and May, G. S. (2007). Enhanced activity of strobilurin and fludioxonil by using berberine and phenolic compounds to target fungal antioxidative stress response. *Lett. Appl. Microbiol.* 45, 134–141. doi:10.1111/j.1472-765X.2007.02159.x

Kirillova, A., Smitz, J. E. J., Sukhikh, G. T., and Mazunin, I. (2021). The role of mitochondria in oocyte maturation. *Cells* 10, 2484. doi:10.3390/cells10092484

Kumar, N., Willis, A., Satbhai, K., Ramalingam, L., Schmitt, C., Moustaid-Moussa, N., et al. (2020). Developmental toxicity in embryo-larval zebrafish (*Danio rerio*) exposed to strobilurin fungicides (azoxystrobin and pyraclostrobin). *Chemosphere* 241, 124980. doi:10.1016/j.chemosphere.2019.124980

Lee, I. W., Jo, Y. J., Jung, S. M., Wang, H. Y., Kim, N. H., and Namgoong, S. (2018). Distinct roles of Cep192 and Cep152 in acentriolar MTOCs and spindle formation during mouse oocyte maturation. *Faseb J.* 32, 625–638. doi:10.1096/fj.201700559RR

Leem, J., Kim, S., Kim, J. S., and Oh, J. S. (2022). ROS-independent cytotoxicity of 9, 10-phenanthrenequinone inhibits cell cycle progression and spindle assembly during meiotic maturation in mouse oocytes. *J. Hazard. Mat.* 436, 129248. doi:10.1016/j.jhazmat.2022.129248

Londoño-Vásquez, D., Rodriguez-Lukey, K., Behura, S. K., and Balboula, A. Z. (2022). Microtubule organizing centers regulate spindle positioning in mouse oocytes. *Dev. Cell.* 57, 197–211.e3. e193. doi:10.1016/j.devcel.2021.12.011

Manandhar, G., Schatten, H., and Sutovsky, P. (2005). Centrosome reduction during gametogenesis and its significance. *Biol. Reprod.* 72, 2–13. doi:10.1095/biolreprod.104.031245

Meyer, J. N., Leung, M. C., Rooney, J. P., Sendoel, A., Hengartner, M. O., Kisby, G. E., et al. (2013). Mitochondria as a target of environmental toxicants. *Toxicol. Sci.* 134, 1–17. doi:10.1093/toxsci/kft102

Mogessie, B., Scheffler, K., and Schuh, M. (2018). Assembly and positioning of the oocyte meiotic spindle. *Annu. Rev. Cell. Dev. Biol.* 34, 381–403. doi:10.1146/annurev-cellbio-100616-060553

Namgoong, S., and Kim, N. H. (2018). Meiotic spindle formation in mammalian oocytes: Implications for human infertility. *Biol. Reprod.* 98, 153–161. doi:10.1093/biolre/iox145

Ou, X. H., Li, S., Xu, B. Z., Wang, Z. B., Quan, S., Li, M., et al. (2010). p38α MAPK is a MTOC-associated protein regulating spindle assembly, spindle length and accurate chromosome segregation during mouse oocyte meiotic maturation. *Cell. Cycle* 9, 4130–4143. doi:10.4161/cc.9.20.13389

Pang, Y. W., Sun, Y. Q., Sun, W. J., Du, W. H., Hao, H. S., Zhao, S. J., et al. (2016). Melatonin inhibits paraquat-induced cell death in bovine preimplantation embryos. *J. Pineal Res.* 60, 155–166. doi:10.1111/jpi.12297

Park, B. K., Kwon, S. H., Yeom, M. S., Joo, K. S., and Heo, M. J. (2022). Detection of pesticide residues and risk assessment from the local fruits and vegetables in Incheon, Korea. *Sci. Rep.* 12, 9613. doi:10.1038/s41598-022-13576-5

Pearson, B. L., Simon, J. M., Mccoy, E. S., Salazar, G., Fragola, G., and Zylka, M. J. (2016). Identification of chemicals that mimic transcriptional changes associated with autism, brain aging and neurodegeneration. *Nat. Commun.* 7, 11173. doi:10.1038/ncomms11173

Pellizzari, E. D., Woodruff, T. J., Boyles, R. R., Kannan, K., Beamer, P. I., Buckley, J. P., et al. (2019). Erratum: "Identifying and prioritizing chemicals with uncertain burden of exposure: Opportunities for biomonitoring and health-related research". *Environ. Health Perspect.* 127, 19002. doi:10.1289/EHP6769

Radford, S. J., Nguyen, A. L., Schindler, K., and Mckim, K. S. (2017). The chromosomal basis of meiotic acentrosomal spindle assembly and function in oocytes. *Chromosoma* 126, 351–364. doi:10.1007/s00412-016-0618-1

Rodrigues, E. T., Lopes, I., and Pardal, M. (2013). Occurrence, fate and effects of azoxystrobin in aquatic ecosystems: A review. *Environ. Int.* 53, 18–28. doi:10.1016/j.envint.2012.12.005

Sathananthan, A. H., and Trounson, A. O. (2000). Mitochondrial morphology during preimplantational human embryogenesis. *Hum. Reprod.* 15, 148–159. doi:10.1093/humrep/15.suppl_2.148

Schuh, M., and Ellenberg, J. (2007). Self-organization of MTOCs replaces centrosome function during acentrosomal spindle assembly in live mouse oocytes. *Cell.* 130, 484–498. doi:10.1016/j.cell.2007.06.025

Shi, X. K., Bian, X. B., Huang, T., Wen, B., Zhao, L., Mu, H. X., et al. (2017). Azoxystrobin induces apoptosis of human esophageal squamous cell carcinoma KYSE-150 cells through triggering of the mitochondrial pathway. *Front. Pharmacol.* 8, 277. doi:10.3389/fphar.2017.00277

Simon, J. M., Paranjape, S. R., Wolter, J. M., Salazar, G., and Zylka, M. J. (2019). High-throughput screening and classification of chemicals and their effects on neuronal gene expression using RASL-seq. *Sci. Rep.* 9, 4529. doi:10.1038/s41598-019-39016-5

Tamura, H., Takasaki, A., Taketani, T., Tanabe, M., Kizuka, F., Lee, L., et al. (2012). The role of melatonin as an antioxidant in the follicle. *J. Ovarian Res.* 5, 5. doi:10.1186/1757-2215-5-5

Usgs (2018). *Estimated annual agricultural pesticide use.* Lawrenceville: Azoxystrobin.

Wang, F., Li, X., Yu, S., He, S., Cao, D., Yao, S., et al. (2021a). Chemical factors affecting uptake and translocation of six pesticides in soil by maize (Zea mays L.). *J. Hazard. Mat.* 405, 124269. doi:10.1016/j.jhazmat.2020.124269

Wang, H., Choe, M. H., Lee, I. W., Namgoong, S., Kim, J. S., Kim, N. H., et al. (2017). CIP2A acts as a scaffold for CEP192-mediated microtubule organizing center assembly by recruiting Plk1 and aurora A during meiotic maturation. *Development* 144, 3829–3839. doi:10.1242/dev.158584

Wang, X., Baumann, C., De La Fuente, R., and Viveiros, M. M. (2021b). Loss of acentriolar MTOCs disrupts spindle pole Aurora A and assembly of the liquid-like meiotic spindle domain in oocytes. *J. Cell. Sci.* 134, jcs256297. doi:10.1242/jcs.256297

Wang, X. H., Yin, S., Ou, X. H., and Luo, S. M. (2020). Increase of mitochondria surrounding spindle causes mouse oocytes arrested at metaphase I stage. *Biochem. Biophys. Res. Commun.* 527, 1043–1049. doi:10.1016/j.bbrc.2020.05.037

Wittmann, T., Hyman, A., and Desai, A. (2001). The spindle: A dynamic assembly of microtubules and motors. *Nat. Cell. Biol.* 3, E28–E34. doi:10.1038/35050669

Xing, C. H., Wang, Y., Liu, J. C., Pan, Z. N., Zhang, H. L., Sun, S. C., et al. (2021). Melatonin reverses mitochondria dysfunction and oxidative stress-induced apoptosis of Sudan I-exposed mouse oocytes. *Ecotoxicol. Environ. Saf.* 225, 112783. doi:10.1016/j.ecoenv.2021.112783

Yin, H., Zhang, T., Wang, H., Hu, X., Hou, X., Fang, X., et al. (2021). Echinoderm microtubule associated protein like 1 is indispensable for oocyte spindle assembly and meiotic progression in mice. *Front. Cell. Dev. Biol.* 9, 687522. doi:10.3389/fcell.2021.687522

Yu, Y., Dumollard, R., Rossbach, A., Lai, F. A., and Swann, K. (2010). Redistribution of mitochondria leads to bursts of ATP production during spontaneous mouse oocyte maturation. *J. Cell. Physiol.* 224, 672–680. doi:10.1002/jcp.22171

Zhang, H. M., and Zhang, Y. (2014). Melatonin: A well-documented antioxidant with conditional pro-oxidant actions. *J. Pineal Res.* 57, 131–146. doi:10.1111/jpi.12162

Zhang, S. X., Ding, Z. M., Ahmad, M. J., Wang, Y. S., Duan, Z. Q., Miao, Y. L., et al. (2020). Bisphenol B exposure disrupts mouse oocyte meiotic maturation *in vitro* through affecting spindle assembly and chromosome alignment. *Front. Cell. Dev. Biol.* 8, 616771. doi:10.3389/fcell.2020.616771

frontiers | Frontiers in Cell and Developmental Biology

TYPE Methods
PUBLISHED 19 January 2023
DOI 10.3389/fcell.2023.1010306

OPEN ACCESS

EDITED BY
Rafael A. Fissore,
University of Massachusetts Amherst,
United States

REVIEWED BY
Pascale Lybaert,
Université libre de Bruxelles, Belgium
Gunda Georg,
University of Minnesota Twin Cities,
United States
Nadine Mundt,
University of California, San Francisco,
United States

*CORRESPONDENCE
Guillermina M. Luque,
gmluque@ibyme.conicet.gov.ar
Mariano G. Buffone,
mgbuffone@ibyme.conicet.gov.ar

SPECIALTY SECTION
This article was submitted to Molecular and Cellular Reproduction, a section of the journal Frontiers in Cell and Developmental Biology

RECEIVED 02 August 2022
ACCEPTED 09 January 2023
PUBLISHED 19 January 2023

CITATION
Luque GM, Schiavi-Ehrenhaus LJ, Jabloñski M, Balestrini PA, Novero AG, Torres NI, Osycka-Salut CE, Darszon A, Krapf D and Buffone MG (2023), High-throughput screening method for discovering CatSper inhibitors using membrane depolarization caused by external calcium chelation and fluorescent cell barcoding.
Front. Cell Dev. Biol. 11:1010306.
doi: 10.3389/fcell.2023.1010306

High-throughput screening method for discovering CatSper inhibitors using membrane depolarization caused by external calcium chelation and fluorescent cell barcoding

Guillermina M. Luque[1]*, Liza J. Schiavi-Ehrenhaus[1], Martina Jabloñski[1], Paula A. Balestrini[1], Analia G. Novero[2], Nicolás I. Torres[1], Claudia E. Osycka-Salut[3], Alberto Darszon[4], Dario Krapf[2] and Mariano G. Buffone[1]*

[1]Instituto de Biología y Medicina Experimental (IBYME-CONICET), Buenos Aires, Argentina, [2]Instituto de Biología Molecular y Celular de Rosario (CONICET-UNR), Rosario, Santa Fe, Argentina, [3]Instituto de Investigaciones Biotecnológicas, Universidad Nacional de San Martín (UNSAM-CONICET), Buenos Aires, Argentina, [4]Instituto de Biotecnología, UNAM, Cuernavaca, Mexico

The exclusive expression of CatSper in sperm and its critical role in sperm function makes this channel an attractive target for contraception. The strategy of blocking CatSper as a male, non-hormonal contraceptive has not been fully explored due to the lack of robust screening methods to discover novel and specific inhibitors. The reason for this lack of appropriate methodology is the structural and functional complexity of this channel. We have developed a high-throughput method to screen drugs with the capacity to block CatSper in mammalian sperm. The assay is based on removing external free divalent cations by chelation, inducing CatSper to efficiently conduct monovalent cations. Since Na^+ is highly concentrated in the extracellular milieu, a sudden influx depolarizes the cell. Using CatSper1 KO sperm we demonstrated that this depolarization depends on CatSper function. A membrane potential (Em) assay was combined with fluorescent cell barcoding (FCB), enabling higher throughput flow cytometry based on unique fluorescent signatures of different sperm samples. These differentially labeled samples incubated in distinct experimental conditions can be combined into one tube for simultaneous acquisition. In this way, acquisition times are highly reduced, which is essential to perform larger screening experiments for drug discovery using live cells. Altogether, a simple strategy for assessing CatSper was validated, and this assay was used to develop a high-throughput drug screening for new CatSper blockers.

KEYWORDS

male contraceptive, membrane potential (EM), sperm, non-hormonal, blocker

Introduction

After ejaculation, sperm acquire the ability to fertilize in the female genital tract in a time-dependent process called capacitation (Chang, 1951; Austin, 1952). During capacitation, sperm undergo a change in the motility pattern into a more vigorous one, with a high-amplitude and asymmetric flagellar beating called hyperactivation (HA), which is critical for fertilization

(Demott and Suarez, 1992; Stauss et al., 1995; Suarez and Ho, 2003). HA requires a Ca^{2+} uptake through the sperm-specific CatSper channel complex (Ren et al., 2001).

CatSper is one of the most complex ion channels characterized at the moment, both structurally and functionally. It comprises multiple subunits; the pore is formed by four homologous subunits: CatSper α 1–4 (Navarro et al., 2008; Kirichok and Lishko, 2011), that are accompanied by several auxiliary subunits: CatSper β, CatSper ɣ, CatSper δ (Liu et al., 2007; Wang et al., 2009; Chung et al., 2011), CatSper ε, CatSper ζ, EFCAB9 (Chung et al., 2017; Hwang et al., 2019) and the most recently described CatSper τ (Hwang et al., 2022; Yang et al., 2022), CatSper η, SLCO6C1 and TMEM249 (Zhao et al., 2022). Multiple testis-specific genes encode these CatSper proteins, which localize in the plasma membrane of the principal piece of mature sperm (Quill et al., 2001; Ren et al., 2001; Lobley et al., 2003; Hwang et al., 2022; Yang et al., 2022), except for CatSper ζ and EFCAB9, which are small-soluble proteins (Chung et al., 2017; Hwang et al., 2019). In addition, CatSper proteins form a unique pattern of four columns of Ca^{2+} signaling nanodomains in the plasma membrane, along the principal piece of the flagellum (Chung et al., 2014; Chung et al., 2017; Hwang et al., 2019). Sperm derived from mice lacking any of the CatSper α 1–4 genes (Ren et al., 2001; Quill et al., 2003; Qi et al., 2007) as well as human males with mutations affecting CatSper function (Avidan et al., 2003; Avenarius et al., 2009; Smith et al., 2013) are unable to hyperactivate and therefore infertile.

Furthermore, there might be species-specific adaptations of CatSper to adjust to a distinct set of stimulators within the female reproductive tract (Lishko and Mannowetz, 2018). In both rodents and primates, CatSper channels are strongly activated by intracellular alkalinization (Kirichok et al., 2006; Lishko et al., 2010), while only in primates exogenous compounds such as progesterone and prostaglandins also behave as activators (Lishko et al., 2011; Miller et al., 2015).

Since its discovery, CatSper has been considered an attractive target for male contraception because it is critical for sperm motility and is only expressed in sperm. However, the strategy of using CatSper to find a male contraceptive has not been fully implemented so far. The complex structural organization of CatSper has impeded its heterologous reconstitution and therefore the study of its regulation *in vitro*. Currently, the only accurate and specific method to evaluate CatSper function relies on patch clamp techniques. Although this approach univocally and specifically assesses CatSper function, it is time-consuming and requires sophisticated equipment and well-trained personnel. This technical limitation has hindered the development of powerful screening methods for drug discovery. However, recent advances have started to overcome this problem. For example, the rise in intracellular Ca^{2+} concentration ($[Ca^{2+}]_i$) after exposure to an alkaline-high K^+ solution was evaluated as an indirect measure of CatSper function in a high-throughput drug screening (Carlson et al., 2022). Here, we propose an alternative method to specifically evaluate CatSper opening. We developed a method based on the combination of two remarkable tools: 1) the fluorescent cell barcoding (FCB) approach using flow cytometry; 2) the membrane potential (Em) assay. This powerful combination will be used to develop a high-throughput screening method for CatSper channels blockers.

FCB enables high-throughput flow cytometry increasing data robustness as well as minimizing reagent consumption (Krutzik and Nolan, 2006; Krutzik et al., 2011). This technique encodes different cell samples with a unique fluorescent signature before mixing these samples in a single tube for simultaneous data acquisition. Therefore, differences in staining volume and probes concentration that result in sample-to-sample variation are eliminated while reducing acquisition times. This enables entire 96 well plates to be run in ~10 min. Altogether, these advantages makes FCB suitable to perform larger screening experiments for drug discovery (Krutzik et al., 2011). Up to now, this powerful technique has never been used to evaluate new drugs in mammalian sperm.

In FCB, cells labeled with unique signatures or "barcodes" of fluorescent dyes are exposed to distinct compounds from a library. The fluorescent dyes used in FCB are *N*-hydroxysuccinimide-derived, meaning reactive to amine functional groups (forming stable amide bonds) located mainly at the N-terminus and on protein lysine side chains. Cell samples with unique dye intensity distributions are obtained due to staining each of them with different concentrations of reactive fluorescent dye. Mixing differentially labeled samples into a single tube for probe staining and subsequent data acquisition is possible since the reacted dye is covalently attached to the cells enabling the non-reacted dye to be washed away. Each sample is distinguishable in the subsequent software analysis based on their fluorescence intensity in each barcoding channel (Krutzik et al., 2011).

The Em assay is based on the removal of external divalent cations by EGTA allowing CatSper to efficiently conduct monovalent cations (Kirichok et al., 2006). The magnitude of the Na^+ influx that depolarizes the cells depends on the extent of CatSper opening (Espinosa and Darszon, 1995; Torres-Flores et al., 2011). This simple CatSper function assay has not been extensively used due to the fact that it was only validated using the non-selective pharmacological CatSper inhibitors available (Torres-Flores et al., 2011; Ernesto et al., 2015). Using CatSper1 KO sperm, we demonstrate for the first time that the depolarization induced by EGTA addition is strongly CatSper dependent.

In the present work, a simple strategy for assessing CatSper was validated, and this assay was used to develop a high-throughput drug screening for new CatSper blockers.

Materials and methods

Reagents

Chemicals were obtained from the following sources: bovine serum albumin (BSA) A7906 and ethylene glycol-bis (2-aminoethylether)-N,N,N,N'tetraacetic acid (EGTA) were purchased from Sigma-Aldrich (St. Louis, MO, United States), while HC-056456 from MedKoo Biosciences (Morrisville, NC, United States). Fluo-4 AM, 3,3-dipropylthiadicarbocyanine iodide ($DiSC_3(5)$), CellTrace™ CFSE (C34554), CellTrace™ Violet (C34557), and pluronic acid from Invitrogen, Thermo Fisher Scientific (Waltham, MA, United States); while propidium iodide (PI) from Santa Cruz Biotechnology (Dallas, TX, United States). FDA-Approved Drug Library Mini (HY-L022M) was purchased from MedChemExpress (Monmouth Junction, NJ, United States). RU 1968 was kindly provided by Dr. Timo Strünker. HC-056456, RU 1968, Fluo-4 AM, $DiSC_3(5)$, CellTrace™ CFSE, CellTrace™ Violet, and pluronic acid were dissolved in DMSO; EGTA and PI were dissolved in hexa-distilled water.

Animals

Hybrid F1 (BALB/c female × C57BL/6 male) mature (10–12 weeks-old) male mice were used for all the experiments involving FCB. CatSper1 KO (Ren et al., 2001) mice and their corresponding heterozygous (HET) siblings (C57BL/6) mature (10–12 weeks-old) male mice were also used. We have established a colony of CatSper1 KO and CatSper1 HET mice in our laboratory from founders kindly provided by Dr. Celia Santi, who obtained them from Jackson Laboratory. In one supplementary experiment, wild-type C57BL/6 mature (10–12 weeks-old) male mice were used. In all cases, mice were housed in groups of 4 or 5 in a temperature-controlled room (23°C) with lights on at 07:00 a.m. and off at 07:00 p.m. and had free access to tap water and laboratory rodent chow. All experimental procedures were carried out according to institutional animal care guidelines and were reviewed and approved by the Ethical Committees of the Instituto de Biología y Medicina Experimental, Buenos Aires #32/2021. Experiments were performed strictly following the Guide for Care and Use of Laboratory Animals approved by the National Institutes of Health (NIH).

Sperm capacitation

The non-capacitating medium (NC medium) used in this study was a modified Toyoda–Yokoyama–Hosi (TYH) containing 119.3 mM NaCl, 4.7 mM KCl, 1.71 mM $CaCl_2.2H_2O$, 1.2 mM KH_2PO_4, 1.2 mM $MgSO_4.7H_2O$, 0.51 mM sodium pyruvate, 5.56 mM glucose, 20 mM HEPES and 10 μg/ml gentamicin (NC TYH medium). For capacitating conditions, 15 mM $NaHCO_3$ and 5 mg/ml BSA were added (CAP TYH medium). In all cases, pH was adjusted to 7.4 with NaOH.

Animals were euthanized and both cauda epididymis were placed in 1 ml of NC TYH medium (without $NaHCO_3$ and BSA). After 15 min of incubation at 37°C (swim-out), epididymis were removed, and sperm concentration was determined with a Neubauer chamber (1:20 dilution of swim-out sperm suspension with distilled water). Then, sperm concentration was adjusted to reach a final maximum concentration of 1×10^7 cells/ml in a final volume of 100 μl of NC medium. An equal volume (100 μl) of NC or two-fold concentrated CAP medium (CAP 2X: 30 mM $NaHCO_3$ and 10 mg/ml BSA) was added. Finally, sperm were incubated for 90 min at 37°C.

Determination of $[Ca^{2+}]_i$ by flow cytometry

Sperm $[Ca^{2+}]_i$ was assessed using Fluo-4 AM as previously described (Luque et al., 2018). Briefly, after incubation in the appropriate medium, samples were washed by centrifugation, the supernatant discarded and resuspended in NC medium containing 1 μM Fluo-4 AM and 0.02% pluronic acid for 20 min at 37°C. Samples were washed again and resuspended in NC medium. Before collecting data, 3 μM of PI was added to monitor viability. Data were recorded as individual cellular events using a BD FACSCanto II TM cytometer (Biosciences; Becton, Dickinson and Company). Side-scatter area (SSC-A) and forward-scatter area (FSC-A) data were collected from 20,000 events per sample in order to define sperm population as previously described (Escoffier et al., 2012). In all cases, doublet exclusion was performed by analyzing two-dimensional dot plot FSC-A vs. forward-scatter height (FSC-H). Positive cells for Fluo-4 were collected using the filter for fluorescein isothiocyanate (FITC; 530/30), and for PI the filter for peridinin chlorophyll protein complex (PerCP; 670LP) was used. The two indicators had minimal emission overlap, but compensation was still done using single-stained controls. Data were analyzed using FlowJo software (V10.0.7).

CatSper opening through determination of Em by flow cytometry

Sperm Em changes were assessed using $DiSC_3(5)$ respectively as previously described (Puga Molina et al., 2018). Briefly, after incubation in the appropriate medium, 50 nM $DiSC_3(5)$ was added. CatSper inhibitors (HC-056456 or RU 1968) or vehicle were used, prior dye loading, when required. In these experiments $DiSC_3(5)$ was not washed. Before collecting data, 3 μM of PI was added to monitor viability. Data were recorded as individual cellular events using a BD FACSCanto II TM cytometer (Biosciences; Becton, Dickinson and Company). First, basal Em was obtained after 30 s of continuous recording. Afterwards, Ca^{2+} was chelated with 3.5 mM of EGTA (pH adjusted with NaOH to ~10 so that media pH does not change upon H^+ release in exchange for Ca^{2+}) to a value of free Ca^{2+} of 138 nM (MaxChelator) (Patton et al., 2004), and acquisition continued for additional 150 s. The sperm population was gated and doublet exclusion was performed as described above for $[Ca^{2+}]_i$ measurements. Positive cells for $DiSC_3(5)$ were collected using the filter for allophycocyanine (APC; 660/20), and for PI the filter for peridinin chlorophyll protein complex (PerCP; 670LP) was used. Compensation was done. Data were analyzed using FlowJo software (V10.0.7). Finally, $DiSC_3(5)$ fluorescence mean was determined in the sperm population with higher $DiSC_3(5)$ fluorescence before (time = 0 s) and after addition of 3.5 mM EGTA. In each condition, the fluorescence mean was normalized to the basal fluorescence (0 s).

CatSper opening through determination of Em by spectrofluorometer

Sperm Em changes were assessed using $DiSC_3(5)$, as previously described (Ritagliati et al., 2018). Cells were loaded with 1 μM of the Em-sensitive dye $DiSC_3(5)$ for 2 min. An incubation with CatSper inhibitor (10 μM HC-056456) or vehicle was conducted, prior dye loading, when required. Sperm were transferred to a gently stirred cuvette at 37°C, and the fluorescence was monitored with a Varian Cary Eclipse fluorescence spectrophotometer at 620/670 nm excitation/emission wavelengths. CCCP (0.5 μM) was added as mitochondrial un-coupler to avoid mitochondrial contribution to recorded Em. Recordings were initiated when steady-state fluorescence was reached. Ca^{2+} was chelated with 3.5 mM of EGTA (pH adjusted with NaOH to ~10 so that media pH does not change upon H^+ release in exchange for Ca^{2+}) to a value of free Ca^{2+} of 138 nM (MaxChelator) (Patton et al., 2004). The fluorescence change after EGTA addition was presented as ΔAFU (delta arbitrary fluorescence units), $F_{EGTA} - F_R$, where F_{EGTA} represents fluorescence intensity after EGTA addition and F_R is the mean of 1 min of acquisition before the addition of EGTA (Torres-Flores et al., 2011; Ernesto et al., 2015). We wait for

~1 min after EGTA addition to get a stable signal and that point is used for calculation (F_{EGTA}). A normalization to the mean obtained in the control condition (CatSper1 HET or NC) was used.

FCB protocol in combination with Em assay by flow cytometry

Preparation of the plate with reagents

A library of compounds was used. These drugs were provided either in DMSO or aqueous medium at a concentration of 10 mM. After the appropriate intermediate dilution (0.19 mM), a volume of 5 µl was added to each well to reach a final concentration of 10 µM.

Preparation of the cells

Cells were obtained by swim-out as previously described.

Preparation of the barcoding dyes

Two different dyes were used to produce 12 barcodes: three increasing concentrations of CellTrace™ CFSE (C34554) in combination with four increasing concentrations of CellTrace™ Violet (C34557).

In 1.5 ml microcentrifuge tubes, a three-fold serial dilution of the 5 mM stock solution of CellTrace™ CFSE (in DMSO) was performed in NC TYH medium to generate solutions at the following concentrations (3X of the final concentration that will be used to barcode the cells): CellTrace™ CFSE tube 1: 0.003 µM (final concentration 0.001 µM); CellTrace™ CFSE tube 2: 0.75 µM (final concentration 0.25 µM); CellTrace™ CFSE tube 3: 3 µM (final concentration 1 µM).

In 1.5 ml microcentrifuge tubes, a four-fold serial dilution of the 5 mM stock solution of CellTrace™ Violet (in DMSO) was performed in NC TYH medium to generate solutions at the following concentrations (3X of the final concentration that will be used to barcode the cells): CellTrace™ Violet tube 1: 0.075 µM (final concentration 0.025 µM); CellTrace™ Violet tube 2: 3 µM (final concentration 1 µM); CellTrace™ Violet tube 3: 15 µM (final concentration 5 µM); CellTrace™ Violet tube 4: 60 µM (final concentration 20 µM).

Thirty µl of each corresponding FCB dye was added to each well.

Different lots of fluorescent dyes or probes may have distinct levels of reactivity, so it is recommended that every time a new batch is opened to be tested and optimized before use.

Addition of samples to each barcoding dye combination

A volume of 30 µl of sperm suspension at a final concentration between 20–30 × 10^6/ml was added to each well carefully, submerging the pipette tip in the FCB dye solution (Supplementary Figures S1A, B). Sperm concentration was determined with a Neubauer chamber (1:20 dilution of swim-out sperm suspension with distilled water). Every well contained: 30 µl sperm sample + 30 µl CellTrace™ Violet 3X + 30 µl CellTrace™ CFSE 3X + 5 µl compound (final volume 95 µl, with sperm suspension at a final concentration between 6–9 × 10^6/ml in each well). An incubation for 20 min at 37°C in the dark was performed, making sure that the plate was well covered to avoid loss of volume by evaporation. Then, 205 µl of NC TYH medium was added to each well.

Combination of the barcoded samples

Immediately after, barcoded samples were combined by transferring all the volume from each well to a 15 ml tube containing additional 5 ml of warmed NC TYH medium. The total volume was 8.6 ml in the new combined tube (300 µl × 12 + 5 ml). Mouse sperm were washed by centrifugation for 15 min at 700 g at room temperature to remove the excess of unbound dyes. Immediately after centrifugation, without removing supernatant 150 µl of the pellet was transferred to a new 1.5 ml microcentrifuge tube containing 50 µl of $DiSC_3(5)$ 4X (200 nM, final concentration 50 nM).

Flow cytometry acquisition

Before collecting data, 3 µM of PI was added to monitor viability. Data were recorded as individual cellular events using a BD FACSCanto II TM cytometer (Biosciences; Becton, Dickinson and Company). Positive cells for CellTrace™ CFSE were collected using the filter for fluorescein isothiocyanate (FITC; 530/30), for CellTrace™ Violet the filter for Pacific Blue™ AmCyan (450/50), for $DiSC_3(5)$ the filter for allophycocyanine (APC; 660/20) and for PI the filter for peridinin chlorophyll protein complex (PerCP; 670LP) were used.

For CatSper opening assay, after 30 s of continuous recording (basal Em), Ca^{2+} was chelated with 3.5 mM of EGTA to a value of free Ca^{2+} of 138 nM (MaxChelator) (Patton et al., 2004), and acquisition continued for additional 150 s.

Data analysis

In all cases, doublet exclusion was performed by analyzing two-dimensional dot plot FSC-A vs. FSC-H. Compensation was done by performing the appropriate unmixed barcoded samples compensation controls in each experiment. Data were analyzed using FlowJo software (V10.0.7).

Statistical analysis

Statistical analyses were performed using the GraphPad Prism 6 software (La Jolla, CA, United States). Data are expressed as mean ± standard error of the mean (SEM) of at least five independent experiments from different mice for all determinations. The differences between means of only two groups were analyzed using a *t*-test. Two-way analysis of variance (ANOVA) for independent measures was performed to analyze normalized median fluorescence intensity of Fluo-4 and percentage of sperm with high Fluo-4 fluorescence, for the effects of medium × genotype. Post hoc Sidak's test was used when necessary. A probability (p) value of $p < 0.05$ was considered statistically significant. Parametric or non-parametric comparisons were used as dictated by data distribution using D'Agostino and Pearson omnibus normality test.

Results

The membrane potential (Em) assay is a specific and sensitive tool for analyzing CatSper function

The Em sensitive probe, $DiSC_3(5)$, is a positively charged carbocyanine dye that partitions into sperm cells according to their Em but independently on the nature of ionic fluxes, making it suitable

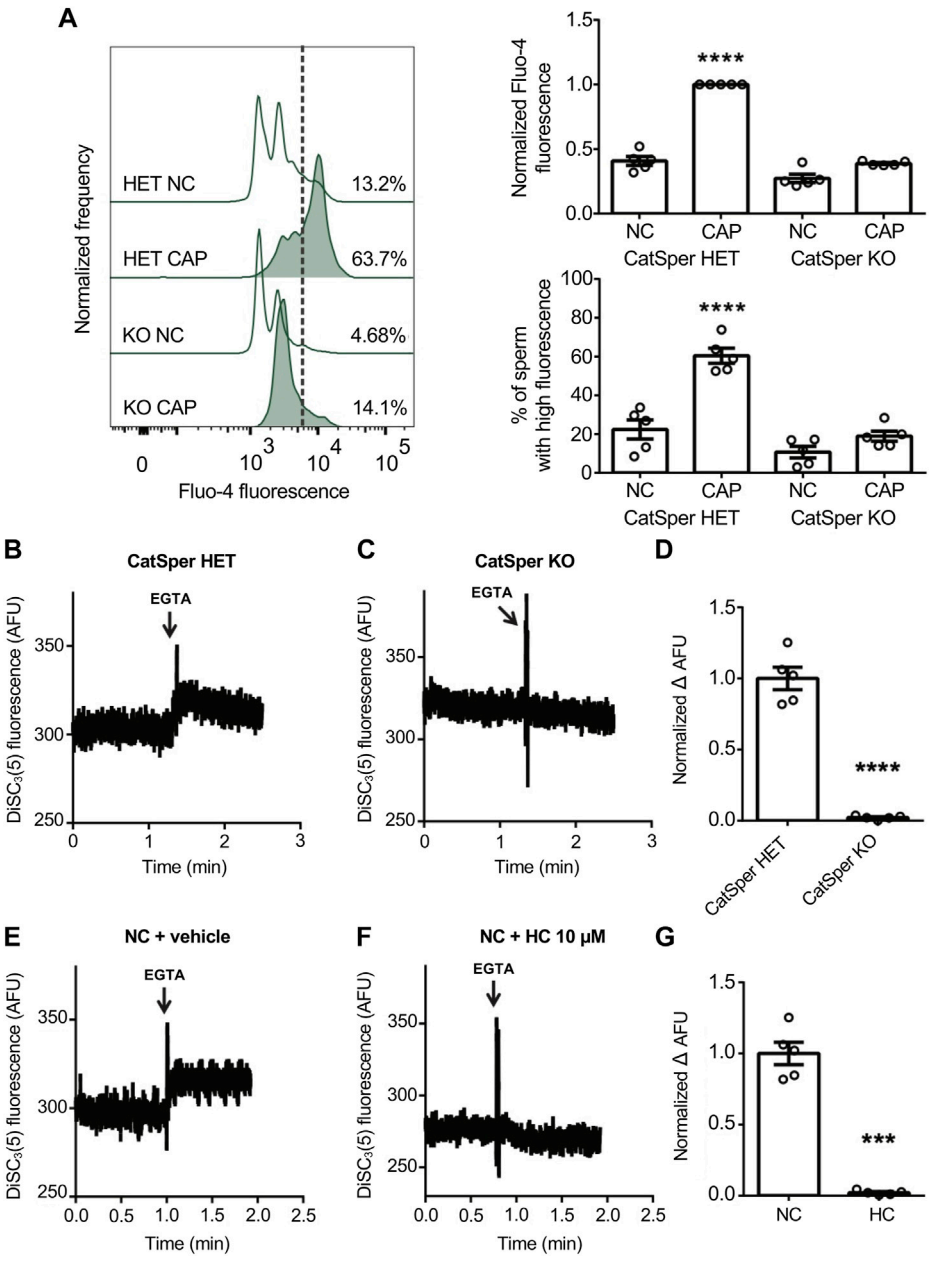

FIGURE 1
CatSper activity was analyzed by measuring Em in a population assay by spectrofluorometry, where extracellular $DiSC_3(5)$ fluorescence was determined. Effect of Ca^{2+} removal by EGTA 3.5 mM addition on NC sperm loaded with 1 µM $DiSC_3(5)$. **(A)** Sperm incubated for 90 min under capacitating conditions (CAP) or non-capacitating conditions (NC) were analyzed. Representative histograms of normalized frequency vs. Fluo-4 fluorescence of non-PI-stained sperm (live), with the corresponding percentage of sperm that increased Fluo-4 fluorescence, are shown. Normalized median fluorescence intensity, compared with the control condition (CatSper1 HET CAP), of Fluo-4. The percentage of sperm that responds by increasing the $[Ca^{2+}]_i$ was established in the CAP control condition (CatSper1 HET CAP) and extrapolated to the other conditions (dashed line). Values represent the mean ± SEM of 5 independent experiments. Two-way ANOVA showed a significant interaction (genotype × medium), $P_{interaction} < 0.001$. ****$p < 0.0001$ represents statistical significance between control (CatSper1 HET CAP condition) and all other conditions. Sidak's multiple comparisons test was performed. **(B, C)** Representative Em recordings are shown: $DiSC_3(5)$ fluorescence traces (AFU: arbitrary fluorescence units) through time in CatSper1 HET **(B)** and CatSper1 KO **(C)** sperm. **(D)** Summary of normalized ΔAFU after EGTA addition (F_{EGTA}) and before (resting: F_R) compared to the mean obtained in the control condition (CatSper1 HET). Data represents the mean ± SEM of 5 independent experiments. ****$p < 0.0001$ represents statistical significance vs. control (CatSper1 HET). Unpaired *t*-test was performed. **(E, F)** Representative Em recordings are shown: $DiSC_3(5)$ fluorescence traces (AFU, arbitrary fluorescence units) through time in control (NC + vehicle) **(E)** and 10 µM HC-056456 **(F)** treated sperm. **(G)** Normalized ΔAFU after EGTA addition (F_{EGTA}) and before (resting: F_R) compared to the mean obtained in the control condition (NC + DMSO). Data represents the mean ± SEM of 5 independent experiments. ***$p < 0.001$ represents statistical significance vs. control (NC + DMSO). Paired *t*-test was performed.

for potential measurements of the plasma membrane. Em measurement with $DiSC_3(5)$ has long been used in mouse sperm being a robust and reproducible technique (Demarco et al., 2003; De La Vega-Beltran et al., 2012; Stival et al., 2015; Ritagliati et al., 2018; Stival et al., 2018; Luque et al., 2021). Em depolarization favors the efflux of dye out of the cell, resulting in an increase of $DiSC_3(5)$

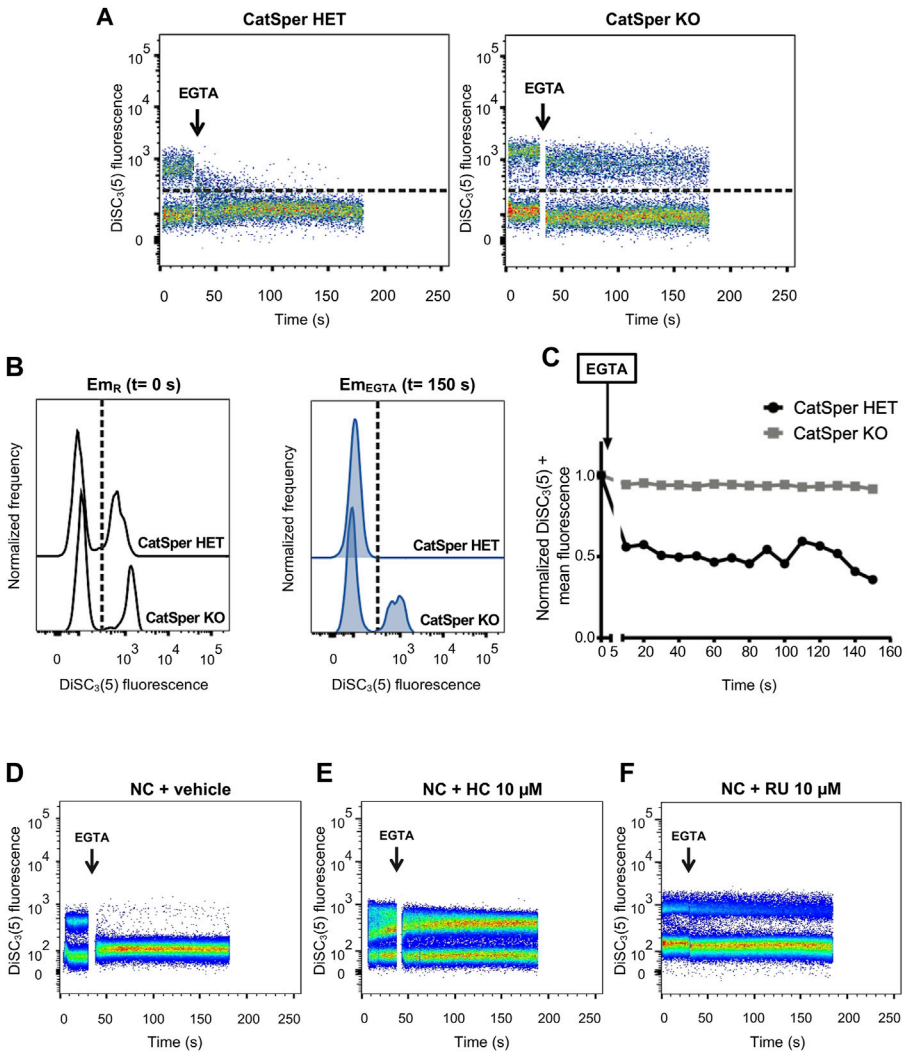

FIGURE 2
CatSper activity was assessed by measuring Em in individual live cells by flow cytometry, where intracellular $DiSC_3(5)$ fluorescence was determined. **(A)** Representative 2D dot plot of $DiSC_3(5)$ fluorescence vs. time (seconds) analysis, from 5 independent experiments, are shown. The addition of 3.5 mM EGTA is indicated using a black arrow. The population of sperm that responds by decreasing the fluorescence values was established in the CatSper1 HET control condition and used as a reference for the other conditions (dashed line). Sperm cells above the dashed line [higher $DiSC_3(5)$ fluorescence] were arbitrarily identified as $DiSC_3(5)$ +. **(B)** Histogram analysis depicting normalized frequency of sperm vs. $DiSC_3(5)$ fluorescence before EGTA addition (resting: Em_R) and after (Em_{EGTA}) were performed for both CatSper1 HET and CatSper1 KO samples. **(C)** $DiSC_3(5)$ fluorescence mean was determined in the sperm population with higher $DiSC_3(5)$ fluorescence: $DiSC_3(5)$ + [dashed line in **(A)**] before (time = 0 s) and after (black arrow) addition of 3.5 mM EGTA. In each condition, the fluorescence mean was normalized to the basal fluorescence (0 s). **(D, F)** Representative 2D dot plot of $DiSC_3(5)$ fluorescence vs. time (seconds) analysis in the absence or presence of pharmacological CatSper blockers. The addition of 3.5 mM EGTA (black arrow) provokes a decrease in the population of sperm with high $DiSC_3(5)$ fluorescence due to Em depolarization in the control condition **(D)** but not in the presence of 10 µM HC-056456 **(E)** or 10 µM RU 1968 **(F)**.

extracellular fluorescence that correlates with a decrease of the intracellular one (Stam et al., 2011; Mei et al., 2015). Previous results from our and other groups employed this approach using CatSper inhibitors (Torres-Flores et al., 2011; Ernesto et al., 2015; Ritagliati et al., 2018; Stival et al., 2018). However, the ultimate validation using sperm from CatSper KO mice was not yet achieved. First, the phenotype of the mice used in the following experiment was corroborated by flow cytometry $[Ca^{2+}]_i$ assessment using the Ca^{2+}-sensitive probe Fluo-4. Under capacitating conditions the absence of the functional CatSper channel (CatSper1 KO) displayed a significant decrease in $[Ca^{2+}]_i$ in comparison with the capacitation-induced rise observed in heterozygous mice (CatSper1 HET) (Figure 1A). This can be visualized by a decrease in the normalized median fluorescence intensity of Fluo-4, as well as in the percentage of sperm that displayed a rise in $[Ca^{2+}]_i$ (Figure 1A). Second, by measuring extracellular $DiSC_3(5)$ fluorescence by spectrofluorometry, it was determined that CatSper1 HET sperm displayed a Em depolarization caused by the rapid Na^+ influx (Figures 1B, D). In contrast, sperm from CatSper1 KO mice failed to increase extracellular $DiSC_3(5)$ fluorescence after the addition of EGTA (Figures 1C, D).

Furthermore, consistent with previous reports using pharmacological CatSper blockers (Ritagliati et al., 2018; Stival et al., 2018), the addition of the CatSper inhibitor HC-056456 in wild-type sperm significantly decreased the magnitude of depolarization (Figures 1E–G).

10.3389/fcell.2023.1010306

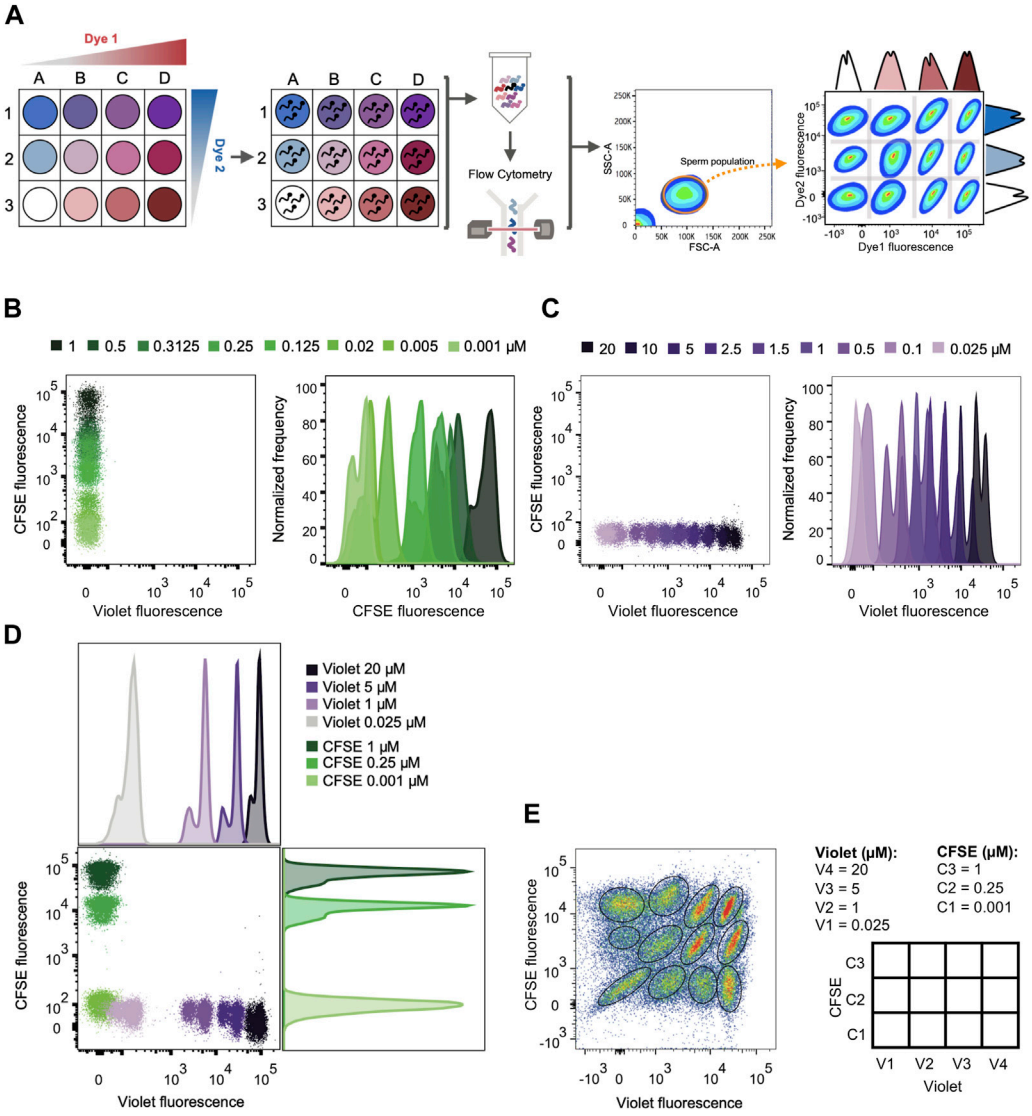

FIGURE 3
FCB set up in mouse sperm. **(A)** Schematic diagram of the high-throughput screening method: First, each well is given one unique fluorescent signature by the combination of dyes used in different concentrations. Second, sperm samples are distributed in the different wells and loaded with a distinct combination of dyes. After loading, all samples are grouped in a single tube and analyzed by flow cytometry. Following data acquisition, a sperm population is selected from all the events. Each sperm sample is able to be distinguished through their corresponding dye fluorescence signature. **(B)** Representative 2D dot plot of CellTrace™ Violet vs. CellTrace™ CFSE fluorescence (left) and representative histograms of normalized frequency vs. CellTrace™ CFSE fluorescence (right). Sperm were incubated with increasing µM concentrations of CellTrace™ CFSE and its fluorescence raised in a dose dependent manner. **(C)** Representative 2D dot plot of CellTrace™ Violet vs. CellTrace™ CFSE fluorescence (left) and representative histograms of normalized frequency vs. CellTrace™ Violet fluorescence (right). Sperm were incubated with increasing µM concentrations of CellTrace™ Violet and its fluorescence raised in a dose dependent manner. **(D)** Representative 2D dot plot of CellTrace™ Violet (Dye 1) vs. CellTrace™ CFSE (Dye 2) fluorescence, with their corresponding histogram analysis depicting normalized frequency of sperm vs. dye fluorescence. The concentrations selected for CellTrace™ Violet and CellTrace™ CFSE are shown, with no overlapping between each other. **(E)** Representative 2D dot plot of CellTrace™ Violet vs. CellTrace™ CFSE fluorescence of a 4 × 3 matrix, where the population of sperm with each dye combination/signature was defined. The diagram with the dye concentration in each well is depicted on the right as a double-entry table.

Determination of CatSper function using flow cytometry

This Em assay was adapted for flow cytometry that has the advantage of discriminating between live and dead sperm, as well as analyzing the intracellular fluorescence in individual cells.

When sperm were loaded with $DiSC_3(5)$ and analyzed by flow cytometry, two clearly distinguishable populations were observed in basal conditions: a subset of cells with low $DiSC_3(5)$ fluorescence that corresponds to sperm with less hyperpolarized Em and another with higher fluorescence representing more hyperpolarized Em sperm (Figures 2A, B).

When CatSper is functionally present (CatSper1 HET), the addition of EGTA promotes that most of the cells (~70%–90%) that displayed high $DiSC_3(5)$ fluorescence migrate to the low fluorescence subset as a result of the depolarization produced by Na^+ influx upon Ca^{2+} chelation (Figures 2A–C). This is not observed when CatSper is absent (CatSper1 KO), in which a population of sperm with high $DiSC_3(5)$ fluorescence remained

detectable after EGTA addition (Figures 2A–C). Similarly, pharmacological inhibition of CatSper using HC-056456 or RU 1968 (Rennhack et al., 2018; Curci et al., 2021) (two well characterized CatSper inhibitors), also prevented the EGTA-induced depolarization (Figures 2D–F). This pharmacological approach was also tested using two different mouse strains, C57BL/6 and hybrid F1 (BALB/c female × C57BL/6 male), and no relevant differences were found (Supplementary Figure S2). In our screening, we have chosen 10 μM HC-056456 as a positive control presented in all the experiments. As shown in Supplementary Figure S3, HC-056456 inhibits CatSper in a concentration-dependent manner.

Fluorescent cell barcoding (FCB) flow cytometry in live mouse sperm

Flow cytometry is a high-content, multiparameter platform that allows the analysis of multiple biosignatures at the single-cell level. FCB dramatically reduces reagent consumption, improves flow cytometry experiments throughput, and eliminates staining variabilities between samples (Krutzik and Nolan, 2006). This technique has been widely used in multiple cellular systems (cell lines and primary cell samples) and for different applications in the development of high-throughput screening methods (Krutzik and Nolan, 2006; Krutzik et al., 2008; Clutter et al., 2010; Irish et al., 2010; Stam et al., 2011; Mei et al., 2015). The FCB method is usually used in fixed and permeabilized cells, although FCB of live cells is possible. As detailed in the diagram of Figure 3A, mouse sperm samples were labeled with different intensities of two FCB markers (namely Dye 1 and Dye 2) by incubation with increasing concentrations of these fluorescent dyes. As a result, each sample was labeled with a unique fluorescent signature. Due to their specific characteristics, FCB markers remain covalently attached to the cells, allowing the combination of these multiple sperm samples in a single analysis tube, from which the acquisition by flow cytometry was performed.

For setting FCB, mouse sperm were stained with two dyes that are compatible with the use of propidium iodide (PI) as a viability marker and $DiSC_3(5)$ as a Em reporter, since their respective spectrum of emission do not overlap and can be easily analyzed by flow cytometry: CellTrace™ CFSE (C34554) and CellTrace™ Violet (C34557). The addition of either dye produced an increase in emission in a concentration-dependent manner (Figures 3B, C). Since the ultimate objective is to identify each sperm sample, 3 concentrations of CellTrace™ CFSE (0.001, 0.25 and 1 μM) were selected in combination with 4 concentrations of CellTrace™ Violet (0.025, 1, 5 and 20 μM), which displayed discrete fluorescent peaks in the histogram (Figure 3D) that can be gated when all the samples were combined (Figure 3E). This combination of dyes allowed us to simultaneously analyze 12 different sperm samples that were clearly identified afterwards (Figure 3E). A maximum concentration of CellTrace™ CFSE 1 μM was used since it was the higher concentration that allowed a proper fluorescence compensation with PI (Supplementary Figure S4).

High-throughput screening method to identify novel compounds that inhibit CatSper channels

To develop a high-throughput method to screen drugs with the capacity to block CatSper channels, FCB flow cytometry in combination with the potentiometric probe $DiSC_3(5)$ as a reporter of Em was employed. The sequence of procedures is summarized in Figure 4, where the process was divided into 8 steps as follows:

Step 1: Dilutions for each compound were performed in the appropriate medium as previously described in the Mat&Met section.

Step 2: Each well was labeled with unique signatures or "barcodes" of fluorescent dyes. Two different dyes were used to produce 12 barcodes: CellTrace™ CFSE (C34554) and CellTrace™ Violet (C34557), as previously described in the Mat&Met section.

Step 3: The appropriate concentration of mouse sperm ($6–9 \times 10^6$/ml final concentration per well) in NC TYH medium was added to each well and incubated to allow both compounds and dyes to be simultaneously incorporated into sperm. The omission of BSA is critical in this step since this protein may bind to these compounds decreasing the effective concentration in the well. Each 12-well matrix also included one positive and one negative control. As positive control (CatSper inhibition), sperm were incubated in the presence of 10 μM HC-056456. As a negative control (normal CatSper activity), sperm were incubated in the presence of the vehicle used to dissolve the drugs (either DMSO or water).

Step 4: After incubation, NC TYH medium was added to each well and the content of one 12-well matrix was combined into one tube containing additional NC TYH medium. Sperm were washed by centrifugation to remove the excess of unbound dyes. Then, sperm samples were resuspended in NC TYH medium and the Em-sensitive probe $DiSC_3(5)$ was added. At this point, PI was added to differentiate between live and dead sperm. The tube was further analyzed by flow cytometry to acquire basal Em, and after EGTA 3.5 mM addition to promote the depolarizing influx of Na^+ through CatSper, acquisition continued for 150 additional seconds.

Step 5: The analysis of the FCB experiment was performed with FlowJo software. In the FSC-A vs. SSC-A dot plot, the sperm population was selected.

Step 6: Those cells that uptake PI (dead sperm) were gated out and the following analysis was only performed with the population of live sperm (PI negative).

Step 7: During software analysis the samples were distinguishable based on their fluorescence intensity in each FCB marker channel. Sperm within each well possess a unique fluorescent signature. Using the FlowJo software, plotting the corresponding channel for Dye 1 (CellTrace™ Violet) vs. the corresponding channel for Dye 2 (CellTrace™ CFSE) revealed distinct populations that correspond to the original wells that were barcoded.

Step 8: Once gated, the populations were analyzed according to $DiSC_3(5)$ fluorescence before and after the EGTA addition. As an example, two different conditions are displayed. On the bottom, a situation where a given compound inhibits CatSper function is displayed, whereas on top, a representative example where a given compound is not blocking CatSper is shown.

Figure 5A shows an example of a single 4 × 3 matrix where different sperm populations can be distinguished depending on

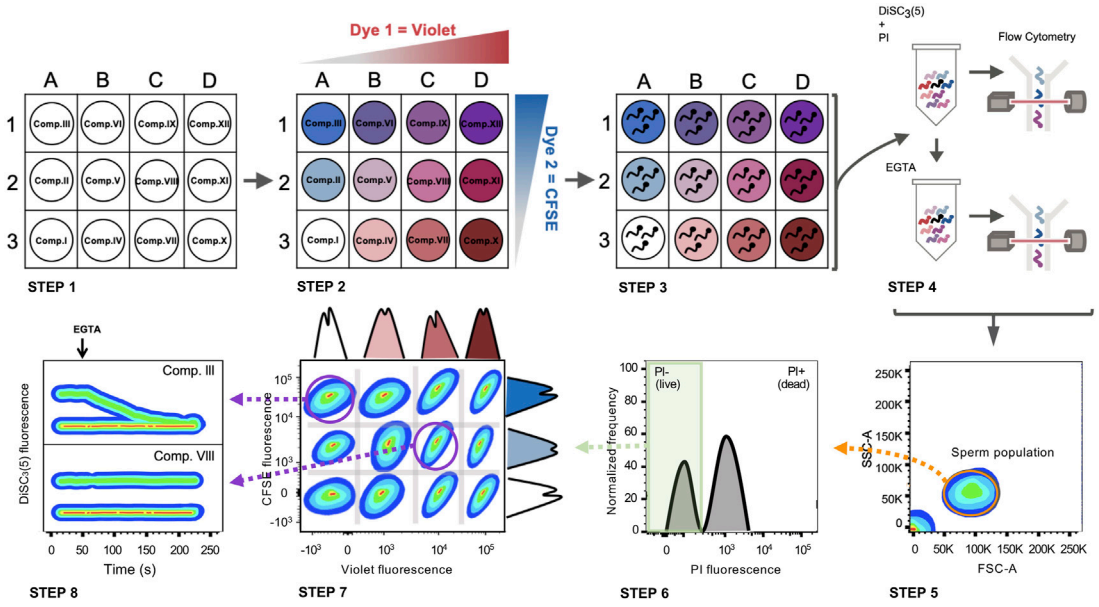

FIGURE 4
FCB in combination with Em analysis by flow cytometry in mouse sperm. Schematic diagram: STEP 1) A 96 well plate is prepared with a different compound in each well. STEP 2) Each well is loaded with a unique combination of dyes (CellTrace™ Violet and CellTrace™ CFSE). STEP 3) Sperm samples are distributed in different wells and incubated with the compounds while loading with a distinct combination of dyes. STEP 4) After loading, all samples are grouped in a single tube, loaded with $DiSC_3(5)$ (Em indicator) and PI (viability marker) and analyzed by flow cytometry (basal recording of 30 s). After basal Em acquisition, EGTA 3.5 mM is added and immediately analyzed by flow cytometry again (for 150 s). STEP 5) Following data acquisition, the sperm population is selected from all the events recorded. STEP 6) The live sperm population is selected by gating PI-negative sperm. STEP 7) Live sperm samples can be distinguished through their corresponding dye fluorescence signature. STEP 8) $DiSC_3(5)$ fluorescence before and after EGTA addition is determined in each population, discriminating if there is any compound that promotes CatSper closure. Comp. III = does not inhibit CatSper. Comp. VIII = CatSper inhibitor.

their barcoding dyes concentration. The position of a given treatment within the matrix is diagrammed in Figure 5B as a double-entry table, where it can be defined through its corresponding CellTrace™ Violet—CellTrace™ CFSE signature. For example, in V3-C3 position no sperm were added as a control to corroborate proper sperm sample identification (Figure 5A, dashed-line circle). In V3-C1, a well-known CatSper inhibitor (10 μM HC-056456) was added as a positive control, while as a negative control only DMSO (vehicle) was added in position V1-C1. After selecting the appropriate population, distinguished by its unique signature provided by the FCB (which corresponds to a specific position of the initial microplate), $DiSC_3(5)$ fluorescence was monitored over time (Figure 5C). The mean $DiSC_3(5)$ fluorescence of the hyperpolarized subset of cells was quantified and displayed in Figure 5D. As observed, the presence of the CatSper inhibitor blocked the EGTA-induced depolarization (Figures 5C, D, HC). In contrast, addition of DMSO (Figures 5C, D, Ctrl) did not inhibit CatSper and displayed a robust depolarization. By using a 96-well microplate, eight 4 × 3 matrices could be included. If one positive control (HC-056456 or CatSper1 KO sperm) and one negative control (NC + DMSO) are used per matrix, a total of 80 compounds could be tested in 40 min. A representative example of this procedure is presented in Figure 6, where 80 compounds from a FDA-Approved Drug Library were tested (Supplementary Table S1). To assess intra-experiment variability, the mean of the $DiSC_3(5)$ + fluorescence from the eight NC and HC controls was calculated and displayed in Supplementary Figure S5.

Discussion

It is currently estimated that one in four pregnancies is unplanned worldwide (Shah and Åhman, 2010; Bearak et al., 2018), based on studies that analyzed data bases from 1990–2014 in more than 100 countries. In addition, available male contraceptive methods are scarce, resulting in a gender imbalance in decision-making related to family planning. Nowadays, most men confirm that they would be interested in using new fertility control methods, if available (Heinemann et al., 2005), while many women would be willing to rely on their partner on this matter (Glasier, 2010). Initially, most efforts were directed to the development of male hormonal contraceptives, resembling the female birth control pill. However due to several side effects associated with hormonal treatments none have reached the market, and the acceptance among users is low. More recently, research has been focused on the discovery of non-hormonal targets, particularly compounds directed to block sperm production on the testis, sperm maturation on the epididymis, and/or sperm function (Long et al., 2021). A male contraceptive must be specific, effective, safe, reversible, and accessible. Taking this into consideration CatSper emerges as an attractive male contraceptive target since it is a sperm-specific Ca^{2+} channel, only localized in the flagellum, and essential for sperm fertilizing ability. Targeted disruption of each of the four murine CatSper ion channel proteins was shown to lead to infertility. Similarly, humans with CatSper loss-of-function mutations have shown male infertility due to hyperactivation impairment, without systemic effects (Avidan et al., 2003; Avenarius et al., 2009; Smith et al., 2013). Therefore, a pharmacological CatSper inhibitor

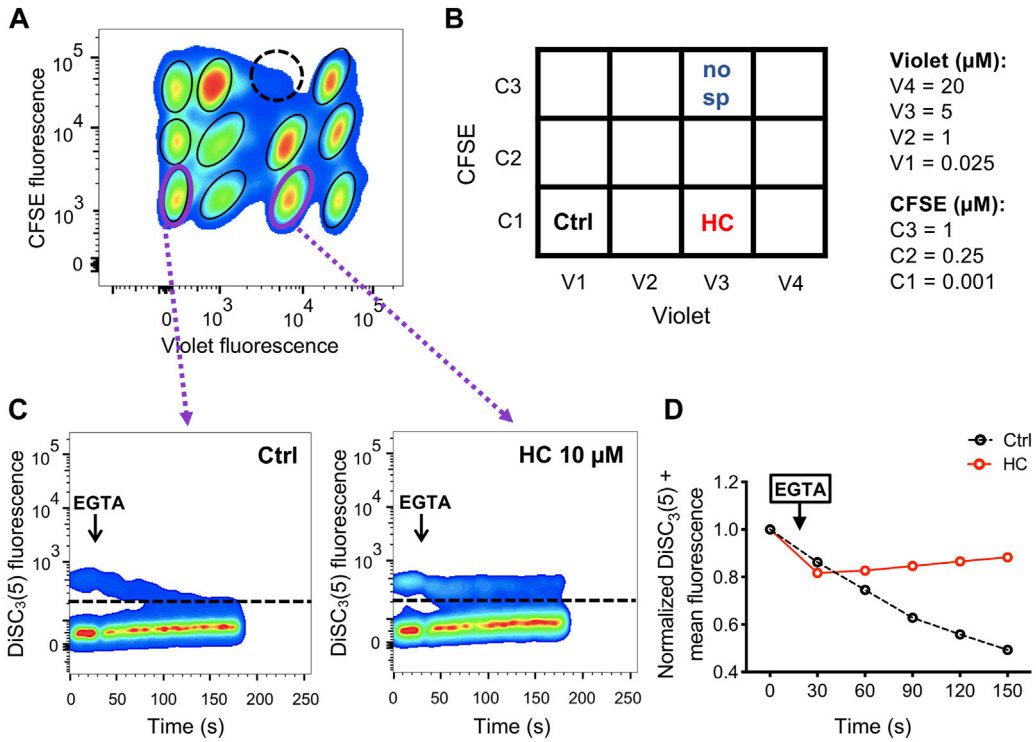

FIGURE 5
(A) Representative 2D dot plot of CellTrace™ Violet vs. CellTrace™ CFSE fluorescence of a 4 × 3 matrix, where the population of sperm with each dye combination/signature was defined. As an additional control of proper identification in the matrix, in one well sperm were not added (dashed-line circle). **(B)** Diagram showing the arrangement of compounds (HC: CatSper inhibitor; Ctrl: NC + DMSO vehicle; no sp: no sperm were added) within the 4 × 3 matrix. The dye concentration in each well is depicted as a double-entry table. **(C)** Representative 2D dot plot of $DiSC_3(5)$ fluorescence vs. time (seconds) analysis for the positive (HC) and negative (Ctrl) controls. The addition of 3.5 mM EGTA (black arrow) induced a decrease in the population of sperm with high $DiSC_3(5)$ fluorescence due to Em depolarization in the NC control condition (with only vehicle) but not in sperm that were incubated with 10 μM HC-056456. The population of sperm that responds by decreasing the Em was established in the NC control condition and extrapolated to the other conditions (dashed line). Sperm cells above the dashed line [higher $DiSC_3(5)$ fluorescence] were arbitrarily identified as $DiSC_3(5)$ +. **(D)** $DiSC_3(5)$ fluorescence mean was determined in the sperm population with higher $DiSC_3(5)$ fluorescence: $DiSC_3(5)$ + [dashed line in **(C)**] before (time = 0 s) and after (black arrow) addition of 3.5 mM EGTA. In each condition, the fluorescence mean was normalized to the basal fluorescence (0 s).

might be used as an on-demand male contraceptive and/or as a female treatment to prevent sperm migration through the oviduct.

It is well established that CatSper regulation is promiscuous since it can be non-specifically inhibited or activated by numerous compounds (Rennhack et al., 2018; Rahban et al., 2021). This channel's intrinsic feature makes it challenging to discover specific candidates to inhibit its function. For example, some of the pharmacological CatSper inhibitors available nowadays are not specific, such as Mibefradil (Carlson et al., 2009) and NNC 55-0396 (Huang et al., 2004), which are T- and L-type Ca^{2+} channel blockers. CatSper inactivation with HC-056456 (Carlson et al., 2009) was recently investigated showing that intrauterine insemination of treated sperm resulted in a reduced percentage of fertilized oocytes (Curci et al., 2021), but further *in vivo* experiments are required. Others such as RU 1968 (Rennhack et al., 2018), have not been well characterized and tested *in vivo*.

In addition, the high structural complexity of CatSper has impeded its heterologous expression making *in vitro* studies difficult. In this regard, patch clamp electrophysiology is the gold standard technique for direct measurement of channel ionic currents. Still, conventional manual patch clamp requires highly skilled personnel, it is time-consuming and therefore has low throughput. Recently, the advent of automated patch clamp technologies enabled high-throughput direct measurement of ion channel function (Mathes, 2006; Picones et al., 2016). Although this technique has been applied to a wide variety of cell types, it presents additional challenges when it comes to sperm, a very tiny cell with scarce cytoplasm and constant movement. One way around this has been the use of high-throughput assays with alternative measures of CatSper function such as $[Ca^{2+}]_i$ (Carlson et al., 2022). Although informative, this parameter does not directly assess CatSper channel function and has key limitations, as several compounds can generate changes in $[Ca^{2+}]_i$ without significant effects on CatSper.

Data presented in this paper have also validated the indirect assessment of CatSper function through Em determination. This approach has been used in previous reports from our group (Torres-Flores et al., 2011; Ernesto et al., 2015; Ritagliati et al., 2018; Stival et al., 2018; Luque et al., 2021) to determine the inhibitory effect of proteins or compounds. Possible and valid concerns about this method are related to the existence of other ion channels that may also become permeable to monovalent ions when Ca^{2+} is chelated. Now, we fully validated this functional assay using CatSper1 KO mice. The depolarizing Na^+ influx occurs mainly through CatSper channels since many sperm remained hyperpolarized in CatSper1 KO. This observation suggests that, although we cannot rule out the contribution of other channels, it

10.3389/fcell.2023.1010306

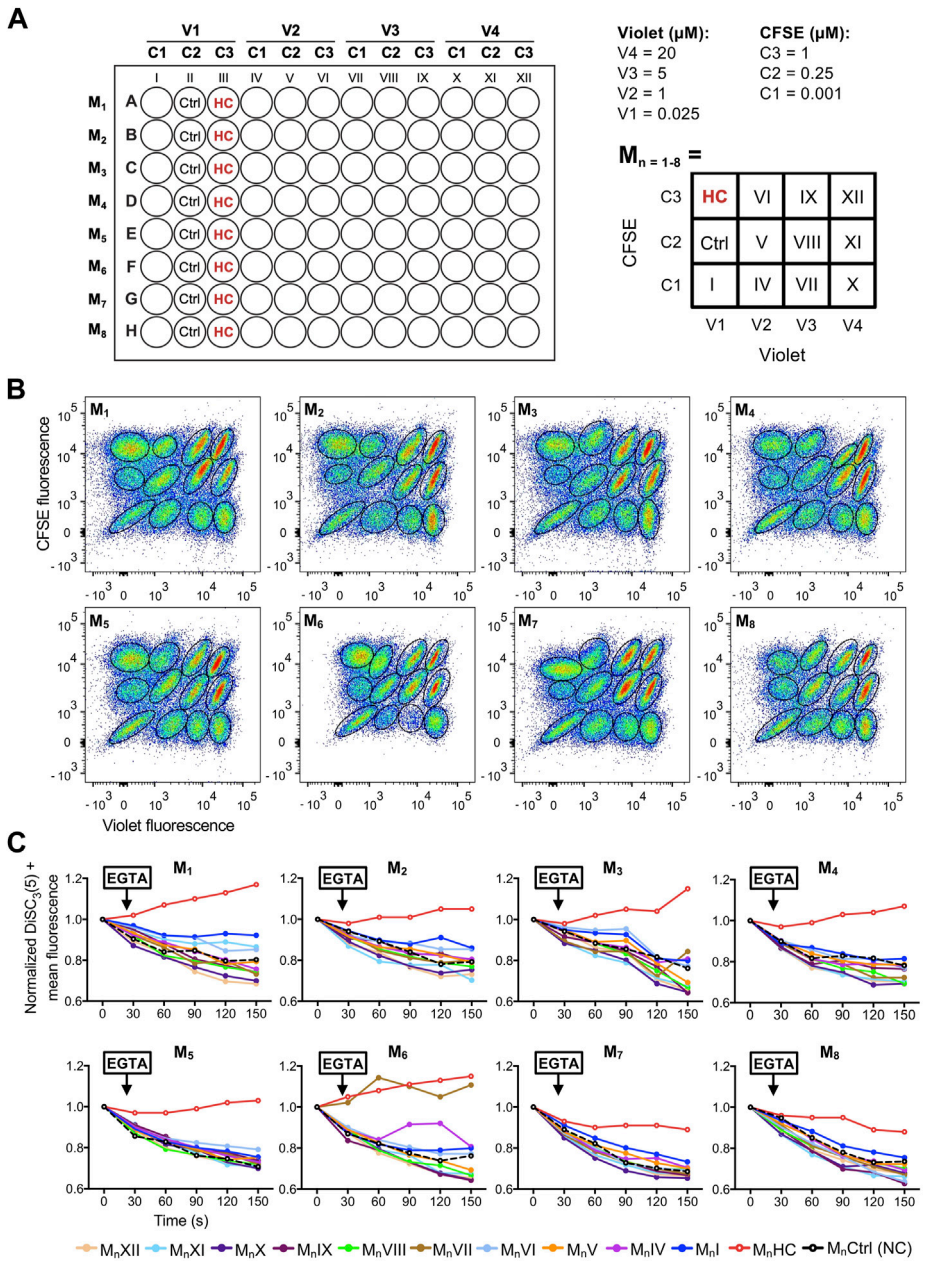

FIGURE 6
(A) Left-panel: schematic diagram of a 96-well plate showing the arrangement of compounds (all tested at 10 μM), dyes (V1-4: CellTrace™ Violet concentrations; C1-3: CellTrace™ CFSE concentrations), and controls (Ctrl: NC + DMSO vehicle; HC: 10 μM HC-056456). Each row corresponds to a different matrix ($M_{n=1-8}$). Right-panel: schematic diagram of the compound arrangement within each 4 × 3 matrix. The dye concentration in each location is depicted as a double-entry table. **(B)** Representative 2D dot plots of CellTrace™ Violet vs. CellTrace™ CFSE fluorescence of the eight 4 × 3 matrixes from the 96-well plate, where the population of sperm with each dye combination/signature was defined. **(C)** $DiSC_3(5)$ fluorescence mean was determined in $DiSC_3(5)$ + population before (time = 0 s) and after (black arrow) addition of 3.5 mM EGTA. In each condition, the fluorescence mean was normalized to the basal fluorescence (0 s). Each color represents a different compound (M_nI-XII; *n* = 1–8) obtained through its corresponding dye fluorescence signature.

may not be significant in magnitude to alter the results obtained by this methodology. Thus, Em determination before and after EGTA addition (Em assay) is a reliable, simple, reproducible, and robust functional assay for measuring indirectly the CatSper opening extent, by both spectrofluorometry and flow cytometry. It is essential to consider that there might be compounds with the ability to change basal sperm Em through the blockage of other channels or electrogenic exchangers, which could compromise the sensitivity of the test.

FBC combined with the Em assay provides a new high-throughput tool for discovering novel CatSper blockers. This phenotypic assay presents future challenges such as hit validation that require follow-up testing (Moffat et al., 2017). In addition, FBC in live sperm itself emerges as a limitless and therefore valuable tool. Considering only the proper

combination of fluorophores, this system could be applied in the future to determine novel blockers of acrosome reaction (by using for example the mouse model with EGFP in their acrosomes (Hasuwa et al., 2010) or FM4-64 when the desired extension to humans is performed (Balestrini et al., 2021)), intracellular $[Ca^{2+}]_i$ increase (Fluo-4, Fluo-3 or Fura), intracellular pH alkalinization (BCECF), as well as other biochemical and/or functional events associated with sperm capacitation.

Data availability statement

The original contributions presented in the study are included in the article/Supplementary Material, further inquiries can be directed to the corresponding authors.

Ethics statement

The animal study was reviewed and approved by Ethical Committees of the Instituto de Biología y Medicina Experimental, Buenos Aires #32/2021.

Author contributions

GL, LS-E, MJ, PB, AN, and NT performed experiments; GL, LS-E, MJ, PB, and AN analyzed the data; GL, LS-E, and MB prepared the manuscript with contributions of all other authors; AD and DK discussed results and contributed with ideas; GL and MB designed the study; GL, CO-S, DK, and MB acquired the funding.

Funding

This work was supported by Male Contraceptive Initiative (Sokal Innovation Award 2020 to MB), and Agencia Nacional de Promoción Científica y Tecnológica (PICT 2017-3047 and 2021-00014 to MB; 2018-1988 to GL; 2017-3217 and 2019-1779 to DK).

Acknowledgments

We would like to thank Gabriel Rabinovich for his assistance in the flow cytometry experiments, and Micaela Carruba with her assistance with fluorimetry measurements. We would like to thank the Williams and Rene Baron Foundations and other members of our lab for critically reading the manuscript. We are grateful to Timo Strünker (University of Münster, Germany) for providing RU 1968. We also would like to thank Male Contraceptive Initiative for their continuous support.

Conflict of interest

The authors declare that the research was conducted in the absence of any commercial or financial relationships that could be construed as a potential conflict of interest.

Publisher's note

Supplementary material

The Supplementary Material for this article can be found online at: https://www.frontiersin.org/articles/10.3389/fcell.2023.1010306/full#supplementary-material

SUPPLEMENTARY FIGURE S1
Difference between depositing the sperm in the corresponding well containing the dye from above without submerging the tip (BEFORE) and submerging the tip (AFTER). The sperm population results in a more homogeneous loading when submerging the tip. Representative 2D dot plot of CellTrace™ Violet vs. CellTrace™ CFSE fluorescence, with their corresponding histogram analysis depicting the normalized frequency of sperm vs. dye fluorescence. **(A)** Sperm sample loaded with CellTrace™ CFSE 1 μM. **(B)** Sperm sample loaded with CellTrace™ Violet 20 μM.

SUPPLEMENTARY FIGURE S2
The Em assay was evaluated in two different mouse strains: A) C57BL/6 and B) Hybrid F1 (C57BL/6 male × BALB/c female) mature (10–12 weeks-old) male mice were used. Representative 2D dot plots of $DiSC_3(5)$ fluorescence vs. time (seconds) analysis are shown. The addition of 3.5 mM EGTA (black arrow) provokes a decrease in the population of sperm with high $DiSC_3(5)$ fluorescence due to Em depolarization in the control condition (DMSO vehicle; left), but not in the presence of 10 μM HC-056456 (right).

SUPPLEMENTARY FIGURE S3
CatSper activity was assessed by measuring Em in individual live cells by flow cytometry. **(A)** Representative 2D dot plot of $DiSC_3(5)$ fluorescence vs. time (seconds) analysis. The addition of 3.5 mM EGTA (black arrow) provokes a decrease in the population of sperm with high $DiSC_3(5)$ fluorescence due to Em depolarization in the control condition (DMSO vehicle). The addition of the specific CatSper inhibitor HC-056456 prevents this decay in a concentration-dependent manner, where at 10 μM the maximum effect is reached. **(B)** Quantification of at least 3 independent experiments (mean ± SEM) is shown. The population of sperm that responds by decreasing the Em was established in the control condition and extrapolated to the other conditions [**(A)**, dashed line]. $DiSC_3(5)$ fluorescence mean was determined in $DiSC_3(5)$ + population before (time = 0 s) and after (black arrow) addition of 3.5 mM EGTA. In each condition, the fluorescence mean was normalized to the basal fluorescence (0 s). No differences were found between HC 10 μM vs. time matched HC 20 μM. Both, HC 10 μM and HC 20 μM were significantly different vs. time matched control condition (DMSO). Two-way ANOVA with repeated-measures in combination with Tukey's multiple comparison test was performed.

SUPPLEMENTARY FIGURE S4
CellTrace™ CFSE has some emission overlap with PI. Representative 2D dot plot of CellTrace™ CFSE vs. PI fluorescence before and after compensation. Increasing concentrations of CellTrace™ CFSE are shown. The higher concentration of CellTrace™ CFSE that allows optimal discrimination of populations in combination with PI is 1 μM.

SUPPLEMENTARY FIGURE S5
Quantification of the eight NC and HC controls used in the 96-well plate to evaluate intra-experiment variability. $DiSC_3(5)$ fluorescence mean was determined in $DiSC_3(5)$ + population before (time = 0 s) and after (black arrow) addition of 3.5 mM EGTA. In each condition, the fluorescence mean was normalized to the basal fluorescence (0 s). Mean ± SEM is shown.

SUPPLEMENTARY TABLE S1
List of the 80 compounds from the FDA-Approved Drug Library used in the representative screening-experiment shown in Figure 6.

References

Austin, C. R. (1952). The capacitation of the mammalian sperm. *Nature* 170, 326. doi:10.1038/170326a0

Avenarius, M. R., Hildebrand, M. S., Zhang, Y., Meyer, N. C., Smith, L. L. H., Kahrizi, K., et al. (2009). Human male infertility caused by mutations in the CATSPER1 channel protein. *Am. J. Hum. Genet.* 84, 505–510. doi:10.1016/j.ajhg.2009.03.004

Avidan, N., Tamary, H., Dgany, O., Cattan, D., Pariente, A., Thulliez, M., et al. (2003). CATSPER2, a human autosomal nonsyndromic male infertility gene. *Eur. J. Hum. Genet.* 11, 497–502. doi:10.1038/sj.ejhg.5200991

Balestrini, P. A., Sanchez-Cardenas, C., Luque, G. M., Baro Graf, C., Sierra, J. M., Hernández-Cruz, A., et al. (2021). Membrane hyperpolarization abolishes calcium oscillations that prevent induced acrosomal exocytosis in human sperm. *FASEB J.* 35, e21478. doi:10.1096/fj.202002333rr

Bearak, J., Popinchalk, A., Alkema, L., and Sedgh, G. (2018). Global, regional, and subregional trends in unintended pregnancy and its outcomes from 1990 to 2014: Estimates from a bayesian hierarchical model. *Lancet. Glob. heal.* 6, e380–e389. doi:10.1016/S2214-109X(18)30029-9

Carlson, A. E., Burnett, L. A., del Camino, D., Quill, T. A., Hille, B., Chong, J. A., et al. (2009). Pharmacological targeting of native CatSper channels reveals a required role in maintenance of sperm hyperactivation. *PLoS One* 4, e6844. doi:10.1371/JOURNAL.PONE.0006844

Carlson, E. J., Francis, R., Liu, Y., Li, P., Lyon, M., Santi, C. M., et al. (2022). Discovery and characterization of multiple classes of human CatSper blockers. *ChemMedChem* 17, e202000499. doi:10.1002/CMDC.202000499

Chang, M. C. (1951). Fertilizing capacity of spermatozoa deposited into the fallopian tubes. *Nature* 168, 697–698. doi:10.1038/168697b0

Chung, J.-J. J., Shim, S.-H. H., Everley, R. A., Gygi, S. P., Zhuang, X., and Clapham, D. E. (2014). Structurally distinct Ca2+ signaling domains of sperm flagella orchestrate tyrosine phosphorylation and motility. *Cell* 157, 808–822. doi:10.1016/j.cell.2014.02.056

Chung, J.-J., Miki, K., Kim, D., Shim, S.-H., Shi, H. F., Hwang, J. Y., et al. (2017). CatSperζ regulates the structural continuity of sperm Ca2+ signaling domains and is required for normal fertility. *Elife* 6, e23082. doi:10.7554/eLife.23082

Chung, J.-J., Navarro, B., Krapivinsky, G., Krapivinsky, L., and Clapham, D. E. (2011). A novel gene required for male fertility and functional CATSPER channel formation in spermatozoa. *Nat. Commun.* 2, 153. doi:10.1038/ncomms1153

Clutter, M. R., Heffner, G. C., Krutzik, P. O., Sachen, K. L., and Nolan, G. P. (2010). Tyramide signal amplification for analysis of kinase activity by intracellular flow cytometry. *Cytom. A* 77, 1020–1031. doi:10.1002/cyto.a.20970

Curci, L., Carvajal, G., Sulzyk, V., Gonzalez, S. N., and Cuasnicú, P. S. (2021). Pharmacological inactivation of CatSper blocks sperm fertilizing ability independently of the capacitation status of the cells: Implications for non-hormonal contraception. *Front. Cell Dev. Biol.* 9, 686461. doi:10.3389/FCELL.2021.686461

De La Vega-Beltran, J. L., Sánchez-Cárdenas, C., Krapf, D., Hernandez-González, E. O., Wertheimer, E., Treviño, C. L., et al. (2012). Mouse sperm membrane potential hyperpolarization is necessary and sufficient to prepare sperm for the acrosome reaction. *J. Biol. Chem.* 287, 44384–44393. doi:10.1074/jbc.M112.393488

Demarco, I. A., Espinosa, F., Edwards, J., Sosnik, J., de la Vega-Beltrán, J. L., Hockensmith, J. W., et al. (2003). Involvement of a Na+/HCO3- cotransporter in mouse sperm capacitation. *J. Biol. Chem.* 278, 7001–7009. doi:10.1074/jbc.M206284200

Demott, R. P., and Suarez, S. S. (1992). Hyperactivated sperm progress in the mouse oviduct. *Biol. Reprod.* 46, 779–785. doi:10.1095/biolreprod46.5.779

Ernesto, J. I., Weigel Munoz, M., Battistone, M. A., Vasen, G., Martinez-López, P., Orta, G., et al. (2015). CRISP1 as a novel CatSper regulator that modulates sperm motility and orientation during fertilization. *J. Cell Biol.* 210, 1213–1224. doi:10.1083/jcb.201412041

Escoffier, J., Krapf, D., Navarrete, F., Darszon, A., and Visconti, P. E. (2012). Flow cytometry analysis reveals a decrease in intracellular sodium during sperm capacitation. *J. Cell Sci.* 125, 473–485. doi:10.1242/jcs.093344

Espinosa, F., and Darszon, A. (1995). Mouse sperm membrane potential: Changes induced by Ca2+. *FEBS Lett.* 372, 119–125. doi:10.1016/0014-5793(95)00962-9

Glasier, A. (2010). Acceptability of contraception for men: A review. *Contraception* 82, 453–456. doi:10.1016/j.contraception.2010.03.016

Hasuwa, H., Muro, Y., Ikawa, M., Kato, N., Tsujimoto, Y., and Okabe, M. (2010). Transgenic mouse sperm that have green acrosome and red mitochondria allow visualization of sperm and their acrosome reaction *in vivo*. *Exp. Anim.* 59, 105–107. doi:10.1538/expanim.59.105

Heinemann, K., Saad, F., Wiesemes, M., White, S., and Heinemann, L. (2005). Attitudes toward male fertility control: Results of a multinational survey on four continents. *Hum. Reprod.* 20, 549–556. doi:10.1093/humrep/deh574

Huang, L., Keyser, B. M., Tagmose, T. M., Hansen, J. B., Taylor, J. T., Zhuang, H., et al. (2004). NNC 55-0396 [(1S, 2S)-2-(2-(N-[(3-benzimidazol-2-yl)propyl]-N-methylamino) ethyl)-6-fluoro-1, 2, 3, 4-tetrahydro-1-isopropyl-2-naphtyl cyclopropanecarboxylate dihydrochloride]: A new selective inhibitor of T-type calcium channels. *J. Pharmacol. Exp. Ther.* 309, 193–199. doi:10.1124/jpet.103.060814

Hwang, J. Y., Mannowetz, N., Zhang, Y., Everley, R. A., Gygi, S. P., Bewersdorf, J., et al. (2019). Dual sensing of physiologic pH and calcium by EFCAB9 regulates sperm motility. *Cell* 177, 1480–1494. doi:10.1016/j.cell.2019.03.047

Hwang, J. Y., Wang, H., Lu, Y., Ikawa, M., and Chung, J. J. (2022). C2cd6-encoded CatSperτ targets sperm calcium channel to Ca 2+ signaling domains in the flagellar membrane. *Cell Rep.* 38. 110226. doi:10.1016/j.celrep.2021.110226

Irish, J. M., Myklebust, J. H., Alizadeh, A. A., Houot, R., Sharman, J. P., Czerwinski, D. K., et al. (2010). B-cell signaling networks reveal a negative prognostic human lymphoma cell subset that emerges during tumor progression. *Proc. Natl. Acad. Sci. U. S. A.* 107, 12747–12754. doi:10.1073/pnas.1002057107

Kirichok, Y., and Lishko, P. V. (2011). Rediscovering sperm ion channels with the patch-clamp technique. *Mol. Hum. Reprod.* 17, 478–499. doi:10.1093/molehr/gar044

Kirichok, Y., Navarro, B., and Clapham, D. E. (2006). Whole-cell patch-clamp measurements of spermatozoa reveal an alkaline-activated Ca2+ channel. *Nature* 439, 737–740. doi:10.1038/nature04417

Krutzik, P. O., Clutter, M. R., Trejo, A., and Nolan, G. P. (2011). Fluorescent cell barcoding for multiplex flow cytometry. *Curr. Protoc. Cytom.* Chapter 6, Unit 6.31. doi:10.1002/0471142956.CY0631S55

Krutzik, P. O., Crane, J. M., Clutter, M. R., and Nolan, G. P. (2008). High-content single-cell drug screening with phosphospecific flow cytometry. *Nat. Chem. Biol.* 4, 132–142. doi:10.1038/nchembio.2007.59

Krutzik, P. O., and Nolan, G. P. (2006). Fluorescent cell barcoding in flow cytometry allows high-throughput drug screening and signaling profiling. *Nat. Methods.* 3, 361–368. doi:10.1038/nmeth872

Lishko, P. V., and Mannowetz, N. (2018). CatSper: A unique calcium channel of the sperm flagellum. *Curr. Opin. Physiol.* 2, 109–113. doi:10.1016/j.cophys.2018.02.004

Lishko, P. V., Botchkina, I. L., Fedorenko, A., and Kirichok, Y. (2010). Acid extrusion from human spermatozoa is mediated by flagellar voltage-gated proton channel. *Cell* 140, 327–337. doi:10.1016/j.cell.2009.12.053

Lishko, P. V., Botchkina, I. L., and Kirichok, Y. (2011). Progesterone activates the principal Ca2+ channel of human sperm. *Nature* 471, 387–391. doi:10.1038/nature09767

Liu, J., Xia, J., Cho, K.-H., Clapham, D. E., and Ren, D. (2007). CatSperbeta, a novel transmembrane protein in the CatSper channel complex. *J. Biol. Chem.* 282, 18945–18952. doi:10.1074/jbc.M701083200

Lobley, A., Pierron, V., Reynolds, L., Allen, L., and Michalovich, D. (2003). Identification of human and mouse CatSper3 and CatSper 4 genes: Characterisation of a common interaction domain and evidence for expression in testis. *Reprod. Biol. Endocrinol.* 10, 53. doi:10.1186/1477-7827-1-53

Long, J. E., Lee, M. S., and Blithe, D. L. (2021). Update on novel hormonal and nonhormonal male contraceptive development. *J. Clin. Endocrinol. Metab.* 106, E2381–E2392. doi:10.1210/clinem/dgab034

Luque, G. M., Dalotto-Moreno, T., Martín-Hidalgo, D., Ritagliati, C., Puga Molina, L. C., Romarowski, A., et al. (2018). Only a subpopulation of mouse sperm displays a rapid increase in intracellular calcium during capacitation. *J. Cell. Physiol.* 233, 9685–9700. doi:10.1002/jcp.26883

Luque, G. M., Xu, X., Romarowski, A., Gervasi, M. G., Orta, G., De la Vega-Beltrán, J. L., et al. (2021). Cdc42 localized in the CatSper signaling complex regulates cAMP-dependent pathways in mouse sperm. *FASEB J.* 35, e21723. doi:10.1096/fj.202002773RR

Mathes, C. (2006). QPatch: The past, present and future of automated patch clamp. *Expert Opin. Ther. Targets.* 10, 319–327. doi:10.1517/14728222.10.2.319

Mei, H. E., Leipold, M. D., Schulz, A. R., Chester, C., and Maecker, H. T. (2015). Barcoding of live human peripheral blood mononuclear cells for multiplexed mass cytometry. *J. Immunol.* 194, 2022–2031. doi:10.4049/jimmunol.1402661

Miller, M. R., Mansell, S. A., Meyers, S. A., and Lishko, P. V. (2015). Flagellar ion channels of sperm: Similarities and differences between species. *Cell Calcium* 58, 105–113. doi:10.1016/j.ceca.2014.10.009

Moffat, J. G., Vincent, F., Lee, J. A., Eder, J., and Prunotto, M. (2017). Opportunities and challenges in phenotypic drug discovery: An industry perspective. *Nat. Rev. Drug Discov.* 16, 531–543. doi:10.1038/nrd.2017.111

Navarro, B., Kirichok, Y., Chung, J.-J., and Clapham, D. E. (2008). Ion channels that control fertility in mammalian spermatozoa. *Int. J. Dev. Biol.* 52, 607–613. doi:10.1387/ijdb.072554bn

Patton, C., Thompson, S., and Epel, D. (2004). Some precautions in using chelators to buffer metals in biological solutions. *Cell Calcium* 35, 427–431. doi:10.1016/j.ceca.2003.10.006

Picones, A., Loza-Huerta, A., Segura-Chama, P., and Lara-Figueroa, C. O. (2016). Contribution of automated technologies to ion channel drug discovery. *Adv. Protein Chem. Struct. Biol.* 104, 357–378. doi:10.1016/bs.apcsb.2016.01.002

Puga Molina, L. D., Pinto, N. A., Torres, N. I., Ana, L. G. C., Luque, G. M., Balestrini, P. A., et al. (2018). CFTR/ENaC-dependent regulation of membrane potential during human sperm capacitation is initiated by bicarbonate uptake through NBC. *J. Biol. Chem.* 293, 9924–9936. doi:10.1074/jbc.RA118.003166

Qi, H., Moran, M. M., Navarro, B., Chong, J. A., Krapivinsky, G., Krapivinsky, L., et al. (2007). All four CatSper ion channel proteins are required for male fertility and sperm cell hyperactivated motility. *Proc. Natl. Acad. Sci. U. S. A.* 104, 1219–1223. doi:10.1073/pnas.0610286104

Quill, T. A., Ren, D., Clapham, D. E., and Garbers, D. L. (2001). A voltage-gated ion channel expressed specifically in spermatozoa. *Proc. Natl. Acad. Sci. U. S. A.* 98, 12527–12531. doi:10.1073/pnas.221454998

Quill, T. A., Sugden, S. A., Rossi, K. L., Doolittle, L. K., Hammer, R. E., and Garbers, D. L. (2003). Hyperactivated sperm motility driven by CatSper2 is required for fertilization. *Proc. Natl. Acad. Sci. U. S. A.* 100, 14869–14874. doi:10.1073/pnas.2136654100

Rahban, R., Rehfeld, A., Schiffer, C., Brenker, C., Egeberg Palme, D. L., Wang, T., et al. (2021). The antidepressant Sertraline inhibits CatSper Ca2+ channels in human sperm. *Hum. Reprod.* 36, 2638–2648. doi:10.1093/humrep/deab190

Ren, D., Navarro, B., Perez, G., Jackson, A. C., Hsu, S., Shi, Q., et al. (2001). A sperm ion channel required for sperm motility and male fertility. *Nature* 413, 603–609. doi:10.1038/35098027

Rennhack, A., Schiffer, C., Brenker, C., Fridman, D., Nitao, E. T., Cheng, Y. M., et al. (2018). A novel cross-species inhibitor to study the function of CatSper Ca2+ channels in sperm. *Br. J. Pharmacol.* 175, 3144–3161. doi:10.1111/bph.14355

Ritagliati, C., Luque, G. M., Stival, C., Baro Graf, C., Buffone, M. G., and Krapf, D. (2018). Lysine acetylation modulates mouse sperm capacitation. *Sci. Rep.* 8, 13334. doi:10.1038/s41598-018-31557-5

Shah, I., and Åhman, E. (2010). Unsafe abortion in 2008: Global and regional levels and trends. *Reprod. Health Matters* 18, 90–101. doi:10.1016/S0968-8080(10)36537-2

Smith, J. F., Syritsyna, O., Fellous, M., Serres, C., Mannowetz, N., Kirichok, Y., et al. (2013). Disruption of the principal, progesterone-activated sperm Ca2+ channel in a CatSper2-deficient infertile patient. *Proc. Natl. Acad. Sci. U. S. A.* 110, 6823–6828. doi:10.1073/pnas.1216588110

Stam, J., Abdulahad, W., Huitema, M. G., Roozendaal, C., Limburg, P. C., van Stuijvenberg, M., et al. (2011). Fluorescent cell barcoding as a tool to assess the age-related development of intracellular cytokine production in small amounts of blood from infants. *PLoS One* 6, e25690. doi:10.1371/JOURNAL.PONE.0025690

Stauss, C. R., Votta, T. J., and Suarez, S. S. (1995). Sperm motility hyperactivation facilitates penetration of the hamster zona pellucida. *Biol. Reprod.* 53, 1280–1285. doi:10.1095/biolreprod53.6.1280

Stival, C., La Spina, F. A., Baró Graf, C., Arcelay, E., Arranz, S. E., Ferreira, J. J., et al. (2015). Src kinase is the connecting player between Protein Kinase A (PKA) activation and hyperpolarization through SLO3 potassium channel regulation in mouse sperm. *J. Biol. Chem.* 290, 18855–18864. doi:10.1074/jbc.M115.640326

Stival, C., Ritagliati, C., Xu, X., Gervasi, M. G., Luque, G. M., Baro Graf, C., et al. (2018). Disruption of protein kinase A localization induces acrosomal exocytosis in capacitated mouse sperm. *J. Biol. Chem.* 293, 9435–9447. doi:10.1074/jbc.RA118.002286

Suarez, S. S., and Ho, H. C. (2003). Hyperactivation of mammalian sperm. *Cell. Mol. Biol. (Noisy-le-grand)* 49, 351–356.

Torres-Flores, V., Picazo-Juárez, G., Hernández-Rueda, Y., Darszon, A., and González-Martínez, M. T. (2011). Sodium influx induced by external calcium chelation decreases human sperm motility. *Hum. Reprod.* 26, 2626–2635. doi:10.1093/humrep/der237

Wang, H., Liu, J., Cho, K.-H., and Ren, D. (2009). A novel, single, transmembrane protein CATSPERG is associated with CATSPER1 channel protein. *Biol. Reprod.* 81, 539–544. doi:10.1095/biolreprod.109.077107

Yang, F., Gracia Gervasi, M., Orta, G., Tourzani, D. A., De la Vega-Beltrán, J. L., Ruthel, G., et al. (2022). C2CD6 regulates targeting and organization of the CatSper calcium channel complex in sperm flagella. *Development* 149, dev199988. doi:10.1242/DEV.199988

Zhao, Y., Wang, H., Wiesehoefer, C., Shah, N. B., Reetz, E., Hwang, J. Y., et al. (2022). 3D structure and *in situ* arrangements of CatSper channel in the sperm flagellum. *Nat. Commun.* 13, 3439. doi:10.1038/S41467-022-31050-8

frontiers | Frontiers in Cell and Developmental Biology

TYPE Review
PUBLISHED 03 February 2023
DOI 10.3389/fcell.2023.1107312

OPEN ACCESS

EDITED BY
Shao-Chen Sun,
Nanjing Agricultural University, China

REVIEWED BY
Jianqiang Bao,
University of Science and Technology of China, China
Lena Arévalo,
University Hospital Bonn, Germany

*CORRESPONDENCE
Katherine A. Maniates,
maniates@waksman.rutgers.edu

SPECIALTY SECTION
This article was submitted to Molecular and Cellular Reproduction, a section of the journal Frontiers in Cell and Developmental Biology

RECEIVED 24 November 2022
ACCEPTED 24 January 2023
PUBLISHED 03 February 2023

CITATION
Maniates KA and Singson A (2023), Where are all the egg genes?
Front. Cell Dev. Biol. 11:1107312.
doi: 10.3389/fcell.2023.1107312

Where are all the egg genes?

Katherine A. Maniates* and Andrew Singson

Waksman Institute of Microbiology, Rutgers University, Piscataway, NJ, United States

Complementary forward and reverse genetic approaches in several model systems have resulted in a recent burst of fertilization gene discovery. The number of genetically validated gamete surface molecules have more than doubled in the last few years. All the genetically validated sperm fertilization genes encode transmembrane or secreted molecules. Curiously, the discovery of genes that encode oocyte molecules have fallen behind that of sperm genes. This review discusses potential experimental biases and inherent biological reasons that could slow egg fertilization gene discovery. Finally, we shed light on current strategies to identify genes that may result in further identification of egg fertilization genes.

KEYWORDS

egg, oocyte, fertilization, *C. elegans*, mouse, *zebrafish*, sperm

1 Introduction

1.1 The big questions and fertilization gene discovery

Understanding the genetic underpinnings of fertilization is essential for developing infertility treatments, contraceptive targets, understanding speciation, and mechanisms of cell-cell interactions (Schultz and Williams, 2002; Krauchunas et al., 2016; Bhakta et al., 2019; Findlay et al., 2019). In the last several years there has been a rapid increase in the discovery of genetically validated fertilization molecules in several key model systems (Deneke and Pauli, 2021; Mei and Singson, 2021). While fertilization is studied in many model systems, forward and reverse genetic approaches in worms, zebrafish, and mice have recently led the charge. Sterile mutants obtained through mutant screens or genetic knockouts are the modern gold standard to demonstrate the requirement of a gene to encode a factor in fertilization. The progress from genetic screens and knockouts has also established that there are fertilization genes that are deeply conserved from nematode worms to mammals (Mei and Singson, 2021). For example, there are several immunoglobulin superfamily molecules that were independently identified with roles in fertilization in several different species (Ellerman et al., 2003; Krauchunas et al., 2016; Binner et al., 2022). The DCSTAMP sperm molecules *spe-42* and *spe-49* (Kroft et al., 2005; Wilson et al., 2018) have essentially the same sperm sterile mutant phenotype to DCST1/2 mutants in flies, fish, and mice (Inoue et al., 2021; Mei and Singson, 2021; Noda et al., 2022). Progress in fertility gene discovery has also uncovered a high degree of molecular complexity required for sperm egg interactions. This was the inspiration for the concept of the fertilization synapse as the intellectual framework to understand how many newly discovered fertility gene products work in conjunction at the interface of sperm and egg plasma membranes (Krauchunas et al., 2016). Sperm and egg interactions have parallels with other cellular synapses (neural and immune) that include specialized cell structures, integrated with adhesion, secretion, and cell signaling. Understanding the fertilization synapse will require knowing what molecules interact either in cis with other molecules on the same gamete or in trans with molecules of the opposite gamete. The realization of the fertilization synapse also opens new questions. How are all the sperm and egg components assembled into complexes and at the right time and place? Genes are being discovered that may impact the processing and assembly of the fertilization synapse (Gleason et al., 2006; Contreras et al., 2022; Schreier et al.,

2022). For example, Frey can regulate the assembly of Izumo1, a key protein involved in fertilization on the surface of the sperm (Contreras et al., 2022). It does this by helping to assemble Izumo into the correct protein complex. The road to the identification of genes involved in fertilization faces many challenges which researchers must overcome.

1.2 Difficulties in determining genes involved in fertilization

Unlike some other biological processes, fertilization comprises multiple cellular processes including gamete activation, recognition, binding, and fusion. These processes must be executed very precisely to combine one sperm and one egg. This requires that the space, time, and the concentration of proteins during fertilization be exact. The transient interactions and combination of proteins at the correct level can be difficult to recapitulate *in vitro*. Genes must be expressed specifically on the surface of the cell and often shift after fertilization. As there are multiple processes that require very specific interactions, it is of no surprise that the sperm and egg also require multiple protein interactions. Beyond the transient interactions, redundancy, pleiotropy, and maintaining sterile mutants have been roadblocks for gene discovery on both gametes.

1.3 Current fertilization molecules and open questions

As of writing this review, going by the sterile mutant gold standard, there are ten mouse genes (Bianchi and Wright, 2020; Deneke and Pauli, 2021) and 12 *C. elegans* genes that encode transmembrane or secreted proteins that are required for fertilization and are components of the fertilization synapse (Mei and Singson, 2021) (Figure 1). For complete recent information about the fertilization proteins, please see recent reviews by Deneke and Pauli (2021); Mei and Singson (2021). Anyone would agree that when it comes to fertilization, it takes two to tango as sperm and egg are the ultimate in complementary cells. However, gazing at the molecules in the emerging fertilization synapse of worms, fish, and mouse shown in Figure 1 there is a striking asymmetry. Most currently known fertilization genes encode sperm factors. Ten of twelve genes in worms and seven of ten genes in mice are on the sperm surface (Figure 1). Here we review why we currently observe this gene discovery asymmetry between known sperm and egg genes. As of writing this review, only five egg surface molecules have been discovered: *egg-1/2* in *C.* elegans, Bouncer in Zebrafish, and Juno and CD9 in mouse (Naour et al., 2000; Kadandale et al., 2005; Bianchi et al., 2014; Herberg et al., 2018) (Table 1). These genes encode a multitude of different types of proteins. *Egg-1* and *egg-2* have LDL receptor repeats, Bouncer a Ly6/uPAR protein, Juno, is related to folate receptors, and CD9 is a tetraspanin (Naour et al., 2000; Kadandale et al., 2005; Bianchi et al., 2014; Herberg et al., 2018). However, these genes are not sufficient for all the different functions of fertilization. Therefore, the search for egg genes continues. There are other proteins such as Phospholipid C zeta which is a sperm specific soluble enzyme that can trigger oocyte activation (Yoon et al., 2008; Yoon et al., 2012; Hachem et al., 2017; Sanders et al., 2018). This review in particular focuses only on proteins that are expressed on the surface of the gamete. This asymmetry underscores the importance of studies in females. Female processes have been historically understudied. This has been a focus of the NIH since 2016 when they published their policy on sex as a biological variable (Arnegard et al., 2020). The gap in egg gene discovery is an important subject that we, as researchers, should examine and work to close. In this review, we discuss different biological mechanisms such as redundancy, pleiotropy, and how the evolution of sperm expressed genes have impacted the identification of fertilization genes in the oocyte. A likely source of lagging egg gene discovery is also experimental bias either in methods or the model organisms. Potential experimental biases could include maintenance and propagation of sterile mutants, screening strategies, and difficulty in identifying fertilization phenotypes. While many of these experimental biases are not an exclusive challenge to discovering egg genes, we think that these are important ideas to bring to the forefront of the research community. Finally, we conclude by discussing new experimental approaches and options that could address the question of where are all the egg genes?

2 Challenges in the identification of egg genes

2.1 Fertilization and redundant genes

Fertilization is an essential process and redundant genes can help protect against deleterious mutations. The same protection that redundancy provides may make it more difficult to identify egg genes with genetic approaches. For sexually reproducing organisms, loss of fertility is evolutionarily devastating, rendering animals unable to pass on their genes to future generations. One random mutation could render an animal sterile and subsequently bring their fitness level to zero. Therefore, like other genes that have essential functions, gene duplication and redundant copies can decrease the likelihood of extinction occurring over many generations. This has been observed across many different organisms in fertility and particularly in the previously identified egg genes. In *C. elegans, egg-1* and *egg-2* function redundantly with one another. The loss of *egg-1* which encodes an LDL receptor repeat-containing protein that functions redundantly with *egg-2* another LDL receptor. These genes encode a protein with 67% similarity (Kadandale et al., 2005). The initial observation by RNAi of *egg-1* also knocks down *egg-2* generating a sterile phenotype, however genetic loss of only *egg-1* or *egg-2* decreases fertility but does not cause sterility.

On the oocyte surface, one abundant group of proteins that were at the forefront of fertilization research for many years were integrins on the egg surface. Interest in this group of proteins arose due to a disintegrin domain in ADAM2/Fertilin that was found on the sperm surface (Blobel et al., 1992). Investigation of this class of integrin proteins which were expressed in eggs revealed 24 different integrin combinations. The complexity made this a difficult area to study (Evans, 2002). Individual knockouts of integrins generated modest decreases in fertility and multiple knockouts generated other fertility defects such as embryonic lethality making this challenging to elucidate their exact role during fertilization (Miller et al., 2000; Hynes, 2002; He et al., 2003; Vjugina and Evans, 2008). While redundancy is not the singular reason that it has been difficult to identify egg genes, we hypothesize that it is one of the most prevalent reasons.

On the sperm side of the equation, there have also been genes that act redundantly with one another. One example is the CRISP (Cysteine-RIch

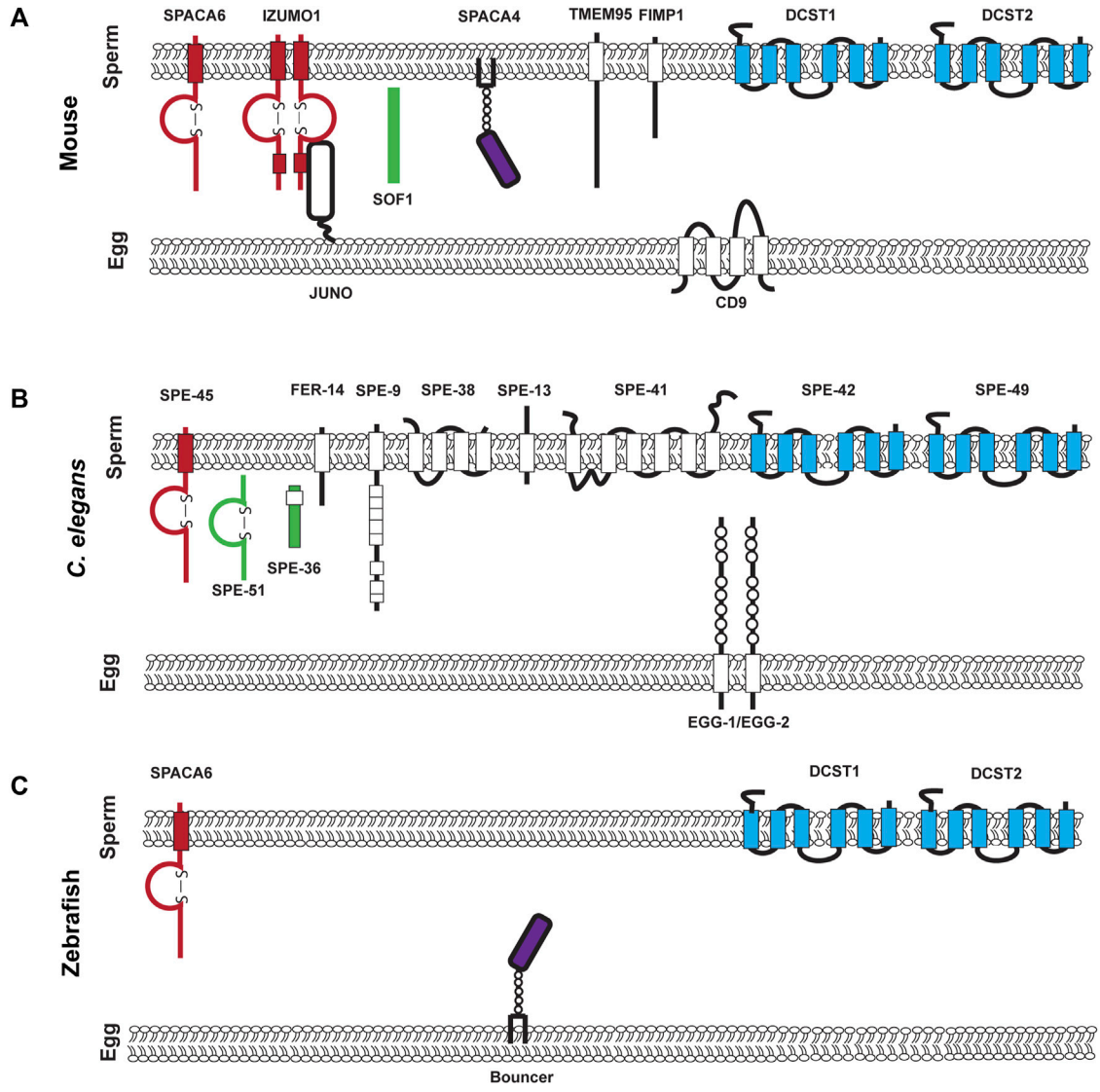

FIGURE 1
Known components of the mouse, *C. elegans*, and Zebrafish fertilization synapse. **(A)**. Mouse fertilization synapse, **(B)**. *C. elegans* fertilization synapse, and **(C)**. Zebrafish fertilization synapse. For **(A–C)** each of the molecules that are denoted have been experimentally validated though loss of function mutations. Proteins on the left of each synapse in red contain an immunoglobulin domain, proteins in green are secreted, proteins in purple are in the uPAR/Ly6 family and on the right in blue are conserved DCSTAMP proteins.

Secretory Protein) gene family which regulates calcium channels in fertilization. In mouse, there are four CRISP family members, knockout of one member of the family reduces fertility but does not completely abolish it, however knockout of three or four of the family members completely disrupts male fertility demonstrating their redundant or compensatory functions (Ros et al., 2008; Curci et al., 2020). Interestingly in humans there are three CRISP genes which are all located on the same chromosome, therefore it would take a large deletion or rare collection of point mutations in all three genes to remove all function rendering them infertile (Gibbs et al., 2008; Curci et al., 2020). Redundant or compensatory genes may be a big challenge in our field in discovering egg genes as well as additional sperm genes. With the rise of CRISPR/Cas9 gene editing, it may be valuable to look for homologues and potential gene families and then knockout multiple genes in these family groups to examine for fertility phenotypes.

2.2 Less gene expression and pleiotropy

Oocytes enter a period of transcriptional quiescence usually during which fertilization, egg activation, and early embryonic development must occur (Kim and You, 2022). This contrasts with sperm cells which have a short period of quiescence, however their function largely ends after fertilization. The oocyte must provide all the proteins necessary for these very diverse cellular processes. One way that this could be accomplished is through pleiotropy, where one gene regulates multiple functions. As the first genomes were sequenced, researchers were surprised that there are far fewer genes than previously predicted, pleiotropy is one explanation for this phenomenon (Lander et al., 2001).

A related reason that it might be difficult to identify egg genes is that there may be tissue or stage specific isoforms of genes. This is

where one isoform of a gene functions in development and another during adulthood, or one isoform in a somatic cell and other functions in the germline. For example, Juno in mouse is widely expressed in tissues other than just oocytes including the thymus, spleen, and lung however loss of Juno in these tissues does not appear to solicit additional loss of function phenotypes (Spiegelstein et al., 2000; Bianchi et al., 2014). If multiple phenotypes are exhibited this can complicate our ability to interpret gene functions. For example, in *C. elegans, nhr-23* is expressed during the process of molting which takes place during larval development and precedes much of germ cell differentiation. Later in development *nhr-23* also functions as a transcription factor during spermatogenesis (Ragle et al., 2020). The earlier molting defects exhibited by *nhr-23* had been established for many years prior to its function during spermatogenesis. The function during spermatogenesis was not as evident as animals arrested prior to adulthood (Kostrouchova et al., 1998; Kostrouchova et al., 2001). Finally, as mentioned before in Section 2.1, loss of integrins on the egg surface identified pleiotropic functions in oogenesis and embryonic development. Mutant phenotypes that are exhibited in other tissues or earlier in development can make the isolation of specific genes involved in fertilization more difficult and these pleiotropic defects may obscure specific genes roles in fertilization. The limited number of genes that are expressed in the oocyte make this a compelling reason why egg expressed gene roles have been difficult to identify.

2.3 Differential cell expression, opposing sex specific expression patterns, and homotypic interactions can make elucidating gene function difficult

Another reason that identifying egg genes could be difficult is that different proteins or protein domains maybe used in various species. Further it may be where two identical structural elements of individual monomers are interchanged to stabilize protein complexes (Bennett et al., 1994). The puzzle of molecular swapping between two gametes underscores the importance of studying fertilization in different organisms to understand the mechanism of cell-cell interactions between sperm and oocytes.

For example, Bouncer, a Ly6/uPAR protein in Zebrafish is essential for sperm-egg interactions which facilitate sperm binding to the oolemma when expressed on the egg surface (Herberg et al., 2018). SPACA4, the mammalian homologue of Bouncer is actually expressed on the sperm surface in mice and functions to penetrate the Zona Pellucida (ZP) for binding to the egg surface in mouse (Fujihara et al., 2021). At this point, the mechanism underlying opposing sex specific expression patterns for Bouncer and SPACA4 is not clear. Hypotheses surrounding this include it being due to different environments for fertilization as Zebrafish have a micropyle and therefore the sperm do not need to pass through the egg surface whereas mammals need penetration of the ZP and the acrosome reaction to occur. Another hypothesis is that this is a sperm specific loss of function that was retained in the egg during evolution.

In the same vein, homotypic interactions where either two proteins or protein domains interact with one on each of the opposing sperm and egg cells acting to signal for binding or fusion to occur. No homotypic interactions have been observed in fertilization thus far. However, this has been observed in cadherin signaling for polarity in *Drosophila* (Chen et al., 2008). Polarity is also required for fertilization and establishing egg activation. Another example related to cell-cell fusion is EFF-1 in *C. elegans* which mediates cell-cell fusion in the Soma (Segev et al., 2018). The EFF-1 interactions are structurally homologous to HAP2/GCS1 in flowering plants which is a sperm-egg fusogen in plants (Brukman et al., 2022). Homotypic interactions and sex specific expression patterns can make it difficult for identification of egg molecules as homotypic mutant animals would be sterile in both sexes and be very difficult to generate and maintain.

2.4 *De novo* gene formation in the testis and the co-evolution of fertilization receptors create complex genetic dynamics

Gene duplication and deletion events often drive evolution and establish new biological functions and phenotypes. Interestingly, it has been shown that *de novo* gene synthesis occurs much more often in the male lineage particularly through the testes (Kondo et al., 2017). This may also be referred to as the out of the testis hypothesis. It can be hypothesized that the abundant number of new genes in the male lineage may provide opportunities for these newly synthesized genes to be adopted into fertilization synapse complex working to stabilize this process and further define speciation. The male germline has several attributes that can facilitate new gene synthesis. These include histone modifications, demethylation of CpG islands, and increased expression of transcription associated proteins, as well as increased selective pressure from sperm competition (Kleene, 2001; Haerty et al., 2007; Kondo et al., 2017; Nyberg and Carthew, 2017). In contrast to gene synthesis, in gene loss, genes which no longer have biological functions can occur. Gene loss is less likely to occur in oocytes and primarily impacts multi-copy gene families (Assis, 2019). These results may demonstrate that while over time more sperm surface genes may be involved in fertilization, the genes on the oocyte side of the equation are less likely to change and may have strong levels of conservation and be involved in multiple processes such as both oogenesis and fertilization. It has also been hypothesized from observations in marine invertebrates that there is a co-evolution “arms race” of the male and female fertilization proteins in different species which may drive species specificity and could make identification of conserved fertilization molecules more difficult to identify (Wilburn and Swanson, 2016). The long-term evolutionary consequences of these changes in genes can both drive speciation and impact the genes that are involved in fertilization. These, however, are unlikely to be phenotypes that can be picked up in genetic screens but would require analysis of different species and genomes.

2.5 Sterile animals require active maintenance in the lab

As anyone who works in fertilization and gamete activation knows, maintaining mutant animals that are sterile or have lethal mutations requires active thought and coordination by researchers for each generation. To overcome these difficulties, there are a few very clever ways to maintain sterile animals for experimental analysis. One example is the identification conditional mutations. These conditional mutants can be temperature sensitive (ts) mutations that can be more

easily screened for in microbes, worms, and flies. These ts animals are sterile when cultured at high temperatures but fertile when cultured at lower temperatures (also see Section 2.7 below) (Suzuki and Procunier, 1969; O'Connell et al., 1998; Mei and Singson, 2021). A second approach is through inducible systems such as Cre-Lox, GAL4/UAS, and Auxin Inducible Degrons which use either site specific recombinases, DNA binding activation sites, or chemical induction to induce sterile phenotypes (Brand and Perrimon, 1993; Zhang et al., 2015; Kim et al., 2018). Finally, we can use balancer chromosomes which are rearranged chromosomes often with morphological and fluorescent tags which can be used to maintain recessive lethal or sterile mutations as heterozygotes without recombination (Dejima et al., 2018; Miller et al., 2019). Unfortunately, all of these techniques have their limitations. Temperature sensitive mutations rely on protein misfolding at differential temperatures and there are relatively few model organisms where this is a practical approach (body temperature conforms to ambient temperature). Furthermore, not all genes are able to be mutated to become temperature sensitive, this favors proteins with hydrophobic residues and higher free energy levels (Varadarajan et al., 1996). Inducible systems require knowledge of the specific gene and favor reverse genetic approaches which can bias gene identification. Some balancer chromosomes rely on active maintenance of mutant animals as heterozygotes. Finally, collecting enough mutant animals for analysis may require specific breeding schemes as in the case of mice and the amount of space and resources required can limit the amount of exploration that can occur. For egg surface genes, extra care must be taken in order to maintain a set of fertile-heterozygotes in order to generate mutants for the next generation. This sibling selection may require constant costly and laborious molecular genotyping.

2.6 Gametogenesis and fertilization are often inherently temperature sensitive, egg genes might be more specifically unable to become temperature sensitive

One way that researchers working on worms, flies, and fish have managed to keep sterile animal lines going is through temperature sensitive mutations as described in Section 2.5 (Mei and Singson, 2021). While this has been an extremely useful tool, not all proteins can be mutated to become temperature sensitive. In fact, spermatogenesis and sperm activation are inherently more temperature sensitive than egg processes (Nakamura et al., 1987; Kurhanewicz et al., 2020; Hirano et al., 2022). The ability of oocytes to buffer temperature may make it more difficult to identify mutations but may also reveal information about the biology of oocytes. In many male-female organisms, oocytes are available in a limited number, therefore protecting the viability of oocytes becomes essential for an animal's reproductive success, consequently our techniques of temperature stress may not be as efficient for egg specific genes.

2.7 Egg fertilization genes may be mischaracterized as embryonic lethal and meiosis mutants

Despite the difficulties in maintaining sterile animals, the field still engages in both forward and reverse genetic screens identify additional genes involved in fertilization. This has often required creative techniques such as temperature sensitive mutants, sibling selection, balancing all mutants prior to analysis, and using CRISPR/Cas9 to knock out all candidate genes to capture sterile alleles for future analysis (Mei and Singson, 2021). After mutagenesis one limitation is that it can be difficult to differentiate between genes that are embryonic lethal or have meiosis defects from fertilization specific genes at a high level since they often display similar terminal phenotypes. This can lead to a bottleneck in assessing mutations in a screen. Furthermore, on the flipside, when researchers are conducting screens for other phenotypes, they may encounter sterile mutants but not have the experimental tools to keep these mutations from getting dropped out of the population. It is possible that the egg surface genes that we are interested in may have been discarded in screens looking for embryonic lethal or meiosis genes.

2.8 Laboratory environments may not mimic environmental conditions that the animal might experience in the wild

Labs are often sterile environments that researchers work hard to keep free from contamination. However, this does not mimic the natural environment that our experimental organisms experience in the wild. Animals in laboratory environments do not face competition for food, contamination by parasites and bacteria, the temperature is stable, and light-dark cycles are controlled. These environmental stresses can often decrease fertility in the wild through changes in immune response, diet, and seasonality (Amaral et al., 2014). Therefore, in laboratory environments, we may be unable to recapitulate the environmental stressors that may impact fertility by modulating gene responses.

2.9 Egg fertility proteins may be sensitive to one mutant copy and quickly become sterile

In contrast to the idea that we're unable to capture egg genes due to redundancy where there is no observable phenotype because there's another copy of the gene which is compensating for the loss of one copy is a dominant sterile mutation. In a dominant sterile mutation, the loss of one copy of a gene through mutation renders an animal sterile or lethal (Erdélyi and Szabad, 1989). Capturing dominant sterile mutations may occur in genetic screens but lead to a dead end. It is incredibly difficult to keep dominant sterile strains alive. Maintaining a dominant sterile mutation requires the gene to have sex restricted expression where one sex is not sterile. For example, a dominant negative sperm mutation would not impact females, therefore the mutation could be carefully maintained in the maternal lineage and then crossed to a wild-type male and analyze their male progeny which would have one copy of the gene. One example of this is *wee-1.3* in *C. elegans*. The *wee-1.3* gene encodes a kinase that functions during spermatogenesis, a dominant mutation in this gene renders an animal infertile (Lamitina and L'Hernault, 2002). The hermaphrodite-male androdiecious reproductive mode in *C. elegans* is the only way that these mutant animals were able to be maintain. These limitations therefore preclude anything, that is, homotypic and expressed in both gametes. If prepared, it is possible to generate conditional mutants, however this excludes forward genetic screens and simple knockouts for analyses.

TABLE 1 Egg surface fertilization molecules.

Gene	Species	Protein domains and features	References
egg-1	*C. elegans*	Transmembrane protein with LDL repeats	Kadandale et al. (2005)
egg-2	*C. elegans*	Transmembrane protein with LDL repeats	Kadandale et al. (2005)
Juno	Mouse	GPI anchored folate receptor	Bianchi et al. (2014)
CD9	Mouse	Tetraspanin	Naour et al. (2000), Bianchi et al. (2014)
CD81	Mouse	Tetraspanin	Tanigawa et al. (2008)
Bouncer	Zebrafish	GPI anchored, Ly6 Superfamily	Herberg et al. (2018)

TABLE 2 Solutions to identifying egg genes.

Unbiased forward genetic screens utilizing genetic tools such as balancer chromosomes to identify non-conditional mutants
Systematic knockout of all oocyte expressed genes and gene pairs using CRISPR/Cas9
Immunoprecipitation and proximity labeling to identify candidates followed by genetic validation

2.10 Small proteins are less likely to be mutated in genetic screens and less likely to be identified with biochemical methods

In fertilization small genes (less than 200 amino acids) have been shown to have important roles for fertilization. In Zebrafish, Bouncer, the Ly6/uPAR protein on the egg surface is 80 amino acids (Herberg et al., 2018). On the sperm side of the equation, *spe-13* in *C. elegans* is 130 amino acids (Singson Lab unpublished observation) and *fimp-1* in mouse with 111 amino acids are also small proteins involved in fertilization (Fujihara et al., 2020). Despite their important roles, small proteins are more likely to be missed in both genetic screens as well as mass spectrometry or ribosomal profiling (Jorgensen and Mango, 2002; Harney et al., 2019). In genetic screens the smaller number of nucleotides in each gene decreases the probability that individual base pairs will be mutated in the right region for sterility to occur. For mass spectrometry and ribosome profiling, this is also an issue as RNA based methods are more likely occurring with amplified RNA which can filter out smaller RNAs, and small transcripts may be beyond the sensitivity of the equipment (Ahrens et al., 2021). The emergence of the importance of small proteins may be a good avenue for future analysis.

2.11 Mutations in egg fertilization genes may generate extremely subfertile animals but not be labeled fertilization defects

The question of what constitutes a sterile phenotype may also mire the picture of what genes are involved with fertilization on the egg's surface. Infertility is clinically defined as failure to conceive after 12 months of unprotected intercourse (Mélodie and Christine, 2018). This also discounts couples that may be able to have one child but then experience secondary infertility. A significant drop in the number of progeny that an animal produces due to a genetic mutation while not completely sterilizing an animal could make it difficult to determine if involvement is technically in fertilization. There is some debate in what should be considered subfertile or sterile, particularly in animals with larger broods and faster rates of ovulation. For example, mice ovulate at 8 times the rate of humans with more than one egg at a time, a decrease in litter size here could look like clinical infertility in humans (Vjugina and Evans, 2008). Similarly in *C. elegans* which have a brood size of ~300 progeny in their reproductive lifetime, a decrease to two progeny in their lifetime would be very likely to be considered clinically infertile if modeled in humans. Thus, we encourage careful analysis of animals with fertility defects and a careful analysis of the phenotypes in determining their role at the molecular level.

2.12 Previous biochemical analysis has often been unable to be genetically validated

Previous biochemical analysis primarily in sea urchin and abalone identified a multitude of proteins such as Bindin, speract and resact, VERL and lysin through analysis of cell extracts using monoclonal antibodies to inhibit fertilization (Vacquier and Moy, 1977; Hansbrough and Garbers, 1981). These approaches were valiant and groundbreaking to our understanding of protein candidates for fertilization. However, when genetic knockouts were examined for many of these genes, the animals were still fertile (Deneke and Pauli, 2021). Monoclonal antibodies to gamete surface antigens were helpful in identifying and validating IZUMO (Okabe et al., 1988). CD81 was also identified through monoclonal antibodies but is not essential but still can contribute to fertilization (Takahashi et al., 2001; Rubinstein et al., 2006). As we continue our search for all the genes that are involved in fertilization these contributions help us to understand the redundancy of the process and the contributing factors.

2.13 Historical narratives surrounding the roles of females may impact current egg gene discovery

Both historically and currently, females are understudied (Ah-King et al., 2014). Despite awareness and advocacy of this issue from individual researchers to as well as organizations such as the NIH, this gap has persisted (Arnegard et al., 2020). Commonly described reasons for why females continue to be understudied include that there is a stronger interest in male processes of reproduction, and that eggs are presumed to be less complex and passive receivers of sperm whose biology has already been fully characterized (Méndez

and Córdoba-Aguilar, 2004). These reasons are not evidence based and fail to take into account recent gene discovery in fertilization, egg activation, and blocks to polyspermy which still have largely unknown mechanisms and complex cell signaling and organization. Perpetuating these ideas minimizes the role of females and can be potentially harmful in the treatment of female reproductive health.

3 Addressing the sperm and egg gene discovery question

To address the difficulty in identifying egg genes (and in fact sperm genes), there are several approaches that can be and are currently being taken (Table 2). For example, in *C. elegans* we are employing an approach which will involve doing random mutagenesis and then using balancer chromosomes to generate stable balanced lines of mutants, in contrast to previous screens which have identified temperature sensitive mutants that are typically not genetic nulls. This approach in invertebrate systems can allow for higher throughput of mutations to be screened as well as help differentiate embryonic lethal and meiosis mutants. In parallel with characterization of genetic mutants, Whole Genome Sequencing (WGS) can be employed to identify the causative mutation. Another approach being undertaken is to use CRISPR-Cas9 to generate knockouts of all testes expressed genes as is being undertaken by several labs to ascertain which knockouts impact fertilization (Miyata et al., 2016; Abbasi et al., 2020). A similar approach could be taken to knock out all oocyte expressed genes. This is however an expensive approach and can miss redundant or pleiotropic genes. Redundancy and pleiotropy remain problems which are difficult to address. A bioinformatic approach identifying potential gene pairs could aid in prioritizing generating double mutants could partially address this issue. Finally, for pleiotropic genes, conditional systems such as those mentioned in Section 2.6 can be employed. One caveat to this approach is that it is limited in the number of candidates that this would be feasible for as these can be labor intensive strains to build. Complementary to these approaches, utilizing biochemical approaches such as immunoprecipitation and proximity labeling will help us to better understand other proteins that are involved in fertilization. Taking advantage of biochemical approaches now supported by complementary genetic approaches will bring all available tools to bear on our understanding of how nature does conception.

4 Conclusion

Is this question of where are all the egg genes an experimental problem or a true biological asymmetry? We imagine that it might be a combination of both possibilities. Will this asymmetry of sperm and egg molecules also be seen in other species such as fish, frogs, and humans? We have great faith in the determination and productivity of the reproductive biology community to continue with its rapid and transforming fertility gene discovery. Exciting new experimental approaches to aid in egg gene discovery are rapidly coming into play. The future discoveries of egg genes will greatly enhance our understanding of fertilization to aid in the development of infertility treatments and novel contraceptive techniques as well as provide further understanding of how two morphologically distinct cells interact with each other.

Author contributions

KM and AS prepared and revised the manuscript. KM generated the figures.

Funding

This work was supported by funding from an NIH Grant to AS (R01HD054681) and KM was also supported by an NIH Institutional Research and Academic Career Development Award (K12GM093854) Fellowship.

Conflict of interest

The authors declare that the research was conducted in the absence of any commercial or financial relationships that could be construed as a potential conflict of interest.

Publisher's note

References

Abbasi, F., Kodani, M., Emori, C., Kiyozumi, D., Mori, M., Fujihara, Y., et al. (2020). CRISPR/Cas9-Mediated genome editing reveals oosp family genes are dispensable for female fertility in mice. *Cells* 9, 821. doi:10.3390/cells9040821

Ah-King, M., Barron, A. B., and Herberstein, M. E. (2014). Genital evolution: Why are females still understudied? *Plos Biol.* 12, e1001851. doi:10.1371/journal.pbio.1001851

Ahrens, C. H., Wade, J. T., Champion, M. M., and Langer, J. D. (2021). A practical guide to small protein discovery and characterization using mass spectrometry. *J. Bacteriol.* 204, e0035321. doi:10.1128/jb.00353-21

Amaral, F. G., Castrucci, A. M., Cipolla-Neto, J., Poletini, M. O., Mendez, N., Richter, H. G., et al. (2014). Environmental control of biological rhythms: Effects on development, fertility and metabolism. *J. Neuroendocrinol.* 26, 603–612. doi:10.1111/jne.12144

Arnegard, M. E., Whitten, L. A., Hunter, C., and Clayton, J. A. (2020). Sex as a biological variable: A 5-year progress report and call to action. *J. Women's Heal* 29, 858–864. doi:10.1089/jwh.2019.8247

Assis, R. (2019). Out of the testis, into the ovary: Biased outcomes of gene duplication and deletion in Drosophila. *Evolution* 73, 1850–1862. doi:10.1111/evo.13820

Bennett, M. J., Choe, S., and Eisenberg, D. (1994). Domain swapping: Entangling alliances between proteins. *Proc. Natl. Acad. Sci.* 91, 3127–3131. doi:10.1073/pnas.91.8.3127

Bhakta, H. H., Refai, F. H., and Avella, M. A. (2019). The molecular mechanisms mediating mammalian fertilization. *Development* 146, dev176966. doi:10.1242/dev.176966

Bianchi, E., Doe, B., Goulding, D., and Wright, G. J. (2014). Juno is the egg Izumo receptor and is essential for mammalian fertilization. *Nature* 508, 483–487. doi:10.1038/nature13203

Bianchi, E., and Wright, G. J. (2020). Find and fuse: Unsolved mysteries in sperm–egg recognition. *Plos Biol.* 18, e3000953. doi:10.1371/journal.pbio.3000953

Binner, M. I., Kogan, A., Panser, K., Schleiffer, A., Deneke, V. E., and Pauli, A. (2022). The sperm protein Spaca6 is essential for fertilization in zebrafish. *Front. Cell Dev. Biol.* 9, 806982. doi:10.3389/fcell.2021.806982

Blobel, C. P., Wolfsberg, T. G., Turck, C. W., Myles, D. G., Primakoff, P., and White, J. M. (1992). A potential fusion peptide and an integrin ligand domain in a protein active in sperm–egg fusion. *Nature* 356, 248–252. doi:10.1038/356248a0

Brand, A. H., and Perrimon, N. (1993). Targeted gene expression as a means of altering cell fates and generating dominant phenotypes. *Development* 118, 401–415. doi:10.1242/dev.118.2.401

Brukman, N. G., Li, X., and Podbilewicz, B. (2022). Fusexins, HAP2/GCS1 and evolution of gamete fusion. *Front. Cell Dev. Biol.* 9, 824024. doi:10.3389/fcell.2021.824024

Chen, W.-S., Antic, D., Matis, M., Logan, C. Y., Povelones, M., Anderson, G. A., et al. (2008). Asymmetric homotypic interactions of the atypical cadherin flamingo mediate intercellular polarity signaling. *Cell* 133, 1093–1105. doi:10.1016/j.cell.2008.04.048

Lander, E. S., Linton, L. M., Birren, B., Zody, M. C., Devon, K., Dewar, K., et al. (2001). Initial sequencing and analysis of the human genome. *Nature* 409, 860–921. doi:10.1038/35057062

Contreras, W., Wiesehöfer, C., Schreier, D., Leinung, N., Peche, P., Wennemuth, G., et al. (2022). C11orf94/Frey is a key regulator for male fertility by controlling Izumo1 complex assembly. *Sci. Adv.* 8, eabo6049. doi:10.1126/sciadv.abo6049

Curci, L., Brukman, N. G., Muñoz, M. W., Rojo, D., Carvajal, G., Sulzyk, V., et al. (2020). Functional redundancy and compensation: Deletion of multiple murine Crisp genes reveals their essential role for male fertility. *Faseb J.* 34, 15718–15733. doi:10.1096/fj.202001406r

Dejima, K., Hori, S., Iwata, S., Suehiro, Y., Yoshina, S., Motohashi, T., et al. (2018). An aneuploidy-free and structurally defined balancer chromosome toolkit for *Caenorhabditis elegans*. *Cell Rep.* 22, 232–241. doi:10.1016/j.celrep.2017.12.024

Deneke, V. E., and Pauli, A. (2021). The fertilization enigma: How sperm and egg fuse. *Annu. Rev. Cell Dev. Bi* 37, 391–414. doi:10.1146/annurev-cellbio-120219-021751

Ellerman, D. A., Ha, C., Primakoff, P., Myles, D. G., and Dveksler, G. S. (2003). Direct binding of the ligand PSG17 to CD9 requires a CD9 site essential for sperm-egg fusion. *Mol. Biol. Cell* 14, 5098–5103. doi:10.1091/mbc.e03-04-0244

Erdélyi, M., and Szabad, J. (1989). Isolation and characterization of dominant female sterile mutations of *Drosophila melanogaster*. I. Mutations on the third chromosome. *Genetics* 122, 111–127. doi:10.1093/genetics/122.1.111

Evans, J. P. (2002). The molecular basis of sperm–oocyte membrane interactions during mammalian fertilization. *Hum. Reprod. Update* 8, 297–311. doi:10.1093/humupd/8.4.297

Findlay, J. K., Holland, M. K., and Wong, B. B. M. (2019). Reproductive science and the future of the planet. *Reproduction* 1, R91–R96. doi:10.1530/rep-18-0640

Fujihara, Y., Herberg, S., Blaha, A., Panser, K., Kobayashi, K., Larasati, T., et al. (2021). The conserved fertility factor SPACA4/Bouncer has divergent modes of action in vertebrate fertilization. *Proc. Natl. Acad. Sci.* 118, e2108777118. doi:10.1073/pnas.2108777118

Fujihara, Y., Lu, Y., Noda, T., Oji, A., Larasati, T., Kojima-Kita, K., et al. (2020). Spermatozoa lacking Fertilization Influencing Membrane Protein (FIMP) fail to fuse with oocytes in mice. *Proc. Natl. Acad. Sci.* 117, 9393–9400. doi:10.1073/pnas.1917060117

Gibbs, G. M., Roelants, K., and O'Bryan, M. K. (2008). The CAP superfamily: Cysteine-rich secretory proteins, antigen 5, and pathogenesis-related 1 proteins—roles in reproduction, cancer, and immune defense. *Endocr. Rev.* 29, 865–897. doi:10.1210/er.2008-0032

Gleason, E. J., Lindsey, W. C., Kroft, T. L., Singson, A. W., and L'Hernault, S. W. (2006). spe-10 encodes a DHHC–CRD zinc-finger membrane protein required for endoplasmic reticulum/golgi membrane morphogenesis during *Caenorhabditis elegans* spermatogenesis. *Genetics* 172, 145–158. doi:10.1534/genetics.105.047340

Hachem, A., Godwin, J., Ruas, M., Lee, H. C., Buitrago, M. F., Ardestani, G., et al. (2017). PLCζ is the physiological trigger of the Ca2+ oscillations that induce embryogenesis in mammals but conception can occur in its absence. *Development* 144, 2914–2924. doi:10.1242/dev.150227

Haerty, W., Jagadeeshan, S., Kulathinal, R. J., Wong, A., Ram, K. R., Sirot, L. K., et al. (2007). Evolution in the fast lane: Rapidly evolving sex-related genes in Drosophila. *Genetics* 177, 1321–1335. doi:10.1534/genetics.107.078865

Hansbrough, J. R., and Garbers, D. L. (1981). Speract. Purification and characterization of a peptide associated with eggs that activates spermatozoa. *J. Biol. Chem.* 256, 1447–1452. doi:10.1016/s0021-9258(19)69983-7

Harney, D. J., Hutchison, A. T., Su, Z., Hatchwell, L., Heilbronn, L. K., Hocking, S., et al. (2019). Small-protein enrichment assay enables the rapid, unbiased analysis of over 100 low abundance factors from human plasma. *Mol. Cell Proteomics* 18, 1899–1915. doi:10.1074/mcp.tir119.001562

He, Z.-Y., Brakebusch, C., Fässler, R., Kreidberg, J. A., Primakoff, P., and Myles, D. G. (2003). None of the integrins known to be present on the mouse egg or to be ADAM receptors are essential for sperm–egg binding and fusion. *Dev. Biol.* 254, 226–237. doi:10.1016/s0012-1606(02)00043-x

Herberg, S., Gert, K. R., Schleiffer, A., and Pauli, A. (2018). The Ly6/uPAR protein Bouncer is necessary and sufficient for species-specific fertilization. *Science* 361, 1029–1033. doi:10.1126/science.aat7113

Hirano, K., Nonami, Y., Nakamura, Y., Sato, T., Sato, T., Ishiguro, K., et al. (2022). Temperature sensitivity of DNA double-strand break repair underpins heat-induced meiotic failure in mouse spermatogenesis. *Commun. Biol.* 5, 504. doi:10.1038/s42003-022-03449-y

Hynes, R. O. (2002). Integrins bidirectional, allosteric signaling machines. *Cell* 110, 673–687. doi:10.1016/s0092-8674(02)00971-6

Inoue, N., Hagihara, Y., and Wada, I. (2021). Evolutionarily conserved sperm factors, DCST1 and DCST2, are required for gamete fusion. *Elife* 10, e66313. doi:10.7554/elife.66313

Jorgensen, E. M., and Mango, S. E. (2002). The art and design of genetic screens: *Caenorhabditis elegans*. *Nat. Rev. Genet.* 3, 356–369. doi:10.1038/nrg794

Kadandale, P., Stewart-Michaelis, A., Gordon, S., Rubin, J., Klancer, R., Schweinsberg, P., et al. (2005). The egg surface LDL receptor repeat-containing proteins EGG-1 and EGG-2 are required for fertilization in *Caenorhabditis elegans*. *Curr. Biol.* 15, 2222–2229. doi:10.1016/j.cub.2005.10.043

Kim, H., Kim, M., Im, S.-K., and Fang, S. (2018). Mouse cre-LoxP system: General principles to determine tissue-specific roles of target genes. *Lab. Anim. Res.* 34, 147–159. doi:10.5625/lar.2018.34.4.147

Kim, J., and You, Y.-J. (2022). Oocyte quiescence: From formation to awakening. *Endocrinology* 163, bqac049. doi:10.1210/endocr/bqac049

Kleene, K. C. (2001). A possible meiotic function of the peculiar patterns of gene expression in mammalian spermatogenic cells. *Mech. Dev.* 106, 3–23. doi:10.1016/s0925-4773(01)00413-0

Kondo, S., Vedanayagam, J., Mohammed, J., Eizadshenass, S., Kan, L., Pang, N., et al. (2017). New genes often acquire male-specific functions but rarely become essential in Drosophila. *Gene Dev.* 31, 1841–1846. doi:10.1101/gad.303131.117

Kostrouchova, M., Krause, M., Kostrouch, Z., and Rall, J. E. (1998). CHR3: A *Caenorhabditis elegans* orphan nuclear hormone receptor required for proper epidermal development and molting. *Development* 125, 1617–1626. doi:10.1242/dev.125.9.1617

Kostrouchova, M., Krause, M., Kostrouch, Z., and Rall, J. E. (2001). Nuclear hormone receptor CHR3 is a critical regulator of all four larval molts of the nematode *Caenorhabditis elegans*. *Proc. Natl. Acad. Sci.* 98, 7360–7365. doi:10.1073/pnas.131171898

Krauchunas, A. R., Marcello, M. R., and Singson, A. (2016). The molecular complexity of fertilization: Introducing the concept of a fertilization synapse. *Mol. Reprod. Dev.* 83, 376–386. doi:10.1002/mrd.22634

Kroft, T. L., Gleason, E. J., and L'Hernault, S. W. (2005). The spe-42 gene is required for sperm–egg interactions during *C. elegans* fertilization and encodes a sperm-specific transmembrane protein. *Dev. Biol.* 286, 169–181. doi:10.1016/j.ydbio.2005.07.020

Kurhanewicz, N. A., Dinwiddie, D., Bush, Z. D., and Libuda, D. E. (2020). Elevated temperatures cause transposon-associated DNA damage in *C. elegans* spermatocytes. *Curr. Biol.* 30, 5007–5017. doi:10.1016/j.cub.2020.09.050

Lamitina, S. T., and L'Hernault, S. W. (2002). Dominant mutations in the *Caenorhabditis elegans* Myt1 ortholog wee-1.3 reveal a novel domain that controls M-phase entry during spermatogenesis. *Development* 129, 5009–5018. doi:10.1242/dev.129.21.5009

Mei, X., and Singson, A. W. (2021). The molecular underpinnings of fertility: Genetic approaches in *Caenorhabditis elegans*. *Adv. Genet.* 2, e10034. doi:10.1002/ggn2.10034

Mélodie, V. B., and Christine, W. (2018). Fertility and infertility: Definition and epidemiology. *Clin. Biochem.* 62, 2–10. doi:10.1016/j.clinbiochem.2018.03.012

Méndez, V., and Córdoba-Aguilar, A. (2004). Sexual selection and animal genitalia. *Trends Ecol. Evol.* 19, 224–225. doi:10.1016/j.tree.2004.03.012

Miller, B. J., Georges-Labouesse, E., Primakoff, P., and Myles, D. G. (2000). Normal fertilization occurs with eggs lacking the integrin alpha6beta1 and is CD9-dependent. *J. Cell Biol.* 149, 1289–1296. doi:10.1083/jcb.149.6.1289

Miller, D. E., Cook, K. R., and Hawley, R. S. (2019). The joy of balancers. *Plos Genet.* 15, e1008421. doi:10.1371/journal.pgen.1008421

Miyata, H., Castaneda, J. M., Fujihara, Y., Yu, Z., Archambeault, D. R., Isotani, A., et al. (2016). Genome engineering uncovers 54 evolutionarily conserved and testis-enriched genes that are not required for male fertility in mice. *Proc. Natl. Acad. Sci.* 113, 7704–7710. doi:10.1073/pnas.1608458113

Nakamura, M., Namiki, M., Okuyama, A., Matsui, T., Doi, Y., Takeyama, M., et al. (1987). Temperature sensitivity of human spermatogonia and spermatocytes *in vitro*. *Arch. Androl.* 19, 127–132. doi:10.3109/01485018708986808

Naour, F. L., Rubinstein, E., Jasmin, C., Prenant, M., and Boucheix, C. (2000). Severely reduced female fertility in CD9-deficient mice. *Science* 287, 319–321. doi:10.1126/science.287.5451.319

Noda, T., Blaha, A., Fujihara, Y., Gert, K. R., Emori, C., Deneke, V. E., et al. (2022). Sperm membrane proteins DCST1 and DCST2 are required for sperm-egg interaction in mice and fish. *Commun. Biol.* 5, 332. doi:10.1038/s42003-022-03289-w

Nyberg, K. G., and Carthew, R. W. (2017). Out of the testis: Biological impacts of new genes. *Gene Dev.* 31, 1825–1826. doi:10.1101/gad.307496.117

O'Connell, K. F., Leys, C. M., and White, J. G. (1998). A genetic screen for temperature-sensitive cell-division mutants of *Caenorhabditis elegans*. *Genetics* 149, 1303–1321. doi:10.1093/genetics/149.3.1303

Okabe, M., Yagasaki, M., Oda, H., Matzno, S., Kohama, Y., and Mimura, T. (1988). Effect of a monoclonal anti-mouse sperm antibody (OBF13) on the interaction of mouse sperm with zona-free mouse and hamster eggs. *J. Reprod. Immunol.* 13, 211–219. doi:10.1016/0165-0378(88)90002-2

Ragle, J. M., Aita, A. L., Morrison, K. N., Martinez-Mendez, R., Saeger, H. N., Ashley, G. A., et al. (2020). The conserved molting/circadian rhythm regulator NHR-23/NR1F1 serves as an essential co-regulator of *C. elegans* spermatogenesis. *Development* 147, dev193862. doi:10.1242/dev.193862

Ros, V. G. D., Maldera, J. A., Willis, W. D., Cohen, D. J., Goulding, E. H., Gelman, D. M., et al. (2008). Impaired sperm fertilizing ability in mice lacking Cysteine-RIch Secretory Protein 1 (CRISP1). *Dev. Biol.* 320, 12–18. doi:10.1016/j.ydbio.2008.03.015

Rubinstein, E., Ziyyat, A., Prenant, M., Wrobel, E., Wolf, J.-P., Levy, S., et al. (2006). Reduced fertility of female mice lacking CD81. *Dev. Biol.* 290, 351–358. doi:10.1016/j.ydbio.2005.11.031

Sanders, J. R., Ashley, B., Moon, A., Woolley, T. E., and Swann, K. (2018). PLCζ induced Ca2+ oscillations in mouse eggs involve a positive feedback cycle of Ca2+ induced InsP3 formation from cytoplasmic PIP2. *Front. Cell Dev. Biol.* 6, 36. doi:10.3389/fcell.2018.00036

Schreier, J., Dietz, S., Boermel, M., Oorschot, V., Seistrup, A.-S., Domingues, A. M. de J., et al. (2022). Membrane-associated cytoplasmic granules carrying the Argonaute protein WAGO-3 enable paternal epigenetic inheritance in *Caenorhabditis elegans*. *Nat. Cell Biol.* 24, 217–229. doi:10.1038/s41556-021-00827-2

Schultz, R. M., and Williams, C. J. (2002). The science of ART. *Science* 296, 2188–2190. doi:10.1126/science.1071741

Segev, N., Avinoam, O., and Podbilewicz, B. (2018). Fusogens. *Curr. Biol.* 28, R37–R380. doi:10.1016/j.cub.2018.01.024

Spiegelstein, O., Eudy, J. D., and Finnell, R. H. (2000). Identification of two putative novel folate receptor genes in humans and mouse. *Gene* 258, 117–125. doi:10.1016/s0378-1119(00)00418-2

Suzuki, D. T., and Procunier, D. (1969). Temperature-sensitive mutations in *Drosophila melanogaster*. 3. Dominant lethals and semilethals on chromosome 2*†. *Proc. Natl. Acad. Sci.* 62, 369–376. doi:10.1073/pnas.62.2.369

Takahashi, Y., Bigler, D., Ito, Y., and White, J. M. (2001). Sequence-specific interaction between the disintegrin domain of mouse ADAM 3 and murine eggs: Role of beta1 integrin-associated proteins CD9, CD81, and CD98. *Mol. Biol. Cell* 12, 809–820. doi:10.1091/mbc.12.4.809

Tanigawa, M., Miyamoto, K., Kobayashi, S., Sato, M., Akutsu, H., Okabe, M., et al. (2008). Possible involvement of CD81 in acrosome reaction of sperm in mice. *Mol. Reprod. Dev.* 75, 150–155. doi:10.1002/mrd.20709

Vacquier, V. D., and Moy, G. W. (1977). Isolation of bindin: The protein responsible for adhesion of sperm to sea urchin eggs. *Proc. Natl. Acad. Sci.* 74, 2456–2460. doi:10.1073/pnas.74.6.2456

Varadarajan, R., Nagarajaram, H. A., and Ramakrishnan, C. (1996). A procedure for the prediction of temperature-sensitive mutants of a globular protein based solely on the amino acid sequence. *Proc. Natl. Acad. Sci.* 93, 13908–13913. doi:10.1073/pnas.93.24.13908

Vjugina, U., and Evans, J. P. (2008). New insights into the molecular basis of mammalian sperm-egg membrane interactions. *Front. Biosci.* 13, 462–476. doi:10.2741/2693

Wilburn, D. B., and Swanson, W. J. (2016). From molecules to mating: Rapid evolution and biochemical studies of reproductive proteins. *J. Proteomics* 135, 12–25. doi:10.1016/j.jprot.2015.06.007

Wilson, L. D., Obakpolor, O. A., Jones, A. M., Richie, A. L., Mieczkowski, B. D., Fall, G. T., et al. (2018). The *Caenorhabditis elegans* spe-49 gene is required for fertilization and encodes a sperm-specific transmembrane protein homologous to SPE-42. *Mol. Reprod. Dev.* 85, 563–578. doi:10.1002/mrd.22992

Yoon, S.-Y., Eum, J. H., Lee, J. E., Lee, H. C., Kim, Y. S., Han, J. E., et al. (2012). Recombinant human phospholipase C zeta 1 induces intracellular calcium oscillations and oocyte activation in mouse and human oocytes. *Hum. Reprod.* 27, 1768–1780. doi:10.1093/humrep/des092

Yoon, S.-Y., Jellerette, T., Salicioni, A. M., Lee, H. C., Yoo, M., Coward, K., et al. (2008). Human sperm devoid of PLC, zeta 1 fail to induce Ca2+ release and are unable to initiate the first step of embryo development. *J. Clin. Invest.* 118, 3671–3681. doi:10.1172/jci36942

Zhang, L., Ward, J. D., Cheng, Z., and Dernburg, A. F. (2015). The auxin-inducible degradation (AID) system enables versatile conditional protein depletion in *C. elegans*. *Development* 142, 4374–4384. doi:10.1242/dev.129635

frontiers | Frontiers in Cell and Developmental Biology

TYPE Original Research
PUBLISHED 17 February 2023
DOI 10.3389/fcell.2023.1072456

OPEN ACCESS

EDITED BY
Rafael A. Fissore,
University of Massachusetts Amherst, United States

REVIEWED BY
Marianne Malartre,
UMR9198 Institut de Biologie Intégrative de la Cellule (I2BC), France
Elizabeth Tweedie Ables,
East Carolina University, United States

*CORRESPONDENCE
Tina L. Tootle,
tina-tootle@uiowa.edu

†PRESENT ADDRESS
Bailey J. Vormezeele, Department of Medicine, University of Colorado, Anschutz Medical Campus, Aurora, CO, United States; Garrett C. Kimble, Department of Molecular Biology, University of Texas Southwestern Medical Center, Dallas, TX, United States; Daniel J. Kelpsch, Department of Embryology, Carnegie Institution for Science, Baltimore, MD, United States

‡These authors have contributed equally to this work and share first authorship

SPECIALTY SECTION
This article was submitted to Molecular and Cellular Reproduction, a section of the journal Frontiers in Cell and Developmental Biology

RECEIVED 17 October 2022
ACCEPTED 06 February 2023
PUBLISHED 17 February 2023

CITATION
Talbot DE, Vormezeele BJ, Kimble GC, Wineland DM, Kelpsch DJ, Giedt MS and Tootle TL (2023), Prostaglandins limit nuclear actin to control nucleolar function during oogenesis. *Front. Cell Dev. Biol.* 11:1072456. doi: 10.3389/fcell.2023.1072456

Prostaglandins limit nuclear actin to control nucleolar function during oogenesis

Danielle E. Talbot‡, Bailey J. Vormezeele†‡, Garrett C. Kimble†, Dylane M. Wineland, Daniel J. Kelpsch†, Michelle S. Giedt and Tina L. Tootle*

Anatomy and Cell Biology, University of Iowa Carver College of Medicine, Iowa City, IA, United States

Prostaglandins (PGs), locally acting lipid signals, regulate female reproduction, including oocyte development. However, the cellular mechanisms of PG action remain largely unknown. One cellular target of PG signaling is the nucleolus. Indeed, across organisms, loss of PGs results in misshapen nucleoli, and changes in nucleolar morphology are indicative of altered nucleolar function. A key role of the nucleolus is to transcribe ribosomal RNA (rRNA) to drive ribosomal biogenesis. Here we take advantage of the robust, *in vivo* system of *Drosophila* oogenesis to define the roles and downstream mechanisms whereby PGs regulate the nucleolus. We find that the altered nucleolar morphology due to PG loss is not due to reduced rRNA transcription. Instead, loss of PGs results in increased rRNA transcription and overall protein translation. PGs modulate these nucleolar functions by tightly regulating nuclear actin, which is enriched in the nucleolus. Specifically, we find that loss of PGs results in both increased nucleolar actin and changes in its form. Increasing nuclear actin, by either genetic loss of PG signaling or overexpression of nuclear targeted actin (NLS-actin), results in a round nucleolar morphology. Further, loss of PGs, overexpression of NLS-actin or loss of Exportin 6, all manipulations that increase nuclear actin levels, results in increased RNAPI-dependent transcription. Together these data reveal PGs carefully balance the level and forms of nuclear actin to control the level of nucleolar activity required for producing fertilization competent oocytes.

KEYWORDS

prostaglandins, nucleolus, nuclear actin, oogenesis, *Drosophila* prostaglandins limit nucleolar function

Introduction

Prostaglandins (PGs) are a conserved class of lipid signaling molecules that signal locally near their sites of synthesis (Funk, 2001). PGs are produced by a series of synthases and signal *via* G protein-coupled receptors (GPCRs). Specifically, the fatty acid arachidonic acid serves as the substrate for cyclooxygenase (COX) enzymes, which produce the PG intermediate. PG-type specific synthases convert this intermediate into bioactive PGs which activate PG-type specific GPCRs.

PGs regulate almost every aspect of female reproduction (Tootle, 2013). For example, loss of PG synthesis blocks mammalian follicle maturation and ovulation (Lim et al., 1997; Langenbach et al., 1999; Takahashi et al., 2010). Further, COX inhibitors (non-steroidal anti-inflammatory drugs) cause reversible infertility in women due to similar defects (Akil et al.,

1996; Smith et al., 1996; Pall et al., 2001). While it is clear how PGs are produced and initiate signaling cascades, the cellular roles of PGs during follicle development remain unclear.

One poorly understood cellular target of PG signaling is the nucleolus. The nucleolus is the largest nuclear organelle and is best known for its role in ribosomal RNA (rRNA) transcription and ribosome biogenesis (Pederson, 2011; Tiku and Antebi, 2018). It forms by liquid-liquid phase separation (Lafontaine et al., 2021). This phase separation is driven by interactions between intrinsically disordered proteins and rRNA. These interactions are driven by nucleolar function, specifically rRNA transcription. Thus, if the function of the nucleolus is perturbed, its morphology is changed. PG signaling, from flies to humans, regulates nucleolar morphology (Stark et al., 2001; Stark and Dunlop, 2005; Thoms et al., 2007; Khandelwal et al., 2011; Groen et al., 2015), suggesting it controls nucleolar functions. Dynamic regulation of nucleolar activity, including ribosome biogenesis, is a conserved process during oogenesis (Sanchez et al., 2016; Mercer et al., 2021). Specifically, nucleolar function within the oocyte is essential for producing sufficient ribosomes necessary for embryonic development outside of the mother, or for preimplantation embryonic development in placental mammals (Fulka and Aoki, 2016; Kresoja-Rakic and Santoro, 2019; Fulka et al., 2020). As both nucleolar functions and PGs are critical for producing viable oocytes, and PGs regulate nucleolar morphology in other contexts, one cellular role of PG signaling may be to regulate nucleolar function during oogenesis.

To uncover the roles of PGs and their downstream effectors in regulating the nucleolus, we use the robust, *in vivo* genetic system of *Drosophila* oogenesis. Adult female flies have a pair of ovaries, each comprised of ~15 ovarioles or chains of sequentially developing follicles (also referred to as egg chambers). There are 14 morphologically distinct stages of follicle development. Each follicle is comprised of 16 germline cells—15 nurse cells and one oocyte–which are surrounded by a somatic epithelium of ~650 follicle cells (Spradling, 1993). We previously identified Pxt as the sole COX-like enzyme in *Drosophila*; thus, loss of Pxt results in a lack of all PG synthesis and signaling (Tootle and Spradling, 2008). Pxt, like mammalian COX enzymes (Tootle, 2013; Prates et al., 2014; Sugimoto et al., 2015), is required for successful follicle development and fertility (Tootle and Spradling, 2008; Tootle et al., 2011). Loss of Pxt results in striking nucleolar morphology changes; the nucleoli in the nurse cells shift from a tubular to a rounded morphology (Groen et al., 2015), strongly suggesting nucleolar function is altered.

PG signaling also plays a conserved and critical role in regulating actin (Peppelenbosch et al., 1993; Pierce et al., 1999; Dormond et al., 2002; Tamma et al., 2003; Bulin et al., 2005; Birukova et al., 2007). Loss of Pxt results in severe defects in actin cytoskeletal remodeling, blocking normal follicle morphogenesis (Tootle and Spradling, 2008; Groen et al., 2012; Spracklen et al., 2014b; Spracklen et al., 2019). In addition to being a key component of the cytoskeleton, actin localizes to, and has numerous conserved functions within the nucleus (Kelpsch and Tootle, 2018; Green et al., 2021). The nuclear localization of actin is highly regulated. Cofilin-actin complexes are imported into the nucleus by Importin 9 (Imp9, (Dopie et al., 2012)), whereas Profilin-actin complexes are exported from the nucleus by Exportin 6 (Exp6, (Stuven et al., 2003)). Additionally, a recent study suggests that in *Drosophila* there are multiple mechanisms controlling nuclear actin import and export to ensure levels are tightly regulated (Borkuti et al., 2022). Inside the nucleus, actin promotes general transcription, is an active component of multiple chromatin remodeling complexes, participates in DNA damage repair, and contributes to nuclear structure (Kelpsch and Tootle, 2018; Green et al., 2021). Given this wide range of nuclear activities, it is not surprising that nuclear actin is emerging as a key regulator of differentiation and cell fate, including during oogenesis (Sen et al., 2015; Misu et al., 2017; Sen et al., 2017; Duan et al., 2020). Further, nuclear actin regulates chromatin movement during meiosis (Mogessie and Schuh, 2017), and plays critical roles in the structure and organization of large oocyte nuclei (Bohnsack et al., 2006); indeed perturbing nuclear actin causes chromatin and nucleolar coalescence (Maslova and Krasikova, 2012; Feric and Brangwynne, 2013). While nuclear actin has many functions, how these functions are regulated, and which are important for oocyte development remain poorly understood.

During *Drosophila* oogenesis, we previously found that there are three pools of endogenous nuclear actin that localize to the nucleolus with distinct developmental patterns (Wineland et al., 2018). These findings suggest that nuclear actin likely functions in the nucleolus. Supporting this idea, actin localizes to nucleoli in many organisms (Jockusch et al., 1971; Funaki et al., 1995; Andersen et al., 2002; Scherl et al., 2002; Andersen et al., 2005; Cruz and Moreno Diaz de la Espina, 2009; Belin et al., 2015; Wineland et al., 2018), numerous actin binding proteins are found in the nucleolus (Hubert et al., 2008; Deng et al., 2012; Groen et al., 2015; Kitamura et al., 2015), and actin promotes RNA Polymerase I (RNAPI) activity (Fomproix and Percipalle, 2004; Philimonenko et al., 2004; Almuzzaini et al., 2016). Given the relationships between PGs, actin, and the nucleolus, we hypothesize that PG signaling regulates nuclear actin to control nucleolar function and morphology during oogenesis.

We find PG signaling negatively regulates nuclear actin to restrict nucleolar activity to the correct level during *Drosophila* follicle development. Loss of Pxt, the *Drosophila* COX-like enzyme, causes striking changes in nucleolar morphology, and surprisingly, these nucleoli have increased rRNA transcription and normal nucleolar localization of a key RNAPI regulator. This ultimately results in increased protein translation. Loss of PG signaling also increases the level and/or expands the developmental pattern of the three pools of nuclear actin, raising the possibility that these changes in nuclear actin drive the alterations in nucleolar function and morphology. Supporting this idea, increasing nuclear actin levels by two different means or co-reduction of Pxt and Exp6, an export factor for nuclear actin (Stuven et al., 2003), results in *pxt*-like increases in rRNA transcription. Together these data lead to the model that PG signaling tightly controls nuclear actin–preventing the accumulation of too much of any nuclear actin pool–to limit nucleolar activity to the levels needed for successful *Drosophila* follicle development. We speculate that this pathway likely regulates oocyte development across organisms, as all the components–PGs, nuclear actin, and nucleolar activity–play conserved roles in oogenesis and fertility.

Results

Prostaglandin signaling restricts nucleolar transcription and protein synthesis

PGs regulate the structure of the nucleolus, including in *Drosophila* (Stark et al., 2001; Stark and Dunlop, 2005; Thoms

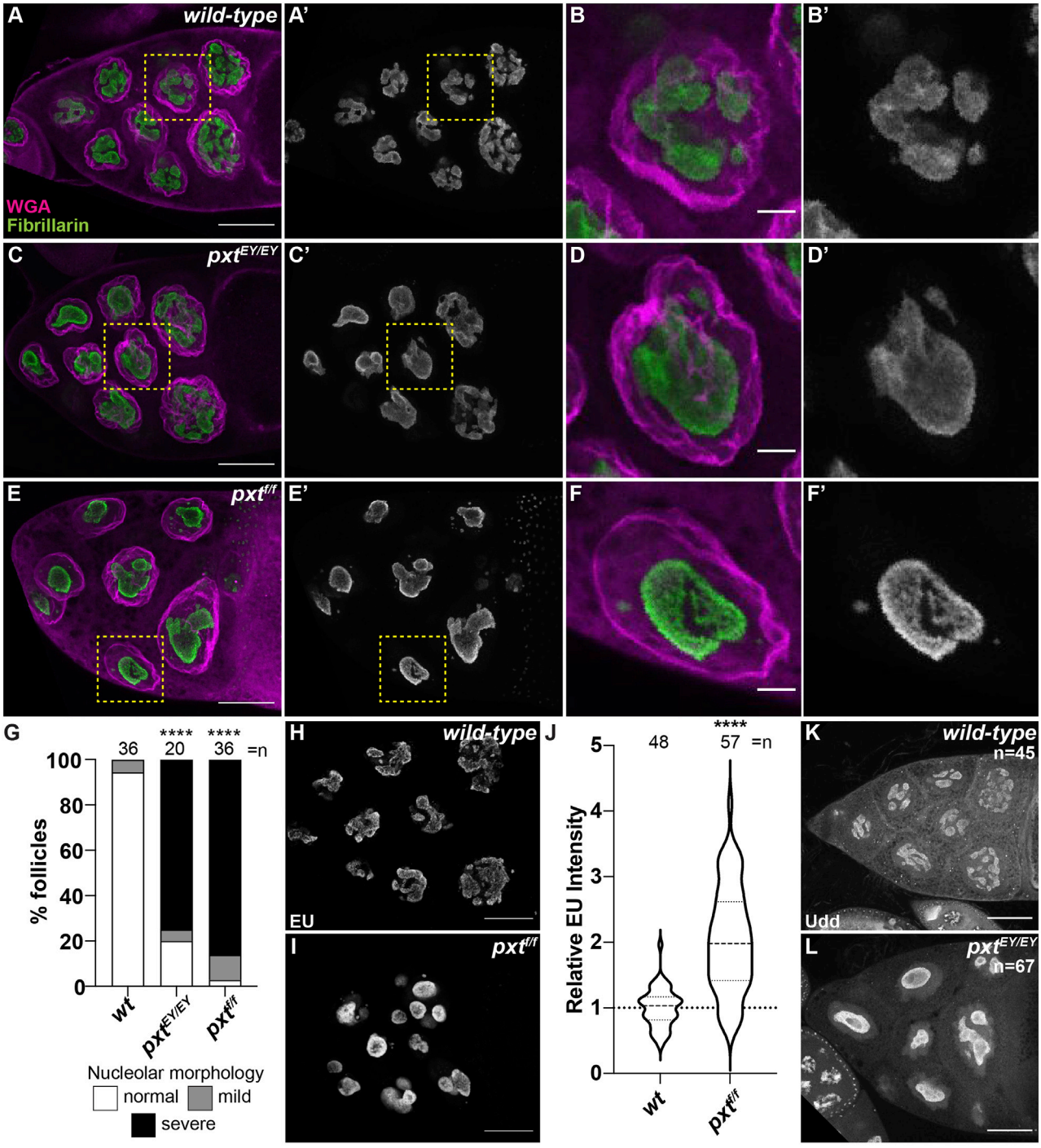

FIGURE 1
Prostaglandins regulate nucleolar structure and limit rRNA transcription. **(A–F′), (H,I,K,L)**. Maximum projections of 2-4 confocal slices of wild-type (*yw*) and *pxt* mutant ($pxt^{EY/EY}$ and $pxt^{f/f}$ as indicated) S10B follicles stained for: nucleolus (Fibrillarin, green in merge and white in single channel) and nuclear envelope wheat germ agglutinin (WGA), magenta in merge) in **(A–F′)**, nascent RNA (EU) in **(H,I)**, and Udd, a RNAPI regulatory complex component in **(K,L)**. Yellow boxed regions in **(A, C, E)** are shown as zoomed in images in **(B-B′, D-D′, F-F′)**, respectively. Scale bars = 50 μm except in **(B-B′, D-D′, F-F′)** where scale bars = 10 μm. **(G)**. Graph quantifying the percentage of follicles exhibiting normal (white) vs. mild (gray) or severe (black) defects in nucleolar morphology. **(J)**. Graph of quantification of relative EU intensity. ****$p < 0.0001$ (unpaired t-test). *n* = number of follicles. Loss of Pxt results in a rounded nucleolar morphology **(A–G)**, increased nascent nucleolar RNA **(H–J)**, and normal nucleolar localization of Udd **(K,L)**.

et al., 2007; Khandelwal et al., 2011; Groen et al., 2015). In the nurse cells of developing follicles nucleoli appear reticular in early stages (Supplementary Figures 1A-A′, D-D′) and in later stages (from Stage 9 [S9] onward) exhibit an interconnected tubular morphology (Supplementary Figure 1E-E′; Figure 1A-B′ and data not shown). Loss of Pxt by either of two alleles (pxt^{EY} and pxt^{f})and thereby, loss of

10.3389/fcell.2023.1072456

all PG synthesis, results in severe changes in nucleolar morphology throughout oogenesis (Supplementary Figure S1 and Figure 1), but the changes are most striking at S10B when almost all nurse cells exhibit rounded nucleoli (Figure 1C-F″) (Groen et al., 2015). Quantification reveals that 80% of pxt^{EY} mutant S10B follicles and ~97% of pxt^{f} mutant S10B follicles exhibit nucleolar morphology changes, with the majority of the changes being severe (Figure 1G); the phenotype of the two *pxt* alleles are not statistically different from each other so throughout the study, in most cases, they are used interchangeably and data from the two alleles is often combined and presented as *pxt*−/−. As nucleolar structure is highly dependent on its functions, we sought to identify the changes in nucleolar function that drive the morphological alteration when PGs are lost.

The best understood role of the nucleolus is to transcribe rRNA. Using a nucleotide incorporation assay (Click-iT EU), we assessed nascent RNA production in the nucleolus. In S10B nurse cells nascent RNA is restricted to the nucleolus (Figure 1H), as previously observed (Zhang et al., 2014; Sanchez et al., 2016). Further supporting this approach labels nascent rRNA, inhibition of RNAPII by α-amanitin does not impact the level of nucleolar RNA, whereas inhibition of RNAPI with actinomycin D blocks nucleolar RNA labeling (Supplementary Figures 2A-D) (Zhang et al., 2014; Sanchez et al., 2016). Based on the altered nucleolar morphology in *pxt* mutants, we expected impaired rRNA transcription. Instead, our data shows that loss of Pxt results in increased EU intensity (Figures 1H–J). This finding could indicate an increase in RNAPI activity and rRNA production or it could be an artifact due to the altered nucleolar volume due to the morphology change. To address if nucleolar volume impacts EU intensity we took advantage of the fact that within a wild-type follicle the anterior nurse cell, and therefore its nucleolus, is significantly smaller than more posterior nurse cells. Indeed, the mean nucleolar volume of the anterior-most wild-type nurse cell is 4,211 μm^3, whereas in the posterior nurse cells it is 5,340 μm^3 ($p = 0.0098$, paired t-test). We compared EU intensity between these two populations of nurse cells and find that it is similar, indicating that EU intensity and nascent rRNA production is consistent within a follicle, reflecting its stage in development and not the specific nucleolar volume of individual nurse cells (Supplementary Figure S3). These data lead us to favor the model that loss of Pxt results in increased rRNA production. Further supporting that the rounded nucleolar morphology in *pxt* mutants is not due to impaired rRNA production, directly inhibiting RNAPI results in distinct nucleolar morphology changes. Specifically, treatment of wild-type S10B follicles with actinomycin D results in the formation of multiple small, round nucleoli per cell (Supplementary Figure 2E, F). Finally, Udd, a component of the RNAPI regulatory complex (Zhang et al., 2014), remains highly enriched in the nucleoli when Pxt is lost (Figure 1K,L). These findings support the model that loss of Pxt results in increased RNAPI activity.

Our findings in *Drosophila* are consistent with what has been observed in colon cancer cells upon aspirin treatment, which inhibits COX activity and thus PG synthesis (Brighenti et al., 2016). Aspirin treatment results in a reduction of the small ribosomal subunit protein RpS6 compared to the large subunit protein RpL11. This imbalance in ribosomal proteins leads to the buildup of an rRNA intermediate (Brighenti et al., 2016). To

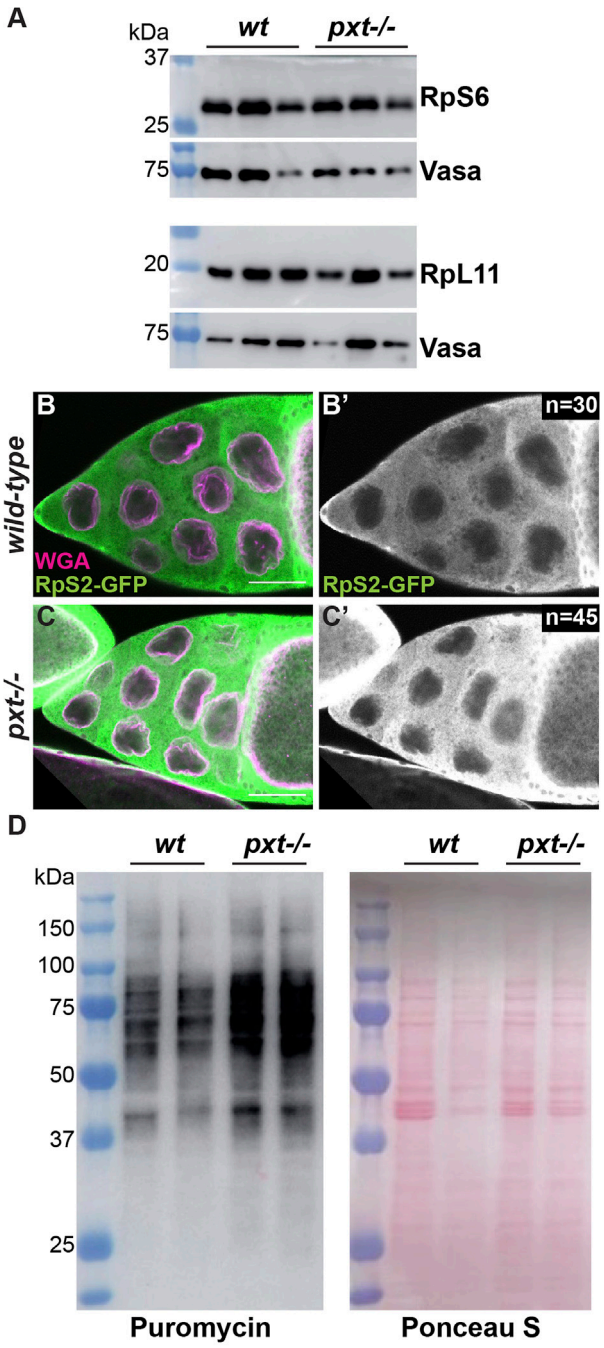

FIGURE 2
Prostaglandins restrict protein translation levels. **(A)**. Western blots of wild-type and pxt^{EY} mutant whole ovary lysates for RpS6 and RpL11; the Vasa blots serve as the loading controls. For RpS6, the blot was cut horizontally at the 37 kDa ladder band, with the top stained for Vasa and the bottom for RpS6. For RpL11, two gels were loaded with the same samples. **(B-C')**. Single confocal slice of wild-type and pxt^{f} mutant S10B follicles stained for: RpS2-GFP (anti-GFP) in green in merge and white in single channel **(B',C')** and WGA, which marks the nuclear envelope, in magenta in merge. Scale bars = 50 μm. **(D)**. Representative western blot for Puromycin and Ponceau S stained blot (loading control) of puromycin incorporation assay on wild-type and pxt^{EY} mutant whole ovary samples. In **(A,D)**, molecular weight ladder (kDa) is BioRad Precision Plus Protein Standard. Loss of Pxt results in no change in RpS6 compared to RpL11 levels **(A)**, normal cytoplasmic localization of RpS2 **(B-C')**, and increased protein translation **(D)**.

determine if the increased nascent nucleolar RNA we observe in *pxt* mutants is due to the same mechanism we assessed RpS6 and RpL11 levels. We find RpS6 remains highly expressed when Pxt is lost (Figure 2A), suggesting loss of Pxt during *Drosophila* oogenesis results in nucleolar changes distinct from those in cancer cells due to aspirin treatment.

We next assessed the role of PGs in ribosomal biogenesis and activity. If ribosome formation is impaired, ribosomal proteins are retained in the nucleolus (Zhang et al., 2014). Using a GFP protein trap in the ribosomal protein RpS2, we find that RpS2 leaves the nucleolus and localizes to the cytoplasm in both wild-type and *pxt* mutant follicles (Figure 2B-C'). This finding suggests that there are no defects in ribosomal biogenesis when Pxt is lost. We then assessed ribosomal activity by visualizing protein translation levels using a puromycin incorporation assay (Schmidt et al., 2009; Jang et al., 2021). Puromycin is a tRNA analog that is incorporated into polypeptide chains during translation. This incorporation results in the premature termination of translation and a puromycin-labeled polypeptide. These puromycin-labeled polypeptide chains can be detected *via* western blot using a puromycin antibody, revealing the relative rates of translation (Aviner, 2020). Loss of Pxt results in increased puromycin incorporation (Figure 2D), suggesting an increased rate of protein synthesis. Together, these findings support the model that PGs normally restrict RNAPI activity, ribosome production, and protein translation during *Drosophila* oogenesis.

Prostaglandins regulate nuclear actin accumulation in the nucleolus and its polymerization state

We previously discovered that during *Drosophila* oogenesis, PG signaling regulates actin cytoskeletal remodeling, (Tootle and Spradling, 2008; Groen et al., 2012; Spracklen et al., 2014b), and nuclear actin is both dynamic and enriched in the nucleolus (Wineland et al., 2018). These findings led us to hypothesize that PG signaling regulates nuclear actin to modulate nucleolar activities.

During *Drosophila* oogenesis there are three pools of endogenous nuclear actin recognized by DNase I, anti-actin C4 and anti-actin AC15, and all three pools exhibit nucleolar localization (Wineland et al., 2018). DNase I tightly binds to monomeric or G-actin (Hitchcock, 1980). We find that in addition to labeling G-actin in the cytoplasm, in the nucleus DNase I is enriched throughout the nucleolus and colocalizes with Fibrillarin in every single cell during oogenesis (Figure 3A-A″, Supplementary Figure 4A-B″). This finding indicates monomeric nuclear actin is enriched in the nucleolus (Wineland et al., 2018). Like DNase I, anti-actin C4 labels G-actin in both the cytoplasm and nucleus during oogenesis. However, the C4 antibody colocalizes with Fibrillarin, and thus, labels the whole nucleolus, in only a subset of mitotic follicle cells and in some of the nurse cells during S5-9 (Figure 3B-B″ yellow arrow, Supplementary Figure S4C-D″); in these instances, it overlaps with DNase I staining (Wineland et al., 2018). It is important to note that while in any fixed image only some of the nurse cell nucleoli are C4 positive, but based on the pattern of the staining being either middle vs. anterior and posterior nurse cells, we suspect that every nurse cell nucleolus at some point (and likely multiple points) in development has C4 positivity. C4 also labels polymeric actin in undifferentiated germ cells and in the germinal vesicle (Kelpsch et al., 2016; Wineland et al., 2018). We have previously validated the specificity of the C4 antibody for immunofluorescence during *Drosophila* oogenesis (Kelpsch et al., 2016). We next assessed anti-actin AC15 (see Supplementary Figure S5 for validation of AC15 antibody specificity). We find that anti-actin AC15 labels polymeric nuclear actin in every nurse and follicle cell starting weakly around S6, with higher levels in the nurse cells (Wineland et al., 2018). The AC15 levels increase in both the nurse and follicle cells during the subsequent stages with maximal labeling at S10 (Wineland et al., 2018). While AC15 nuclear actin primarily localizes to the chromatin, during mid-oogenesis AC15 nuclear actin puncta are also observed within the nurse cells in regions lacking DNA (Wineland et al., 2018). Previously, we speculated that these AC15 puncta were within the nucleolus (Wineland et al., 2018). To test this, we co-labeled follicles for the nucleolar protein Fibrillarin and AC15. Indeed, we find that AC15 labels puncta within the nurse cell nucleoli during S9-12 (Figure 3C-C″ blue arrows, Supplementary Movie S1, Supplementary Figure S4E-E" and data not shown). Together, these findings reveal that all three pools of endogenous nuclear actin localize to the nucleolus during follicle development, suggesting nuclear actin functions within the nucleolus.

We next asked whether PGs regulate the three pools of nuclear actin. Loss of Pxt results in increased nucleolar G-actin, as seen by DNase I and C4 labeling (Figure 4). We performed DNase I staining of *wild-type* and *pxt* mutant ovaries in the same tube; co-labeling with the Pxt antibody to distinguish the genotypes. Loss of Pxt results in subtle but significant increase in nucleolar DNase I staining in the nurse cells (Figure 4B-B′ compared to Figure 4A-A'), and a higher nucleolar to cytoplasmic DNase I fluorescence intensity ratio compared to *wild-type* (Figure 4C). We next examined the role of PGs in regulating C4 nuclear actin. We did not observe differences between C4 labeling in wild-type and *pxt* mutant follicle cells (data not shown). However, loss of Pxt results an increased frequency of nurse cells exhibiting nucleolar C4 staining (Figures 4E, F). These data indicate that loss of Pxt results in a change in the nucleolar G-actin that leads to increased C4 labeling.

Having found that PGs play a critical role in regulating nuclear G-actin, we assessed if PGs similarly affects polymeric nuclear actin recognized by AC15. Loss of Pxt results in earlier and more uniform AC15 labeling during *Drosophila* oogenesis (Figure 5A-D'); the *wild-type* and *pxt* mutant follicles were stained in the same tube, indicating the difference is not due to a staining artifact. We quantified the AC15 level in different developmental stages on a five-point scale (see methods for details). Loss of Pxt results in increased nuclear AC15 labeling prior to S5 and in S5/6 nurse and follicle cells, while the later stages are similar to wild-type (Figures 5E, F). These data suggest that loss of Pxt increases the amount of polymeric nuclear actin in the earlier stages of oogenesis, suggesting PGs regulate the form of nuclear actin. Given that AC15 labels puncta within nucleoli during mid-oogenesis (Figure 3C-C″ blue arrows, Movie 1, and Supplementary Figure S4E-E"), we next examined whether PGs regulate AC15 nucleolar actin. In wild-type follicles, there are little to no AC15 nucleolar puncta during S7/8, small puncta are observed in the majority of

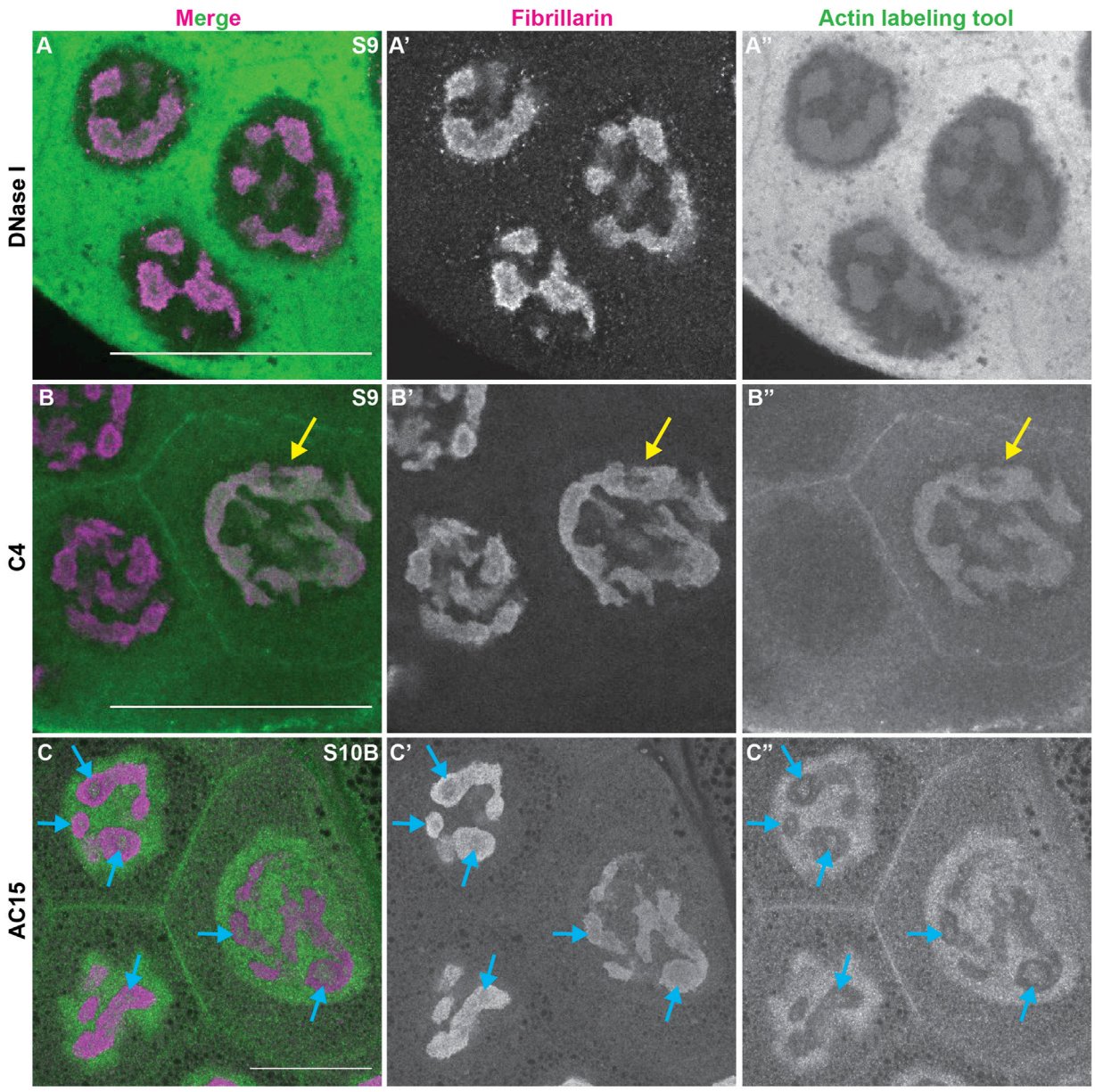

FIGURE 3
Nuclear actin is enriched in the nucleolus. **(A-C")**. Maximum projections of 2-5 confocal slices of zoomed in regions of a few nurse cells of wild-type follicles of the indicated stages (S) stained for the nucleolus (Fibrillarin, magenta in merge) and three different nuclear actin labeling tools (green in merge): DNase I **(A-A")**, anti-actin C4 (C4, **(B-B")**), and anti-actin AC15 (AC15, **(C-C")**); scale bars = 50 μm. Yellow arrow indicates a C4 positive nucleolus and blue arrows indicate AC15 positive nucleolar puncta. DNase I, which labels all monomeric actin, is enriched throughout the nucleolus of every cell **(A-A")**, whereas C4 labels whole nucleoli of a subset of nurse cells (yellow arrow, (B-B")). AC15 nuclear actin is largely localized to the chromatin, but in mid-oogenesis it labels puncta within every nurse cell nucleoli **(C-C")**, blue arrows).

S9 follicles, and by S10, all follicles exhibit puncta and most puncta are large (Figures 5G, H, K). Loss of Pxt results in earlier and increased AC15 nucleolar puncta, and these puncta are larger than those in wild-type follicles (Figures 5I–K).

Together our studies reveal that PGs play an important role in limiting the level of nucleolar actin and regulating its form–G-actin vs. C4 G-actin and monomeric vs. polymeric actin (AC15). We speculate that increased nucleolar actin affects both the stage it is observed in and later stages due to downstream effects of the impacted processes. Indeed, the nucleolar morphology defects observed in *pxt* mutants are more striking in the later stages (Kelpsch et al., 2016).

Increased nuclear actin levels alter nucleolar activity

We next sought to determine if the PG-dependent modulation of nucleolar morphology and function is due to regulation of nuclear actin.

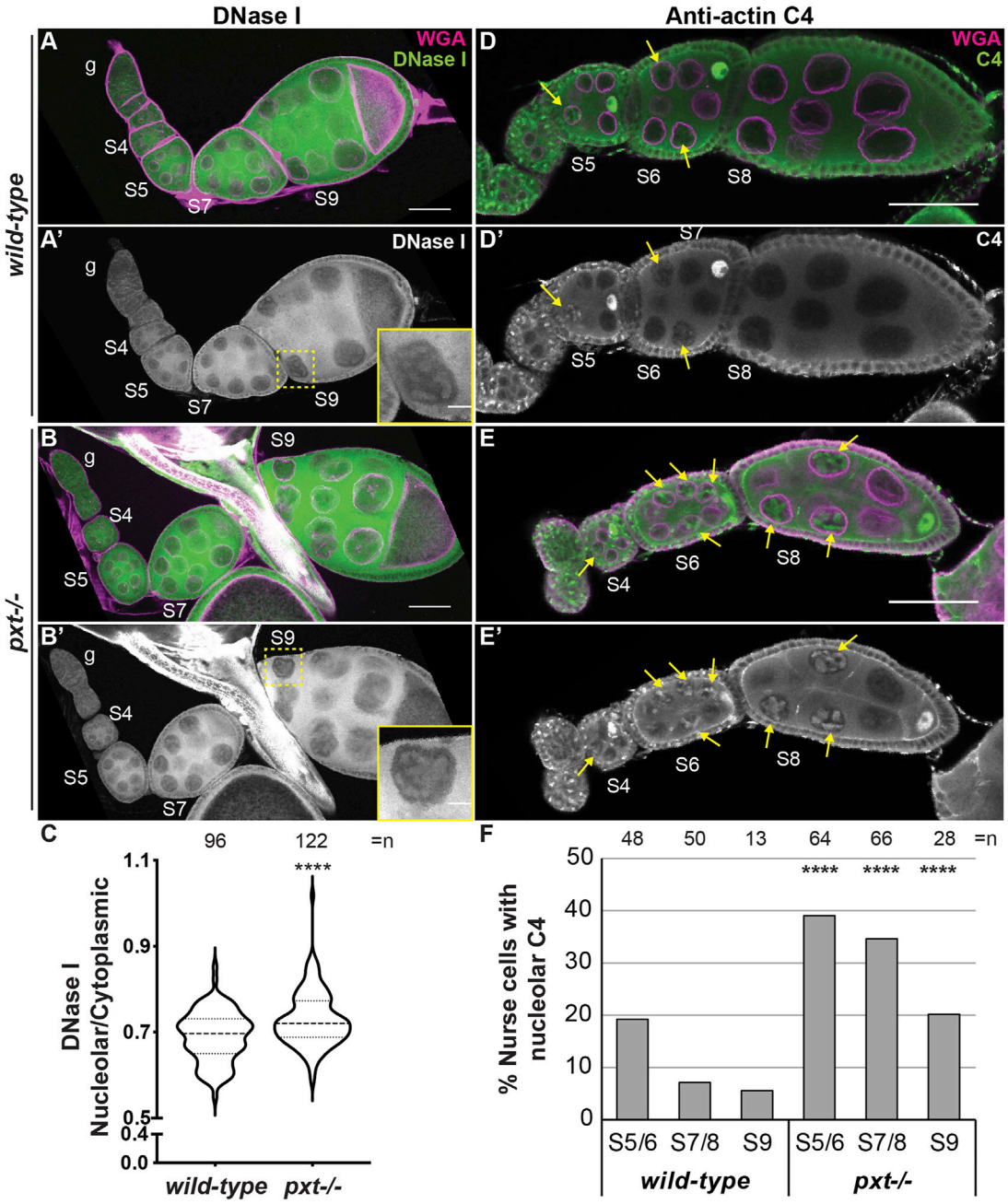

FIGURE 4
Prostaglandins restrict the amount of nuclear G-actin. **(A-B')**, **(D-E')**. Maximum projections of two confocal slices of wild-type and *pxt*^{EY} mutant follicles of the indicated stages (S, germarium = g) stained for: nuclear envelope (WGA) in magenta in merge and either DNase I **(A-B')** or anti-actin C4 (C4, **(D-E')** in green in merge and white in single channel. In **(A',B')**, yellow dashed box indicates nurse cell in inset. In **(D-E')**, yellow arrows indicate C4 positive nurse cell nucleoli. Scale bars = 50μm, except in inset where scale bars = 10 μm. **(C)**. Graph quantifying the ratio of nucleolar to cytoplasmic DNase I fluorescence intensity in S7/8 follicles, ****$p < 0.0001$ (unpaired t-test with Welch's correction). n = number of nurse cells; three nurse cells were measured per follicle. **(D)**. Graph quantifying the percentage of nurse cells in S5/6, S7/8, and S9 with C4 nucleolar staining, ****$p < 0.0001$ (Pearson's Chi-squared test). *n* = number of follicles. In **(C,D)**, data from both *pxt* alleles were combined. Loss of Pxt results in increased nucleolar DNase I levels **(A–C)**, and an increased frequency of C4 positive nurse cell nucleoli **(D–F)**.

If this is the case, then increasing nuclear actin levels alone will drive *pxt*-like changes in nucleolar morphology and/or function. To increase nuclear actin levels, we took two approaches, overexpression of nuclear targeted actin and loss of a nuclear actin export factor, Exp6 (encoded by *Drosophila ellipsoid body open* or *ebo*; (Stuven et al., 2003)).

First, we used the UAS/GAL4 system to overexpress nuclear targeted actin (UASp NLS-flag-Actin 5C, referred to as NLS-Actin) in the germline using two different transgenic insertions. Increasing nuclear actin levels results in altered nucleolar morphology (Figures 6A-C). The nucleoli go from a tubular to

10.3389/fcell.2023.1072456

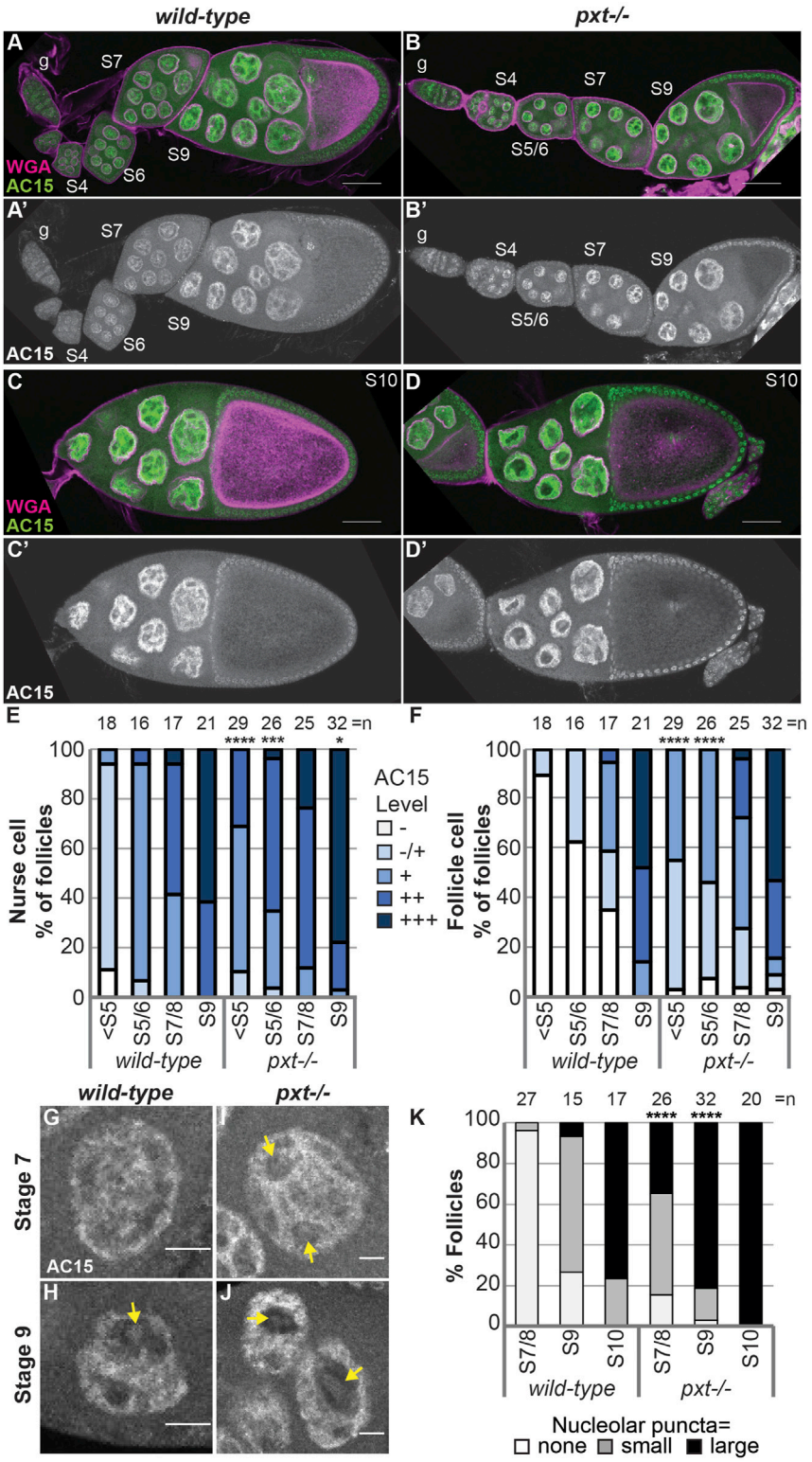

FIGURE 5
Prostaglandins restrict the developmental pattern and level of AC15 nuclear actin. **(A-D')**. Maximum projections of two confocal slices of wild-type and *pxt*^{f} mutant follicles of the indicated stages (S, germarium = g) stained for: nuclear envelope (WGA) in magenta in merge and AC15 in green in merge and white in single channel; scale bars = 50 µm. **(E,F)**. Graphs quantifying the percentage of follicles at the indicated stages with different levels of AC15 (–, –/+, +, ++, +++, white to dark blue) staining for nurse cells **(E)** and follicle cells **(F)**, ****$p < 0.0001$, ***$p < 0.001$, **$p < 0.01$ (Fisher's exact test). n = number of follicles. **(G–J)**. Maximum projections of two confocal slices of wild-type and *pxt*^{f} mutant nurse cells of the indicated stages stained for anti-actin AC15 (AC15) from the same images in **(A',B')**. Yellow arrows indicate puncta. Scale bars = 10 µm. **(K)**. Quantification of the percentage of follicles of the indicated stages exhibiting no (white), small (gray) or large (black) nucleolar puncta, ****$p < 0.0001$ (Pearson's Chi-squared test). *n* = number of follicles. In **(E, F, K)**, data from both *pxt* alleles were combined. Loss of Pxt results in earlier and stronger nuclear AC15 staining in both the nurse and follicle cells **(A–F)**, and earlier, larger, and more nucleolar AC15 puncta **(G–K)**.

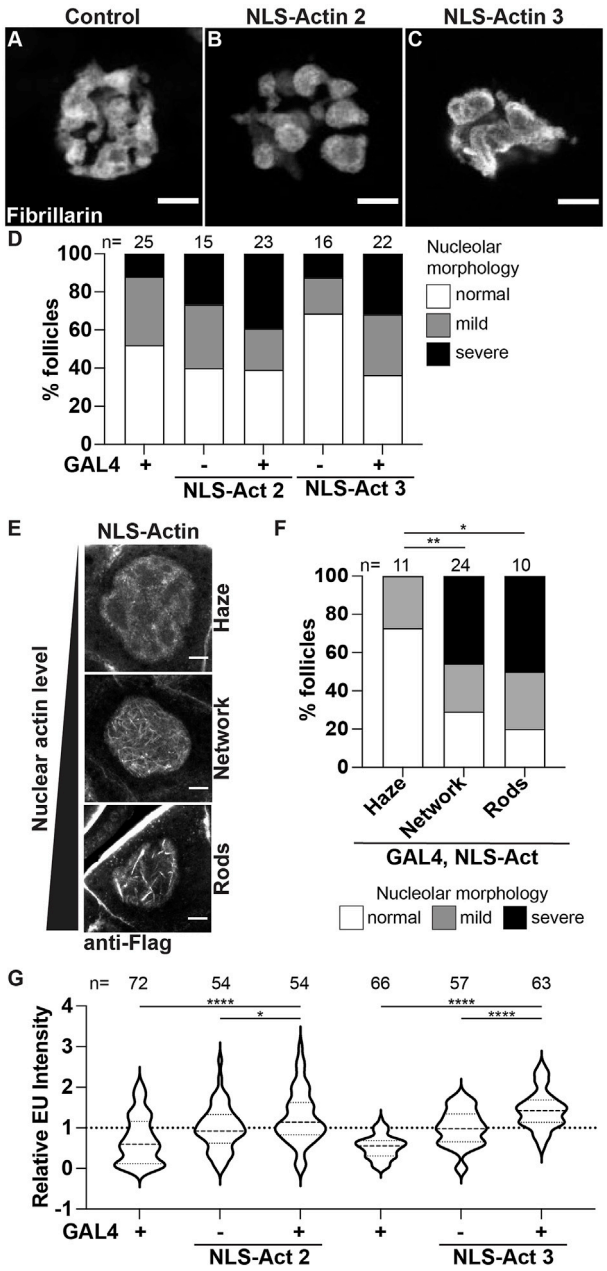

FIGURE 6
Increasing nuclear actin levels alters nucleolar morphology and increases nucleolar activity. **(A–C)**. Maximum projections of 2-4 confocal slices of Control (*osk GAL4/+*) and NLS-Actin (*osk GAL4/+; UAS NLS-flag-Actin 5C/+*) overexpressing single S10B nurse cells stained for the nucleolus (Fibrillarin). **(D)**. Graph quantifying the percentage of follicles exhibiting normal (white) vs. mild (gray) or severe (black) defects in nucleolar morphology. **(E)**. Maximum projections of 2-3 confocal slices of NLS-Actin overexpressing S10B nurse cells stained for Flag that exhibit varying levels of nuclear actin: haze (no obvious filaments), network of thin filaments, and rods (thick filaments). **(F)**. Graph quantifying the percentage of follicles exhibiting normal (white) vs. mild (gray) or severe (black) defects in nucleolar morphology when all the NLS-Actin overexpressing follicle data was combined and binned based on the level/structure of nuclear actin observed: haze, network of filaments, or rods $^{**}p < 0.01$, $^{*}p < 0.05$ (unpaired t-test). n = number of follicles. **(G)**. Graph quantifying the relative EU fluorescence intensity of the indicated genotypes, $^{****}p < 0.0001$, $^{*}p < 0.05$ (unpaired t-test). *n* = number of follicles. Overexpression of NLS-tagged Actin results in variable alterations in

(*Continued*)

FIGURE 6 (Continued)
nucleolar morphology, including pebbling **(B)** and coalescence **(C)**; these changes are not statistically significant **(D)**. However, when the level of nuclear actin is considered, follicles with increased nuclear actin, as observed by filament networks and rods, nucleolar morphology is altered **(E,F)**. Further, nascent nucleolar RNA levels are increased when nuclear targeted actin is expressed **(G)**. Scale bars = 10 μm.

a pebbled morphology, and in a few cases trended towards a *pxt*-like rounded phenotype. Notably, these nucleolar changes are only observed in a subset of the nurse cells; this is in contrast to *pxt* mutants in which all the nurse cell nucleoli within a follicle are affected. Quantification of the penetrance of the morphological changes across the nurse cells within a follicle reveals that while increased morphology changes are observed when NLS-Actin is overexpressed, but these changes are not significantly different than the controls (Figure 6D). To determine if this subtle change in nucleolar morphology was due to the variable level of nuclear actin resulting from NLS-Actin expression, we combined the NLS-Actin overexpression data and binned it based on the level of nuclear actin. As expected from previous work (Spracklen et al., 2014a; Kelpsch et al., 2016), when exogenous nuclear actin levels are low, only a nuclear actin haze is observed, whereas increasing nuclear actin levels results in a nuclear actin filament network (many thin actin filaments) or nuclear actin rod formation (fewer, thick actin structures) in the nurse cells (Figure 6E). We find that follicles with apparent nuclear F-actin structures have nucleolar morphology changes (i.e. the presence of nuclear actin filament networks and rods correlates with severe changes in nucleolar morphology), supporting that increased nuclear actin and/or changes in nuclear actin structure cause nucleolar alterations (Figure 6F). We next assessed if these changes in nucleolar structure reflect *pxt*-like increases in nucleolar activity. Overexpression of NLS-Actin results in increased nascent nucleolar RNA (Figure 6G).

We then assessed how loss of Exp6 impacts nucleolar morphology and function. Loss of Exp6 results in mild and variable alterations in nucleolar morphology, with a few follicles exhibiting nurse cells with pebbled nucleoli (Supplementary Figure S6A-C'); notably, these morphological changes are not statistically significant. This lack of phenotype could be due to the nature of the *exp6* allele (*exp6^{f}*). To test this possibility, we assessed Exp6 levels in this and other alleles; we find that *exp6^{f}* is a strong hypomorph with little to no protein present (Supplementary Figure S7A). Thus, the allele is not the reason for the lack of nucleolar morphology change. Instead, we speculate it is due to only minor alterations in nuclear actin levels. Indeed, it has been shown that loss of Exp6 only increases total nuclear actin levels by ~20% (Borkuti et al., 2022). We next assessed nucleolar function and find loss of Exp6 results in a significant increase in nascent nucleolar RNA (Supplementary Figure S6D). Together these data reveal that tight regulation of nuclear actin is critical for maintaining normal nucleolar activity, and when significantly perturbed impacts nucleolar morphology.

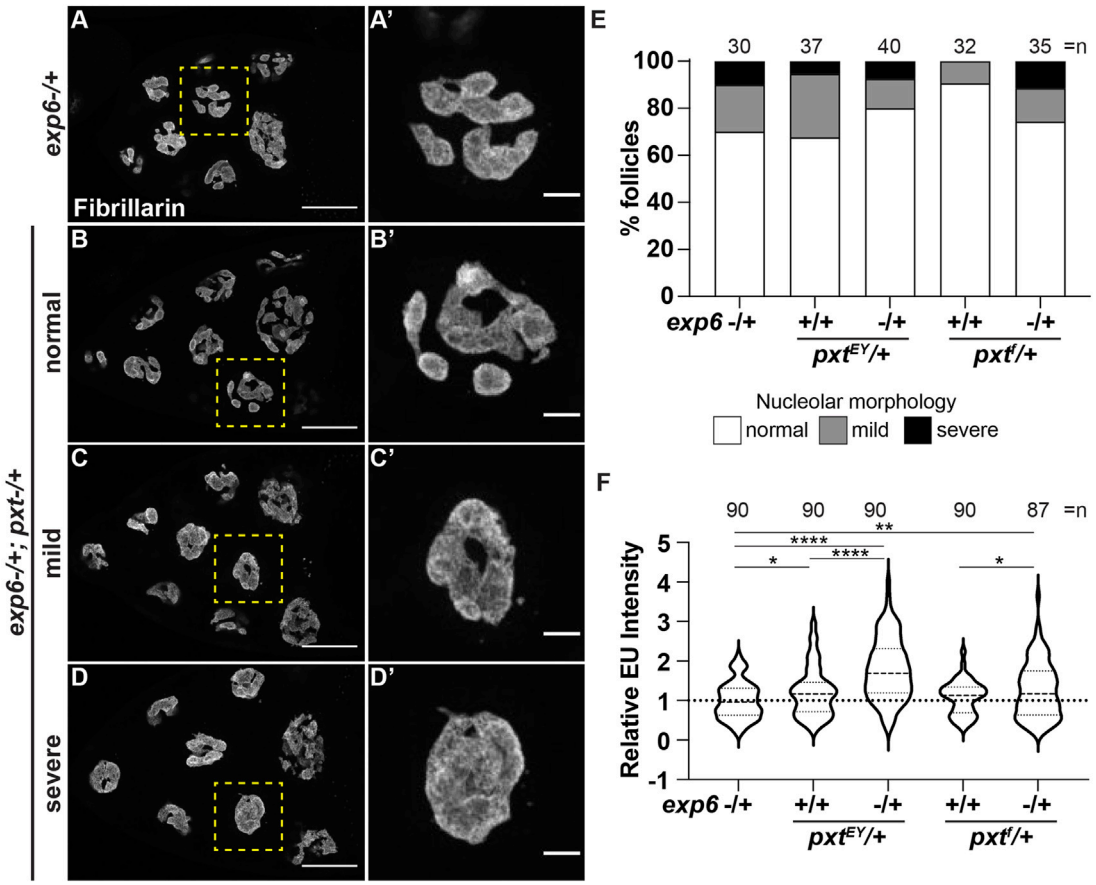

FIGURE 7
Prostaglandins limit nuclear actin to control nucleolar activity. **(A-D')**. Maximum projections of 3-4 confocal slices of *exp6–/+* (control) and *exp6–/+; pxt^{EY}/+* S10B follicles **(A–D)**, scale bars = 50 μm, or zoomed in images of single nurse cells boxed in yellow **(A'-D')**, scale bars = 10 μm, stained for the nucleolus (Fibrillarin). Examples of the varying nucleolar morphologies observed in the double heterozygotes are shown, normal vs. mild or severe defects. **(E)**. Graph quantifying the percentage of follicles exhibiting normal (white) vs. mild (gray) or severe (black) defects in nucleolar morphology; n = number of follicles. **(F)**. Graph quantifying the relative EU fluorescence intensity of the indicated genotypes, $^{****}p < 0.0001$, $^{**}p < 0.01$, $^{*}p < 0.05$ (unpaired t-test). n = number of follicles. Heterozygosity for *exp6* has little effect on nucleolar structure **(A-A')**, whereas follicles from double heterozygotes of *exp6* and *pxt* exhibit varying nucleolar morphologies, from normal to severe defects **(B-D')**; quantification of the level of defects indicates these changes are not statistically significant **(E)**. In contrast, double heterozygotes of *exp6* and *pxt* exhibit increased nascent nucleolar RNA **(F)**.

PGs regulate nuclear actin to control nucleolar functions

While our data reveal that PGs and nuclear actin both regulate nucleolar function/morphology and PGs control nuclear actin levels, it remains possible that PGs and nuclear actin act independently to regulate the nucleolus. To test if the nuclear actin changes in *pxt* mutants drive the observed changes in nucleolar activity, we assessed dominant genetic interactions between Pxt and Exp6. Heterozygosity for mutations in either *pxt* or *exp6* should weakly increase nuclear actin levels and therefore, have little to no effect on nucleolar morphology or function. If increasing nuclear actin drives nucleolar changes, then simultaneously reducing these two factors that normally limit nuclear actin levels is expected to increase nuclear actin and cause nucleolar defects. We find that there are variable nucleolar morphology changes in the double heterozygotes (*exp6–/+;;pxt–/+*), ranging from normal to severe *pxt*-like rounded nucleoli (Figure 7A-D'), but these changes are not statistically significant (Figure 7E). However, the double heterozygotes exhibit increased nascent nucleolar RNA levels (Figure 7F). This genetic interaction could suggest that PGs regulate Exp6; however, we think this is unlikely, as the phenotypes of the single heterozygotes are not statistically different from wild-type follicles (*yw*, *n* = 90), and as the most established means of regulating Exp6 activity is by modulating its expression (Bohnsack et al., 2006; Fiore et al., 2017) and Exp6 levels are unchanged in *pxt* mutants (Supplementary Figure S7B). Together, these findings lead to the model that PG signaling restricts nuclear actin to control nucleolar activity, specifically rRNA transcription, and modulates nucleolar morphology (Figure 8).

Discussion

While the systemic effects of PGs are well characterized, such as their role in regulating female fertility and oocyte development (Tootle, 2013), the cellular mechanisms remain unclear. Here we

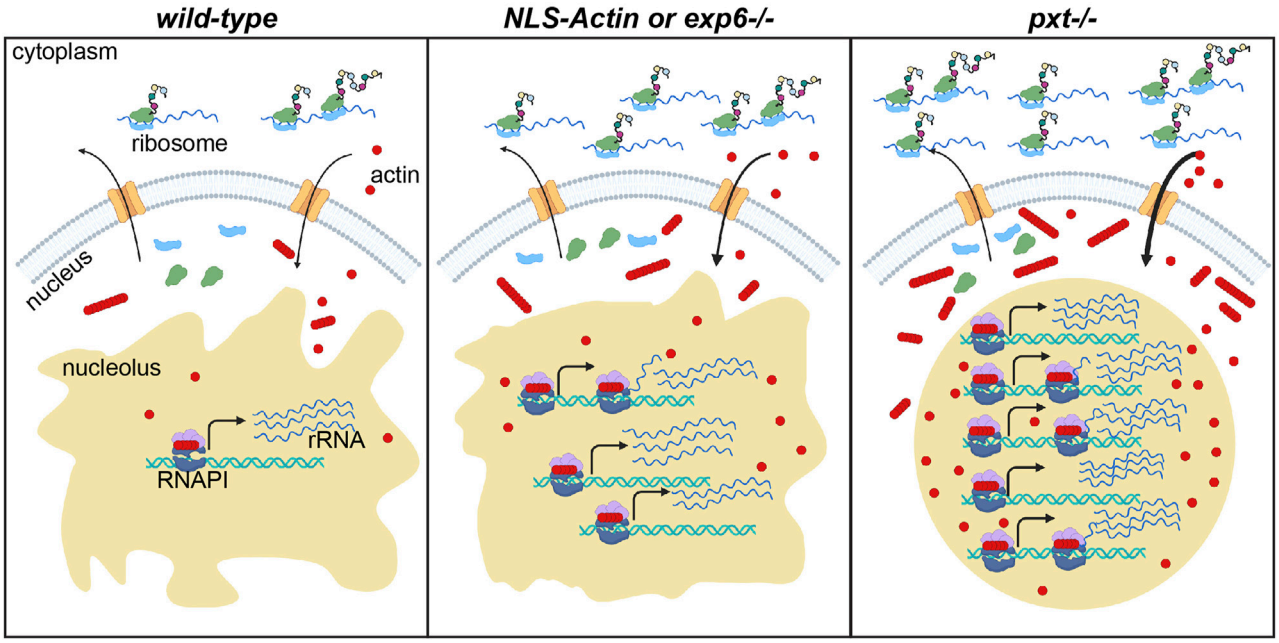

FIGURE 8
Nuclear actin levels must be tightly regulated to coordinate nucleolar activity with development. Schematic of the resulting model for how nuclear actin levels and/or form correspond to the level of rRNA transcription and protein translation in wild-type, increased nuclear actin (NLS-Actin overexpression or Exportin 6 [Exp6] loss), and *pxt* mutant contexts. The cytoplasm (top) and nucleus (bottom) are diagramed for a single cell in each context. Nuclear envelope = gray, nuclear pores = orange; nucleolus = tan; RNAPI complex: polymerase = dark blue, regulatory factors = light purple, ribosomal DNA (rDNA) = teal helix, rRNA = blue lines; actin (monomers and polymers) = red circles and lines of red circles; ribosomal subunits = light green and light blue; nascent proteins = colored circles on black lines emerging from ribosomes. In wild-type follicles, tight regulation of nuclear actin maintains the correct levels of monomeric and polymeric nucleolar actin to ensure correct rRNA production, a tubular nucleolar structure, and normal ribosome biogenesis and protein translation levels. When nuclear actin levels are slightly increased, by expression of NLS-Actin or loss of Exp6, there is increased nuclear and nucleolar actin, a modest change in nucleolar structure, and increased rRNA production. When Pxt is lost, nuclear actin levels increase and the form of nuclear actin is altered; this results in increased rRNA production, a rounding of the nucleolus, increased ribosome biogenesis (predicted but not tested) and increased protein translation levels.

provide the first evidence that PGs and nuclear actin are critical regulators of the nucleolus during egg development. Specifically, we discovered PGs tightly control the level and forms of nuclear actin. This tight control of nuclear actin is necessary to maintain normal nucleolar functions and morphology. Increasing nuclear actin, through genetic loss of PG signaling or overexpression of an NLS-targeted actin, results in a round nucleolar morphology. Moreover, we find that loss of PGs, overexpression of an NLS-target actin, or loss of Exp6, all manipulations that increase nuclear actin levels, results in an increase in RNAPI-dependent transcription. Further, loss of PGs does not inhibit ribosome formation and maturation, but increases global translation, despite the gross changes in nucleolar morphology. We demonstrate that these changes in the nucleolus are a result of Pxt-dependent nuclear actin regulation. Together, these findings lead to the model that during *Drosophila* oogenesis, PGs limit nuclear actin to promote proper nurse cell nucleolar function and morphology. When these factors become disrupted, it leads to changes in nucleolar function and morphology. These disruptions likely contribute to the sterility in *pxt* mutants (Tootle and Spradling, 2008; Tootle et al., 2011). Given the conservation of PGs, nuclear actin, and the nucleolus, it is tempting to speculate these same mechanisms regulate oocyte development and female fertility across organisms.

PGs control the functions of the nucleolus

The function of the nucleolus is intimately linked to its structure. The nucleolus is non-membrane bound, and forms by liquid-liquid phase separation (Dubois and Boisvert, 2016; Stochaj and Weber, 2020; Lafontaine et al., 2021). Specifically, rDNA transcription allows intrinsically disordered nucleolar proteins, including Fibrillarin, to coalesce and form the discreet compartments of the nucleolus. This connection between function and structure led to the prevailing notion that changes in nucleolar morphology are indicative of dysfunction (Yuan et al., 2005; Boulon et al., 2010; Grummt, 2013). This idea, along with the prior work showing aspirin impairs nucleolar function in cancer cells (Brighenti et al., 2016; Chen et al., 2018), led us to initially hypothesize the rounded nucleolar morphology observed in *pxt* mutants was the result of impaired nucleolar activity. This is not the case. Instead, we find loss of Pxt results in increased rRNA transcription, normal ribosome biogenesis, and increased protein translation (Figures 1, 2).

The increased transcription observed in the rounded nucleoli of *pxt* mutants is not the first instance of enhanced nucleolar function being associated with altered nucleolar morphology. For example, during *Drosophila* oogenesis, loss of RpS5b, a small ribosomal subunit protein paralog, results in a rounded nucleolar morphology, and increased Udd levels, rRNA transcription, and global translation (Jang et al., 2021).

Additionally, cancer cells have striking changes in nucleolar morphology, and increased rates of translation and ribosome production; this is linked to disease progression (Orsolic et al., 2016; Lindstrom et al., 2018; Lafita-Navarro and Conacci-Sorrell, 2022). It is thought that increased flux of RNA, proteins, and other molecules important for rRNA transcription, processing, and maturation within the nucleolus results in a more liquid-like nucleolar state, driving the enlarged and rounded structure (Lafontaine et al., 2021). Similarly, the nucleoli of *Xenopus laevis* oocytes are more rounded and liquid-like than other cell types, and this nucleolar structure is essential for oocyte development and maturation (Brangwynne et al., 2011; Feric et al., 2016). Conversely, solid-like nucleoli are thought to reduce the flux of factors into and out of the nucleolus, and thereby, decrease rRNA transcription and processing, ribosomal precursor release, and ribosome biogenesis; this is observed in patients with ribosomopathies (Lafontaine et al., 2021). Given the rounded morphology of the nucleoli and increased nucleolar functions in *pxt* mutants, it is tempting to speculate that the nucleoli have a liquid-like state whereas wild-type cells have more solid-like nucleoli.

Our finding that genetic loss of COX activity during *Drosophila* oogenesis results in increased nucleolar functions is at odds with the known effects of inhibiting COX activity in cancer cells. Aspirin treatment of both hepatocarcinoma and colorectal cancer cells results in decreased numbers but increased size of nucleoli (Brighenti et al., 2016; Chen et al., 2018). Further, in the colorectal cancer study, aspirin decreases RpS6 expression compared to RpL11; this misbalance in ribosomal proteins impairs ribosome maturation. These ribosomal biogenesis defects feed back to the nucleolus, resulting in the accumulation of a rRNA intermediate (Brighenti et al., 2016). Conversely, we find that loss of Pxt does not result in decreased RpS6 or impaired ribosome activity, but instead increases protein translation (Figure 2). This difference could simply be due to aspirin reducing but not eliminating PG signaling. Furthermore, higher eukaryotes have two COX enzymes, COX1 and COX2. COX1 is more sensitive to aspirin inhibition (Vane and Botting, 2003), and COX2 is highly upregulated in cancer (Hashemi Goradel et al., 2019). COX1 and COX2 also have tendencies to couple with distinct downstream synthases, resulting in the production of different bioactive PGs (Ueno et al., 2001; Yuan and Smith, 2015). Thus, aspirin treatment may result in the reduction of specific PGs but not the loss of all PGs, as occurs in the *Drosophila pxt* mutants. Finally, the cellular context may drive the differences observed. Cancer cell nucleoli are less responsive to mechanical signaling than normal cells (Jaecker et al., 2022). Further, cancer cells are mitotic, and nucleolar stress can drive the death of individual cells. In contrast, the nurse cells in the *Drosophila* follicle are post-mitotic, and can only undergo synchronous cell death (i.e. all the nurse cells in a follicle) at specific developmental time points (Jenkins et al., 2013). Future studies are needed to explore the roles of genetic loss vs. pharmacologic inhibition of PG synthesis in diverse contexts to decipher both the common and cell-specific roles of PGs in regulating the nucleolus.

What are the consequences of increased rRNA transcription and protein translation?

The level of rRNA transcription and protein translation are tightly tuned for each cell-type, differentiation status, and developmental stage (Buszczak et al., 2014; Mercer et al., 2021). During development, cells significantly increase the level of protein translation as they differentiate. For example, the *Drosophila* ovarian germline stem cells (GSCs) exhibit high levels of rRNA transcription but lower levels of protein translation, whereas the differentiating daughter cells decrease rRNA transcription and increase protein translation (Zhang et al., 2014). Misregulation of this developmental change in nucleolar activity and protein translation impairs germ cell differentiation (Zhang et al., 2014; Sanchez et al., 2016). In aged animals, loss of Pxt results in early oogenesis defects that resemble germ cell differentiation mutants (Tootle and Spradling, 2008); perhaps this phenotype is due to alterations in rRNA transcription and protein translation. The nurse cells of developing *Drosophila* follicles also likely require specific levels of nucleolar and ribosomal activities. Supporting this idea, loss of RpS5b increases rRNA transcription and protein translation, and these changes dramatically impair oogenesis and result in sterility (Kong et al., 2019; Jang et al., 2021). Specifically, it causes mid-oogenesis checkpoint arrest, meaning follicle development stops at S8 and these follicles undergo cell death. Loss of Pxt results in increased mid-oogenesis checkpoint death (Spracklen et al., 2014b), raising the possibility that this phenotype is due to its altered nucleolar activity. Increased rRNA transcription and protein translation also consume lots of the cellular energy, and thereby, reduce what is available for other processes. Indeed, in *RpS5b* mutants the distribution and shape of mitochondria within the nurse cells are severely altered, and there is elevated reactive oxygen species (Kong et al., 2019). While it remains unknown whether loss of PGs causes similar changes, other energy dependent processes are impaired. In particular, actin cytoskeletal remodeling consumes large amounts of ATP and is severely disrupted in *pxt* mutants (Tootle and Spradling, 2008; Groen et al., 2012; Spracklen et al., 2014b). Finally, increased protein translation in the context of RpS5b loss alters the translational efficiencies of specific mRNAs. Of particular interest is that multiple cytoskeletal genes exhibit decreases translation efficiency. This raises another possible mechanism whereby loss of PGs results in actin cytoskeletal defects. Future studies are needed to determine how the increased rRNA transcription and protein translation in the *pxt* mutants impacts oogenesis and fertility.

PGs regulate nuclear actin

While PGs have been widely implicated in regulating cytoplasmic actin dynamics (Peppelenbosch et al., 1993; Pierce et al., 1999; Dormond et al., 2002; Tamma et al., 2003; Bulin et al., 2005; Birukova et al., 2007), including during *Drosophila* oogenesis (Tootle and Spradling, 2008; Groen et al., 2012; Spracklen et al., 2014b; Spracklen et al., 2019), here we provide the first evidence that PGs control nuclear actin levels and form (monomeric vs. polymeric). Indeed, loss of Pxt, the enzyme required for all PG synthesis in *Drosophila*, results in increased G-actin in the nucleolus, as seen by DNase I and C4 staining (Figure 4) and increased polymeric actin (AC15) on the chromatin and puncta in the nucleolus (Figure 5). Further supporting that the form of nuclear actin is critical for regulating the nucleolus, nucleolar morphology is altered when NLS-Actin expression results in filamentous nuclear actin (Figure 6). These data lead to the model that PGs are required to coordinate the level and form of nuclear actin with follicle development.

The mechanisms whereby PGs tightly control nuclear actin remain unknown, but there are several possibilities. First, PG regulation of cytoplasmic actin dynamics may control the pool of G-actin available for nuclear import. Supporting that such a mechanism can regulate nuclear actin, in mammalian cells, activation of integrin receptors drives cytoskeletal changes that lead to the rapid accumulation of F-actin in the nucleus (Plessner et al., 2015). Second, PG signaling could regulate the nuclear import or export of actin. Indeed, PGs regulate the actin binding protein Fascin (*Drosophila* Singed) (Groen et al., 2012) and Fascin acts with Cofilin, the cofactor for the nuclear import of actin by Imp9, to alter nuclear actin levels (Kelpsch et al., 2016). Third, PG signaling may induce the nuclear retention of actin by altering post-translational modifications on actin or its nuclear binding partners, or by controlling the levels or localization of these partners. Indeed, PGs regulate the nuclear localization of Fascin (Groen et al., 2015), making it tempting to speculate PGs regulate other nuclear actin binding proteins. Future studies will define how PGs modulate nuclear actin levels and forms.

PG regulation of nuclear actin modifies the functions of the nucleolus

We find that PG signaling tightly controls the level and form of nuclear actin to limit rRNA transcription and protein translation, yet directly manipulating nuclear actin levels does not fully recapitulate the nucleolar phenotype in *pxt* mutants. These phenotypic differences could be due to redundant mechanism regulating nuclear actin trafficking in and out of the nucleus. Indeed, a recent study found that numerous import factors contribute to the nuclear localization of actin (Borkuti et al., 2022). Alternatively, in addition to controlling nuclear actin levels and form, PGs may also regulate the functions of actin in the nucleolus. Such regulation would remain intact when nuclear actin levels are increased in the presence of normal PG signaling.

Downstream of PG signaling, how does nuclear actin modulate nucleolar activity? One possibility is that increased nuclear actin simply increases RNAPI activity. Indeed, actin is a required cofactor for all three RNAPs, however the form of actin present in the different complex remains unclear (Kelpsch and Tootle, 2018; Green et al., 2021). Data supports that monomeric actin is bound to gene promoters and mediates RNAPII recruitment (Sokolova et al., 2018), whether this is true for RNAPI remains unknown. Actin polymerization is required for RNAPI transcription (Percipalle, 2013). Based on these findings, monomeric actin (DNase I and C4) in the nucleolus may mark and recruit RNAPI and therefore, determine which rRNA genes are transcribed, whereas polymeric actin (AC15) may function within the RNAPI complex to drive rRNA transcription. Supporting this idea, during S10B when the nurse cells are producing large quantities of mRNAs, proteins, and organelles to provide to the oocyte in S11, AC15 nucleolar puncta are observed. These puncta appear earlier in development, at an increased number, and are larger when Pxt is lost (Figures 5G–K). We speculate that these puncta are at the sites of active rRNA transcription. Monomeric actin (DNase I and C4) may also play a role in rRNA processing, as it associates with ribonucleoproteins (RNPs) (Percipalle et al., 2002; Obrdlik et al., 2008; Qi et al., 2011). RNPs splice and process 3′-ends of mRNAs. Monomeric actin also interacts with spliceosomal small nuclear RNPs and spliceosomal assembly and activation factors, and either increasing or decreasing nuclear actin impairs splicing (Viita et al., 2019). Monomeric actin remains associated with RNPs and the associated mRNA as they are transported out of the nucleus. These findings raise the possibility that nucleolar monomeric actin regulates rRNA processing and translocation to the cytoplasm. Supporting this idea, actin is present in 40S pre-mRNP/RNP ribosomal fractions (Percipalle, 2013). Together, these findings suggest monomeric nucleolar actin may regulate RNAPI activity, rRNA processing, and rRNA translocation, while polymeric nucleolar actin is required for transcription by RNAPI.

Another possibility is that nucleolar actin regulates the phase separation of the nucleolus. Nuclear actin could alter nucleolar phase separation by increasing RNAPI activity (discussed above), changing nucleolar protein-protein interactions, altering heterochromatin associated with the nucleolus, or increasing the number of actively transcribed rDNA genes (Lafontaine et al., 2021). We speculate that monomeric actin (DNase I and C4) may interact with specific nucleolar factors, driving biomolecular condensates that ultimately form and control the morphology and functions of the nucleolus. Further, monomeric actin could regulate the heterochromatin associated with the nucleolus, as it is required for the activity of multiple chromatin remodeling complexes (Kelpsch and Tootle, 2018; Green et al., 2021). Changes in chromatin architecture, along with the above discussed ability of monomeric actin to license genes for transcription, may also regulate which and how many rRNA loci are transcribed. These data lead us to hypothesize that in the context of Pxt loss, the increased nucleolar monomeric actin (DNase I and C4) alters the phase separation of the nucleolus by some or all of these mechanisms, transitioning it from a more solid-like to liquid-like state, thereby promoting rRNA transcription.

While there are many possible functions for monomeric actin in the nucleolus, one question that remains is what is the difference between DNase I and C4 monomeric actin? C4 nucleolar actin is only present in a subset of the nurse cells of any given follicle, either labeling both the anterior-most and posterior-most nurse cells or the middle nurse cells (Kelpsch et al., 2016; Wineland et al., 2018). From looking at sequential follicles within an ovariole, it seems like this C4 positivity oscillates between these two localization patterns. This spatial and temporal pattern of C4 nucleolar staining is reminiscent of what is seen for the cell cycle marker Cyclin E (Dej and Spradling, 1999), raising the possibility that C4 nucleolar actin has a cell cycle specific role in the nucleolus. The nurse cells undergo endocycling, meaning the DNA is replicated but the cell doesn't divide. So unlike during mitosis, the nucleolus does not disassemble in the nurse cells. Thus, we speculate that C4 monomeric actin acts by an unknown means to maintain the nucleolus, and perhaps modulate nucleolar activity, during endocyling.

The literature provides many possibilities for the form-specific functions of actin within the nucleolus. Future studies are essential for determining the mechanisms whereby monomeric actin (DNase I), C4 positive monomeric actin, and AC15 positive polymeric actin modulate nucleolar function and morphology during *Drosophila* oogenesis, and whether these functions are conserved in other tissues and organisms.

PGs, nuclear actin, nucleolar function, and oogenesis

PGs, nuclear actin, and nucleolar function are critical and conserved factors required for oocyte development and fertility. Indeed, knockout mouse models of PG synthesis and signaling components exhibit impaired follicle maturation and ovulation failure (Lim et al., 1997; Langenbach et al., 1999; Takahashi et al., 2010). Similarly, in humans, usage of non-steroidal inflammatory drugs, which inhibit COX enzymes, results in aberrant follicle maturation and delayed ovulation of fertilization incompetent oocytes (Akil et al., 1996; Smith et al., 1996; Pall et al., 2001). Nuclear actin is also emerging as a key factor in egg development. In organisms with large oocytes, like frogs and birds, actin forms a mesh or network in the nucleus that is critical for maintaining the chromatin and nucleolar distribution (Bohnsack et al., 2006; Maslova and Krasikova, 2012; Feric and Brangwynne, 2013). Nuclear F-actin is also required in mouse oocytes. There nuclear actin forms a second spindle structure to segregate chromosomes during meiosis (Mogessie and Schuh, 2017). Nuclear actin also serves to buffer the level of G-actin in the cytoplasm to prevent aberrant dense cytoplasmic F-actin networks that preclude oocyte development (Scheffler et al., 2022). Like nuclear actin and PGs, nucleolar functions, including ribosome biogenesis, play critical roles in oocytes (Mercer et al., 2021). Nucleolar activity within the oocyte is required to produce enough ribosomes to support early, preimplantation embryonic development in placental mammals and embryonic development that occurs completely outside the mother (Fulka and Aoki, 2016; Kresoja-Rakic and Santoro, 2019; Fulka et al., 2020). Further supporting the role of the nucleolus in oocyte development, mutations in human UTP14, a pre-18S rRNA processing factor, are linked to both the ribosomopathy scleroderma and infertility (Joseph et al., 2014). Thus, the nucleolus, nuclear actin, and PGs play key roles in oocyte development and fertility across organisms. This conservation of function leads us to speculate that the pathway we uncovered in *Drosophila*–where PGs tightly control the level and form of nuclear actin to coordinate nucleolar rRNA transcription and downstream protein translation rates with development to ensure the production of a high-quality oocyte–is likely to be widely used, from simple eukaryotes to humans.

Materials and methods

For product information on the reagents used in this study please refer to Supplementary Table S1.

Fly stocks

Fly stocks were maintained on cornmeal-agar-yeast food at 21°C. Prior to immunofluorescence or western blot analysis, flies were fed wet yeast paste daily for 3–4 days. Unless otherwise noted, *yw* (RRID: BDSC_1495) was used as the wild-type control. The following stocks were obtained from the Bloomington *Drosophila* Stock Center (Bloomington, IN): $pxt^{EY03052}$ (referred to as pxt^{EY}, RRID: BDSC_15620), *matαGAL4* (RRID: BDSC_7063); and UASp RNAi *actin 5C* (TRiP.HMS02487; RRID: BDSC_42651). pxt^{f01000} (referred to as pxt^{f}) and ebo^{f07537} (referred to as $exp6^{f}$) stocks were obtained from the Harvard Exelixis collection (Boston, MA). The *oskarGal4* (second and third chromosome) lines were a generous gift from Anne Ephrussi (Telley et al., 2012), and the UASp NLS-flag-Actin 5C (second and third chromosome) lines were a generous gift from Maria Vartiainen. Expression of UASp RNAi *actin 5C* was achieved by crossing to *matαGal4*, maintaining fly crosses at 21°C and maintaining progeny at 29°C for 5-6 days. Expression of UASp NLS-flag-Actin 5C was achieved by crossing to *oskarGal4* flies, maintaining fly crosses at 21°C, and maintaining progeny at 25°C for 5–6 days.

Immunofluorescence

Whole-mount *Drosophila* ovary samples were dissected into room temperature Grace's insect medium (Lonza, Walkersville, MD). In the cases of drug treatment, follicles were treated with either 0.4% dimethyl sulfoxide (DMSO) or 20 μg/ml Actinomycin D (Sigma-Aldrich, A1410) diluted in modified Grace's medium containing 1X penicillin/streptomycin (100x, Gibco) and 10% fetal bovine serum (FBS, Atlanta Biologicals) for 60 min prior to antibody staining. Samples were fixed for 10 min at room temperature in 4% paraformaldehyde in Grace's insect medium, except for the instance of methanol fixation which was done for 10 min at 4 °C in -20°C methanol. Briefly, samples were blocked by washing in antibody wash (1X phosphate-buffered saline [PBS], 0.1% Triton X-100, and 0.1% bovine serum albumin [BSA]) six times for 10 min each at room temperature. Primary antibodies were incubated overnight at 4°C, except for Actin C4, Actin AC15, and rabbit anti-fibrillarin which were incubated for a minimum of 20 h at 4°C. The following additional antibodies and concentrations were used: rabbit anti-Pxt (pre-absorbed on *pxt* mutant ovaries at 1: 50 and used 1:50-1:100, (Spracklen et al., 2014b),), mouse anti-Actin C4 1:50 (RRID: AB_2223041; Millipore); mouse anti-Actin AC15 1: 100 (RRID: AB_476744; Sigma-Aldrich); mouse anti-fibrillarin 72B9 1:25 (a generous gift from Patrick DiMario); rabbit anti-fibrillarin 1:250 (RRID: AB_2105785; Abcam, Cambridge, MA); and rabbit anti-flag (preabsorbed on yw ovaries at 1:20 and used at 1:20, RRID: AB_F7425; Sigma-Aldrich). After six washes in antibody wash (10 min each), secondary antibodies were incubated overnight at 4°C or for ~4 h at room temperature. The following secondary antibodies were used at 1:250-1:500: AlexaFluor 488:goat anti-mouse (RRID: AB_2534069), AlexaFluor 568:goat anti-mouse (RRID: AB_2534072), AlexaFluor 488:goat anti-rabbit (RRID:AB_2576217), and AlexaFluor 568:goat anti-rabbit (RRID: AB_10563566) (ThermoFisher Scientific, Waltham, MA). When used, AlexaFluor488-conjugated DNase I (1:500; ThermoFisher Scientific), AlexaFluor555-or AlexaFluor657-conjugated Phalloidin (1:500; ThermoFisher Scientific) and AlexaFluor555-or AlexaFluor647-conjugated wheat germ agglutinin, WGA (1:500; ThermoFisher Scientific) were included with the primary and secondary antibodies. Following six washes in antibody wash (10 min each), 4′,6-diamidino-2-phenylindole (DAPI, 5 mg/ml) staining was performed at a concentration of 1:5,000 in 1X PBS

for 10 min at room temperature. Samples were then rinsed in 1X PBS and mounted in 1 mg/ml phenylenediamine in 50% glycerol, pH 9 (Platt and Michael, 1983). For each experiment ~5 pairs of ovaries were stained, imaged, and analyzed, and all experiments were performed a minimum of three independent times.

Click-iT nascent RNA staining

Whole mount *Drosophila* ovary samples (5-10 ovaries per sample) were either treated with 0.2-2 μg/ml of Actinomycin D diluted in Grace's medium, 250 μg/ml Alpha-amanitin (Sigma-Aldrich, A2263) in Grace's medium or the same dilution of DMSO for 10 min prior to, or were directly incubated with 2 mM 5-ethynyl uridine (EU) for 15 min and washed twice with Grace's medium. Samples were fixed in 4% paraformaldehyde diluted in Grace's medium for 15 min. Samples were washed 6 times for 10 min each with Triton Wash (1X PBS, 0.5% Triton X-100), and then rinsed once with 1X PBS before incubating for 30 min in the Click-iT reaction cocktail, prepared according to product specifications (Thermo Fisher Scientific, Click-iT™ RNA Alexa Fluor™ 488 Imaging Kit, C10329). Samples were rinsed twice with Click-iT Reaction Rinse Buffer and twice with 1X PBS, and then washed for 30 min in 1X PBS. Samples were either stained for antibodies starting at the antibody wash step (see above) or immediately stained with Hoechst 33342 (1:1000 in PBS) for 15 min to label DNA and then rinsed 3 times in 1X PBS before mounting as described in the immunofluorescence section.

Image acquisition and processing

Microscope images of fixed *Drosophila* follicles were obtained using Zen software on a Zeiss 880 mounted on Zeiss Axio Observer.Z1 using Plan-Apochromat 20x/0.8 working distance (WD) = 0.55 M27, Plan-Apochromat 40x/1.3 Oil DIC WD = 2.0, or Plan-Apochromat 63x/1.4 Oil DIC f/ELYRA objectives (Carl Zeiss Microscopy, Thornwood, NY), on a Zeiss 700 mounted on an Axio Observer.Z1 using a Plan-Aprochromat 20x/0.8 WD = 0.55 M27 (Carl Zeiss Microscopy, Thornwood, NY) or LAS AF SPE Core software on a Leica TCS SPE mounted on a Leica DM2500 using an ACS APO 20×/0.60 IMM CORR -/D or an ACS APO 63×/1.30 Oil CS 0.17/E objective (Leica Microsystems, Buffalo Grove, IL). Maximum projections, merged images, rotation, and cropping were performed using ImageJ software (Abramoff et al., 2004, FIJI, RRID: SCR_002285). All fluorescent images were brightened by 30% in Photoshop (Adobe, RRID: SCR_010279) to improve visualization, except Figure 1; Supplementary Figures S1, S4 where the images were brightened by 50%.

Quantification of nuclear actin from immunofluorescence

Genotypically de-identified images were analyzed using ImageJ (Abramoff et al., 2004) for DNase I, C4 and AC15 for specific stages of oogenesis. Follicle staging was assigned based on morphology and size.

DNase I nucleolar to cytoplasmic ratios were quantified from single confocal slices in S7/8 follicles by measuring the integrated density of fluorescence within a square in the nucleolus, compared to a square in the adjacent cytoplasm; the focal planes chosen had the strongest nucleolar DNase I signal. Three paired measurements were made per cell and the average nucleolar/cytoplasmic ratio was determined. Three cells per follicle were measured. DNase I data were analyzed and statistical analysis performed using Prism (Graphpad, RRID: SCR_002798).

Quantification of C4 nucleolar actin was performed on confocal image stacks of follicles stained with anti-actin C4, WGA, and Phalloidin; as necessary, brightness and contrast were adjusted to score all the C4 nucleolar actin present. Data were collected for S5-6, S7-8, and S9 follicles. For each follicle the number of nurse cells exhibiting structured nucleolar C4 actin was scored.

Quantification of AC15 nuclear actin level and nucleolar puncta presence/size was performed on confocal image stacks of follicles stained with anti-actin AC15, WGA, and DAPI. For AC15 nuclear actin level, data were collected for S5-6, S7-8, and S9 follicles. For each follicle the nurse cells and the follicle cells were scored for their level of AC15 staining on a 5-point scale ranging from background levels typical of what is observed in wild-type S3 follicles (-) to the strongest staining typical of what is observed in wild-type S10 follicles (+++). For AC15 puncta, data were collected for S7/8, S9, and S10 follicles; as necessary, brightness, contrast and zoom were adjusted to score the puncta. Each follicle was scored as having either no AC15 puncta, small puncta, or large/obvious puncta in the nurse cells. C4 and AC15 data were analyzed using Excel (Microsoft, RRID: SCR_016137) and statistical analysis was preformed using R (Vienna, Austria, RRID: 001905).

Quantification of nucleolar morphology

Confocal image stacks of S10B follicles stained for fibrillarin or EU were genotypically blinded and each follicle was assigned a nucleolar defect severity score according to the number of nurse cell nucleoli with morphological changes; the four posterior nurse cells were excluded from the analysis as their morphology is distinct. The nucleolar morphology categories included: normal (0-1 disrupted nucleoli), mild (2-4 disrupted nucleoli), and severe (5 or more disrupted nucleoli). Morphology defects included nucleoli that are pebbled (several smaller, disconnected portions of nucleolus) or rounded (single, nearly spherical nucleolus). In the context of NLS Actin overexpression (Figure 6), we assessed nucleolar morphology in relation to the level of nuclear actin. The level of nuclear actin was categorized as low which exhibits a nuclear actin haze, medium which exhibits a network of thin nuclear actin filaments, and high which exhibits thick nuclear actin filamentous structures termed rods. Quantification of nucleolar volume was performed using Imaris (Oxford, RRID:SCR_007370) on *yw* S10B follicles stained for EU. The single anterior-most nurse cell was compared to the average volume of four posterior nurse cells (from the third row of nurse cells).

Quantification of Click-iT nascent RNA staining

Click-iT EU intensity was quantified from genotypically de-identified confocal image stacks of S10 follicles. For a given follicle, the EU intensity of three nurse cells was measured, excluding the four posterior-most and single anterior-most nurse cells. For each nurse cell, three nucleolar and three cytoplasmic intensity

measurements of a square ROI (4.788 square pixels) were taken and averaged. The average cytoplasmic intensity measurement was subtracted from the averaged nucleolar intensity measurement, resulting in a single nucleolar relative EU intensity value per nurse cell.

Puromycin incorporation assay

From 1-2 day old flies, 10-15 ovary pairs were dissected per sample in Grace's insect medium. Samples were transferred to a 9-well plate containing 5 µg/ml puromycin dihydrochloride (Sigma-Aldrich) diluted in Grace's medium and incubated with shaking for 40 min. Samples were then washed with 1X PBS and then transferred to 1.5 ml microcentrifuge tubes. The PBS solution was removed from sample tubes and 50 µL 1X Laemmli buffer was added. The samples were ground by hand with a plastic pestle, and then boiled for 10 min. Samples were stored at -20°C until used for western blotting.

Western blotting

Whole ovaries were dissected from flies fed wet yeast paste for 2-3 days, unless otherwise noted. Ovaries were dissected in room temperature Grace's insect medium and transferred to a 1.5 ml microcentrifuge tube containing 50 µL of Grace's media. Grace's media was removed and replaced with 50 µL 1X Laemmli buffer. The tissue was lysed by grinding with a plastic pestle and boiled for 10 min. Samples were run on a 10% SDS-PAGE gel; in some cases, initial western blot analysis was used to dilute samples to normalize protein levels. The molecular weight ladder used in all experiments was the Precision Plus Protein All Blue Prestained Protein Standard (BioRad, 1610373). Western blots were performed using standard methods (Biorad system). For the puromycin incorporation experiments, prior to blocking and antibody incubation blots were stained with 0.1% Ponceau S solution in 1% acetic acid for 10 min and photographed using an iPhone 13 Pro; Ponceau S solution was washed off prior to antibody stains. The following primary antibodies were obtained from the Developmental Studies Hybridoma Bank (DSHB) developed under the auspices of the National Institute of Child Health and Human Development and maintained by the Department of Biology, University of Iowa (Iowa City, IA): mouse anti-Puromycin 0.5ug/mL (MY-2A4, Yewdell, J, (David et al., 2012)) and rat anti-vasa 1:100 (vasa, Spradling, A.C/Williams, D, (Aruna et al., 2009)). The following primary antibodies were also used: mouse anti-actin AC15 1:200, rabbit anti-RpL11 1:1000 (RRID:AB_2042832, Abcam, Cambridge, MA), mouse anti-RpS6 1:500 (RRID: AB_2238583, Cell Signaling), rabbit anti-Exp6 1:50,000 (Yves, a generous gift from Dirk Goerlich (Stuven et al., 2003)), and mouse anti-alpha tubulin 1:5000 (RRID: AB_477593, Sigma-Aldrich). All blots were blocked and incubated in primary antibody in 5% milk diluted in 1X Tris-buffered saline (1X TBS) with 0.1% Tween 20, except for anti-actin AC15, anti-RpS6, anti-RpL11, and anti-Exp6, blots which were blocked and incubated in primary antibody in 3% BSA diluted in 1X TBS with 0.1% Tween 20. The following secondary antibodies were obtained from Jackson ImmunoResearch Laboratories (West Grove, PA) and used 1: 5,000: Peroxidase-AffiniPure Goat Anti-Mouse IgG (H + L) (RRID: AB_10015289), Peroxidase-AffiniPure Goat Anti-Rabbit IgG (H + L) (RRID: AB_2307391), and Peroxidase-AffiniPure Goat Anti-Guinea Pig (H + L) (RRID: AB_2337402), except for the anti-RpS6 and anti-RpL11 western blots where secondary antibodies were used at 1:10,000. Blots were developed with SuperSignal West Pico or Femto Chemiluminescent Substrate (Thermo Scientific, Waltham, MA) and imaged using the Amersham Imager 600 (GE Healthcare Life Sciences, Chicago, IL). A minimum of three independent experiments were performed for each Western blotting experiment. Where not shown as full blots in the figures, full blots are provided in Supplementary Figure S8.

Data availability statement

The original contributions presented in the study are included in the article/Supplementary Material, further inquiries can be directed to the corresponding author.

Author contributions

DT, BV, GK, DW, DK, and TT performed experiments and analyzed data. MG performed statistical analyses and designed figures. TT conceived the study and designed figures. DT, BV, and TT wrote the manuscript.

Funding

This project was supported by National Institutes of Health (NIH) R01 GM116885 (TT), and National Science Foundation MCB2017797 (TT). MG was supported by NIH T32 CA078586 Free Radical and Radiation Biology, University of Iowa.

Acknowledgments

We thank the Dunnwald lab for helpful discussions, and Dr. Martine Dunnwald and the Tootle Lab for helpful discussions and careful review of the manuscript. Stocks obtained from the Bloomington Drosophila Stock Center (NIH P40OD018537) were used in this study. The Carver Center for Imaging Imaris image processing system and software were provided by the generous support of the Roy J. Carver Charitable Trust. At the University of Iowa, Information Technology Services–Research Services provided data storage support.

Conflict of interest

The authors declare that the research was conducted in the absence of any commercial or financial relationships that could be construed as a potential conflict of interest.

Publisher's note

All claims expressed in this article are solely those of the authors and do not necessarily represent those of their

affiliated organizations, or those of the publisher, the editors and the reviewers. Any product that may be evaluated in this article, or claim that may be made by its manufacturer, is not guaranteed or endorsed by the publisher.

Supplementary material

The Supplementary Material for this article can be found online at: https://www.frontiersin.org/articles/10.3389/fcell.2023.1072456/full#supplementary-material

References

Abramoff, M., Magalhaes, P., and Ram, S. (2004). Image processing with ImageJ. *Biophot. Int.* 11, 36–42.

Akil, M., Amos, R. S., and Stewart, P. (1996). Infertility may sometimes be associated with NSAID consumption. *Br. J. Rheumatol.* 35, 76–78. doi:10.1093/rheumatology/35.1.76

Almuzzaini, B., Sarshad, A. A., Rahmanto, A. S., Hansson, M. L., Von Euler, A., Sangfelt, O., et al. (2016). In beta-actin knockouts, epigenetic reprogramming and rDNA transcription inactivation lead to growth and proliferation defects. *FASEB J. Off. Publ. Fed. Am. Soc. Exp. Biol.* 30, 2860–2873. doi:10.1096/fj.201600280R

Andersen, J. S., Lyon, C. E., Fox, A. H., Leung, A. K., Lam, Y. W., Steen, H., et al. (2002). Directed proteomic analysis of the human nucleolus. *Curr. Biol.* 12, 1–11. doi:10.1016/s0960-9822(01)00650-9

Andersen, J. S., Lam, Y. W., Leung, A. K., Ong, S. E., Lyon, C. E., Lamond, A. I., et al. (2005). Nucleolar proteome dynamics. *Nature* 433, 77–83. doi:10.1038/nature03207

Aruna, S., Flores, H. A., and Barbash, D. A. (2009). Reduced fertility of *Drosophila melanogaster* hybrid male rescue (Hmr) mutant females is partially complemented by Hmr orthologs from sibling species. *Genetics* 181, 1437–1450. doi:10.1534/genetics.108.100057

Aviner, R. (2020). The science of puromycin: From studies of ribosome function to applications in biotechnology. *Comput. Struct. Biotechnol. J.* 18, 1074–1083. doi:10.1016/j.csbj.2020.04.014

Belin, B. J., Lee, T., and Mullins, R. D. (2015). DNA damage induces nuclear actin filament assembly by Formin -2 and Spire-½ that promotes efficient DNA repair. [corrected]. *eLife* 4, e07735. doi:10.7554/eLife.07735

Birukova, A. A., Zagranichnaya, T., Fu, P., Alekseeva, E., Chen, W., Jacobson, J. R., et al. (2007). Prostaglandins PGE(2) and PGI(2) promote endothelial barrier enhancement via PKA- and Epac1/Rap1-dependent Rac activation. *Exp. Cell Res.* 313, 2504–2520. doi:10.1016/j.yexcr.2007.03.036

Bohnsack, M. T., Stuven, T., Kuhn, C., Cordes, V. C., and Gorlich, D. (2006). A selective block of nuclear actin export stabilizes the giant nuclei of Xenopus oocytes. *Nat. Cell Biol.* 8, 257–263. doi:10.1038/ncb1357

Borkuti, P., Kristo, I., Szabo, A., Bajusz, C., Kovacs, Z., Rethi-Nagy, Z., et al. (2022). Parallel import mechanisms ensure the robust nuclear localization of actin in Drosophila. *Front. Mol. Biosci.* 9, 963635. doi:10.3389/fmolb.2022.963635

Boulon, S., Westman, B. J., Hutten, S., Boisvert, F. M., and Lamond, A. I. (2010). The nucleolus under stress. *Mol. Cell* 40, 216–227. doi:10.1016/j.molcel.2010.09.024

Brangwynne, C. P., Mitchison, T. J., and Hyman, A. A. (2011). Active liquid-like behavior of nucleoli determines their size and shape in *Xenopus laevis* oocytes. *Proc. Natl. Acad. Sci. U. S. A.* 108, 4334–4339. doi:10.1073/pnas.1017150108

Brighenti, E., Giannone, F. A., Fornari, F., Onofrillo, C., Govoni, M., Montanaro, L., et al. (2016). Therapeutic dosages of aspirin counteract the IL-6 induced pro-tumorigenic effects by slowing down the ribosome biogenesis rate. *Oncotarget* 7, 63226–63241. doi:10.18632/oncotarget.11441

Bulin, C., Albrecht, U., Bode, J. G., Weber, A. A., Schror, K., Levkau, B., et al. (2005). Differential effects of vasodilatory prostaglandins on focal adhesions, cytoskeletal architecture, and migration in human aortic smooth muscle cells. *Arterioscler. Thromb. Vasc. Biol.* 25, 84–89. doi:10.1161/01.ATV.0000146814.81581.68

Buszczak, M., Signer, R. A., and Morrison, S. J. (2014). Cellular differences in protein synthesis regulate tissue homeostasis. *Cell* 159, 242–251. doi:10.1016/j.cell.2014.09.016

Chen, J., Lobb, I. T., Morin, P., Novo, S. M., Simpson, J., Kennerknecht, K., et al. (2018). Identification of a novel TIF-IA-NF-κB nucleolar stress response pathway. *Nucleic Acids Res.* 46, 6188–6205. doi:10.1093/nar/gky455

Cruz, J. R., and Moreno Diaz de la Espina, S. (2009). Subnuclear compartmentalization and function of actin and nuclear myosin I in plants. *Chromosoma* 118, 193–207. doi:10.1007/s00412-008-0188-y

David, A., Dolan, B. P., Hickman, H. D., Knowlton, J. J., Clavarino, G., Pierre, P., et al. (2012). Nuclear translation visualized by ribosome-bound nascent chain puromycylation. *J. Cell Biol.* 197, 45–57. doi:10.1083/jcb.201112145

Dej, K. J., and Spradling, A. C. (1999). The endocycle controls nurse cell polytene chromosome structure during Drosophila oogenesis. *Development* 126, 293–303. doi:10.1242/dev.126.2.293

Deng, W., Lopez-Camacho, C., Tang, J. Y., Mendoza-Villanueva, D., Maya-Mendoza, A., Jackson, D. A., et al. (2012). Cytoskeletal protein filamin A is a nucleolar protein that suppresses ribosomal RNA gene transcription. *Proc. Natl. Acad. Sci. U. S. A.* 109, 1524–1529. doi:10.1073/pnas.1107879109

Dopie, J., Skarp, K. P., Rajakyla, E. K., Tanhuanpaa, K., and Vartiainen, M. K. (2012). Active maintenance of nuclear actin by importin 9 supports transcription. *Proc. Natl. Acad. Sci. U. S. A.* 109, E544–E552. doi:10.1073/pnas.1118880109

Dormond, O., Bezzi, M., Mariotti, A., and Ruegg, C. (2002). Prostaglandin E2 promotes integrin alpha Vbeta 3-dependent endothelial cell adhesion, rac-activation, and spreading through cAMP/PKA-dependent signaling. *J. Biol. Chem.* 277, 45838–45846. doi:10.1074/jbc.M209213200

Duan, T., Green, N. M., Tootle, T. L., and Geyer, P. (2020). Nuclear architecture as an intrinsic regulator of Drosophila female germline stem cell maintenance. *Curr Opin Insect Sci.* 37, 30–38. doi:10.1016/j.cois.2019.11.007

Dubois, M.-L., and Boisvert, F.-M. (2016). The nucleolus: Structure and function. *Funct. Nucl.*, 29–49. doi:10.1007/978-3-319-38882-3_2

Feric, M., and Brangwynne, C. P. (2013). A nuclear F-actin scaffold stabilizes ribonucleoprotein droplets against gravity in large cells. *Nat. Cell Biol.* 15, 1253–1259. doi:10.1038/ncb2830

Feric, M., Vaidya, N., Harmon, T. S., Mitrea, D. M., Zhu, L., Richardson, T. M., et al. (2016). Coexisting liquid phases underlie nucleolar subcompartments. *Cell* 165, 1686–1697. doi:10.1016/j.cell.2016.04.047

Fiore, A., Spencer, V. A., Mori, H., Carvalho, H. F., Bissell, M. J., and Bruni-Cardoso, A. (2017). Laminin-111 and the level of nuclear actin regulate epithelial quiescence via exportin-6. *Cell Rep.* 19, 2102–2115. doi:10.1016/j.celrep.2017.05.050

Fomproix, N., and Percipalle, P. (2004). An actin-myosin complex on actively transcribing genes. *Exp. Cell Res.* 294, 140–148. doi:10.1016/j.yexcr.2003.10.028

Fulka, H., and Aoki, F. (2016). Nucleolus precursor bodies and ribosome biogenesis in early mammalian embryos: Old theories and new discoveries. *Biol. Reprod.* 94, 143. doi:10.1095/biolreprod.115.136093

Fulka, H., Rychtarova, J., and Loi, P. (2020). The nucleolus-like and precursor bodies of mammalian oocytes and embryos and their possible role in post-fertilization centromere remodelling. *Biochem. Soc. Trans.* 48, 581–593. doi:10.1042/BST20190847

Funaki, K., Katsumoto, T., and Iino, A. (1995). Immunocytochemical localization of actin in the nucleolus of rat oocytes. *Biol. Cell* 84, 139–146. doi:10.1016/0248-4900(96)89423-8

Funk, C. D. (2001). Prostaglandins and leukotrienes: Advances in eicosanoid biology. *Science* 294, 1871–1875. doi:10.1126/science.294.5548.1871

Green, N. M., Kimble, G. C., Talbot, D. E., and Tootle, T. L. (2021). "Nuclear actin," in *eLS*, 958–967.

Groen, C. M., Spracklen, A. J., Fagan, T. N., and Tootle, T. L. (2012). Drosophila Fascin is a novel downstream target of prostaglandin signaling during actin remodeling. *Mol. Biol. Cell* 23, 4567–4578. doi:10.1091/mbc.E12-05-0417

Groen, C. M., Jayo, A., Parsons, M., and Tootle, T. L. (2015). Prostaglandins regulate nuclear localization of Fascin and its function in nucleolar architecture. *Mol. Biol. Cell* 26, 1901–1917. doi:10.1091/mbc.E14-09-1384

Grummt, I. (2013). The nucleolus—guardian of cellular homeostasis and genome integrity. *Chromosoma* 122, 487–497. doi:10.1007/s00412-013-0430-0

Hashemi Goradel, N., Najafi, M., Salehi, E., Farhood, B., and Mortezaee, K. (2019). Cyclooxygenase-2 in cancer: A review. *J. Cell. Physiol.* 234, 5683–5699. doi:10.1002/jcp.27411

Hitchcock, S. E. (1980). Actin deoxyroboncuclease I interaction. Depolymerization and nucleotide exchange. *J. Biol. Chem.* 255, 5668–5673. doi:10.1016/s0021-9258(19)70681-4

Hubert, T., Van Impe, K., Vandekerckhove, J., and Gettemans, J. (2008). The F-actin filament capping protein CapG is a bona fide nucleolar protein. *Biochem. Biophys. Res. Commun.* 377, 699–704. doi:10.1016/j.bbrc.2008.10.048

Jaecker, F. F., Almeida, J. A., Krull, C. M., and Pathak, A. (2022). Nucleoli in epithelial cell collectives respond to tumorigenic, spatial, and mechanical cues. *Mol. Biol. Cell* 33, br19. doi:10.1091/mbc.E22-02-0070

Jang, S., Lee, J., Mathews, J., Ruess, H., Williford, A. O., Rangan, P., et al. (2021). The Drosophila ribosome protein S5 paralog RpS5b promotes germ cell and follicle cell differentiation during oogenesis. *Development* 148, dev199511. doi:10.1242/dev.199511

Jenkins, V. K., Timmons, A. K., and McCall, K. (2013). Diversity of cell death pathways: insight from the fly ovary. *Trends Cell Biol.* 23, 567–574. doi:10.1016/j.tcb.2013.07.005

Jockusch, B. M., Brown, D. F., and Rusch, H. P. (1971). Synthesis and some properties of an actin-like nuclear protein in the slime mold Physarum polycephalum. *J. Bacteriol.* 108, 705–714. doi:10.1128/jb.108.2.705-714.1971

Joseph, C. G., Darrah, E., Shah, A. A., Skora, A. D., Casciola-Rosen, L. A., Wigley, F. M., et al. (2014). Association of the autoimmune disease scleroderma with an immunologic response to cancer. *Science* 343, 152–157. doi:10.1126/science.1246886

Kelpsch, D. J., and Tootle, T. L. (2018). Nuclear actin: From discovery to function. *Anat. Rec. Hob.* 301, 1999–2013. doi:10.1002/ar.23959

Kelpsch, D. J., Groen, C. M., Fagan, T. N., Sudhir, S., and Tootle, T. L. (2016). Fascin regulates nuclear actin during Drosophila oogenesis. *Mol. Biol. Cell* 27, 2965–2979. doi:10.1091/mbc.E15-09-0634

Khandelwal, N., Simpson, J., Taylor, G., Rafique, S., Whitehouse, A., Hiscox, J., et al. (2011). Nucleolar NF-κB/RelA mediates apoptosis by causing cytoplasmic relocalization of nucleophosmin. *Cell death Differ.* 18, 1889–1903. doi:10.1038/cdd.2011.79

Kitamura, H., Matsumori, H., Kalendova, A., Hozak, P., Goldberg, I. G., Nakao, M., et al. (2015). The actin family protein ARP6 contributes to the structure and the function of the nucleolus. *Biochem. Biophys. Res. Commun.* 464, 554–560. doi:10.1016/j.bbrc.2015.07.005

Kong, J., Han, H., Bergalet, J., Bouvrette, L. P. B., Hernandez, G., Moon, N. S., et al. (2019). A ribosomal protein S5 isoform is essential for oogenesis and interacts with distinct RNAs in *Drosophila melanogaster*. *Sci. Rep.* 9, 13779. doi:10.1038/s41598-019-50357-z

Kresoja-Rakic, J., and Santoro, R. (2019). Nucleolus and rRNA gene chromatin in early embryo development. *Trends Genet.* 35, 868–879. doi:10.1016/j.tig.2019.06.005

Lafita-Navarro, M. C., and Conacci-Sorrell, M. (2022). Nucleolar stress: From development to cancer. *Semin. Cell Dev. Biol.* 136, 64–74. doi:10.1016/j.semcdb.2022.04.001

Lafontaine, D. L. J., Riback, J. A., Bascetin, R., and Brangwynne, C. P. (2021). The nucleolus as a multiphase liquid condensate. *Nat. Rev. Mol. Cell Biol.* 22, 165–182. doi:10.1038/s41580-020-0272-6

Langenbach, R., Loftin, C., Lee, C., and Tiano, H. (1999). Cyclooxygenase knockout mice: models for elucidating isoform-specific functions. *Biochem. Pharmacol.* 58, 1237–1246. doi:10.1016/s0006-2952(99)00158-6

Lim, H., Paria, B. C., Das, S. K., Dinchuk, J. E., Langenbach, R., Trzaskos, J. M., et al. (1997). Multiple female reproductive failures in cyclooxygenase 2-deficient mice. *Cell* 91, 197–208. doi:10.1016/s0092-8674(00)80402-x

Lindstrom, M. S., Jurada, D., Bursac, S., Orsolic, I., Bartek, J., and Volarevic, S. (2018). Nucleolus as an emerging hub in maintenance of genome stability and cancer pathogenesis. *Oncogene* 37, 2351–2366. doi:10.1038/s41388-017-0121-z

Maslova, A., and Krasikova, A. (2012). Nuclear actin depolymerization in transcriptionally active avian and amphibian oocytes leads to collapse of intranuclear structures. *Nucleus* 3, 300–311. doi:10.4161/nucl.20393

Mercer, M., Jang, S., Ni, C., and Buszczak, M. (2021). The dynamic regulation of mRNA translation and ribosome biogenesis during germ cell development and reproductive aging. *Front. Cell Dev. Biol.* 9, 710186. doi:10.3389/fcell.2021.710186

Misu, S., Takebayashi, M., and Miyamoto, K. (2017). Nuclear actin in development and transcriptional reprogramming. *Front. Genet.* 8, 27. doi:10.3389/fgene.2017.00027

Mogessie, B., and Schuh, M. (2017). Actin protects mammalian eggs against chromosome segregation errors. *Science* 357, eaal1647. doi:10.1126/science.aal1647

Obrdlik, A., Kukalev, A., Louvet, E., Farrants, A. K., Caputo, L., and Percipalle, P. (2008). The histone acetyltransferase PCAF associates with actin and hnRNP U for RNA polymerase II transcription. *Mol. Cell. Biol.* 28, 6342–6357. doi:10.1128/MCB.00766-08

Orsolic, I., Jurada, D., Pullen, N., Oren, M., Eliopoulos, A. G., and Volarevic, S. (2016). The relationship between the nucleolus and cancer: Current evidence and emerging paradigms. *Semin. Cancer Biol.* 37-38, 36–50. doi:10.1016/j.semcancer.2015.12.004

Pall, M., Friden, B. E., and Brannstrom, M. (2001). Induction of delayed follicular rupture in the human by the selective COX-2 inhibitor rofecoxib: A randomized double-blind study. *Hum. Reprod.* 16, 1323–1328. doi:10.1093/humrep/16.7.1323

Pederson, T. (2011). The nucleolus. *Cold Spring Harb. Perspect. Biol.* 3, a000638. doi:10.1101/cshperspect.a000638

Peppelenbosch, M. P., Tertoolen, L. G., Hage, W. J., and de Laat, S. W. (1993). Epidermal growth factor-induced actin remodeling is regulated by 5-lipoxygenase and cyclooxygenase products. *Cell* 74, 565–575. doi:10.1016/0092-8674(93)80057-l

Percipalle, P., Jonsson, A., Nashchekin, D., Karlsson, C., Bergman, T., Guialis, A., et al. (2002). Nuclear actin is associated with a specific subset of hnRNP A/B-type proteins. *Nucleic acids Res.* 30, 1725–1734. doi:10.1093/nar/30.8.1725

Percipalle, P. (2013). Co-transcriptional nuclear actin dynamics. *Nucleus* 4, 43–52. doi:10.4161/nucl.22798

Philimonenko, V. V., Zhao, J., Iben, S., Dingova, H., Kysela, K., Kahle, M., et al. (2004). Nuclear actin and myosin I are required for RNA polymerase I transcription. *Nat. Cell Biol.* 6, 1165–1172. doi:10.1038/ncb1190

Pierce, K. L., Fujino, H., Srinivasan, D., and Regan, J. W. (1999). Activation of FP prostanoid receptor isoforms leads to Rho-mediated changes in cell morphology and in the cell cytoskeleton. *J. Biol. Chem.* 274, 35944–35949. doi:10.1074/jbc.274.50.35944

Platt, J. L., and Michael, A. F. (1983). Retardation of fading and enhancement of intensity of immunofluorescence by p-phenylenediamine. *J. Histochem. Cytochem. Off. J. Histochem. Soc.* 31, 840–842. doi:10.1177/31.6.6341464

Plessner, M., Melak, M., Chinchilla, P., Baarlink, C., and Grosse, R. (2015). Nuclear F-actin formation and reorganization upon cell spreading. *J. Biol. Chem.* 290, 11209–11216. doi:10.1074/jbc.M114.627166

Prates, E. G., Nunes, J. T., and Pereira, R. M. (2014). A role of lipid metabolism during cumulus-oocyte complex maturation: impact of lipid modulators to improve embryo production. *Mediat. Inflamm.* 2014, 692067. doi:10.1155/2014/692067

Qi, T., Tang, W., Wang, L., Zhai, L., Guo, L., and Zeng, X. (2011). G-actin participates in RNA polymerase II-dependent transcription elongation by recruiting positive transcription elongation factor b (P-TEFb). *J. Biol. Chem.* 286, 15171–15181. doi:10.1074/jbc.M110.184374

Sanchez, C. G., Teixeira, F. K., Czech, B., Preall, J. B., Zamparini, A. L., Seifert, J. R., et al. (2016). Regulation of ribosome biogenesis and protein synthesis controls germline stem cell differentiation. *Cell Stem Cell* 18, 276–290. doi:10.1016/j.stem.2015.11.004

Scheffler, K., Giannini, F., Lemonnier, T., and Mogessie, B. (2022). The prophase oocyte nucleus is a homeostatic G-actin buffer. *J. Cell Sci.* 135, jcs259807. doi:10.1242/jcs.259807

Scherl, A., Coute, Y., Deon, C., Calle, A., Kindbeiter, K., Sanchez, J. C., et al. (2002). Functional proteomic analysis of human nucleolus. *Mol. Biol. Cell* 13, 4100–4109. doi:10.1091/mbc.e02-05-0271

Schmidt, E. K., Clavarino, G., Ceppi, M., and Pierre, P. (2009). SUnSET, a nonradioactive method to monitor protein synthesis. *Nat. methods* 6, 275–277. doi:10.1038/nmeth.1314

Sen, B., Xie, Z., Uzer, G., Thompson, W. R., Styner, M., Wu, X., et al. (2015). Intranuclear actin regulates osteogenesis. *Stem cells* 33, 3065–3076. doi:10.1002/stem.2090

Sen, B., Uzer, G., Samsonraj, R. M., Xie, Z., McGrath, C., Styner, M., et al. (2017). Intranuclear actin structure modulates mesenchymal stem cell differentiation. *Stem cells* 35, 1624–1635. doi:10.1002/stem.2617

Smith, G., Roberts, R., Hall, C., and Nuki, G. (1996). Reversible ovulatory failure associated with the development of luteinized unruptured follicles in women with inflammatory arthritis taking non-steroidal anti-inflammatory drugs. *Br. J. Rheumatol.* 35, 458–462. doi:10.1093/rheumatology/35.5.458

Sokolova, M., Moore, H. M., Prajapati, B., Dopie, J., Merilainen, L., Honkanen, M., et al. (2018). Nuclear actin is required for transcription during Drosophila oogenesis. *iScience* 9, 63–70. doi:10.1016/j.isci.2018.10.010

Spracklen, A. J., Fagan, T. N., Lovander, K. E., and Tootle, T. L. (2014a). The pros and cons of common actin labeling tools for visualizing actin dynamics during Drosophila oogenesis. *Dev. Biol.* 393, 209–226. doi:10.1016/j.ydbio.2014.06.022

Spracklen, A. J., Kelpsch, D. J., Chen, X., Spracklen, C. N., and Tootle, T. L. (2014b). Prostaglandins temporally regulate cytoplasmic actin bundle formation during Drosophila oogenesis. *Mol. Biol. Cell* 25, 397–411. doi:10.1091/mbc.E13-07-0366

Spracklen, A. J., Lamb, M. C., Groen, C. M., and Tootle, T. L. (2019). Pharmacogenetic screen to uncover actin regulators targeted by prostaglandins during Drosophila oogenesis. *G3* 9, 3555–3565. doi:10.1534/g3.119.400704

Spradling, A. C. (1993). "Developmental genetics of oogenesis," in *The development of* Drosophila melanogaster. Editor B. Martinez-Arias (Cold Spring Harbor Laboratory Press), 1–70.

Stark, L. A., and Dunlop, M. G. (2005). Nucleolar sequestration of RelA (p65) regulates NF-kappaB-driven transcription and apoptosis. *Mol. Cell. Biol.* 25, 5985–6004. doi:10.1128/MCB.25.14.5985-6004.2005

Stark, L. A., Din, F. V., Zwacka, R. M., and Dunlop, M. G. (2001). Aspirin-induced activation of the NF-kappaB signaling pathway: A novel mechanism for aspirin-mediated apoptosis in colon cancer cells. *FASEB J. Off. Publ. Fed. Am. Soc. Exp. Biol.* 15, 1273–1275. doi:10.1096/fj.00-0529fje

Stochaj, U., and Weber, S. C. (2020). Nucleolar organization and functions in Health and disease. *Cells* 9, 526. doi:10.3390/cells9030526

Stuven, T., Hartmann, E., and Gorlich, D. (2003). Exportin 6: A novel nuclear export receptor that is specific for profilin.actin complexes. *EMBO J.* 22, 5928–5940. doi:10.1093/emboj/cdg565

Sugimoto, Y., Inazumi, T., and Tsuchiya, S. (2015). Roles of prostaglandin receptors in female reproduction. *J. Biochem.* 157, 73–80. doi:10.1093/jb/mvu081

Takahashi, T., Igarashi, H., Amita, M., Hara, S., and Kurachi, H. (2010). Roles of prostaglandins during oocyte maturation: Lessons from knockout mice. *J. Mamm. Ova Res.* 27, 11–20. doi:10.1274/jmor.27.11

Tamma, G., Wiesner, B., Furkert, J., Hahm, D., Oksche, A., Schaefer, M., et al. (2003). The prostaglandin E2 analogue sulprostone antagonizes vasopressin-induced antidiuresis through activation of Rho. *J. Cell Sci.* 116, 3285–3294. doi:10.1242/jcs.00640

Telley, I. A., Gaspar, I., Ephrussi, A., and Surrey, T. (2012). Aster migration determines the length scale of nuclear separation in the Drosophila syncytial embryo. *J. Cell Biol.* 197, 887–895. doi:10.1083/jcb.201204019

Thoms, H. C., Dunlop, M. G., and Stark, L. A. (2007). p38-mediated inactivation of cyclin D1/cyclin-dependent kinase 4 stimulates nucleolar translocation of RelA and apoptosis in colorectal cancer cells. *Cancer Res.* 67, 1660–1669. doi:10.1158/0008-5472.CAN-06-1038

Tiku, V., and Antebi, A. (2018). Nucleolar function in lifespan regulation. *Trends Cell Biol.* 28, 662–672. doi:10.1016/j.tcb.2018.03.007

Tootle, T. L., and Spradling, A. C. (2008). Drosophila pxt: A cyclooxygenase-like facilitator of follicle maturation. *Development* 135, 839–847. doi:10.1242/dev.017590

Tootle, T. L., Williams, D., Hubb, A., Frederick, R., and Spradling, A. (2011). Drosophila eggshell production: identification of new genes and coordination by pxt. *PloS one* 6, e19943. doi:10.1371/journal.pone.0019943

Tootle, T. L. (2013). Genetic insights into the *in vivo* functions of prostaglandin signaling. *Int. J. Biochem. Cell Biol.* 45, 1629–1632. doi:10.1016/j.biocel.2013.05.008

Ueno, N., Murakami, M., Tanioka, T., Fujimori, K., Tanabe, T., Urade, Y., et al. (2001). Coupling between cyclooxygenase, terminal prostanoid synthase, and phospholipase A2. *J. Biol. Chem.* 276, 34918–34927. doi:10.1074/jbc.M100429200

Vane, J. R., and Botting, R. M. (2003). The mechanism of action of aspirin. *Thromb. Res.* 110, 255–258. doi:10.1016/s0049-3848(03)00379-7

Viita, T., Kyheroinen, S., Prajapati, B., Virtanen, J., Frilander, M. J., Varjosalo, M., et al. (2019). Nuclear actin interactome analysis links actin to KAT14 histone acetyl transferase and mRNA splicing. *J. Cell Sci.* 132, jcs226852. doi:10.1242/jcs.226852

Wineland, D. M., Kelpsch, D. J., and Tootle, T. L. (2018). Multiple pools of nuclear actin. *Anat. Rec. Hob.* 301, 2014–2036. doi:10.1002/ar.23964

Yuan, C., and Smith, W. L. (2015). A cyclooxygenase-2-dependent prostaglandin E2 biosynthetic system in the Golgi apparatus. *J. Biol. Chem.* 290, 5606–5620. doi:10.1074/jbc.M114.632463

Yuan, X., Zhou, Y., Casanova, E., Chai, M., Kiss, E., Gröne, H. J., et al. (2005). Genetic inactivation of the transcription factor TIF-IA leads to nucleolar disruption, cell cycle arrest, and p53-mediated apoptosis. *Mol. Cell* 19, 77–87. doi:10.1016/j.molcel.2005.05.023

Zhang, Q., Shalaby, N. A., and Buszczak, M. (2014). Changes in rRNA transcription influence proliferation and cell fate within a stem cell lineage. *Science* 343, 298–301. doi:10.1126/science.1246384

frontiers | Frontiers in Cell and Developmental Biology

TYPE Original Research
PUBLISHED 21 April 2023
DOI 10.3389/fcell.2023.1134051

OPEN ACCESS

EDITED BY
Rafael A. Fissore,
University of Massachusetts Amherst,
United States

REVIEWED BY
Bart M. Gadella,
Utrecht University, Netherlands
Manabu Yoshida,
The University of Tokyo, Japan

*CORRESPONDENCE
Lonny R. Levin,
llevin@med.cornell.edu

RECEIVED 29 December 2022
ACCEPTED 12 April 2023
PUBLISHED 21 April 2023

CITATION
Ritagliati C, Ayoub S, Balbach M, Buck J and Levin LR (2023), *In vivo* characterization of sAC null sperm. *Front. Cell Dev. Biol.* 11:1134051. doi: 10.3389/fcell.2023.1134051

In vivo characterization of sAC null sperm

Carla Ritagliati, Sylvia Ayoub, Melanie Balbach, Jochen Buck and Lonny R. Levin*

Department of Pharmacology, Weill Cornell Medicine, New York, NY, United States

Targeted disruption of the soluble adenylyl cyclase (ADCY10; sAC) gene results in male-specific sterility without affecting spermatogenesis, mating behavior, or spermatozoa morphology and count; however, it dramatically impairs sperm motility and prevents capacitation. These phenotypes were identified in sperm from sAC null mice surgically extracted from the epididymis and studied *in vitro*. Epididymal sperm are dormant, and never exposed to physiological activators in semen or the female reproductive tract. To study sAC null sperm under conditions which more closely resemble natural fertilization, we explored phenotypes of ejaculated sAC null sperm *in vivo* post-coitally as well as *ex vivo*, collected from the female reproductive tract. *Ex vivo* ejaculated sAC null sperm behaved similarly to epididymal sAC null sperm, except with respect to the physiologically induced acrosome reaction. These studies suggest there is a sAC-independent regulation of acrosome responsiveness induced upon ejaculation or exposure to factors in the female reproductive tract. We also studied the behavior of sAC null sperm *in vivo* post-coitally by taking advantage of transgenes with fluorescently labelled sperm. Transgenes expressing GFP in the acrosome and DsRed2 in the mitochondria located in the midpiece of sperm (DsRed2/Acr3-EGFP) allow visualization of sperm migration through the female reproductive tract after copulation. As previously reported, sperm from wild type (WT) double transgenic mice migrated from the uterus through the uterotubular junction (UTJ) into the oviduct within an hour post-copulation. In contrast, sperm from sAC null double transgenic mice were only found in the uterus. There were no sAC null sperm in the oviduct, even 8 h after copulation. These results demonstrate that sAC KO males are infertile because their sperm do not migrate to the fertilization site.

KEYWORDS

***in vivo* migration, motility, soluble adenylyl cyclase, hyperactivation, acrosome reaction**

1 Introduction

Morphologically mature sperm are stored, in a dormant state, in the cauda epididymis which is characterized by an extremely low (≤5 mM) bicarbonate (HCO_3^-) concentration (Levine and Kelly, 1978). Upon ejaculation, sperm mix with seminal plasma, which contains 25 mM bicarbonate along with various nutrients that initiate and support sperm motility. Ejaculated motile sperm are still not capable of fertilizing an oocyte. Mammalian sperm acquire fertilization competence in the female genital tract, in a process known as capacitation, which involves molecular, cellular, and physiological changes. During this process sperm increase their flagellar beat frequency; switch their motility pattern to a fast whip-like asymmetrical movement, known as hyperactivation; and gain acrosomal responsiveness to a physiological stimulus.

Studying sperm physiology is greatly enhanced by using mouse genetics to study phenotypes of sperm devoid of key proteins. For most studies, sperm are surgically isolated from the epididymis, and the process of capacitation is defined by conditions which are sufficient to support sperm functions essential for *in vitro* fertilization. While such studies have revealed molecular hallmarks of capacitation, they may miss physiologically relevant processes that sperm undergo prior to fertilizing the oocyte in the oviduct *in vivo*. For example, migration through the female reproductive tract is a key element of natural fertilization which is not mimicked in the test tube.

After being deposited in the vagina during coitus, mammalian sperm must travel through the female's reproductive tract to reach the site of fertilization, the ampullary region of the uterine tube. To reach and penetrate the oocyte, sperm migration along the female tract is thought to depend upon contractions of the myometrium (Lyons et al., 1991; Kunz et al., 1996; Ishikawa et al., 2016), interactions between sperm and the female tract (Yamaguchi et al., 2009; Fujihara et al., 2013; Okabe, 2015) and sperm motility (Gaddum-Rosse, 1981). Among the semen parameters motility is considered to be a strong predictor of male fertility potential. Sperm dysfunction has consistently been identified as a common cause of infertility, with asthenozoospermia (the medical term for reduced sperm motility), among the predominant contributing factors for male infertility (Dcunha et al., 2022).

The complex signaling cascade leading to initiation of motility and capacitation is stimulated upon ejaculation when cauda epididymal sperm encounter seminal plasma, where elevated HCO_3^- activates soluble adenylyl cyclase (sAC or ADCY10) (Visconti et al., 1995; 2011; Chen et al., 2000). sAC activity is directly stimulated by bicarbonate (Chen et al., 2000; Kleinboelting et al., 2014), which induces an allosteric change facilitating catalysis (Kleinboelting et al., 2014). In the absence of sAC, mammalian sperm are unable to fertilize, and sAC knock-out (KO) mice exhibit male-specific sterility. Targeted disruption of the sAC gene or pharmacological inhibition of sAC does not affect spermatogenesis, mating behavior, nor spermatozoa morphology and count; however, it dramatically impairs sperm motility, prevents capacitation, and results in sperm which cannot fertilize zona-intact oocytes (Esposito et al., 2004; Xie et al., 2006; Marquez and Suarez, 2008; Ramos-Espiritu et al., 2016; Balbach et al., 2021; 2023). These deficits were identified by studying epididymal sAC null sperm; thus, until now, mouse sAC null sperm were only studied in the context of *in vitro* capacitating conditions.

The role of sAC in male fertility was also genetically and pharmacologically confirmed in humans (Akbari et al., 2019; Balbach et al., 2021; 2023). Two infertile male patients were found to be homozygous for a frameshift mutation in the exonic region of ADCY10, leading to premature termination and interruption of the catalytic domains. Sperm from these patients are immotile, similar to sperm from sAC KO mice, and their motility defect could be rescued with cell-permeable cAMP analogs, consistent with the loss of sAC disrupting motility and causing infertility (Akbari et al., 2019). Interestingly, unlike mouse sAC null sperm which were studied only after exposure to bicarbonate in the capacitating media *in vitro,* human sAC null sperm were studied following ejaculation, after the sperm were already exposed to the bicarbonate and nutrients present in seminal plasma.

Two advances in mouse physiology facilitate studying sperm in more physiological contexts. Post-ejaculated mouse sperm can be studied *ex vivo* and *in vivo*. Recovering ejaculated mouse sperm from the female reproductive tract post-coitus affords the opportunity to study mouse sperm *ex vivo* after exposure to seminal plasma as well as factors derived from the female reproductive tract. *In vivo*, mouse sperm migration through the female reproductive tract can be visualized post-coitally with the aid of fluorescent markers. Using these methods to more accurately reflect natural fertilization, we characterized the *in vivo* phenotypes of sAC null sperm.

2 Materials and methods

2.1 Animals

The transgenic C1 sAC null mouse line, in which exons 2–4 are deleted, was generated at Lexicon Genetics (The Woodlands, TX). The transgenic mouse line whose sperm express green fluorescent protein (GFP) in their acrosome and red fluorescent protein (RFP) in their mitochondria (B6D2F1-Tg (CAG/Su9-DsRed2, Acr3-EGFP) RBGS002Osb) (Hasuwa et al., 2010) is from M. Okabe (Osaka U, Japan) via the RIKEN Institute. Animal experiments were approved by Weill Cornell Medicine's Institutional Animal Care and Use Committee (IACUC).

2.2 Reagents

3-Isobutyl-1-methylxanthine (IBMX), bovine serum albumin (BSA), $NaHCO_3$ and Progesterone were purchased from Sigma-Aldrich (St. Louis, MO, United States). 8-Bromo-cAMP (sodium salt) and cAMP Elisa kit from Cayman Chemical (Ann Arbor, MI, United States). β-mercaptoethanol from Thermo Fisher Scientific (Waltham, MA, United States). PBS buffer was purchased from Corning (Radnor, PA, United States). Rabbit monoclonal anti-phospho-PKA substrates (anti-pPKA substrates) (clone 100G7E) and Horseradish peroxidase-conjugated anti-mouse and anti-rabbit IgG, were purchased from Cell Signaling Technology (Danvers, MA). Mouse anti-phospho Tyrosine (anti-pTyr) (clone 4G10) was from EMD Millipore.

2.3 Generation of the double fluorescent transgenic sAC KO line

Crossing sAC KO females with Acr-EGFP/Su9-DsRed2 males generated Acr-EGFP/Su9-DsRed2/$sAC^{-/-}$ mice. The presence of the transgenes expressing fluorescent tags as well as disruption of sAC gene in the germline were confirmed by PCR analysis.

2.4 Sperm preparation

Mouse sperm were isolated by incision of the cauda epididymis of male mice or from the female genital tract after copulation, followed by a swim-out in 500 µL Toyoda Yokoyama Hoshi (TYH) medium (in mM: 119.3 NaCl, 4.7 KCl, 1.7 $CaCl_2$, 1.2 KH_2PO_4,

1.2 $MgSO_4$, 5.6 glucose, 0.5 pyruvate, 20 HEPES, pH 7.4 adjusted with NaOH), prewarmed at 37°C and counted using a hematocytometer. For capacitation, sperm were incubated in TYH containing 5 mg/mL BSA and 20 mM $NaHCO_3$ or 0.5 mM 8Br-cAMP and 0.5 µM IBMX at 37°C.

2.5 Sperm cAMP quantification

Aliquots of 3–4 x 10^6 WT or $sAC^{-/-}$ double transgenic sperm were incubated for 15 min in the presence of 0.5 µM IBMX in non-capacitating (TYH-) or capacitating (TYH + HCO_3/BSA) buffer. Sperm were sedimented by centrifugation at 2000 x g for 3 min and lysed in 50–100 µL of 0.1 M HCl for 10 min. Sperm lysates were centrifuged at 2000 x g for 3 min and the cAMP in the supernatant was acetylated and quantified using the Direct cAMP ELISA Kit (Cayman) according to the manufacturer's instructions.

2.6 Western blot analysis

Aliquots of 1–2 x 10^6 WT or $sAC^{-/-}$ double transgenic sperm were incubated for 60 min in TYH buffer in the absence or presence of 5 mg/mL BSA and 20 mM $NaHCO_3$ or 0.5 mM 8Br-cAMP and 0.5 µM IBMX. Sperm were collected by centrifugation for 3 min at 2000 x g, washed twice with 1 mL TBS, and resuspended with Laemmli sample buffer without β-mercaptoethanol, vortexed for 10 s and boiled for 3 min. After centrifugation, 5% β-mercaptoethanol was added to the supernatants and boiled again for 5 min. Protein extracts equivalent to 0.5–1 x 10^6 sperm/lane were subjected to SDS-PAGE and electrotransferred to PVDF membranes at 250 mA for 90 min. Membranes were blocked with 3% BSA in TBS containing 0.1% Tween-20 (T-TBS). Antibodies were diluted in T-TBS as follows: 1/5,000 for anti-pTyr and 1/3,000 for anti-pPKA substrates. Secondary antibodies were diluted 1/10,000 in T-TBS and the membranes analyzed using an enhanced chemiluminescence detection kit (SuperSignal West Femto Maximun Sensitivity Substrate, Thermo Scientific) according to manufacturer's instructions.

2.7 Sperm motility analysis

Sperm suspensions were loaded on a 100-µm deep Leja slides and placed on a microscope stage at 37°C. Sperm movements were examined using an IVOSII Hamilton Thorne. Parameters used were as follows: 45 frames acquired, frame rate of 60 Hz, and cell size of 25–200 μm^2. At least 5 microscopy fields and a minimum of 500 sperm were analyzed in each experiment. The following parameters were measured: mean path velocity (VAP, µm/sec), curvilinear velocity (VCL, µm/sec), straight-line velocity (VSL, µm/sec), linearity (LIN, %), amplitude of lateral head displacement (ALH, µm), beat cross frequency (BCF, Hz) and straightness (STR, %). Sperm were considered hyperactivated when presenting VCL ≥271 µm/s, LIN <50%, and ALH ≥3.5 µm and progressive when presenting VAP ≥50 µm/s and STR >80%.

2.8 Acrosomal status assay

After incubating WT and $sAC^{-/-}$ sperm under non-capacitating or capacitating (+HCO_3^-/BSA or +8Br-cAMP/IBMX) conditions for 60 min, sperm were incubated for an additional 30 min in the absence or presence of 25 µM progesterone (Pg). Sperm were sedimented by centrifugation at 1,000 x g for 5 min, washed twice with PBS, and seeded on 8-well glass slides. After adhesion, sperm were incubated with PBS containing DAPI for 10 min. Before mounting, samples were washed with PBS (four times for 5 min each time). Epifluorescence microscopy was used to assess acrosomal status, distinguished by the presence or absence of green fluorescence of intact acrosomes. At least 300 sperm were analyzed in each condition.

2.9 *In vivo* sperm migration assay

Single-caged double transgenic DsRed2/Acr3-EGFP WT or $sAC^{-/-}$ males were combined with WT females in estrous and vaginal plug formation was checked every 30 min. Once plug formation was confirmed, the male was separated from the female. The uteri and oviducts were excised various times after coitus (1.5, 4, and 8 h), transferred to slides, and examined for the presence of fluorescent sperm expressing mitochondrial DsRed2 and/or acrosomal EGFP markers in the female reproductive tract (IX73 Olympus). The experiments were repeated at least 3 times with 3 different males.

3 Results

3.1 Fluorescently tagged double transgenic sAC KO sperm do not display molecular hallmarks associated with capacitation

To be able to study sAC null sperm *in vivo,* we crossed transgenes which label the acrosome and mitochondria (located in the midpiece) of spermatozoa with green and red fluorescent proteins, respectively (DsRed2/Acr3-EGFP) (Hasuwa et al., 2010), into $sAC^{-/-}$ (KO) mice (Esposito et al., 2004; Hess et al., 2005) as well as into our isogenic C57Bl/6 strain. The resultant double transgenic sAC KO mouse line exhibited no overt developmental abnormalities. As previously reported, sAC KO males were infertile despite producing epididymal spermatozoa with the same count and morphology as wild type (WT) males (Supplementary Figures S1A, B) and showing normal mating behavior with successful ejaculation and vaginal plug formation (Supplementary Figure S1C).

Also similar to spermatozoa from sAC KO mice, epididymal spermatozoa from DsRed2/Acr3-EGFP/sAC KO males did not display molecular hallmarks normally associated with capacitation when incubated in the presence of HCO_3^-: they did not increase cAMP levels and they did not produce the prototypical pattern of phosphorylation of PKA substrates and tyrosines. As expected, addition of membrane-permeable cAMP, the product of sAC, rescued the phosphorylation of PKA substrates and tyrosines (Figure 1), confirming that any defects observed in sperm from

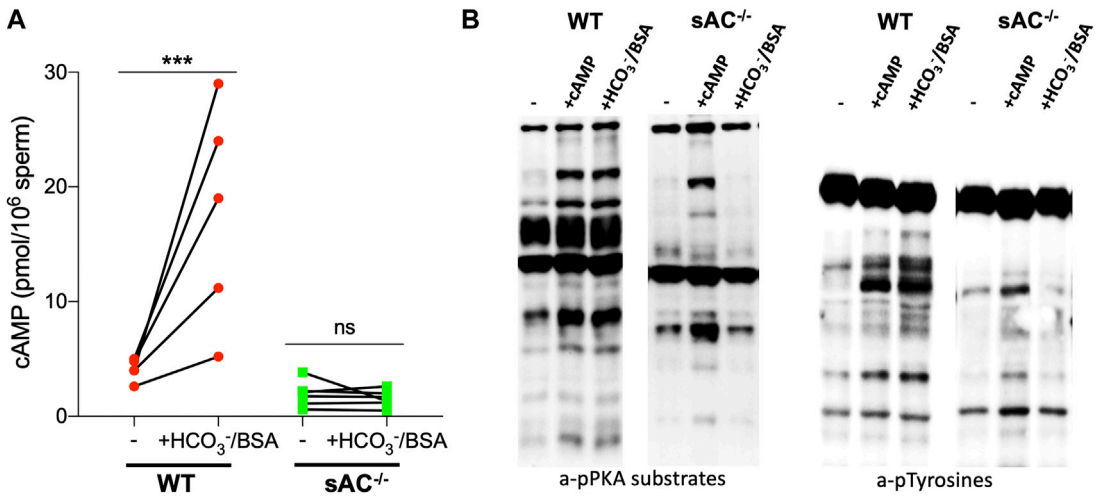

FIGURE 1
(A) Intracellular cAMP levels in WT (red circles) and sAC$^{-/-}$ (green squares) sperm after incubation for 15 min in the presence of 0.5 μM IBMX in non-capacitating (–) or capacitating (+HCO_3^-/BSA) media. Individual replicates indicated by symbols, N = 5. Ratio paired Student's t test was performed between indicated conditions: ***$p < 0.001$, ns (non-significant). **(B)** Western blot analysis using anti-pPKA substrates and anti-pTyrosines antibodies. Sperm were incubated for 60 min in the absence (–) or presence of 0.5 mM 8Br-cAMP and 0.5 μM IBMX (+cAMP) or 20 mM HCO_3^- and 5 mg/mL BSA (+HCO_3^-/BSA).

double transgenic sAC KO mice come from the absence of sAC. These results validate that the double transgenic, fluorescently tagged sAC KO line phenotypically reflect previously characterized sAC KO mice (Esposito et al., 2004; Hess et al., 2005; Xie et al., 2006).

3.2 Both epididymal and ejaculated double transgenic sAC KO sperm are immotile

Sperm surgically extracted from the epididymis are isolated prior to ejaculation so they have never been exposed to the HCO_3^- in seminal plasma. Like other WT epididymal sperm, epididymal sperm from double transgenic WT males are motile, and the fraction of sperm exhibiting hyperactivated motility increases in the presence of HCO_3^- (Figure 2; Supplementary Movies S1, S2). To compare epididymal sperm with ejaculated mouse sperm, we mated double transgenic males with WT females and recovered sperm from the uterus post-copulation. As expected, ejaculated WT sperm were motile, but remarkably they did not display the bicarbonate-induced increases in total and progressive motility seen in epididymal sperm. In addition, they showed only a slight increase in hyperactivation (Figure 2; Supplementary Movies S1, S2). Presumably ejaculated sperm are less sensitive to bicarbonate because they have already been exposed to bicarbonate-dependent stimulation upon mixing with seminal plasma and fluids in the female tract.

We used the same methods to isolate and characterize ejaculated sAC null sperm. When we mated sAC$^{-/-}$ double transgenic males with WT females, we observed *bona fide* plugs and plumped uteri after copulation (Supplementary Figure S2), and we successfully obtained sAC null sperm from uteri of receptive females. We recovered the same amount of ejaculated sperm from the female tract after mating with WT and sAC KO males (Supplementary Figure S2), confirming that sAC ablation does not affect mating or ejaculatory behaviors. In agreement with previous reports for epididymal sAC KO sperm (Esposito et al., 2004; Hess et al., 2005; Marquez and Suarez, 2008), both epididymal and ejaculated double transgenic sAC$^{-/-}$ sperm were immotile, showing only vibratory movements (Figure 2; Supplementary Movies S1, S2). Motility was restored by addition of a cell-permeable cAMP analog, proving the motility defect is due to the absence of sAC. Thus, double-transgenic sAC KO sperm are immotile even after ejaculation.

3.3 Ejaculated sAC KO sperm display bicarbonate-independent acrosomal responsiveness to progesterone

Another hallmark of capacitation is the ability to undergo a physiologically induced acrosome reaction (AR). WT epididymal sperm exhibited progesterone (Pg) induced AR following incubation with bicarbonate or after addition of exogenous membrane permeable cAMP (Figure 3A). In contrast, with epididymal sAC KO sperm, we only observed the Pg-induced AR in the presence of exogenous cAMP. These data demonstrate that there is a cAMP-dependent component to enable acrosomal responsiveness, which is mediated via sAC following bicarbonate stimulation. In ejaculated WT sperm, which were already exposed to bicarbonate in seminal plasma and fluids in the female reproductive tract, acrosomal responsiveness to Pg was observed in non-capacitating media (Figure 3B). Addition of bicarbonate enhanced the Pg-induced increase in AR (Supplementary Figure S3). Surprisingly, ejaculated sAC null sperm displayed a degree of Pg responsiveness in both non-capacitating and capacitating media

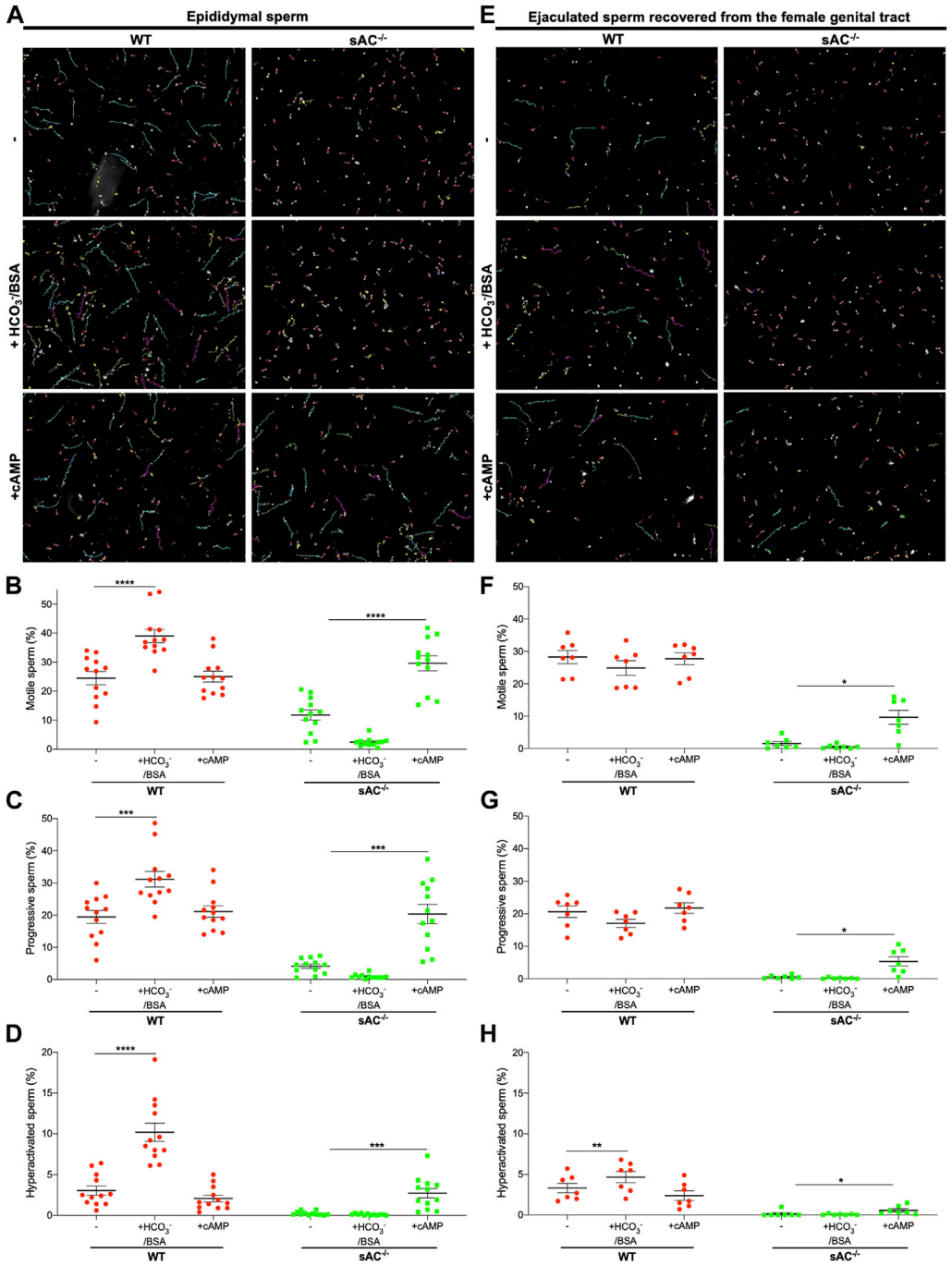

FIGURE 2
Epididymal and ejaculated WT (red circles) and sAC$^{-/-}$ (green squares) sperm incubated in the absence (–) or presence of 20 mM HCO_3^- and 5 mg/mL BSA (+HCO_3^-/BSA) or 0.5 mM 8Br-cAMP and 0.5 μM IBMX (+cAMP) for 20 min **(A,E)** Representative images with motility tracks of the CASA obtained with IVOSII Hamilton Thorne. Track´s color code: motile (green), progressive (turquoise), hyperactivated (pink), static (red), not counted (yellow). Bar graphs show percent total motility **(B,F)**, progressive motility **(C,G)** and hyperactivation **(D,H)** with the individual values for each experiment indicated. Data shown as mean ± SEM, representative of at least 7 independent experiments. More than 500 sperm in at least 5 fields were analyzed. Hyperactivated sperm are defined by: VCL ≥271 μm/s, LIN <50%, and ALH ≥5 μm.

(Figure 3). Thus, there also appears to be a sAC-independent mechanism regulating AR associated with ejaculation or residence in the female reproductive tract. As expected, epididymal and ejaculated sAC KO sperm lost any bicarbonate-induced increase in Pg-stimulated AR (Supplementary Figure S3), but in both cases, Pg responsiveness was increased by cell-permeable cAMP, corroborating the idea that there are both cAMP-dependent and cAMP-independent mechanisms for increasing the response to Pg.

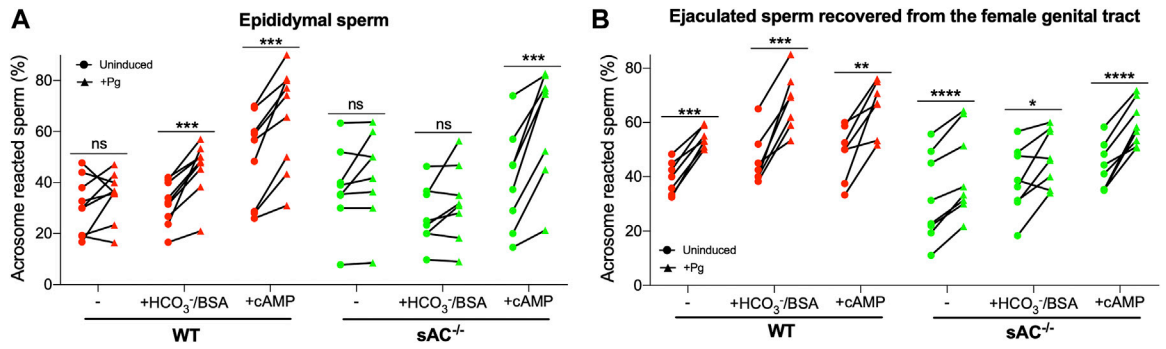

FIGURE 3
Progesterone-induced AR of epididymal **(A)** and ejaculated **(B)** WT (red symbols) and sAC$^{-/-}$ (green symbols) sperm incubated in the absence (–) or presence of 20 mM HCO_3^- and 5 mg/mL BSA (+HCO_3^-/BSA) or 0.5 mM 8Br-cAMP and 0.5 μM IBMX (+cAMP) for 60 min, 25 μM Progesterone (+Pg) or DMSO (Uninduced) were added, and then further incubated for 30 min. Data shown as mean ± SEM, representative of at least 7 independent experiments. Paired Student's t test was performed between indicated conditions: *$p < 0.05$, **$p < 0.005$, ***$p < 0.001$, ns (non-significant).

3.4 sAC KO sperm do not progress into the oviduct

Finally, to explore the *in vivo* roll of sAC, we studied sperm migration through the female reproductive tract following matings between WT or sAC KO double transgenic males with receptive WT females. Sperm ejaculated from WT mice migrated from the uterus through the uterotubular junction (UTJ) into the oviduct within an hour post-copulation, and by 4 h sperm were observed all the way from the oviduct to the ampulla. In contrast, while sperm ejaculated from sAC$^{-/-}$ double transgenic mice were present inside the uterus, few were infrequently observed in the UTJ, and none successfully progressed into the oviduct even 8 h after copulation (Figure 4; Supplementary Figures S4, S5).

4 Discussion

sAC null male mice and men are infertile (Esposito et al., 2004; Hess et al., 2005; Akbari et al., 2019). Previously, the specific defects in sAC null mouse sperm were studied in sperm isolated from the epididymis. Epididymal sperm are dormant, the signaling cascades which initiate motility and capacitation are activated by factors in seminal plasma and/or the female reproductive tract. Epididymal sperm genetically or pharmacologically devoid of sAC activity are immotile, do not capacitate, and do not fertilize oocytes in mouse IVF experiments (Esposito et al., 2004; Hess et al., 2005; Xie et al., 2006; Marquez and Suarez, 2008; Ramos-Espiritu et al., 2016; Balbach et al., 2021; 2023). We now explored phenotypes of sAC null sperm in states which better reflect natural fertilization. sAC null sperm collected post-coitally from the female reproductive tract revealed the existence of a sAC-independent, acrosome responsiveness in ejaculated sperm, and using transgenic mice expressing GFP and DsRed we demonstrate that sAC null sperm are unable to penetrate beyond the UTJ to reach the fertilization site.

As expected, sAC KO mouse sperm do not respond to bicarbonate in capacitating media. Neither epididymal nor ejaculated sAC KO sperm altered motility or acrosomal responsiveness in media containing bicarbonate. This observation reinforces the idea that sAC mediates the bicarbonate-induced changes during capacitation (Visconti et al., 1999; 2011; Ferreira et al., 2021). However, unlike epididymal sAC null sperm, ejaculated sAC null sperm recovered from the female genital tract can undergo a low level of progesterone-induced acrosome reaction. Thus, there appears to be a sAC-independent mechanism caused by ejaculation and/or residence in the female genital tract.

A major difference between mouse and human reproduction is the anatomy of the female reproductive tract. In humans, females possess a cervical restriction, and it is speculated that the sperm's progressive motility allows them to pass through the cervix to escape the inhospitable environment of the vagina. In contrast, mouse females lack a cervical restriction so ejaculated sperm deposited in the vagina are rapidly swept unimpeded into the uterus. Sperm accumulate at the UTJ, which can be considered a major selective barrier to mouse sperm migration through the female reproductive tract drastically reducing the number of sperm entering the oviduct (Suarez and Pacey, 2006; Mahé et al., 2021). Because immotile sAC null sperm fail to cross beyond the UTJ, we conclude that sperm must at least have progressive motility to pass through the UTJ.

There are three processes which appear to contribute to sperm's ability to travel through the female reproductive tract to reach the fertilization site: interactions between sperm and the female tract (Yamaguchi et al., 2009; Fujihara et al., 2013; Okabe, 2015), contractions of the myometrium and oviduct (myosalpinx) (Lyons et al., 1991; Kunz et al., 1996; Ishikawa et al., 2016), and sperm motility (Gaddum-Rosse, 1981). A number of distinct KO mouse lines with defects in binding to the oocyte's zona pellucida fail to enter the UTJ (Okabe, 2015). These lines display no detectable abnormalities in motility or morphology, implying that their migration defect is due to a lack of specific interactions between sperm and the epithelium of the female tract (Muro et al., 2016). These interactions seem to be essential for successful sperm entry into and passing through the UTJ. Once across the UTJ, myosalpinx contractions help the transport of sperm from the uterus to the isthmus and the middle region of the oviduct (Ishikawa et al., 2016).

Completely immotile rat sperm failed to cross the UTJ (Gaddum-Rosse, 1981); thus, it was proposed that most spermatozoa require self-propulsion to get through the UTJ into

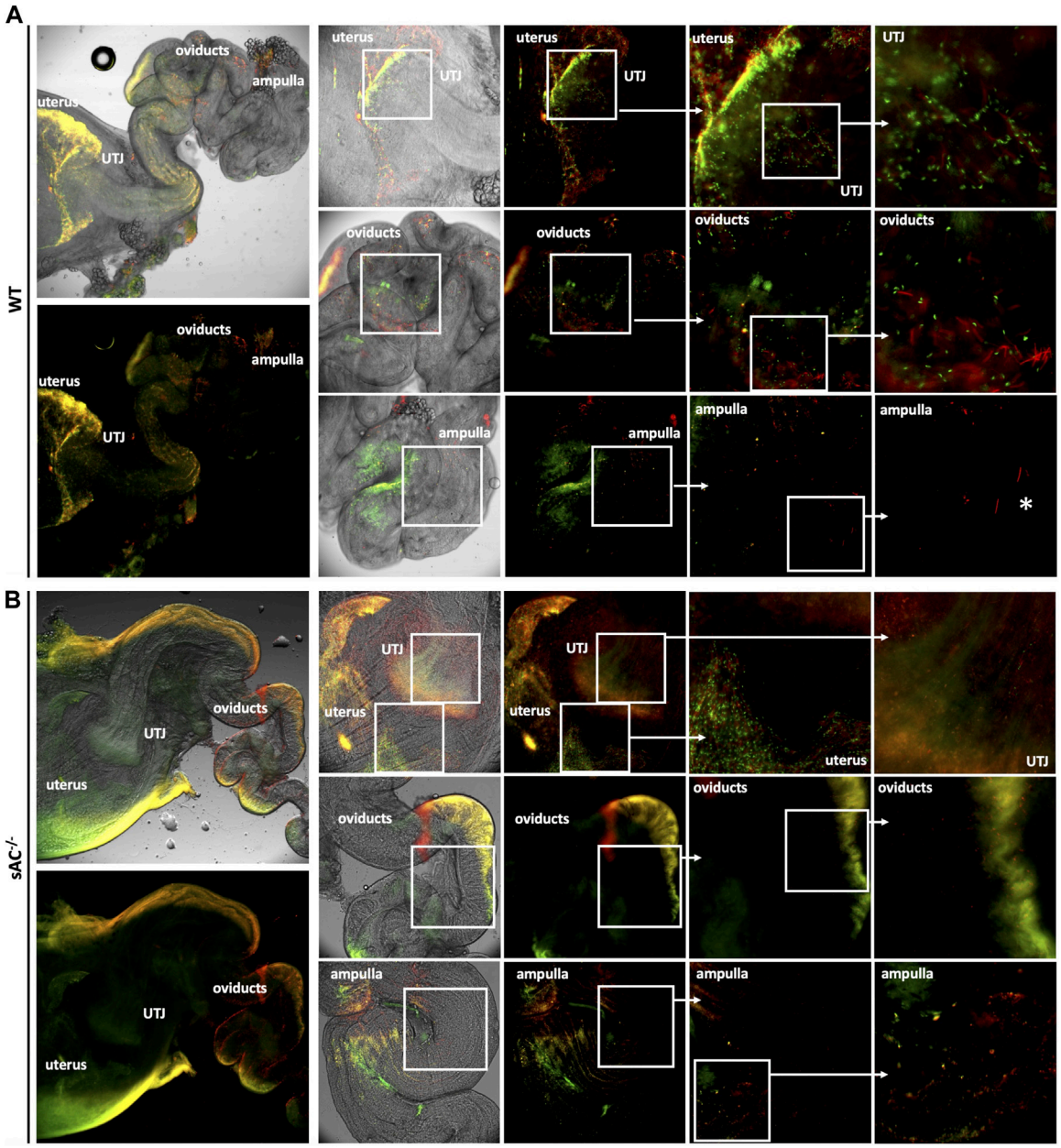

FIGURE 4
Migration of DsRed2/Acr3-EGFP/WT **(A)** and sAC$^{-/-}$ **(B)** sperm in the female genital tract 4 h post-copulation. Males were caged with WT females in estrous and after vaginal plug detection, they were separated. Four hours post-copulation, the female genital tracts were dissected and mounted for fluorescence microscopy analysis using an IX73 Olympus microscope. The indicated squared regions were digitally magnified and shown to the right. White asterisks depict acrosome reacted WT sperm in the ampulla. Images representative of at least 3 independent experiments.

the oviduct. However, this study relied upon killing sperm to render them immotile. CatSper1-null sperm, which are motile but do not hyperactivate, can migrate through the UTJ and reach the ampulla, though less effectively (Chung et al., 2014). A number of mouse strains with KOs of sperm-specific metabolic enzymes (phosphoglycerate Kinase 2, glyceraldehyde 3-phosphate dehydrogenase, and lactate dehydrogenase C) display sperm motility defects which correlate to male-specific infertility (Miki et al., 2004; Odet et al., 2008; Danshina et al., 2010), but *in vivo* migration has not been studied. We predict that migration of sperm from these strains will be impaired due to their motility defect. In our study, sAC null sperm, which are alive but immotile, are unable to migrate through the UTJ to the fertilization site.

While the UTJ represents the major barrier to sperm migration in rodents, the cervical restriction represents the major barrier to sperm migration in humans. Our demonstration that sAC KO male mice are infertile because their sperm do not penetrate beyond the UTJ suggests that human's sAC KO men are infertile because their sperm will not cross the cervix to enter the uterus to be able to ever reach the oviduct and the fertilization site. Because the vagina

reacidifies following intercourse, in the absence of sAC, human sperm are not likely to survive long after sex.

Data availability statement

The raw data supporting the conclusion of this article will be made available by the authors, without undue reservation.

Ethics statement

The animal study was reviewed and approved by Weill Cornell Medicine's Institutional Animal Care and Use Committee (IACUC).

Author contributions

Conceptualization: CR, MB, LL, and JB. Methodology: CR and SA. Visualization: CR. Funding acquisition: LL and JB. Supervision: LL and JB. Writing–original draft: CR, LL, and JB.

Funding

This work was supported by Grants from National Institutes of Health (P50 HD100549 to LL and JB) and Male Contraceptive Initiative (MCI) Grants to LL & JB, and CR.

Acknowledgments

We wish to thank Samuel Nidorf for maintaining the mouse colony. Jean-Ju Chung, Pablo Visconti, and the Levin/Buck laboratory for helpful advice.

Conflict of interest

Buck and Levin are co-founders of Sacyl Pharmaceuticals, Inc. Established to develop sAC inhibitors into on-demand contraceptives.

Publisher's note

Supplementary material

The Supplementary Material for this article can be found online at: https://www.frontiersin.org/articles/10.3389/fcell.2023.1134051/full#supplementary-material

References

Akbari, A., Pipitone, G. B., Anvar, Z., Jaafarinia, M., Ferrari, M., Carrera, P., et al. (2019). ADCY10 frameshift variant leading to severe recessive asthenozoospermia and segregating with absorptive hypercalciuria. *Hum. Reprod.* 34, 1155–1164. doi:10.1093/humrep/dez048

Balbach, M., Ghanem, L., Rossetti, T., Kaur, N., Ritagliati, C., Ferreira, J., et al. (2021). Soluble adenylyl cyclase inhibition prevents human sperm functions essential for fertilization. *Mol. Hum. Reprod.* 27, gaab054–13. doi:10.1093/MOLEHR/GAAB054

Balbach, M., Rossetti, T., Ferreira, J., Ghanem, L., Ritagliati, C., Myers, R. W., et al. (2023). On-demand male contraception via acute inhibition of soluble adenylyl cyclase. *Nat. Commun.* 14, 637. doi:10.1038/S41467-023-36119-6

Chen, Y., Cann, M. J., Litvin, T. N., Iourgenko, V., Sinclair, M. L., Levin, L. R., et al. (2000). Soluble adenylyl cyclase as an evolutionarily conserved bicarbonate sensor. *Science* 289, 625–628. doi:10.1126/science.289.5479.625

Chung, J. J., Shim, S. H., Everley, R. A., Gygi, S. P., Zhuang, X., and Clapham, D. E. (2014). Structurally distinct Ca2+ signaling domains of sperm flagella orchestrate tyrosine phosphorylation and motility. *Cell* 157, 808–822. doi:10.1016/j.cell.2014.02.056

Danshina, P. V., Geyer, C. B., Dai, Q., Goulding, E. H., Willis, W. D., Kitto, G. B., et al. (2010). Phosphoglycerate kinase 2 (PGK2) is essential for sperm function and male fertility in mice. *Biol. Reprod.* 82, 136–145. doi:10.1095/BIOLREPROD.109.079699

Dcunha, R., Hussein, R. S., Ananda, H., Kumari, S., Adiga, S. K., Kannan, N., et al. (2022). Current insights and latest updates in sperm motility and associated applications in assisted reproduction. *Reprod. Sci.* 29, 7–25. doi:10.1007/S43032-020-00408-Y

Esposito, G., Jaiswal, B. S., Xie, F., Krajnc-Franken, M. A. M., Robben, T. J. A. A., Strik, A. M., et al. (2004). Mice deficient for soluble adenylyl cyclase are infertile because of a severe sperm-motility defect. *Proc. Natl. Acad. Sci. U. S. A.* 101, 2993–2998. doi:10.1073/pnas.0400050101

Ferreira, J. J., Lybaert, P., Puga-Molina, L. C., and Santi, C. M. (2021). Conserved mechanism of bicarbonate-induced sensitization of CatSper channels in human and mouse sperm. *Front. Cell Dev. Biol.* 9, 733653. doi:10.3389/FCELL.2021.733653

Fujihara, Y., Tokuhiro, K., Muro, Y., Kondoh, G., Araki, Y., Ikawa, M., et al. (2013). Expression of TEX101, regulated by ACE, is essential for the production of fertile mouse spermatozoa. *Proc. Natl. Acad. Sci. U. S. A.* 110, 8111–8116. doi:10.1073/PNAS.1222166110

Gaddum-Rosse, P. (1981). Some observations on sperm transport through the uterotubal junction of the rat. *Am. J. Anat.* 160, 333–341. doi:10.1002/AJA.1001600309

Hasuwa, H., Muro, Y., Ikawa, M., Kato, N., Tsujimoto, Y., and Okabe, M. (2010). Transgenic mouse sperm that have green acrosome and red mitochondria allow visualization of sperm and their acrosome reaction *in vivo*. *Exp. Anim.* 59, 105–107. doi:10.1538/expanim.59.105

Hess, K. C., Jones, B. H., Marquez, B., Chen, Y., Ord, T. S., Kamenetsky, M., et al. (2005). The "soluble" adenylyl cyclase in sperm mediates multiple signaling events required for fertilization. *Dev. Cell* 9, 249–259. doi:10.1016/j.devcel.2005.06.007

Ishikawa, Y., Usui, T., Yamashita, M., Kanemori, Y., and Baba, T. (2016). Surfing and swimming of ejaculated sperm in the mouse oviduct. *Biol. Reprod.* 94, 89. doi:10.1095/BIOLREPROD.115.135418

Kleinboelting, S., Diaz, A., Moniot, S., Van Den Heuvel, J., Weyand, M., Levin, L. R., et al. (2014). Crystal structures of human soluble adenylyl cyclase reveal mechanisms of catalysis and of its activation through bicarbonate. *Proc. Natl. Acad. Sci. U. S. A.* 111, 3727–3732. doi:10.1073/PNAS.1322778111

Kunz, G., Beil, D., Deininger, H., Wildt, L., and Leyendecker, G. (1996). The dynamics of rapid sperm transport through the female genital tract: Evidence from vaginal sonography of uterine peristalsis and hysterosalpingoscintigraphy. *Hum. Reprod.* 11, 627–632. doi:10.1093/HUMREP/11.3.627

Levine, N., and Kelly, H. (1978). Measurement of pH in the rat epididymis *in vivo*. *J. Reprod. Fertil.* 52, 333–335. doi:10.1530/JRF.0.0520333

Lyons, E. A., Taylor, P. J., Zheng, X. H., Ballard, G., Levi, C. S., and Kredentser, J. V. (1991). Characterization of subendometrial myometrial contractions throughout the menstrual cycle in normal fertile women. *Fertil. Steril.* 55, 771–774. doi:10.1016/S0015-0282(16)54246-0

Mahé, C., Zlotkowska, A. M., Reynaud, K., Tsikis, G., Mermillod, P., Druart, X., et al. (2021). Sperm migration, selection, survival, and fertilizing ability in the mammalian oviduct †. *Biol. Reprod.* 105, 317–331. doi:10.1093/biolre/ioab105

Marquez, B., and Suarez, S. S. (2008). Soluble adenylyl cyclase is required for activation of sperm but does not have a direct effect on hyperactivation. *Reprod. Fertil. Dev.* 20, 247–252. doi:10.1071/RD07146

Miki, K., Qu, W., Goulding, E. H., Willis, W. D., Bunch, D. O., Strader, L. F., et al. (2004). Glyceraldehyde 3-phosphate dehydrogenase-S, a sperm-specific glycolytic

enzyme, is required for sperm motility and male fertility. *Proc. Natl. Acad. Sci. U. S. A.* 101, 16501–16506. doi:10.1073/PNAS.0407708101

Muro, Y., Hasuwa, H., Isotani, A., Miyata, H., Yamagata, K., Ikawa, M., et al. (2016). Behavior of mouse spermatozoa in the female reproductive tract from soon after mating to the beginning of fertilization. *Biol. Reprod.* 94, 80–81. doi:10.1095/biolreprod.115.135368

Odet, F., Duan, C., Willis, W. D., Goulding, E. H., Kung, A., Eddy, E. M., et al. (2008). Expression of the gene for mouse lactate dehydrogenase C (Ldhc) is required for male fertility. *Biol. Reprod.* 79, 26–34. doi:10.1095/BIOLREPROD.108.068353

Okabe, M. (2015). Mechanisms of fertilization elucidated by gene-manipulated animals. *Asian J. Androl.* 17, 646–652. doi:10.4103/1008-682X.153299

Ramos-Espiritu, L., Kleinboelting, S., Navarrete, F. A., Alvau, A., Visconti, P. E., Valsecchi, F., et al. (2016). Discovery of LRE1 as a specific and allosteric inhibitor of soluble adenylyl cyclase. *Nat. Chem. Biol.* 12, 838–844. doi:10.1038/nchembio.2151

Suarez, S. S., and Pacey, A. A. (2006). Sperm transport in the female reproductive tract. *Hum. Reprod. Update* 12, 23–37. doi:10.1093/HUMUPD/DMI047

Visconti, P. E., Bailey, J. L., Moore, G. D., Pan, D., Olds-clarke, P., and Kopf, G. S. (1995). Capacitation of mouse spermatozoa I. Correlation between the capacitation state and protein tyrosine phosphorylation. *Development* 121, 1129–1137. doi:10.1242/dev.121.4.1129

Visconti, P. E., Krapf, D., de la Vega-Beltrán, J. L., Acevedo, J. J., and Darszon, A. (2011). Ion channels, phosphorylation and mammalian sperm capacitation. *Asian J. Androl.* 13, 395–405. doi:10.1038/aja.2010.69

Visconti, P. E., Stewart-Savage, J., Blasco, A., Battaglia, L., Miranda, P., Kopf, G. S., et al. (1999). Roles of bicarbonate, cAMP, and protein tyrosine phosphorylation on capacitation and the spontaneous acrosome reaction of hamster sperm. *Biol. Reprod.* 61, 76–84. doi:10.1095/biolreprod61.1.76

Xie, F., Garcia, M. A., Carlson, A. E., Schuh, S. M., Babcock, D. F., Jaiswal, B. S., et al. (2006). Soluble adenylyl cyclase (sAC) is indispensable for sperm function and fertilization. *Dev. Biol.* 296, 353–362. doi:10.1016/j.ydbio.2006.05.038

Yamaguchi, R., Muro, Y., Isotani, A., Tokuhiro, K., Takumi, K., Adham, I., et al. (2009). Disruption of ADAM3 impairs the migration of sperm into oviduct in mouse. *Biol. Reprod.* 81, 142–146. doi:10.1095/BIOLREPROD.108.074021

frontiers | Frontiers in Cell and Developmental Biology

TYPE Original Research
PUBLISHED 05 May 2023
DOI 10.3389/fcell.2023.1156060

OPEN ACCESS

EDITED BY
Rafael A. Fissore,
University of Massachusetts Amherst,
United States

REVIEWED BY
Alan D. Ealy,
Virginia Tech, United States
Kasey Lane DeAtley,
California State University, Chico,
United States

*CORRESPONDENCE
Sarah E. Moorey,
smoorey5@utk.edu

†These authors share first authorship

RECEIVED 01 February 2023
ACCEPTED 11 April 2023
PUBLISHED 05 May 2023

CITATION
Hessock EA, Edwards JL, Schrick FN, Payton RR, Campagna SR, Pollock AB, Clark HM, Stokes AE, Klabnik JL, Hill KS, Roberts SR, Hinson MG and Moorey SE (2023), Metabolite abundance in bovine preovulatory follicular fluid is influenced by follicle developmental progression post estrous onset in cattle.
Front. Cell Dev. Biol. 11:1156060.
doi: 10.3389/fcell.2023.1156060

Metabolite abundance in bovine preovulatory follicular fluid is influenced by follicle developmental progression post estrous onset in cattle

Emma A. Hessock[1†], J. Lannett Edwards[1], F. Neal Schrick[1], Rebecca R. Payton[1], Shawn R. Campagna[2], Abigayle B. Pollock[1], Hannah M. Clark[1], Allyson E. Stokes[1], Jessica L. Klabnik[1], Kennedy S. Hill[1], Samantha R. Roberts[1], Meredith G. Hinson[1] and Sarah E. Moorey[1*†]

[1]Department of Animal Science, University of Tennessee, Knoxville, TN, United States, [2]Department of Chemistry, University of Tennessee, Knoxville, TN, United States

Introduction: Preovulatory follicle response to the luteinizing hormone (LH) surge leads to metabolic, molecular, and functional changes in the oocyte and somatic follicular cells from the onset of estrus to ovulation. Follicular fluid contains metabolites, miRNAs, proteins, and hormones that are byproducts of follicular metabolism and support cellular processes of oocyte, cumulus, and granulosa constituents. Numerous studies have highlighted the importance of follicular fluid composition to support fertility, but critical gaps exist toward understanding dynamic modifications in the follicular fluid metabolome from estrous onset to ovulation. The hypothesis was that abundance of follicular fluid metabolites is dependent on follicle progression post LH surge and variability in follicular fluid metabolome profiles indicate key processes required for preparation of the follicle and oocyte for optimal fertility. The objective was to generate preovulatory follicular fluid metabolome profiles and discern differences in the metabolome of preovulatory follicular fluid samples collected at onset of estrus, 11 h post estrous onset, and 18 h post estrous onset.

Methods: Estrus was synchronized in non-lactating Jersey cows (n=40) and follicular fluid was collected immediately after the first observed standing mount (hr 0) or at approximately h 11 or 18 after the first standing mount. Ultra-High-Performance Liquid Chromatography-High Resolution Mass Spectrometry was performed on preovulatory follicular fluid samples (n = 9 collected at hr 0, 9 at h 11, and 10 at h 18) and a multiple linear model was performed to determine if time post estrous onset impacted metabolite abundance.

Results: Metabolites influenced by time post estrous onset were tested for enrichment in KEGG pathways. Ninety metabolites were identified in follicular fluid samples. Twenty metabolites differed in abundance among timepoints post estrous onset ($p \leq 0.05$). Pathways corresponding to amino acid and energy metabolism were enriched with metabolites impacted by time post estrous onset (FDR ≤ 0.10).

Discussion: Results from the current study indicate early response to the LH surge to increase bioavailability of amino acids and metabolites used by the cumulus and granulosa cells for energy production and shuttled into the oocyte to support meiotic maturation. Such metabolites may later be used by the ovulatory follicle for protein production.

KEYWORDS

preovulatory follicle, follicular fluid, metabolome, cow, estrus, ovulation

1 Introduction

Optimal fertility in cattle, humans, and other mammalian species relies on dynamic transformations in the oocyte, preovulatory follicle's somatic cells, and follicular fluid milieu during the days leading up to estrus and the hours between estrus and ovulation. In bovine, estrous onset is a key developmental milestone in the follicle's progression toward ovulation. This is because the preovulatory gonadotropin surge closely follows onset of estrus (Dieleman et al., 1986; Rajamahendran et al., 1989; Stevenson et al., 1998; Mondal et al., 2006) and signals the cascade of events within the follicle that commence in the ovulation of a mature oocyte from a follicle, that is, transitioning into a functional corpus luteum (Richards et al., 1998; Duffy et al., 2018; Robker et al., 2018). Specifically, the luteinizing hormone (LH) surge serves as the stimulant for the onset of oocyte maturation, follicle cell luteinization, increased follicular vascularity, and breakdown of the follicle wall that leads to ovulation (Richards et al., 1998; Duffy et al., 2018; Robker et al., 2018). In cattle that displayed estrus, the first elevation of circulating LH concentrations that was followed by higher LH values was observed to occur approximately 2 h after the onset of estrus, and the LH surge peak was reported at approximately 4.5 h after the onset of estrus (Dieleman et al., 1983).

Progression of the follicle and oocyte toward ovulation can be roughly divided into intrafollicular events occurring pre-LH surge exposure, in early response to the LH surge, and in later response to the LH surge as ovulation nears. Before the LH surge, follicular granulosa cells remain in a proliferative phase. The oocyte and surrounding cumulus cells are intimately connected to each other via paracrine signaling and direct transfer of metabolites, RNAs, and signaling molecules such as cyclic AMP (cAMP) and cyclic GMP through gap junctional complexes that span the zona pellucida (Eppig, 1985; Gilchrist et al., 2004; Macaulay et al., 2014). Rising LH levels associated with the preovulatory gonadotropin surge act through binding of receptors on the granulosa cells to initiate ovulatory events. Granulosa cells cease dividing and undergo differentiation in preparation for future secretory roles in the corpus luteum, their metabolism and the synthesis of amino acids increases, and granulosa mediated pathways signal for follicular angiogenesis and inflammation. Cumulus cell expansion, breakdown of gap junctional transfer from the cumulus cells to the oocyte, and a drop in cAMP in the oocyte that leads to onset of oocyte nuclear maturation also result from granulosa cells mediated response to the LH surge (Eppig, 1985; Granot and Dekel, 2002; Norris et al., 2009). The dramatic follicular response to the LH surge ranges from changes in gene expression that take place almost immediately to biological processes that occur over multiple hours. Physically identifiable differences in oocyte maturation have been reported at approximately 9–12 and 18–20 h after the peak LH surge. Disconnection of junctions between the oocyte and cumulus cells, alongside breakdown of the oocyte nucleus, was first reported between 9 and 12 h after the peak LH surge (Callesen et al., 1986; Hyttel et al., 1986). By 15 h after peak LH surge, spatial rearrangements of organelles were observed in the oocyte's cytoplasm (Hyttel et al., 1986), and by 18–20 h after peak LH surge the first polar body was extruded (Callesen et al., 1986; Hyttel et al., 1986). Similarly, granulosa cells exhibit a time dependent response to the LH surge. Leading up to estrus, and the LH surge, follicular estradiol production rises to peak around the onset of estrus (Henricks et al., 1971; Wettemann et al., 1972; Ginther et al., 2013). However, 6 h post estrous onset, intrafollicular hormone concentrations of estradiol and progesterone have abruptly shifted to favor progesterone production. Accumulation of members of the vascular endothelial cell family of growth factors to promote angiogenesis (Duffy et al., 2018) and production of the enzyme prostaglandin synthase two that catalyzes conversion of membrane lipids to prostaglandin H2 (Richards, 1997) also occur quickly after the LH surge.

The currently known post-LH surge intrafollicular changes in steroid hormone profiles, somatic molecular blueprint, cumulus-oocyte association, and oocyte maturation likely lead to or are accompanied by further transient modifications in the follicular fluid to further promote optimal fertility. In recent years, much progress has been made toward understanding the follicular fluid's composition and role in fertility. This highly complex biofluid contains numerous molecules and components such as enzymes, amino acids, extracellular vesicles, hormones, proteins, and lipids (Revelli et al., 2009; Ambekar et al., 2013). A number of studies have linked abundance of specific proteins, metabolites, and mRNAs to roles in the follicle that support oocyte developmental competence and pregnancy outcome (Leroy et al., 2005; Bender et al., 2010; Hung et al., 2015; Kafi et al., 2017; Bou Nemer et al., 2019; Rispoli et al., 2019; Afedi et al., 2021; Read et al., 2021; Read et al., 2022). Related to cycle specific impacts on the follicular fluid metabolome, composition naturally varies across the estrous cycle in cows (Orsi et al., 2005), but no known studies have examined post LH surge progression on the bovine follicular fluid metabolome.

Given the importance of the follicular fluid metabolic constituents and known transitions in follicular cell function and metabolism during the time from estrus to ovulation, it is essential to further characterize time specific modifications in the follicular fluid metabolome of bovine preovulatory follicles from the time of estrous onset throughout oocyte and follicle maturation. The hypothesis of this study was that abundance of follicular fluid metabolites is

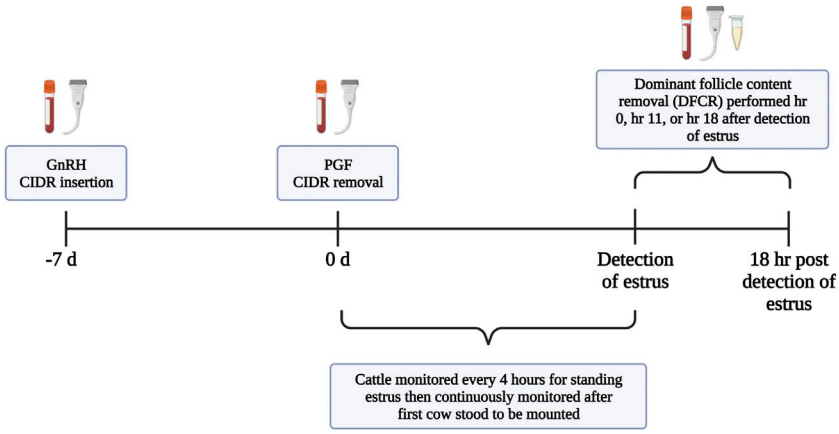

FIGURE 1
Timeline for synchronization of estrus and follicular fluid collection.

dependent on follicle progression post LH surge and that variability in follicular fluid metabolome profiles indicate key processes required for optimal preparation of the follicle and oocyte for optimal fertility post ovulation. Therefore, a study was performed with the objective to generate preovulatory follicular fluid metabolome profiles and discern differences in the metabolome of preovulatory follicular fluid samples collected at onset of estrus, 11 h post estrous onset, and 18 h post estrous onset.

2 Materials and methods

2.1 Experimental design

The primary objective of this study was to determine time specific modifications in the metabolome of preovulatory follicular fluid collected from cattle at the onset of estrus to approximately 18 h after estrous onset. Estrus was synchronized in 40 non-lactating Jersey cows (mean age = 5.21 years; mean lactations = 1.61) and the preovulatory follicle's fluid was collected either immediately after the first observed standing mount (hr 0) or at approximately hr 11 or 18 after the first observed standing mount. Ultra-High-Performance Liquid Chromatography - High Resolution Mass Spectrometry (UHPLC-HRMS) was performed on preovulatory follicular fluid samples that were successfully collected at either hr 0, hr 11, or hr 18 after an animal first displayed standing estrus. Metabolites were identified and quantified using Metabolomic Analysis and Visualization Engine (MAVEN). Prior to statistical analyses, samples were filtered based on follicular fluid estradiol to progesterone ratio to ensure that follicles were non-atretic and of hormone profiles expected for their assigned stage post estrous onset. Statistical analyses were performed on 8 samples collected at hr 0, 6 samples collected at hr 11, and 6 samples collected at hr 18. Sparse Partial Least Squares Discriminant Analysis (sPLS-DA) was performed to allow visual clustering of samples based on time post estrous onset. A step down multiple linear model, followed by analysis of variance (ANOVA; type III sum of squares) was performed on all metabolites to determine if time post estrous onset impacted the abundance each follicular fluid metabolite. Tukey's Honest Significant Difference *post hoc* test (Tukey's HSD) was conducted to determine pairwise differences between hr 0 vs. hr 11, hr 0 vs. hr 18, and hr 11 vs. hr 18 follicular fluid metabolites. Metabolites influenced by time post estrous onset were then tested for enrichment in Kyoto Encyclopedia of Genes and Genomes (KEGG) pathways.

2.2 Synchronization of estrus and follicular development

All protocols and procedures were approved by the Institutional Animal Care and Use Committee at the University of Tennessee. Non-lactating Jersey cows (n = 40; mean age = 5.21 years; mean lactations = 1.61) which were maintained as a grazing herd at one of the University of Tennessee AgResearch and Education Centers underwent pre-synchronization, synchronization of estrus, and dominant follicle content removal (DFCR; Figure 1). Throughout the study's duration cattle were provided with *ad libitum* access to fescue-based pasture, hay, and water. Cows were maintained in multiple, interconnected large pens where the gates remained open to allow for free movement of the animals. Cows were moved to an adjacent working area to perform all procedures and upon completion were returned back to the pens where they remained until completion of the study. Pre-synchronization was performed by administration of gonadotropin releasing hormone (GnRH; Cystorelin®; 100 ug; i.m.; Boehringer Ingelheim; Ingelheim am Rhein, Germany) and insertion of a controlled internal drug release (CIDR intervaginal insert; 1.38 g progesterone; Eazi-Breed™ CIDR®; Zoetis Animal Health, Kalamazoo, MI, United States). Nine days later, the CIDR was removed and Prostaglandin F2α (PGF; 12.5 mg of dinoprost tromethamine/mL Lutalyse® HighCon; Zoetis Animal Health, Kalamazoo, MI, United States) was administered. Forty-8 hr after PGF administration and CIDR removal, when animals were expected to be in the follicular phase of the estrous cycle, cows were

administered GnRH and a CIDR was inserted (d-7). Seven days later (d0) the CIDR was removed, PGF was administered, and an Estrotect™ patch (Estrotect; Rockway Inc.; spring Valley, WI, United States) was adhered to the tailhead. Cows were visually monitored for estrus every 4 h in a pen containing pasture and dry dirt areas until estrous activity began, then monitoring occurred continuously. All personnel were trained in visual observation of estrus based on standing heat. Patches were used to assist with visual detection of estrus but were not the sole or main method to detect estrus. Patches were scored using a 1–4 scale (score 1 = <25% rubbed off, score 2 = 25%–50% rubbed off, score 3 = 50%–75% rubbed off, score 4 = >75% rubbed off). Secondary signs of estrus (mounting, riding other cows, and chin resting on the tailhead) were also recorded, and onset of estrus was defined as the time of first recorded instance of an animal visually standing to be mounted. Cattle underwent DFCR via transvaginal ultrasound guided aspiration either within 2 h 55 min of first observed standing mount (hr 0; 1 h 47 ±15 min; 11 min–2h 55 min) or between 10 h 18 min–12 h 50 min (hr 11; 11 h 29 min ±16 min) or 17 h 49 min–18 h 44 min (hr 18; 18 h 14 min ±5 min) after first observed standing mount.

2.3 Blood collection, ovarian mapping, cow weight, and body condition

Blood was collected and ovarian status recorded at the time of GnRH administration and CIDR insertion on d −7, CIDR removal and PGF administration on d 0, onset of estrus, and when DFCR occurred. Blood was collected via venipuncture in the coccygeal vein of the tail, and approximately 10 mL of blood was collected into BD Vacutainer® serum collection tubes using BD Vacutainer® single-sample 18-gauge 1-inch needles attached to a collar (BD, Franklin Lakes, NJ, United States). Blood samples remained at room temperature for 1 h to allow for clotting to occur. Samples were then stored at 4°C for 24 h before undergoing centrifugation at 1,200 x g for 25 min at 4°C. Serum was collected and stored in borosilicate glass tubes at −20°C for hormone analysis. Transrectal ultrasonography was performed using an IBEX EVO® II ultrasound and the eL7 linear probe (E.I Medical Imaging, Loveland, CO, United States). For both ovaries, follicles >7 mm were measured in millimeters using the average of the largest diameter of the follicle and the diameter perpendicular to the largest diameter. Other notable structures such as small cohorts of follicles and all corpora lutea were recorded. Animal weight (kg) and body condition score were assessed at the onset of synchronization, and records for age at DFCR were acquired. Body condition score was measured using the dairy body condition score scale of 1–5 where a score of 1 indicates severe under condition and 5 indicates severe over condition; (Wildman et al., 1982).

2.4 Dominant follicle content removal via transvaginal aspiration

After estrus was detected, cattle underwent DFCR at hr 0, hr 11, or hr 18 via transvaginal aspiration which was performed by a trained technician (Read et al., 2021; Horn et al., 2022; Read et al., 2022). Cows were administered a spinal block using 5 mL of 2% lidocaine in the first intercoccygeal space of the tailhead prior to transvaginal aspiration. The perineal and vulvar area was thoroughly cleaned to remove potential contaminants from entering the vagina. An ultrasound guided transvaginal aspiration apparatus encompassing a CFA-9 convex ultrasound probe connected to a Samsung HM70A ultrasound, 18-gauge spinal needle, and plastic tubing for follicular fluid collection was inserted into the anterior vagina. Using the ultrasound for visualization, the ovary was manipulated until the follicle of interest was in the best position for aspiration. The needle was advanced through the vaginal wall and ovarian cortex until the tip was inserted in the follicular antrum. Follicular fluid was aspirated into a 5 mL syringe until the follicle was visualized to have fully collapsed. The transvaginal aspiration device was cleaned with chlorhexidine and rinsed with water, and all tubing was completely flushed with sterile water between each cow.

2.5 Processing of follicular fluid

After aspiration, follicular fluid in the 5 mL syringe was distributed into one well of a 4 well Petri dish. A trained technician searched the dish under a microscope for the cumulus oocyte complex, which if found was removed and collected for future use in a different study. The follicular fluid was collected from the 4 well Petri dish and distributed into 1.7 mL Eppendorf tubes which were centrifuged at 500 x g for 5 min at 4°C to pellet potential cellular debris within the sample. Supernatant was aliquoted into multiple tubes, snap frozen in liquid nitrogen, and stored at −80°C for future analyses. Specifically, 60 µL of follicular fluid supernatant was placed in a 2 mL microcentrifuge tube for metabolomic analyses, 100 µL was placed in a 2 mL microcentrifuge tube for follicular fluid estradiol and progesterone assays, and remaining follicular fluid was divided amongst 2 mL polypropylene cryovials (Stellar Scientific, Baltimore, MD, United States) for procedures outside the scope of this study.

2.6 Profiling of the follicular fluid metabolome

Ultra-High-Performance Liquid Chromatography—High Resolution Mass Spectrometry (UHPLC-HRMS) was performed on follicular fluid samples at the Biological and Small Molecule Mass Spectrometry Core (RRID: SCR_021368) at the University of Tennessee, Knoxville. Sixty µL aliquots of follicular fluid samples (n = 29) were thawed at room temperature, and metabolites within each sample were extracted using a 40:40:20 methanol/acetonitrile/water solution with 0.1 M formic acid following a previously reported procedure (Rabinowitz and Kimball, 2007; Lu et al., 2010). An extraction solvent was added to the samples which underwent agitation and vortexing before samples were then chilled at −20°C for 20 min. Once samples were properly chilled, the tubes were centrifuged to form pellets and remove debris from the sample. A second set of 2 mL microcentrifuge tubes were used to collect the supernatant from the first set of tubes. The extraction solvent was again dispensed into the first set of tubes, which contained the pellet, and the mixture was pipetted to resuspend the pellet. The tubes were

then re-submitted to agitation and vortexing, chilling, and centrifugation as described above. The supernatant from the tube was added to the second set of tubes which contained the previous supernatant. The first tube set with the final pellet was then discarded. The second set of tubes containing the supernatant underwent drying using nitrogen gas. Once dried, tubes were filled with MilliQ water to resuspend samples and moved to new autosampler vials. Metabolomic samples were separated using columns (Synergi Hydro RP, 2.5 µm, 100 mm × 2.0 mm column; Phenomenex, Torrance, CA, United States) which were maintained at 25°C. Solvents to elute metabolites during the mobile phase were 1) 97: 3 methanol/water with 15 mM acetic acid and 11 mM tributylamine and 2) 100% methanol. At a flow rate of 0.2 µL/min, the solvent gradient was 1) 100% and 2) 0% from 0 to 5 min, 1) 80% and 2) 20% from 5 to 13 min, 1) 45% and 2) 55% from 13 to 15.5 min, 1) 5% and 2) 95% from 15.5 to 19 min, and 1) 100% and 2) 0% from 19 to 25 min. An Exactive Plus Orbitrap mass spectrometer (Thermo Fisher Scientific, Waltham, MA, United States) with an electrospray ionization probe attached was used, operating in negative mode with a scan range between 72 and 1,000 m/z, a resolution of 140,000, and an acquisition gain control of 3×10^6.

2.7 Initial analysis of metabolome data

The mass spectrometry generated Xcalibur (RAW) files were converted to an open source mzML format (msconvert software; ProteoWizard package). The converted files were processed using the Metabolomic Analysis and Visualization Engine (MAVEN; mzroll software, Princeton University) to complete an untargeted analysis of the liquid chromatography mass spectrometry data. MAVEN identifies metabolites using a variety of factors including peak shape, retention time, and signal-to-noise-ratio. The program then generated pre-processed peak data tables which were used for statistical analysis.

2.8 Follicular fluid and serum hormone profile evaluation

Serum and follicular fluid progesterone concentrations were evaluated using the ImmuChem progesterone double antibody radioimmunoassay kit (MP Biomedicals, Costa Mesa, CA, United States) and following manufacturer's specifications. Serum progesterone intra- and inter-assay coefficients of variation (CV) were 8.00% and 4.18%, respectively. Follicular fluid progesterone intra- and inter-assay CVs were 4.42% 5.70%, respectively. Serum estradiol concentration was determined using methods previously validated and described (Kirby et al., 1997). Serum estradiol intra- and inter-assay CVs were 3.55% and 6.70%, respectively. Follicular fluid samples underwent dilution from 1:2500 to 1:50000 before follicular fluid estradiol concentration was quantified using The DetectX® Serum 17β-Estradiol ELISA Kit (Arbor Assays, Ann Arbor, MI, United States) according to manufacturer's specifications. Intra- and inter-assay CVs for follicular fluid estradiol were 1.65% and 7.33%, respectively.

2.9 Statistical analysis

All statistical procedures were performed using R Studio version 4.1.2, (R Team, 2020), or MetaboAnalyst 5.0 (Pang et al., 2021). Data was first processed to remove samples that lacked hormone data on follicular fluid due to inadequate volume ($n = 1$ at h 11 and 2 at h 18) or had follicular fluid estradiol to progesterone (FF E2:P4) ratios indicative of potentially less or more advanced progression post estrous onset (Fortune and Hansel, 1985) compared to their cohort and assigned time ($n = 2$ at h 0, 2 at h 11, and 2 at h 18). Though this procedure reduced sample numbers to 7 samples at hr 0, 6 samples at hr 11, and 6 samples at hr 18, it was essential to enhance confidence in time classification by combining visual estrous observation efforts with confirmation of follicular fluid hormones. Such procedures removed samples with FF E2:P4 ratios that overlapped with other timepoints and that may have originated from animals first detected in estrous hours before or after first actual mount and who would have been at variable progression relative to estrous onset compared to other animals within their treatment cohort. Samples removed from hr 0 based on FF E2: P4 ratio had ratios of 7.22 and 9.03, compared to hr 0 cohorts with ratios of 17.1–65.07. Samples removed from hr 11 based on ratio had FF E2:P4 ratios of 3.12 and 14.27, compared to hr 11 cohorts with ratios from 4.47 to 9.35. Samples removed from hr 18 based on FF E2:P4 ratio had ratios of 0.2 and 15.9, compared to hr 18 cohorts that ranged from 2.51 to 3.77.

Mean age, body condition score, serum estradiol concentration at follicle collection, and serum progesterone concentration at follicle collection were calculated, and differences among timepoints post estrous onset were determined using ANOVA. The effect of timepoint was considered significant if $p \leq 0.05$. Post hoc comparisons between hr 0 vs. hr 11, hr 0 vs. hr 18, and hr 11 vs. hr 18-time groups were performed using the "emeans" function in R, which utilized Tukey's HSD and provided least squares means for trait analyzed at each time point. Differences between phenotypic timepoint comparisons were considered significant if Tukey's HSD $p \leq 0.05$.

Peak area data for samples selected for statistical analyses was then input into MetaboAnalyst 5.0, filtered for relative standard deviation, and log transformed before performing sPLS-DA and plotting samples based on 2 components and 10 variables per component (Lê Cao et al., 2011). Ninety-five percent confidence intervals were then calculated and drawn around clustered samples from each timepoint.

Using R Studio, data were tested for normality using Shapiro Wilke test, and metabolites that failed normality assumption were log transformed. Due to detection of outliers for metabolite abundance within treatment (hr 0, hr 11, hr 18) that hindered achieving normality and influenced statistical results, samples with outlier metabolite abundance compared to their time group were removed for analyses of the specific metabolite in which the outlier was identified. Initial linear models were performed to detect potential relationships between abundance of each metabolite and independent variables of cow age, weight, body condition score (BCS), serum and follicular fluid steroid hormone concentrations, and follicle diameter. We then designed a multiple linear model for each metabolite with metabolite abundance as the dependent variable and time group (hr 1, hr 11, hr 18) alongside the above variables with $p < 0.10$ as independent variables. Covariates were

10.3389/fcell.2023.1156060

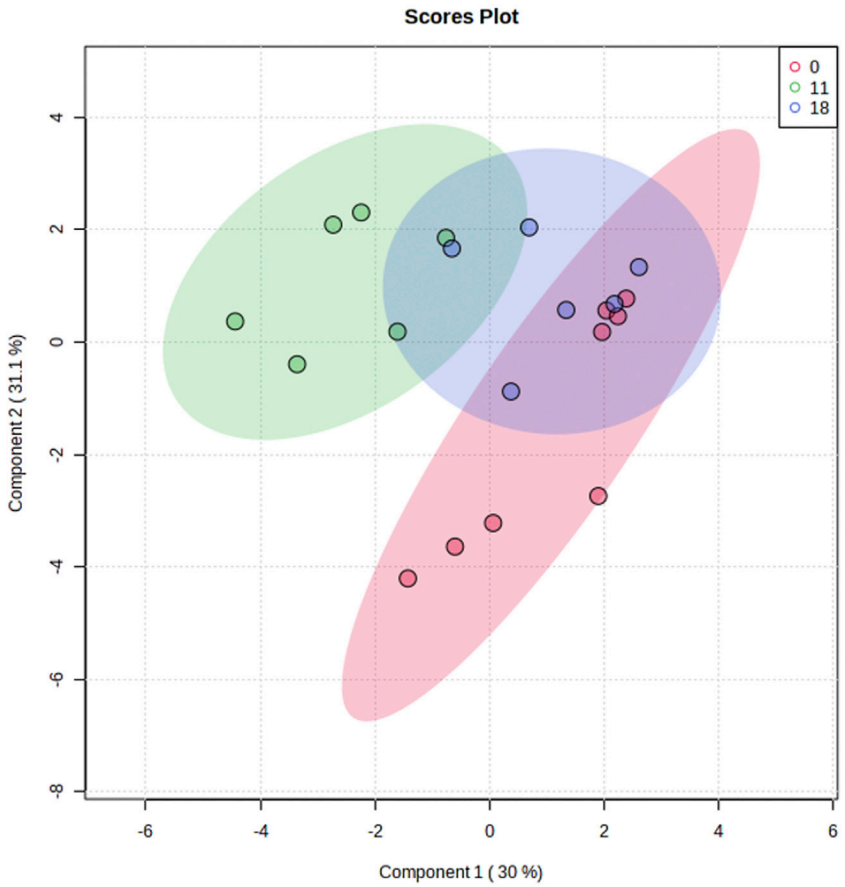

FIGURE 2
Sparse Partial Least Squares Discriminant Analysis of follicular fluid metabolome profiles from preovulatory follicular fluid samples collected at onset of estrus (hr 0), hr 11 after estrous onset, or hr 18 after estrous onset. Shaded ellipses indicate 95% confidence area around each timepoint cluster.

removed from the model in a stepwise fashion with the least significant variable removed each time until only covariates where $p \leq 0.05$ remained in the final model alongside the variable of interest (time group). If time group was significant ($p \leq 0.05$) based on the ANOVA function utilizing Type III Sum of Squares, *post hoc* comparisons between hr 0 vs. hr 11, hr 0 vs. hr 18, and hr 11 vs. hr 18-time groups were performed using the "emeans" function in R, which utilized Tukey's HSD and provided least squares means for metabolite abundance at each time point. Differences between timepoint comparisons were considered significant or trending if Tukey's HSD $p \leq 0.05$ or $0.05 \leq p \leq 0.10$, respectively.

Three KEGG pathway enrichment analyses of metabolites influenced by time post estrous were performed using MetaboAnalyst 5.0 with the *Bos taurus* reference metabolome. Based on results of metabolite statistical analysis, 3 lists of metabolites influenced by time post estrous onset were interrogated for pathway enrichment analysis: 1) all metabolites that differed among timepoints post estrous onset, 2) metabolites that rose in abundance from hr 0 to hr 11, and 3) metabolites that rose in abundance from hr 0 to hr 11 and then decreased in abundance from hr 11 to hr 18. Pathways were reported if false discovery rate (FDR) ≤ 0.10.

A secondary analysis was performed that classified samples into categories based on FF E2:P4 ratio. Samples with FF E2:P4 ratio >10 were classified into a cohort based on FF E2:P4 expected at onset of estrus. Samples with FF E2:P4 ratio >4 and <10 were classified into a second cohort based on FF E2:P4 expected approximately 11 h post onset of estrus, and samples with FF E2:P4 ratio <4 were categorized into a third cohort based on FF E2:P4 expected approximately 18 h post onset of estrus. Statistical analyses were performed as described above to determine relationships between FF E2:P4 category and metabolome profiles. Metabolites that differed among FF E2:P4 classifications were utilized to perform 3 KEGG pathway enrichment analyses, as described above, utilizing lists of all differentially abundance metabolites, metabolites that rose from FF E2:P4 classification indicative of estrous onset to FF E2:P4 classification indicative of hr 11 post estrous onset, and metabolites that rose from FF E2:P4 classification indicative of estrous onset to FF E2:P4 classification indicative of hr 11 post estrous onset and then decreased in abundance from FF E2:P4 classification indicative of hr 11 post estrous onset to FF E2:P4 classification indicative of hr 18 post estrous onset.

3 Results

3.1 Description of cow phenotypes, hormone profiles, and preovulatory follicular fluid metabolome profiles at 0, 11, and 18 h post onset of estrus

Mean age and BCS of cows classified and included in analyses as hr 0, 11, or 18 post estrous onset was 2012 ± 19 days and 3.11 ± 0.07, respectively. Mean serum progesterone concentration at the time of dominant follicle content removal was 0.10 ± 0.02 ng/mL. Neither age (p = 0.96), BCS (p = 0.49), or serum progesterone at follicle content removal (p = 0.28) differed among collection timepoints. Mean serum estradiol concentration at the timepoint of dominant follicle content removal was 6.62 ± 0.02 pg/mL. Serum estradiol concentration differed among collection timepoints (p = 0.037), such that samples collected at hr 18 had lower serum estradiol concentration than samples collected at hr 0.

Ninety metabolites were identified in preovulatory follicular fluid samples collected at onset of estrous and hr 11 and 18 following estrous onset. Metabolites consisted primarily of amino acids, byproducts of glucose metabolism and the tricarboxylic acid (TCA) cycle, and varied other small molecules such as myo-Inositol, Cholate, and the nucleosides Uridine and Deoxyuridine. Plotting of samples utilizing sPLS-DA revealed independent clustering of samples collected at the onset of estrous from those collected 11 h post estrous onset (Figure 2). Samples collected at 18 h post estrous onset clustered such that their 95% confidence interval intersected confidence intervals surrounding both hr 0 and 11 samples. While most hr 11 and 18 samples clustered tightly, hr 0 samples dispersed along the y-axis (Component 2) to form two subclusters. Further interrogation of hr 0 samples belonging to each subcluster did not reveal visually identifiable differences in cow phenotype, follicle dynamics, or hormone profiles between the two subgroups.

3.2 Preovulatory follicular fluid metabolites influenced by time post estrous onset

Of the 90 metabolites identified in preovulatory follicular fluid, 20 differed in abundance based on time post onset of estrus (Table 1). The most profound finding was that 17 of these 20 metabolites rose in abundance from hr 0 to hr 11 after first instance of standing estrus (myo-Inositol, Lactate, Pyruvate, N-acetyl-D-glucosamine 6-phosphate, Alpha-Ketoglutarate, Cholate, Glycerol-3-phosphate, Hydroxyphenylacetate, Deoxyuridine, Orotate, Xylitol, Aconitate, 3-Hydroxyisovalerate, Kynurenine, Cysteine, Phosphorylethanolamine, Glutamate; Figure 3).

Aside from Deoxyuridine and Glycerol-3-phosphate which tended to remain elevated at hr 18 compared to hr 0, all other metabolites that initially rose were no longer different in abundance between hr 0 and 18 post estrous onset. Ten metabolites declined or tended to decline in abundance from hr 11 to 18 (myo-Inositol, Lactate, Pyruvate, N-acetyl-D-glucosamine 6-phosphate, Alpha-Ketoglutarate, Cholate, Orotate, Xylitol, Aconitate, Kynurenine; Figure 3A). The 5 remaining metabolites that rose from hr 0 to hr 11 remained at a level such that no differences were observed between hr 18 and either hr 0 or hr 11 follicular fluid (Hydroxyphenylacetate, 3-Hydroxyisovalerate, Cysteine, Phosphorylethanolamine, Glutamate; Figure 3B).

Few metabolites influenced by time post estrous onset followed a different trend in abundance. Aspartate was elevated at hr 18 compared to onset of estrus (Figure 4A). Though, a consistent rise in Aspartate was observed there were no statistical differences between hr 0 and 11 or hr 11 and 18 follicular fluid Aspartate level. Lysine decreased in abundance between hr 0 and 11 post first standing mount, but quantity of follicular fluid Lysine was no different between hr 18 and hr 0 or 11 (Figure 4B). Two, 3-Dihydroxybenzoate dropped in abundance from hr 11 to hr 18, but did not differ between hr 0 and either 11 or 18 (Figure 4C).

3.3 Pathway enrichment analysis of preovulatory follicular fluid metabolites influenced by time post estrous onset

Pathway analyses of all follicular fluid metabolites influenced by time post estrous onset revealed enrichment of 6 KEGG pathways, including "Alanine, Aspartate, and Glutamate Metabolism", "Arginine Biosynthesis", "D-Glutamine and D-Glutamate Metabolism", "Citrate Cycle (TCA Cycle)", "Aminoacyl-tRNA Synthesis", and "Glyoxylate and Dicarboxylate Metabolism" (Table 2). Pathway analyses of only metabolites that rose in abundance from hr 0 to hr 11 or that rose in abundance from hr 0 to 11 and then decreased in abundance from hr 11 to 18 demonstrated similar enriched pathways including "Citrate Cycle (TCA Cycle)", "D-Glutamine and D-Glutamate Metabolism", "Alanine, Aspartate, and Glutamate Metabolism", and "Glyoxylate and Dicarboxylate Metabolism" (Table 2). "Arginine Biosynthesis" and "Butanoate Metabolism" pathways were also enriched with metabolites that had increased abundance from hr 0 to 11 followed by decreased abundance from hr 11 to 18 (Table 2). Though multiple metabolic pathways were enriched with metabolites whose abundance varied across timepoint, relatively few metabolites contributed to observed enrichment. Pyruvate, Alpha-Ketoglutarate, Aspartate, Glutamate, Cysteine, Aconitate, and Lysine were the metabolites influenced by time post estrous onset that appeared in KEGG pathways identified by enrichment analysis.

3.4 Preovulatory follicular fluid metabolites influenced by FF E2:P4 ratio classification

Eighteen preovulatory follicular fluid metabolites differed in abundance based on follicular fluid E2:P4 ratio classification (Table 3). Fourteen of these metabolites also differed in abundance among collection timepoints post estrous onset (myo-Inositol, Lactate, Pyruvate, N-acetyl-D-glucosamine 6-phosphate, Alpha-Ketoglutarate, Cholate, Glycerol-3-phosphate, Hydroxyphenylacetate, Aspartate, 2,3 Dihydroxybenzoate, Aconitate, Kynurenine, Orotate, and Phosphorylethanolamine; Table 1; Table 3). Similar to the results from analysis of metabolites based on time post estrous onset, a

TABLE 1 Preovulatory follicular fluid metabolites that varied in abundance among collection times post estrous onset.

Metabolite	†Least squares means			
	0	11	18	*P
myo-Inositol	123,311 ± 27,711^{a}	692,126 ± 33,253^{b}	112,739 ± 41,567^{a}	<0.001
Lactate	27,092,488 ± 1,705,098^{a}	68,150,779 ± 2,046,118^{b}	29,618,133 ± 2,046,118^{a}	<0.001
Pyruvate	4,494,127 ± 210,682^{a}	7,303,056 ± 245,795^{b}	4,123,317 ± 245,795^{a}	0.003
N-acetyl-D-glucosamine 6-phosphate	1.7 ± 264^{a}	2,183 ± 264^{b}	82 ± 329^{a}	0.003
Alpha-Ketoglutarate	39,869 ± 4,353^{a}	98,500 ± 5,079^{b}	31,092 ± 5,079^{a}	0.003
Cholate	24,199 ± 5,584^{a}	63,485 ± 3,722^{b}	19,617 ± 4,467^{a}	0.0030
Lysine	43,270 ± 2,618^{a}	11,162 ± 3,055^{b}	22,285 ± 3,055^{ab}	0.005
Glycerol-3-phosphate	1,099 ± 1,399^{a}	13,002 ± 1,166^{b}	4,860 ± 1,166^{Ab}	0.006
Hydroxyphenylacetate	91,242 ± 8,226^{a}	167,493 ± 5,965^{b}	117,551 ± 5,431^{ab}	0.013
Deoxyuridine	324 ± 167^{a}	1,536 ± 151^{b}	549 ± 138^{Ab}	0.013
Aspartate	76,716 ± 4,158^{a}	107,629 ± 4,511^{ab}	123,471 ± 4,103^{b}	0.020
Xylitol	67,279 ± 1,863^{a}	87,249 ± 2,235^{b}	69,446 ± 2,235^{aB}	0.020
2,3-Dihydroxybenzoate	10,828 ± 914^{ab}	16,255 ± 914^{b}	8,090 ± 914^{a}	0.020
Aconitate	32,802 ± 1,659^{a}	46,684 ± 1,659^{b}	33,734 ± 1,105^{a}	0.023
3-Hydroxyisovalerate	1,548,328 ± 30,540^{a}	1,788,369 ± 20,360^{b}	1,612,064 ± 30,540^{ab}	0.025
Kynurenine	8,059 ± 1,324^{a}	19,025 ± 1,324^{b}	6,593 ± 1,589^{aB}	0.031
Cysteine	166 ± 64^{a}	667 ± 54^{b}	424 ± 64^{ab}	0.034
Orotate	1,402 ± 626^{a}	5,719 ± 522^{b}	818 ± 522^{a}	0.015
Phosphorylethanolamine	6,279 ± 1,495^{a}	20,837 ± 1,869^{b}	17,154 ± 1,869^{ab}	0.036
Glutamate	116,870 ± 16,746^{a}	28,0252 ± 16,746^{b}	197,926 ± 16,746^{ab}	0.041

†Least squares mean ± standard error of the mean for metabolite peak area.
*P value reported for main effect of time classification.
$^{ab}P \leq 0.05$.
$^{aA \text{ or } bB}$ $P \leq 0.10$. Pairwise comparison p values were adjusted using Tukey's Honest Significant Difference post hoc test.

majority of metabolites that differed among FF E2:P4 ratios rose or tended to rise in abundance as FF E2:P4 ratio decreased from values expected near the onset of estrus to values expected nearing 11 h after first standing mount (myo-Inositol, Lactata, Pyruvate, N-acetyl-D-glucosamine 6-phosphate, Alpha-Ketoglutarate, Cholate, Glycerol-3-phosphate, Hydroxyphenylacetate, Aconitate, Kynurenine, Orotate, Phosphorylethanolamine). One distinction between analyses based on time post estrous onset and FF E2:P4 ratio was that myo-Inositol, Lactate, N-acetyl-D-glucosamine 6-phosphate, Cholate, and Kynurenine all dropped in abundance from hr 11 to hr 18 in the analysis based on time, whereas these metabolites did not significantly decrease in abundance between FF E2:P4 classifications indicative of approximately 11 and 18 h post estrous onset (Table 1; Table 3). As with the analysis based on time post estrous onset, Aspartate was elevated in the FF E2:P4 classification expected at hr 18 compared to onset of estrus (Table 3).

3.5 Pathway enrichment analysis of preovulatory follicular fluid metabolites influenced by FF E2:P4 ratio

The KEGG pathway "Citrate Cycle (TCA Cycle)" was enriched in pathway analyses including all metabolites that differed among FF E2:P4 classifications, metabolites that rose from FF E2:P4 classification indicating onset of estrus to FF E2:P4 classification indicating hr 11, and metabolites that rose from FF E2:P4 classifications indicating hrs 0 and 11 but also decreased from FF E2:P4 classifications indicating hrs 11 and 18 (Table 4). The pathway "Alanine, Aspartate, and Glutamate Metabolism" was enriched with metabolites that differed among FF E2:PR ratio classifications and metabolites that rose from FF E2:P4 classifications indicating hrs 0 and 11 but also decreased from FF E2:P4 classifications indicating hrs 11 and 18 (Table 4). Three additional pathways including "Glyoxylate and Dicarboxylate Metabolism", "Cysteine and Methionine Metabolism", and

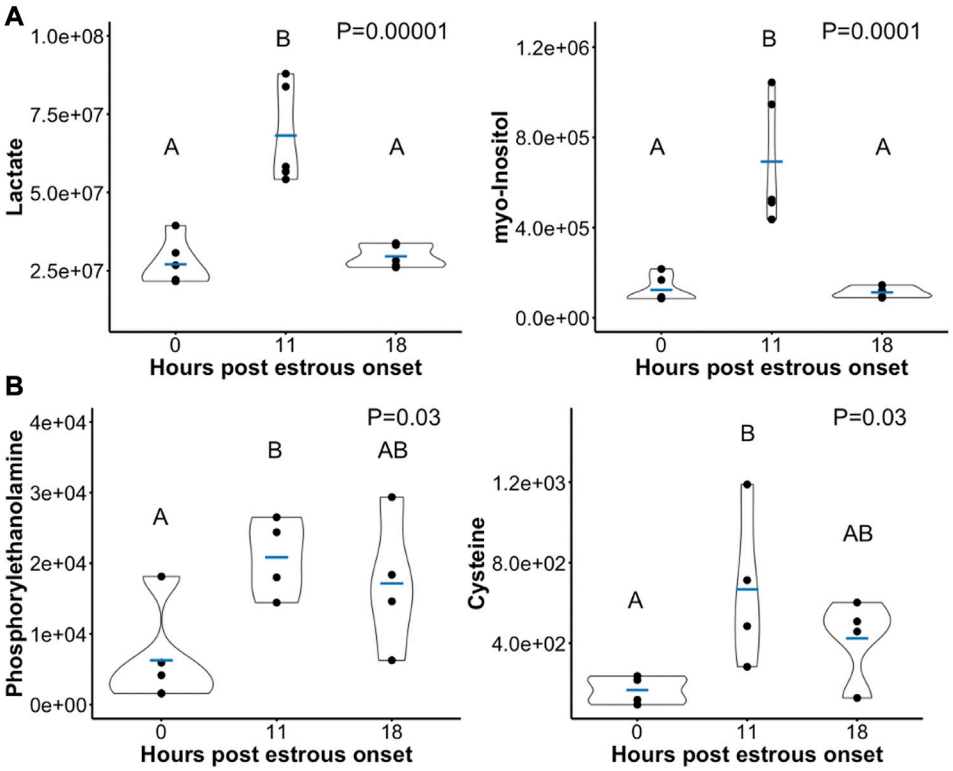

FIGURE 3
Scatterplots depicting peak area (*y*-axis) of example preovulatory follicular fluid metabolites that rose in abundance from hr 0 to hr 11 post onset of estrus. A subset of metabolites dropped in abundance after hr 11 such that metabolite levels at hr 18 were significantly lower than at hr 11 **(A)**. In other metabolites, abundance was not different between hr 18 and either hr 0 or hr 11 **(B)**. Mean metabolite abundance at timepoints with different letters are statistically different (Tukey's Honest Significant Difference *post hoc* test $p \leq 0.05$).

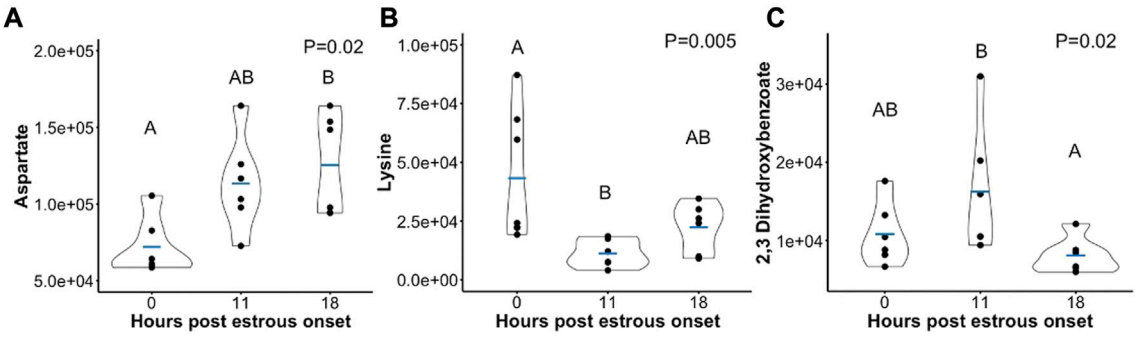

FIGURE 4
Scatterplots depicting peak area (*y*-axis) of metabolites that either **(A)** rose in abundance from hr 0 to hr 18 **(B)** dropped in abundance from hr 0 to hr 11, or **(C)** dropped in abundance from hr 11 to hr 18 post estrous onset. Mean metabolite abundance at timepoints with different letters are statistically different (Tukey's Honest Significant Difference *post hoc* test $p \leq 0.05$).

"Glycine, Serine and Threonine Metabolism" were also enriched with metabolites that rose from FF E2:P4 classifications indicating hrs 0 and 11 and decreased from FF E2:P4 classifications indicating hrs 11 and 18 (Table 4). As observed in the primary analysis based on time post estrous onset, multiple metabolic pathways were enriched with metabolites whose abundance varied across FF E2:P4 ratio classifications and relatively few metabolites contributed to observed enrichment. Pyruvate, Alpha-Ketoglutarate, Aconitate, Aspartate, and Cystathionine were the metabolites influenced by FF E2:P4 ration classification that appeared in KEGG pathways identified by enrichment analysis.

TABLE 2 KEGG pathways significantly enriched with preovulatory follicular fluid metabolites that differed in abundance among collection times post estrous onset.

Pathway	Pathway name	*Match status	FDR	Differentially abundant metabolites in pathway
bta00250	Alanine, Aspartate and Glutamate Metabolism	[a]4/28 [bc]3/28	[a]0.020 [b]0.076 [c]0.040	[abc]C00026 (Alpha-Ketoglutarate) [a]C00049 (Aspartate) [abc]C00025 (Glutamate) [abc]C00022 (Pyruvate)
bta00220	Arginine Biosynthesis	[a]3/14 [c]2/14	[a]0.020 [c]0.094	[ac]C00026 (Alpha-Ketoglutarate) [a]C00049 (Aspartate) [ac]C00025 (Glutamate)
bta00471	D-Glutamine and D-Glutamate Metabolism	[abc]2/5	[a]0.030 [b]0.043 [c]0.030	[abc]C00026 (Alpha-Ketoglutarate) [abc]C00025 (Glutamate)
bta00020	Citrate Cycle (TCA Cycle)	[abc]3/20	[a]0.030 [b]0.043 [c]0.028	[abc]C00026 (Alpha-Ketoglutarate) [abc]C00022 (Pyruvate) [abc]C00417 (Aconitate)
bta00970	Aminoacyl-tRNA Biosynthesis	[a]4/48	[a]0.033	[a]C00049 (Aspartate) [a]C00025 (Glutamate) [a]C00097 (Cysteine) [a]C00047 (Lysine)
bta00630	Glyoxylate and Dicarboxylate Metabolism	[abc]3/32	[a]0.080 [b]0.084 [c]0.044	[abc]C00417 (Aconitate) [abc]C00025 (Glutamate) [abc]C00022 (Pyruvate)
bta00650	Butanoate Metabolism	[c]2/15	[c]0.094	[c]C00026 (Alpha-Ketoglutarate) [c]C00025 (Glutamate)

*Number of differentially abundant metabolites in pathway/total number of metabolites in pathway.
[a]data representative of pathway enrichment analysis using all metabolites that differed in abundance among timepoints.
[b]data representative of pathway enrichment analysis using metabolites that increased in abundance from h 0 to h 11.
[c]data representative of pathway enrichment analysis using metabolites that increased in abundance from h 0 to h 11 and also decreased in abundance from h 11 to h 18.

4 Discussion

This study is the first of our knowledge to interrogate preovulatory follicular fluid metabolome profiles to determine metabolites whose abundance differed based on time post estrous onset in cattle. As somatic follicular cell differentiation and oocyte maturation commence following the LH surge, it is not surprising that preovulatory follicular fluid metabolome profiles at hr 0 (assumed pre-LH surge) and hr 11 (assumed post-LH surge) were distinct. Pyruvate, Alpha-Ketoglutarate, and Glutamate all varied in abundance according to time post estrous onset. These metabolites were the key contributors to significant pathway enrichment analysis in each KEGG pathway identified. The combination of metabolite enrichment in multiple metabolic related KEGG pathways and the change in abundance of key metabolites in glucose metabolism, the TCA cycle, and amino acid synthesis throughout post estrous follicle differentiation demonstrates essential shifts in intrafollicular metabolism during the hours leading up to and following the LH surge (Figure 5). In all of the above metabolites, greatest abundance was observed at 11 h after the first standing mount.

A rise in follicular fluid metabolites involved in energy and amino acid production during the early LH surge response is in line with increased follicular metabolism and need for such byproducts to support the energetically demanding transformations in the oocyte, cumulus, and granulosa cells in response to the LH surge (Figure 5). The transition of granulosa cells from proliferative function pre-LH surge to elevated metabolism, amino acid production, and increased vascularity at 6 h post surge (Gilbert et al., 2011) may partly explain the rise in many follicular fluid metabolites from hr 0 to hr 11 in the current study. Though differences in follicular progression from hr 6 post LH surge to hr 11 post estrous onset must be considered, follicular samples collected at hr 11 after first standing mount should be within approximately 7 h of the peak LH surge and thus quite similar in developmental progression as those collected at 6 h post LH surge. Since follicular fluid composition is heavily influenced by secretions of granulosa cells, increased metabolic activity and amino acid synthesis of granulosa cells likely contributes to the increased abundance of metabolites such as Pyruvate, Alpha-Ketoglutarate, Aspartate, Glutamate, Cysteine, Aconitate, and additional amino acids. Increased vascularity of the ovulatory follicle due to granulosa cell expression of vascular endothelial growth factor in response to LH surge (Schams et al., 2001) following estrous onset may have also positively influenced follicular fluid metabolite abundance via increased opportunity for transfer of small, neutral to slightly negatively charged molecules via the blood follicle barrier (Cran et al., 1976; Shalgi et al., 1977; Hess et al., 1998). All metabolites found to differ among time points post estrous onset were <1 kDA in mass, and all had a net charge or 0 or -1 except myo-Inositol which had a net charge of −6. Though much remains to be discovered about the selectivity and time dependent permeability of the blood follicle barrier, composition of follicular fluid is influenced by passing of systemic molecules through this barrier

TABLE 3 Preovulatory follicular fluid metabolites that varied in abundance among follicular fluid E2:P4 ratio classifications.

Metabolite	†Least squares means			
	0	11	18	*P
Hydroxyphenylacetate	92,331 ± 4,806^{a}	163,878 ± 3,816^{b}	109,006 ± 4,109^{a}	<0.001
Aspartate	77,830 ± 3,687^{a}	101,532 ± 4,213^{ab}	137,786 ± 3,687^{b}	0.001
N-acetyl-D-glucosamine 6-phosphate	27 ± 149^{a}	1,592 ± 171^{b}	228 ± 199^{ab}	0.003
Pyruvate	4,564,570 ± 171,529^{a}	6,997,512 ± 192,971^{b}	4,637,113 ± 192,971^{a}	0.006
Alpha-Ketoglutarate	42,689 ± 3,548^{a}	91,608 ± 3,992^{b}	43,466 ± 3,992^{a}	0.006
Glycerol-3-phosphate	2,517 ± 1,019^{a}	12,952 ± 891^{b}	7,598 ± 891^{Ab}	0.007
myo-Inositol	159,336 ± 51,110^{a}	647,828 ± 58,411^{b}	567,821 ± 51,110^{ab}	0.008
Lactate	30,895,067 ± 3,202,428^{a}	66,276,567 ± 3,659,918^{b}	56,820,210 ± 3,202,428^{ab}	0.009
Phosphorylethanolamine	13,673 ± 3,310^{a}	24,237 ± 3,782^{Ab}	51,496 ± 3,310^{b}	0.012
Orotate	964 ± 305^{a}	5,779 ± 346^{b}	836 ± 370^{a}	0.012
Jasmonate	15,988,962 ± 19,434^{a}	15,888,480 ± 31,094^{ab}	15,734,453 ± 19,434^{b}	0.014
2,3-Dihydroxybenzoate	11,125 ± 458^{ab}	14,255 ± 523^{a}	8,266 ± 523^{b}	0.017
Succinate/Methylmalonate	1,488,465 ± 4,879^{a}	1,551,601 ± 7,318^{b}	1,486,125 ± 5,489^{a}	0.021
Aconitate	39,475 ± 1,160^{ab}	51,923 ± 1,590^{A}	35,550 ± 1,488^{b}	0.029
Cholate	27,381 ± 3,592^{a}	62,050 ± 3,143^{b}	39,536 ± 3,143^{ab}	0.034
Cystathionine	9,825 ± 1,223^{a}	18,744 ± 1,070^{A}	8,203 ± 1,426^{a}	0.034
Homocitrulline	223 ± 43^{a}	644 ± 37^{b}	545 ± 37^{ab}	0.035
Kynurenine	10,805 ± 1,388^{a}	21,616 ± 1,388^{b}	11,805 ± 1,388^{ab}	0.044

†Least squares mean ± standard error of the mean for metabolite peak area.

*P value reported for main effect of FF E2:P4 ratio classification.

$^{ab}P \leq 0.05$.

$^{aA \text{ or } bB}P \leq 0.10$. Pairwise comparison p values were adjusted using Tukey's Honest Significant Difference post hoc test.

and both follicular invasion of blood vessels and blood follicle barrier permeability have been reported to increase following the LH surge (Duffy et al., 2018).

An increase in follicular fluid metabolites following the LH surge could certainly also hold a functional role in metabolic supportive of cumulus expansion and final metabolic preparation of the oocyte for maturation, fertilization, and early embryonic cell divisions. Undoubtedly, the metabolic contributions of the somatic follicular components support oocyte energy production prior to the LH surge and breakdown of cumulus-oocyte connections (Sutton-McDowall et al., 2004; Thompson et al., 2007; Sutton-McDowall et al., 2010). This support, however, is likely equally important in the early hours post LH surge. Since disconnection of the oocyte and cumulus was first reported at approximately 9–12 h after peak LH surge (Hyttel et al., 1986), samples collected at hr 11 in the current study should represent follicular fluid encasing intact cumulus oocyte complexes or those early in the process of cumulus expansion and gap junctional breakdown. The oocyte relies on oxidative phosphorylation using substrates derived from cumulus cell glycolysis to metabolize glucose (Thompson et al., 2007). Therefore, elevated abundance of follicular fluid Pyruvate, Alpha-Ketoglutarate, Aspartate, Glutamate, Lactate, Cysteine, and Aconitate at hr 11 vs. 0 may be partially produced by elevated cumulus metabolism and metabolic transfer to the oocyte and surrounding follicular fluid. Elevations of such metabolites from granulosa metabolism and systemic uptake may also serve a supportive role in oocyte metabolism by transfer through the cumulus or direct uptake by the oocyte.

Interestingly, metabolites involved in glucose metabolism and TCA cycle pathways have previously been identified by our lab to differ in abundance based on preovulatory follicle developmental status prior to a LH surge induced by exogenous GnRH administration (Read et al., 2021; Read et al., 2022). Follicles with higher estradiol production or larger diameter immediately prior to GnRH administration contained greater quantity of Pyruvate, Alpha-ketoglutarate, Glutamate, and other TCA cycle intermediates than did their less developed counterparts. Increased abundance of metabolic compounds in the follicular fluid of developmentally superior follicles is hypothesized to contribute to the superior fertility and oocyte developmental competence for embryo production in such animals. In fact pathways of "Alanine, aspartate, and glutamate metabolism", "Arginine biosynthesis", "D-Glutamine and D-Glutamate Metabolism", "Citrate cycle (TCA cycle)", and "Aminoacyl-tRNA

TABLE 4 KEGG pathways significantly enriched with preovulatory follicular fluid metabolites that differed in abundance among follicular fluid E2:P4 ratio classifications.

Pathway	Pathway name	*Match status	FDR	Differentially abundant metabolites in pathway
bta00020	Citrate Cycle (TCA Cycle)	[abc]3/20	[a]0.055 [b]0.044 [c]0.002	[abc]C00026 (Alpha-Ketoglutarate) [abc]C00022 (Pyruvate) [abc]C00417 (Aconitate)
bta00250	Alanine, Aspartate and Glutamate Metabolism	[a]3/28 [c]2/28	[a]0.076 [c]0.079	[ac]C00026 (Alpha-Ketoglutarate) [a]C00049 (Aspartate) [ac]C00022 (Pyruvate)
bta00270	Cysteine and Methionine Metabolism	[c]2/33	[c]0.079	[c]C00022 (Pyruvate) [c]C02291 (Cystathionine)
bta00630	Glyoxylate and Dicarboxylate Metabolism	[c]2/32	[c]0.079	[c]C00417 (Aconitate) [c]C00022 (Pyruvate)
bta00260	Glycine, Serine and Threonine Metabolism	[c]2/34	[c]0.079	[c]C00022 (Pyruvate) [c]C02291 (Cystathionine)

*Number of differentially abundant metabolites in pathway/total number of metabolites in pathway.

[a]Data representative of pathway enrichment analysis using all metabolites that differed in abundance among FF E2:P4 classifications.

[b]Data representative of pathway enrichment analysis using metabolites that increased in abundance from FF E2:P4 ratio classification expected at h 0 to FF E2:P4 ratio classification expected at h 11.

[c]Data representative of pathway enrichment analysis using metabolites that increased in abundance from FF E2:P4 ratio classification expected at h 0 to FF E2:P4 ratio classification expected at h 11 and also decreased in abundance from FF E2:P4 ratio classification expected at h 11to FF E2:P4 ratio classification expected at h 18.

synthesis" which were enriched with metabolites influenced by time post estrous in the current study were previously reported to be enriched with metabolites increased in physiologically superior follicles that enclosed an oocyte with greater abundance of ATP (Read et al., 2021; Read et al., 2022). The detection of metabolites enriched within glucose and amino acid metabolism related pathways in both the current study and past complementary studies emphasizes the intrafollicular metabolic milieu directly leading up to and following the LH surge as essential for fertility in cattle.

In addition to the increased bioavailability of glucose metabolism, TCA cycle, and amino acid metabolites from hr 0 to 11, myo-Inositol increased from hr 0 to hr 11 and then decreased from hr 11 to hr 18. Myo-Inositol is critical for numerous cellular functions through its role in cell signaling pathways, such as oocyte maturation and fertilization, that rely on intracellular calcium release (Berridge, 1993; Whitaker, 2006). Indeed, increased levels of follicular fluid myo-Inositol and *in vitro* supplementation of myo-Inositol in oocyte maturation media were related to or improved oocyte maturation and ability to produce a quality embryo (Pesty et al., 1994; Holm et al., 1999; Chiu et al., 2002). An increased level of myo-Inositol in hr 11 follicular fluid likely serves similar function to the elevated abundance of amino acids and energetic metabolites at this time point for oocyte final preparation to complete the essential process of meiotic maturation. Additionally, functions of myo-Inositol to combat oxidative stress and reduce abundance of free radicals such as hydrogen peroxide could contribute to maintenance of an oxidatively balanced follicular environment when follicular metabolism in maximized at hr 11 post estrous onset (Jiang et al., 2013; Mohammadi et al., 2019).

It is interesting that hr 18 preovulatory follicular fluid samples were not distinct from hr 0 or hr 11 when sPLSDA was performed. Regardless, a small number of metabolites, especially those that were amino acids or were involved in glucose metabolism or the TCA cycle, differed in abundance between hr 11 and 18 samples. Decrease in select metabolite levels from hr 11 to hr 18 suggests a potential slowing of the cellular production or blood follicle barrier uptake of those specific metabolites by the follicle or a ratio of follicular metabolite usage that strongly exceeds production. Previous studies have suggested that the increased bioavailability of glucose metabolism byproducts and amino acids in the follicular fluid as part of an early to intermediate response to the LH surge may hold multiple roles in the preovulatory follicle including shuttle to the oocyte while gap junctions remain intact (Eppig et al., 2005; D'Aniello et al., 2007) and subsequent usage in later hours post LH surge for protein synthesis (Gilbert et al., 2011). By the time follicles in the current study reached hr 18 post estrous onset, amino acids or metabolic byproducts could have been utilized to meet granulosa and/or oocyte needs for developmental progression. Such metabolites could be lower in abundance at hr 18 vs. hr 11 because they had been previously utilized and were no longer as necessary for follicular processes required for fertility. Though most metabolites did not differ in abundance between hr 0 and hr 18 samples, Aspartate increased from hr 0 to hr 18. Higher Aspartate levels in hr 18 follicular fluid supports the previous results of others indicating increased transcripts for granulosa cell preparation for ovulation and further luteal function at 22 h after the LH surge (Assidi et al., 2010). Aspartate has previously been implicated to function in endocrine tissues to promote hormone biosynthesis and may be functionally relevant to promote progesterone production in granulosa cells approaching ovulation (D'Aniello et al., 2000; D'Aniello et al., 2007). Further, potentially elevated Aspartate levels in ovulated follicular fluid may have positive impacts on the sperm quality (D'Aniello et al., 2005).

One weakness of the current study is the variation of LH surge timing relative to estrous onset. It is generally accepted that the pre-

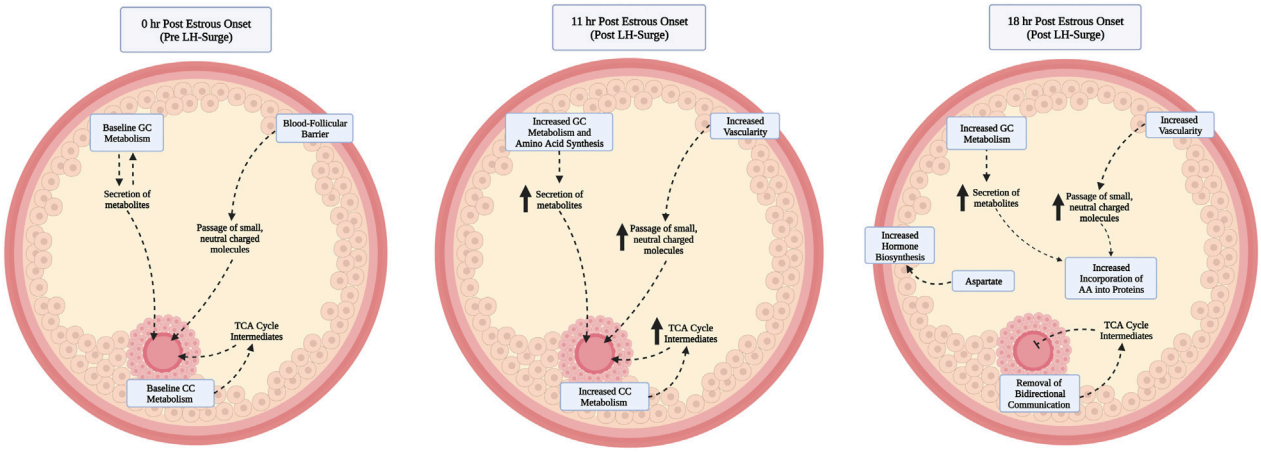

FIGURE 5
Proposed model of contributors to and functional relevance of elevated levels of follicular fluid metabolites at hr 11 vs. 0 post onset of estrus. As the preovulatory follicle launches an early response to the luteinizing hormone surge, granulosa and cumulus cells increase metabolism, amino acids are produced, and increased blood follicle barrier permeability leads to increased bioavailability of metabolites to be shuttled to the oocyte before breakdown of gap junctional transfer between the cumulus and oocyte, readily used by the cumulus for expansion, or to be used by hr 18 post estrous onset for incorporation into proteins. By hr 18, the follicular fluid metabolite milieu remains similar to that of hr 11, with the exception of decreased abundance of a small number of metabolites that are hypothesized to have been utilized by the follicular cells and oocyte during previous hours or whose production has slowed such that usage exceeds metabolite accumulation.

ovulatory gonadotropin surge occurs near the onset of estrus in bovine [within ~0.5–5 h (Mondal et al., 2006; Rajamahendran et al., 1989; Dieleman et al., 1986; Stevenson et al.)]. Some studies have indicated occurrence of the surge before estrus (Saumande and Humblot, 2005) or the onset of surge to occur before the onset of estrus (Rajamahendran et al., 1989). Timing of the LH surge could have been more controlled if animal were not allowed adequate time to display estrus and GnRH was administered to induce the LH surge. Estrous expression was the preferred method of LH surge induction and timing due to a strong relationship between preovulatory follicle status at GnRH administration to induce ovulation and animal fertility, oocyte competence, and the follicular fluid metabolome. Since the majority of studies indicate the LH surge to occur within 0.5–5 h post estrous onset, mild variation in LH surge timing relative to estrus was preferred to reduce variability in preovulatory follicle physiological status. Nevertheless, some cows may be more or less inclined to mount or stand to be ridden based on weather conditions, age, or dominance. Low inclination to be mounted could lead to an animal being detected in estrus hours after a more sexually active animal. In such instances, the LH surge could have occurred before the animal was visually detected in estrus. To add confidence in the current study, we performed a secondary analysis that classified follicular fluid samples based on FF E2: P4 ratio. Analysis of metabolome profiles of the FF E2:P4 ratio categorized samples followed a remarkably similar trend to those analyzed based on collection timepoint. This similarity further points to the dynamic changes in intrafollicular metabolite milieu as preovulatory follicles respond to the LH surge and prepare for ovulation.

5 Conclusion

Outcomes of the current study highlight the myriad of intrafollicular changes that occur following onset of estrus in cattle. Dynamic changes in abundance of metabolites from estrus to hr 11 post estrous onset highlight the essentiality of follicular metabolism in early response to the LH surge and pose metabolites of key interest for future studies. Continued efforts to elucidate the biological function of each metabolite's rise and/or fall in abundance throughout oocyte maturation and follicle progression to ovulation will provide invaluable opportunity to 1 day improve the intrafollicular environment for oocyte maturation, better support the developing corpus luteum, provide more physiological culture conditions for *in vitro* oocyte maturation, and thus improve fertility in cattle and other mammalian species.

Data availability statement

The original contributions presented in the study are publicly available. This data can be found here: [https://doi.org/doi:10.5061/dryad.1vhhmgqz0].

Ethics statement

The animal study was reviewed and approved by The University of Tennessee IACUC.

Author contributions

SM, JE, and FS contributed to conception and design of the study. EH, JE, RP, SC, JK, and SM collected samples and performed wet lab procedures. EH, RP, AP, HC, AS, and SM organized the data. EH, HC, AS, KH, SR, MH, and SM performed the statistical analyses. EH and SM wrote the first draft of the manuscript. All authors contributed to manuscript revision, read, and approved the submitted version.

Funding

This research was supported by the USDA NIFA Multistate project 1022068 (NE1727), the University of Tennessee AgResearch, and the University of Tennessee Department of Animal Science.

Acknowledgments

The authors would like to thank Hector Castro, Courtney Christopher, and Sara Howard for their assistance with the UHPLC-HRMS metabolomics processing. The authors would also like to thank Kevin Thompson, Wes Gilliam, David Johnson, and Nolan Rinks of the Middle Tennessee AgResearch and Education Center for providing the cattle and their assistance in processing the cattle for this study, Justin Rhinehart and Courtnie Bridges for assisting with a portion of dominant follicle aspirations, and Casey Read, Megan Mills, Claire Hunkler, Afroza Akter, and Jake Watts for their assistance with sample collection and processing.

Conflict of interest

The authors declare that the research was conducted in the absence of any commercial or financial relationships that could be construed as a potential conflict of interest.

Publisher's note

References

Afedi, P. A., Larimore, E. L., Cushman, R. A., Raynie, D., and Perry, G. A. (2021). iTRAQ-based proteomic analysis of bovine pre-ovulatory plasma and follicular fluid. *Domest. Anim. Endocrinol.* 76, 106606. doi:10.1016/j.domaniend.2021.106606

Ambekar, A. S., Nirujogi, R. S., Srikanth, S. M., Chavan, S., Kelkar, D. S., Hinduja, I., et al. (2013). Proteomic analysis of human follicular fluid: A new perspective towards understanding folliculogenesis. *J. Proteomics.* 87, 68–77. doi:10.1016/j.jprot.2013.05.017

Assidi, M., Dieleman, S. J., and Sirard, M. A. (2010). Cumulus cell gene expression following the LH surge in bovine preovulatory follicles: Potential early markers of oocyte competence. *Reprod* 140 (6), 835–852. doi:10.1530/rep-10-0248

Bender, K., Walsh, S., Evans, A. C. O., Fair, T., and Brennan, L. (2010). Metabolite concentrations in follicular fluid may explain differences in fertility between heifers and lactating cows. *Reproduction* 139 (6), 1047–1055. doi:10.1530/rep-10-0068

Berridge, M. J. (1993). Inositol trisphosphate and calcium signalling. *Nature* 361 (6410), 315–325. doi:10.1038/361315a0

Bou Nemer, L., Shi, H., Carr, B. R., Word, R. A., and Bukulmez, O. (2019). Effect of body weight on metabolic hormones and fatty acid metabolism in follicular fluid of women undergoing *in vitro* fertilization: A pilot study. *Reprod. Sci.* 26 (3), 404–411. doi:10.1177/1933719118776787

Callesen, H., Greve, T., and Hyttel, P. (1986). Preovulatory endocrinology and oocyte maturation in superovulated cattle. *Theriogenology* 25 (1), 71–86. doi:10.1016/0093-691X(86)90184-6

Chiu, T. T. Y., Rogers, M. S., Law, E. L. K., Briton-Jones, C. M., Cheung, L. P., and Haines, C. J. (2002). Follicular fluid and serum concentrations of myo-inositol in patients undergoing IVF: Relationship with oocyte quality. *Hum. Reprod.* 17 (6), 1591–1596. doi:10.1093/humrep/17.6.1591

Cran, D. G., Moor, R. M., and Hay, M. F. (1976). Permeability of ovarian follicles to electron-dense macromolecules. *Acta. Endocrinol. (Copenh)* 82 (3), 631–636. doi:10.1530/acta.0.0820631

D'Aniello, A., Di Fiore, M. M., Fisher, G. H., Milone, A., Seleni, A., D'Aniello, S., et al. (2000). Occurrence of D-aspartic acid and N-methyl-D-aspartic acid in rat neuroendocrine tissues and their role in the modulation of luteinizing hormone and growth hormone release. *Faseb J.* 14 (5), 699–714. doi:10.1096/fasebj.14.5.699

D'Aniello, G., Grieco, N., Di Filippo, M., Cappiello, F., Topo, E., D'Aniello, E., et al. (2007). Reproductive implication of d-aspartic acid in human pre-ovulatory follicular fluid. *Hum. Reprod.* 22, 3178–3183. doi:10.1093/humrep/dem328

D'Aniello, G., Ronsini, S., Guida, F., Spinelli, P., and D'Aniello, A. (2005). Occurrence of D-aspartic acid in human seminal plasma and spermatozoa: Possible role in reproduction. *Fert. Steril.* 84 (5), 1444–1449. doi:10.1016/j.fertnstert.2005.05.019

Dieleman, S. J., Bevers, M. M., Poortman, J., and Van Tol, H. T. M. (1983). Steroid and pituitary hormone concentrations in the fluid of preovulatory bovine follicles relative to the peak of LH in the peripheral blood. *Reprod* 69 (2), 641–649. doi:10.1530/jrf.0.0690641

Dieleman, S. J., Bevers, M. M., Van Tol, H. T. M., and Willemse, A. H. (1986). Peripheral plasma concentrations of oestradiol, progesterone, cortisol, LH and prolactin during the oestrous cycle in the cow, with emphasis on the peri-oestrous period. *Anim. Reprod. Sci.* 10 (4), 275–292. doi:10.1016/0378-4320(86)90003-5

Duffy, D. M., Ko, C., Jo, M., Brannstrom, M., and Curry, T. E., Jr. (2018). Ovulation: Parallels with inflammatory processes. *Endocr. Rev.* 40 (2), 369–416. doi:10.1210/er.2018-00075

Eppig, J. J. (1985). Oocyte-somatic cell interactions during oocyte growth and maturation in the mammal. *Oogenesis* 1, 313–347. doi:10.1007/978-1-4615-6814-8_7

Eppig, J., Pendola, F., Wigglesworth, K., and Pendola, J. (2005). Mouse oocytes regulate metabolic cooperativity between granulosa cells and oocytes: Amino acid transport. *Biol. Reprod.* 73, 351–357. doi:10.1095/biolreprod.105.041798

Fortune, J. E., and Hansel, W. (1985). Concentrations of steroids and gonadotropins in follicular fluid from normal heifers and heifers primed for superovulation. *Biol. Reprod.* 32 (5), 1069–1079. doi:10.1095/biolreprod32.5.1069

Gilbert, I., Robert, C., Dieleman, S., Blondin, P., and Sirard, M. A. (2011). Transcriptional effect of the LH surge in bovine granulosa cells during the peri-ovulation period. *Reprod* 141 (2), 193–205. doi:10.1530/rep-10-0381

Gilchrist, R. B., Ritter, L. J., and Armstrong, D. T. (2004). Oocyte-somatic cell interactions during follicle development in mammals. *Anim. Reprod. Sci.* 82-83, 431–446. doi:10.1016/j.anireprosci.2004.05.017

Ginther, O. J., Pinaffi, F. L., Khan, F. A., Duarte, L. F., and Beg, M. A. (2013). Follicular-phase concentrations of progesterone, estradiol-17β, LH, FSH, and a PGF2α metabolite and daily clustering of prolactin pulses, based on hourly blood sampling and hourly detection of ovulation in heifers. *Theriogenology* 79 (6), 918–928. doi:10.1016/j.theriogenology.2012.12.015

Granot, I., and Dekel, N. (2002). The ovarian gap junction protein connexin43: Regulation by gonadotropins. *Trends Endocrinol. Metab.* 13 (7), 310–313. doi:10.1016/s1043-2760(02)00623-9

Henricks, D. M., Dickey, J. F., and Hill, J. R. (1971). Plasma estrogen and progesterone levels in cows prior to and during estrus. *Endocrinol* 89 (6), 1350–1355. doi:10.1210/endo-89-6-1350

Hess, K. A., Chen, L., and Larsen, W. J. (1998). The ovarian blood follicle barrier is both charge- and size-selective in mice. *Biol. Reprod.* 58 (3), 705–711. doi:10.1095/biolreprod58.3.705

Holm, P., Booth, P. J., Schmidt, M. H., Greve, T., and Callesen, H. (1999). High bovine blastocyst development in a static *in vitro* production system using SOFaa medium supplemented with sodium citrate and myo-inositol with or without serum-proteins. *Theriogenology* 52 (4), 683–700. doi:10.1016/s0093-691x(99)00162-4

Horn, E. J., Read, C. C., Edwards, J. L., Schrick, F. N., Rhinehart, J. D., Payton, R. R., et al. (2022). Preovulatory follicular fluid and serum metabolome profiles in lactating beef cows with thin, moderate, and obese body condition. *Journ. Anim. Sci.* 100 (7), skac152. doi:10.1093/jas/skac152

Hung, W.-T., Hong, X., Christenson, L. K., and McGinnis, L. K. (2015). Extracellular vesicles from bovine follicular fluid support cumulus expansion. *Biol. Reprod.* 93 (5), 117. doi:10.1095/biolreprod.115.132977

Hyttel, P., Callesen, H., and Greve, T. (1986). Ultrastructural features of preovulatory oocyte maturation in superovulated cattle. *J. Reprod. Fertil.* 76 (2), 645–656. doi:10.1530/jrf.0.0760645

Jiang, W. D., Kuang, S. Y., Liu, Y., Jiang, J., Hu, K., Li, S. H., et al. (2013). Effects of myo-inositol on proliferation, differentiation, oxidative status and antioxidant capacity of carp enterocytes in primary culture. *Aquac. Nutr.* 19 (1), 45–53. doi:10.1111/j.1365-2095.2011.00934.x

Kafi, M., Azari, M., Chashnigir, O., Gharibzadeh, S., Aghabozorgi, Z., Asaadi, A., et al. (2017). Inherent inferior quality of follicular fluid in repeat breeder heifers as evidenced by low rates of *in vitro* production of bovine embryos. *Theriogenology* 102, 29–34. doi:10.1016/j.theriogenology.2017.07.011

Lê Cao, K.-A., Boitard, S., and Besse, P. (2011). Sparse PLS discriminant analysis: Biologically relevant feature selection and graphical displays for multiclass problems. *BMC Bioinform* 12 (1), 253. doi:10.1186/1471-2105-12-253

Leroy, J., Vanholder, T., Mateusen, B., Christophe, A., Opsomer, G., de Kruif, A., et al. (2005). Non-esterified fatty acids in follicular fluid of dairy cows and their effect on developmental capacity of bovine oocytes *in vitro*. *Reprod* 130, 485–495. doi:10.1530/rep.1.00735

Lu, W., Clasquin, M. F., Melamud, E., Amador-Noguez, D., Caudy, A. A., and Rabinowitz, J. D. (2010). Metabolomic analysis via reversed-phase ion-pairing liquid chromatography coupled to a stand alone orbitrap mass spectrometer. *Anal. Chem.* 82 (8), 3212–3221. doi:10.1021/ac902837x

Macaulay, A. D., Gilbert, I., Caballero, J., Barreto, R., Fournier, E., Tossou, P., et al. (2014). The gametic synapse: RNA transfer to the bovine oocyte. *Biol. Reprod.* 91 (4), 90. doi:10.1095/biolreprod.114.119867

Mohammadi, F., Varanloo, N., Heydari Nasrabadi, M., Vatannejad, A., Amjadi, F. S., Javedani Masroor, M., et al. (2019). Supplementation of sperm freezing medium with myoinositol improve human sperm parameters and protects it against DNA fragmentation and apoptosis. *Cell Tissue Bank.* 20 (1), 77–86. doi:10.1007/s10561-018-9731-0

Mondal, M., Rajkhowa, C., and Prakash, B. S. (2006). Oestrous behaviour and timing of ovulation in relation to onset of oestrus and LH peak in Mithun (*Bos frontalis*) cows. *Reprod. Domest. Anim.* 41 (6), 479–484. doi:10.1111/j.1439-0531.2006.00678.x

Norris, R. P., Ratzan, W. J., Freudzon, M., Mehlmann, L. M., Krall, J., Movsesian, M. A., et al. (2009). Cyclic GMP from the surrounding somatic cells regulates cyclic AMP and meiosis in the mouse oocyte. *Dev* 136 (11), 1869–1878. doi:10.1242/dev.035238

Orsi, N. M., Gopichandran, N., Leese, H. J., Picton, H. M., and Harris, S. E. (2005). Fluctuations in bovine ovarian follicular fluid composition throughout the oestrous cycle. *Reprod* 129 (2), 219–228. doi:10.1530/rep.1.00460

Pang, Z., Chong, J., Zhou, G., de Lima Morais, D. A., Chang, L., Barrette, M., et al. (2021). MetaboAnalyst 5.0: Narrowing the gap between raw spectra and functional insights. *Nucleic Acids Res.* 49 (W1), W388–W396. doi:10.1093/nar/gkab382

Pesty, A., Lefèvre, B., Kubiak, J., Géraud, G., Tesarik, J., and Maro, B. (1994). Mouse oocyte maturation is affected by lithium via the polyphosphoinositide metabolism and the microtubule network. *Mol. Reprod. Dev.* 38 (2), 187–199. doi:10.1002/mrd.1080380210

R Team (2020). *RStudio*. Boston, MA: Integrated development for R. RStudio, PBC.

Rabinowitz, J. D., and Kimball, E. (2007). Acidic acetonitrile for cellular metabolome extraction from *Escherichia coli*. *Anal. Chem.* 79 (16), 6167–6173. doi:10.1021/ac070470c

Rajamahendran, R., Robinson, J., Desbottes, S., and Walton, J. S. (1989). Temporal relationships among estrus, body temperature, milk yield, progesterone and luteinizing hormone levels, and ovulation in dairy cows. *Theriogenology* 31 (6), 1173–1182. doi:10.1016/0093-691X(89)90086-1

Read, C. C., Edwards, J. L., Schrick, F. N., Rhinehart, J. D., Payton, R. R., Campagna, S. R., et al. (2022). Preovulatory serum estradiol concentration is positively associated with oocyte ATP and follicular fluid metabolite abundance in lactating beef cattle. *J. Anim. Sci.* 100 (7), skac136. doi:10.1093/jas/skac136

Read, C. C., Edwards, L., Schrick, N., Rhinehart, J. D., Payton, R. R., Campagna, S. R., et al. (2021). Correlation between pre-ovulatory follicle diameter and follicular fluid metabolome profiles in lactating beef cows. *Metabolites* 11 (9), 623. doi:10.3390/metabo11090623

Revelli, A., Piane, L. D., Casano, S., Molinari, E., Massobrio, M., and Rinaudo, P. (2009). Follicular fluid content and oocyte quality: From single biochemical markers to metabolomics. *Reprod. Biol. Endocrinol.* 7 (1), 40. doi:10.1186/1477-7827-7-40

Richards, J. S. (1997). Editorial: Sounding the alarm—Does induction of prostaglandin endoperoxide synthase-2 control the mammalian ovulatory clock? *Endocrinol* 138 (10), 4047–4048. doi:10.1210/endo.138.10.5515

Richards, J. S., Russell, D. L., Robker, R. L., Dajee, M., and Alliston, T. N. (1998). Molecular mechanisms of ovulation and luteinization. *Mol. Cell. Endocrinol.* 145 (1), 47–54. doi:10.1016/S0303-7207(98)00168-3

Rispoli, L. A., Edwards, J. L., Pohler, K. G., Russell, S., Somiari, R. I., Payton, R. R., et al. (2019). Heat-induced hyperthermia impacts the follicular fluid proteome of the periovulatory follicle in lactating dairy cows. *PLoS One* 14 (12), e0227095. doi:10.1371/journal.pone.0227095

Robker, R. L., Hennebold, J. D., and Russell, D. L. (2018). Coordination of ovulation and oocyte maturation: A good egg at the right time. *Endocrinol* 159 (9), 3209–3218. doi:10.1210/en.2018-00485

Saumande, J., and Humblot, P. (2005). The variability in the interval between estrus and ovulation in cattle and its determinants. *Anim. Reprod. Sci.* 85 (3), 171–182. doi:10.1016/j.anireprosci.2003.09.009

Schams, D., Kosmann, M., Berisha, B., Amselgruber, W. M., and Miyamoto, A. (2001). Stimulatory and synergistic effects of luteinising hormone and insulin like growth factor 1 on the secretion of vascular endothelial growth factor and progesterone of cultured bovine granulosa cells. *Exp. Clin. Endocrinol. Diabetes.* 109 (3), 155–162. doi:10.1055/s-2001-14839

Shalgi, R., Kaplan, R., and Kraicer, P. F. (1977). Proteins of follicular, bursal and ampullar fluids of rats. *Biol. Reprod.* 17 (3), 333–338. doi:10.1095/biolreprod17.3.333

Stevenson, J. S., Lamb, G. C., Kobayashi, Y., and Hoffman, D. P. (1998). Luteolysis during two stages of the estrous cycle: Subsequent endocrine profiles associated with radiotelemetrically detected estrus in heifers. *J. Dairy Sci.* 81 (11), 2897–2903. doi:10.3168/jds.S0022-0302(98)75850-3

Sutton-McDowall, M. L., Gilchrist, R. B., and Thompson, J. G. (2004). Cumulus expansion and glucose utilisation by bovine cumulus–oocyte complexes during *in vitro* maturation: The influence of glucosamine and follicle-stimulating hormone. *Reprod* 128 (3), 313–319. doi:10.1530/rep.1.00225

Sutton-McDowall, M. L., Gilchrist, R. B., and Thompson, J. G. (2010). The pivotal role of glucose metabolism in determining oocyte developmental competence. *Reprod* 139 (4), 685–695. doi:10.1530/rep-09-0345

Thompson, J. G., Lane, M., and Gilchrist, R. B. (2007). Metabolism of the bovine cumulus-oocyte complex and influence on subsequent developmental competence. *Soc. Reprod. Fertil. Suppl.* 64, 179–190. doi:10.5661/rdr-vi-179

Wettemann, R. P., Hafs, H. D., Edgerton, L. A., and Swanson, L. V. (1972). Estradiol and progesterone in blood serum during the bovine estrous cycle. *J. Anim. Sci.* 34 (6), 1020–1024. doi:10.2527/jas1972.3461020x

Whitaker, M. (2006). Calcium at fertilization and in early development. *Physiol. Rev.* 86 (1), 25–88. doi:10.1152/physrev.00023.2005

Wildman, E. E., Jones, G. M., Wagner, P. E., Boman, R. L., Troutt, H. F., Jr., and Lesch, T. N. (1982). A dairy cow body condition scoring system and its relationship to selected production characteristics. *J. Dairy Sci.* 65 (3), 495–501. doi:10.3168/jds.S0022-0302(82)82223-6

frontiers | Frontiers in Cell and Developmental Biology

TYPE Review
PUBLISHED 15 May 2023
DOI 10.3389/fcell.2023.1166232

OPEN ACCESS

EDITED BY
Fredrick Rosario-Joseph,
University of Colorado Denver,
United States

REVIEWED BY
Mariana Camargo,
Federal University of São Paulo, Brazil
Korah Pushpamangalam Kuruvilla,
University of Colorado Anschutz Medical Campus, United States

*CORRESPONDENCE
Débora J. Cohen,
dcohen@dna.uba.ar
Vanina Zaremberg,
vzarembe@ucalgary.ca

RECEIVED 15 February 2023
ACCEPTED 26 May 2023
PUBLISHED 15 May 2023

CITATION
Horta Remedios M, Liang W, González LN, Li V, Da Ros VG, Cohen DJ and Zaremberg V (2023), Ether lipids and a peroxisomal riddle in sperm. *Front. Cell Dev. Biol.* 11:1166232. doi: 10.3389/fcell.2023.1166232

Ether lipids and a peroxisomal riddle in sperm

Mayrene Horta Remedios[1], Weisheng Liang[1], Lucas N. González[2], Victoria Li[1], Vanina G. Da Ros[2], Débora J. Cohen[2]* and Vanina Zaremberg[1]*

[1]Department of Biological Sciences, University of Calgary, Calgary, AB, Canada, [2]Instituto de Biología y Medicina Experimental (IByME-CONICET), Buenos Aires, Argentina

Sperm are terminally differentiated cells that lack most of the membranous organelles, resulting in a high abundance of ether glycerolipids found across different species. Ether lipids include plasmalogens, platelet activating factor, GPI-anchors and seminolipid. These lipids play important roles in sperm function and performance, and thus are of special interest as potential fertility markers and therapeutic targets. In the present article, we first review the existing knowledge on the relevance of the different types of ether lipids for sperm production, maturation and function. To further understand ether-lipid metabolism in sperm, we then query available proteomic data from highly purified sperm, and produce a map of metabolic steps retained in these cells. Our analysis pinpoints the presence of a truncated ether lipid biosynthetic pathway that would be competent for the production of precursors through the initial peroxisomal core steps, but devoid of subsequent microsomal enzymes responsible for the final synthesis of all complex ether-lipids. Despite the widely accepted notion that sperm lack peroxisomes, the thorough analysis of published data conducted herein identifies nearly 70% of all known peroxisomal resident proteins as part of the sperm proteome. In view of this, we highlight open questions related to lipid metabolism and possible peroxisomal functions in sperm. We propose a repurposed role for the truncated peroxisomal ether-lipid pathway in detoxification of products from oxidative stress, which is known to critically influence sperm function. The likely presence of a peroxisomal-derived remnant compartment that could act as a sink for toxic fatty alcohols and fatty aldehydes generated by mitochondrial activity is discussed. With this perspective, our review provides a comprehensive metabolic map associated with ether-lipids and peroxisomal-related functions in sperm and offers new insights into potentially relevant antioxidant mechanisms that warrant further research.

KEYWORDS

sperm, ether lipid, peroxisome, metabolism, oxidative stress, fertility

Introduction

Sperm are terminally differentiated haploid cells with a unique structure necessary for the different stages of fertilization and early embryonic development. To achieve fertilization, sperm leaving the testis must first undergo a series of physiological changes in the epididymis and the female tract, known as maturation and capacitation, respectively (Yanagimachi, 1994). As a consequence of these processes, sperm become able to undergo the acrosome reaction, an exocytotic event that takes place in their head, and to develop a specific flagellar movement termed hyperactivation.

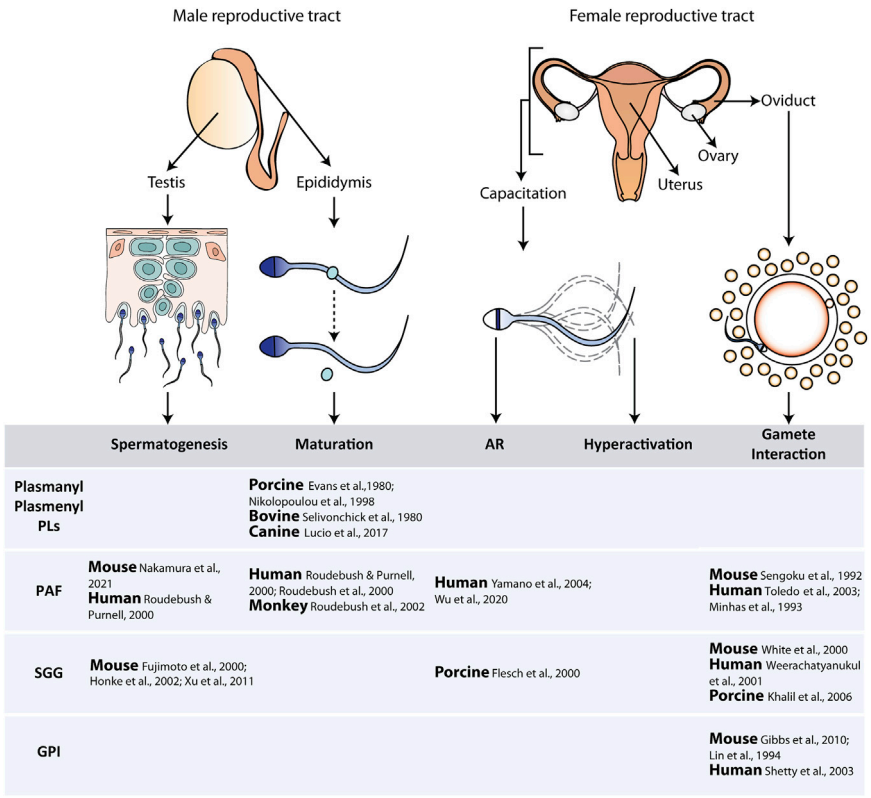

FIGURE 1
Schematic representation of the different steps involved in sperm production, maturation, and fertilization. The described roles for the different types of ether lipids in these steps are included in the table. Abbreviations: AR, acrosomal reaction; PLs, phospholipids; PAF, platelet activating factor; SGG, sulfogalactosylglycerolipid; GPI, glycosylphosphatidylinositol.

These physiological changes enable sperm to cross the *cumulus oophorus* that surrounds the egg, then bind to and penetrate the *zona pellucida*, and finally fuse with the egg's plasma membrane (Figure 1). In this regard, it is important to mention that, since sperm are transcriptionally and translationally silent cells, signal transduction cascades and metabolic pathways, among others, are essential for the regulation of the changes conducive to fertilization. Moreover, sperm function is critically influenced by reactive oxygen species (ROS) mainly derived from aerobic metabolism in the mitochondria. Small quantities of ROS are needed for normal sperm function, stimulating both sperm capacitation and fertilization reviewed by O'Flaherty and Scarlata (2022). However, high levels of ROS induce an oxidative stress state that has a detrimental effect on sperm motility, capacitation, acrosome reaction and DNA integrity, leading to male infertility reviewed by Aitken et al., (2022). As terminally differentiated cells, sperm are particularly vulnerable to ROS attack. Since the late 70's, evidence has been accumulating showing the critical role of lipid peroxidation in both combating and propagating this damage (Jones and Mann, 1976; Aitken et al., 1989; Gomez et al., 1998; Aitken and Baker, 2006). Therefore, a delicate balance between ROS production and antioxidant mechanisms should exist in normal sperm to ensure sperm survival for successful fertilization.

As a result of several studies focusing on the evaluation of sperm lipid composition, increased attention has been given to the relationship between sperm lipid composition and fertility (Rivera-Egea et al., 2018; Lopalco et al., 2019). Thus, lipids are of special interest as potential fertility markers and therapeutic targets not only because of their structural functions in sperm, but also because they are sensitive to external and environmental signals, many of which can be recreated *in vitro*. Ether lipids are a particularly highly abundant subclass of glycerophospholipids found in sperm of different species, such as humans, boars, stallions, bulls, and lions (Parks and Lynch, 1992; Leßig et al., 2004; Oresti et al., 2011; Jakop et al., 2022), suggesting they play a critical role in sperm physiology. In other cell types, ether lipids are key components of cell membranes, providing unique structural attributes with effects on membrane dynamics, including membrane fluidity and membrane fusion, facilitating signaling processes, regulating cell differentiation, and protecting membranes from oxidation by acting as potential endogenous antioxidants reviewed by Dean and Lodhi, (2018), Jiménez-Rojo and Riezman, (2019). Structurally, ether-phospholipids are characterized by the presence of an ether bond at the *sn-1* position of the glycerol backbone (Figure 2). Lipids with distinctive ether linkages may be categorized into a variety of subspecies that include: a) plasmanyl and plasmenyl

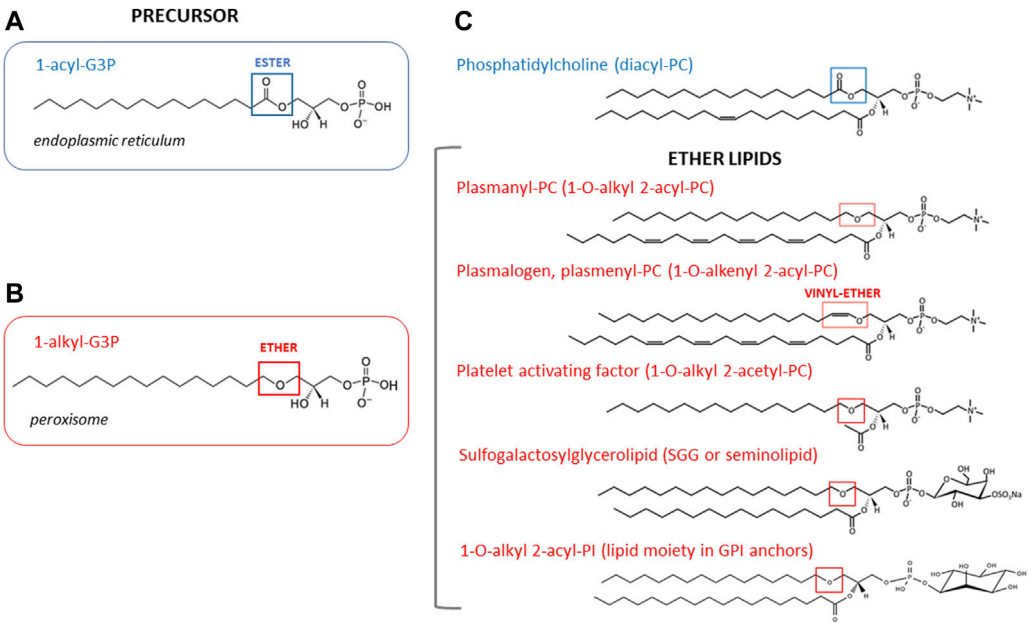

FIGURE 2
Chemical structures of ether and diacyl glycerophospholipids and their precursors. The acyl precursor of diacyl phospholipids, 1-acyl-G3P (also known as lysophosphatidic acid) is shown for comparison. This precursor is mainly made in the endoplasmic reticulum. Blue box points to the ester bond at the *sn-1* position of the glycerol backbone **(A)**. The precursor of all ether lipids is 1-alkyl-glycerol-3-phosphate (1-alkyl-G3P) which is synthesized in peroxisomes. Red box points to ether linkage at the *sn-1* position of the glycerol backbone **(B)**. Structures of representative ether lipid species discussed in this review are shown with the ether linkage boxed in red **(C)**. Note that in the case of plasmenyl glycerophospholipids a vinyl ether bond is found at the *sn-1* position.

(plasmalogens) glycerophospholipids that compose approximately 20% of the mammalian total phospholipid pool (Dean and Lodhi, 2018), b) platelet-activating factor (PAF) that mediates inflammatory responses (Kelesidis et al., 2015), c) glycosylphosphatidylinositol (GPI) anchors, a lipid anchor for many cell-surface proteins added via posttranslational modifications (Kinoshita, 2016), and d) sulfogalactosylglycerolipid (SGG), also known as seminolipid, which is a testis-specific sulfoglycolipid essential for germ cell function in spermatogenesis (Zhang et al., 2005) (Figure 2). It is not clear when and where this array of ether lipids present in sperm is synthesized. The enzymes responsible for the initial steps in the synthesis of ether lipids are localized to the peroxisome where the alkyl precursor, 1-alkyl-glycerol-3-phosphate (1-alkyl-G3P), is made, and then is transported to the endoplasmic reticulum (ER) and Golgi, where it is consumed to produce complex ether lipids. It is currently accepted that sperm are devoid of these organelles, as these are lost with the residual body and cytoplasmic droplet during spermiogenesis and epididymal maturation, along with other membranous organelles such as lysosomes (Aveldano et al., 1992; Lüers et al., 2006), precluding the idea that they can synthesize ether lipids for themselves. As such, the source of ether lipids in sperm may be linked to early stages of the spermatogenesis or to acquisition during epididymal transit, particularly since the incorporation of exogenous phospholipids is possible through extracellular vesicles such as epididymosomes (Sullivan and Saez, 2013). Intriguingly, reports on sperm proteomes from different species have consistently identified peroxisomal resident proteins, including the enzymes involved in the production of ether lipids (Chauvin et al., 2012; Amaral et al., 2013; 2014; Castillo et al., 2018; Martín-Cano et al., 2020; Greither et al., 2023). Therefore, sperm seem to preserve selected peroxisomal pathways relevant for lipid metabolism. Here, we first summarize existing knowledge on the biological significance of ether lipid species plasmanyl and plasmenyl glycerophospholipids, PAF, SGG and GPI, particularly regarding sperm maturation and fertilization and their impact on male fertility and sperm performance. Using published data from highly purified human and mice sperm, we then embark in a thorough analysis of the sperm proteome identifying peroxisomal resident proteins and ether-lipid metabolic enzymes. This analysis unveils the presence of a truncated biosynthetic pathway where peroxisomal steps capable of producing ether lipid precursors are present, while late ER/Golgi steps are missing. Lastly, we discuss open questions related to lipid metabolism and peroxisomal functions in sperm, which require further research to be answered.

Ether lipids in the male reproductive system and in sperm

The vast majority of reports on ether lipids in the male reproductive system and sperm date back from two decades ago. The relatively recent identification of genes coding for all the enzymes involved in the biosynthesis of ether lipids (Dean and Lodhi, 2018), combined with powerful techniques using proteomics

and lipidomics of sperm samples has revamped research in this field, providing unique opportunities to advance in our knowledge on the role of these relegated lipids highly abundant in sperm.

Examples of the known roles of ether lipids in the different stages of sperm production and function are included in Figure 1.

a) Plasmanyl and plasmenyl phospholipids

During epididymal maturation, the number of phospholipids per cell decreases by around 50% in ram, bull, and rat sperm (Scott et al., 1967; Poulos et al., 1973; Aveldano et al., 1992) due to the loss of the cytoplasmic droplet. Interestingly, this reduction of phospholipids during epididymal transit is selective for diacyl phospholipids whereas plasmalogen levels do not significantly change, resulting in an increase in its proportion. In fact, early lipid analyses have revealed that both plasmanyl (O-) and plasmenyl (P-) forms of phosphatidylcholine and phosphatidylethanolamine are the major phospholipid classes in mature porcine and bovine sperm (Evans et al., 1980; Selivonchick et al., 1980). More recent lipidomics analysis of sperm from humans and other species have confirmed the prevalence of these ether lipids (Wood et al., 2016; Rivera-Egea et al., 2018; Ramal-Sanchez et al., 2020). Although the precise biological function of plasmanyl and plasmenyl glycerophospholipids in the male reproductive system has yet to be elucidated, it is hypothesized that the high proportion of these lipids in mature sperm protects these cells against oxidative damage due to their known antioxidant properties (Shan et al., 2021). Based on their chemical structure, plasmalogens have been considered to act as endogenous antioxidants. Due to their vinyl-ether linkage, plasmalogens are prone to oxidation serving as scavengers for radical species while protecting membrane lipids (Skaff et al., 2008; Broniec et al., 2011). It has been proposed that the susceptibility of plasmalogens to oxidative damage is due to a low hydrogen bond dissociation energy at the carbon adjacent to the vinyl ether bond (Murphy, 2001). Furthermore, the vinyl ether bond might be more exposed to the oxidative agents due to its proximity to the water-lipid interface, making them the first targets of ROS (Lankalapalli et al., 2009). In this regard, oxidation of plasmalogen by interaction with singlet oxygen/ROS occurs significantly faster than their diacyl counterparts (Broniec et al., 2011). However, the formation of further toxic molecules like fatty aldehydes generated from plasmalogens oxidation has also been reported, questioning their role towards a pro-oxidative effect (Stadelmann-Ingrand et al., 2004). This is relevant for sperm, considering the critical effect of ROS, oxidative stress and lipid peroxidation on sperm function, and their high content of polyunsaturated fatty acids incorporated to plasmalogens reviewed by Gibb et al., (2020), Gautier and Aurich, (2022).

Further challenging the idea that all plasmanyl/plasmenyl species play similar roles, is the fact that specific ether lipid species have been linked to opposite phenotypes in sperm performance. For example, 40:4 plasmanyl-PC [(O-40:4)] and 40:5 plasmenyl-PC [(P-40:5)] were identified as potential motility markers in canine spermatozoa (Lucio et al., 2017) while PC (O-42:4) and PE (P-34:2) were found to be significantly higher in sperm from patients without pregnancy success after intracytoplasmic sperm injection (Rivera-Egea et al., 2018). In addition, lack of plasmenyl species did not seem to affect sperm viability (Werner et al., 2020).

In summary, it is possible that ether lipid species with specific length and degree of unsaturation of their fatty acid tails may differentially affect the physical and functional properties of sperm. Indeed, it is known that sperm lipid composition can be influenced by factors such as the intake of dietary lipids (Saez and Drevet, 2019). As such, future investigations may be directed towards establishing a link between ether lipid saturation and alkyl/acyl chain length, the reproductive performance of sperm and its dependence on diet.

b) Platelet activating factor (PAF).

Studies in different species, including humans, have drawn a positive relationship between PAF content and sperm motility (Minhas et al., 1991; 1993; Roudebush et al., 2002), fertilization rates (Toledo et al., 2003) and clinical pregnancy after assisted reproduction treatments (Roudebush and Purnell, 2000). PAF acts through binding to its receptor, which has been found to be concentrated in the proximal head and midpiece of sperm from different species (Reinhardt et al., 1999; Levine et al., 2002). Human sperm samples with less than 50% forward motility possess low PAF receptor levels (Roudebush et al., 2000), leading to the hypothesis that this ether lipid is relevant for sperm function. This has been further supported by the presence of enzymes responsible for PAF catabolism and remodeling in human sperm and seminal plasma (Gujrati et al., 1987).

The association between PAF and sperm function has been studied using experiments where exogenous PAF was added during capacitation. Incubation of mouse sperm in a medium containing PAF resulted in an increase in fertilization rate, while incubation with a PAF receptor antagonist significantly decreased motility and fertilization rate, which was reversed with the addition of PAF (Sengoku et al., 1992). In this regards, PAF-acetylhydrolase, the primary enzyme responsible for inactivating PAF, has been proposed as a decapacitation factor (Letendre et al., 1992; Roudebush and Purnell, 2000; Zhu et al., 2006). More recently, PAF was found to dose-dependently induce the acrosome reaction in capacitated human spermatozoa and has been proposed to be associated with ERK-signaling pathways (Wu et al., 2020).

c) Sulfogalactosylglycerolipid (SGG)

SGG (also known as seminolipid) is an anionic glycolipid found selectively on the outer leaflet of mammalian primary spermatocytes membranes (Ishizuka, 1997; Tanphaichitr et al., 2003). SGG levels reach a maximum in round spermatids and remain constant in sperm (Iwamori et al., 2020; Kongmanas et al., 2021). Saturated C16:0-alkyl-C16:0-acyl is the primary species, with SGG containing other alkyl/acyl chain lengths comprising less than 10% of the total SGG content (Goto-Inoue et al., 2009).

SGG is essential in sperm production as spermatogenesis is arrested in animals lacking SGG synthesis, leading to infertility (Fujimoto et al., 2000; Honke et al., 2002). Moreover, male animals defective in SGG turnover are subfertile (Xu et al., 2011). Altogether, these results support the notion that SGG homeostasis in the testis is critical for normal spermatogenesis.

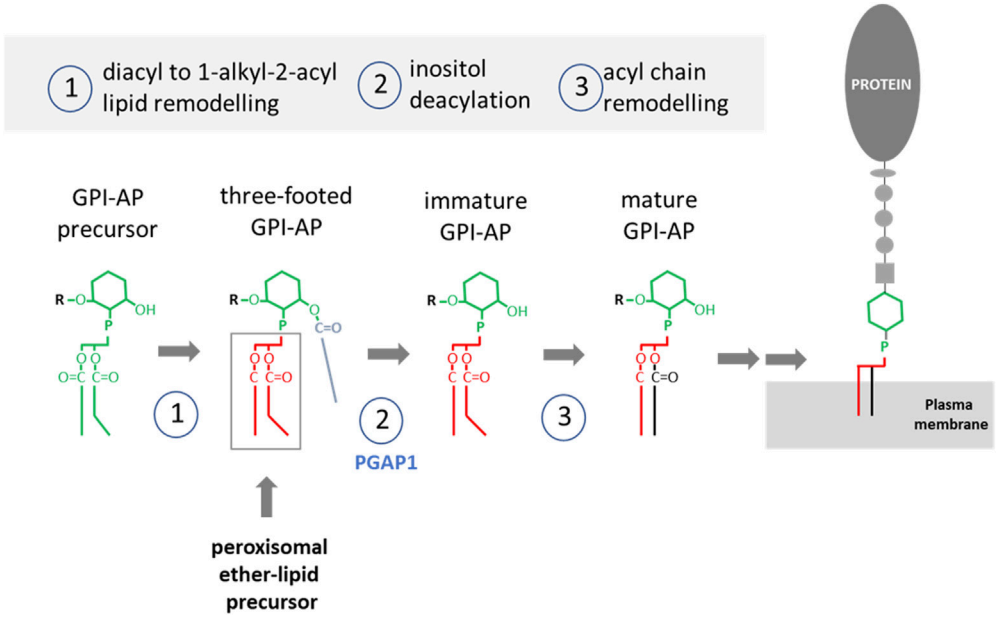

FIGURE 3
Key steps in the synthesis of GPI-APs. The lipid precursor is phosphatidylinositol (PI, green) containing two acyl tails with mostly unsaturated fatty acids in *sn-2*. 1) A diacyl to alkyl/acyl occurs through lipid remodelling involving a peroxisomal precursor. In addition the inositol ring gets palmitoylated. 2) The deacylase PGAP1 removes the acyl tail. 3) Further acyl tail remodeling occurs to introduce a saturated fatty acid in position sn-2. Once mature, the GPI-AP can be delivered to the plasma membrane. Modified from (Kinoshita, 2020).

In addition, SGG involvement in capacitation and fertilization has also been proposed. Several studies have shown that during capacitation, SGG migrates to the equatorial region of the sperm head (Flesch and Gadella, 2000), likely to allow the acrosome reaction to occur. Moreover, most SGG is localized in low-density detergent resistant membranes in capacitated sperm cells, reflecting the ability of SGG to form lipid rafts (Khalil et al., 2006). A role for SGG in sperm-ZP interaction has also been proposed (White et al., 2000; Weerachatyanukul et al., 2001).

In humans, the ratio of cholesterol to SGG is found to be a potential biomarker for semen quality. Oligoasthenozoospermic (i.e., low sperm number and motility) patients were found to have a five-fold higher cholesterol to SGG ratio than individuals with normal sperm motility values, although this ratio has not been implicated to affect fertility (Lopalco et al., 2019).

d) Glycosylphosphatidylinositol (GPI)

GPI is a lipid anchor added post-translationally to many cell-surface proteins (Figure 2). The GPI anchors are assembled on a phosphatidylinositol (PI) lipid in the ER, and then covalently attached to the carboxyl terminus of proteins possessing a GPI-attachment signal peptide (Kinoshita, 2016). In mammals, despite the fact that most free cellular phosphatidylinositols contain unsaturated diacyl glycerol forms, GPI anchors have mainly 1-alkyl-2-acyl phosphatidylinositol with saturated fatty acid tails that make them raft-compatible lipid structures (Kanzawa et al., 2009). GPI anchored proteins (GPI-AP) are typically associated with membrane microdomains or lipid rafts (Kinoshita, 2020).

GPI-APs have been described to play different roles in sperm function. Their origin on the sperm surface is primarily from *de novo* synthesis by spermatogenic cells and/or by transfer from epididymal exosomes (epididymosomes) (Martin-DeLeon, 2015; Yoshitake and Araki, 2020). Database analysis showed more than 25 GPI-APs from testicular origin, and many of them are present in sperm (Yoshitake and Araki, 2020). Among them, TEX101 and Ly6K are essential for male fertility as sperm from knockout mice are unable to reach the fertilization site in the oviduct (Fujihara et al., 2014). Other GPI-APs have been implicated in different steps of gamete interaction (i.e., GLIPR1-like protein 1, SPAM1, SPACA4) (Phelps et al., 1988; Lin et al., 1994; Shetty et al., 2003; Gibbs et al., 2010).

The key steps in the synthesis of GPI anchors are summarized in Figure 3 (Kinoshita, 2020). GPI-AP synthesis is initiated with a phosphatidylinositol precursor that is converted to a 1-alkyl 2- acyl "three-footed" PI moiety where the inositol ring is acylated in addition to the two alkyl/acyl tails of PI (Kinoshita, 2020). Incorporation of the alkyl-based lipid moiety in the GPI anchor occurs through a remodeling pathway. Although the exact enzymatic steps of this remodeling are unclear, it is known that the peroxisomal alkyl-phospholipid biosynthetic pathway is required for biosynthesis of mammalian GPI anchors (Kanzawa et al., 2009). The inositol ring in the GPI precursor first gets deacylated by the GPI inositol-deacylase Pgap1. Interestingly, Pgap1 has been detected in the proteome of mouse sperm (Chauvin et al., 2012) and PGAP1 knockout mice showed male infertility (Ueda et al., 2007). Therefore, lack of deacylation of the GPI anchor may abolish the subsequent fatty acid remodeling to incorporate the ether lipid moiety, which has been shown to be

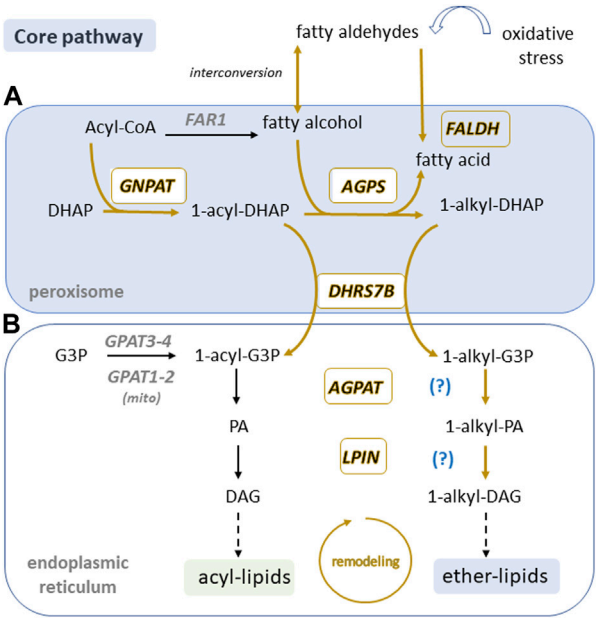

FIGURE 4
Peroxisomal core ether lipid biosynthetic pathway is present in sperm. In somatic cells, ether lipid biosynthesis is initiated in peroxisomes **(A)** and is finalized in the endoplasmic reticulum **(B)** where enzymes may be able to use both acyl and alkyl precursors (question mark). Boxed enzymes and pathways labelled in gold are found in sperm according to Chauvin et al., 2012; Amaral et al., 2013, 2014; Castillo et al., 2018; Martín-Cano et al., 2020 and Greither et al., 2023. Note peroxisome and ER compartments are believed to be missing in sperm. DHAP, Dihydroxyacetone phosphate; G3P, glycerol 3-phosphate; PA, phosphatidic acid; DAG, diacylglycerol; GNPAT, DHAP acyltransferase; AGPS, alkyl-DHAP synthase; DHRS7B, acyl/alkyl DHAP reductase; FAR; fatty acyl-CoA reductase; FALDH fatty aldehyde dehydrogenase; GPAT, G3-P acyltransferase; AGPAT, 1-acyl G3-P acyltransferase; LPIN, lipin PA phosphatase.

critical for raft association of GPI-APs (Maeda et al., 2007). This highlights the relevance of alkyl-GPI anchors in male fertility.

Ether lipid biosynthesis: the core peroxisomal pathway

The synthesis of all ether lipids is initiated by a core pathway that operates in peroxisomes and is conserved along evolution (Figure 4). In the first step of this pathway, dihydroxyacetone phosphate (DHAP) is acylated at the *sn*-1 position by the enzyme DHAP acyltransferase (GNPAT/DHAPAT) encoded by the mammalian *GNPAT* gene (Dean and Lodhi, 2018). The acyl group on 1-acyl-DHAP is subsequently exchanged for a fatty alcohol via alkyl-DHAP synthase (AGPS/ADHAPS) encoded by the *AGPS* gene. Therefore, this second step is responsible for the characteristic ether bond at the *sn*-1 position, generating the intermediate 1-alkyl-DHAP (Dean and Lodhi, 2018). Studies involving patients deficient in either GNPAT or AGPS revealed a dependence on the presence of the catalytically competent AGPS for the stability and maximal activity of GNPAT (Itzkovitz et al., 2012), leading to the hypothesis that the two enzymes form a functional complex in order to channel 1-acyl-DHAP from GNPAT to AGPS. Both enzymes are localized on the luminal side of the peroxisomal membrane (de Vet E. C. et al., 1997; Thai et al., 1997; Braverman and Moser, 2012) and may exist as a heterotrimeric complex in a 2:1 ratio of GNPAT to AGPS (Biermann et al., 1999; Piano et al., 2016).

The fatty alcohol (AGPS substrate), typically restricted to C16:0, C18:0, and C18:1 species, is generated from a peroxisomal membrane-associated fatty acyl-CoA reductase (FAR), which catalyzes the reduction of acyl-CoA (Cheng and Russell, 2004). Two isoforms, FAR1 and FAR2, with a 58% sequence identity are ubiquitously expressed, albeit at varying levels in different tissues (Cheng and Russell, 2004). FAR1 activity is regulated by the cellular levels of ether lipids as its degradation has been associated with high levels of plasmenyl-PE (Honsho et al., 2010). Therefore, FAR1 is strongly implicated to be the rate-limiting step in ether lipid biosynthesis (Honsho et al., 2013). Another source of fatty alcohols is derived from the interconversion with fatty aldehydes. Evidence supporting the presence of this FAR-independent pathway comes from patients with the inherited metabolic disease Sjögren–Larsson Syndrome (SLS) (Weustenfeld et al., 2019), characterized by a deficiency in the enzyme fatty aldehyde dehydrogenase (FALDH) which oxidizes fatty aldehydes to fatty acids (Keller et al., 2014; Weustenfeld et al., 2019). FALDH deficiency results in an increase of fatty alcohols inducing ether lipid synthesis, reflected by the accumulation of ether lipids in the brain of SLS patients (Staps et al., 2020; Koch et al., 2022).

The last step in the core peroxisomal pathway for ether lipid biosynthesis involves the conversion of 1-alkyl-DHAP to 1-alkyl-glycerol-3 phosphate (1-alkyl-G3P), mediated by an acyl/alkyl DHAP reductase (DHRS7B/ADHAPR) encoded by the *DHRS7B* gene (Lodhi et al., 2012; Honsho et al., 2020). This reductase has the capacity to also reduce 1-acyl-DHAP to 1-acyl-G3P, which is a precursor for the synthesis of phosphatidic acid and all derived acyl-glycerophospholipids (Figure 4). Although the expression of enzymes involved in the previous steps in the pathway are non-tissue specific, *DHRS7B* expression is high in thyroid, muscle, testis, epididymis, and seminal vesicle (Sjöstedt et al., 2020; Human Protein Atlas, 2022). 1-alkyl-G3P is exported from the peroxisome for further acylation and dephosphorylation in the ER, giving rise to the different species of ether lipids discussed above (Honsho et al., 2020).

Peroxisomal disorders associated with ether lipid deficiency typically result in severe clinical phenotypes, highlighting its significance in human pathophysiology. The deficiency of ether lipids could be due to mutations in the biosynthetic peroxisomal proteins (Figure 4) or defects in peroxisomal import complexes. Patients afflicted with Zellweger spectrum disorder lack the ability to assemble functional peroxisomes due to pathogenic variants of *PEX* genes, which encode proteins known as peroxins (Kim and Hettema, 2015). Among these genes are *PEX5* and *PEX7*, coding for cytosolic receptors that recognize **P**eroxisomal **T**argeting **S**ignals, PTS1 or PTS2, respectively, which are necessary for the import of matrix proteins to the peroxisome (Hasan et al., 2013). The core enzymes for the biosynthesis of ether lipids display peroxisomal import signals. Whereas GNPAT contains a PTS1 in its C-end, AGPS presents a PTS2 in its N-end (de Vet E. C. J. M. et al., 1997; Thai et al., 1997; Ofman et al., 1998). A second disorder, rhizomelic chondrodysplasia punctata (RCDP), corresponds specifically to

defects in the core ether lipid biosynthesis pathway. Five types of RCDP have been identified; RCDP1 and RCDP5 are associated with defects in the *PEX7* and *PEX5*, respectively, with their abnormal function preventing the import of GNPAT and AGPS to the peroxisomal matrix. Mutations leading to deficiencies in GNPAT, AGPS, and FAR1 are respectively referred to as RCDP2, RCDP3, and RCDP4 (Barøy et al., 2015). Clinical characteristics of RCDP include the shortening of limbs (rhizomelia), premature calcifications of the epiphyseal cartilage, microcephaly, facial dysmorphism, congenital cataracts, and psychomotor retardation (Dean and Lodhi, 2018). Approximately 50% of affected patients succumb by age six due to the severity of these phenotypes, and most do not survive past adolescence (Braverman and Moser, 2012). Studies to elucidate the underlying mechanisms that result in these phenotypes were primarily conducted in knockout mouse models. Mice deficient in GNPAT displayed symptoms observed in RCDP patients, such as dwarfism, cataract formation, and abnormalities in myelination (Rodemer et al., 2003; Teigler et al., 2009). Another symptom of ether lipid deficiency displayed in the mouse models includes male sterility, a characteristic not studied in humans due to the premature mortality associated with the disorder. A targeted disruption of the *GNPAT* gene results in abnormalities of the male reproductive system, including testicular atrophy, decreased seminiferous tubule diameter and absence of sperm in the epididymis (Rodemer et al., 2003). Based on the presence of apoptotic, multinucleated cells within the seminiferous epithelium and a lack of mature sperm or elongating spermatids, a spermatogenic arrest is hypothesized to occur between the pachytene spermatocytes and round spermatid stages (Rodemer et al., 2003). Blind-sterile2 (*bs2*) mice which express aberrantly spliced *AGPS* transcripts exhibited similar phenotypes (Liegel et al., 2011). These observations indicate an essential role of ether lipids in the male reproductive system, raising the question of whether they can serve as valid fertility markers.

A peroxisomal connection in sperm

As stated before, it is currently accepted that sperm are devoid of peroxisomes, but reports on the proteome of these cells from different species have consistently identified peroxisomal proteins (Chauvin et al., 2012; Amaral et al., 2013; 2014; Castillo et al., 2018; Martín-Cano et al., 2020; Greither et al., 2023). Based on available data on peroxisomal residents at the time, Amaral and others highlighted the presence of fifteen proteins with exclusive peroxisomal localization in the human sperm tail proteome. Furthermore, the expression of peroxisomal membrane protein 11 (PEX11) and peroxisomal 3-ketoacyl-CoA thiolase (ACAA1) was confirmed via immunocytochemistry (PEX11 and ACAA1) and Western blot (ACAA1) in highly purified sperm samples (Amaral et al., 2013). Consistent with MS/MS results using sperm tails, both Pex11 and Acaa1 proteins localized to sperm midpiece and in the case of Acaa1, the full protein was detected by Western blot, indicating it is potentially functional. In order to better define the extent of the peroxisomal presence in the sperm proteome we conducted a meticulous analysis of published proteomic data from human and mouse sperm (Chauvin et al., 2012; Amaral et al., 2013; 2014; Castillo et al., 2018; Greither et al., 2023) and compared it to the known mammalian peroxisomal resident list of proteins (Yifrach et al., 2018). Out of 195 peroxisomal residents, 138 proteins (~71%) were detected at least once in sperm from humans or mice, representing a much larger incidence than previously anticipated (Supplementary Table S1). It is worth noting that 12 peroxins are present in sperm, with only 4 remaining undetected. Interestingly, two of the missing peroxins (Pex2 and Pex10) belong to the Really Interesting Genes (RING) finger E3 ligases family, and have been recently shown to act as sensors of intracellular FAs, regulating lipolysis in response to ROS levels (Ding et al., 2021). Therefore sperm are equipped with a large set of peroxisomal proteins, with its most abundant matrix proteins (e.g.,.ACOX1, HSD17B4, CAT, THIKA, EPHX2), membrane proteins (ABCD1, ABCD3, ACBD5) and biogenesis associated peroxins in addition to the enzymes from the ether lipid pathway. This probably reflects the presence of a previously undetected peroxisomal remnant compartment which based on previous immunocytochemistry (PEX11 and ACAA1) may be localized to the midpiece in close proximity to mitochondria. Consistently among all sperm proteomes analyzed was the absence of the peroxisomal enzymes FAR1 and FAR2. As highlighted in Figure 4, the core enzymes GNPAT, AGPS and DHRS7B have all been detected in sperm proteomic studies, but the pathway seems to be FAR-independent, suggesting a detrimental role for fatty alcohols in sperm. Our analysis also points to a truncated ether-lipid biosynthetic pathway, with few extra peroxisomal steps present in sperm. A large set of LysoPA acyltransferases (AGPAT1, 2, 3, and 5) and a PA phosphohydrolase (LPIN1), which are the putative enzymes responsible for the production of diacyl- and 1-alkyl-2 acyl- PA and DAG respectively, are also present in sperm (Figure 4). After these steps, the enzymes of the Kennedy pathway known to consume the acyl- and alkyl-DAG intermediates in the ER/Golgi, as well as PEDS, the desaturase that introduces the vinyl bond for the synthesis of plasmalogens (Werner et al., 2020), all seem to be missing from the sperm proteome.

The presence of this truncated ether-lipid biosynthetic pathway suggests a divergent role for the peroxisomal core pathway in sperm. Given the pathway is FAR-independent it must consume an alternative source of fatty-alcohols at the AGPS step. The production of both fatty-aldehydes and fatty-alcohols from the catabolism of membrane lipids in sperm has been documented (Evans et al., 2021). Interestingly, mitochondrial cytochrome c has been found to act as a plasmalogenase that cleaves plasmenylcholine and plasmenylethanolamine at the *sn-1* vinyl ether linkage, releasing fatty aldehydes in response to oxidative stress (Jenkins et al., 2018). The presence of peroxisomal FALDH in sperm also supports a role of a putative peroxisomal-like compartment in the detoxification of fatty aldehydes.

We therefore propose that sperm contain a repurposed FAR-independent ether lipid core pathway, probably localized to a peroxisome-remnant compartment intimately connected to mitochondria in order to act as a sink for toxic fatty alcohols and fatty aldehydes produced from lipid catabolism (Figure 5). Although somehow limited, evidence on the midpiece localization of the peroxisomal residents PEX11 and

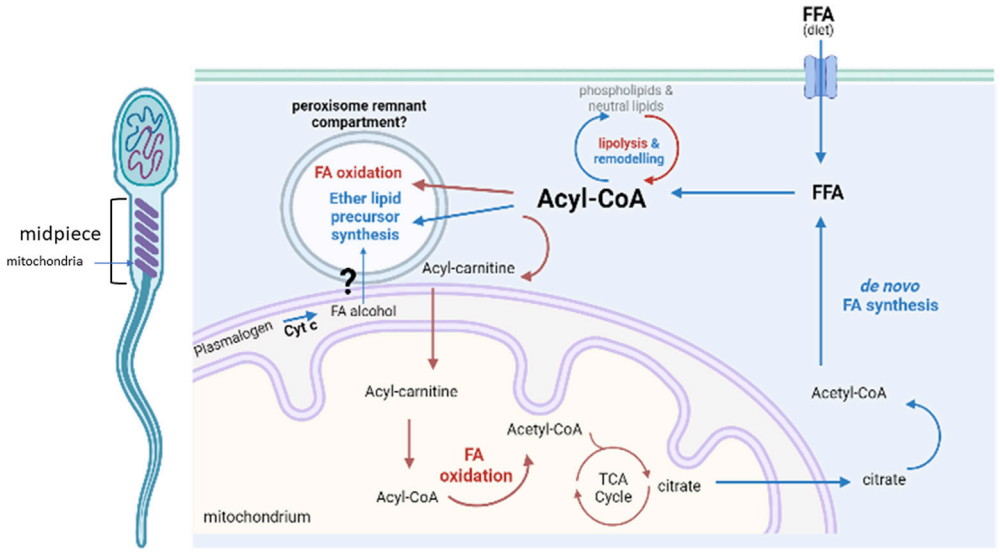

FIGURE 5
Metabolic lipid pathways present in sperm. Proposed localization of the core peroxisomal pathway to a remnant peroxisomal compartment in close contact with mitochondria, for the synthesis ether lipid precursors with a main fatty alcohol detoxifying role. Abbreviations: Cyt c, cytochrome c; FFA, free fatty acid; FA, fatty acid; TCA, tri-carboxylic acids; CoA, coenzyme A. Created with BioRender.com.

ACAA1 supports the close proximity of such compartment to mitochondria (Amaral et al., 2013).

In summary, sperm ether lipids, produced in early stages of spermatogenesis and/or provided by the epididymis, play a variety of roles in sperm function included in this review, and probably others to be elucidated in future studies. In addition, this review puts forward the concept that an enhanced collaboration between mitochondria and peroxisomal-like remnant structures may exist in sperm, in order to deal with the oxidative stress burden generated during sperm performance by the high mitochondrial activity (Balbach et al., 2020; Ferreira et al., 2021; Giaccagli et al., 2021).

Concluding remarks

Ether lipids are particularly abundant in sperm. As we have described in the first sections of this review, their diversity and relevance for sperm production, maturation, and function have been addressed by different laboratories over time. Many outstanding questions remain regarding the regulation of their synthesis and metabolism during the various steps preparing sperm for fertilization. The analysis of available sperm proteomic data carried out in this review identified key lipid metabolic pathways, opening new avenues in this regard. It is well known that sperm damage generated by oxidative stress as a consequence of a systemic inflammation produced by exogenous insults is one of the main causes of male infertility (Agarwal et al., 2018; Su et al., 2022). Therefore, the potential involvement of peroxisomal enzymes in a new antioxidant mechanism to help sperm deal with this damage contributes critical information that has the potential of significantly improving the diagnosis and treatment of male infertility. Future research is needed to challenge the proposed hypothesis and to further investigate the localization of the large peroxisomal subproteome present in sperm.

Search methods

We performed this study by searching for keywords from PubMed and Web of Science on all articles in English published prior to April 2023. Search terms were based on the following keywords: Ether lipids, Plasmanyl, Plasmenyl, Plasmalogen, Platelet-activating factor, Sulfogalactosylglycerolipid, Seminolipid, Glycosylphosphatidylinositol, GNPAT/DHAPAT, AGPS, DHRS7B, fatty alcohols, oxidative stress, proteomics, and peroxisome combined to male reproductive tract, sperm and fertilization. In all cases, references cited in the analyzed articles were also considered.

Author contributions

DC and VZ: conceptualization, data curation, funding acquisition, investigation, writing—original draft, review and editing. MH, WL, LG, and VL: data curation, investigation, and writing—original draft. VD: data curation, funding acquisition and writing—review and editing. All authors contributed to the article and approved the submitted version.

Funding

This study was partially supported by National Agency for Scientific and Technological Promotion (ANPCyT) Grant PICT 2019-1508 to DC, and the National Research Council (PIP 2022-2024) of Argentina to DC and VD and by a Discovery Grant and a

Discovery Accelerator Supplement from the Natural Sciences and Engineering Research Council (NSERC) PIN303585-2016 to VZ.

Acknowledgments

The authors would like to thank Alina Bertolesi for insightful comments about this manuscript.

Conflict of interest

The authors declare that the research was conducted in the absence of any commercial or financial relationships that could be construed as a potential conflict of interest.

Publisher's note

Supplementary material

The Supplementary Material for this article can be found online at: https://www.frontiersin.org/articles/10.3389/fcell.2023.1166232/full#supplementary-material

References

Agarwal, A., Rana, M., Qiu, E., AlBunni, H., Bui, A. D., and Henkel, R. (2018). Role of oxidative stress, infection and inflammation in male infertility. *Andrologia* 50, 13126. doi:10.1111/and.13126

Aitken, R. J., and Baker, M. A. (2006). Oxidative stress, sperm survival and fertility control. *Mol. Cell. Endocrinol.* 250, 66–69. doi:10.1016/j.mce.2005.12.026

Aitken, R. J., Clarkson, J. S., and Fishel, S. (1989). Generation of reactive oxygen species, lipid peroxidation, and human sperm function. *Biol. Reprod.* 41, 183–197. doi:10.1095/biolreprod41.1.183

Aitken, R. J., Drevet, J. R., Moazamian, A., and Gharagozloo, P. (2022). Male infertility and oxidative stress: A focus on the underlying mechanisms. *Antioxidants* 11, 306. doi:10.3390/antiox11020306

Amaral, A., Castillo, J., Estanyol, J. M., Ballesca, J. L., Ramalho-Santos, J., and Oliva, R. (2013). Human sperm tail proteome suggests new endogenous metabolic pathways. *Mol. Cell. Proteomics* 12, 330–342. doi:10.1074/mcp.M112.020552

Amaral, A., Castillo, J., Ramalho-Santos, J., and Oliva, R. (2014). The combined human sperm proteome: Cellular pathways and implications for basic and clinical science. *Hum. Reprod. Update* 20, 40–62. doi:10.1093/humupd/dmt046

Aveldano, M. I., Rotstein, N. P., and Vermouth, N. T. (1992). Lipid remodelling during epididymal maturation of rat spermatozoa. Enrichment in plasmenylcholines containing long-chain polyenoic fatty acids of the n-9 series. *Biochem. J.* 283, 235–241. doi:10.1042/bj2830235

Baba, D., Kashiwabara, S., Honda, A., Yamagata, K., Wu, Q., Ikawa, M., et al. (2002). Mouse sperm lacking cell surface hyaluronidase PH-20 can pass through the layer of cumulus cells and fertilize the egg. *J. Biol. Chem.* 277, 30310–30314. doi:10.1074/jbc.M204596200

Balbach, M., Gracia Gervasi, M., Hidalgo, D. M., Visconti, P. E., Levin, L. R., and Buck, J. (2020). Metabolic changes in mouse sperm during capacitation. *Biol. Reprod.* 103, 791–801. doi:10.1093/biolre/ioaa114

Barøy, T., Koster, J., Strømme, P., Ebberink, M. S., Misceo, D., Ferdinandusse, S., et al. (2015). A novel type of rhizomelic chondrodysplasia punctata, RCDP5, is caused by loss of the PEX5 long isoform. *Hum. Mol. Genet.* 24, 5845–5854. doi:10.1093/hmg/ddv305

Biermann, J., Just, W. W., Wanders, R. J. A., and Van Den Bosch, H. (1999). Alkyl-dihydroxyacetone phosphate synthase and dihydroxyacetone phosphate acyltransferase form a protein complex in peroxisomes. *Eur. J. Biochem.* 261, 492–499. doi:10.1046/j.1432-1327.1999.00295.x

Braverman, N. E., and Moser, A. B. (2012). Functions of plasmalogen lipids in health and disease. *Biochim. Biophys. Acta - Mol. Basis Dis.* 1822, 1442–1452. doi:10.1016/j.bbadis.2012.05.008

Broniec, A., Klosinski, R., Pawlak, A., Wrona-Krol, M., Thompson, D., and Sarna, T. (2011). Interactions of plasmalogens and their diacyl analogs with singlet oxygen in selected model systems. *Free Radic. Biol. Med.* 50, 892–898. doi:10.1016/j.freeradbiomed.2011.01.002

Castillo, J., Jodar, M., and Oliva, R. (2018). The contribution of human sperm proteins to the development and epigenome of the preimplantation embryo. *Hum. Reprod. Update* 24, 535–555. doi:10.1093/humupd/dmy017

Chauvin, T., Xie, F., Liu, T., Nicora, C. D., Yang, F., Camp II, D. G., et al. (2012). A systematic analysis of a deep mouse epididymal sperm proteome. *Biol. Reprod.* 87, 141. doi:10.1095/biolreprod.112.104208

Cheng, J. B., and Russell, D. W. (2004). Mammalian wax biosynthesis: I. Identification of two fatty acyl-coenzyme A reductases with different substrate specificities and tissue distributions. *J. Biol. Chem.* 279, 37789–37797. doi:10.1074/jbc.M406225200

de Vet, E. C., Biermann, J., and van den Bosch, H. (1997a). Immunological localization and tissue distribution of alkyldihydroxyacetonephosphate synthase and deficiency of the enzyme in peroxisomal disorders. *Eur. J. Biochem.* 247, 511–517. doi:10.1111/j.1432-1033.1997.00511.x

de Vet, E. C. J. M., van den Broek, B. T. E., and van den Bosch, H. (1997b). Nucleotide sequence of human alkyl-dihydroxyacetonephosphate synthase cDNA reveals the presence of a peroxisomal targeting signal 2. *Biochim. Biophys. Acta - Lipids Lipid Metab.* 1346, 25–29. doi:10.1016/S0005-2760(97)00014-3

Dean, J. M., and Lodhi, I. J. (2018). Structural and functional roles of ether lipids. *Protein Cell* 9, 196–206. doi:10.1007/s13238-017-0423-5

Ding, L., Sun, W., Balaz, M., He, A., Klug, M., Wieland, S., et al. (2021). Peroxisomal β-oxidation acts as a sensor for intracellular fatty acids and regulates lipolysis. *Nat. Metab.* 3, 1648–1661. doi:10.1038/s42255-021-00489-2

Evans, H. C., Dinh, T. T. N., Hardcastle, M. L., Gilmore, A. A., Ugur, M. R., Hitit, M., et al. (2021). Advancing semen evaluation using lipidomics. *Front. Vet. Sci.* 8, 601794. doi:10.3389/fvets.2021.601794

Evans, R. W., Weaver, D. E., and Clegg, E. D. (1980). Diacyl, alkenyl, and alkyl ether phospholipids in ejaculated, *in utero*-and *in vitro*-incubated porcine spermatozoa. *J. Lipid Res.* 21, 223–228. doi:10.1016/s0022-2275(20)39828-x

Ferreira, J. J., Cassina, A., Irigoyen, P., Ford, M., Pietroroia, S., Peramsetty, N., et al. (2021). Increased mitochondrial activity upon CatSper channel activation is required for mouse sperm capacitation. *Redox Biol.* 48, 102176. doi:10.1016/j.redox.2021.102176

Flesch, F. M., and Gadella, B. M. (2000). Dynamics of the mammalian sperm plasma membrane in the process of fertilization. *Biochim. Biophys. Acta* 1469, 197–235. doi:10.1016/s0304-4157(00)00018-6

Fujihara, Y., Okabe, M., and Ikawa, M. (2014). GPI-anchored protein complex, LY6K/TEX101, is required for sperm migration into the oviduct and male fertility in mice. *Biol. Reprod.* 90, 60. doi:10.1095/biolreprod.113.112888

Fujihara, Y., Tokuhiro, K., Muro, Y., Kondoh, G., Araki, Y., Ikawa, M., et al. (2013). Expression of TEX101, regulated by ACE, is essential for the production of fertile mouse spermatozoa. *Proc. Natl. Acad. Sci.* 110, 8111–8116. doi:10.1073/pnas.1222166110

Fujimoto, H., Tadano-Aritomi, K., Tokumasu, A., Ito, K., Hikita, T., Suzuki, K., et al. (2000). Requirement of seminolipid in spermatogenesis revealed by UDP-galactose: ceramide galactosyltransferase-deficient mice. *J. Biol. Chem.* 275, 22623–22626. doi:10.1074/jbc.C000200200

Gautier, C., and Aurich, C. (2022). Fine feathers make fine birds – the mammalian sperm plasma membrane lipid composition and effects on assisted reproduction. *Anim. Reprod. Sci.* 246, 106884. doi:10.1016/j.anireprosci.2021.106884

Giaccagli, M. M., Gómez-Elías, M. D., Herzfeld, J. D., Marín-Briggiler, C. I., Cuasnicú, P. S., Cohen, D. J., et al. (2021). Capacitation-Induced mitochondrial activity is required for sperm fertilizing ability in mice by modulating hyperactivation. *Front. Cell Dev. Biol.* 9, 767161. doi:10.3389/fcell.2021.767161

Gibb, Z., Griffin, R. A., Aitken, R. J., and De Iuliis, G. N. (2020). Functions and effects of reactive oxygen species in male fertility. *Anim. Reprod. Sci.* 220, 106456. doi:10.1016/j.anireprosci.2020.106456

Gibbs, G. M., Lo, J. C. Y., Nixon, B., Jamsai, D., O'Connor, A. E., Rijal, S., et al. (2010). Glioma pathogenesis-related 1-like 1 is testis enriched, dynamically modified, and redistributed during male germ cell maturation and has a potential role in sperm-oocyte binding. *Endocrinology* 151, 2331–2342. doi:10.1210/en.2009-1255

Gomez, E., Irvine, D. S., and Aitken, R. J. (1998). Evaluation of a spectrophotometric assay for the measurement of malondialdehyde and 4-hydroxyalkenals in human spermatozoa: Relationships with semen quality and sperm function. *Int. J. Androl.* 21, 81–94. doi:10.1046/j.1365-2605.1998.00106.x

Goto-Inoue, N., Hayasaka, T., Zaima, N., and Setou, M. (2009). The specific localization of seminolipid molecular species on mouse testis during testicular maturation revealed by imaging mass spectrometry. *Glycobiology* 19, 950–957. doi:10.1093/glycob/cwp089

Greither, T., Dejung, M., Behre, H. M., Butter, F., and Herlyn, H. (2023). The human sperm proteome—toward a panel for male fertility testing. Androl. *n/a*. doi:10.1111/andr.13431

Gujrati, V. R., Naukam, R. J., and Sastry, B. V. R. R. (1987). Enzymatic deacetylation and acetylation of ether phospholipids related to platelet-activating factor in human semen with short and long liquefaction times. *Ann. N. Y. Acad. Sci.* 513, 583–585. doi:10.1111/j.1749-6632.1987.tb25114.x

Hasan, S., Platta, H. W., and Erdmann, R. (2013). Import of proteins into the peroxisomal matrix. *Front. Physiol.* 4, 261. doi:10.3389/fphys.2013.00261

Honke, K., Hirahara, Y., Dupree, J., Suzuki, K., Popko, B., Fukushima, K., et al. (2002). Paranodal junction formation and spermatogenesis require sulfoglycolipids. *Proc. Natl. Acad. Sci. U. S. A.* 99, 4227–4232. doi:10.1073/pnas.032068299

Honsho, M., Asaoku, S., and Fujiki, Y. (2010). Posttranslational regulation of fatty acyl-CoA reductase 1, Far1, controls ether glycerophospholipid synthesis. *J. Biol. Chem.* 285, 8537–8542. doi:10.1074/jbc.M109.083311

Honsho, M., Asaoku, S., Fukumoto, K., and Fujiki, Y. (2013). Topogenesis and homeostasis of fatty Acyl-CoA reductase 1. *J. Biol. Chem.* 288, 34588–34598. doi:10.1074/jbc.M113.498345

Honsho, M., Tanaka, M., Zoeller, R. A., and Fujiki, Y. (2020). Distinct functions of acyl/alkyl dihydroxyacetonephosphate reductase in peroxisomes and endoplasmic reticulum. *Front. Cell Dev. Biol.* 8, 855. doi:10.3389/fcell.2020.00855

Human Protein Atlas (2022). Hum. Protein atlas. Available at: https://www.proteinatlas.org/.

Hunnicutt, G. R., Primakoff, P., and Myles, D. G. (1996). Sperm surface protein PH-20 is bifunctional: One activity is a hyaluronidase and a second, distinct activity is required in secondary sperm-zona binding. *Biol. Reprod.* 55, 80–86. doi:10.1095/biolreprod55.1.80

Ishizuka, I. (1997). Chemistry and functional distribution of sulfoglycolipids. *Prog. Lipid Res.* 36, 245–319. doi:10.1016/S0163-7827(97)00011-8

Itzkovitz, B., Jiralerspong, S., Nimmo, G., Loscalzo, M., Horovitz, D. D. G., Snowden, A., et al. (2012). Functional characterization of novel mutations in GNPAT and AGPS, causing rhizomelic chondrodysplasia punctata (RCDP) types 2 and 3. *Hum. Mutat.* 33, 189–197. doi:10.1002/humu.21623

Iwamori, M., Adachi, S., Lin, B., Tanaka, K., Aoki, D., and Nomura, T. (2020). Spermatogenesis-associated changes of fucosylated glycolipids in murine testis. *Hum. Cell* 33, 23–28. doi:10.1007/s13577-019-00304-x

Jakop, U., Müller, K., Müller, P., Neuhauser, S., Rodríguez, I. C., Grunewald, S., et al. (2022). Seminal lipid profiling and antioxidant capacity: A species comparison. *PLoS One* 17 (3), e0264675. doi:10.1371/journal.pone.0264675

Jenkins, C. M., Yang, K., Liu, G., Moon, S. H., Dilthey, B. G., and Gross, R. W. (2018). Cytochrome c is an oxidative stress-activated plasmalogenase that cleaves plasmenylcholine and plasmenylethanolamine at the sn-1 vinyl ether linkage. *J. Biol. Chem.* 293, 8693–8709. doi:10.1074/jbc.RA117.001629

Jiménez-Rojo, N., and Riezman, H. (2019). On the road to unraveling the molecular functions of ether lipids. *FEBS Lett.* 593, 2378–2389. doi:10.1002/1873-3468.13465

Jones, R., and Mann, T. (1976). Lipid peroxides in spermatozoa; formation, role of plasmalogen, and physiological significance. *Proc. R. Soc. Lond. - Biol. Sci.* 193, 317–333. doi:10.1098/rspb.1976.0050

Kanzawa, N., Maeda, Y., Ogiso, H., Murakami, Y., Taguchi, R., and Kinoshita, T. (2009). Peroxisome dependency of alkyl-containing GPI-anchor biosynthesis in the endoplasmic reticulum. *Proc. Natl. Acad. Sci. U. S. A.* 106, 17711–17716. doi:10.1073/pnas.0904762106

Kelesidis, T., Papakonstantinou, V., Detopoulou, P., Fragopoulou, E., Chini, M., Lazanas, M. C., et al. (2015). The role of platelet-activating factor in chronic inflammation, immune activation, and comorbidities associated with HIV infection. *AIDS Rev.* 17, 191–201.

Keller, M. A., Zander, U., Fuchs, J. E., Kreutz, C., Watschinger, K., Mueller, T., et al. (2014). A gatekeeper helix determines the substrate specificity of Sjögren–Larsson Syndrome enzyme fatty aldehyde dehydrogenase. *Nat. Commun.* 5, 4439. doi:10.1038/ncomms5439

Khalil, M. B., Chakrabandhu, K., Xu, H., Weerachatyanukul, W., Buhr, M., Berger, T., et al. (2006). Sperm capacitation induces an increase in lipid rafts having zona pellucida binding ability and containing sulfogalactosylglycerolipid. *Dev. Biol.* 290, 220–235. doi:10.1016/j.ydbio.2005.11.030

Kim, P. K., and Hettema, E. H. (2015). Multiple pathways for protein transport to peroxisomes. *J. Mol. Biol.* 427, 1176–1190. doi:10.1016/j.jmb.2015.02.005

Kinoshita, T. (2020). Biosynthesis and biology of mammalian GPI-anchored proteins. *Open Biol.* 10, 190290. doi:10.1098/rsob.190290

Kinoshita, T. (2016). Glycosylphosphatidylinositol (GPI) anchors: Biochemistry and cell biology: Introduction to a thematic review series. *J. Lipid Res.* 57, 4–5. doi:10.1194/jlr.E065417

Koch, J., Watschinger, K., Werner, E. R., and Keller, M. A. (2022). Tricky isomers—the evolution of analytical strategies to characterize plasmalogens and plasmanyl ether lipids. *Front. Cell Dev. Biol.* 10, 864716. doi:10.3389/fcell.2022.864716

Kongmanas, K., Saewu, A., Kiattiburut, W., Baker, M. A., Faull, K. F., Burger, D., et al. (2021). Accumulation of seminolipid in sertoli cells is associated with increased levels of reactive oxygen species and male subfertility: Studies in aging arsa null male mice. *Antioxidants* 10, 912. doi:10.3390/antiox10060912

Lankalapalli, R. S., Eckelkamp, J. T., Sircar, D., Ford, D. A., Subbaiah, P. V., and Bittman, R. (2009). Synthesis and antioxidant properties of an unnatural plasmalogen analogue bearing a trans O-vinyl ether linkage. *Org. Lett.* 11, 2784–2787. doi:10.1021/ol9009078

Letendre, E. D., Miron, P., Roberts, K. D., and Langlais, J. (1992). Platelet-activating factor acetylhydrolase in human seminal plasma. *Fertil. Steril.* 57, 193–198. doi:10.1016/S0015-0282(16)54800-6

Levine, A. S., Kort, H. I., Toledo, A. A., and Roudebush, W. E. (2002). A review of the effect of platelet-activating factor on male reproduction and sperm function. *J. Androl.* 23, 471–476. doi:10.1002/j.1939-4640.2002.tb02262.x

Leßig, J., Gey, C., Süß, R., Schiller, J., Glander, H.-J., and Arnhold, J. (2004). Analysis of the lipid composition of human and boar spermatozoa by MALDI-TOF mass spectrometry, thin layer chromatography and 31P NMR spectroscopy. *Comp. Biochem. Physiol. Part B Biochem. Mol. Biol.* 137, 265–277. doi:10.1016/j.cbpc.2003.12.001

Liegel, R., Chang, B., Dubielzig, R., and Sidjanin, D. J. (2011). Blind sterile 2 (bs2), a hypomorphic mutation in Agps, results in cataracts and male sterility in mice. *Mol. Genet. Metab.* 103, 51–59. doi:10.1016/j.ymgme.2011.02.002

Lin, Y., Mahan, K., Lathrop, W. F., Myles, D. G., and Primakoff, P. (1994). A hyaluronidase activity of the sperm plasma membrane protein PH-20 enables sperm to penetrate the cumulus cell layer surrounding the egg. *J. Cell Biol.* 125, 1157–1163. doi:10.1083/jcb.125.5.1157

Lodhi, I. J., Yin, L., Jensen-Urstad, A. P. L., Funai, K., Coleman, T., Baird, J. H., et al. (2012). Inhibiting adipose tissue lipogenesis reprograms thermogenesis and PPARγ activation to decrease diet-induced obesity. *Cell Metab.* 16, 189–201. doi:10.1016/j.cmet.2012.06.013

Lopalco, P., Vitale, R., Cho, Y. S., Totaro, P., Corcelli, A., and Lobasso, S. (2019). Alteration of cholesterol sulfate/seminolipid ratio in semen lipid profile of men with oligoasthenozoospermia. *Front. Physiol.* 10, 1344. doi:10.3389/fphys.2019.01344

Lucio, C. F., Brito, M. M., Angrimani, D. S. R., Belaz, K. R. A., Morais, D., Zampieri, D., et al. (2017). Lipid composition of the canine sperm plasma membrane as markers of sperm motility. *Reprod. Domest. Anim.* 52, 208–213. doi:10.1111/rda.12860

Lüers, G. H., Thiele, S., Schad, A., Völkl, A., Yokota, S., and Seitz, J. (2006). Peroxisomes are present in murine spermatogonia and disappear during the course of spermatogenesis. *Histochem. Cell Biol.* 125, 693–703. doi:10.1007/s00418-005-0114-9

Maeda, Y., Tashima, Y., Houjou, T., Fujita, M., Yoko-o, T., Jigami, Y., et al. (2007). Fatty acid remodeling of GPI-anchored proteins is required for their raft association. *Mol. Biol. Cell* 18, 1497–1506. doi:10.1091/mbc.e06-10-0885

Martín-Cano, F. E., Gaitskell-Phillips, G., Ortiz-Rodríguez, J. M., Silva-Rodríguez, A., Román, Á., Rojo-Domínguez, P., et al. (2020). Proteomic profiling of stallion spermatozoa suggests changes in sperm metabolism and compromised redox regulation after cryopreservation. *J. Proteomics* 221, 103765. doi:10.1016/j.jprot.2020.103765

Martin-DeLeon, P. (2015). Epididymosomes: Transfer of fertility-modulating proteins to the sperm surface. *Asian J. Androl.* 17, 720–725. doi:10.4103/1008-682X.155538

Minhas, B. S., Kim, H. N., Zhu, Y. P., Ripps, B. A., and Buster, J. E. (1993). Platelet activating factor treatment of spermatozoa enhances fertilization rates of rabbit oocytes utilizing subzonal insertion of sperm. *Theriogenology* 39, 269. doi:10.1016/0093-691x(93)90124-n

Minhas, B. S., Kumar, R., Ricker, D. D., Robertson, J. L., and Dodson, M. G. (1991). The presence of platelet-activating factor-like activity in human spermatozoa. *Fertil. Steril.* 55, 372–376. doi:10.1016/s0015-0282(16)54132-6

Minhas, B. S. (1993). Platelet-activating factor treatment of human spermatozoa enhances fertilization potential. *Am. J. Obstet. Gynecol.* 168, 1314–1317. doi:10.1016/0002-9378(93)90387-x

Murphy, R. C. (2001). Free-radical-Induced oxidation of arachidonoyl plasmalogen phospholipids: Antioxidant mechanism and precursor pathway for bioactive eicosanoids. *Chem. Res. Toxicol.* 14, 463–472. doi:10.1021/tx000250t

Nakamura, Y., Yoshida, M., Tanigawa, K., Harada, A., Kihara-Negishi, F., Maruyama, K., et al. (2021). Deficiency of type I platelet-activating factor-acetylhydrolase catalytic subunits causes an increase in body weight. *Biol. Pharm. Bull.* 44, 920–925. doi:10.1248/bpb.b20-00936

Nikolopoulou, M., Soucek, D. A., and Vary, J. C. (1985). Changes in the lipid content of boar sperm plasma membranes during epididymal maturation. *Biochim. Biophys. Acta* 815, 486–498. doi:10.1016/0005-2736(85)90377-3

O'Flaherty, C., and Scarlata, E. (2022). Oxidative stress and reproductive function: The protection of mammalian spermatozoa against oxidative stress. *Reproduction* 164, F67–F78. doi:10.1530/REP-22-0200

Ofman, R., Hettema, E. H., Hogenhout, E. M., Caruso, U., Muijsers, A. O., and Wanders, R. J. A. (1998). Acyl-CoA:Dihydroxyacetonephosphate acyltransferase: Cloning of the human cDNA and resolution of the molecular basis in rhizomelic chondrodysplasia punctata type 2. *Hum. Mol. Genet.* 7, 847–853. doi:10.1093/hmg/7.5.847

Oresti, G. M., Luquez, J. M., Furland, N. E., and Aveldaño, M. I. (2011). Uneven distribution of ceramides, sphingomyelins and glycerophospholipids between heads and tails of rat spermatozoa. *Lipids* 46, 1081–1090. doi:10.1007/s11745-011-3601-x

Parks, J. E., and Lynch, D. V. (1992). Lipid composition and thermotropic phase behavior of boar, bull, stallion, and rooster sperm membranes. *Cryobiology* 29, 255–266. doi:10.1016/0011-2240(92)90024-v

Phelps, B. M., Primakoff, P., Koppel, D. E., Low, M. G., and Myles, D. G. (1988). Restricted lateral diffusion of PH-20, a PI-anchored sperm membrane protein. *Sci. (80-.)* 240, 1780–1782. doi:10.1126/science.3381102

Piano, V., Nenci, S., Magnani, F., Aliverti, A., and Mattevi, A. (2016). Recombinant human dihydroxyacetonephosphate acyl-transferase characterization as an integral monotopic membrane protein. *Biochem. Biophys. Res. Commun.* 481, 51–58. doi:10.1016/j.bbrc.2016.11.019

Poulos, A., Voglmayr, J. K., and White, I. G. (1973). Phospholipid changes in spermatozoa during passage through the genital tract of the bull. *Biochim. Biophys. Acta (BBA)-Lipids Lipid Metab.* 306, 194–202. doi:10.1016/0005-2760(73)90225-7

Ramal-Sanchez, M., Bernabo, N., Tsikis, G., Blache, M.-C. C., Labas, V., Druart, X., et al. (2020). Progesterone induces sperm release from oviductal epithelial cells by modifying sperm proteomics, lipidomics and membrane fluidity. *Mol. Cell. Endocrinol.* 504, 110723. doi:10.1016/j.mce.2020.110723

Reinhardt, J. C., Cui, X., and Roudebush, W. E. (1999). Immunofluorescent evidence of the platelet-activating factor receptor on human spermatozoa. *Fertil. Steril.* 71, 941–942. doi:10.1016/S0015-0282(99)00096-5

Rivera-Egea, R., Garrido, N., Sota, N., Meseguer, M., Remohí, J., and Dominguez, F. (2018). Sperm lipidic profiles differ significantly between ejaculates resulting in pregnancy or not following intracytoplasmic sperm injection. *J. Assist. Reprod. Genet.* 35, 1973–1985. doi:10.1007/s10815-018-1284-4

Rodemer, C., Thai, T. P., Brugger, B., Kaercher, T., Werner, H., Nave, K. A., et al. (2003). Inactivation of ether lipid biosynthesis causes male infertility, defects in eye development and optic nerve hypoplasia in mice. *Hum. Mol. Genet.* 12, 1881–1895. doi:10.1093/hmg/ddg191

Roudebush, W. E., Gerald, M. S., Cano, J. A., Lussier, I. D., Westergaard, G., and Higley, J. D. (2002). Relationship between platelet-activating factor concentration in rhesus monkey (*Macaca mulatta*) spermatozoa and sperm motility. *Am. J. Primatol.* 56, 1–7. doi:10.1002/ajp.1059

Roudebush, W. E., and Purnell, E. T. (2000). Platelet-activating factor content in human spermatozoa and pregnancy outcome. *Fertil. Steril.* 74, 257–260. doi:10.1016/S0015-0282(00)00646-4

Roudebush, W. E., Wild, M. D., and Maguire, E. H. (2000). Expression of the platelet-activating factor receptor in human spermatozoa: Differences in messenger ribonucleic acid content and protein distribution between normal and abnormal spermatozoa. *Fertil. Steril.* 73, 967–971. doi:10.1016/S0015-0282(00)00485-4

Saez, F., and Drevet, J. R. (2019). Dietary cholesterol and lipid overload: Impact on male fertility. *Oxid. Med. Cell. Longev.* 2019, 4521786. doi:10.1155/2019/4521786

Scott, T. W., Voglmayr, J. K., and Setchell, B. P. (1967). Lipid composition and metabolism in testicular and ejaculated ram spermatozoa. *Biochem. J.* 102, 456–461. doi:10.1042/bj1020456

Selivonchick, D. P., Schmid, P. C., Natarajan, V., and Schmid, H. H. O. (1980). Structure and metabolism of phospholipids in bovine epididymal spermatozoa. *Biochim. Biophys. Acta (BBA)/Lipids Lipid Metab.* 618, 242–254. doi:10.1016/0005-2760(80)90030-2

Sengoku, K., Ishikawa, M., Tamate, K., and Shimizu, T. (1992). Effects of platelet activating factor on mouse sperm function. *J. Assist. Reprod. Genet.* 9, 447–453. doi:10.1007/BF01204050

Shan, S., Xu, F., Hirschfeld, M., and Brenig, B. (2021). Sperm lipid markers of male fertility in mammals. *Int. J. Mol. Sci.* 22, 8767. doi:10.3390/ijms22168767

Shetty, J., Wolkowicz, M. J., Digilio, L. C., Klotz, K. L., Jayes, F. L., Diekman, A. B., et al. (2003). SAMP14, a novel, acrosomal membrane-associated, glycosylphosphatidylinositol-anchored member of the Ly-6/urokinase-type plasminogen activator receptor superfamily with a role in sperm-egg interaction. *J. Biol. Chem.* 278, 30506–30515. doi:10.1074/jbc.M301713200

Sjöstedt, E., Zhong, W., Fagerberg, L., Karlsson, M., Mitsios, N., Adori, C., et al. (2020). An atlas of the protein-coding genes in the human, pig, and mouse brain. *Science* 367, 5947. doi:10.1126/science.aay5947

Skaff, O., Pattison, D. I., and Davies, M. J. (2008). The vinyl ether linkages of plasmalogens are favored targets for myeloperoxidase-derived oxidants: A kinetic study. *Biochemistry* 47, 8237–8245. doi:10.1021/bi800786q

Stadelmann-Ingrand, S., Pontcharraud, R., and Fauconneau, B. (2004). Evidence for the reactivity of fatty aldehydes released from oxidized plasmalogens with phosphatidylethanolamine to form Schiff base adducts in rat brain homogenates. *Chem. Phys. Lipids* 131, 93–105. doi:10.1016/j.chemphyslip.2004.04.008

Staps, P., Rizzo, W. B., Vaz, F. M., Bugiani, M., Giera, M., Heijs, B., et al. (2020). Disturbed brain ether lipid metabolism and histology in Sjögren-Larsson syndrome. *J. Inherit. Metab. Dis.* 43, 1265–1278. doi:10.1002/jimd.12275

Su, Y., Liu, Z., Xie, K., Ren, Y., Li, C., and Chen, W. (2022). Ferroptosis: A novel type of cell death in male reproduction. *Genes (Basel)* 14, 43. doi:10.3390/genes14010043

Sullivan, R., and Saez, F. (2013). Epididymosomes, prostasomes, and liposomes: Their roles in mammalian male reproductive physiology. *Reproduction* 146, R21–R35. doi:10.1530/REP-13-0058

Tanphaichitr, N., Khalil, M. B., Weerachatyanukul, W., Kates, M., Xu, H., Carmona, E., et al. (2003). Physiological and biophysical properties of male germ cell sulfogalactosylglycerolipid. *Male Fertil. lipid Metab.*, 125–148.

Teigler, A., Komljenovic, D., Draguhn, A., Gorgas, K., and Just, W. W. (2009). Defects in myelination, paranode organization and Purkinje cell innervation in the ether lipid-deficient mouse cerebellum. *Hum. Mol. Genet.* 18, 1897–1908. doi:10.1093/hmg/ddp110

Thai, T. P., Heid, H., Rackwitz, H. R., Hunziker, A., Gorgas, K., and Just, W. W. (1997). Ether lipid biosynthesis: Isolation and molecular characterization of human dihydroxyacetonephosphate acyltransferase. *FEBS Lett.* 420, 205–211. doi:10.1016/S0014-5793(97)01495-6

Toledo, A. A., Mitchell-Leef, D., Elsner, C. W., Slayden, S. M., and Roudebush, W. E. (2003). Fertilization potential of human sperm is correlated with endogenous platelet-activating factor content. *J. Assist. Reprod. Genet.* 20, 192–195. doi:10.1023/A:1023622126870

Ueda, Y., Yamaguchi, R., Ikawa, M., Okabe, M., Morii, E., Maeda, Y., et al. (2007). PGAP1 knock-out mice show otocephaly and male infertility. *J. Biol. Chem.* 282, 30373–30380. doi:10.1074/jbc.M705601200

Weerachatyanukul, W., Rattanachaiyanont, M., Carmona, E., Furimsky, A., Mai, A., Shoushtarian, A., et al. (2001). Sulfogalactosylglycerolipid is involved in human gamete interaction. *Mol. Reprod. Dev.* 60, 569–578. doi:10.1002/mrd.1122

Werner, E. R., Keller, M. A., Sailer, S., Lackner, K., Koch, J., Hermann, M., et al. (2020). The TMEM189 gene encodes plasmanylethanolamine desaturase which introduces the characteristic vinyl ether double bond into plasmalogens. *Proc. Natl. Acad. Sci. U. S. A.* 117, 7792–7798. doi:10.1073/pnas.1917461117

Weustenfeld, M., Eidelpes, R., Schmuth, M., Rizzo, W. B., Zschocke, J., and Keller, M. A. (2019). Genotype and phenotype variability in Sjögren-Larsson syndrome. *Hum. Mutat.* 40, 177–186. doi:10.1002/humu.23679

White, D., Weerachatyanukul, W., Gadella, B., Kamolvarin, N., Attar, M., and Tanphaichitr, N. (2000). Role of sperm sulfogalactosylglycerolipid in mouse sperm-zona pellucida binding. *Biol. Reprod.* 63, 147–155. doi:10.1095/biolreprod63.1.147

Wood, P. L., Scoggin, K., Ball, B. A., Troedsson, M. H., and Squires, E. L. (2016). Lipidomics of equine sperm and seminal plasma: Identification of amphiphilic (O-acyl)-ω-hydroxy-fatty acids. *Theriogenology* 86, 1212–1221. doi:10.1016/j.theriogenology.2016.04.012

Wu, H., Gao, J., Wang, X., Leung, T. Y., Duan, Y. G., and Chiu, P. C. N. (2020). Platelet-activating factor induces acrosome reaction via the activation of extracellular signal-regulated kinase in human spermatozoa. *Andrologia* 52, e13565–e13567. doi:10.1111/and.13565

Xu, H., Kongmanas, K., Kadunganattil, S., Smith, C. E., Rupar, T., Goto-Inoue, N., et al. (2011). Arylsulfatase A deficiency causes seminolipid accumulation and a lysosomal storage disorder in Sertoli cells. *J. Lipid Res.* 52, 2187–2197. doi:10.1194/jlr.M019661

Yamano, S., Yamazaki, J., Irahara, M., Tokumura, A., Nakagawa, K., and Saito, H. (2004). Human spermatozoa capacitated with progesterone or a long incubation show accelerated internalization by an alkyl ether lysophospholipid. *Fertil. Steril.* 81, 605–610. doi:10.1016/j.fertnstert.2003.07.036

Yanagimachi, R. (1994). Mammalian fertilization. *Physiol. Reprod.* 1, 273–279.

Yifrach, E., Fischer, S., Oeljeklaus, S., Schuldiner, M., Zalckvar, E., and Warscheid, B. (2018). Defining the mammalian peroxisomal proteome. *Subcell. Biochem.* 89, 47–66. doi:10.1007/978-981-13-2233-4_2

Yoshitake, H., and Araki, Y. (2020). Role of the glycosylphosphatidylinositol-anchored protein TEX101 and its related molecules in spermatogenesis. *Int. J. Mol. Sci.* 21, 6628. doi:10.3390/ijms21186628

Zhang, Y., Hayashi, Y., Cheng, X., Watanabe, T., Wang, X., Taniguchi, N., et al. (2005). Testis-specific sulfoglycolipid, seminolipid, is essential for germ cell function in spermatogenesis. *Glycobiology* 15, 649–654. doi:10.1093/glycob/cwi043

Zhu, J., Massey, J. B., Mitchell-Leef, D., Elsner, C. W., Kort, H. I., and Roudebush, W. E. (2006). Platelet-activating factor acetylhydrolase activity affects sperm motility and serves as a decapacitation factor. *Fertil. Steril.* 85, 391–394. doi:10.1016/j.fertnstert.2005.07.1303

frontiers | Frontiers in Cell and Developmental Biology

TYPE Original Research
PUBLISHED 23 May 2023
DOI 10.3389/fcell.2023.1125988

OPEN ACCESS

EDITED BY
Rafael A. Fissore,
University of Massachusetts Amherst,
United States

REVIEWED BY
Alexander Travis,
Cornell University, United States
Elizabeth Grace Bromfield,
The University of Newcastle, Australia

*CORRESPONDENCE
Claudia Nora Tomes,
ctomes@fcm.uncu.edu.ar

RECEIVED 16 December 2022
ACCEPTED 09 May 2023
PUBLISHED 23 May 2023

CITATION
Buzzatto MV, Berberián MV, Di Bartolo AL, Masone D and Tomes CN (2023), α-Synuclein is required for sperm exocytosis at a post-fusion stage. *Front. Cell Dev. Biol.* 11:1125988. doi: 10.3389/fcell.2023.1125988

α-Synuclein is required for sperm exocytosis at a post-fusion stage

Micaela Vanina Buzzatto[1,2], María Victoria Berberián[1,2,3], Ary Lautaro Di Bartolo[2], Diego Masone[1,4] and Claudia Nora Tomes[1,2]*

[1]Instituto de Histología y Embriología de Mendoza (IHEM)-CONICET-Universidad Nacional de Cuyo, Mendoza, Argentina, [2]Facultad de Ciencias Exactas y Naturales, Universidad Nacional de Cuyo, Mendoza, Argentina, [3]Instituto de Ciencias Básicas (ICB)-CONICET-Universidad Nacional de Cuyo, Mendoza, Argentina, [4]Facultad de Ingeniería, Universidad Nacional de Cuyo, Mendoza, Argentina

The sperm acrosome is a large dense-core granule whose contents are secreted by regulated exocytosis at fertilization through the opening of numerous fusion pores between the acrosomal and plasma membranes. In other cells, the nascent pore generated when the membrane surrounding a secretory vesicle fuses with the plasma membrane may have different fates. In sperm, pore dilation leads to the vesiculation and release of these membranes, together with the granule contents. α-Synuclein is a small cytosolic protein claimed to exhibit different roles in exocytic pathways in neurons and neuroendocrine cells. Here, we scrutinized its function in human sperm. Western blot revealed the presence of α-synuclein and indirect immunofluorescence its localization to the acrosomal domain of human sperm. Despite its small size, the protein was retained following permeabilization of the plasma membrane with streptolysin O. α-Synuclein was required for acrosomal release, as demonstrated by the inability of an inducer to elicit exocytosis when permeabilized human sperm were loaded with inhibitory antibodies to human α-synuclein. The antibodies halted calcium-induced secretion when introduced after the acrosome docked to the cell membrane. Two functional assays, fluorescence and transmission electron microscopies revealed that the stabilization of open fusion pores was responsible for the secretion blockage. Interestingly, synaptobrevin was insensitive to neurotoxin cleavage at this point, an indication of its engagement in *cis* SNARE complexes. The very existence of such complexes during AE reflects a new paradigm. Recombinant α-synuclein rescued the inhibitory effects of the anti-α-synuclein antibodies and of a chimeric Rab3A-22A protein that also inhibits AE after fusion pore opening. We applied restrained molecular dynamics simulations to compare the energy cost of expanding a nascent fusion pore between two model membranes and found it higher in the absence than in the presence of α-synuclein. Hence, our results suggest that α-synuclein is essential for expanding fusion pores.

KEYWORDS

acrosome exocytosis, cell permeabilization, exocytosis, fusion pore, sperm, α-synuclein

Abbreviations: AE, acrosome exocytosis; BoNT/B, botulinum toxin B; BSA, bovine serum albumin; FITC, fluorescein isothiocyanate; HTF, human tubal fluid; IPTG, isopropyl-β-D-thio-galactoside; NP-EGTA-AM, O-nitrophenyl EGTA-acetoxymethyl ester; PBS, phosphate buffer saline; PSA, *Pisum sativum* agglutinin; SDS-PAGE, sodium dodecyl sulfate-polyacrylamide gel electrophoresis; PVP, polyvinylpyrrolidone; SLO, streptolysin O; SNARE, SNAP receptor; TeTx, tetanus toxin.

Introduction

Exocytosis is a widespread process that most cells utilize to deliver membranes, lipids, and soluble molecules to the cell surface and the extracellular space. It is mediated by membranous carriers—secretory vesicles—of different sizes and shapes. In regulated exocytosis, vesicles fuse with the plasma membrane in response to extracellular stimuli. This type of exocytosis occurs in specialized cells in order to satisfy specific physiological tasks, such as neurotransmission, respiration, digestion, reproduction, immune responses, and many others (Porat-Shliom et al., 2013). Exocytosis consists of multiple kinetically, functionally and/or morphologically definable stages, the latest of which include docking of secretory vesicles with the plasma membrane and calcium-triggered membrane fusion, followed by release of the granules' contents (Rizo, 2018; Silva et al., 2021).

During the fusion of a vesicle with the plasma membrane, the lumen of the former initially connects to the extracellular space via a narrow fusion pore (Quevedo et al., 2016; Alvarez de et al., 2018; Karatekin, 2018; Sharma and Lindau, 2018). Low-molecular-weight substances can permeate the narrow pore, which is sometimes stable for several tens of milliseconds before it expands. An Ω-shaped membrane profile may occasionally be captured by electron microscopy. Exocytosis may occur in distinct ways: full-collapse fusion or kiss-and-run. In the former, the fusion pore rapidly dilates, allowing the vesicle membrane to flatten and integrate its lipid and proteins into the planar surface of the plasma membrane. In the kiss-and-run mode, a narrow fusion pore allows the vesicle to retain its gross morphological shape while it releases its contents; the pore is transient and it eventually reseals (Alabi and Tsien, 2013). Large molecules or those packed into dense matrices can only be released by full fusion. Although various members of the fusion machinery have been implicated in fusion pore opening and dilation, the mechanisms involved are far from being elucidated [(Quevedo et al., 2016) and references therein].

The accumulation and aggregation of α-synuclein in the brain characterize devastating neurodegenerative disorders such as Parkinson's disease, dementia with Lewy bodies, and multiple system atrophy (Masaracchia et al., 2018; Runwal and Edwards, 2021). α-Synuclein is a small (≈15 kDa), cytosolic protein, unstructured in solution, whose amino terminal region folds into two antiparallel α-helices in the presence of highly curved membranes with acidic phospholipid headgroups. Synuclein promotes, as well as senses, membrane curvature (Gallea et al., 2018; Alza et al., 2019). Although the precise normal function of α-synuclein is not well established, evidence toward its involvement in the exocytotic pathway is beginning to emerge [see (Gallea et al., 2018; Alza et al., 2019) for functions attributed to α-synuclein]. Of particular interest to this study is α-synuclein's involvement in fusion pore dilation, a phenomenon observed in artificial membranes (Khounlo et al., 2021) and during exocytosis in cultured rat hippocampal neurons and mouse adrenal chromaffin cells (Logan et al., 2017).

A discrete number of highly conserved protein families involved in the late stages of the exocytotic cascade has been identified; within them, the SNAREs constitute the core of the fusion machinery in all cells [reviewed in (Barclay et al., 2012; Jahn and Fasshauer, 2012; Rizo and Xu, 2015; Zhang and Hughson, 2021)]. Synaptobrevin-2, syntaxin1, and SNAP-25 families are the synaptic isoforms of the SNARE superfamily. Synaptobrevins are classified as R-SNAREs (arginine-containing SNAREs) and syntaxins and SNAPs as Q-SNAREs (glutamine-containing SNAREs) based on the identity of highly conserved residues (Fasshauer et al., 1998). The Q- and R-SNAREs join into parallel four-helix bundles; Q-SNAREs contribute three helices whereas R-SNAREs contribute the remaining one. When Q-SNARES are located in one membrane and the cognate R-SNARE in the other, complexes are in a *trans* configuration. SNARE proteins zipper progressively from the amino terminus portion of the molecules toward the membranes. The energy barrier for bilayer mixing is overcome by the zippering of *trans* SNARE complexes (Sorensen et al., 2006; Walter et al., 2010; Gao et al., 2012; Rizo, 2022). SNAREs are engaged in a functionally inactive *cis* configuration when all cognates are located on the same membrane. Although they have a role in pre-fusion events (Haynes et al., 1998; Xu et al., 1999a; De Blas et al., 2005; Tomes et al., 2005; Jun and Wickner, 2019), *cis* SNARE complexes are often only viewed as by-products of exocytosis (Sorensen, 2009). Disentangling *cis* complexes so that monomeric SNAREs would be available to engage in productive *trans* complexes requires metabolic energy; this energy is provided by the hydrolysis of ATP catalyzed by NSF. α-SNAP bridges the SNARE complex to NSF and stimulates the ATPase activity of the latter (Ryu et al., 2016; Zhao and Brunger, 2016).

Sperm contain a single, large dense-core secretory granule (the acrosome) whose contents are released by regulated exocytosis (acrosomal exocytosis, AE) in the female tract at fertilization or in response to an increase in calcium levels in the test tube (Vardjan et al., 2013; Chiang et al., 2014). The topology of the AE fits neither full collapse nor kiss and run modes because the acrosomal and sperm's plasma membranes merge through a unique membrane fusion mechanism. Briefly, the AE proceeds through a series of steps that include the swelling of the acrosome and remodeling of its membrane, the docking of the outer acrosomal to the overlying plasma membrane, and the genesis of pores at the points of apposition (Buffone et al., 2012; Zhao et al., 2016). In most dense-core secretion events, the pores widen and the granule contents discharge. In sperm, however, the granule membrane is as large as the section of the plasma membrane it must fuse with, therefore Ω-shaped structures are never observed. Pore expansion leads to the fenestration of the fusing membranes and joining of pores to generate a reticulum of tubules and hybrid plasma-outer acrosomal membrane vesicles. Exactly at which point after the opening of fusion pores do acrosomal contents begin to be released has been a matter of intense study in the field [reviewed in (Buffone et al., 2014; Foster and Gerton, 2016; Hirohashi, 2016)]. When the vesiculated membranes and acrosomal contents are lost, the inner acrosomal membrane becomes the leading edge of the sperm and the AE is fully accomplished (Harper et al., 2008; Tomes, 2015; Belmonte et al., 2016; La Spina et al., 2016). Although no direct evidence supported the claim, it was believed that sperm fusion pores dilated spontaneously. We have been able to dispute this notion by means of a chimeric protein consisting of the amino-terminal portion of Rab3A fused to the carboxy-terminal portion of Rab22A. Thanks to this tool, we have demonstrated that sperm fusion pores are subjected to post-fusion regulation, as happens in many other cells (Quevedo et al., 2016).

Due to their highly specific, zinc-dependent, proteolytic cleavage of the neuronal isoforms of SNARE proteins, tetanus (TeTx) and botulinum (BoNT) toxins are potent inhibitors of secretory vesicle release (Ahnert-Hilger et al., 2013; Pantano and Montecucco, 2014; Pirazzini et al., 2022). Monomeric SNAREs are sensitive—whereas those in *cis* complexes are resistant—to all toxins (Hayashi et al., 1994). Because SNAREs cycle through toxin-sensitive stages, exocytosis is blocked by neurotoxins in neuroendocrine cells. In contrast, SNAREs do not cycle in capacitated human sperm; instead, they are engaged in toxin-resistant *cis* complexes on both the granule and the cell membranes (De Blas et al., 2005). This is because NSF's dissociating activity is kept dormant by tyrosine phosphorylation. Once AE is initiated, protein tyrosine phosphatase 1B (PTP1B) dephosphorylates NSF, which derepresses its activity (Zarelli et al., 2009). The monomeric SNAREs thus generated are free to assemble in *trans* and achieve the docking of the acrosome to the plasma membrane (Zanetti and Mayorga, 2009). Monomeric synaptobrevin and that engaged in partially assembled *trans* complexes exhibit differential sensitivity to BoNT/B and TeTx (Xu et al., 1999b; Sorensen et al., 2006; Gaisano, 2014; Bombardier and Munson, 2015). These toxins cleave a peptide bond exposed in both configurations (Schiavo et al., 2000; Fabris et al., 2022; Pirazzini et al., 2022), but to sever the bond toxins must bind their substrate. TeTx binds to the N-terminal, whereas BoNT/B binds the C-terminal portion of synaptobrevin's coil domain. Because SNARE complex assembly begins at the N-terminus, the TeTx-recognition site is hidden in partially assembled SNARE complexes while the BoNT/B recognition site is exposed. This feature is responsible for synaptobrevin's differential sensitivity to toxins: TeTx only cleaves free synaptobrevin while BoNT/B also cuts synaptobrevin loosely assembled in complexes (Hua and Charlton, 1999; De Blas et al., 2005; Giraudo et al., 2006; Wu et al., 2016). At a very late stage during the AE, downstream the full zippering of SNARE proteins in *trans* and the subsequent opening of fusion pores, sperm SNAREs are engaged in *cis* complexes (Quevedo et al., 2016).

Here, we combined *in silico* with biochemical, functional and microscopy-based methods employing recombinant proteins, neurotoxins, lectins and antibodies to show that human sperm α-synuclein is required for fusion pore expansion during a very late stage of the AE.

Materials and methods

Reagents

Recombinant streptolysin O (SLO) was obtained from Dr. Bhakdi (University of Mainz, Mainz, Germany). The rabbit polyclonal antibody directed towards human α-synuclein (purified on protein A) was from Axxora, LLC (Farmingdale, NY). The mouse monoclonal anti-synaptobrevin-2 antibody (clone 69.1, purified IgG) and the rabbit polyclonal anti-complexin I/II (purified IgG) were from Synaptic Systems (Göttingen, Germany). HisTrap columns, FF, Cytiva (formerly GE healthcare Life Sciences) were purchased from ALLSCIENCE, LLC (Doral, FL). FITC-coupled *Pisum sativum* agglutinin (FITC-PSA) was from Vector Labs (BIOARS S.A, Buenos Aires, Argentina). PSA coupled to 20 nm colloidal gold was from glycoMatrix (Dublin, OH). Horseradish peroxidase- and Cy™3-conjugated goat anti-rabbit, as well as Cy™3-conjugated goat anti-mouse IgGs (H + L) were from Jackson ImmunoResearch (West Grove, PA). *O*-nitrophenyl EGTA-acetoxymethyl ester (NP-EGTA-AM) was purchased from Life Technologies (Buenos Aires, Argentina). Ni-NTA-agarose was from GE Healthcare. Prestained molecular weight markers were from Bio-Rad (Tecnolab, Buenos Aires, Argentina). All other chemicals were from Sigma-Aldrich™ Argentina S.A., Genbiotech, or Tecnolab (Buenos Aires, Argentina).

Recombinant proteins

The light chains of BoNT/B and TeTx fused to His_6 in a pQE3 vector were generously provided by Dr. T. Binz (Medizinische Hochschule Hannover, Hannover, Germany). The cDNA encoding human α-synuclein fused to His_6 and to the TAT-transduction domain of HIV virus in a pET11a plasmid was a kind gift of Dr. L. Pollegioni (Università degli Studi dell'Insubria, Varese, Italy). Purified, recombinant Rab3A-22A fused to glutathione S-transferase was a kind gift from Dr. M.F. Quevedo (IHEM, Mendoza, Argentina).

Expression and purification of recombinant His_6-BoNT/B and His_6-TeTx were as in (De Blas et al., 2005). The plasmid encoding His_6-TAT-α-synuclein was transformed into *Escherichia coli* BL21 (DE3) and protein expression was induced with 0.5 mM IPTG 4 h at 37°C. Recombinant-α-synuclein is mostly located in the periplasmic space (Ren et al., 2007). We recovered the periplasm of transformed bacteria by osmotic shock as in (Caldinelli et al., 2013), made it 20 mM TrisHCl, pH 7.4 and run it through a metal-chelating HisTrap column. Twenty volumes of 20 mM TrisHCl, pH 7.4, 1 M NaCl, and 5 volumes each of 20 mM TrisHCl, pH 7.4 plus 125 mM, 250 mM and 500 mM imidazole were applied to the column. Purified His_6-TAT-α-synuclein eluted with 500 mM imidazole was added 10% glycerol, aliquoted and stored at −80°C until use.

Human sperm sample preparation procedures

Semen samples were donated by normal healthy men. Semen was allowed to liquefy by incubating at 37°C for 30–60 min. Highly motile cells were isolated from semen following a swim-up protocol. Sperm concentrations were adjusted to 7×10^6/mL before incubating for at least 2 h under capacitating conditions (37°C, 5% CO_2/95% air) in Human Tubal Fluid media (Serendipia Lab, Vedia, Argentina) supplemented with 0.5% bovine serum albumin (BSA, HTF media). Sperm were permeabilized with SLO as follows: after washing twice with PBS, sperm were incubated for 15 min at 4°C in cold PBS containing 3 U/mL SLO. Cells were washed once with PBS, resuspended in ice-cold sucrose buffer (20 mM Hepes-K, pH 7, 250 mM sucrose, 0.5 mM EGTA) and permeabilized by activating the SLO bound to their plasma membrane with 2 mM DTT. The reagents to test were added sequentially as indicated in the figure legends, and incubated for 8–15 min at 37°C after each addition. Samples were processed for AE assays, immunofluorescence and for

transmission electron microscopy. To obtain the results shown in Figure 2B, photosensitive NP-EGTA-AM was supplied to SLO-permeabilized sperm at the beginning of the experiments, ensuring that all subsequent procedures were carried out in the dark. After the last incubation, photolysis was induced by exposing twice (1 min each) to an UV lamp, mixing, and incubating for 5 min at 37°C.

Indirect AE assay

Sperm were spotted on teflon-printed slides, air dried, and fixed/permeabilized in ice-cold methanol for 20 s. Acrosomal status was assessed by staining with 25 µg/mL FITC-PSA in PBS for 40 min at room temperature and washing for 20 min in water (Mendoza et al., 1992). PSA binds α-methyl mannoside moieties in proteins present in the acrosomal matrix (Cross et al., 1986). At least 200 cells per condition were scored manually using an upright Zeiss microscope equipped with epifluorescence optics. All experiments included a basal (no stimulation) and a positive (0.5 mM $CaCl_2$ [corresponding to 10 µM free calcium]) controls. AE indices were calculated by subtracting the number of spermatozoa that lost their acrosome spontaneously ("control"; assigned 0% for normalization) from all values and expressing the results as a percentage of the AE observed with 0.5 mM $CaCl_2$ ("Ca", assigned 100% for normalization). Our analysis only included results derived from experiments that produced similar responses and where the difference between basal (7%–19% before normalization) and stimulated conditions was of at least 8–10 percentage points (Supplementary Figure S1B). SLO did not affect the PSA staining patterns (see images of PSA-stained SLO-permeabilized sperm in Supplementary Figure S1A; compare "-SLO and "+SLO" FITC-PSA panels in Figure 1B). Data were evaluated before normalization with the program GraphPad Prism 8, using the one way Anova, Dunnett's multiple comparisons test. Bar plots represent the mean ± SEM of at least three independent experiments. Different letters indicate statistical significance ($p < 0.05$).

Direct AE assay

SLO-permeabilized sperm were bathed in 30 µg/mL FITC-PSA for all the incubation time. Cells were loaded with 5 nM anti-α-synuclein antibodies followed by 0.5 mM $CaCl_2$ and incubated for 15 min at 37°C after each addition. At the end of the second incubation, sperm were spotted on teflon-printed slides, air dried overnight and fixed/permeabilized in 2% paraformaldehyde for 10 min, followed by a 5 min-wash in water. AE indices and statistical analysis were as described above.

Indirect immunofluorescence

For anti-synaptobrevin-2 immunofluorescence, capacitated and SLO-permeabilized sperm samples were processed as described for indirect AE assays, adding reagents and $CaCl_2$ sequentially, and incubating for 10 min at 37°C after each addition. α-Synuclein immunofluorescence was performed on cells subjected or not to SLO permeabilization. Samples were fixed in 2% paraformaldehyde in PBS for 15 min at room temperature, centrifuged and resuspended in PBS containing 100 mM glycine to neutralize the fixative. Cells (5×10^5 per condition) were attached to poly-L-lysine-coated, 12 mm round coverslips by incubating for 30 min at room temperature in a moisturized chamber. Exposure to 0.1% Triton X-100 in PBS for 10 min at room temperature was used to permeabilize the plasma membrane. After the detergent, sperm were washed three times with PBS containing 0.1% polyvinylpyrrolidone (PVP, average M.W. = 40,000; PBS/PVP). Incubation in 3% BSA in PBS/PVP for 1 h at 37°C was used to reduce nonspecific staining. Anti-α-synuclein (10 µg/mL) and anti-synaptobrevin-2 (25 µg/mL) antibodies were diluted in 2% BSA in PBS/PVP, added to the coverslips, and incubated for 1 h at 37°C in a moisturized chamber. After washing (three times, 6 min each) with PBS/PVP, 2.5 µg/mL Cy™3-conjugated anti-rabbit (synuclein) or mouse (synaptobrevin) IgGs in 1% BSA in PBS/PVP) were added and incubated for 1 h at room temperature protected from light. Coverslips were washed (three times, 6 min each) with PBS/PVP. The acrosomal membrane was permeabilized with ice-cold methanol for 1 min, and the acrosomal contents stained with FITC-PSA as described in "Indirect AE assay" (but without air drying). Coverslips were washed (three times, 10 min each) with PBS/PVP, mounted with Mowiol® 4–88 in PBS containing 2 µM Hoechst 33342, and stored at room temperature in the dark. Samples were examined with an 80i Nikon microscope equipped with a Plan Apo 60x/1.40 oil objective. Images were captured with a Nikon DS-Fi1 camera operated with NIS software (Nikon). ImageJ (freeware from N.I.H.) was used to subtract background and adjust brightness/contrast to render all-or nothing labeling patterns. The presence of immunostaining in the acrosomal region was scored in digital images from at least ≈100 cells contained in 10 fields. Data were evaluated before normalization with the program GraphPad Prism 8 using the one way Anova, Dunnett's multiple comparisons test.

SDS-PAGE and western blot

Proteins were resolved by electrophoresis on 15% Tris-glycine-SDS-gels and electro-transferred to 0.22 µm nitrocellulose membranes (Hybond, GE Healthcare) on a semi-dry apparatus (Amersham Biosciences) for 35 min at 25 mA. Because α-synuclein monomers tend to detach from blotted membranes, resulting in no or very poor detection (Lee and Kamitani, 2011), membranes were treated with 0.4% paraformaldehyde for 30 min at room temperature immediately after transfer. Non-specific reactivity was blocked with 2% BSA dissolved in washing buffer (PBS, pH 7.6, 0.2% Tween 20) for 1 h at room temperature. Blots were incubated with 1 µg/mL anti-α-synuclein in blocking solution overnight at 4°C. Horseradish peroxidase-conjugated goat-anti-rabbit IgG (0.1 µg/mL in washing buffer) was used as secondary antibody with 1 h incubation at room temperature. Excess first and second antibodies were removed by rocking three times, 10 min each in washing buffer. Detection was accomplished with a chemiluminescence kit from Kalium Technologies (Biolumina, Buenos Aires, Argentina) on a Luminescent Image Analyzer LAS-4000 (Fujifilm, Tokyo, Japan).

Transmission electron microscopy

For experiments summarized in Figure 4, we processed capacitated and SLO-permeabilized human sperm (5×10^6 cells in 250 µL per condition) as described for "Indirect AE assays". For experiments summarized in Figure 5, we incubated the cells with 20 µg/mL PSA-colloidal gold as described in the legend. Reactions were stopped by fixing in 2.5% glutaraldehyde in 0.1 M sodium phosphate buffer and incubating overnight at 4°C or 2 h at room temperature. Samples were washed in PBS (three times, 20 min each) and postfixed in 1% OsO_4 in PBS for 1 h at room temperature, washed as before, dehydrated in a graded acetone series and embedded in a low viscosity epoxy resin (Pelco International, Fresno, CA) (Spurr, 1969). Polymerization was performed at 70°C for 48 h. Ultrathin sections with interference color gray were cut with an ultramicrotome (Ultracut R; Leica, Wien, Austria), mounted on grids and stained with uranyl acetate and lead citrate (Reynolds, 1963). Grids were examined by transmission electron microscopy at 80 kV in a 900 Zeiss microscope (Jena, Germany). We included negative (not stimulated) and positive (stimulated with 0.5 mM $CaCl_2$) controls in all experiments.

Computational methods

We conducted umbrella sampling molecular dynamics using GROMACS (GROningen Machine for Chemical Simulations)-2020.5 (Van Der et al., 2005; Pronk et al., 2013), PLUMED-2.7.2 (Tribello et al., 2014) and the Martini 3 coarse-grained model (Souza et al., 2021). In all cases, we modeled two 1024-lipid bilayers patches composed of 87.5% of 1-palmitoyl-2-oleoyl-glycero-3-phosphocholine (POPC), 10% of 1-palmitoyl-2-oleoyl-sn-glycero-3-phospho-L-serine (POPS) and 2.5% of the recently developed phosphatidylinositol 4,5-bisphosphate ($PI(4,5)P_2$, or PIP_2) model (Borges-Araujo et al., 2022). This arrangement, previously used in our laboratory (Di Bartolo et al., 2022; Di Bartolo and Masone, 2022) follows the experimental membrane composition reported by Jahn and collaborators to trap Syt1 to the plasma membrane in the presence of calcium (Perez-Lara et al., 2016). These bilayer patches of ~17 × 17 nm ensure negligible finite-size effects due to interactions between periodic images of the fusion pore (Caparotta et al., 2020b). Solvation fulfilled the ample water condition for Martini (Ingolfsson et al., 2014) and the inter-membrane separation was adjusted to equilibrate at ~3.9 nm (Di Bartolo and Masone, 2022). See Supplementary Material for more technical details.

Results

α-Synuclein is localized to the acrosomal region of human sperm

We investigated the presence of α-synuclein in human sperm by Western blot using a polyclonal antibody raised against recombinant human α-synuclein as probe. Immunoblot analysis of whole cell extracts detected a single protein band with an apparent molecular mass of 15 kDa (Figure 1A, lane 2). The recombinant protein used as positive control showed decreased electrophoretic mobility compared to that of the endogenous form (Figure 1A, lane 1). This is because α-synuclein expressed in *E. coli* contains the TAT peptide and therefore has a higher molecular weight (≃ 17.8 kDa) than sperm α-synuclein.

To explore the localization of α-synuclein in sperm, we performed indirect immunofluorescence experiments using anti-α-synuclein as primary and anti-rabbit-Cy3 IgGs as secondary antibodies (Figure 1B, red, left panels). FITC-coupled PSA, a lectin that binds the acrosomal matrix, allowed visualization of the acrosomes (Figure 1B, green, central panels). Hoechst 33342 stained the nuclei and accounted for all cells in each field (Figure 1B, blue, right panels). α-Synuclein was detected in the acrosomal region of the sperm head in over 60% of the cells (Figure 1C); this is the expected localization for a protein with a role in exocytosis. No head staining was observed in sperm that lost their acrosomes either spontaneously (6%) or upon inducing AE with the calcium ionophore A23187 (20%) (not shown). These results suggest that the subcellular compartments that bear α-synuclein shed in cells that undergo exocytosis. Very few cells unexposed to primary antibodies showed fluorescence in the acrosomal domain, indicating that the staining was specific (Figures 1B, C). The percentage of cells labeled by the anti-α-synuclein antibodies was identical whether or not the plasma membrane had been permeabilized with SLO, which indicated that despite its small size, α-synuclein did not diffuse out of cells upon treatment with SLO (Figure 1C).

α-Synuclein is required for the human sperm AE at a late stage

To investigate the requirement of α-synuclein for AE, we introduced anti-α-synuclein antibodies into SLO-permeabilized sperm before inducing exocytosis with calcium. The antibodies inhibited the AE in a dose-response fashion, reaching 77% inhibition at 5 nM and 90% inhibition at 7.5 nM (Figure 2A). Preincubation of the antibody with recombinant α-synuclein abolished the IgG's ability to prevent the AE (Supplementary Figure S2). His_6-TAT-α-synuclein did not affect either the spontaneous or calcium-induced AE. Nor did imidazole, used in the purification of the protein, or a nonimmune rabbit IgG (Supplementary Figure S2). Antibodies to complexin bind the endogenous protein and decorate the acrosomal domain of the head in human sperm (Roggero et al., 2007). In contrast to anti-α-synuclein antibodies, 7.5 nM anti-complexin (cpx) antibodies did not affect the AE (Supplementary Figure S2). Thus, we concluded that the negative effect of the anti-α-synuclein antibodies on sperm secretion was due to binding to endogenous α-synuclein and therefore specific. Our results revealed that α-synuclein exhibits a role in human sperm AE.

The acrosome behaves as an internal calcium reservoir; release from this store is necessary for the AE [reviewed in (Darszon et al., 2011; Correia et al., 2015)] after the outer acrosomal membrane docks to the plasma membrane and before they fuse (De Blas et al., 2005; Zanetti and Mayorga, 2009; Rodriguez et al., 2011). NP-EGTA-AM is a membrane permeant, photolabile calcium chelator that crosses the plasma (because it is permeabilized with

10.3389/fcell.2023.1125988

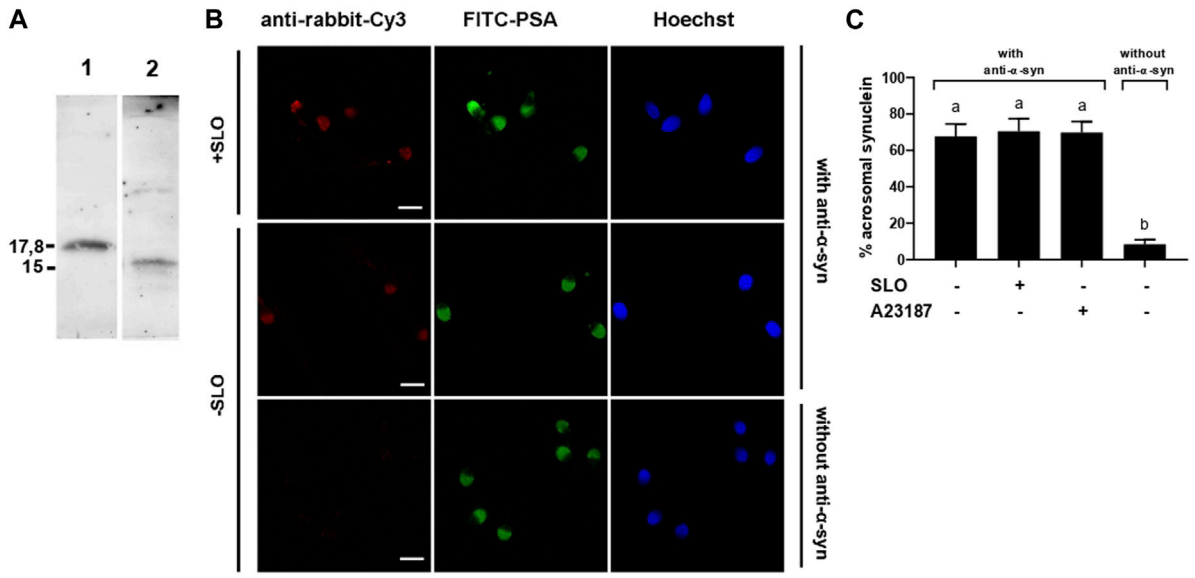

FIGURE 1
α-synuclein is present in the acrosomal domain of human sperm that retain the acrosome. **(A)** 0.7 μg of recombinant, purified α-synuclein (lane 1) and proteins from unfractionated sperm extracts (20×10^6 cells, lane 2) were immunoblotted with anti-α-synuclein antibodies. Shown are Western blots representative of three repetitions. **(B)** SLO permeabilized (+SLO) and non permeabilized (-SLO) capacitated human sperm were triple stained with (top and middle rows) or without (bottom row, negative control) antibodies to α-synuclein followed by a fluorescent secondary antibody (anti-rabbit-Cy3, red, left panels), FITC-PSA (to assess the integrity of the acrosome; green, central panels), and Hoechst 33,342 (to visualize all cells in the field; blue, right panels). Shown are epifluorescence micrographs of typically stained cells. Bars = 5 μm. **(C)** Quantification of the percentage of non-exocytosed sperm with α-synuclein staining. + SLO: SLO-permeabilized sperm; + A23187: non-SLO-permeabilized cells challenged with a calcium ionophore, an AE inducer. The data represent the mean ± SEM of at least three independent experiments. Statistical difference between the groups was non-significant ($p > 0.05$) except when comparing with the background control without primary antibodies.

SLO) and outer acrosomal (due to the AM moiety) membranes. After this, the AM group is removed and NP-EGTA accumulates inside the acrosome, where it halts the AE by chelating intra-acrosomal calcium for as long as the system is kept in the dark. Photolysis of the chelator by exposure to UV light rapidly replenishes the acrosomal calcium pool and allows exocytosis to resume (De Blas et al., 2002; Ackermann et al., 2008; Hu et al., 2010; Sosa et al., 2015). In sperm loaded with NP-EGTA-AM and kept in the dark, challenging with $CaCl_2$ allowed exocytosis to advance up to the stage that requires intracellular calcium mobilization. Subsequent incubation with anti-α-synuclein antibodies prevented exocytosis even after illuminating the tubes to photolyse the chelator (Figure 2B, black bar). These results indicate that α-synuclein is required at a late stage of the AR, likely after docking and intra-acrosomal calcium release. Interestingly, this is the same timeframe in which the chimeric protein Rab3A-22A halts the AE (Bustos et al., 2014; Quevedo et al., 2016).

Sperm SNAREs are engaged in *cis* complexes by the time α-synuclein exhibits its role in the AE

When introduced into SLO-permeabilized human sperm, recombinant α-synuclein reversed the exocytotic block imposed by the anti-α-synuclein antibodies on the AE (Figure 3A, black bar). The reversibility of the effect of the antibodies by bacterially expressed α-synuclein was instrumental to interpret the findings described below.

Results summarized in Figure 2B indicated that α-synuclein controls a post-docking stage during the human sperm AR. Molecularly, docking corresponds to a state where the outer acrosomal and plasma membranes are bridged together by partially assembled *trans* SNARE complexes in preparation for fusion. When in this configuration, SNARE proteins are sensitive to BoNTs but resistant to TeTx. To scrutinize the configuration of the SNARE complex at the post-docking stage governed by α-synuclein, we combined anti-α-synuclein antibodies, BoNT/B and TeTx in a functional assay (Figure 3A). When reagents were introduced into SLO-permeabilized sperm in the sequence anti-α-synuclein → calcium → BoNT/B or TeTx → α-synuclein, the AE proceeded normally (Figure 3A, striped bars). These results revealed that synaptobrevin-2 was protected from either toxin cleavage, which only happens when engaged in SNARE complexes in a *cis* configuration.

We have established in the past that monitoring SNARE proteins' sensitivity to neurotoxins by indirect immunofluorescence is a suitable assay to determine their configuration. Following a triple staining strategy similar to that used to gather the data compiled in Figures 1B, C, we scrutinized if the introduction of anti-α-synuclein antibodies into SLO-permeabilized sperm affected the susceptibility of synaptobrevin-2 to BoNT/B. The monoclonal antibody used in these experiments recognizes an epitope located in a portion of the molecule severed by the toxin and therefore detects

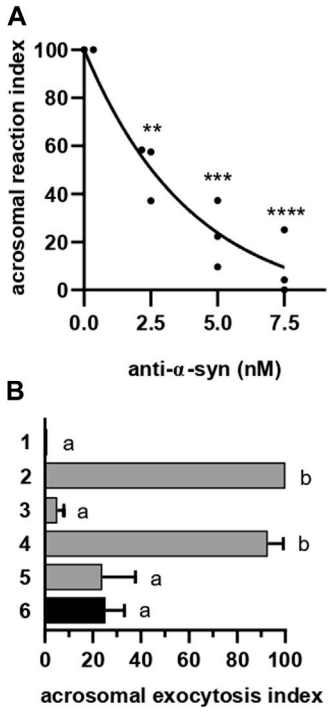

FIGURE 2
α-synuclein is required for the AE at a late stage. **(A)** Anti-α-synuclein antibodies were introduced into SLO-permeabilized sperm incubating at 37°C for 15 min before initiating the AE by adding 0.5 mM $CaCl_2$ and incubating as before. After fixing, the AE was measured as described in "indirect AE assay". Data were evaluated before normalization with the program GraphPad Prism 8 using the one way Anova, Tukey's test multiple comparisons test. Statistically significant differences against the control without anti-α-synuclein antibodies were $^{**}p < 0.02$, $^{***}p < 0.0002$ and $^{****}p < 0.0001$. **(B)** Permeabilized spermatozoa were loaded with 10 μM NP-EGTA-AM (NP) for 10 min at 37°C before initiating the AE with 0.5 mM $CaCl_2$. After another incubation at 37°C, sperm were treated with 5 nM anti-α-synuclein antibodies. All procedures were carried out protecting the tubes from the light. Photolysis of the chelator by UV light (*hv*) was induced at the end (6: NP→Ca^{2+}→ anti-α-syn→*hv*, black bar). Gray bars represent controls: 1 = background; 2 = AE stimulated by 0.5 mM $CaCl_2$; 3 = inhibitory effect of NP in the dark (NP→Ca→dark); 4 = the recovery upon illumination (NP→Ca→*hv*); 5 = inhibitory effect of the antibodies when present throughout the experiment (NP→ anti-α-syn→Ca→*hv*). The AE was measured as in "**A**".

intact—but not BoNT/B-cleaved—synaptobrevin-2. Representative images are shown in Figure 3B. As we have reported before, the anti-synaptobrevin-2 antibody decorated the acrosomal region despite pretreatment with BoNT/B because SNAREs are in a *cis* configuration in resting sperm. When sperm were treated with the toxin plus $CaCl_2$, the proportion of cells exhibiting synaptobrevin-2 labeling dropped significantly because the initiation of the AE sensitized this SNARE to BoNT/B. In contrast, when anti-α-synuclein antibodies were introduced into sperm before $CaCl_2$, synaptobrevin was insensitive to BoNT/B cleavage (Figure 3C). These results suggest that when $CaCl_2$ advanced the AE until it reached the stage blocked by the anti-α-synuclein antibodies, synaptobrevin was in a BoNT/B-resistant configuration. Once again, our findings indicate that the anti-α-synuclein antibodies halted the AE at a stage when SNAREs were likely engaged in a *cis* configuration. This arrangement is characteristic of two exocytotic stages: an early one in resting cells and a late, post-fusion, one. Only the latter is consistent with the findings reported here and therefore we conclude that α-synuclein exhibits its role in the AE after the opening of fusion pores between the acrosomal and plasma membranes.

α-Synuclein exhibits its role in the AE after the opening of fusion pores

Anti-α-synuclein antibodies froze sperm SNAREs in toxin-resistant, *cis* complexes (Figure 3). We used fluorescence and transmission electron microscopies to further explore the premise that the antibodies affect a post-fusion event. FITC-PSA reveals the presence of the acrosomal matrix *after fixation* in the standard (indirect) functional assay: sperm without acrosomes are not stained whereas sperm with acrosomes, are (see diagram). On the contrary, in the direct functional assay, PSA reaches the acrosomal matrix of sperm undergoing exocytosis *without fixation*: only these sperm stain. This is because PSA enters the acrosomes through the fusion pores and remains attached to the matrix (see diagram) (Sanchez-Cardenas et al., 2014; Pelletan et al., 2015; Sosa et al., 2015). Thus, the read outs of both protocols are complementary. Sperm loaded with anti-α-synuclein antibodies and challenged with $CaCl_2$ evinced fluorescent acrosomes under both staining methods: cells incorporated the lectin through the fusion pores (direct protocol, Figure 4B); yet, they retained their acrosomal matrix (indirect staining, Figure 4A). Taken together these results support our hypothesis that the exocytotic cascade advanced to a post-fusion—and before acrosomal dispersion—stage. Similar results are obtained when permeabilized sperm are incubated with the chimaeric protein Rab3A-22A before challenging with $CaCl_2$ (Quevedo et al., 2016).

We resorted to transmission electron microscopy to gain further insights into the exocytotic stage halted by the anti-α-synuclein antibodies. Micrograph labeled "intact" in Figure 4C shows the typical aspect of the heads of a resting cell, where the acrosome is planar. This pattern is the most abundant in unperturbed cells (Figure 4D, I). The cell photographed in the panel "fully exocytosed" has completed the AE. As expected, this stage was predominantly observed in samples challenged with calcium (Figure 4D, IV). Panel "swollen and waving" illustrates a cell that underwent acrosomal swelling/deformation in response to external calcium, but it could not complete the AE. This pattern is seldom observed in cells undergoing exocytosis spontaneously and those challenged with calcium, because swelling is transient (Figure 4D, II) and (Sosa et al., 2015). Interestingly, this was the predominant pattern in cells preloaded with anti-α-synuclein antibodies before adding $CaCl_2$ (Figure 4D, black bars). This response resembled that observed when using recombinant Rab3A-22A instead of anti-α-synuclein antibodies (Quevedo et al., 2016). Few cells completed the AE because the antibodies prevented it. We visualized diffuse, localized and electron dense material adhered to the surface of a subpopulation of cells with swollen and waving acrosomes, exclusively upon treatment with anti-α-synuclein antibodies and

10.3389/fcell.2023.1125988

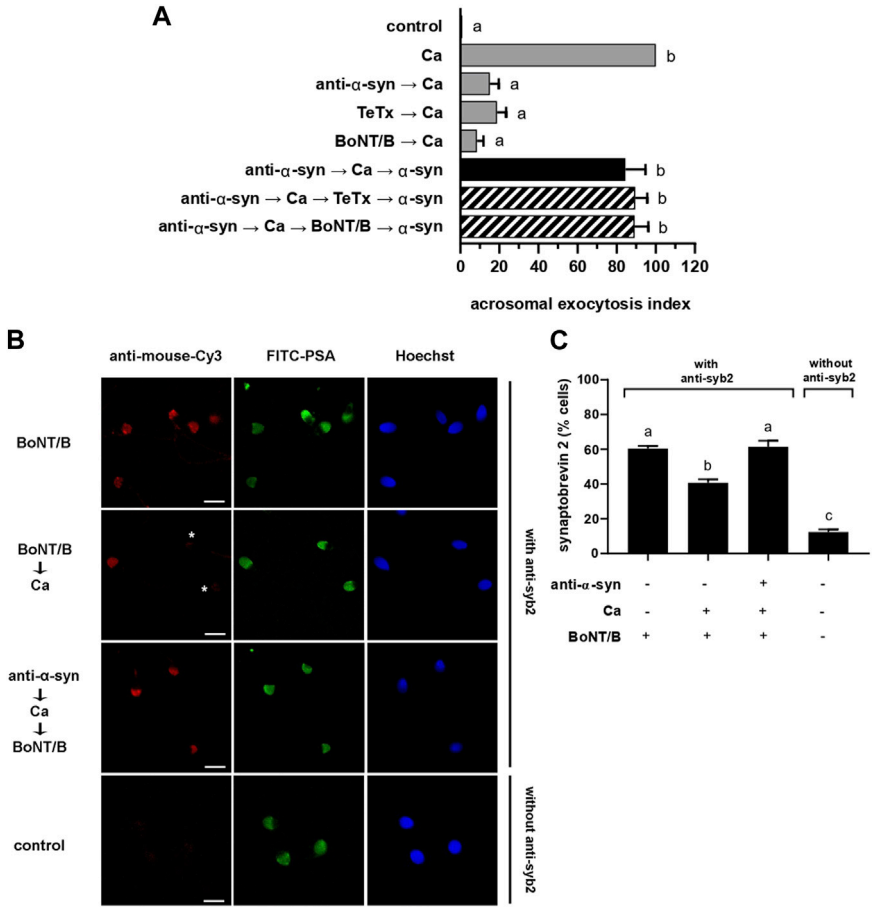

FIGURE 3
anti-α-synuclein antibodies halt exocytosis at a stage when synaptobrevin-2 is engaged in *cis* SNARE complexes. **(A)** Sperm with their plasma membrane permeabilized with SLO were incubated sequentially with 7.5 nM anti-α-synuclein antibodies, 0.5 mM $CaCl_2$, and 20 nM recombinant α-synuclein (15 min at 37°C after each addition; black bar). When indicated, 100 nM TeTx or BoNT/B were added after $CaCl_2$ and before recombinant α-synuclein (striped bars). Gray bars represent controls. The AE was measured as indicated in the legend to Figure 2A. **(B)** Sperm incubated as indicated in the figure key, were fixed and triple stained without (bottom row, negative control) or with (all the rest) an anti-synaptobrevin-2 (syb2) antibody followed by a fluorescent secondary antibody (anti-mouse-Cy3, red, left panels), FITC-PSA (green, central panels), and Hoechst 33,342 (blue, right panels). Shown are representative images of sperm with intact acrosomes i) with synaptobrevin-2 staining or ii) without synaptobrevin-2 immunostaining due to toxin cleavage (asterisks). Bars = 5 μm. **(C)** Quantification of the percentage of non-exocytosed sperm with synaptobrevin-2 staining. The left to right order of the bars corresponds to the top to bottom order of the pictures in panel **(B)**. The data represent the mean ± SEM of at least three independent experiments. Statistical difference between the groups was non-significant ($p > 0.05$) except when comparing the % sperm with intact synaptobrevin between the condition BoNT/B →Ca against all the rest and when comparing synaptobrevin-2 labeling against the background control without primary antibodies ($p < 0.05$).

calcium (Figure 4C, pattern "swollen, waving and diffuse (III)", arrows, quantified in Figure 4D, III).

Considering that the anti-α-synuclein antibodies stabilized open—but not expanded—fusion pores (Figure 4B), we hypothesized that the electron dense material characteristic of pattern III might correspond to acrosomal components that diffuse out of the cells through those pores. To test this premise, we adapted for electron microscopy experiments similar to those summarized in Figure 4B, only that PSA coupled to 20 nm colloidal gold particles substituted for FITC-PSA. The membranes of intact sperm (pattern I in Figure 4C) showed absence of gold nanoparticles (images not shown but included in quantifications to compose Figure 5B), which indicates that they were not ruptured by SLO-permeabilization or processing for transmission electron microscopy. Likewise, PSA-gold did not bind sperm that had completed the AE (pattern IV in Figure 4C; images not shown but included in quantifications to compose Figure 5B), which suggests that no acrosomal matrix remained associated to the inner acrosomal membrane. Interestingly, one or more gold particles were consistently found adjacent to the surface of cells exhibiting swollen and waving acrosomes (patterns II and III in Figure 4C, undistinguishable here). A gallery of typical images illustrating this subpopulation of sperm is shown in Figure 5A, with arrows pointing to gold nanoparticles. Quantification of hundreds of electron micrographs showed that the proportion of gold-labelled cells (+AuNP) was low in sperm that underwent no treatment (Figure 5B, control) or were exposed to the AE inducer (Figure 5B, Ca). This is consistent with the observations that bins II and III were the least abundant of the histogram shown in Figure 4C. In contrast, gold nanoparticles decorated the extracellular face of the

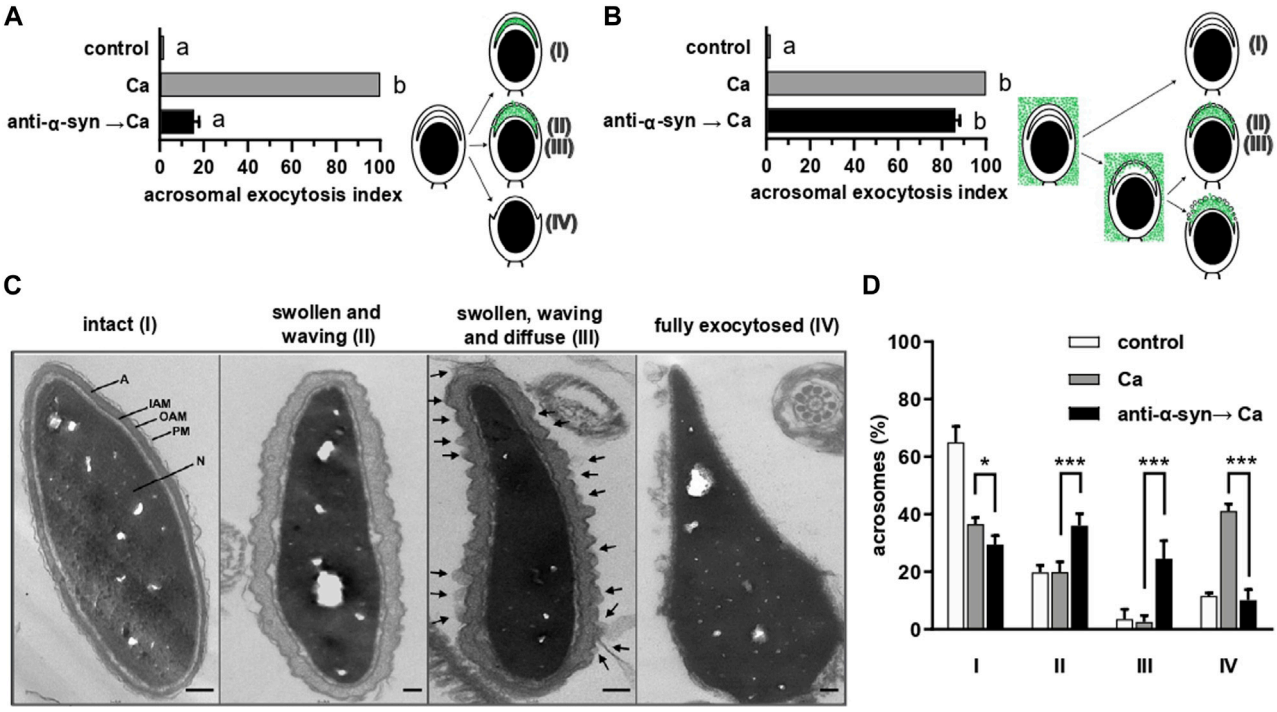

FIGURE 4
treatment with anti-α-synuclein antibodies allows the efflux of electron dense material from the acrosome of sperm undergoing AE through stabilized fusion pores. **(A)** Sperm were treated with 5 nM anti-α-synuclein antibodies and 0.5 mM $CaCl_2$ and incubated 15 min at 37°C after each addition. After fixing, the AE was measured as described in the legend to Figure 2A. The diagram represents the staining patterns of sperm with intact acrosomes, and undergoing intermediate exocytosis stages and after losing the acrosome. Roman numerals are as in panel **(C)**. **(B)** Spermatozoa were bathed in 30 µg/mL FITC-PSA and incubated (15 min at 37°C after each addition) with 5 nM anti-α-synuclein antibodies and 0.5 mM $CaCl_2$. The AE was measured as described in "direct AE assay". The diagram represents the staining patterns of sperm with intact acrosomes, and undergoing intermediate exocytosis stages. Roman numerals are as in panel **(C)**. With this staining method, exocytosis halts at the vesiculated stage, more advanced than II and III but never reaching stage IV. **(C)** Transmission electron micrographs of human sperm heads representative of the four patterns distinguished in this study. Sperm with a flat acrosome (intact, I), sperm with swollen and waving acrosome (II), sperm with swollen and waving acrosome plus electron dense material diffusing out of the cell (III, arrows point to this material), sperm that lost its acrosome completely (fully exocytosed IV). Bars = 200 nm. A acrosome; IAM: inner acrosomal membrane; OAM: outer acrosomal membrane; PM: plasma membrane; N: nucleus. **(D)** Frequency histogram of the percentage of sperm in each of the four categories shown in **C** when cells were incubated with 0.5 mM $CaCl_2$ (Ca, gray bars) or pretreated with 15 nM anti-α-synuclein antibodies before adding 0.5 mM $CaCl_2$ (anti-α-syn→Ca, black bars). Open bars (control) represent the percentage of sperm in each category in untreated samples. The data represent mean values ±SEM, calculated from four independent experiments with at least 100 cells analyzed in each repetition. Two-way ANOVA shows statistically significant differences between "anti-α-syn→Ca" vs. "Ca" groups for all the samples analyzed, $*p < 0.05$ and $***p < 0.0001$ (Tukey's test).

acrosomal region in a high percentage of cells that had initiated the AE but could not complete it because the anti-α-synuclein prevented it (Figure 5B, anti-α-syn → Ca). This is consistent with the distribution shown in Figure 4C, where bins II and III were the most abundant under these experimental conditions. Because colloidal gold was coupled to a probe that exclusively binds the acrosomal matrix, these results support our hypothesis that the acrosomal contents targeted by PSA had diffused out of the sperm (diffuse material, arrows in pattern III, Figure 4C). Similar patterns of detection of extracellular acrosomal contents attributed to efflux through fusion pores have been described with anti-acrosin antibodies (Tesarik et al., 1988) and PSA coupled to paramagnetic beads (Kohn et al., 1996). Colloidal gold present in the medium bathing the cells was seldom observed inside acrosomes, which reflects its inability to traverse the pores opened between the plasma and acrosomal membranes. Soluble PSA permeated through fusion pores and reached the acrosomal membrane (Figure 4B) but that bound to gold nanoparticles did not; these observations suggest that the latter was excluded because of size. The pores were large enough to allow efflux of acrosomal material but too small to allow influx of 20 nm gold nanoparticles. Thus, we conclude that the fusion pores stabilized by anti-α-synuclein antibodies were smaller than 20 nm, the size of the gold nanoparticles used in this study.

α-Synuclein is required for fusion pore dilation

We have shown that the inhibition of the AE by anti-α-synuclein antibodies is a post-fusion event because they freeze sperm SNAREs in toxin-resistant, *cis* complexes (Figure 3) and allow the influx of an acrosomal probe (Figure 4B) as well as the efflux of the acrosomal matrix (Figure 5). Is α-synuclein required after bilayer fusion to dilate the fusion pores? We tested this hypothesis with computational and experimental approaches. We have recently implemented into PLUMED the reaction coordinate ξ_e to study

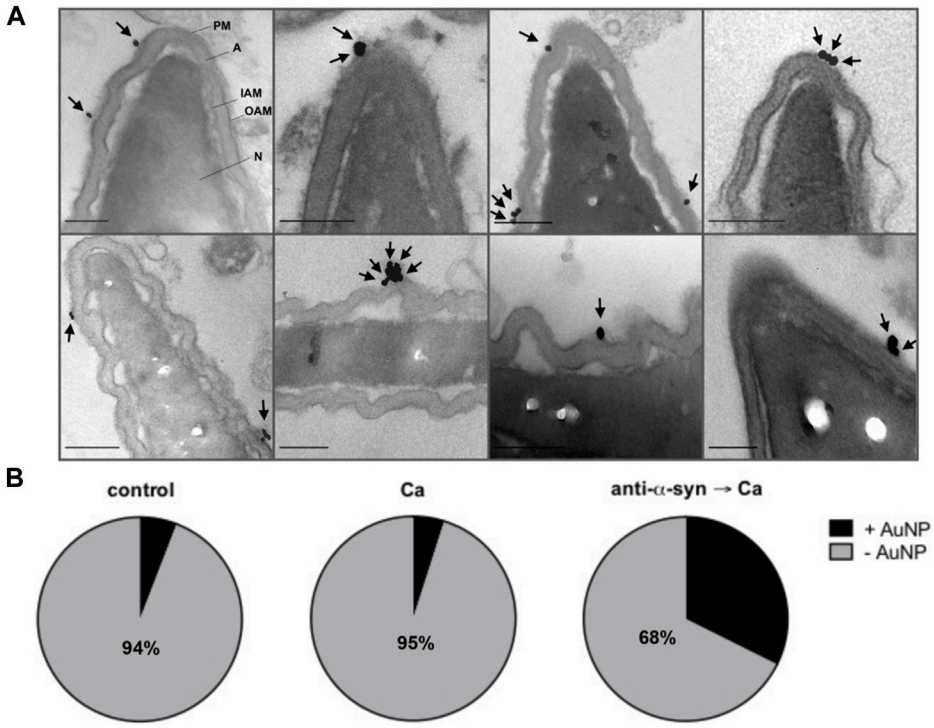

FIGURE 5
PSA-gold binds the electron dense material that diffuses out of sperm. Spermatozoa were incubated for 15 min at 37°C with culture medium or 15 nM anti-α-synuclein antibodies (α-syn) followed by 20 μg/mL PSA-gold nanoparticles (AuNP) and a 15 min at 37°C incubation. When indicated, 0.5 mM $CaCl_2$ (Ca) was added and incubations continued for 30 min at 37°C. **(A)** Gallery showing gold nanoparticles (arrows) bound to the surface in the acrosomal region of sperm heads with swollen and waving acrosomes. Bars = 200 nm. **(B)** Quantification: grey area: cells without gold nanoparticles (-AuNP, numbers indicate the percentage of cells in this category); black area: cells with gold nanoparticles (+AuNP). "Control" 102 cells scored, "Ca", 101 cells scored, "anti-α-syn→Ca", 102 cells scored. Statistical analysis was performed using GraphPad Prism. Chi-square test was applied for proportions. *p*-value < 0.0001 were considered statistically significant.

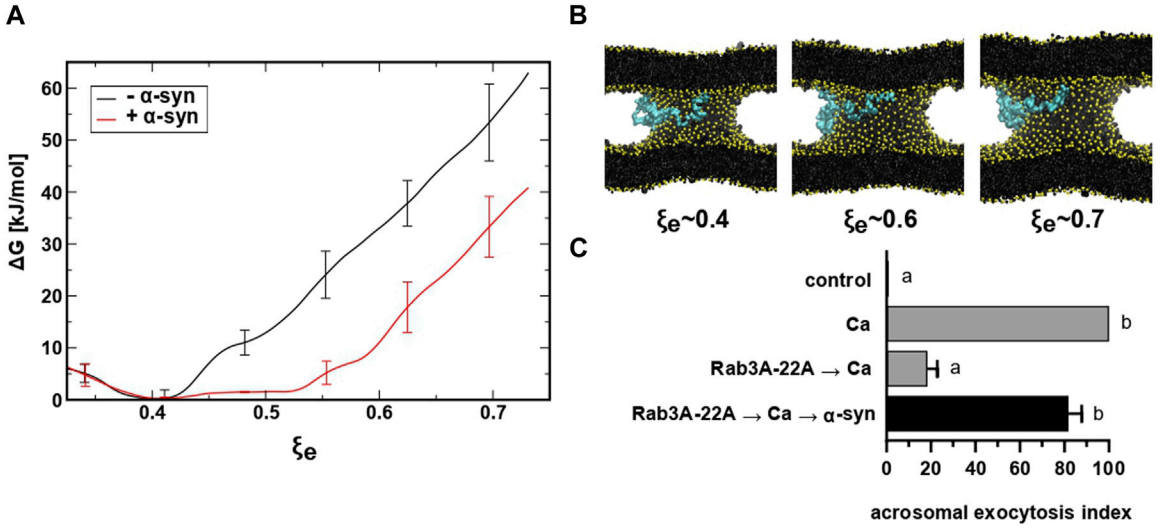

FIGURE 6
restrained molecular dynamics simulations reveal that α-synuclein favors the expansion of the fusion pore. **(A)** Free energy profiles for fusion pore expansion with (red line) and without (black line) full-length α-synuclein. **(B)** Molecular dynamics snapshots for different stages of the expanded fusion pore. Lipids are colored in black with phosphate groups in yellow and α-synuclein in cyan. For clarity, water molecules are not shown. **(C)** SLO-permeabilized sperm were incubated with 300 nM Rab3A-22A, 0.5 mM $CaCl_2$, and 50 nM α-synuclein (10 min at 37°C after each addition, black bar). Gray bars represent controls. The AE was measured as indicated in the legend to Figure 2A.

the thermodynamics of the expansion of the fusion pore using restrained molecular dynamics (Di Bartolo et al., 2022). ξ_e is a dimensionless parameter approximately proportional to the radius (R, in nm) of a toroid-shaped fusion pore (see Eq. 1) [for mathematical details on ξ_e see Masone and collaborators (Di Bartolo et al., 2022)]

$$R \simeq 0.75\xi_e + 0.2 \quad (1)$$

To investigate the influence of α-synuclein, we expanded a fusion pore nucleated between two lipid bilayers using molecular dynamics simulations and the collective variable ξ_e. We inserted a Martini model of α-synuclein between the bilayers (in the cytosolic space) generated from the human micelle-bound α-synuclein (PDB ID: 1xq8) (Ulmer et al., 2005). Figure 6A shows the Gibbs free energy needed to expand a fusion pore with (red) and without (black) α-synuclein in system. A significant reduction (~ 20 kJ/mol) of the free energy occurred as the fusion pore expanded from $\xi_e \sim 0.4$ ($R \simeq 0.5$ nm) to $\xi_e \sim 0.75$ ($R \simeq 0.75$ nm) in the presence of the protein. Snapshots of the expanding pore at three different values of ξ_e are shown in panel B. Notice that the protein, initially situated in the "cytoplasm" (between the bilayers), freely adsorbed on the phospholipid surface of the pore. This location is consistent with experimental data that show strong binding of α-synuclein to highly curved lipid membranes (Middleton and Rhoades, 2010; Caparotta et al., 2020a). These findings suggest that α-synuclein facilitates the expansion of fusion pores that connect two pure lipid membranes.

When introduced into SLO-permeabilized human sperm, the chimeric protein Rab3A-22A halts the AE elicited by calcium at a stage after membrane fusion/pore opening but before pore expansion/membrane vesiculation (Quevedo et al., 2016). Addition of recombinant α-synuclein after Rab3A-22A and calcium rescued the exocytotic block imposed by the chimaera (Figure 6C). Taken together, our results suggest that α-synuclein is required at a post-fusion stage during sperm exocytosis and that its unavailability inhibits the AE because pores do not expand.

Discussion

Exocytosis involves fusion of cargo-loaded vesicles and granules with the plasma membrane. Despite similar molecular machineries, exocytosis proceeds at different speeds, being much faster in synaptic vesicles (~40 nm diameter, high curvature) than in chromaffin and insulin granules (~100–300 nm diameter, low curvature) (Kreutzberger et al., 2019). The fusion pore that opens between the fusing membranes and connects the granule's lumen with the extracellular space can evolve in various ways: it can dilate—slowly or rapidly—to allow full cargo release (full fusion), it can reseal (kiss and run) or open and close repeatedly (flickering) (Karatekin, 2018; Mion et al., 2022). Among other factors, pore dynamics, vesicle size and curvature of the membrane determine the kinetics of cargo release. The acrosome is a very large, electron dense granule that surrounds the elongated nucleus in the apical domain of the sperm head. The head of the human sperm is oval, 3.7–4.7 μm long and 2.5–3.2 μm wide, with the acrosomal domain comprising 40%–70% of the head (Bellastella et al., 2010). Owing to its large size, exocytosis of the acrosome is very slow (minutes instead of seconds or milliseconds) (Harper et al., 2008; Sosa et al., 2015; Romarowski et al., 2016). Rather than being spherical like most vesicles and granules, it resembles a horseshoe in longitudinal sections of resting sperm observed by transmission electron microscopy. The anterior acrosome, or acrosomal cap, is involved in AE, whereas the posterior acrosome, or equatorial segment, is involved in fusion with the oolema. The acrosomal membrane of resting cells exhibits low curvature, except for the anterior tip, the region where fusion with the plasma membrane begins in human sperm (Yudin et al., 1988; Harper et al., 2008). Once the AE has initiated, the acrosome swells and its outer membrane waves profusely, acquiring high curvature. Swelling, fusion and vesiculation do not extend to the equatorial segment, which remains intact after AE, with plasma, inner and outer acrosomal membranes close to one another in a parallel, linear array (Yudin et al., 1988). As stated before, the fate of the fusion pores that open during the AE does not fit into full fusion, kiss and run or flickering modes. Despite these differences, exocytosis of the acrosome relies on the same molecular machinery as that in endocrine and neuroendocrine cells and also depends on the opening and dilation of fusion pores between the acrosomal and plasma membranes.

Modulation of fusion pore opening and dilation during exocytosis has been attributed to various members of the fusion machinery (reviewed in (Karatekin, 2018; Chowdhury and Zorec, 2020; Risselada and Mayer, 2020)), Epac2 (Gucek et al., 2019) and α-synuclein. A study conducted in rat hippocampal primary neurons and mouse adrenal chromaffin cells shows that both, overexpressed and endogenous α-synucleins accelerate the dilation of the fusion pores, whereas loss of all three synuclein isoforms increases the likelihood of pore closure events without affecting the time to closure. Fusion pore dilation would not be expected to influence the release of classical transmitters, such as glutamate, that escape rapidly even through small pores. In contrast, it would affect the release of monoamines and peptides that dissociate slowly from a luminal matrix (Logan et al., 2017). Likewise, in an *in vitro* system that uses TIRF microscopy to study the fusion between single vesicles containing synaptobrevin-2 and flat artificial membranes containing syntaxin1a and SNAP-25, α-synuclein promotes the probability of opening, duration and expansion of large (6 nm) fusion pores (Khounlo et al., 2021). Lastly, overexpression of α-synuclein quickens the post-fusion discharge of brain-derived neurotrophic factor in bovine chromaffin cells detected by videomicroscopy in live cells (Abbineni et al., 2019). Although these observations are consistent with an increase in fusion pore expansion, the authors of this report failed to capture such expansion by TIRF microscopy.

α-Synuclein adopts a bent helix structure when bound to highly curved micelles but adopts an elongated helix structure when bound to membranes with low curvature (Trexler and Rhoades, 2009). It has been hypothesized that at the highly curved membranes surrounding the fusion pore, α-synuclein adopts a bent α-helix structure that binds to the vesicle on one side and to the plasma membrane on the other. Its transition to an extended state would drive pore dilation (Runwal and Edwards, 2021). The authors of this very insightful review put forth an alternative mechanism by which α-synuclein may regulate SNARE complex dynamics after fusion (Runwal and Edwards, 2021). Given the high curvature of the outer membrane in swollen acrosomes (Figures 4C, 5) and the resistance of synaptobrevin to toxin cleavage (Figure 3) in sperm treated with

anti-α-synuclein and calcium, both hypotheses would be worth exploring.

Despite its small size, α-synuclein failed to diffuse out of SLO-permeabilized human sperm (Figure 1C), perhaps reflecting its interaction with sperm membranes. Alternatively, α-synuclein may engage in large molecular weight complexes unable to exit the cell through the toxin-generated pores. No loss of protein by diffusion accounted for the access of the anti-α-synuclein antibodies to their intracellular target. By obstructing the function of sperm α-synuclein, the antibodies inhibited the AE because they impaired a post-docking (Figure 2B), post-fusion pore opening (Figures 4A, B) step of the pathway. It is licit to speculate that the electron dense material appreciated in the "swollen, waving and diffuse" classification in Figure 4 may correspond, at least partially, to the acrosomal contents recognized by the gold-coupled lectin (Figure 5). Taken together, these findings strongly suggest that treatment with anti-α-synuclein antibodies stabilizes fusion pores during the calcium-induced AE. It was through these pores that FITC-PSA entered (Figure 4B) and electron dense material diffused out of (Figure 5) the acrosomal granule. These findings are reminiscent of those attained when Rab3A-22A substituted for anti-α-synuclein antibodies (Quevedo et al., 2016). Addition of recombinant α-synuclein rescued the block imposed by the antibodies (Figure 3A). One possible explanation for these findings is that the recombinant protein (which did not influence the percentage of AE *per se* in our end-point assay, see Supplementary Figure S2) added at the end of the incubation displaced the antibody from sperm synuclein and allowed the exocytotic cascade to resume. Exogenous α-synuclein also rescued the block imposed by Rab3A-22A (Figure 6C), which supports the more attractive notion that the protein directly or indirectly expanded the pores. Results from computational analysis also agree with this view (Figures 6A, B).

The novel findings reported here are: i) α-synuclein regulates a post-fusion stage of the AE to dilate the pores; ii) when endogenous α-synuclein is unavailable, SNARE proteins are engaged in post-fusion *cis* complexes; iii) when endogenous α-synuclein is unavailable, electron dense contents diffuse out of the acrosome through open, stable fusion pores. As happens in other cells, sperm fusion pores are subjected to post-fusion regulation.

Misfolded α-synuclein species can spread between cells in a prion-like manner and seed the aggregation of endogenous protein in recipient cells. This cell-to-cell transmission and propagation of misfolded α-synuclein mirrors the spread of human neurodegenerative diseases such as Parkinson's (Bras et al., 2020; Oliveira et al., 2021). Many pathogenic mutations have been discovered in the α-synuclein-encoding gene *SNCA* in cases of familial Parkinson's disease. *SNCA* overexpression and its mutants were introduced in animal models of neurodegeneration [reviewed in (Oliveira et al., 2021) (Runwal and Edwards, 2021; Gasser, 2023]. Neither aggregation of synuclein in the male germline nor the fertility of these animals have been reported to date. Single α-synuclein (Abeliovich et al., 2000), double αγ-synuclein (Papachroni et al., 2005) and triple αβγ-synuclein (Greten-Harrison et al., 2010) null mice are viable and fertile. We would have expected reduced male fertility in these cases. However, overt reproductive phenotypes are rarely observed in mating experiments even when egg- or sperm-specific proteins with well established roles in fertility are knocked out. In contrast, problems are readily detected when gametes of deficient animals are tested in experiments designed to assess their fertility, such as IVF, something that has not been done for synucleins. This is an interesting avenue to pursue in the future.

Data availability statement

The original contributions presented in the study are included in the article/Supplementary Material, further inquiries can be directed to the corresponding author.

Ethics statement

The studies involving human participants were reviewed and approved by Comité de Bioética School of Medicine, Cuyo University. The patients/participants provided their written informed consent to participate in this study.

Author contributions

MaB, MiB, AD, and DM performed the experiments; MaB, MiB, AD, DM, and CT analyzed the data; CT coordinated the project and wrote the paper. All authors contributed to the article and approved the submitted version.

Funding

This study was supported by Agencia Nacional de Promoción Científica y Tecnológica (grant numbers PICT 2017-1179 to CT and PICT2017-1002 to DM, Argentina), CONICET (grant number PIP-0409CO to DM) and Secretaría de Investigación, Internacionales y Posgrado, Universidad Nacional de Cuyo (grant numbers 06/M126 to CT and M007-T1 to MaB, Argentina).

Acknowledgments

The authors thank very specially M.C. Ruete for her generous initial training of MiB, Drs. M.C.Ruete and L. Mayorga for revising this manuscript critically for important intellectual content, Drs. T. Binz, L. Pollegioni for plasmids, M.F. Quevedo for purified GST-Rab3A-22A, and R. Militello, E. Bocanegra, N. Domizio and J. Ibáñez for excellent technical assistance. Supercomputing time for this work was provided by CCAD (Centro de Computación de Alto Desempeño de la Universidad Nacional de Córdoba). The preparation of samples for transmission electron microscopy was carried out by A. Morales and P. López, Servicio de Microscopía Electrónica del Instituto de Histología y Embriología "Mario H. Burgos" (IHEM—CONICET-UNCuyo).

Conflict of interest

The authors declare that the research was conducted in the absence of any commercial or financial relationships that could be construed as a potential conflict of interest.

Publisher's note

All claims expressed in this article are solely those of the authors and do not necessarily represent those of their affiliated organizations, or those of the publisher, the editors and the reviewers. Any product that may be evaluated in this article, or claim that may be made by its manufacturer, is not guaranteed or endorsed by the publisher.

Supplementary material

The Supplementary Material for this article can be found online at: https://www.frontiersin.org/articles/10.3389/fcell.2023.1125988/full#supplementary-material

References

Abbineni, P. S., Bohannon, K. P., Bittner, M. A., Axelrod, D., and Holz, R. W. (2019). Identification of beta-synuclein on secretory granules in chromaffin cells and the effects of alpha- and beta-synuclein on post-fusion BDNF discharge and fusion pore expansion. *Neurosci. Lett.* 699, 134–139. doi:10.1016/j.neulet.2019.01.056

Abeliovich, A., Schmitz, Y., Farinas, I., Choi-Lundberg, D., Ho, W. H., Castillo, P. E., et al. (2000). Mice lacking alpha-synuclein display functional deficits in the nigrostriatal dopamine system. *Neuron* 25, 239–252. doi:10.1016/s0896-6273(00)80886-7

Ackermann, F., Zitranski, N., Heydecke, D., Wilhelm, B., Gudermann, T., and Boekhoff, I. (2008). The Multi-PDZ domain protein MUPP1 as a lipid raft-associated scaffolding protein controlling the acrosome reaction in mammalian spermatozoa. *J. Cell Physiol.* 214, 757–768. doi:10.1002/jcp.21272

Ahnert-Hilger, G., Munster-Wandowski, A., and Holtje, M. (2013). Synaptic vesicle proteins: Targets and routes for botulinum neurotoxins. *Curr. Top. Microbiol. Immunol.* 364, 159–177. doi:10.1007/978-3-642-33570-9_8

Alabi, A. A., and Tsien, R. W. (2013). Perspectives on kiss-and-run: Role in exocytosis, endocytosis, and neurotransmission. *Annu. Rev. Physiol.* 75, 393–422. doi:10.1146/annurev-physiol-020911-153305

Alvarez de, T. G., Montes, M. A., Montenegro, P., and Borges, R. (2018). Phases of the exocytotic fusion pore. *FEBS Lett.* 592, 3532–3541. doi:10.1002/1873-3468.13234

Alza, N. P., Iglesias Gonzalez, P. A., Conde, M. A., Uranga, R. M., and Salvador, G. A. (2019). Lipids at the crossroad of alpha-synuclein function and dysfunction: Biological and pathological implications. *Front. Cell Neurosci.* 13, 175. doi:10.3389/fncel.2019.00175

Barclay, J. W., Morgan, A., and Burgoyne, R. D. (2012). Neurotransmitter release mechanisms studied in *Caenorhabditis elegans*. *Cell Calcium* 52, 289–295. doi:10.1016/j.ceca.2012.03.005

Bellastella, G., Cooper, T. G., Battaglia, M., Strose, A., Torres, I., Hellenkemper, B., et al. (2010). Dimensions of human ejaculated spermatozoa in Papanicolaou-stained seminal and swim-up smears obtained from the Integrated Semen Analysis System (ISAS(®)). *Asian J. Androl.* 12, 871–879. doi:10.1038/aja.2010.90

Belmonte, S. A., Mayorga, L. S., and Tomes, C. N. (2016). The molecules of sperm exocytosis. *Adv. Anat. Embryol. Cell Biol.* 220, 71–92. doi:10.1007/978-3-319-30567-7_4

Bombardier, J. P., and Munson, M. (2015). Three steps forward, two steps back: Mechanistic insights into the assembly and disassembly of the SNARE complex. *Curr. Opin. Chem. Biol.* 29, 66–71. doi:10.1016/j.cbpa.2015.10.003

Borges-Araujo, L., Souza, P. C. T., Fernandes, F., and Melo, M. N. (2022). Improved parameterization of phosphatidylinositide lipid headgroups for the Martini 3 coarse-grain force field. *J. Chem. Theory. Comput.* 18, 357–373. doi:10.1021/acs.jctc.1c00615

Bras, I. C., Dominguez-Meijide, A., Gerhardt, E., Koss, D., Lazaro, D. F., Santos, P. I., et al. (2020). Synucleinopathies: Where we are and where we need to go. *J. Neurochem.* 153, 433–454. doi:10.1111/jnc.14965

Buffone, M. G., Hirohashi, N., and Gerton, G. L. (2014). Unresolved questions concerning mammalian sperm acrosomal exocytosis. *Biol. Reprod.* 90, 112. doi:10.1095/biolreprod.114.117911

Buffone, M. G., Ijiri, T. W., Cao, W., Merdiushev, T., Aghajanian, H. K., and Gerton, G. L. (2012). Heads or tails? Structural events and molecular mechanisms that promote mammalian sperm acrosomal exocytosis and motility. *Mol. Reprod. Dev.* 79, 4–18. doi:10.1002/mrd.21393

Bustos, M. A., Roggero, C. M., De, I., Mayorga, L. S., and Tomes, C. N. (2014). GTP-bound Rab3A exhibits consecutive positive and negative roles during human sperm dense-core granule exocytosis. *J. Mol. Cell Biol.* 6, 286–298. doi:10.1093/jmcb/mju021

Caldinelli, L., Albani, D., and Pollegioni, L. (2013). One single method to produce native and Tat-fused recombinant human alpha-synuclein in *Escherichia coli*. *Bmc. Biotechnol.* 13, 32–13. doi:10.1186/1472-6750-13-32

Caparotta, M., Bustos, D. M., and Masone, D. (2020a). Order-disorder skewness in alpha-synuclein: A key mechanism to recognize membrane curvature. *Phys. Chem. Chem. Phys.* 22 (9), 5255–5263. doi:10.1039/c9cp04951g

Caparotta, M., Tomes, C. N., Mayorga, L. S., and Masone, D. (2020b). The synaptotagmin-1 C2B domain is a key regulator in the stabilization of the fusion pore. *J. Chem. Theory. Comput.* 16, 7840–7851. doi:10.1021/acs.jctc.0c00734

Chiang, H. C., Shin, W., Zhao, W. D., Hamid, E., Sheng, J., Baydyuk, M., et al. (2014). Post-fusion structural changes and their roles in exocytosis and endocytosis of dense-core vesicles. *Nat. Commun.* 5, 3356. doi:10.1038/ncomms4356

Chowdhury, H. H., and Zorec, R. (2020). Exocytotic fusion pore under stress. *Cell Stress* 4, 218–226. doi:10.15698/cst2020.09.230

Correia, J., Michelangeli, F., and Publicover, S. (2015). Regulation and roles of Ca^{2+} stores in human sperm. *Reproduction* 150, 65–76. doi:10.1530/REP-15-0102

Cross, N. L., Morales, P., Overstreet, J. W., and Hanson, F. W. (1986). Two simple methods for detecting acrosome-reacted human sperm. *Gamete Res.* 15, 213–226. doi:10.1002/mrd.1120150303

Darszon, A., Nishigaki, T., Beltran, C., and Treviño, C. L. (2011). Calcium channels in the development, maturation, and function of spermatozoa. *Physiol. Rev.* 91, 1305–1355. doi:10.1152/physrev.00028.2010

De Blas, G. A., Roggero, C. M., Tomes, C. N., and Mayorga, L. S. (2005). Dynamics of SNARE assembly and disassembly during sperm acrosomal exocytosis. *PLoS. Biol.* 3, e323. doi:10.1371/journal.pbio.0030323

De Blas, G., Michaut, M., Treviño, C. L., Tomes, C. N., Yunes, R., Darszon, A., et al. (2002). The intraacrosomal calcium pool plays a direct role in acrosomal exocytosis. *J. Biol. Chem.* 277, 49326–49331. doi:10.1074/jbc.M208587200

Di Bartolo, A. L., and Masone, D. (2022). Synaptotagmin-1 C2B domains cooperatively stabilize the fusion stalk via a master-servant mechanism. *Chem. Sci.* 13, 3437–3446. doi:10.1039/d1sc06711g

Di Bartolo, A. L., Tomes, C. N., Mayorga, L. S., and Masone, D. (2022). Enhanced expansion and reduced kiss-and-run events in fusion pores steered by synaptotagmin-1 C2B domains. *J. Chem. Theory. Comput.* 18, 4544–4554. doi:10.1021/acs.jctc.2c00424

Fabris, F., Sostaric, P., Matak, I., Binz, T., Toffan, A., Simonato, M., et al. (2022). Detection of VAMP proteolysis by tetanus and botulinum neurotoxin type B *in vivo* with a cleavage-specific antibody. *Int. J. Mol. Sci.* 23, 4355. doi:10.3390/ijms23084355

Fasshauer, D., Sutton, R. B., Brunger, A. T., and Jahn, R. (1998). Conserved structural features of the synaptic fusion complex: SNARE proteins reclassified as Q- and R-SNAREs. *Proc. Natl. Acad. Sci. U. S. A.* 95, 15781–15786. doi:10.1073/pnas.95.26.15781

Foster, J. A., and Gerton, G. L. (2016). The acrosomal matrix. *Adv. Anat. Embryol. Cell Biol.* 220, 15–33. doi:10.1007/978-3-319-30567-7_2

Gaisano, H. Y. (2014). Here come the newcomer granules, better late than never. *Trends Endocrinol. Metab.* 25, 381–388. doi:10.1016/j.tem.2014.03.005

Gallea, J. I., Ambroggio, E. E., Vilcaes, A. A., James, N. G., Jameson, D. M., and Celej, M. S. (2018). Amyloid oligomerization of the Parkinson's disease related protein alpha-synuclein impacts on its curvature-membrane sensitivity. *J. Neurochem.* 147, 541–556. doi:10.1111/jnc.14573

Gao, Y., Zorman, S., Gundersen, G., Xi, Z., Ma, L., Sirinakis, G., et al. (2012). Single reconstituted neuronal SNARE complexes zipper in three distinct stages. *Science* 337, 1340–1343. doi:10.1126/science.1224492

Gasser, T. (2023). *Genetic testing for Parkinson's disease in clinical practice*. Vienna: J. Neural Transm.

Giraudo, C. G., Eng, W. S., Melia, T. J., and Rothman, J. E. (2006). A clamping mechanism involved in SNARE-dependent exocytosis. *Science* 313, 676–680. doi:10.1126/science.1129450

Greten-Harrison, B., Polydoro, M., Morimoto-Tomita, M., Diao, L., Williams, A. M., Nie, E. H., et al. (2010). αβγ-Synuclein triple knockout mice reveal age-dependent neuronal dysfunction. *Proc. Natl. Acad. Sci. U. S. A.* 107, 19573–19578. doi:10.1073/pnas.1005005107

Gucek, A., Gandasi, N. R., Omar-Hmeadi, M., Bakke, M., Doskeland, S. O., Tengholm, A., et al. (2019). Fusion pore regulation by cAMP/Epac2 controls cargo release during insulin exocytosis. *Elife* 8, e41711. doi:10.7554/eLife.41711

Harper, C. V., Cummerson, J. A., White, M. R., Publicover, S. J., and Johnson, P. M. (2008). Dynamic resolution of acrosomal exocytosis in human sperm. *J. Cell Sci.* 121, 2130–2135. doi:10.1242/jcs.030379

Hayashi, T., McMahon, H., Yamasaki, S., Binz, T., Hata, Y., Sudhof, T. C., et al. (1994). Synaptic vesicle membrane fusion complex: Action of clostridial neurotoxins on assembly. *EMBO J.* 13, 5051–5061. doi:10.1002/j.1460-2075.1994.tb06834.x

Haynes, L. P., Barnard, R. J., Morgan, A., and Burgoyne, R. D. (1998). Stimulation of NSF ATPase activity during t-SNARE priming. *FEBS Lett.* 436, 1–5. doi:10.1016/s0014-5793(98)01088-6

Hirohashi, N. (2016). Site of mammalian sperm acrosome reaction. *Adv. Anat. Embryol. Cell Biol.* 220, 145–158. doi:10.1007/978-3-319-30567-7_8

Hu, X. Q., Ji, S. Y., Li, Y. C., Fan, C. H., Cai, H., Yang, J. L., et al. (2010). Acrosome formation-associated factor is involved in fertilization. *Fertil. Steril.* 93, 1482–1492. doi:10.1016/j.fertnstert.2009.01.067

Hua, S. Y., and Charlton, M. P. (1999). Activity-dependent changes in partial VAMP complexes during neurotransmitter release. *Nat. Neurosci.* 2, 1078–1083. doi:10.1038/16005

Ingolfsson, H. I., Melo, M. N., van Eerden, F. J., Arnarez, C., Lopez, C. A., Wassenaar, T. A., et al. (2014). Lipid organization of the plasma membrane. *J. Am. Chem. Soc.* 136, 14554–14559. doi:10.1021/ja507832e

Jahn, R., and Fasshauer, D. (2012). Molecular machines governing exocytosis of synaptic vesicles. *Nature* 490, 201–207. doi:10.1038/nature11320

Jun, Y., and Wickner, W. (2019). Sec17 (alpha-SNAP) and Sec18 (NSF) restrict membrane fusion to R-SNAREs, Q-SNAREs, and SM proteins from identical compartments. *Proc. Natl. Acad. Sci. U. S. A.* 116, 23573–23581. doi:10.1073/pnas.1913985116

Karatekin, E. (2018). Toward a unified picture of the exocytotic fusion pore. *FEBS Lett.* 592, 3563–3585. doi:10.1002/1873-3468.13270

Khounlo, R., Hawk, B. J. D., Khu, T. M., Yoo, G., Lee, N. K., Pierson, J., et al. (2021). Membrane binding of α-synuclein stimulates expansion of SNARE-dependent fusion pore. *Front. Cell Dev. Biol.* 9, 663431. doi:10.3389/fcell.2021.663431

Kohn, F. M., Mack, S. R., Hashish, Y. A., Anderson, R. A., and Zaneveld, L. J. (1996). Paramagnetic beads coated with Pisum sativum agglutinin bind to human spermatozoa undergoing the acrosome reaction. *Andrologia* 28, 231–239. doi:10.1111/j.1439-0272.1996.tb02788.x

Kreutzberger, A. J. B., Kiessling, V., Stroupe, C., Liang, B., Preobraschenski, J., Ganzella, M., et al. (2019). *In vitro* fusion of single synaptic and dense core vesicles reproduces key physiological properties. *Nat. Commun.* 10, 3904. doi:10.1038/s41467-019-11873-8

La Spina, F. A., Puga Molina, L. C., Romarowski, A., Vitale, A. M., Falzone, T. L., Krapf, D., et al. (2016). Mouse sperm begin to undergo acrosomal exocytosis in the upper isthmus of the oviduct. *Dev. Biol.* 411, 172–182. doi:10.1016/j.ydbio.2016.02.006

Lee, B. R., and Kamitani, T. (2011). Improved immunodetection of endogenous alpha-synuclein. *PLoS. ONE.* 6, e23939. doi:10.1371/journal.pone.0023939

Logan, T., Bendor, J., Toupin, C., Thorn, K., and Edwards, R. H. (2017). α-Synuclein promotes dilation of the exocytotic fusion pore. *Nat. Neurosci.* 20, 681–689. doi:10.1038/nn.4529

Masaracchia, C., Hnida, M., Gerhardt, E., Lopes da, F. T., Villar-Pique, A., Branco, T., et al. (2018). Membrane binding, internalization, and sorting of alpha-synuclein in the cell. *Acta Neuropathol. Commun.* 6, 79. doi:10.1186/s40478-018-0578-1

Mendoza, C., Carreras, A., Moos, J., and Tesarik, J. (1992). Distinction between true acrosome reaction and degenerative acrosome loss by a one-step staining method using *Pisum sativum* agglutinin. *J. Reprod. Fertil.* 95, 755–763. doi:10.1530/jrf.0.0950755

Middleton, E. R., and Rhoades, E. (2010). Effects of curvature and composition on alpha-synuclein binding to lipid vesicles. *Biophys. J.* 99, 2279–2288. doi:10.1016/j.bpj.2010.07.056

Mion, D., Bunel, L., Heo, P., and Pincet, F. (2022). The beginning and the end of SNARE-induced membrane fusion. *FEBS Open* 12, 1958–1979. doi:10.1002/2211-5463.13447

Oliveira, L. M. A., Gasser, T., Edwards, R., Zweckstetter, M., Melki, R., Stefanis, L., et al. (2021). Alpha-synuclein research: Defining strategic moves in the battle against Parkinson's disease. *NPJ. Park. Dis.* 7, 65. doi:10.1038/s41531-021-00203-9

Pantano, S., and Montecucco, C. (2014). The blockade of the neurotransmitter release apparatus by botulinum neurotoxins. *Cell Mol. Life Sci.* 71, 793–811. doi:10.1007/s00018-013-1380-7

Papachroni, K., Ninkina, N., Wanless, J., Kalofoutis, A. T., Gnuchev, N. V., and Buchman, V. L. (2005). Peripheral sensory neurons survive in the absence of alpha- and gamma-synucleins. *J. Mol. Neurosci.* 25, 157–164. doi:10.1385/JMN:25:2:157

Pelletan, L. E., Suhaiman, L., Vaquer, C. C., Bustos, M. A., De Blas, G. A., Vitale, N., et al. (2015). ADP ribosylation factor 6 (ARF6) promotes acrosomal exocytosis by modulating lipid turnover and Rab3A activation. *J. Biol. Chem.* 290, 9823–9841. doi:10.1074/jbc.M114.629006

Perez-Lara, A., Thapa, A., Nyenhuis, S. B., Nyenhuis, D. A., Halder, P., Tietzel, M., et al. (2016). PtdInsP2 and PtdSer cooperate to trap synaptotagmin-1 to the plasma membrane in the presence of calcium. *Elife* 5, e15886. doi:10.7554/eLife.15886

Pirazzini, M., Montecucco, C., and Rossetto, O. (2022). Toxicology and pharmacology of botulinum and tetanus neurotoxins: An update. *Arch. Toxicol.* 96, 1521–1539. doi:10.1007/s00204-022-03271-9

Porat-Shliom, N., Milberg, O., Masedunskas, A., and Weigert, R. (2013). Multiple roles for the actin cytoskeleton during regulated exocytosis. *Cell Mol. Life Sci.* 70, 2099–2121. doi:10.1007/s00018-012-1156-5

Pronk, S., Pall, S., Schulz, R., Larsson, P., Bjelkmar, P., Apostolov, R., et al. (2013). Gromacs 4.5: A high-throughput and highly parallel open source molecular simulation toolkit. *Bioinformatics* 29, 845–854. doi:10.1093/bioinformatics/btt055

Quevedo, M. F., Lucchesi, O., Bustos, M. A., Pocognoni, C. A., De, l. I., and Tomes, C. N. (2016). The Rab3A-22a chimera prevents sperm exocytosis by stabilizing open fusion pores. *J. Biol. Chem.* 291, 23101–23111. doi:10.1074/jbc.M116.729954

Ren, G., Wang, X., Hao, S., Hu, H., and Wang, C. C. (2007). Translocation of alpha-synuclein expressed in *Escherichia coli*. *J. Bacteriol.* 189, 2777–2786. doi:10.1128/JB.01406-06

Reynolds, E. S. (1963). The use of lead citrate at high pH as an electron-opaque stain in electron microscopy. *J. Cell Biol.* 17, 208–212. doi:10.1083/jcb.17.1.208

Risselada, H. J., and Mayer, A. (2020). SNAREs, tethers and SM proteins: How to overcome the final barriers to membrane fusion? *Biochem. J.* 477, 243–258. doi:10.1042/BCJ20190050

Rizo, J. (2018). Mechanism of neurotransmitter release coming into focus. *Protein Sci.* 27, 1364–1391. doi:10.1002/pro.3445

Rizo, J. (2022). Molecular mechanisms underlying neurotransmitter release. *Annu. Rev. Biophys.* 51, 377–408. doi:10.1146/annurev-biophys-111821-104732

Rizo, J., and Xu, J. (2015). The synaptic vesicle release machinery. *Annu. Rev. Biophys.* 44, 339–367. doi:10.1146/annurev-biophys-060414-034057

Rodriguez, F., Bustos, M. A., Zanetti, M. N., Ruete, M. C., Mayorga, L. S., and Tomes, C. N. (2011). α-SNAP prevents docking of the acrosome during sperm exocytosis because it sequesters monomeric syntaxin. *PLoS. ONE.* 6, e21925. doi:10.1371/journal.pone.0021925

Roggero, C. M., De Blas, G. A., Dai, H., Tomes, C. N., Rizo, J., and Mayorga, L. S. (2007). Complexin/synaptotagmin interplay controls acrosomal exocytosis. *J. Biol. Chem.* 282, 26335–26343. doi:10.1074/jbc.M700854200

Romarowski, A., Sanchez-Cardenas, C., Ramirez-Gomez, H. V., Puga Molina, L. C., Trevino, C. L., Hernandez-Cruz, A., et al. (2016). A specific transitory increase in intracellular calcium induced by progesterone promotes acrosomal exocytosis in mouse sperm. *Biol. Reprod.* 94, 63. doi:10.1095/biolreprod.115.136085

Runwal, G., and Edwards, R. H. (2021). The membrane interactions of synuclein: Physiology and pathology. *Annu. Rev. Pathol.* 16, 465–485. doi:10.1146/annurev-pathol-031920-092547

Ryu, J. K., Jahn, R., and Yoon, T. Y. (2016). Review: Progresses in understanding N-ethylmaleimide sensitive factor (NSF) mediated disassembly of SNARE complexes. *Biopolymers* 105, 518–531. doi:10.1002/bip.22854

Sanchez-Cardenas, C., Servin-Vences, M. R., Jose, O., Treviño, C. L., Hernandez-Cruz, A., and Darszon, A. (2014). Acrosome reaction and Ca^{2+} imaging in single human spermatozoa: New regulatory roles of $[Ca^{2+}]_i$. *Biol. Reprod.* 91, 67. doi:10.1095/biolreprod.114.119768

Schiavo, G., Matteoli, M., and Montecucco, C. (2000). Neurotoxins affecting neuroexocytosis. *Physiol. Rev.* 80, 717–766. doi:10.1152/physrev.2000.80.2.717

Sharma, S., and Lindau, M. (2018). The fusion pore, 60 years after the first cartoon. *FEBS Lett.* 592, 3542–3562. doi:10.1002/1873-3468.13160

Silva, M., Tran, V., and Marty, A. (2021). Calcium-dependent docking of synaptic vesicles. *Trends Neurosci.* 44, 579–592. doi:10.1016/j.tins.2021.04.003

Sorensen, J. B. (2009). Conflicting views on the membrane fusion machinery and the fusion pore. *Annu. Rev. Cell Dev. Biol.* 25, 513–537. doi:10.1146/annurev.cellbio.24.110707.175239

Sorensen, J. B., Wiederhold, K., Muller, E. M., Milosevic, I., Nagy, G., de Groot, B. L., et al. (2006). Sequential N- to C-terminal SNARE complex assembly drives priming and fusion of secretory vesicles. *EMBO J.* 25, 955–966. doi:10.1038/sj.emboj.7601003

Sosa, C. M., Pavarotti, M. A., Zanetti, M. N., Zoppino, F. C., De Blas, G. A., and Mayorga, L. S. (2015). Kinetics of human sperm acrosomal exocytosis. *Mol. Hum. Reprod.* 21, 244–254. doi:10.1093/molehr/gau110

Souza, P. C. T., Alessandri, R., Barnoud, J., Thallmair, S., Faustino, I., Grunewald, F., et al. (2021). Martini 3: A general purpose force field for coarse-grained molecular dynamics. *Nat. Methods* 18, 382–388. doi:10.1038/s41592-021-01098-3

Spurr, A. R. (1969). A low-viscosity epoxy resin embedding medium for electron microscopy. *J. Ultrastruct. Res.* 26, 31–43. doi:10.1016/s0022-5320(69)90033-1

Tesarik, J., Drahorad, J., and Peknicova, J. (1988). Subcellular immunochemical localization of acrosin in human spermatozoa during the acrosome reaction and zona pellucida penetration. *Fertil. Steril.* 50, 133–141. doi:10.1016/s0015-0282(16)60021-3

Tomes, C. N., De Blas, G. A., Michaut, M. A., Farre, E. V., Cherhitin, O., Visconti, P. E., et al. (2005). alpha-SNAP and NSF are required in a priming step during the human sperm acrosome reaction. *Mol. Hum. Reprod.* 11, 43–51. doi:10.1093/molehr/gah126

Tomes, C. N. (2015). The proteins of exocytosis: Lessons from the sperm model. *Biochem. J.* 465, 359–370. doi:10.1042/BJ20141169

Trexler, A. J., and Rhoades, E. (2009). Alpha-synuclein binds large unilamellar vesicles as an extended helix. *Biochemistry* 48, 2304–2306. doi:10.1021/bi900114z

Tribello, G., Bonomi, M., Branduardi, D., Camillioni, C., and Bussi, G. (2014). Plumed 2: New feathers for an old bird. *Comput. Phys. Commun.* 185, 604–613. doi:10.1016/j.cpc.2013.09.018

Ulmer, T. S., Bax, A., Cole, N. B., and Nussbaum, R. L. (2005). Structure and dynamics of micelle-bound human alpha-synuclein. *J. Biol. Chem.* 280, 9595–9603. doi:10.1074/jbc.M411805200

Van Der, S. D., Lindahl, E., Hess, B., Groenhof, G., Mark, A. E., and Berendsen, H. J. (2005). Gromacs: Fast, flexible, and free. *J. Comput. Chem.* 26, 1701–1718. doi:10.1002/jcc.20291

Vardjan, N., Jorgacevski, J., and Zorec, R. (2013). Fusion pores, SNAREs, and exocytosis. *Neuroscientist* 19, 160–174. doi:10.1177/1073858412461691

Walter, A. M., Wiederhold, K., Bruns, D., Fasshauer, D., and Sorensen, J. B. (2010). Synaptobrevin N-terminally bound to syntaxin-SNAP-25 defines the primed vesicle state in regulated exocytosis. *J. Cell Biol.* 188, 401–413. doi:10.1083/jcb.200907018

Wu, Z., Auclair, S. M., Bello, O., Vennekate, W., Dudzinski, N. R., Krishnakumar, S. S., et al. (2016). Nanodisc-cell fusion: Control of fusion pore nucleation and lifetimes by SNARE protein transmembrane domains. *Sci. Rep.* 6, 27287. doi:10.1038/srep27287

Xu, T., Ashery, U., Burgoyne, R. D., and Neher, E. (1999a). Early requirement for alpha-SNAP and NSF in the secretory cascade in chromaffin cells. *EMBO J.* 18, 3293–3304. doi:10.1093/emboj/18.12.3293

Xu, T., Rammner, B., Margittai, M., Artalejo, A. R., Neher, E., and Jahn, R. (1999b). Inhibition of SNARE complex assembly differentially affects kinetic components of exocytosis. *Cell* 99, 713–722. doi:10.1016/s0092-8674(00)81669-4

Yudin, A. I., Gottlieb, W., and Meizel, S. (1988). Ultrastructural studies of the early events of the human sperm acrosome reaction as initiated by human follicular fluid. *Gamete Res.* 20, 11–24. doi:10.1002/mrd.1120200103

Zanetti, N., and Mayorga, L. S. (2009). Acrosomal swelling and membrane docking are required for hybrid vesicle formation during the human sperm acrosome reaction. *Biol. Reprod.* 81, 396–405. doi:10.1095/biolreprod.109.076166

Zarelli, V. E., Ruete, M. C., Roggero, C. M., Mayorga, L. S., and Tomes, C. N. (2009). PTP1B dephosphorylates N-Ethylmaleimide-sensitive factor and elicits SNARE complex disassembly during human sperm exocytosis. *J. Biol. Chem.* 284, 10491–10503. doi:10.1074/jbc.M807614200

Zhang, Y., and Hughson, F. M. (2021). Chaperoning SNARE folding and assembly. *Annu. Rev. Biochem.* 90, 581–603. doi:10.1146/annurev-biochem-081820-103615

Zhao, M., and Brunger, A. T. (2016). Recent advances in deciphering the structure and molecular mechanism of the AAA+ ATPase N-Ethylmaleimide-Sensitive factor (NSF). *J. Mol. Biol.* 428, 1912–1926. doi:10.1016/j.jmb.2015.10.026

Zhao, W. D., Hamid, E., Shin, W., Wen, P. J., Krystofiak, E. S., Villarreal, S. A., et al. (2016). Hemi-fused structure mediates and controls fusion and fission in live cells. *Nature* 534, 548–552. doi:10.1038/nature18598

frontiers | Frontiers in Cell and Developmental Biology

TYPE Original Research
PUBLISHED 02 June 2023
DOI 10.3389/fcell.2023.1148773

OPEN ACCESS

EDITED BY
Rafael A. Fissore,
University of Massachusetts Amherst, United States

REVIEWED BY
Tina Tootle,
The University of Iowa, United States
Arnon Henn,
Technion Israel Institute of Technology, Israel

*CORRESPONDENCE
Graydon B. Gonsalvez,
ggonsalvez@augusta.edu

RECEIVED 20 January 2023
ACCEPTED 18 May 2023
PUBLISHED 02 June 2023

CITATION
Neiswender H, Baker FC, Veeranan-Karmegam R, Allen P and Gonsalvez GB (2023), dTtc1, a conserved tetratricopeptide repeat protein, is required for maturation of *Drosophila* egg chambers via its role in stabilizing electron transport chain components. *Front. Cell Dev. Biol.* 11:1148773. doi: 10.3389/fcell.2023.1148773

dTtc1, a conserved tetratricopeptide repeat protein, is required for maturation of *Drosophila* egg chambers via its role in stabilizing electron transport chain components

Hannah Neiswender, Frederick C. Baker, Rajalakshmi Veeranan-Karmegam, Phylicia Allen and Graydon B. Gonsalvez *

Cellular Biology and Anatomy, Medical College of Georgia, Augusta University, Augusta, GA, United States

We recently identified the *Drosophila* ortholog of TTC1 (dTtc1) as an interacting partner of Egalitarian, an RNA adaptor of the Dynein motor. In order to better understand the function of this relatively uncharacterized protein, we depleted dTtc1 in the *Drosophila* female germline. Depletion of dTtc1 resulted in defective oogenesis and no mature eggs were produced. A closer examination revealed that mRNA cargoes normally transported by Dynein were relatively unaffected. However, mitochondria in dTtc1 depleted egg chambers displayed an extremely swollen phenotype. Ultrastructural analysis revealed a lack of cristae. These phenotypes were not observed upon disruption of Dynein. Thus, this function of dTtc1 is likely to be Dynein independent. Consistent with a role for dTtc1 in mitochondrial biology, a published proteomics screen revealed that dTtc1 interacts with numerous components of electron transport chain (ETC) complexes. Our results indicate that the expression level of several of these ETC components was significantly reduced upon depletion of dTtc1. Importantly, this phenotype was completely rescued upon expression of wild-type GFP-dTtc1 in the depleted background. Lastly, we demonstrate that the mitochondrial phenotype caused by a lack of dTtc1 is not restricted to the germline but is also observed in somatic tissues. Our model suggests that dTtc1, likely in combination with cytoplasmic chaperones, is required for stabilizing ETC components.

KEYWORDS

TRP domain, electron transport chain, Dynein, oocyte, mitochondria

Introduction

The microtubule minus-end motor cytoplasmic Dynein (hereafter Dynein) is involved in transporting numerous types of cargo such as RNAs, proteins, vesicles, and organelles (Cason and Holzbaur, 2022; Jongsma et al., 2023). These cargos are typically linked to Dynein via adaptor proteins (Reck-Peterson et al., 2018; Canty and Yildiz, 2020). One such adaptor expressed in the *Drosophila melanogaster* oocyte and embryo is the RNA binding protein, Egalitarian (Egl) (Mach and Lehmann, 1997). Egl has been shown to link a growing

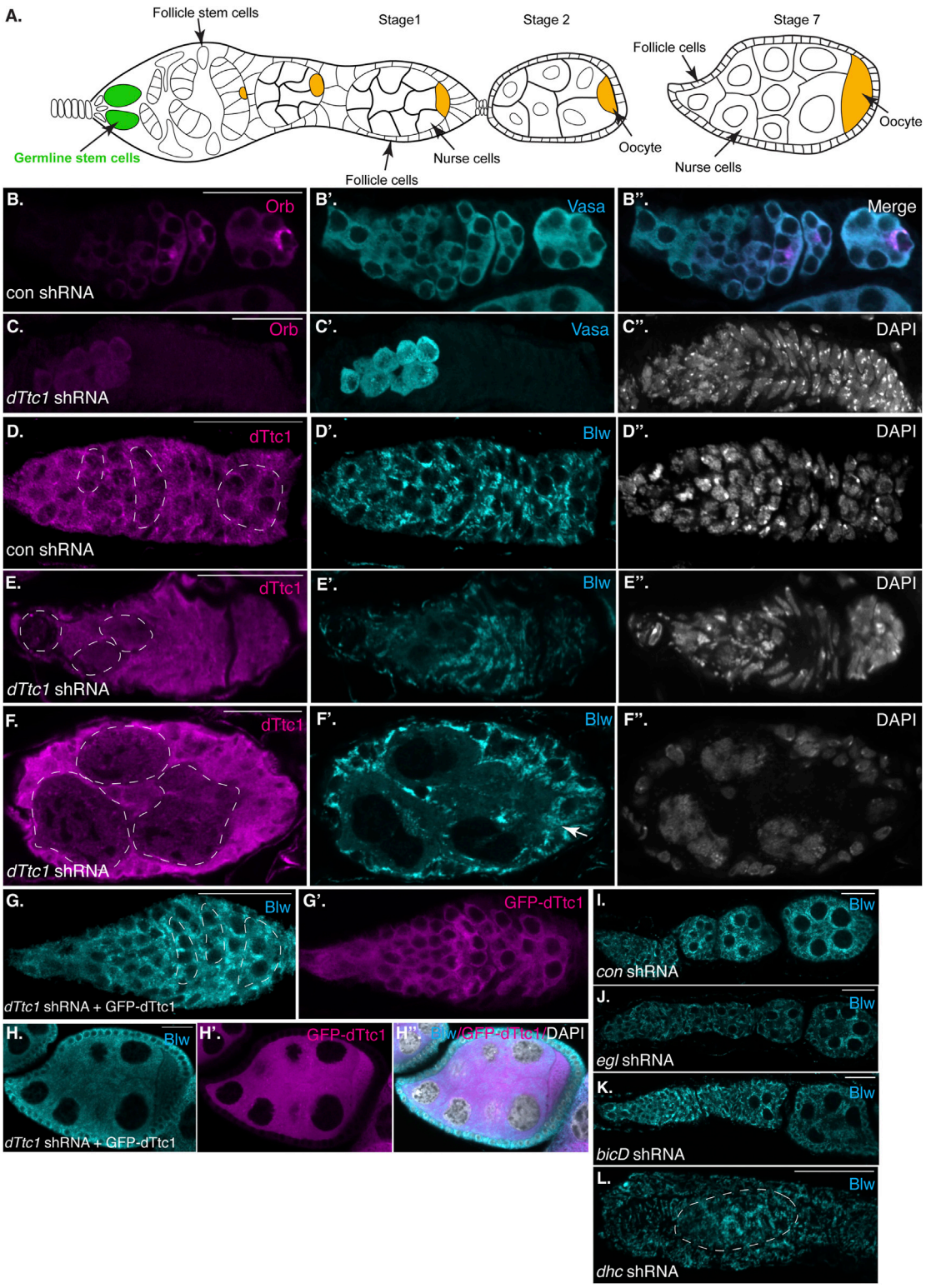

FIGURE 1
Early-stage depletion of dTtc1. **(A)** Schematic of a *Drosophila* female germarium as well as stage 1, 2 and 7 egg chambers. The germline stem cells are colored in green and the oocyte is shown in orange. **(B, C)** Ovaries were dissected and fixed from strains expressing either a control shRNA **(B)** or an shRNA against *dTtc1* **(C)**. The shRNAs were expressed using a driver that is active in the germarium. The egg chambers were processed for immunofluorescence using an antibody against Orb (magenta) and Vasa [cyan, **(B′, B′′, C′)**]. The egg chambers were also counterstained using DAPI to visualize nuclei [greyscale, **(C′′)**]. Depletion of dTtc1 results in defective formation of a 16-cell cyst. **(D–F)** The same control **(D)** and dTtc1 depleted egg chambers **(E, F)** were processed for immunofluorescence using antibodies against dTtc1 (magenta) and Blw [cyan, **(D′, E′, F′)**], a mitochondrial marker protein. The egg chambers were counterstained with DAPI to visualize nuclei **(D′′, E′′, F′′)**. Germline cysts are marked with a dashed line. dTtc1 depleted germline cells were almost completely devoid of mitochondria. By contrast, the surrounding somatic follicle cells contained normal mitochondria (arrows). **(G, H)**
(*Continued*)

FIGURE 1 (Continued)
Ovaries were dissected and fixed from a strain co-expressing the *dTtc1* shRNA and a GFP-dTtc1 transgene. The egg chambers were processed for immunofluorescence using an antibody against Blw (cyan). The channel for GFP-dTtc1 is shown in **(G′, H′)** (magenta). **(H′′)** is a merged image of Blw, GFP-dTtc1 and the DAPI channel (DAPI shown in greyscale). Expression of GFP-dTtc1 rescued the mitochondrial phenotypes. **(I–L)** Ovaries were dissected and fixed from strains expressing shRNAs against eb1(I, control shRNA) *egl* **(J)**, bicD **(L)** or dhc **(L)**. The ovaries were processed for immunofluorescence using an antibody against Blw. Depletion of these components does not produce the same mitochondrial defect as observed upon dTtc1 depletion. The scale bar in these images corresponds to 20 microns.

list of RNAs with the Dynein motor (Dienstbier et al., 2009; Goldman and Gonsalvez, 2017; Vazquez-Pianzola et al., 2017; Goldman et al., 2019; Goldman et al., 2021). Localization of several of these mRNAs is key to establishment of polarity in the oocyte and to specification of the body plan in the embryo (Weil, 2014; Goldman and Gonsalvez, 2017).

In an effort to determine whether Egl also links non-RNA cargo with Dynein, we recently undertook a proteomics screen using *Drosophila* ovaries (Baker et al., 2021). One of the candidates identified in this screen was the uncharacterized gene CG14894. Because this gene is the fly ortholog of human TTC1/TPR1, we named the gene *dTtc1*. Very little is known regarding the function of dTtc1. Although the mammalian protein is similarly under-studied, it has been shown to be present in a complex with the heat shock protein, Hsp90 (Lotz et al., 2008). TTC1 contains tetratricopeptide repeats, a motif that is bound by C-terminal residues within Hsp90 (Scheufler et al., 2000). In addition, TTC1 also interacts with the A and B isoforms of VAP-33 (also referred to as VAPA and VAPB) (Lotz et al., 2008). Studies suggest that a trimeric complex consisting of TTC1, VAP-33, and Hsp90 is involved in vesicle trafficking (Lotz et al., 2008). This complex appears to be conserved in flies as dTtc1 was also found to interact with the fly orthologs of Hsp90 and VAP-33 (Baker et al., 2021).

Our interest in dTtc1 was spurred by the finding that TTC1 was identified in mammalian cells as a component of the Dynein complex (Redwine et al., 2017). We therefore hypothesized that dTtc1 might serve as a cargo or cargo adaptor of the Dynein motor. Surprisingly, however, we found that Dynein-localized mRNAs were not affected upon depletion of dTtc1. However, mitochondria in dTtc1 depleted egg chambers were significantly compromised; their numbers were reduced, they displayed a swollen morphology, and were largely devoid of cristae. Furthermore, the expression of numerous components of electron transport chain (ETC) complexes was greatly reduced in dTtc1 depleted ovaries. This phenotype is not germline specific, because depletion of dTtc1 in somatic tissues is also associated with similar mitochondrial defects. Thus, although our results do not rule out a potential function for dTtc1 in Dynein-related processes, our findings suggest a novel and primary role for dTtc1 in maintaining healthy mitochondria.

Results

dTtc1 is required for formation of the egg chamber

The *Drosophila* egg chamber is composed of fifteen nurse cells and a single oocyte. Formation of the egg chamber involves division of a germline stem cell to produce a daughter cell known as a cystoblast. The cystoblast divides four more times to produce a sixteen-cell cyst. One of these cells will be specified as the oocyte, while the remainder differentiate as supportive cells known as nurse cells (Figure 1A) (Huynh and St Johnston, 2004).

Oocyte specification is a complex process involving numerous factors, including several components and regulators of the microtubule minus-end motor, Dynein (Suter and Steward, 1991; Carpenter, 1994; McGrail and Hays, 1997) (Figure 1A). Among these factors are Bicaudal-D (BicD), a Dynein activating adaptor, and Egalitarian (Egl), an RNA binding protein (Dienstbier et al., 2009; Hoogenraad and Akhmanova, 2016). The current model suggests that Egl binds numerous mRNAs in the *Drosophila* oocyte and embryo and links these mRNAs with Dynein via its interaction with BicD (McClintock et al., 2018; Sladewski et al., 2018; Goldman et al., 2019). However, it is also possible that Egl links non-RNA cargo with the Dynein motor. In order to explore this potential function of Egl, we undertook a proteomics screen using *Drosophila* ovaries to identify interacting partners of Egl. One candidate that was identified in this screen was the *Drosophila* ortholog of human TTC1, which we refer to as dTtc1 (Baker et al., 2021). We demonstrated in a recent publication that dTtc1 was enriched within the oocyte of stage 4 to stage 7 *Drosophila* egg chambers in an Egl-dependent manner (Baker et al., 2021) (Supplementary Figure S1A, arrows).

Relatively little is known regarding the function of dTtc1. However, human TTC1 was also identified in an independent proteomics screen as an interacting partner of Dynein light intermediate chain, as well as an interacting partner of BicD2, the human homolog of *Drosophila* BicD (Redwine et al., 2017). Thus, the association of TTC1 with the Dynein motor complex appears to be conserved between flies and mammals.

In order to identify the molecular function of dTtc1 we depleted this protein in the *Drosophila* germline. Immunofluorescence analysis indicates that the shRNA is capable of depleting endogenous dTtc1 and that the depletion is specific to germline cells (Supplementary Figures S1A, B). We initially used a driver that is active in the germanium, at the earliest stages of egg chamber formation. For simplicity, we will refer to this driver as a "germarium driver" (see Materials and methods for details). In contrast to strains expressing a control shRNA, strains expressing the shRNA against *dTtc1* contained extremely small degenerating ovaries (Supplementary Figure S1C, D). We examined dissected ovaries using an antibody against Orb, a marker for oocytes specification. Control egg chambers contained a single cell that was highly enriched for Orb (Figure 1B). By contrast, strains expressing the *dTtc1* shRNA displayed minimal Orb staining (Figure 1C). A closer examination using an antibody against Vasa, a protein expressed in germ cells, revealed that dTtc1 depleted strains failed to even form a sixteen-cell cyst (Figures 1B′, B″, C′, C″). Egg chamber formation involves a specialized membranous branched structure that

connects germline stem cells and their differentiating progeny referred to as the fusome (Lin et al., 1994). As expected, the fusome was readily detected in egg chambers expressing a control shRNA (Supplementary Figure S2A, arrows). By contrast, the fusome was not formed in dTtc1 depleted egg chambers (Supplementary Figures S2B, B′). Thus, dTtc1 is required at the earliest stages within the germanium for formation of the egg chamber.

In a previous interactome analysis, dTtc1 was shown to interact with numerous mitochondrial proteins (Baker et al., 2021). We therefore examined control and dTtc1 depleted egg chambers using an antibody against Blw, a mitochondrial marker protein and the fly homolog of human ATP5A1. Rather astonishingly, cells within dTtc1 depleted cysts contained relatively few mitochondria (Figures 1D–F, dashed circles). By contrast, the surrounding somatic follicle cells, within which the shRNA is not expressed, displayed normal mitochondrial numbers and morphology (Figures 1E, F, arrow).

In order to test the specificity of this phenotype, we expressed GFP-dTtc1 in these egg chambers. Importantly, the dTtc1 used in this transgenic strain contained silent mutations that makes it refractory to the shRNA. Thus, using this strategy, we are able to deplete endogenous dTtc1 and express a wild-type version of GFP-dTtc1 in the same cells. Co-expressing wild-type GFP-dTtc1 and the *dttc1* shRNA in the germarium completely rescued these phenotypes. Egg chamber maturation occurs normally in these strains and mature oocytes were produced (Figures 1G, H). In addition, these egg chambers contained abundant mitochondria that were morphologically normal (Figures 1G, H). Based on these results, we conclude that the egg chamber degeneration and mitochondrial phenotypes are specifically caused due to depletion of dTtc1.

As noted previously, dTtc1 was identified as an interacting partner of Egl, a Dynein RNA adaptor. Loss of Egl and BicD in the germanium results in defective oocyte specification (Theurkauf et al., 1993). However, mitochondrial defects have not been reported in *egl* and *bicD* null mutants. Consistent with these previous studies, we found that depletion of Egl and BicD using the same germarium driver that was used to deplete dTtc1 produced morphologically normal egg chambers that were lacking an oocyte. Furthermore, we did not observe any overt mitochondrial phenotype in these depleted egg chambers (Figures 1I, J). Depletion of Dynein heavy chain (Dhc), the motor subunit of Dynein, resulted in a much more severe phenotype (Figure 1K). This is also consistent with prior studies indicating a role for Dynein in formation of the sixteen-cell cyst (McGrail and Hays, 1997). However, even in these aberrant egg chambers, the mitochondria appeared relatively normal (Figure 1K). Thus, in contrast to dTtc1 depletion, depletion of Dynein components at these earliest stages of oogenesis does not result in significant mitochondrial loss.

Depletion of dTtc1 in mid-stage egg chambers also results in defective mitochondria

Loss of dTtc1 in the germanium results in extremely small ovaries that are difficult to fully characterize. We therefore expressed the *dttc1* shRNA using a driver that is active at slightly later stages of oogenesis (Sanghavi et al., 2016). For simplicity, we refer to this driver as an early-stage driver (see Materials and methods for details). Using this approach, dTtc1 function in the germanium is preserved, and egg chambers containing a single oocyte can be specified. However, even using this approach, mature eggs are not produced (Supplementary Figure S1, E, F). Consistent with published results (Lu et al., 2022), a similar phenotype was observed upon depleting Dhc using this early-stage driver (Supplementary Figure S1G). We therefore examined dTtc1 and Dhc depleted mid-stage egg chambers using a mitochondria marker antibody. In egg chambers expressing a control shRNA, mitochondria were abundant and were typically clustered in the vicinity of the nurse cell nuclei (Figures 2A, A′, D). However, this clustering phenotype was disrupted in Dhc depleted egg chambers (Figures 2B, D). Despite a lack of clustering, overall mitochondria numbers and morphology appeared unaffected (Figure 2B′; Supplementary Figure S2F). By contrast, egg chambers expressing the *dTtc1* shRNA contained fewer mitochondria (Figure 2C; Supplementary Figure S2F). In addition, the mitochondria that were present displayed a swollen and enlarged phenotype (Figure 2C′). Similar results were obtained using a strain expressing mitochondria labeled with EYFP (Supplementary Figures S2C, D, D′). However, despite the reduced number of mitochondria and their swollen appearance, clustering of mitochondria adjacent to nurse cell nuclei was preserved (Figures 2C, D). We therefore conclude that dTtc1 is required for maintaining adequate mitochondria numbers and normal morphology but not for their localization within the egg chamber. Dynein on the other hand, appears to be mostly involved in mitochondrial positioning.

In order to better understand the nature of the mitochondrial defect, and to examine these phenotypes with greater resolution, we processed control and dTtc1 depleted egg chambers for transmission electron microscopy. As expected, control egg chambers contained numerous mitochondria that were elongated with abundant cristae (Figures 2E, E′). Quantification of EM images revealed that mitochondria in dTtc1 depleted egg chambers were much less abundant, were enlarged, and largely devoid of cristae (Figures 2F, F′; Supplementary Figure S2G). Thus, depletion of dTtc1 in mid-stage egg chambers results in morphologically abnormal mitochondria.

The Dynein motor, Egl, and BicD are required for localization of several mRNAs such as *hts* and *bcd* in mid-stage egg chambers. In order to determine whether dTtc1 is required for these Dynein-mediated processes, we examined control and dTtc1 depleted egg chambers using *in situ* hybridization. In contrast to what is observed upon depletion of Egl (Goldman et al., 2021), *hts* and *bcd* remained correctly localized in dTtc1 depleted egg chambers (Figures 3A, B). Thus, although dTtc1 was identified as an interacting partner of Egl (Baker et al., 2021), depletion of dTtc1 does not appear to compromise Egl and Dynein-mediated mRNA localization.

dTtc1 depletion results in reduced expression of electron transport chain components

Given the mitochondrial phenotype observed upon depletion of dTtc1, we wondered whether dTtc1 localized to mitochondria. Egg

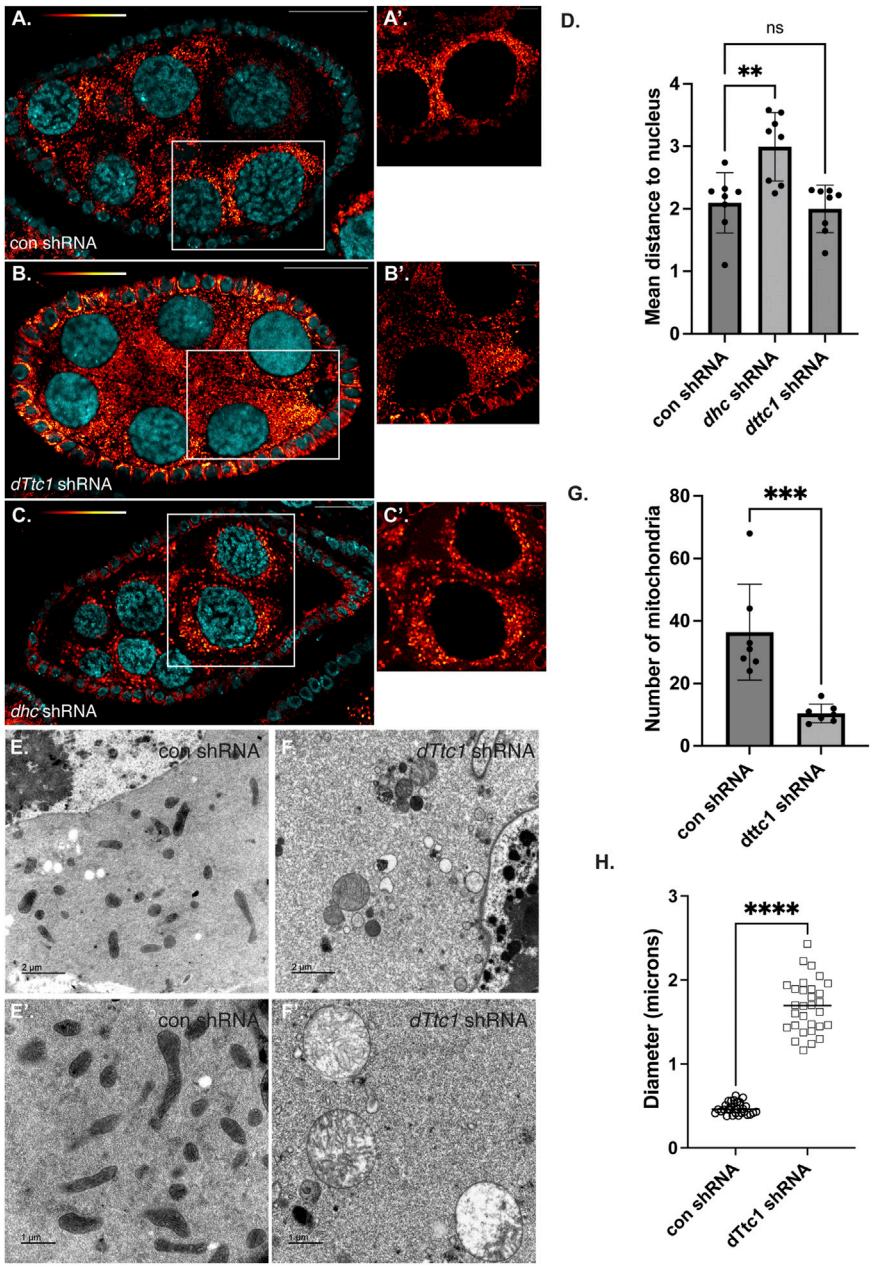

FIGURE 2
Mid-stage depletion of dTtc1. **(A–D)** Ovaries were dissected and fixed from strains expressing a control shRNA **(A)** an shRNA against *dhc* **(B)** or an shRNA against *dTtc1* **(B)** using a driver that is not active in the germanium but is active in early and mid-stage egg chambers (referred to in the Methods as an early-stage driver). The tissues were processed for immunofluorescence using an antibody against Blw (red to white LUT). **(A′–C′)** represent magnified images of the area shown in the white box. Mitochondria cluster in the vicinity of nurse cell nuclei. This clustering phenotype was disrupted in Dhc depleted egg chambers **(D)**. Mitochondrial clustering was not affected in dTtc1 depleted egg chambers **(D)**. However, these egg chambers contained fewer mitochondria that displayed a swollen phenotype. A one-way Anova was used for this analysis; $^{**}p \leq 0.01$, ns = not significant, $n = 8$ egg chambers. **(E–H)** The same control **(E)** and dTtc1 depleted ovaries **(F)** were processed for transmission electron microscopy. In comparison to the control, dTtc1 depleted egg chambers contained fewer mitochondria **(G)**. Note that **(E′,F′)** are from different areas of the slide and do not represent magnified images of the panels in E and **(F)**. An unpaired *t*-test was used for statistical analysis; $^{***}p \leq 0.001$, $n = 7$ individual frames. **(H)** The mitochondrial diameter was determined for control and dTtc1 depleted strains using EM images. Consistent with what was observed using light microscopy, mitochondria in dTtc1 depleted egg chambers are enlarged. An unpaired *t*-test was used for statistical analysis; $^{****}p \leq 0.0001$. $n = 30$ mitochondria were analyzed for each genotype. The scale bar in **(A–C)** is 20 microns; in **(A′–C′)** the scale bar is 5 microns; in **(C,D)** the scale bar is 2 microns; and in **(C′,D′)** the scale bar is 1 micron.

chambers were processed for immunofluorescence using the dTtc1 antibody and a mitochondria marker antibody. High-resolution imaging did not reveal extensive colocalization between dTtc1 and mitochondria (Supplementary Figure S2E). Rather, dTtc1 appeared to be mostly cytoplasmic with occasional foci observed adjacent to mitochondria (Supplementary Figure S2E).

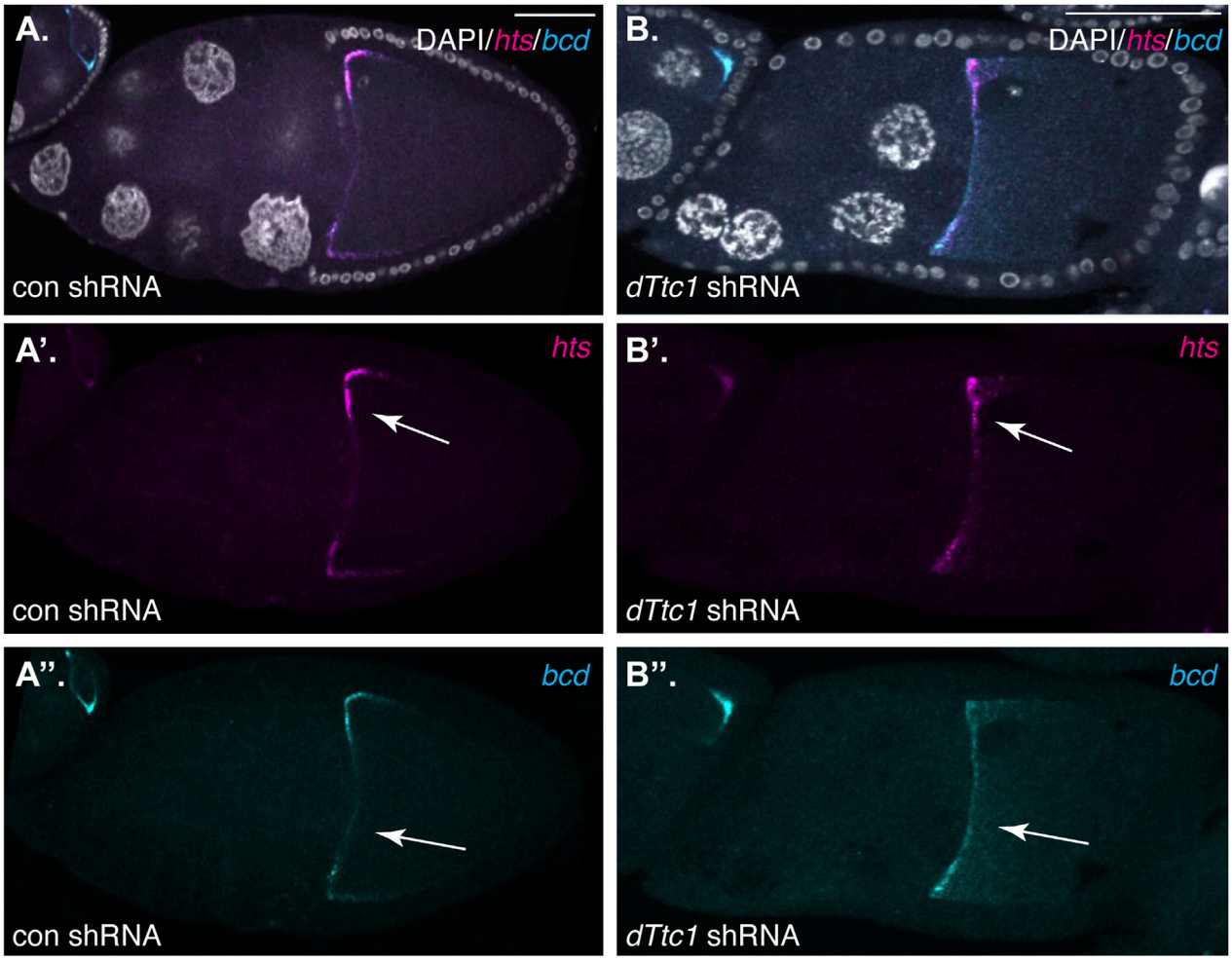

FIGURE 3
(A, B) Ovaries from flies expressing a control shRNA **(A)** or an shRNA against *dTtc1* **(B)** using the early-stage driver were dissected, fixed and processed for *in situ* hybridization using probes against *hts*(magenta) and *bcd* (cyan). The egg chambers were also counterstained with DAPI to visualize nuclei (greyscale). The individual channels for hts and bcd are shown in **(A′, B′, A′′, B′′)**. The anterior localization of these mRNAs was not affected by the depletion of dTtc1 (arrows).

Consistent with these results, fractionation of ovarian lysates revealed that dTtc1 was mostly present in the cytoplasmic fraction, with perhaps a small amount of the protein also present in the mitochondrial fraction (Figure 4A).

Previous studies have shown that dTtc1 interacts with several components of mitochondrial ETC complexes (Supplementary Figure S3A) (Baker et al., 2021). We therefore examined mitochondrial fractions by Western blotting using antibodies against Nd20, Sdha, UQCR-C2, Cox4, ATP synthase beta, and Blw (Figure 4B). Because of the small ovaries present in dTtc1 depleted females, we dissected approximately 1.5x more females from this strain in comparison to the control. In addition, the load was normalized to the total level of protein in the cytoplasmic fraction. As a further validation of equivalent loading, we also examined mitochondrial fractions by silver staining (Supplementary Figure S3B). Under these conditions, we observed that the level of all tested ETC components was reduced to varying degrees (Figures 4B, C). For instance, the level of ND20 was only modestly reduced, whereas the level of Sdha was dramatically reduced (Figures 4B, C). We did not observe an accumulation of these proteins in the cytosolic fraction (data not shown). Thus, the reduced level of these components does not appear to be due to defective mitochondrial import. Expression of GFP-dTtc1 in this background completely rescued this phenotype (Supplementary Figure S3C). Collectively, these results indicate that depletion of dTtc1 in the germline results in mitochondria with defective morphology and reduced expression of ETC components.

We next examined mitochondrial function in these tissues. Live egg chambers from strains expressing an EYFP-mito marker as well as either a control shRNA or an shRNA against *dTtc1* were processed using TMRM. This dye is incorporated into mitochondria dependent upon membrane potential (Garcez et al., 2020). In order to normalize the signal to total mitochondria, the ratio of TMRM signal was compared to the signal for EYFP-mito. Using this strategy, we did not observe a significant difference in mitochondrial membrane potential between the control and dTtc1 depleted strains (Figures 4D, E). Thus, despite the reduced mitochondrial numbers and morphology differences, the membrane

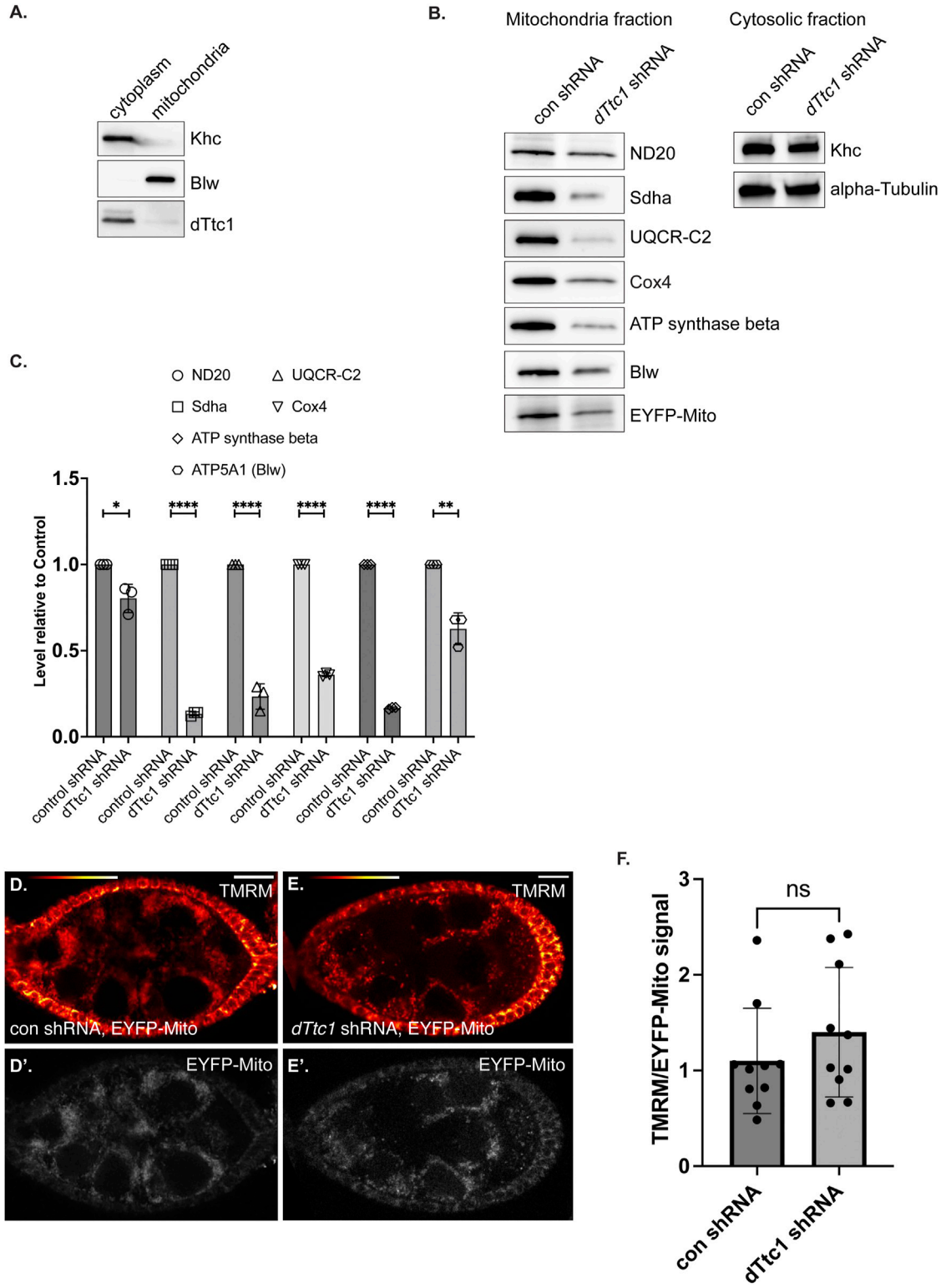

FIGURE 4
Electron transport chain components are expressed at a reduced level in dTtc1 depleted egg chambers. **(A)** Cytoplasmic and mitochondrial fractions were prepared from wild-type fly ovaries and were analyzed by western blotting using the indicated antibodies. dTtc1 is mostly present in the cytoplasmic fraction. **(B, C)** Cytoplasmic and mitochondrial fractions were prepared from ovaries of flies expressing either a control shRNA or an shRNA against *dTtc1* using the early-stage driver. The flies co-expressed mitochondria-targeted EYFP. The fractions were analyzed by western blotting using the indicated antibodies **(B)**. The results from three independent biological replicates were quantified and graphed **(C)**. An unpaired *t* test was used for statistical analysis; $****p \leq 0.0001$, $**p \leq 0.01$, $*p \leq 0.05$. **(D–F)** Live ovaries from the same strains were processed for TMRM labeling. After labeling, the samples were washed in PBS and imaged live on a Leica LSM780 inverted microscope. Signal for TMRM is shown using the red to white LUT **(D, E)** and signal for EYFP is shown using greyscale **(D', E')**. The graph indicates the ratio of TMRM signal to EYFP signal. An unpaired *t* test was used for statistical analysis; ns = not significant. *n* = 10 egg chambers for each genotype.

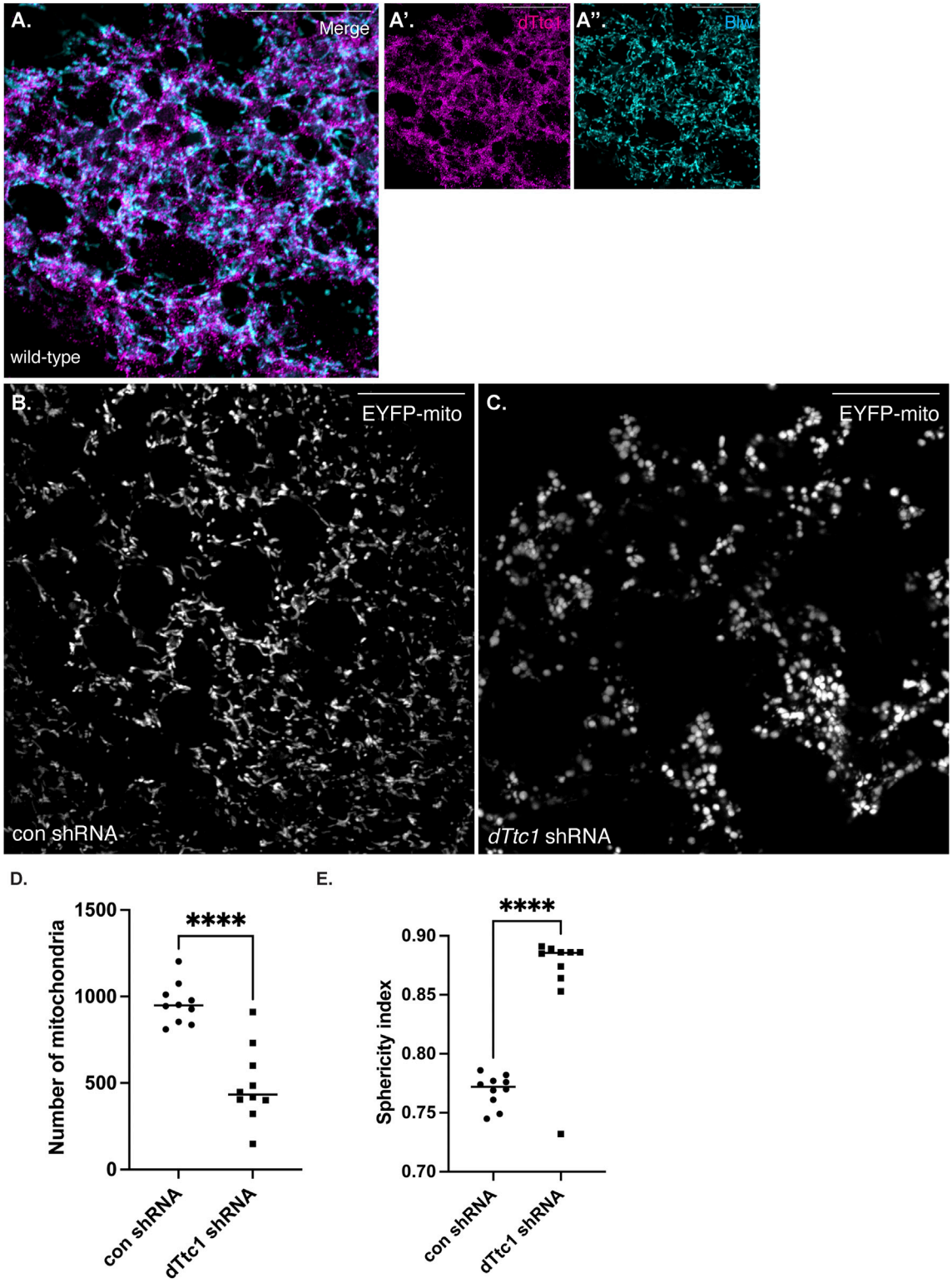

FIGURE 5
dTtc1 is also required for maintaining mitochondrial numbers and morphology in somatic tissues. **(A)** Larval fat body tissue was dissected and processed for immunofluorescence using antibodies against dTtc1 [magenta, **(A')**] and Blw [cyan, **(A'')**]. dTtc1 does not colocalize with mitochondria, but rather is present in foci that are often adjacent to mitochondria. **(B–E)** A strain co-expressing GFP targeted mitochondria and a driver that is active in fat body cells was crossed to a strain expressing a control shRNA **(B)** or an shRNA against *dTtc1* **(C)**. Fat body tissue was dissected from the resulting larvae, fixed and processed for microscopy. In comparison to flies expressing a control shRNA **(B)**, flies expressing the *dTtc1* shRNA **(C)** have reduced numbers of mitochondria **(D)**. In addition, the sphericity index of mitochondria in dTtc1 depleted fat body cells was also higher than the control. This indicates that the mitochondria in dTtc1 depleted cells were less elongated and were more spherical. The scale bar in these images corresponds to 20 microns. An unpaired *t* test was used for statistical analysis; $^{****}p \leq 0.0001$. For **(D)**, 10 individual frames were analyzed for each genotype. The same images were used for the quantification in **(E)**. For this analysis, a total of 9591 mitochondria were scored in the control shRNA background and 4871 mitochondria were scored in the *dTtc1* shRNA background. The plotted sphericity index corresponds to the mean value for each of the 10 individual frames.

potential in mitochondria in dTtc1 depleted egg chambers does not appear to be affected. However, there might be other aspects of mitochondrial function that are defective in dTtc1 depleted egg chambers. Further experimentation will be required to evaluate this.

The mitochondrial role of dTtc1 is not restricted to the germline

Although our initial studies were performed using female germline tissue, dTtc1 appears to be widely expressed (Gerstein et al., 2014; Leader et al., 2018). Larval fat bodies are often used as a model somatic tissue for the study of mitochondrial function (Zhou et al., 2019). We therefore examined the expression and localization of dTtc1 in these cells. As expected, specific signal for dTtc1 could be detected in fat bodies and co-localization analysis revealed that foci of dTtc1 could often be detected adjacent to mitochondria (Figure 5A). We next depleted dTtc1 in these cells using an shRNA and a driver that is active in fat bodies (Zhou et al., 2019). Consistent with what was observed in the egg chamber, depletion of dTtc1 in fat bodies resulted in significantly reduced mitochondrial content (Figures 5B–D). In addition, rather than the longer and filamentous mitochondria observed in control strains, mitochondria in dTtc1 depleted egg chambers displayed a swollen appearance (Figures 5B, C). Consistent with this observation, the sphericity index (see Materials and methods for details) of mitochondria in dTtc1 depleted fat bodies was higher than what was observed in the control strain (Figure 5E). The sphericity index is a measure of how spherical an object is. As such, mitochondria that display a round and swollen appearance will have a higher sphericity index that mitochondria that have a more filamentous morphology. Lastly, bright field imaging revealed that the overall morphology of the fat body was affected upon depletion of dTtc1 (Supplementary Figures S4A, B).

In summary, our results indicate that dTtc1 is a cytosolic protein that plays an important role in controlling the expression level of several ETC components. As a result of this function, depletion of dTtc1 results in morphologically abnormal mitochondria in germline and somatic tissues.

Discussion

In this report, we describe the first characterization of dTtc1 function in germline and somatic tissues using the *Drosophila* egg chamber and fat body cells as models. dTtc1, like its human ortholog, TTC1/TPR1, is a tetratricopeptide repeat (TPR) containing protein. TRP repeats are often involved in mediating protein-protein interaction (Perez-Riba and Itzhaki, 2019). We identified dTtc1 as an interacting partner of Egalitarian (Egl), an RNA adapter for the Dynein motor. Interestingly, the interaction between TTC1 and Dynein appears to be conserved between flies and mammals (Redwine et al., 2017; Baker et al., 2021). Our initial hypothesis was that dTtc1, and perhaps human TTC1, might be involved in linking cargo with Dynein. However, Dynein related processes such as localization of *hu li tai shao* (*hts*) and *bicoid* (*bcd*) mRNAs were unaffected upon depletion of dTtc1. The main defect in dTtc1 depleted tissues appears to be a mitochondrial deficit. Mitochondria numbers are reduced, they display an abnormal enlarged morphology, and the expression level of numerous ETC components is significantly reduced in dTtc1 depleted tissues. Importantly, these defects are rescued upon expression of wild-type GFP-dTtc1. Thus, these phenotypes are specifically due to a lack of dTtc1. Interestingly, depletion of certain ETC components has also been shown to produce a similar enlarged mitochondrial phenotype in fat body cells (Zhou et al., 2019).

In contrast to dTtc1 depletion, loss of either Egl or Dynein components was not associated with similar mitochondrial defects. However, Dhc depletion was associated with a defect in mitochondrial clustering adjacent to nurse cell nuclei. This is consistent with a role for Dynein in transport of mitochondria. Both Kinesin-1 and Dynein have been shown to be required for transporting mitochondria in *Drosophila* axons (Pilling et al., 2006). Both motors are linked to mitochondria via the protein Milton (or its human homologs TRAK1 and TRAK2) (Cox and Spradling, 2006; Fenton et al., 2021; Canty et al., 2023). However, the role of Kinesin-1 and Dynein in mitochondrial transport within the egg chamber is relatively unknown. Our results suggest that in the absence of Dhc, mitochondrial clustering adjacent to nurse cell nuclei is defective. However, from these data we cannot conclude whether this phenotype results from a lack of Dynein-mediated transport towards the nuclei or whether this results from excessive Kinesin transport away from nuclei. Further studies will be required to differentiate between these scenarios.

Why does depletion of dTtc1 result in these profound mitochondrial phenotypes? At present, we do not have a definitive answer to this question. dTtc1 does not co-localize with mitochondria and fractionation suggests that most of the protein resides in the cytosol. Thus, dTtc1 does not appear to be a core mitochondrial protein. In addition, we do not see an obvious accumulation of ETC components in the cytosolic fraction upon depletion of dTtc1. Thus, dTtc1 is not likely to be directly involved in importing proteins into mitochondria. In addition, despite the abnormal morphology of mitochondria in dTtc1 depleted egg chambers, the membrane potential of the mitochondria appeared to be relatively unaffected.

A potential clue to the function of dTtc1 might reside in its conserved interaction with Hsp90. Hsp90 has been shown to bind to human TTC1 via its TRP domains and a proteomics screen identified the *Drosophila* ortholog of Hsp90 (Hsp83) as a potential interaction partner (Lotz et al., 2008; Baker et al., 2021). In addition to Hsp90, ten additional chaperones were also identified as potential interaction partners of dTtc1 in the same screen (Supplementary Figure S4C) (Baker et al., 2021). Based on these observations, we hypothesize that dTtc1 functions primarily as a cytosolic co-chaperone for the folding of key mitochondrial proteins. When dTtc1 is lacking, these mitochondrial proteins are not correctly folded and are subsequently degraded. It would be interesting to determine whether inhibiting proteasomal degradation in dTtc1 depleted flies restores the expression level of ETC components.

Our initial interest in dTtc1 was due to its conserved interaction with the Dynein complex. As noted above, depletion of dTtc1 does not produce overt phenotypes resembling a defect in Dynein mediated processes. However, given the conserved interaction between dTtc1 and Dynein components, it is possible that

dTtc1 and its human ortholog perform a similar co-chaperone function for components of the Dynein motor. Dynein is a very large multi-subunit complex and certain chaperones such as the Prefoldin complex have been shown to interact with newly synthesized Dynein intermediate chains (Ozdemir et al., 2016). In addition, a component of the Chaperonin complex has also been shown to interact with the Dynactin1, a subunit of the large Dynactin complex, a critical regulator of Dynein activity (Echbarthi et al., 2018). Thus, it is possible that dTtc1 associates with Dynein components to assist in their correct folding. However, due to the redundancy of additional chaperones that also function in the folding of Dynein components, loss of dTtc1 might not result in a significant defect in Dynein mediated processes. By contrast, the role of dTtc1in the folding mitochondrial protein might be more central to its function, thus resulting in dramatic mitochondrial phenotypes when dTtc1 is lacking.

Materials and methods

Fly stocks

Endogenous dTtc1 was depleted in the female germline using *dttc1* shRNA expressed using the Valium22 vector (Bloomington stock center; #42763, donor TRiP) and in fat body cells using *dttc1* shRNA expressed using the Valium20 vector (Bloomington stock center; #53005, donor TRiP). For depletion of factors at the earliest stage of oogenesis, within the germarium, expression of the shRNA was driven using P{GAL4::VP16-nanos.UTR}CG6325[MVD1] (Bloomington Stock Center, #4937; donor Ruth Lehmann). We refer to this driver in the results section as a germarium driver. For early and mid-stage depletion, expression of the shRNA was driven using P{w[+mC] = matalpha4-GAL-VP16}V37 (Bloomington Stock Center, #7063; donor Andrea Brand). We refer to this driver in the results sections as the early-stage driver. Depletion of dTtc1 in fat body cells was driven using w [1118]; P{w[+mC] = Cg-GAL4.A}2 (Bloomington Stock Center, #7011; donor Chuck Dearolf). In addition, the following shRNA strains were also used: *egl* shNRA (Bloomington stock center; #43550, donor TRiP), *bicD* shRNA (Bloomington stock center; #35405, donor TRiP) and *dhc* shRNA (Bloomington stock center; #36583, donor TRiP). A strain using mitochondria targeted EYFP (P {sqh-EYFP-Mito}3, Bloomington stock center; #7194, donor Dennis LaJeunesse) was used to validate the swollen mitochondria phenotype. The GFP-dTtc1 used in the rescue experiments was generated in a previous publication (Baker et al., 2021). OR flies were used as the wild-type control. Fly crosses for all experiments were maintained at 25°C. For examination of ovarian phenotypes, female flies were dissected at 3 days of age. Third instar larvae were dissected for examining fat body phenotypes.

Mitochondria fractionation

Ovaries were homogenized in an extraction buffer (5 mM Hepes, pH 7.5, 210 mM mannitol, 70 mM sucrose, and 1 mM EGTA). Next, the lysate was subjected to two rounds of centrifugation, both at 700 g for 5 min at 4°C. The supernatant from each step was transferred into a new microfuge tube. The resulting supernatant was then subjected to a final round of centrifugation at 9,000 g for 10 min at 4°C. The supernatant from this step contains the cytosolic fraction and the pellet contains the mitochondrial fraction. The fractions were mixed with Laemmli buffer, run on a gel and analyzed by Western blotting. All Western blot images were acquired on a Bio Rad ChemiDoc MP.

Antibodies

The following antibodies were used for western analysis: rabbit anti-UQCR-C2 (III) (from Dr. Owusu-Ansah, 1:2,000), rabbit anti-COX IV (from Dr. Owusu-Ansah, 1:2,000), rabbit anti-Sdha(II) (from Dr. Owusu-Ansah, 1:1,500), rabbit anti-ND-20 (I) (from Dr. Owusu-Ansah, 1:2,000) (Murari et al., 2020), mouse anti-ATP synthase beta(V) (Life technologies, 1:2,000), mouse anti-ATP5A1 (Life technologies, 1:30,000 for western, 1:3,000 for immunofluorescence), mouse anti-GFP (Chromotek, 1:5,000), mouse anti-a-Tub (Millipore-Sigma, 1:60,000), rabbit anti-Khc (generated inhouse, 1:5,000), rabbit anti-dTtc1 (1:5,000 for western, 1:100 for immunofluorescence), mouse anti-Orb (Developmental studies hybridoma bank, 1:30 for immunofluorescence), rat anti-Vasa (Developmental studies hybridoma bank, 1:50 for immunofluorescence), and mouse anti-Spectrin (Developmental studies hybridoma bank, 1:20 for immunofluorescence). The following secondary antibodies were used: goat anti-rabbit Alexa 594, 555 and 488 (Life Technologies, 1:400, 1:400 and 1:400 respectively); goat anti-mouse Alexa 594, 555 and 488 (Life Technologies, 1:400, 1:400 and 1:400 respectively); goat anti-rat Alexa 488 (Life Technologies, 1:400); goat anti-mouse HRP (Pierce, 1:5000); and goat anti-rabbit HRP (Pierce, 1:5000).

Immunofluorescence *in situ* hybridization and imaging

Immunofluorescence and RNA *in situ* hybridization on dissected ovaries was performed as described previously (Goldman et al., 2021; Neiswender et al., 2021). Dissected ovaries were fixed in 4% formaldehyde (Pierce) for 20 min at room temperature. For immunofluorescence experiments, the primary antibody was incubated in blocking buffer (PBS +0.1% Triton X-100 + 2% BSA) overnight at 4°C. Next, the samples were washed 3 times in PBST (PBS +0.1% Triton X-100) and incubated overnight with the fluorescent secondary antibody in the same blocking buffer. This was followed by 4 washes with PBST. The tissue was then stained with DAPI, and mounted onto slides using Prolong Diamond (Life technologies).

The fixation step for RNA *in situ* hybridization was the same as described above. After fixation, ovaries were stored in 100% methanol at −20°C for 1 h. Following this, the samples were re-hydrated with three 10 min washes using a solution of PBST and 100% methanol (3:7, 1:1, 7:3) and rinsed 4 times with PBST. Next, the samples were washed for 10 min in Wash Buffer (4xSSC, 35% deionized formamide, 0.1% Tween-20). Fluorescent oligo probes (Stellaris probes) were purchased from Biosearch technologies. Probes diluted in Hybridization Buffer (10% dextran sulfate,

0.1 mg/mL salmon sperm ssDNA, 100 µL vanadyl ribonucleoside (NEB biolabs), 20ug/mL RNAse-free BSA, 4x SSC, 0.1% Tween-20, 35% deionized formamide) were added to the ovaries and incubated overnight at 37°C. The next day, the samples were washed 2 times with pre-warmed wash Buffer for 30 min. After 2 rinses with PBST and 2 rinses with PBS, the samples were counter-stained with DAPI and mounted onto slides using Prolong Diamond.

Immunofluorescence on fat body tissue was also performed using a similar protocol. In brief, fat body tissue was isolated from L3 larvae in cold PBS and fixed with 4% formaldehyde for 40 min without agitation. After fixation, the samples were washed once with PBS and then permeabilized using PBS containing 0.2% Triton X-100. The tissue was incubated with primary antibody in blocking buffer (PBS +0.1% Triton X-100 + 2% BSA) overnight at 4°C. The next day, the samples were washed three times with PBST (PBS +0.1% Triton X-100) and incubated overnight with the fluorescent secondary antibody diluted into the same blocking buffer. Finally, the samples were washed four times with PBST, DAPI stained, and mounted onto slides using Prolong Diamond (Life technologies).

Transmission electron microscopy

Dissected ovaries were processed for transmission electron microscopy as described previously (Liu et al., 2015). Briefly, ovarian tissue was fixed using 4% paraformaldehyde and 2% glutaraldehyde in 0.1 M sodium cacodylate (NaCac) buffer (pH 7.4). Ovarioles were then embedded within agarose. Stage 9 and 10 egg chambers were idenfied and isolated out of the agarose. The samples were post fixed in 2% osmium tetroxide in NaCac, stained with 2% uranyl acetate, dehydrated with a graded ethanol series, and embedded in EponAraldite resin. Next, thin sections were cut using a diamond knife on a Leica EM UC6 ultramicrotome (Leica Microsystems, Bannockburn, IL), collected on copper grids, and stained with uranyl acetate and lead citrate. Egg chambers were observed in a JEM 1230 transmission electron microscope (JEOL USA, Peabody, MA) at 110 kV and imaged with an UltraScan 4000 CCD camera and First Light Digital Camera Controller (Gatan, Pleasanton, CA).

Light microscopy

Light microscopy Images were captured on either an inverted Leica Stellaris confocal microscope or an inverted Zeiss LSM780 equipped with Airyscan. Images were processed for presentation using Fiji, Adobe Photoshop, and Adobe Illustrator. All imaging experiments were performed at the Augusta University Cell Imaging Core.

TMRM live imaging

Ovaries were dissected in Schneider's media (Gibco) containing 15% fetal bovine serum (Corning). Dissected ovaries were incubated in 100 nM of Image-iT™ TMRM Reagent (Invitrogen) for 25 min. After the incubation period, the ovaries were washed 3 times with dissection medium, adhered to a poly lysine coated 35 mm glass bottom dish (1.5 coverslip, MatTek), and immediately imaged on a Zeiss LSM780 inverted microscope.

Silver stain

Mitochondrial fractions were run on a 4%–15% gradient gel (BioRad). Proteins were visualized using the Pierce Silver stain kit following the directions provided by the manufacturer.

Quantifications

Western blot images from the Biorad Chemidoc MP were quantified using the Image lab software from Biorad. Three independent biological replicates were used for quantification. The expression level of ETC components in the dTtc1 shRNA strain was compared to the level of the same protein in the control shRNA strain. The mean distance of the mitochondria to the nucleus was determined using Imaris 10.0. Nuclei were defined using the "surfaces" module and mitochondria were defined using the "spots" module in Imaris. These same data were used to determine the number of mitochondria in each of the indicated genotypes. The number of mitochondria reported in Figure 2 was manually counted using the transmission EM images. The diameter of mitochondria in the transmission electron microscopy images was quantified using Fiji. In order to determine membrane potential, the ratio of the TMRM signal to the EYFP signal was determined between control and dTtc1 depleted live egg chambers. The pixel intensity measurements for this figure were performed using Fiji. The mitochondria number and sphericity index of mitochondria in larval fat bodies were quantified using Imaris 10.0. For Figure 5, mitochondria were defined using the "surface" module of Imaris. This module enabled us to more precisely map the filamentous mitochondria morphologies found in the control strain. In addition, this module enabled us to calculate the sphericity index of mitochondria. In essence, this is an indicator of how spherical an object is and is defined as the ratio of the surface area of a sphere, with the same volume as the given object, to the surface area of the object. The following formula is used by Imaris to calculate the sphericity index:

Vp = volume of object

Ap = surface area of object

Cristae frequency was quantified using our EM images as described by Shi et al. (2022). It is defined as the number of cristae in a given mitochondria divided by the length of the mitochondria. Graphs were assembled using Graphpad Prism9. Statistical analysis was also performed using Prism9.

Data availability statement

The original contributions presented in the study are included in the article/Supplementary Material, further inquiries can be directed to the corresponding author.

Author contributions

HN, FB, RV-K, PA, and GG performed experiments. HN, FB, and GG designed the experimental strategy. HN and GG wrote the paper. All authors contributed to the article and approved the submitted version.

Funding

This work was supported by a grant from the National Institutes of Health to GG (R35GM145340).

Acknowledgments

We would like to thank Dr. Edward Owusu-Ansah for providing antibodies against ND20, Sdha, ATP synthase beta, UQCR-C2 and Cox4. We also thank the Bloomington Stock Center and the Developmental Studies Hybridoma Bank for providing fly strains and antibodies.

Conflict of interest

The authors declare that the research was conducted in the absence of any commercial or financial relationships that could be construed as a potential conflict of interest.

Publisher's note

Supplementary material

The Supplementary Material for this article can be found online at: https://www.frontiersin.org/articles/10.3389/fcell.2023.1148773/full#supplementary-material

SUPPLEMENTARY FIGURE S1

(A,B) Ovaries from flies expressing a control shRNA **(A)** or an shRNA against *dTtc1* **(B)** using the early-stage driver were dissected, fixed and processed for immunofluorescence using an antibody against dTtc1 (red to white LUT). The egg chambers were also counterstained with DAPI to visualize nuclei (cyan). Expression of *dttc1* shRNA results in the germline specific depletion of dTtc1. **(C,D)** Ovaries from flies expressing a control shRNA **(C)** or an shRNA against *dTtc1* **(D)** using the germarium driver were dissected, fixed and stained with DAPI (cyan). Entire ovaries were mounted and imaged. The scale bar in C and D is 100 microns. **(E–G)** Ovaries from flies expressing a control shRNA **(E)**, and shRNA against *dTtc1* **(F)**, or an shRNA against *dhc* **(G)** using the early-stage driver were dissected, fixed and stained with DAPI (cyan). Entire ovaries were mounted and imaged. The scale bar in E-F is 500 microns.

SUPPLEMENTARY FIGURE S2

(A,B) Ovaries from flies expressing a control shRNA **(A)** or an shRNA against *dTtc1* **(B)** using the germarium driver were dissected, fixed and stained using antibodies against Spectrin (cyan) and dTtc1 (greyscale) **(B′)**. The ovaries were counterstained with DAPI (magenta). Spectrin is a marker of the fusome. The fusome fails to form in dTtc1 depleted egg chambers. **(C, D)** Egg chambers from flies co-expressing mitochondria-targeted EYFP and either a control shRNA **(C)** or shRNA against *dttc1* **(D)** driven using the early-stage driver were fixed and imaged. Signal for EYFP is shown using a red to white LUT. Depletion of dTtc1 results in fewer mitochondria per egg chamber. In addition, the mitochondria in the dTtc1 depleted strain display a swollen phenotype **(D′)**. **(E)** Ovaries from wild-type flies were fixed and processed for immunofluorescence using antibodies against dTtc1 (magenta) and Blw (cyan). dTtc1 does not extensively co-localize with mitochondria. The scale bar in D′ is 5 microns. In the rest of the images, the scale bar is 20 microns **(F)**. The number of mitochondria in strains expressing either a control shRNA, an shRNA against *dhc* or an shRNA against *dTtc1* was analyzed using the "spots" module in Imaris. The early-stage driver was used to express the shRNAs. An unpaired *t*-test was used for statistical analysis; $*p \leq 0.05$, ns = not significant, $n = 15$ mitochondria per genotype. **(G)** The cristae frequency was calculated from EM images of egg chambers expressing either the control shRNA or an shRNA against *dTtc1*. The cristae frequency is defined as the number of cristae in each mitochondria divided by the length of the mitochondria (Shi et al., 2022). An unpaired *t*-test was used for statistical analysis; $****p \leq 0.0001$, $n = 15$ mitochondria per genotype.

SUPPLEMENTARY FIGURE S3

(A) A list of the electron transport chain components that were shown to be part of the dTtc1 interactome (Baker et al., 2021). **(B)** Mitochondrial fractions from strains expressing a control shRNA or an shRNA against *dTtc1* were run on a gel and silver stained. These same fractions were also processed for the western blots shown in Figure 4B **(C)** Cytoplasmic and mitochondrial fractions were prepared from ovaries of flies expressing a control shRNA, an shRNA against *dttc1,* or co-expressing *dttc1* shRNA and GFP-dTtc1. Co-expression of GFP-dTtc1 rescues the expression level defect of Cox4 observed upon depletion of endogenous dTtc1.

SUPPLEMENTARY FIGURE S4

(A,B) Larval fat bodies were dissected from strains expressing a control shRNA **(A)** or from larvae expressing an shRNA against *dTtc1* **(B)**. Bright field images are shown. Depletion of dTtc1 results in abnormal morphology of the fat body (arrows). **(C)** A list of chaperone proteins that were shown to be part of the dTtc1 interactome (Baker et al., 2021). The scale bar in these images is 20 microns.

References

Baker, F. C., Neiswender, H., Veeranan-Karmegam, R., and Gonsalvez, G. B. (2021). *In vivo* proximity biotin ligation identifies the interactome of Egalitarian, a Dynein cargo adaptor. *Development* 148, 199935. doi:10.1242/dev.199935

Canty, J. T., Hensley, A., Aslan, M., Jack, A., and Yildiz, A. (2023). TRAK adaptors regulate the recruitment and activation of dynein and kinesin in mitochondrial transport. *Nat. Commun.* 14, 1376. doi:10.1038/s41467-023-36945-8

Canty, J. T., and Yildiz, A. (2020). Activation and regulation of cytoplasmic dynein. *Trends Biochem. Sci.* 45, 440–453. doi:10.1016/j.tibs.2020.02.002

Carpenter, A. T. (1994). Egalitarian and the choice of cell fates in *Drosophila melanogaster* oogenesis. *Ciba Found. Symp.* 182, 223–246.

Cason, S. E., and Holzbaur, E. L. F. (2022). Selective motor activation in organelle transport along axons. *Nat. Rev. Mol. Cell Biol.* 23, 699–714. doi:10.1038/s41580-022-00491-w

Cox, R. T., and Spradling, A. C. (2006). Milton controls the early acquisition of mitochondria by Drosophila oocytes. *Development* 133, 3371–3377. doi:10.1242/dev.02514

Dienstbier, M., Boehl, F., Li, X., and Bullock, S. L. (2009). Egalitarian is a selective RNA-binding protein linking mRNA localization signals to the dynein motor. *Genes Dev.* 23, 1546–1558. doi:10.1101/gad.531009

Echbarthi, M., Vallin, J., and Grantham, J. (2018). Interactions between monomeric CCTδ and p150Glued: A novel function for CCTδ at the cell periphery distinct from the protein folding activity of the molecular chaperone cct. *Exp. Cell Res.* 370, 137–149. doi:10.1016/j.yexcr.2018.06.018

Fenton, A. R., Jongens, T. A., and Holzbaur, E. L. F. (2021). Mitochondrial adaptor TRAK2 activates and functionally links opposing kinesin and dynein motors. *Nat. Commun.* 12, 4578. doi:10.1038/s41467-021-24862-7

Garcez, M., Branco-Santos, J., Gracio, P. C., and Homem, C. C. F. (2020). Mitochondrial dynamics in the Drosophila ovary regulates germ stem cell number, cell fate, and female fertility. *Front. Cell Dev. Biol.* 8, 596819. doi:10.3389/fcell.2020.596819

Gerstein, M. B., Rozowsky, J., Yan, K. K., Wang, D., Cheng, C., Brown, J. B., et al. (2014). Comparative analysis of the transcriptome across distant species. *Nature* 512, 445–448. doi:10.1038/nature13424

Goldman, C. H., and Gonsalvez, G. B. (2017). The role of microtubule motors in mRNA localization and patterning within the Drosophila oocyte. *Results Probl. Cell Differ.* 63, 149–168. doi:10.1007/978-3-319-60855-6_7

Goldman, C. H., Neiswender, H., Baker, F., Veeranan-Karmegam, R., Misra, S., and Gonsalvez, G. B. (2021). Optimal RNA binding by Egalitarian, a Dynein cargo adaptor, is critical for maintaining oocyte fate in Drosophila. *RNA Biol.* 18, 2376–2389. doi:10.1080/15476286.2021.1914422

Goldman, C. H., Neiswender, H., Veeranan-Karmegam, R., and Gonsalvez, G. B. (2019). The Egalitarian binding partners Dynein light chain and Bicaudal-D act sequentially to link mRNA to the Dynein motor. *Development* 146, 176529. doi:10.1242/dev.176529

Hoogenraad, C. C., and Akhmanova, A. (2016). Bicaudal D family of motor adaptors: Linking dynein motility to cargo binding. *Trends Cell Biol.* 26, 327–340. doi:10.1016/j.tcb.2016.01.001

Huynh, J. R., and St Johnston, D. (2004). The origin of asymmetry: Early polarisation of the Drosophila germline cyst and oocyte. *Curr. Biol.* 14, R438–R449. doi:10.1016/j.cub.2004.05.040

Jongsma, M. L. M., Bakker, N., and Neefjes, J. (2023). Choreographing the motor-driven endosomal dance. *J. Cell Sci.* 136, jcs259689. doi:10.1242/jcs.259689

Leader, D. P., Krause, S. A., Pandit, A., Davies, S. A., and Dow, J. a. T. (2018). FlyAtlas 2: A new version of the *Drosophila melanogaster* expression atlas with RNA-seq, miRNA-seq and sex-specific data. *Nucleic Acids Res.* 46, D809–D815. doi:10.1093/nar/gkx976

Lin, H., Yue, L., and Spradling, A. C. (1994). The Drosophila fusome, a germline-specific organelle, contains membrane skeletal proteins and functions in cyst formation. *Development* 120, 947–956. doi:10.1242/dev.120.4.947

Liu, G., Sanghavi, P., Bollinger, K. E., Perry, L., Marshall, B., Roon, P., et al. (2015). Efficient endocytic uptake and maturation in Drosophila oocytes requires dynamitin/p50. *Genetics* 201, 631–649. doi:10.1534/genetics.115.180018

Lotz, G. P., Brychzy, A., Heinz, S., and Obermann, W. M. (2008). A novel HSP90 chaperone complex regulates intracellular vesicle transport. *J. Cell Sci.* 121, 717–723. doi:10.1242/jcs.015610

Lu, W., Lakonishok, M., Serpinskaya, A. S., and Gelfand, V. I. (2022). A novel mechanism of bulk cytoplasmic transport by cortical dynein in Drosophila ovary. *Elife* 11, e75538. doi:10.7554/eLife.75538

Mach, J. M., and Lehmann, R. (1997). An Egalitarian-BicaudalD complex is essential for oocyte specification and axis determination in Drosophila. *Genes Dev.* 11, 423–435. doi:10.1101/gad.11.4.423

Mcclintock, M. A., Dix, C. I., Johnson, C. M., Mclaughlin, S. H., Maizels, R. J., Hoang, H. T., et al. (2018). RNA-directed activation of cytoplasmic dynein-1 in reconstituted transport RNPs. *Elife* 7, e36312. doi:10.7554/eLife.36312

Mcgrail, M., and Hays, T. S. (1997). The microtubule motor cytoplasmic dynein is required for spindle orientation during germline cell divisions and oocyte differentiation in Drosophila. *Development* 124, 2409–2419. doi:10.1242/dev.124.12.2409

Murari, A., Rhooms, S. K., Goparaju, N. S., Villanueva, M., and Owusu-Ansah, E. (2020). An antibody toolbox to track complex I assembly defines AIF's mitochondrial function. *J. Cell Biol.* 219, e202001071. doi:10.1083/jcb.202001071

Neiswender, H., Goldman, C. H., Veeranan-Karmegam, R., and Gonsalvez, G. B. (2021). Dynein light chain-dependent dimerization of Egalitarian is essential for maintaining oocyte fate in Drosophila. *Dev. Biol.* 478, 76–88. doi:10.1016/j.ydbio.2021.06.009

Ozdemir, A., Machida, K., Imataka, H., and Catling, A. D. (2016). Identification of the T-complex protein as a binding partner for newly synthesized cytoplasmic dynein intermediate chain 2. *Biochem. Biophys. Res. Commun.* 469, 126–131. doi:10.1016/j.bbrc.2015.11.082

Perez-Riba, A., and Itzhaki, L. S. (2019). The tetratricopeptide-repeat motif is a versatile platform that enables diverse modes of molecular recognition. *Curr. Opin. Struct. Biol.* 54, 43–49. doi:10.1016/j.sbi.2018.12.004

Pilling, A. D., Horiuchi, D., Lively, C. M., and Saxton, W. M. (2006). Kinesin-1 and Dynein are the primary motors for fast transport of mitochondria in Drosophila motor axons. *Mol. Biol. Cell* 17, 2057–2068. doi:10.1091/mbc.e05-06-0526

Reck-Peterson, S. L., Redwine, W. B., Vale, R. D., and Carter, A. P. (2018). The cytoplasmic dynein transport machinery and its many cargoes. *Nat. Rev. Mol. Cell Biol.* 19, 382–398. doi:10.1038/s41580-018-0004-3

Redwine, W. B., Desantis, M. E., Hollyer, I., Htet, Z. M., Tran, P. T., Swanson, S. K., et al. (2017). The human cytoplasmic dynein interactome reveals novel activators of motility. *Elife* 6, e28257. doi:10.7554/eLife.28257

Sanghavi, P., Liu, G., Veeranan-Karmegam, R., Navarro, C., and Gonsalvez, G. B. (2016). Multiple roles for egalitarian in polarization of the Drosophila egg chamber. *Genetics* 203, 415–432. doi:10.1534/genetics.115.184622

Scheufler, C., Brinker, A., Bourenkov, G., Pegoraro, S., Moroder, L., Bartunik, H., et al. (2000). Structure of TPR domain-peptide complexes: Critical elements in the assembly of the hsp70-hsp90 multichaperone machine. *Cell* 101, 199–210. doi:10.1016/S0092-8674(00)80830-2

Shi, P., Ren, X., Meng, J., Kang, C., Wu, Y., Rong, Y., et al. (2022). Mechanical instability generated by Myosin 19 contributes to mitochondria cristae architecture and OXPHOS. *Nat. Commun.* 13, 2673. doi:10.1038/s41467-022-30431-3

Sladewski, T. E., Billington, N., Ali, M. Y., Bookwalter, C. S., Lu, H., Krementsova, E. B., et al. (2018). Recruitment of two dyneins to an mRNA-dependent Bicaudal D transport complex. *Elife* 7, e36306. doi:10.7554/eLife.36306

Suter, B., and Steward, R. (1991). Requirement for phosphorylation and localization of the Bicaudal-D protein in Drosophila oocyte differentiation. *Cell* 67, 917–926. doi:10.1016/0092-8674(91)90365-6

Theurkauf, W. E., Alberts, B. M., Jan, Y. N., and Jongens, T. A. (1993). A central role for microtubules in the differentiation of Drosophila oocytes. *Development* 118, 1169–1180. doi:10.1242/dev.118.4.1169

Vazquez-Pianzola, P., Schaller, B., Colombo, M., Beuchle, D., Neuenschwander, S., Marcil, A., et al. (2017). The mRNA transportome of the BicD/Egl transport machinery. *RNA Biol.* 14, 73–89. doi:10.1080/15476286.2016.1251542

Weil, T. T. (2014). mRNA localization in the Drosophila germline. *RNA Biol.* 11, 1010–1018. doi:10.4161/rna.36097

Zhou, J., Xu, L., Duan, X., Liu, W., Zhao, X., Wang, X., et al. (2019). Large-scale RNAi screen identified Dhpr as a regulator of mitochondrial morphology and tissue homeostasis. *Sci. Adv.* 5, eaax0365. doi:10.1126/sciadv.aax0365

frontiers | Frontiers in Cell and Developmental Biology

TYPE Original Research
PUBLISHED 15 June 2023
DOI 10.3389/fcell.2023.1178533

OPEN ACCESS

EDITED BY
Wellerson R. Scarano,
São Paulo State University, Brazil

REVIEWED BY
Paul D. Taylor,
King's College London, United Kingdom
Asli Ozmen,
University of South Florida, United States

*CORRESPONDENCE
Fredrick J. Rosario,
✉ Fredrick.joseph@cuanschutz.edu

†These authors have contributed equally to this work

RECEIVED 02 March 2023
ACCEPTED 16 May 2023
PUBLISHED 15 June 2023

CITATION
Kelly A, Chan J, Powell TL, Cox LA, Jansson T and Rosario FJ (2023), Maternal obesity alters the placental transcriptome in a fetal sex-dependent manner.
Front. Cell Dev. Biol. 11:1178533.
doi: 10.3389/fcell.2023.1178533

Maternal obesity alters the placental transcriptome in a fetal sex-dependent manner

Amy Kelly[1,2], Jeannie Chan[3], Theresa L. Powell[2,4], Laura A. Cox[3], Thomas Jansson[2†] and Fredrick J. Rosario[2*†]

[1]Department of Surgery, University of Arizona College of Medicine, Tucson, AZ, United States, [2]Division of Reproductive Sciences, Department of Obstetrics and Gynecology, University of Colorado Anschutz Medical Campus, Aurora, CO, United States, [3]Center for Precision Medicine, Department of Internal Medicine, Section of Molecular Medicine, Wake Forest School of Medicine, Winston-Salem, NC, United States, [4]Section of Neonatology, Department of Pediatrics, University of Colorado Anschutz Medical Campus, Aurora, CO, United States

Infants born to obese mothers have an increased risk of developing obesity and metabolic diseases in childhood and adulthood. Although the molecular mechanisms linking maternal obesity during pregnancy to the development of metabolic diseases in offspring are poorly understood, evidence suggests that changes in the placental function may play a role. Using a mouse model of diet-induced obesity with fetal overgrowth, we performed RNA-seq analysis at embryonic day 18.5 to identify genes differentially expressed in the placentas of obese and normal-weight dams (controls). In male placentas, 511 genes were upregulated and 791 genes were downregulated in response to maternal obesity. In female placentas, 722 genes were downregulated and 474 genes were upregulated in response to maternal obesity. The top canonical pathway downregulated in maternal obesity in male placentas was oxidative phosphorylation. In contrast, sirtuin signaling, NF-kB signaling, phosphatidylinositol, and fatty acid degradation were upregulated. In female placentas, the top canonical pathways downregulated in maternal obesity were triacylglycerol biosynthesis, glycerophospholipid metabolism, and endocytosis. In contrast, bone morphogenetic protein, TNF, and MAPK signaling were upregulated in the female placentas of the obese group. In agreement with RNA-seq data, the expression of proteins associated with oxidative phosphorylation was downregulated in male but not female placentas of obese mice. Similarly, sex-specific changes in the protein expression of mitochondrial complexes were found in placentas collected from obese women delivering large-for-gestational-age (LGA) babies. In conclusion, maternal obesity with fetal overgrowth differentially regulates the placental transcriptome in male and female placentas, including genes involved in oxidative phosphorylation.

KEYWORDS

trophoblast, maternal–fetal exchange, gene expression, mitochondria, fetal growth

Introduction

The worldwide obesity epidemic constitutes a significant public health challenge among pregnant women (Kim et al., 2007). The prevalence of obesity in US women of reproductive age (18–49) increased from 7.4% in 1976 to 27.5% in 2014 (Ogden et al., 2012; Fisher et al., 2013; Ogden et al., 2013; Ogden et al., 2014; National Center for Health Statistics, 2015). Maternal obesity during pregnancy is associated with various pregnancy complications,

including gestational diabetes mellitus (GDM) and preeclampsia (Marchi et al., 2015). In addition, obese women have an increased risk of delivering a large-for-gestational-age (LGA) infant (Yu et al., 2013; Leon-Garcia et al., 2016). Infants of obese mothers are more likely to have poor neonatal outcomes and a greater risk of developing obesity, cancer, insulin resistance, hypertension, and dyslipidemia later in life (Evagelidou et al., 2006; Wang et al., 2007; Alfaradhi and Ozanne, 2011; Bouret et al., 2015). Maternal obesity in women is associated with premature death in adult offspring (Reynolds et al., 2013). Furthermore, animal experiments have shown that diet-induced maternal obesity causes permanent dysregulation of food intake (Kirk et al., 2009), hyperphagia (Samuelsson et al., 2008), adiposity (Samuelsson et al., 2008), non-alcoholic fatty liver (Oben et al., 2010), myocardial dysfunction (Samuelsson et al., 2013), and hypertension (Samuelsson et al., 2010; Taylor et al., 2014) in adult offspring. The molecular mechanisms linking maternal obesity during pregnancy to adverse long-term outcomes in children are poorly understood. However, emerging evidence suggests that changes in the placental structure and function may be involved (Roberts et al., 2011; Wallace et al., 2012; Jansson et al., 2013; Burton et al., 2016; Mitsuya et al., 2017).

The placenta integrates an array of signals from both the mother and fetus to maintain fetal homeostasis (Jansson and Powell, 2013; Diaz et al., 2014). It performs numerous functions critical for normal fetal growth and development, including mediating nutrient and waste transfer, secreting hormones, serving as an immunological barrier, and performing xenobiotic detoxification (Burton et al., 2016). Placental nutrient transport capacity has been reported to be increased in obese women delivering LGA infants and in animal models of diet-induced maternal obesity (Jansson et al., 2013; Aye et al., 2015; Rosario et al., 2015). We developed a mouse model of maternal obesity during pregnancy induced by a high-fat/high-sugar diet, showing extensive similarities to the human condition, including elevated levels of maternal leptin, glucose intolerance, activation of placental insulin and mTOR signaling, increased placental nutrient transport, and fetal overgrowth (Aye et al., 2015; Rosario et al., 2015). Significantly, offspring of obese mice developed metabolic (Paulsen et al., 2019; Dumolt et al., 2022) and cardiovascular diseases in adulthood (Vaughan et al., 2020; Vaughan et al., 2022). Nam and co-workers reported an increased placental expression of nutrient transporters, activation of placental mTOR signaling, and fetal overgrowth in a mouse model of maternal high-fat diet (Nam et al., 2017). These observations are consistent with the possibility that enhanced the placental transfer of nutrients, contributing to fetal overgrowth in maternal obesity.

Experimental animal and human epidemiological studies have demonstrated a sex difference in response to an adverse intrauterine milieu and the subsequent risk of developing diseases later in life (Zhu et al., 2018; Alves et al., 2020). Moreover, gene expression is distinct in male and female placentas (Clifton, 2010; Osei-Kumah et al., 2011; Cox et al., 2013; Barke et al., 2019). Male fetuses grow faster than female fetuses *in utero*, which is believed to place male fetuses at a greater risk in an adverse environment, possibly explaining the increased incidence of adverse perinatal outcomes in male fetuses. Furthermore, emerging evidence suggests that female fetuses adapt better than male fetuses to an adverse intrauterine environment, which could contribute to better perinatal and long-term outcomes in female fetuses, as demonstrated in some studies. Using a mouse model of maternal obesity with fetal overgrowth, we recently demonstrated that male offspring develop obesity, glucose intolerance, and insulin resistance at 3 months of age, whereas the metabolic phenotype in female offspring is much less severe at this age (Paulsen et al., 2019). However, the molecular mechanisms underlying sex-dependent *in utero* growth strategies are largely unknown.

Maternal obesity affects mitochondrial biogenesis, oxidative stress, and antioxidant activity in the placenta in a sexually dimorphic manner (Mele et al., 2014; Evans and Myatt, 2017). Despite the proposed important role of the placenta in mediating the adverse effects of maternal obesity on the long-term health of LGA infants, reports of the impact of maternal obesity on the placental transcriptome in pregnancies with fetal overgrowth are limited (Cox et al., 2019). To address this gap in knowledge, we characterized the placental transcriptome in our mouse model of diet-induced maternal obesity during pregnancy, which is associated with moderate fetal overgrowth and sexual dimorphism in long-term metabolic outcomes.

Materials and methods

Animals and diets

Institutional Animal Care and Use Committee review boards at the University of Texas Health Science Center in San Antonio approved all experimental protocols. Female C57BL/6 J mice (Jackson Laboratory, Bar Harbor, ME, United States of America), which were proven to be breeders with one previous litter, about 12 weeks of age were housed under controlled conditions (25°C, 12-h light/dark cycle). At 13 weeks of age, animals were randomly assigned to a control (D12489B, 10.6 kcal% fat) or high-fat pellet diet (Western Diet D12079B, 41 kcal% fat) with *ad libitum* access to a 20% sucrose solution (high-fat/high-sugar, HF/HS; obese). Sucrose solution was supplemented with vitamins (10 g/4,000 kcal Vitamin Mix V10001) and minerals (35 g/4,000 kcal Mineral Mix S10001). Diets were purchased from Research Diets (New Brunswick, NJ, United States). All animals had free access to water. When female mice on the HF/HS diet had a 25% increase in body weight, obese female mice and age-matched female mice on the control diet were mated with male C57BL/6 J mice on the control diet. Mating was confirmed via the presence of a vaginal plug (embryonic day (E) 0.5), and dams were continued on the respective diets throughout gestation. Body weight increased in pregnant mice at different gestational intervals (Supplementary Figure S1). At E18.5, dams were euthanized for the collection of placentas and fetuses. The weights of fetuses and placentas were recorded. Placentas for molecular analysis were immediately snap-frozen in liquid N_2 and stored at −80°C.

The sex of fetuses was determined by PCR amplification (Hacker et al., 1995) of a fragment of the Y-linked *Zfy-1* gene using genomic DNA isolated from fetal tails by the HotSHOT method (Truett et al., 2000). The primers 5′-TGCTGTTACATGTTGACCTGG-3′ and 5′-TGCTCTCCTGTCTCTCCAAGA-3′ amplified a 451-bp PCR product to indicate the presence of the Y chromosome. Amplicons were loaded on 2% agarose gels and electrophoresed

together with a 100-bp DNA ladder. Under UV illumination, bands were visualized using an ethidium bromide gel stain, and the genotypic sex was identified according to the presence or absence of the *Zfy-1* gene.

RNA extraction

After homogenizing placental tissues (~10 mg) in the TRI reagent, total RNA was purified using the Direct-zol RNA MiniPrep Kits (Zymo Research, Irvine, CA), according to the instructions provided by the manufacturer. Purified RNA was resuspended in 50 µL DNase/RNase-free water. RNA quality was evaluated using an Agilent 2100 Bioanalyzer (Agilent Technologies, Inc., Santa Clara, CA). RNA concentrations were quantified using Qubit RNA HS assay kits and a Qubit 2.0 Fluorometer (Thermo Fisher Scientific, Wilmington, DE) and stored at −80°C until further analysis.

RNA sequencing

One microgram of total RNA was depleted of ribosomal RNA, and PolyA tails of coding RNAs were captured by treatment with oligo-dT beads. Complementary DNA (cDNA) libraries were generated according to the TruSeq Stranded Total RNA sample preparation guide (Illumina, San Diego, CA, United States) and quantified using the KAPA Library Quantification Kit. Multiplex paired-end sequencing was performed using the Illumina HiSeq 2500 instrument (Illumina). Sequence reads were demultiplexed using the CASAVA pipeline (Illumina), and bases with Phred<30 were trimmed from both ends. Paired-end reads were aligned using STAR (PMID: 23104886) against the *Mus musculus* genome (GRCm38). Aligned reads were normalized by the TMM method (PMID: 20196867). After normalization, the gene-specific analysis tool in Partek Flow (Partek Inc., Chesterfield, MO) was used to identify differentially expressed genes (DEGs) by comparing expression in obese vs. control placentas.

KEGG pathway enrichment analysis

Kyoto Encyclopedia of Genes and Genomes (KEGG) pathway enrichment analysis was performed separately for DEGs from male and female placentas using DAVID and GSEA tools (add websites of the online tools). They were entered separately; the cutoff criteria to identify enriched pathways were $p < 0.05$ and FDR <0.01 for DAVID, and nominal $p < 0.05$ and FDR<0.25 for GSEA. A Venn diagram in InteractiVenn (http://www.interactivenn.net/) was used to show the common enriched KEGG pathways between DAVID and GSEA analyses (Heberle et al., 2015).

Gene ontology and functional analyses

DEGs of both male and female placentas were further characterized by gene ontology (GO) and pathway enrichment analyses. Over-represented GO cellular components, biological processes, molecular functions, and KEGG pathways were identified by using WebGestalt, with p-value <0.05 as the criterion for statistical significance after Benjamini–Hochberg correction for multiple testing (Supek et al., 2011). The REVIGO tool was used to filter out redundant GO terms, and enrichment analysis results were visualized using a treemap (Cox et al., 2019). Furthermore, functional analysis was carried out using the ingenuity pathway analysis (IPA, QIAGEN Inc.)

Human placental samples

This study was approved by the Colorado Multiple Institutional Review Board. Women with uncomplicated singleton term (37–40 weeks gestation) pregnancies were recruited, with a written consent prior to delivery. The gestational age was estimated from the date of the last menstrual period and confirmed by ultrasound dating. A total of 36 women with varying BMI (range, 18.4–47.1 kg/m^2) were studied. BMI was calculated based on height and weight measurements from pre-pregnancy medical records. The clinical characteristics of the participants in the study are shown in Table 1. Exclusion criteria for both AGA and obese/LGA groups were smoking, concurrent diseases, such as diabetes or hypertension, development of pregnancy complications, including gestational diabetes, pregnancy-induced hypertension, and pre-eclampsia, and the delivery of small-for-gestational-age (<10th centile) infants, according to published growth curves. Placental tissues were collected and processed within 30 min of delivery. In brief, the decidua basalis and chorionic plate were removed, and villous tissue was dissected and rinsed in cold physiological saline. The villous tissue was transferred to cold buffer D (250 mM sucrose, 10 mM HEPES, pH 7.4) containing 1:100 dilution of protease and phosphatase inhibitors (Sigma-Aldrich, St. Louis, MO) and homogenized on ice with Polytron (Kinematica, Luzern, Switzerland). The placental homogenates were frozen in liquid nitrogen and stored at −80°C until further processing. Mitochondrial electron transport complexes were determined using Western blots, as described in the following paragraph.

Western blotting

The total protein concentration in placental homogenates was determined using the Bradford assay (Bio-Rad). The placental homogenate (10 µg) was separated on 4%–20% precast linear gradient gels (Invitrogen). Membranes were incubated overnight at 4°C with primary antibody diluted in 1% non-fat milk (wt/vol) in TBST and detected using an appropriate peroxidase-conjugated secondary antibody. Products were visualized by ECL chemiluminescence (Millipore). Band intensities were measured using the G-box system (Syngene). Anti-β actin was purchased from Sigma-Aldrich, St. Louis, Mo. Target band densities were normalized using beta-actin to account for any variation in loading and transfer. Additional protein expression analysis was performed using automated capillary-based immunoassay (ProteinSimple, San Jose, CA, catalog #SM-W004-1, #PS-ST01,

TABLE 1 Selected clinical data.

	AGA (male fetus)	Obese (male fetus)	AGA (female fetus)	Obese (female fetus)
Maternal age (years)	26.4 ± 2.2 (18–35)	30.7 ± 1.7 (21–40)	29.0 ± 2.3 (21–40)	33.3 ± 1.23 (21–40)
BMI (kg/m^2) [a]	22.5 ± 0.7[a] (18.7–24.3)	34.2 ± 1.7[b] (28.2–47.1)	23.1 ± 0.5[a] (21.6–24.8)	38.0 ± 1.7[b] (26.9–43.6)
Gestational age (weeks)	39.2 ± 0.28 (37.5–41.6)	38.9 ± 0.44 (37.1–41)	39.0 ± 0.25 (37–40)	38.9 ± 0.27 (37.6–39.4)
Birth weight (kg)	2.9 ± 0.03[a] (2.7–2.9)	4.3 ± 0.19[b] (3.6–5.9)	2.8 ± 0.06[a] (2.7–3.0)	4.1 ± 0.09[b] (3.8–4.5)
Birth weight percentile[b]	19.8 ± 4.1[a] (6–41)	90.2 ± 2.8[b] (73–100)	23.8 ± 5.0[a] (11–46)	92.8 ± 2.5[b] (77–99)
Placental weight (g)	559 ± 37[a] (435–678)	851 ± 47[b] (648–1.15)	518 ± 29[a] (437–625)	854 ± 54[b] (608–1.20)
Fetal/placental ratio	5.25 ± 0.27 (4.36–6.24)	5.12 ± 0.20 (4.35–6.70)	5.64 ± 0.23 (4.75–6.22)	5.00 ± 0.28 (3.74–6.96)

Data are presented as means ± S.E.M; range.
[a]Abbreviations: data from n = AGA (male), 7; obese (male), 11; AGA (female), 6; obese (female), 10.
[b]By corresponding gestational age; means without a common letter differ significantly ($p < 0.05$) by one-way ANOVA, with the Tukey–Kramer multiple comparison *post hoc* test.

and #PN-009–050), as described previously (Castillo-Castrejon et al., 2021). Briefly, Jess plates were run according to the manufacturer's instructions, with minor modification (200 V, 55 min separation time) with 0.1 mg/mL total protein concentration.

Data presentation and statistics

Results from experimental analyses in mice are presented as mean ± SEM. The number of experiments (n) represents the number of litters studied. For each litter, male or female placentas were pooled. Results from human placentas are presented as mean ± SEM. The number of experiments (n) represents the number of individual placentas studied. Variables were analyzed as continuous across the range of BMI and birth weights, and linear relationships between variables were determined using Pearson's correlation coefficients. A $p < 0.05$ value was considered significant. Statistical significance of differences between control and obese groups was assessed using Student's *t*-test. A *p*-value < 0.05 was considered significant. One-way analysis of variance (ANOVA) and Tukey–Kramer multiple comparisons *post hoc* tests were used to compare datasets with more than two groups. $p < 0.05$ was considered significant.

Results

Fetal and placental weights in the mouse model of maternal obesity

Both male and female fetal weights were increased ($p < 0.001$; n = 5 litters in each group) at E18.5 in the obese group as compared to control (Figure 1A). However, placental weights and fetal/placental weight ratios were not significantly different between groups (Figures 1B, C). The increase in fetal weight was not due to a difference in the litter size (Figure 1D), which was similar in control (6.6 ± 0.51, n = 5) and obese groups (6.5 ± 1.2, n = 5).

Analysis of differentially expressed genes

The analysis of RNA-seq data comparing gene expression in obese vs. control placentas without taking the fetal sex into account showed that of 25,099 transcripts (Supplementary Table S1), 1154 were significantly upregulated and 1133 were significantly downregulated (7.6% DEG, $p < 0.05$; Supplementary Table S1) in the obese group. When data were analyzed separately for placentas of male and female fetuses, RNA-seq identified 25,099 transcripts in male placentas with 511 genes significantly upregulated and 791 genes significantly downregulated when comparing the obese group with control (Supplementary Table S2). In female placentas, 25,099 genes were expressed, with 474 genes significantly upregulated and 722 genes significantly downregulated in the obese group as compared with the control group (Supplementary Table S3). Comparing placental DEGs in the mouse maternal obesity model, we observed that 119 DEGs were downregulated in both male and female fetuses (Figure 2; Supplementary Table S4) and 68 DEGs were upregulated in both sexes (Figure 2; Supplementary Table S5).

The top five downregulated genes in male placentas of obese dams were Nudix hydrolase 13 (*Nudt13*, 1080-fold); glutathione S-transferase A3 (*Gsta3*, 233-fold); thromboxane A2 receptor (*Tbxa2r*, 201-fold); roundabout homolog 2 (*Robo2*, 54-fold); and zinc finger and BTB domain-containing protein 7B (*Zbtb7b*, 28-fold). In female placentas of obese dams, the top five downregulated genes were aquaporin-5 (*Aqp5*, 8163-fold); ankyrin repeat family A protein 2 (*Ankra2*, 2896-fold); threonine synthase-like 1 (*Thnsl1*, 2122-fold); zyxin (*Zyx*, 1204-fold); and T-lymphocyte surface antigen Ly-9 (*Ly9*, 913-fold).

The top five upregulated genes in male placentas of obese dams as compared to the control group were myosin light chain 1/3, skeletal muscle isoform (*Myl1*, 12,571-fold); apolipoprotein C-III (*Apoc3*, 6177-fold); kerman protein 2 (*Kremen2*, 5053-fold); disabled homolog 2-interacting protein (*Dab2ip*, 2112-fold); and protein AF-9 (*Mllt3*, 180-fold). In female placentas of obese dams, the top five upregulated genes as compared to the control group were myosin light chain 1/3, skeletal muscle isoform (*Myl1*, 13,482-fold); myosin regulatory light chain 2, skeletal muscle isoform (*Mylpf*, 2381-fold) (*Zmynd15*, 467-fold); RWD domain-

10.3389/fcell.2023.1178533

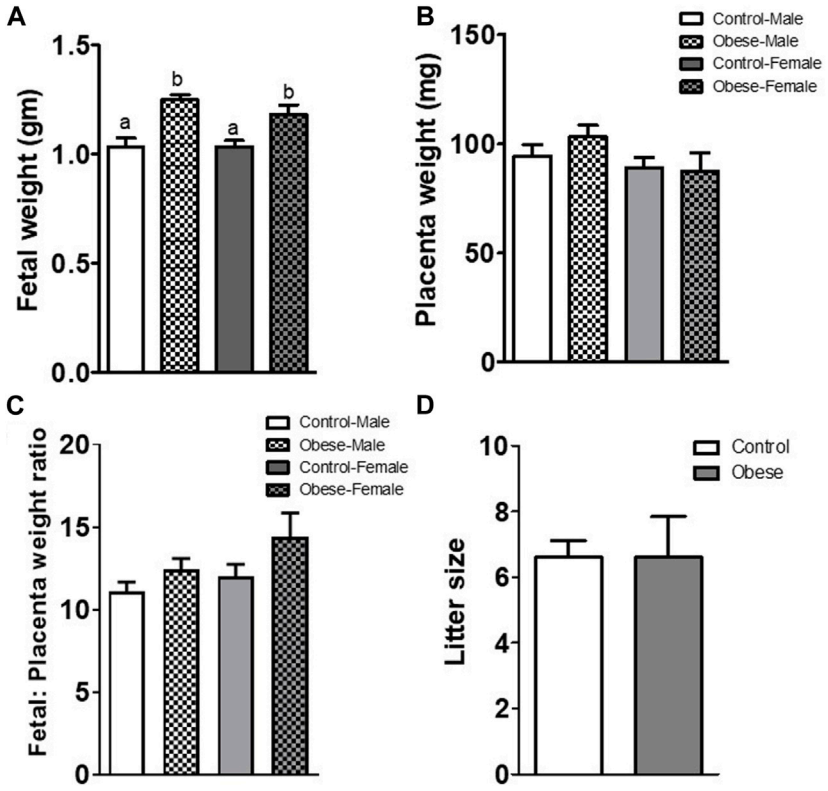

FIGURE 1
Fetal **(A)** and placental **(B)** weights, fetal/placental weight ratio **(C)**, and litter size **(D)** determined at E18.5 in mice from the control and obese groups. Values are means ± SEM, n = 5 in each group, *$p < 0.05$ vs control; unpaired Student's *t*-test. Means without a common letter are statistically different by performing one-way ANOVA with the Tukey–Kramer multiple comparison *post hoc* test ($p < 0.05$).

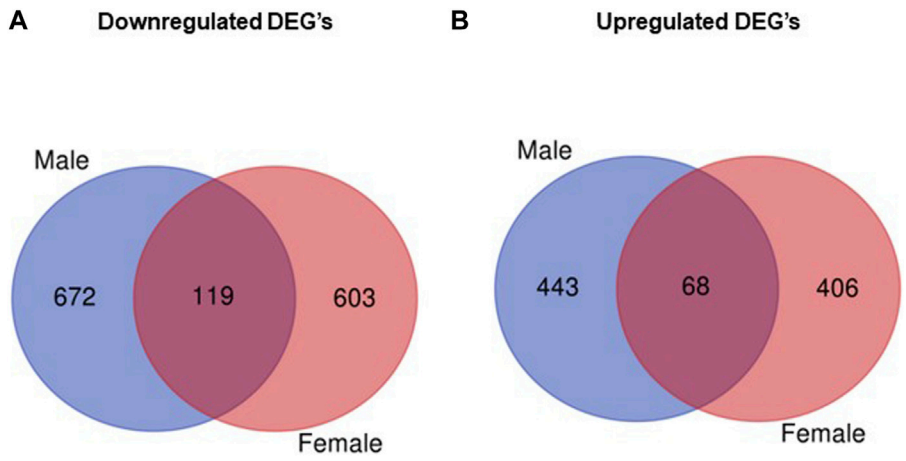

FIGURE 2
Venn diagram illustrating differentially expressed genes that overlap between males and females. **(A)** Number of downregulated genes (obese vs. control) in male and female placentas. **(B)** Number of upregulated genes (obese vs. control) in male and female placentas.

10.3389/fcell.2023.1178533

FIGURE 3
Treemap of GO biological process categories upregulated in male placentas of obese dams. REVIGO was used to remove redundant GO terms and join the cluster representatives (single rectangles) into superclusters (represented by different colors). Each rectangle's size reflects the GO term's false discovery rate (FDR) value (larger for lower FDR), considering a FDR <0.05 as the criterion for statistical significance after Benjamini–Hochberg correction for multiple testing.

containing protein 2A (*Rwdd2a*, 250-fold); and tripartite motif protein 15 isoform (*Trim15*, 223-fold).

GO enrichment analysis for upregulated genes in male placentas of obese dams

Figure 3 shows the most represented non-redundant GO biological process categories upregulated in male placentas of obese dams were signal transduction by a p53 class mediator, positive regulation of the catabolic process, negative regulation of the immune system process, I-kappa kinase/NF-kappa B signaling, the purine-containing compound metabolic process, negative regulation of intracellular signal transduction, and the ErbB signaling pathway. In addition, the critical cellular component GO terms upregulated in male placentas of obese dams were localized in the mitochondrial matrix, lipid droplet, vesicle membrane, actin cytoskeleton, histone deacetylase complex, transcription regulator complex, transcription repressor complex, chromatin, and early endosome (Figure 4). Furthermore, the GO molecular functions of genes associated with an organic acid transmembrane transporter activity, active transmembrane transporter activity, anion transmembrane transporter activity, ribonucleoprotein complex binding, and ATPase activity were increased in male placentas of obese dams as compared to male control placentas (Figure 5).

GO enrichment analysis for downregulated genes in male placentas of obese dams

The non-redundant GO biological processes downregulated in male placentas of obese dams were a response to nutrient, the transmembrane receptor protein serine/threonine kinase signaling pathway, mitochondrial gene expression, hormone-mediated signaling pathway, response to leukemia inhibitory factor, NADH dehydrogenase complex assembly, and regulation of gene expression, epigenetic (Supplementary Figure S2). In addition, many downregulated genes in male placentas of obese dams were located in the heterochromatin, endoplasmic reticulum-Golgi intermediate compartment, vesicle membrane, recycling endosome, oxidoreductase complex, and nuclear periphery (Supplementary Figure S3). Moreover, the GO molecular function of genes associated with the DNA-binding transcription repressor activity, RNA polymerase II-specific transcription, phospholipid binding, peptide receptor activity, metallopeptidase activity, phospholipid binding, active transmembrane transporter activity, hormone receptor binding, and ubiquitin-like protein binding (Supplementary Figure S4).

10.3389/fcell.2023.1178533

FIGURE 4
Treemap of GO cellular component categories upregulated in male placentas of obese dams. REVIGO was used to remove redundant GO terms and join the cluster representatives (single rectangles) into superclusters (represented by different colors). Each rectangle's size reflects the GO term's false discovery rate (FDR) value (larger for lower FDR), considering a FDR <0.05 as the criterion for statistical significance after Benjamini–Hochberg correction for multiple testing.

GO enrichment analysis for upregulated genes in female placentas of obese dams

Supplementary Figure S5 shows the most represented biological process categories upregulated in female placentas of obese dams were the cytoplasmic translation, proteasomal protein catabolic process, response to temperature stimulus, response to acid chemical, synaptic vesicle cycle, and protein import. Furthermore, most of the upregulated genes in the female placentas of obese dams were predominantly localized to the outer membrane, coated vesicle, lytic vacuole, condensed chromosome, endoplasmic reticulum membrane, organelle inner membrane, and cell projection membrane (Supplementary Figure S6). The GO molecular function terms upregulated in female placentas of obese dams were magnesium ion binding, structural constituent of the ribosome, kinase regulator activity, enzyme inhibitor activity, inorganic cation transmembrane transporter activity, chromatin DNA binding, and single-stranded RNA binding (Supplementary Figure S7).

GO enrichment analysis for downregulated genes in female placentas of obese dams

The most enriched non-reductant GO biological functions downregulated in female placentas of obese dams were associated with the muscle system process, chromatin organization, peptidyl serine modification, translational initiation, muscle cell differentiation, sensory system development, regulation of embryonic development, and regulation of the mRNA metabolic process (Supplementary Figure S8). In addition, most downregulated genes in the female placentas of obese dams were predominantly localized to the external side of the plasma membrane, clathrin-coated pit, basolateral plasma membrane, extracellular matrix, cell–substrate junction, myelin sheath, nuclear speck, ribosomes, microtubule-associated complex, and endoplasmic reticulum lumen (Supplementary Figure S9). Furthermore, the GO molecular functions downregulated in the placentas of obese dams were associated with single-stranded RNA binding, GTPase activity, endopeptidase activity, hydrolase activity, acting on carbon–nitrogen (but not peptide) bonds, deubiquitinase activity, helicase activity, glycosaminoglycan binding, growth factor binding, histone binding, and histone deacetylase binding (Supplementary Figure S10).

KEGG pathway enrichment analysis

KEGG pathway analysis for up- and down-regulated genes in both male and female placentas was analyzed using DAVID and GSEA online tools. For upregulated DEGs in male placentas of obese

FIGURE 5
Treemap of GO molecular function categories upregulated in male placentas of obese dams. REVIGO was used to remove redundant GO terms and join the cluster representatives (single rectangles) into superclusters (represented by different colors). Each rectangle's size reflects the GO term's false discovery rate (FDR) value (larger for lower FDR), considering a FDR <0.05 as the criterion for statistical significance after Benjamini–Hochberg correction for multiple testing.

dams, 10 and 27 KEGG pathways were enriched according to GSEA and DAVID, respectively (Supplementary Tables S6, S7). As shown in Supplementary Figure S11, the GSEA and DAVID tool analyses identified eight common upregulated KEGG pathways in male placentas of obese dams: inositol phosphate metabolism, tight junction, adipocytokine, PPAR, phosphatidylinositol, glycosphingolipid biosynthesis–ganglio series, the T-cell receptor, and the Wnt signaling pathway. For downregulated DEGs in male placentas of obese dams, 13 and 36 KEGG pathways were enriched according to GSEA and DAVID analyses, respectively (Supplementary Tables S8, S9). The 12 common downregulated KEGG pathways in male placentas of obese dams identified by GSEA and DAVID analyses were protein export, DNA replication, aminoacyl-tRNA biosynthesis, purine metabolism, pyrimidine metabolism, oxidative phosphorylation, Huntington's disease, Parkinson's disease, RNA polymerase, ubiquitin-mediated proteolysis, Alzheimer's disease, glycolysis, and gluconeogenesis (Supplementary Figure 12).

KEGG pathway analysis using DAVID and GSEA identified 10 and 18 pathways, respectively, that were enriched with upregulated DEGs in female placentas of obese dams (Supplementary Tables S10, S11). The six KEGG pathways (Supplementary Figure S13) that were commonly enriched in GSEA and DAVID analyses were MAPK signaling, Toll-like receptor signaling, homologous recombination, neurotrophin signaling, GnRH signaling, and T-cell receptor signaling. Supplementary Tables S12, S13 show the list of enriched KEGG pathways downregulated in female placentas of obese dams. The GSEA and DAVID analyses identified 7 and 16 KEGG pathways, respectively. Among these pathways, endocytosis, cysteine and methionine metabolism, pyrimidine metabolism, and ubiquitin-mediated proteolysis were common in both analyses (Supplementary Figure S14). Only one KEGG pathway was found to be enriched (FDR<0.01) with downregulated DEGs.

Maternal obesity alters transcriptomic pathways related to mitochondrial dysfunction, oxidative phosphorylation, and protein ubiquitination in male placentas of obese dams.

IPA revealed the differential regulation of 154 significant ($p < 0.05$) canonical pathways in male placentas in response to maternal obesity, including oxidative phosphorylation, ceramide signaling, protein ubiquitination, PKCθ signaling in T lymphocytes, sirtuin, Rac, PDGF signaling, CD27 signaling in lymphocytes, production of nitric oxide and reactive oxygen species in macrophages, p70S6k, angiopoietin, and B-cell receptor signaling (Supplementary Table S14).

The expression of many genes in the placental p21-activated kinases (*Pak*, $p = 1.418$ E-02) and *Rac* ($p = 1.14$ E-02) signaling pathways were upregulated in response to maternal obesity in

10.3389/fcell.2023.1178533

male placentas. PAK are a family of critical effectors of *Rac1* and *Cdc42*. They regulate various cellular functions, such as cytoskeleton dynamics, cell movement and migration, cell proliferation and differentiation, and gene expression. Sixteen of 109 genes in this pathway were differentially expressed, including phosphatidylinositol 3-kinase catalytic subunit type 3 (*Pik3c3*), myosin light chain 1 (*Myl1*), myosin light chain, phosphorylatable, fast skeletal muscle (*Mylpf*), mitogen-activated protein kinase 8 (*Mapk8*), myosin light polypeptide 6 (*Myl6*), P21 (Rac1)-activated kinase 6 (*Pak6*), and RAP2B, a member of the RAS oncogene family (*Rap2b*). In addition, members of *Rac1* signaling pathway genes such as RAS homology family A (*Rhoa*) and CD44 (*Cd44*) were all significantly upregulated in the obese group.

The 70-kDa ribosomal protein S6 kinase (*p70S6K*) signaling pathway (p = 1.84E-03) is known to promote protein synthesis and cell growth. Nineteen of 113 genes in this pathway were differentially expressed. Genes such as ribosomal protein S6 kinase B1 (*Rps6kb1*), casein kinase 2 beta (*Csnk2b*), insulin receptor substrate 2 (*Irs-2*), and protein kinase C Zeta (*Prkcz*) were significantly upregulated in the obese group as compared to control.

A large number of genes, 108 of 171 genes, in the mitochondrial functional pathway (p = 1.86E-05) were downregulated in male placentas of obese dams. Genes such as ATP synthase F1 subunit beta (*Atp5b*), cytochrome c oxidase Subunit 6B1 (*Cox6b1*), NADH dehydrogenase [ubiquinone] 1 alpha subcomplex subunit 3 (*Ndufa3*), NADH dehydrogenase [ubiquinone] 1 alpha subcomplex subunit 7 (*Ndufa7*), cytochrome c oxidase (*Cox15*), NADH: ubiquinone oxidoreductase subunit A11 (*Ndufa11*), and ATP synthase F1 subunit beta (Atp5*f1b*) were all significantly downregulated in the obese group.

Maternal obesity alters transcriptomic pathways related to triacylglycerol biosynthesis and cardiac hypertrophy but not oxidative phosphorylation pathways in female placentas of obese dams.

The IPA analysis of DEGs in female placentas revealed that 63 significant (p < 0.05) canonical pathways were differentially regulated in response to maternal obesity, including sirtuin signaling, triacylglycerol biosynthesis, and phosphatidylglycerol biosynthesis II (Supplementary Table S15).

Eight of 47 genes were differentially expressed in the triacylglycerol biosynthesis pathway (p = 1.27 E-03). The pathway was predicted to be downregulated due to expression of genes such as porcupine O-acyltransferase (*Porcn*), tafazzin (*Taz*), lysocardiolipin acyltransferase 1 (*Lclat1*), phospholipid phosphatase 5 (*Plpp5*), dihydrolipoamide branched chain transacylase E2 (*Dbt*), lysophosphatidylcholine acyltransferase 1 (*Lpcat1*), and lycerol-3-phosphate acyltransferase 4 (*Gpat4*), which were all significantly decreased in female placentas of obese dams.

The expression of 22 out of 242 genes in the cardiac hypertrophy signaling pathway was increased in female placentas of obese dams compared to controls (p = 1.98 E-03). Genes such as myosin light chain 1 (*Myl1*), myosin light chain, phosphorylatable, fast skeletal muscle (*Mylpf*), activating transcription factor 2 (*Atf2*), myocyte enhancer factor 2C (*Mef2c*), RAS homolog family member D (*Rhod*), calcium voltage-gated channel subunit alpha1 D (*Cacna1d*), and mitogen-activated protein kinase 14/8/6/3 (*Mapk14/8/6/3*) were significantly upregulated in response to maternal obesity.

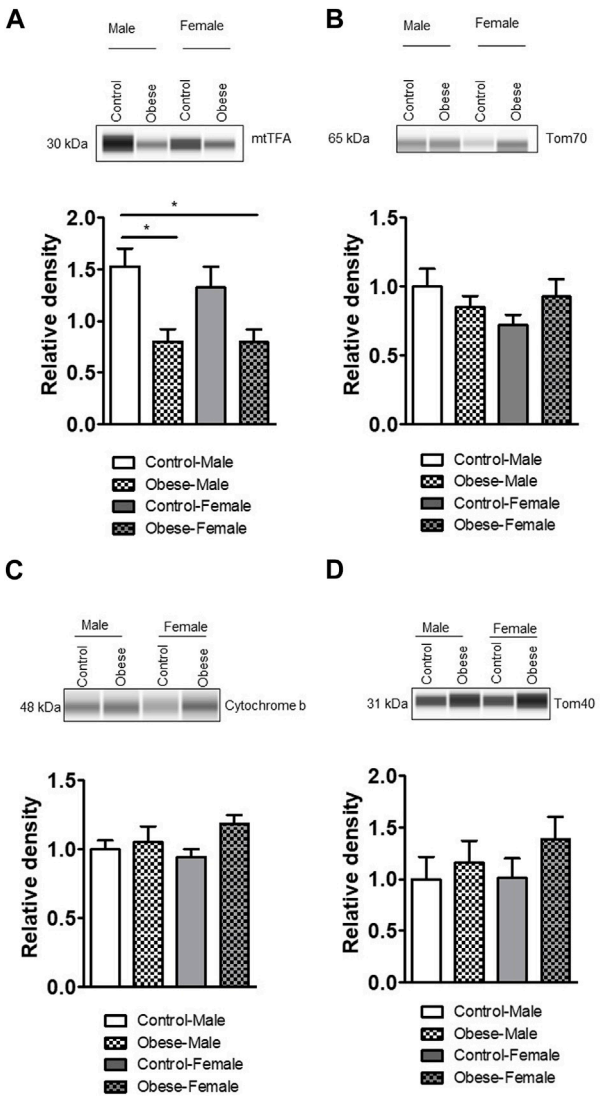

FIGURE 6
Effect of maternal obesity on the expression of placental mtTFA, Tom70, cytochrome b, and Tom40 in pregnant mice. **(A–D)** Protein expression of mtTFA, Tom70, cytochrome b, and Tom40 in the placental homogenates of obese and control groups (n = 7/each group). A representative Western blot is shown. Data are from a representative experiment, and similar results were obtained from six other experiments. Values are means +SEM.; *p < 0.05 vs. control by one-way ANOVA with the Tukey–Kramer multiple comparison *post hoc* test.

Maternal obesity alters upstream regulators in a fetal sex-dependent manner

IPA identified the differential expression of multiple upstream transcriptional regulators that may explain changes in gene expression and illuminate the biological activities occurring in the tissue of interest including serine/threonine-protein kinase/

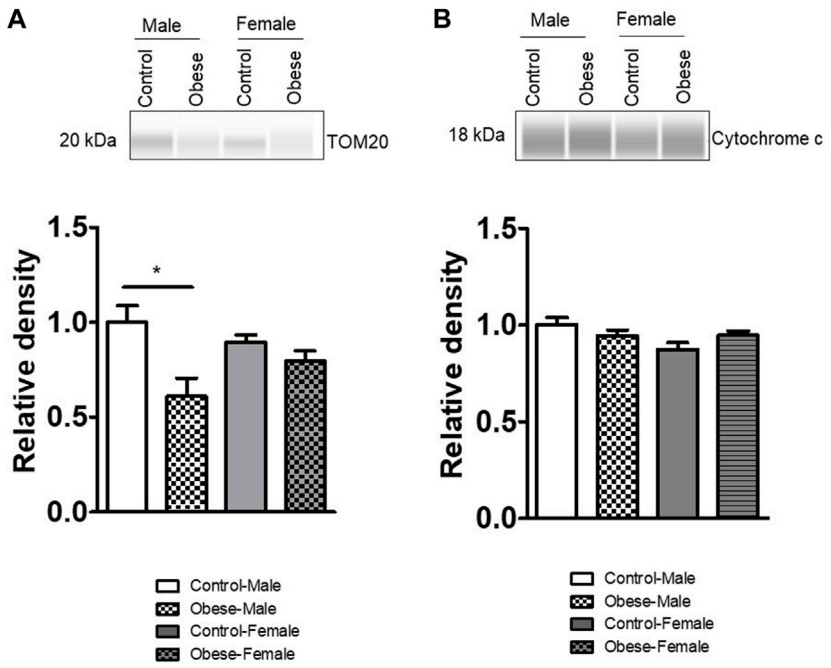

FIGURE 7
Effect of maternal obesity on the placental expression of Tom20 and cytochrome c in pregnant mice. **(A,B)** Protein expression of Tom20 and cytochrome c in the placental homogenates of obese and control groups (n = 7/each group). A representative Western blot is shown. Data are from a representative experiment, and similar results were obtained from six other experiments. *$p < 0.05$ vs. control by one-way ANOVA with the Tukey–Kramer multiple comparison *post hoc* test.

endoribonuclease inositol-requiring enzyme 1α (*ERN1*), interleukin 4 (*IL-4*), activating transcription factor 6 (*ATF6*), thrombospondin-4 (*THSB4*), and hypoxia-inducible factor 1-alpha (*HIF-1 alpha*), which were decreased in both male and female placentas of obese dams. Conversely, the upstream regulators that were activated in both male and female placentas of the obese group were miR-124-3p, miR-1-3p, miR-16-5p, mitogen-activated protein kinase 7 (*MAPK7*), and tumor necrosis factor (ligand) superfamily, member 10 (*TNFSF10*). Interestingly, interleukin-2 (*IL-2*) and peroxisome proliferator-activated receptor gamma coactivator 1-alpha (*PGC-1α*) pathways were activated in male placentas but inhibited in female placentas of obese dams (Supplementary Figure S15).

Effect of maternal obesity on the expression of proteins involved in the mitochondrial function

We measured the protein expression of mtTFA (mitochondrial transcription factor A), Tom (Translocase of outer membrane)-70, cytochrome b, Tom40, Tom20, and cytochrome c in the placental homogenates of obese and control groups (Figures 6, 7). The protein expression levels of mtTFA and Tom20 were significantly reduced in male placentas of obese dams as compared to the control group, whereas maternal obesity did not affect the mtTFA and Tom20 expression levels in female placentas. In contrast, the protein expression levels of Tom70, Tom40, cytochrome b, and cytochrome c were comparable between groups.

Effect of maternal obesity and birth weight on mitochondrial electron transport chain complex expression in the human placenta

To explore the clinical significance of our findings in a mouse model of maternal obesity, we investigated the relationships among maternal obesity, birth weight, and the protein expression of placental mitochondrial electron transport chain (ETC) complexes. Even in this small sample size, maternal BMI was positively correlated with birth weight in both sexes (Figures 8, 9). Figure 8 shows that the protein expression levels of ETC complexes V, II, and I in male placentas were negatively correlated with maternal BMI and birth weight. Male placental, ETC complex III expression was negatively correlated with birth weight but did not correlate with maternal BMI. In contrast (Figure 9), there was no significant relationship between maternal BMI or birth weight and the protein expression of placental mitochondrial, ETC complexes III and V in pregnancies with a female infant. On the other hand, ETC complex I and II expression in the female placenta was negatively correlated with maternal BMI and birth weight.

Discussion

Using a mouse model of high-fat and high-sugar diet-induced maternal obesity with fetal overgrowth, we report that maternal obesity impacts the placental transcriptome in a sex-dependent manner. RNA-seq analysis demonstrated that a total of

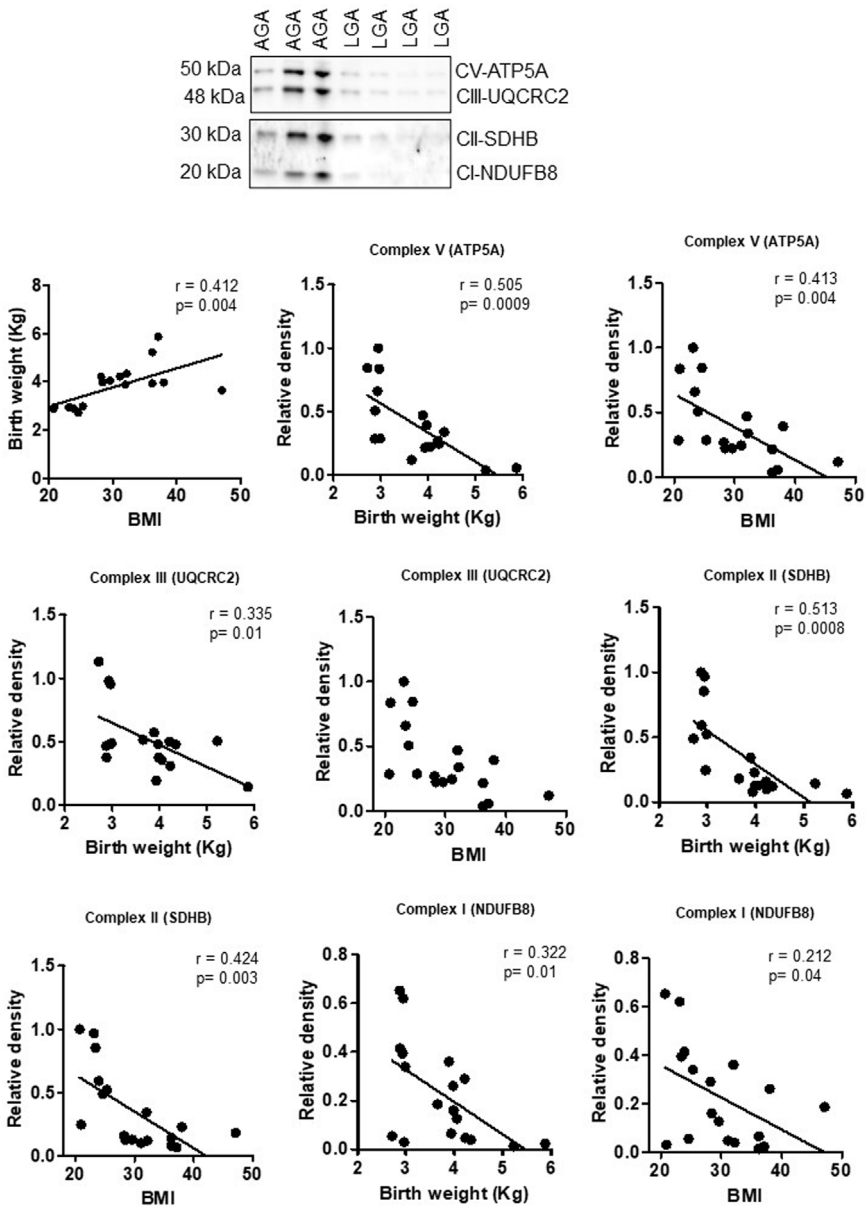

FIGURE 8
Correlation between maternal BMI, birth weight, and placental mitochondrial, ETC complex (V, III, II, and I) protein expression in male placentas of control (AGA, appropriate-for-gestational-age) and LGA (large-for-gestational-age) pregnancy. r = Pearson's correlation coefficient, n = 7–11/each group. Placental mitochondrial, ETC complex subunit protein expression in relation to BMI and birth weight. A representative Western blot for mitochondrial, ETC complex subunits (complex V- ATP5F1A, ATP synthase F1 subunit alpha; complex III- UQCRC2, ubiquinol–cytochrome C reductase core protein 2; complex II- SDHB, succinate dehydrogenase complex iron sulfur subunit B; complex I- NDUFB8, NADH-ubiquinone oxidoreductase subunit B8) in homogenates of placentas from pregnancies with varying maternal BMI and birth weights. There was no significant correlation between BMI and mitochondrial, ETC complex subunit III.

2287 genes were differentially expressed in the placentas of obese dams. We found a significant impact of maternal obesity on genes related to mitochondrial function in male placentas of obese dams, and we provided evidence that the findings in mice have clinical relevance by demonstrating that human placental mitochondrial, ETC expression was downregulated and negatively correlated with maternal pre-pregnancy BMI and birth weights in male infants.

Top downregulated genes (*Nudt*13 and *Gsta3*) in the male placentas of obese dams were associated with mitochondrial dysfunction. *Nudt13* is a NAD(P)H pyrophosphatase that uses mitochondrial NADH and/or NADPH as a substrate. *Nudt13* is an important regulator of the redox state of the cell and may act as a redox sensor for transcriptional control in cells (Abdelraheim et al., 2017).

We found a significant reduction in the transcript levels of genes encoding several mitochondrial proteins such as *Ndufa7, Ndufa9, Ndufa10, Ndufa4l2*, and *Ndufa11* in male placentas of obese dams. In addition, we demonstrated that the protein expression of

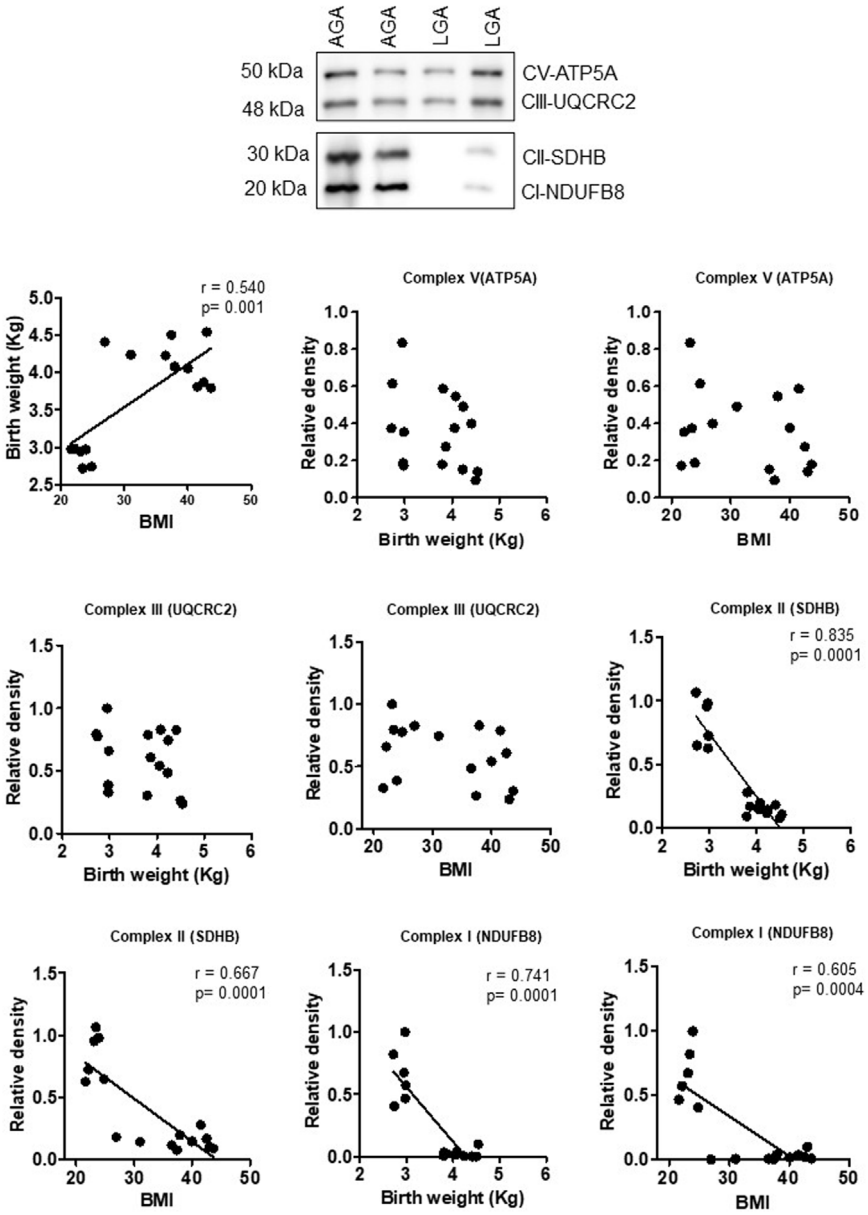

FIGURE 9
Correlation between maternal BMI, birth weight, and placental mitochondrial, ETC complex (V, III, II, and I) protein expression in female placentas of control (AGA, appropriate-for-gestational-age) and LGA (large-for-gestational-age) pregnancy. r = Pearson's correlation coefficient, n = 6–10/each group. Placental mitochondrial, ETC complex subunit protein expression in relation to BMI and birth weight. A representative Western blot for mitochondrial, ETC complex subunits (complex V- ATP5F1A, ATP synthase F1 subunit alpha; complex III- UQCRC2, ubiquinol–cytochrome C reductase core protein 2; complex II- SDHB, succinate dehydrogenase complex iron sulfur subunit B; complex I- NDUFB8, NADH-ubiquinone oxidoreductase subunit B8) in homogenates of placentas from pregnancies with varying maternal BMI and birth weights. There was no significant correlation between BMI or birth weight and mitochondrial, ETC complex subunits II and I.

TOM20 and mtTFA was lower in placentas from male fetuses of obese dams. TOM20 is anchored to the outer membrane as a peripheral subunit of the TOM40 complex (Yamamoto et al., 2011). Recent evidence indicates that the defective mitochondrial import due to the decreased expression of TOM20 contributes to complex I-mediated mitochondrial dysfunction in the brain and the development of neurogenerative disease (Franco-Iborra et al., 2018). Furthermore, reduction in the mitochondrial protein import activity was linked to reduced protein levels of OXPHOS subunits (Schmidt et al., 2010). mtTFA is an essential high-mobility protein that enhances mtDNA transcription, replication, and synthesis of subunits encoded in mtDNA (Alam et al., 2003). The knockout of the mtTFA gene in mice results in the reduction of mtDNA and embryonic lethality (Larsson et al., 1998). Placental mtTFA expression has also been reported to be decreased in pre-eclampsia (Vishnyakova et al., 2016). Our data suggest that exposure to maternal obesity in mice leads to a state of mitochondrial dysfunction in the placentas of male fetuses.

We provided evidence that human placental mitochondrial, ETC complex (V, III, II, and I) expression was downregulated and negatively correlated with maternal pre-pregnancy BMI and birth weight in male infants. Obesity has been reported to be associated with a decrease in the mtDNA copy number, mitochondrial mass, mitochondrial ETC complexes, and mitochondrial activity/biogenesis in white adipose tissue in mouse models and in skeletal muscle of obese men and women (Kelley et al., 2002). Mele et al. showed significant reduction in mitochondrial respiration in cultured primary trophoblasts isolated from pregnancies complicated by maternal obesity (Mele et al., 2014). Thus, reduction in the expression of placental mitochondrial-associated genes in pregnancies complicated by maternal obesity may compromise the placental function and potentially underlying the increased susceptibility of male fetuses of obese mothers to developmental programming in later life (Mele et al., 2014). In addition, maternal obesity stimulates lipotoxicity and increases the activation of inflammatory NF-κB and JNK signaling in the placenta (Liang et al., 2018). NF-κB controls mitochondrial dynamics (Albensi, 2019). Thus, upregulation of the NF-κB signaling pathway may contribute to decreased oxidative phosphorylation reported in the placentas of males in maternal obesity. Alternatively, the downregulation of placental mitochondrial function in male fetuses of obese mice and in women may represent an adaptive response to intermittent hyperglycemia common in maternal obesity, which could be associated with a shift of placental energy production from oxidative phosphorylation to glycolysis.

Other molecular pathways that were downregulated in the male placentas of obese dams are involved in neurodegenerative disorders, namely, Huntington disease and Alzheimer disease pathways. Recent studies indicate that there might be common developmental pathways between the brain and placenta (Burton and Jauniaux, 2018; Maslen, 2018). Moreover, human placenta-derived stem cells differentiate into neural progenitor cells *in vitro*, and the placenta secretes a wide array of neurohormones that regulate fetal brain development (Rosenfeld, 2021). Recent human observational studies suggest that the odds for adverse neurodevelopmental outcome were 17% higher among children of mothers who were overweight or obese during pregnancy (Sanchez et al., 2018). In addition, muscle system processes were among the most enriched downregulated GO biological function in female placentas of obese dams. Although of unclear significance, it is intriguing to note that Shelly and coworkers reported that skeletal muscle signaling and mitochondrial complex II–II linked activity are altered in adult offspring of obese mice (Shelley et al., 2009).

Based on our RNA-seq data, the ceramide signaling pathway is predicted to be upregulated in the male placentas of obese dams. Ceramide is a sphingolipid that functions as an important second messenger known to affect mitochondria, altering both morphology and physiology. The activation of ceramide signaling decreases the mitochondrial oxygen consumption in myotubes (Summers et al., 2019). Thus, it is possible that the upregulation of the ceramide signaling pathway contributes to decreased oxidative phosphorylation reported in placentas of males in maternal obesity (Bucher et al., 2021).

Thermogenesis is another downregulated placental molecular pathway in male fetuses of obese dams. A previous study reported that maternal obesity in mice reduced the expression of genes involved in the thermogenesis of brown adipose tissue (BAT) in offspring (Zhang et al., 2021). Furthermore, decreased thermogenesis in the BAT of fetal mice of obese dams was associated with elevated BAT lipid droplets and reduced mitochondrial DNA and mitochondrial biogenesis markers (Lettieri Barbato et al., 2015). It is therefore plausible that lower oxidative phosphorylation in male placentas of obese dams was caused by the downregulation of the thermogenesis signaling system. Interestingly, decreased thermogenesis was recently highlighted as a possible mechanism underlying altered energy balance in offspring of obese mice (Maragkoudaki et al., 2020).

A top downregulated placental gene in females of obese dams was associated with water transport. Aquaporin 5 (*Aqp5*) belongs to a family of membrane channel proteins that facilitate bulk water transport. *Aqp5* may be involved in energy metabolism, or may be crucial in the clearance of excess lactate in the placental extracellular space (Badaut and Regli, 2004).

Male and female fetuses respond differently to maternal obesity resulting in different risk profiles for developing metabolic diseases later in life (Myatt and Maloyan, 2016). For example, in our mouse model of obesity, male offspring develop obesity, glucose intolerance, and insulin resistance at 3 months of age, whereas the metabolic phenotype in female offspring is much less severe at this age (Paulsen et al., 2019). There is also evidence that the female and male placentas are functionally different with distinct responses to an adverse intrauterine environment such as maternal obesity. Reduced placental mitochondrial function may contribute to impaired glucose metabolism and cardiac dysfunction reported in 3-month-old male offspring born to obese dams (Paulsen et al., 2019; Vaughan et al., 2020).

We also report that the sirtuin signaling pathway was upregulated in the male placentas of obese dams. Sirtuin1 (SIRT1), a class III histone deacetylase, regulates various physiological and pathophysiological processes, including cellular inflammation and metabolism. Recent studies suggest that maternal inflammation is associated with increased placental SIRT1 expression (Park et al., 2020). Furthermore, SIRT1-mediated inflammatory processes may result in placental dysfunction and the release of inflammatory mediators (Ilekis et al., 2016).

In healthy human pregnancies, sex differences in placental size and gene expression are evident throughout the gestation (Buckberry et al., 2014). This is believed to play a role in determining sex differences in intrauterine growth that are apparent from the early stages of development. For example, as early as the pre-implantation stage, male embryos grow faster, demonstrating fundamental differences in growth and metabolism between the sexes (Mittwoch, 1993). In addition, based on the placental weight required to sustain a fetus (Eriksson et al., 2010), male placentas may be more efficient than female placentas.

Studies in rodents suggest that changes in placental morphology and placental inflammation in obese dams are more pronounced in male than female offspring (Kim et al., 2014). In women, Wang et al. demonstrated that fuel utilization in trophoblasts for mitochondrial respiration in human pregnancies complicated by obesity and GDM is sexually dimorphic (Wang et al., 2019). Specifically, as compared to female offspring, male placentas in maternal obesity and GDM

were found to have decreased fuel flexibility with an increased dependency on glucose and limited ability to use glutamine for oxidative phosphorylation (Wang et al., 2019).

Evans and Myatt (2017) demonstrated that in lean women, the male placentas have greater antioxidant defense. However, this protection is lost with maternal obesity, perhaps contributing to the increased incidence of adverse outcomes in male infants (Peacock et al., 2012; Evans and Myatt, 2017). We observed that placental GST (glutathione-S-transferase) gene expression was decreased in males of obese dams. GST is an essential component of the cellular antioxidant defense mechanism that catalyzes the conjugation of reduced glutathione with a large array of xenobiotics and endogenous electrophiles (Yang et al., 2001). GST is also involved in the biosynthesis of leukotrienes, prostaglandins, testosterone, and progesterone, and the degradation of tyrosine (Hayes et al., 2005). The underlying cause for these sexually dimorphic changes in placental gene expression remains to be investigated.

Using the same mouse model of maternal obesity as in the current study, we previously reported the effect of maternal obesity on the fetal liver transcriptome (Kelly et al., 2022). Differentially regulated genes in the liver and placentas in the current study were distinct, with a little overlap. This may reflect that while the placenta is directly exposed to the metabolic changes in the maternal circulation, the fetal liver is not.

The mouse model used in the current study was originally developed to study maternal obesity associated with fetal overgrowth because LGA babies of obese women have a higher risk than appropriate-for-gestational age (AGA) babies to develop cardiovascular diseases later in life. Although obese women are more likely to deliver LGA babies (Yu et al., 2013; Leon-Garcia et al., 2016), the majority of the babies born to obese mothers have a birth weight that is AGA. Importantly, also AGA babies of obese mothers may have increased adiposity and evidence of insulin resistance, predisposing them for cardiometabolic diseases later in life. In the current study, maternal obesity did not alter the fetal/placental ratio. However, maternal obesity in our model causes increased placental glucose and amino acid transport (Rosario et al., 2015), which likely contributes to increased fetal growth. In contrast, using a different mouse model of diet-induced maternal obesity, Lager and coworkers reported normal placental and fetal weights but a lower fetal/placental ratio, suggesting decreased placental efficiency (Lager et al., 2014). It is notable that offspring in this model are programmed for future diseases (Samuelsson et al., 2008; Kirk et al., 2009; Oben et al., 2010; Samuelsson et al., 2010; Reynolds et al., 2013; Samuelsson et al., 2013; Taylor et al., 2014), demonstrating that the link between maternal obesity and offspring cardiometabolic disorders is not limited to infants born large.

In conclusion, our findings have advanced our understanding of the multifaceted effects of maternal obesity on the placental transcriptome that may be crucial to placenta development and function and impacting the developing fetus. We report that maternal obesity with fetal overgrowth differentially regulates the transcriptome in male and female placentas, including genes involved in oxidative phosphorylation. We provide evidence that the findings in mice have clinical relevance by demonstrating that human placental mitochondrial complex expression was downregulated and negatively correlated with maternal pre-pregnancy BMI and birth weight in male infants. This new information could potentially exert efforts to identify new interventions to alleviate the increased risk for poor metabolic health in offspring exposed to maternal obesity.

Data availability statement

The datasets presented in this study can be found in online repositories. The names of the repository/repositories and accession number(s) can be found in the article/Supplementary Material.

Ethics statement

The studies involving human participants were reviewed and approved by the Colorado Multiple Institutional Review Board. The patients/participants provided their written informed consent to participate in this study. The animal study was reviewed and approved by the University of Texas Health Science Center in San Antonio.

Author contributions

Study conception and design: FR, TP, LC, and TJ; data collection: FR, AK, and JC; analysis and interpretation of results: FR, AK, and JC; draft manuscript preparation: FR, TP, LC, JC, TJ, and AK. All authors contributed to the article and approved the submitted version.

Conflict of interest

The authors declare that the research was conducted in the absence of any commercial or financial relationships that could be construed as a potential conflict of interest.

Publisher's note

Supplementary material

The Supplementary Material for this article can be found online at: https://www.frontiersin.org/articles/10.3389/fcell.2023.1178533/full#supplementary-material

References

Abdelraheim, S. R., Spiller, D. G., and McLennan, A. G. (2017). Mouse Nudt13 is a mitochondrial Nudix hydrolase with NAD(P)H pyrophosphohydrolase activity. *Protein J.* 36, 425–432. doi:10.1007/s10930-017-9734-x

Alam, T. I., Kanki, T., Muta, T., Ukaji, K., Abe, Y., Nakayama, H., et al. (2003). Human mitochondrial DNA is packaged with TFAM. *Nucleic Acids Res.* 31, 1640–1645. doi:10.1093/nar/gkg251

Albensi, B. C. (2019). What is nuclear factor kappa B (NF-kappaB) doing in and to the mitochondrion? *Front. Cell Dev. Biol.* 7, 154. doi:10.3389/fcell.2019.00154

Alfaradhi, M. Z., and Ozanne, S. E. (2011). Developmental programming in response to maternal overnutrition. *Front. Genet.* 2, 27. doi:10.3389/fgene.2011.00027

Alves, J. M., Luo, S., Chow, T., Herting, M., Xiang, A. H., and Page, K. A. (2020). Sex differences in the association between prenatal exposure to maternal obesity and hippocampal volume in children. *Brain Behav.* 10, e01522. doi:10.1002/brb3.1522

Aye, I. L., Rosario, F. J., Powell, T. L., and Jansson, T. (2015). Adiponectin supplementation in pregnant mice prevents the adverse effects of maternal obesity on placental function and fetal growth. *Proc. Natl. Acad. Sci. U. S. A.* 112, 12858–12863. doi:10.1073/pnas.1515484112

Badaut, J., and Regli, L. (2004). Distribution and possible roles of aquaporin 9 in the brain. *Neuroscience* 129, 971–981. doi:10.1016/j.neuroscience.2004.06.035

Barke, T. L., Money, K. M., Du, L., Serezani, A., Gannon, M., Mirnics, K., et al. (2019). Sex modifies placental gene expression in response to metabolic and inflammatory stress. *Placenta* 78, 1–9. doi:10.1016/j.placenta.2019.02.008

Bouret, S., Levin, B. E., and Ozanne, S. E. (2015). Gene-environment interactions controlling energy and glucose homeostasis and the developmental origins of obesity. *Physiol. Rev.* 95, 47–82. doi:10.1152/physrev.00007.2014

Bucher, M., Montaniel, K. R. C., Myatt, L., Weintraub, S., Tavori, H., and Maloyan, A. (2021). Dyslipidemia, insulin resistance, and impairment of placental metabolism in the offspring of obese mothers. *J. Dev. Orig. Health Dis.* 12, 1–10. doi:10.1017/S2040174420001026

Buckberry, S., Bianco-Miotto, T., Bent, S. J., Dekker, G. A., and Roberts, C. T. (2014). Integrative transcriptome meta-analysis reveals widespread sex-biased gene expression at the human fetal-maternal interface. *Mol. Hum. Reprod.* 20, 810–819. doi:10.1093/molehr/gau035

Burton, G. J., Fowden, A. L., and Thornburg, K. L. (2016). Placental origins of chronic disease. *Physiol. Rev.* 96, 1509–1565. doi:10.1152/physrev.00029.2015

Burton, G. J., and Jauniaux, E. (2018). Development of the human placenta and fetal heart: Synergic or independent? *Front. Physiol.* 9, 373. doi:10.3389/fphys.2018.00373

Castillo-Castrejon, M., Yamaguchi, K., Rodel, R. L., Erickson, K., Kramer, A., Hirsch, N. M., et al. (2021). Effect of type 2 diabetes mellitus on placental expression and activity of nutrient transporters and their association with birth weight and neonatal adiposity. *Mol. Cell Endocrinol.* 532, 111319. doi:10.1016/j.mce.2021.111319

Clifton, V. L. (2010). Review: Sex and the human placenta: Mediating differential strategies of fetal growth and survival. *Placenta* 31, S33–S39. doi:10.1016/j.placenta.2009.11.010

Cox, B., Tsamou, M., Vrijens, K., Neven, K. Y., Winckelmans, E., de Kok, T. M., et al. (2019). A Co-expression analysis of the placental transcriptome in association with maternal pre-pregnancy BMI and newborn birth weight. *Front. Genet.* 10, 354. doi:10.3389/fgene.2019.00354

Cox, L. A., Li, C., Glenn, J. P., Lange, K., Spradling, K. D., Nathanielsz, P. W., et al. (2013). Expression of the placental transcriptome in maternal nutrient reduction in baboons is dependent on fetal sex. *J. Nutr.* 143, 1698–1708. doi:10.3945/jn.112.172148

Diaz, P., Powell, T. L., and Jansson, T. (2014). The role of placental nutrient sensing in maternal-fetal resource allocation. *Biol. Reprod.* 91, 82. doi:10.1095/biolreprod.114.121798

Dumolt, J., Powell, T. L., Jansson, T., and Rosario, F. J. (2022). Normalization of maternal adiponectin in obese pregnant mice prevents programming of impaired glucose metabolism in adult offspring. *FASEB J.* 36, e22383. doi:10.1096/fj.202200326R

Eriksson, J. G., Kajantie, E., Osmond, C., Thornburg, K., and Barker, D. J. (2010). Boys live dangerously in the womb. *Am. J. Hum. Biol.* 22, 330–335. doi:10.1002/ajhb.20995

Evagelidou, E. N., Kiortsis, D. N., Bairaktari, E. T., Giapros, V. I., Cholevas, V. K., Tzallas, C. S., et al. (2006). Lipid profile, glucose homeostasis, blood pressure, and obesity-anthropometric markers in macrosomic offspring of nondiabetic mothers. *Diabetes Care* 29, 1197–1201. doi:10.2337/dc05-2401

Evans, L., and Myatt, L. (2017). Sexual dimorphism in the effect of maternal obesity on antioxidant defense mechanisms in the human placenta. *Placenta* 51, 64–69. doi:10.1016/j.placenta.2017.02.004

Fisher, S. C., Kim, S. Y., Sharma, A. J., Rochat, R., and Morrow, B. (2013). Is obesity still increasing among pregnant women? Prepregnancy obesity trends in 20 states. *Prev. Med.* 56, 372–378. doi:10.1016/j.ypmed.2013.02.015

Franco-Iborra, S., Cuadros, T., Parent, A., Romero-Gimenez, J., Vila, M., and Perier, C. (2018). Defective mitochondrial protein import contributes to complex I-induced mitochondrial dysfunction and neurodegeneration in Parkinson's disease. *Cell Death Dis.* 9, 1122. doi:10.1038/s41419-018-1154-0

Hacker, A., Capel, B., Goodfellow, P., and Lovell-Badge, R. (1995). Expression of Sry, the mouse sex determining gene. *Development* 121, 1603–1614. doi:10.1242/dev.121.6.1603

Hayes, J. D., Flanagan, J. U., and Jowsey, I. R. (2005). Glutathione transferases. *Annu. Rev. Pharmacol. Toxicol.* 45, 51–88. doi:10.1146/annurev.pharmtox.45.120403.095857

Heberle, H., Meirelles, G. V., da Silva, F. R., Telles, G. P., and Minghim, R. (2015). InteractiVenn: A web-based tool for the analysis of sets through Venn diagrams. *BMC Bioinforma.* 16, 169. doi:10.1186/s12859-015-0611-3

Ilekis, J. V., Tsilou, E., Fisher, S., Abrahams, V. M., Soares, M. J., Cross, J. C., et al. (2016). Placental origins of adverse pregnancy outcomes: Potential molecular targets: An executive workshop summary of the eunice kennedy shriver national institute of child health and human development. *Am. J. Obstet. Gynecol.* 215, S1-S46–S46. doi:10.1016/j.ajog.2016.03.001

Jansson, N., Rosario, F. J., Gaccioli, F., Lager, S., Jones, H. N., Roos, S., et al. (2013). Activation of placental mTOR signaling and amino acid transporters in obese women giving birth to large babies. *J. Clin. Endocrinol. Metab.* 98, 105–113. doi:10.1210/jc.2012-2667

Jansson, T., and Powell, T. L. (2013). Role of placental nutrient sensing in developmental programming. *Clin. Obstet. Gynecol.* 56, 591–601. doi:10.1097/GRF.0b013e3182993a2e

Kelley, D. E., He, J., Menshikova, E. V., and Ritov, V. B. (2002). Dysfunction of mitochondria in human skeletal muscle in type 2 diabetes. *Diabetes* 51, 2944–2950. doi:10.2337/diabetes.51.10.2944

Kelly, A. C., J Rosario, F., Chan, J., Cox, L. A., Powell, T. L., and Jansson, T. (2022). Transcriptomic responses are sex-dependent in the skeletal muscle and liver in offspring of obese mice. *Am. J. Physiol. Endocrinol. Metab.* 323, E336–E353. doi:10.1152/ajpendo.00263.2021

Kim, D. W., Young, S. L., Grattan, D. R., and Jasoni, C. L. (2014). Obesity during pregnancy disrupts placental morphology, cell proliferation, and inflammation in a sex-specific manner across gestation in the mouse. *Biol. Reprod.* 90, 130. doi:10.1095/biolreprod.113.117259

Kim, S. Y., Dietz, P. M., England, L., Morrow, B., and Callaghan, W. M. (2007). Trends in pre-pregnancy obesity in nine states, 1993-2003. *Obes. (Silver Spring)* 15, 986–993. doi:10.1038/oby.2007.621

Kirk, S. L., Samuelsson, A. M., Argenton, M., Dhonye, H., Kalamatianos, T., Poston, L., et al. (2009). Maternal obesity induced by diet in rats permanently influences central processes regulating food intake in offspring. *PLoS One* 4, e5870. doi:10.1371/journal.pone.0005870

Lager, S., Samulesson, A. M., Taylor, P. D., Poston, L., Powell, T. L., and Jansson, T. (2014). Diet-induced obesity in mice reduces placental efficiency and inhibits placental mTOR signaling. *Physiol. Rep.* 2, e00242. doi:10.1002/phy2.242

Larsson, N. G., Wang, J., Wilhelmsson, H., Oldfors, A., Rustin, P., Lewandoski, M., et al. (1998). Mitochondrial transcription factor A is necessary for mtDNA maintenance and embryogenesis in mice. *Nat. Genet.* 18, 231–236. doi:10.1038/ng0398-231

Leon-Garcia, S. M., Roeder, H. A., Nelson, K. K., Liao, X., Pizzo, D. P., Laurent, L. C., et al. (2016). Maternal obesity and sex-specific differences in placental pathology. *Placenta* 38, 33–40. doi:10.1016/j.placenta.2015.12.006

Lettieri Barbato, D., Tatulli, G., Vegliante, R., Cannata, S. M., Bernardini, S., Ciriolo, M. R., et al. (2015). Dietary fat overload reprograms Brown fat mitochondria. *Front. Physiol.* 6, 272. doi:10.3389/fphys.2015.00272

Liang, T., Jinglong, X., Shusheng, D., and Aiyou, W. (2018). Maternal obesity stimulates lipotoxicity and up-regulates inflammatory signaling pathways in the full-term swine placenta. *Anim. Sci. J.* 89, 1310–1322. doi:10.1111/asj.13064

Maragkoudaki, X., Naylor, M., Papacleovoulou, G., Stolarczyk, E., Rees, D., Pombo, J. M., et al. (2020). Supplementation with a prebiotic (polydextrose) in obese mouse pregnancy improves maternal glucose homeostasis and protects against offspring obesity. *Int. J. Obes. (Lond)* 44, 2382–2393. doi:10.1038/s41366-020-00682-5

Marchi, J., Berg, M., Dencker, A., Olander, E. K., and Begley, C. (2015). Risks associated with obesity in pregnancy, for the mother and baby: A systematic review of reviews. *Obes. Rev.* 16, 621–638. doi:10.1111/obr.12288

Maslen, C. L. (2018). Recent advances in placenta-heart interactions. *Front. Physiol.* 9, 735. doi:10.3389/fphys.2018.00735

Mele, J., Muralimanoharan, S., Maloyan, A., and Myatt, L. (2014). Impaired mitochondrial function in human placenta with increased maternal adiposity. *Am. J. Physiol. Endocrinol. Metab.* 307, E419–E425. doi:10.1152/ajpendo.00025.2014

Mitsuya, K., Parker, A. N., Liu, L., Ruan, J., Vissers, M. C. M., and Myatt, L. (2017). Alterations in the placental methylome with maternal obesity and evidence for metabolic regulation. *PLoS One* 12, e0186115. doi:10.1371/journal.pone.0186115

Mittwoch, U. (1993). Blastocysts prepare for the race to be male. *Hum. Reprod.* 8, 1550–1555. doi:10.1093/oxfordjournals.humrep.a137889

Myatt, L., and Maloyan, A. (2016). Obesity and placental function. *Semin. Reprod. Med.* 34, 42–49. doi:10.1055/s-0035-1570027

Nam, J., Greenwald, E., Jack-Roberts, C., Ajeeb, T. T., Malysheva, O. V., Caudill, M. A., et al. (2017). Choline prevents fetal overgrowth and normalizes placental fatty acid and glucose metabolism in a mouse model of maternal obesity. *J. Nutr. Biochem.* 49, 80–88. doi:10.1016/j.jnutbio.2017.08.004

National Center for Health Statistics (2015). The national health interview survey, questionnaires, datasets, and related documentation: 1976-2014 public use data files. Available at: http://www.cdc.gov/nchs/nhis/nhis_questionnaires.htm.

Oben, J. A., Mouralidarane, A., Samuelsson, A. M., Matthews, P. J., Morgan, M. L., McKee, C., et al. (2010). Maternal obesity during pregnancy and lactation programs the development of offspring non-alcoholic fatty liver disease in mice. *J. Hepatol.* 52, 913–920. doi:10.1016/j.jhep.2009.12.042

Ogden, C. L., Carroll, M. D., Kit, B. K., and Flegal, K. M. (2014). Prevalence of childhood and adult obesity in the United States, 2011-2012. *JAMA* 311, 806–814. doi:10.1001/jama.2014.732

Ogden, C. L., Carroll, M. D., Kit, B. K., and Flegal, K. M. (2013). *Prevalence of obesity among adults: United States, 2011-2012.* United States: NCHS Data Brief, 1–8.

Ogden, C. L., Carroll, M. D., Kit, B. K., and Flegal, K. M. (2012). *Prevalence of obesity in the United States, 2009-2010.* United States: NCHS Data Brief, 1–8.

Osei-Kumah, A., Smith, R., Jurisica, I., Caniggia, I., and Clifton, V. L. (2011). Sex-specific differences in placental global gene expression in pregnancies complicated by asthma. *Placenta* 32, 570–578. doi:10.1016/j.placenta.2011.05.005

Park, S., Daewon, H., Seok-Rae, P., Jongdae, S., Sung Ki, L., Hwan-Woo, P., et al. (2020). SIRT1 alleviates LPS-induced IL-1beta production by suppressing NLRP3 inflammasome activation and ROS production in trophoblasts. *Cells* 9, 1. doi:10.3390/cells9030728

Paulsen, M. E., Rosario, F. J., Wesolowski, S. R., Powell, T. L., and Jansson, T. (2019). Normalizing adiponectin levels in obese pregnant mice prevents adverse metabolic outcomes in offspring. *FASEB J.* 33, 2899–2909. doi:10.1096/fj.201801015R

Peacock, J. L., Marston, L., Marlow, N., Calvert, S. A., and Greenough, A. (2012). Neonatal and infant outcome in boys and girls born very prematurely. *Pediatr. Res.* 71, 305–310. doi:10.1038/pr.2011.50

Reynolds, R. M., Allan, K. M., Raja, E. A., Bhattacharya, S., McNeill, G., Hannaford, P. C., et al. (2013). Maternal obesity during pregnancy and premature mortality from cardiovascular event in adult offspring: Follow-up of 1 323 275 person years. *BMJ* 347, f4539. doi:10.1136/bmj.f4539

Roberts, K. A., Riley, S. C., Reynolds, R. M., Barr, S., Evans, M., Statham, A., et al. (2011). Placental structure and inflammation in pregnancies associated with obesity. *Placenta* 32, 247–254. doi:10.1016/j.placenta.2010.12.023

Rosario, F. J., Kanai, Y., Powell, T. L., and Jansson, T. (2015). Increased placental nutrient transport in a novel mouse model of maternal obesity with fetal overgrowth. *Obes. (Silver Spring)* 23, 1663–1670. doi:10.1002/oby.21165

Rosenfeld, C. S. (2021). The placenta-brain-axis. *J. Neurosci. Res.* 99, 271–283. doi:10.1002/jnr.24603

Samuelsson, A. M., Clark, J., Rudyk, O., Shattock, M. J., Bae, S. E., South, T., et al. (2013). Experimental hyperleptinemia in neonatal rats leads to selective leptin responsiveness, hypertension, and altered myocardial function. *Hypertension* 62, 627–633. doi:10.1161/HYPERTENSIONAHA.111.00691

Samuelsson, A. M., Matthews, P. A., Argenton, M., Christie, M. R., McConnell, J. M., Jansen, E. H. J. M., et al. (2008). Diet-induced obesity in female mice leads to offspring hyperphagia, adiposity, hypertension, and insulin resistance: A novel murine model of developmental programming. *Hypertension* 51, 383–392. doi:10.1161/HYPERTENSIONAHA.107.101477

Samuelsson, A. M., Morris, A., Igosheva, N., Kirk, S. L., Pombo, J. M. C., Coen, C. W., et al. (2010). Evidence for sympathetic origins of hypertension in juvenile offspring of obese rats. *Hypertension* 55, 76–82. doi:10.1161/HYPERTENSIONAHA.109.139402

Sanchez, C. E., Barry, C., Sabhlok, A., Russell, K., Majors, A., Kollins, S. H., et al. (2018). Maternal pre-pregnancy obesity and child neurodevelopmental outcomes: A meta-analysis. *Obes. Rev.* 19, 464–484. doi:10.1111/obr.12643

Schmidt, O., Pfanner, N., and Meisinger, C. (2010). Mitochondrial protein import: From proteomics to functional mechanisms. *Nat. Rev. Mol. Cell Biol.* 11, 655–667. doi:10.1038/nrm2959

Shelley, P., Martin-Gronert, M. S., Rowlerson, A., Poston, L., Heales, S. J. R., Hargreaves, I. P., et al. (2009). Altered skeletal muscle insulin signaling and mitochondrial complex II-III linked activity in adult offspring of obese mice. *Am. J. Physiol. Regul. Integr. Comp. Physiol.* 297, R675–R681. doi:10.1152/ajpregu.00146.2009

Summers, S. A., Chaurasia, B., and Holland, W. L. (2019). Metabolic messengers: Ceramides. *Nat. Metab.* 1, 1051–1058. doi:10.1038/s42255-019-0134-8

Supek, F., Bosnjak, M., Skunca, N., and Smuc, T. (2011). REVIGO summarizes and visualizes long lists of gene ontology terms. *PLoS One* 6, e21800. doi:10.1371/journal.pone.0021800

Taylor, P. D., Samuelsson, A. M., and Poston, L. (2014). Maternal obesity and the developmental programming of hypertension: A role for leptin. *Acta Physiol. (Oxf)* 210, 508–523. doi:10.1111/apha.12223

Truett, G. E., Heeger, P., Mynatt, R. L., Truett, A. A., Walker, J. A., and Warman, M. L., Preparation of PCR-quality mouse genomic DNA with hot sodium hydroxide and tris (HotSHOT). *Biotechniques* 29, 52. doi:10.2144/00291bm092000).

Vaughan, O. R., Rosario, F. J., Chan, J., Cox, L. A., Ferchaud-Roucher, V., Zemski-Berry, K. A., et al. (2022). Maternal obesity causes fetal cardiac hypertrophy and alters adult offspring myocardial metabolism in mice. *J. Physiol.* 600, 3169–3191. doi:10.1113/JP282462

Vaughan, O. R., Rosario, F. J., Powell, T. L., and Jansson, T. (2020). Normalisation of circulating adiponectin levels in obese pregnant mice prevents cardiac dysfunction in adult offspring. *Int. J. Obes. (Lond)* 44, 488–499. doi:10.1038/s41366-019-0374-4

Vishnyakova, P. A., Volodina, M. A., Tarasova, N. V., Marey, M. V., Tsvirkun, D. V., Vavina, O. V., et al. (2016). Mitochondrial role in adaptive response to stress conditions in preeclampsia. *Sci. Rep.* 6, 32410. doi:10.1038/srep32410

Wallace, J. M., Horgan, G. W., and Bhattacharya, S. (2012). Placental weight and efficiency in relation to maternal body mass index and the risk of pregnancy complications in women delivering singleton babies. *Placenta* 33, 611–618. doi:10.1016/j.placenta.2012.05.006

Wang, X., Liang, L., Junfen, F. U., and Lizhong, D. U. (2007). Metabolic syndrome in obese children born large for gestational age. *Indian J. Pediatr.* 74, 561–565. doi:10.1007/s12098-007-0108-9

Wang, Y., Bucher, M., and Myatt, L. (2019). Use of glucose, glutamine, and fatty acids for trophoblast respiration in lean women, women with obesity, and women with gestational diabetes. *J. Clin. Endocrinol. Metab.* 104, 4178–4187. doi:10.1210/jc.2019-00166

Yamamoto, H., Itoh, N., Kawano, S., Yatsukawa, Y. i., Momose, T., Makio, T., et al. (2011). Dual role of the receptor Tom20 in specificity and efficiency of protein import into mitochondria. *Proc. Natl. Acad. Sci. U. S. A.* 108, 91–96. doi:10.1073/pnas.1014918108

Yang, Y., Cheng, J. Z., Singhal, S. S., Saini, M., Pandya, U., Awasthi, S., et al. (2001). Role of glutathione S-transferases in protection against lipid peroxidation. Overexpression of hGSTA2-2 in K562 cells protects against hydrogen peroxide-induced apoptosis and inhibits JNK and caspase 3 activation. *J. Biol. Chem.* 276, 19220–19230. doi:10.1074/jbc.M100551200

Yu, Z., Han, S., Zhu, J., Sun, X., Ji, C., and Guo, X. (2013). Pre-pregnancy body mass index in relation to infant birth weight and offspring overweight/obesity: A systematic review and meta-analysis. *PLoS One* 8, e61627. doi:10.1371/journal.pone.0061627

Zhang, Q., Xiao, X., Zheng, J., Li, M., Yu, M., Ping, F., et al. (2021). Maternal high-fat diet disturbs the DNA methylation profile in the Brown adipose tissue of offspring mice. *Front. Endocrinol. (Lausanne)* 12, 705827. doi:10.3389/fendo.2021.705827

Zhu, C., Han, T. L., Zhao, Y., Zhou, X., Mao, X., Qi, H., et al. (2018). A mouse model of pre-pregnancy maternal obesity combined with offspring exposure to a high-fat diet resulted in cognitive impairment in male offspring. *Exp. Cell Res.* 368, 159–166. doi:10.1016/j.yexcr.2018.04.019

frontiers | Frontiers in Cell and Developmental Biology

TYPE Original Research
PUBLISHED 27 June 2023
DOI 10.3389/fcell.2023.1160154

OPEN ACCESS

EDITED BY
Rafael A. Fissore,
University of Massachusetts Amherst, United States

REVIEWED BY
Vanina Gabriela Da Ros,
CONICET Institute of Biology and Experimental Medicine (IBYME), Argentina
Maximiliano Tourmente,
Universidad Nacional de Córdoba, Argentina

*CORRESPONDENCE
Lonny R. Levin,
llevin@med.cornell.edu

†PRESENT ADDRESS
Melanie Balbach,
Department of Biochemistry and Molecular Biology, Michigan State University, East Lansing, MI, United States

RECEIVED 06 February 2023
ACCEPTED 12 June 2023
PUBLISHED 27 June 2023

CITATION
Balbach M, Ghanem L, Violante S, Kyaw A, Romarowski A, Cross JR, Visconti PE, Levin LR and Buck J (2023), Capacitation induces changes in metabolic pathways supporting motility of epididymal and ejaculated sperm.
Front. Cell Dev. Biol. 11:1160154.
doi: 10.3389/fcell.2023.1160154

Capacitation induces changes in metabolic pathways supporting motility of epididymal and ejaculated sperm

Melanie Balbach[1†], Lubna Ghanem[1], Sara Violante[2], Aye Kyaw[2], Ana Romarowski[3], Justin R. Cross[2], Pablo E. Visconti[3], Lonny R. Levin[1*] and Jochen Buck[1]

[1]Department of Pharmacology, Weill Cornell Medicine, New York, NY, United States, [2]Donald B. and Catherine C. Marron Cancer Metabolism Center, Memorial Sloan Kettering Cancer Center, New York, NY, United States, [3]Department of Veterinary and Animal Science, Integrated Sciences Building, University of Massachusetts, Amherst, MA, United States

Mammalian sperm require sufficient energy to support motility and capacitation for successful fertilization. Previous studies cataloging the changes to metabolism in sperm explored ejaculated human sperm or dormant mouse sperm surgically extracted from the cauda epididymis. Due to the differences in methods of collection, it remains unclear whether any observed differences between mouse and human sperm represent species differences or reflect the distinct maturation states of the sperm under study. Here we compare the metabolic changes during capacitation of epididymal *versus* ejaculated mouse sperm and relate these changes to ejaculated human sperm. Using extracellular flux analysis and targeted metabolic profiling, we show that capacitation-induced changes lead to increased flux through both glycolysis and oxidative phosphorylation in mouse and human sperm. Ejaculation leads to greater flexibility in the ability to use different carbon sources. While epididymal sperm are dependent upon glucose, ejaculated mouse and human sperm gain the ability to also leverage non-glycolytic energy sources such as pyruvate and citrate.

KEYWORDS

capacitation, sperm maturation, hyperactivation, metabolic profiling, extracellular flux analysis

Introduction

Mammalian sperm leaving the male reproductive tract upon ejaculation are morphologically mature but functionally immature and cannot fertilize the oocyte. During ejaculation, sperm mix with seminal and prostatic fluids containing elevated levels of bicarbonate. Bicarbonate stimulates Soluble Adenylyl Cyclase (sAC; ADCY10), which activates sperm motility and initiates the maturation processes required for successful fertilization (i.e., capacitation) (Chang, 1951; Austin and Bishop, 1958). The early molecular changes during capacitation, including increased levels of intracellular cAMP and calcium (Gervasi and Visconti, 2016; Balbach et al., 2018), are followed by functional changes. Freshly ejaculated sperm exhibit a low-amplitude and symmetrical flagellar beat, resulting in a progressive movement called activated motility (Publicover et al., 2007; Dey et al., 2019). During capacitation, sperm modify their motility pattern into an asymmetric flagellar beat, representing a swimming mode termed hyperactivation (Yanagimachi, 1970; Ishijima et al.,

2002). Hyperactivation is a fast whip-like movement of the flagellum with an irregular trajectory, which generates the propulsive forces that are needed for sperm to reach the oocyte and overcome its vestments; i.e., the cumulus oophorous and the zona pellucida (Ho and Suarez, 2001; Suarez, 2008). Hyperactivation may also facilitate penetration of the mucus in the oviductal lumen and the release of sperm from the oviductal storage reservoir.

Sperm motility is directly dependent upon the availability of chemical energy obtained through ATP hydrolysis and accounts for the majority of ATP consumed (Bohnensack and Halangk, 1986). Thus, mammalian sperm are dependent on sufficient energy production to maintain flagellar movement within the female genital tract and to complete their journey to the oocyte (reviewed in (Visconti, 2012; du Plessis et al., 2015)). Mammalian sperm possess the metabolic machinery to generate ATP and other compounds supplying chemical energy via both glycolysis and the mitochondrial Krebs cycle and oxidative phosphorylation (oxphos). Metabolic studies demonstrated that externally supplied glycolytic substrates are sufficient to support *in vitro* capacitation, acrosomal exocytosis, progressive motility, and hyperactivation of sperm from both men and mice (Peterson and Freund, 1970; Hoppe, 1976; Fraser and Quinn, 1981; Rogers and Perreault, 1990; Williams and Ford, 2001; Mukai and Okuno, 2004; Goodson et al., 2012). However, it remains unclear how each species specifically utilizes its metabolic machinery to generate ATP for each of these energy-demanding processes. For example, while mouse sperm ceased moving after 30–40 min in media without an exogenous energy source (Navarrete et al., 2019), human sperm remained motile for at least 24 h in the absence of exogenous nutrients (Suter et al., 1979; Ford and Harrison, 1981; Navarrete et al., 2019; Carrageta et al., 2020; Marín-Briggiler et al., 2021), suggesting they possess stored energy reserves. Comparative studies also identified a difference between mouse and human sperm's ability to utilize exogenous pyruvate. While mouse sperm seemed surprisingly unaffected by pyruvate supplementation (Balbach et al., 2020a), addition of pyruvate to glucose-containing media enhances progressive motility and hyperactivation of human sperm (Hereng et al., 2011).

Metabolic discrepancies between mouse and human sperm may reflect species-specific metabolic requirements or regulation. Alternatively, these differences may derive from the experimental conditions utilized. Previous experiments studied human sperm purified from ejaculated semen. The fluid portion of semen, seminal plasma, contains high amounts of fructose and citrate, in addition to glucose, lactate, and free amino acids, and the bicarbonate which initiates the molecular changes of capacitation (Owen and Katz, 2005). Human sperm metabolism was studied in sperm separated from seminal plasma prior to experiments; however, these studies assessed metabolism after human sperm were exposed to these metabolites, and after the bicarbonate in seminal plasma initiated capacitation. In contrast, mouse sperm metabolic experiments have been performed on sperm surgically extracted from the cauda epididymis, which are stored in a dormant, inactivated state, exposed only to the purification media, right until the start of the experiment. These different metabolic and activation states complicate interpretations of experiments comparing dormant epididymal mouse sperm with ejaculated human sperm. Ejaculated mouse sperm can be isolated from the female genital tract following copulation (YANAGIMACHI and CHANG, 1963; Whittingham, 1968; King et al., 1994). Like ejaculated human sperm, mouse sperm recovered from the female genital tract were exposed to the metabolites and activating bicarbonate levels in semen. Ejaculated mouse sperm isolated from the female tract proved informative in a recent study of the sperm Ca^{2+} channel CatSper. Activation of CatSper had been thought to differ between mouse and human; however, by comparing epididymal *versus* ejaculated mouse with human sperm, CatSper activation was shown to be conserved between mouse and human sperm, and was dependent on the sperm maturation state (Ferreira et al., 2021a). These findings motivate a detailed analysis of the metabolic pathways utilized during capacitation in human sperm compared to mouse sperm before and after ejaculation.

We recently developed a minimally invasive technique using an extracellular flux analyzer to observe real-time changes in sperm metabolism during capacitation (Balbach et al., 2020b). Focusing exclusively on recently dormant epididymal mouse sperm, we showed that both glycolysis and oxphos increase during capacitation (Balbach et al., 2020a). The increase in both metabolic pathways was dependent on glycolytic substrates, and the increase in oxphos was dependent on glycolysis (Balbach et al., 2020a), providing evidence for a direct link between oxphos and glycolysis in sperm. Here we extend these results by using extracellular flux analysis and targeted metabolic profiling to compare the metabolic requirements for capacitation between ejaculated human sperm, epidydimal mouse sperm and ejaculated mouse sperm recovered from the female genital tract. We find that among the metabolic changes during ejaculation, sperm gain greater flexibility in utilizing diverse carbon sources.

Results

Epididymal mouse sperm, uterine mouse sperm and ejaculated human sperm rely on both glycolysis and oxphos to generate chemical energy

Motility is the major consumer of ATP in activated sperm (Bohnensack and Halangk, 1986). We used computer-assisted sperm analysis (CASA) to track, quantify and compare motility of *Mus musculus* mouse sperm isolated from the cauda epididymis (epidydimal mouse sperm), mouse sperm ejaculated into the female uterus (uterine mouse sperm), and ejaculated human sperm incubated in non-capacitating (mouse: TYH, human: HTF) and conditions which induce molecular hallmarks of capacitation (i.e., elevated cAMP, increased progressive and hyperactivated motility) (mouse: TYH + BSA + HCO_3^-, human: HTF + HSA + HCO_3^-). Mammalian sperm possess the molecular machinery to generate ATP via glycolysis and oxidative phosphorylation (oxphos). By inhibiting glycolysis with 2-deoxyglucose (2-DG) or blocking the electron transport chain with rotenone (Rot) and antimycin A (AntA), we were able to compare the relative contributions of glycolysis and oxphos to progressive and hyperactive motility. In all sperm samples, the percentage of hyperactivated sperm increased after exposure to media which

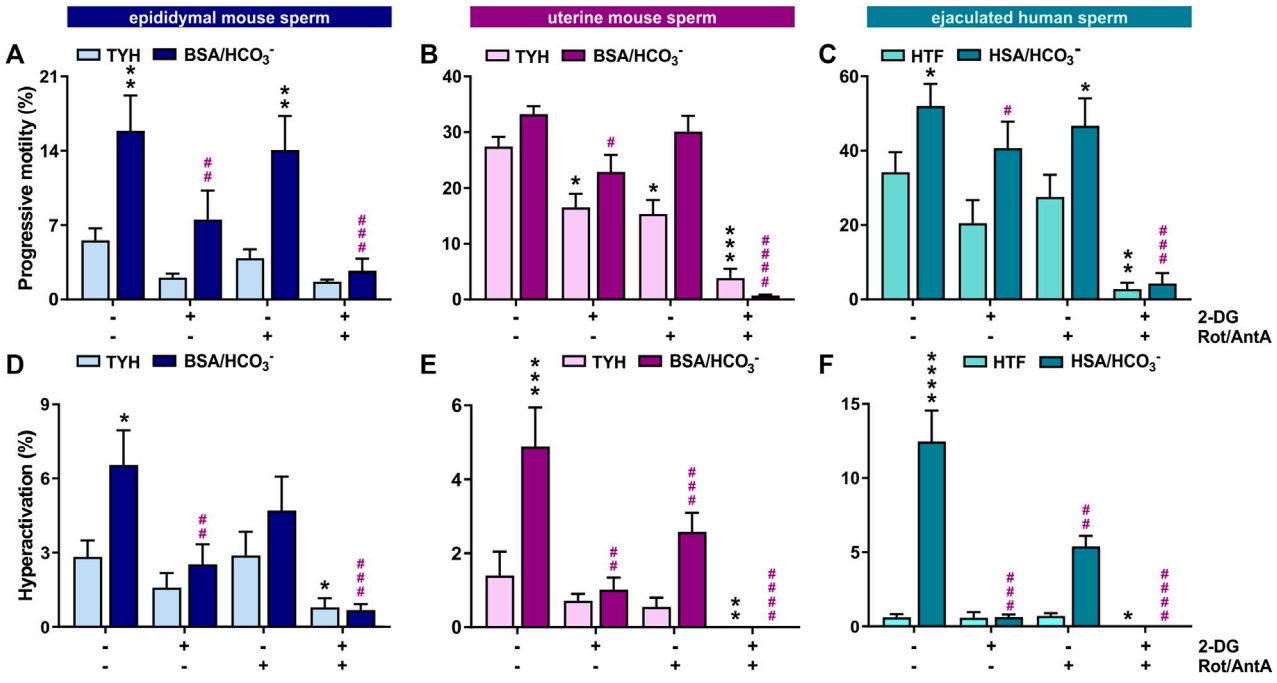

FIGURE 1
In mouse and human sperm, hyperactivated motility is dependent on glycolysis and oxphos **(A–C)** Percentage of progressively motile **(A)** epididymal mouse sperm, **(B)** uterine mouse sperm, or **(C)** ejaculated human sperm incubated for 30 min (mouse) or 60 min (human) in non-capacitating (mouse sperm: TYH, human sperm: HTF) or capacitating media (mouse sperm: TYH + BSA + HCO_3^-, human sperm: HTF + HSA + HCO_3^-) with glucose (mouse) or glucose/pyruvate (human) in the presence or absence of 2-DG (mouse: 56 mM, human: 28 mM) and/or Rot/AntA (0.5 μM); mean +SEM (n ≥ 7). **(D–F)** Percentage of hyperactivated **(D)** epididymal mouse sperm, **(E)** uterine mouse sperm, or **(F)** ejaculated human sperm incubated for 30 min (mouse) or 60 min (human) in non-capacitating or capacitating media in the presence or absence of 2-DG or AntA/Rot; mean +SEM (n ≥ 7). Differences between conditions were analyzed using one-way ANOVA compared to the DMSO-treated non-capacitated (black asterisk) or capacitated (purple pound sign) control,*$p < 0.05$, **$p < 0.01$, ***$p < 0.001$, ****$p < 0.0001$.

induces capacitation hallmarks containing glucose (mouse sperm) and glucose/pyruvate (human sperm) as energy source. The percentage of progressively motile sperm increased in epididymal mouse and ejaculated human sperm in capacitating media. The level of progressively motile sperm in uterine mouse sperm was elevated in non-capacitating conditions (Figures 1A, B); this difference may represent a physiological change induced by motility-enhancing factors in the seminal plasma or female genital tract, and/or it may be due to selection of motile sperm during ejaculation. Human sperm exhibited the highest percentage of progressively motile sperm (Figure 1C). Whether this difference reflects a true distinction between the species is unclear because the progressive motility of C57Bl/6 *M. musculus* sperm is low relative to other mouse species (Odet et al., 2008; Park et al., 2012; Fan et al., 2015; Tourmente et al., 2015) and motile human sperm are enriched during purification from semen. Inhibiting glycolysis greatly diminished the percentage of progressively motile sperm in capacitating conditions in all three sperm samples, consistent with previous studies of epididymal mouse sperm (Mukai and Okuno, 2004; Goodson et al., 2012). In all three samples, in capacitating conditions motility was unaffected when oxphos was blocked, suggesting that oxphos is not essential for generating the ATP which supports motility; however, when both glycolysis and oxphos were inhibited, progressive motility was reduced to nearly zero. This indicates that the ATP generated via oxphos can support at least some progressive motility, particularly when glycolysis is inactive.

Hyperactivated motility is the asymmetric, more powerful flagellar beating that increases energy demand. In all three sperm samples, the capacitation-induced stimulation of hyperactivated motility was entirely dependent upon glycolysis and partially dependent upon oxphos (Figures 1D–F), and as expected, hyperactivated motility was completely absent when both pathways were blocked. Thus, both glycolysis and oxphos can contribute ATP to support motility, and there appears to be synergy between the two pathways in sperm. Particularly during hyperactivated motility with its high energy demand, chemical energy is supplied by the combination of glycolysis and oxphos.

Glycolysis and oxidative phosphorylation increase during capacitation of epididymal mouse sperm, uterine mouse sperm and ejaculated human sperm

We used an extracellular flux analyzer to compare how glycolysis and oxphos change during capacitation in epididymal and uterine mouse sperm as well as ejaculated human sperm. The Seahorse XFe96 extracellular flux analyzer detects the extracellular acidification rate (ECAR), i.e., H^+ extruded into the assay media

10.3389/fcell.2023.1160154

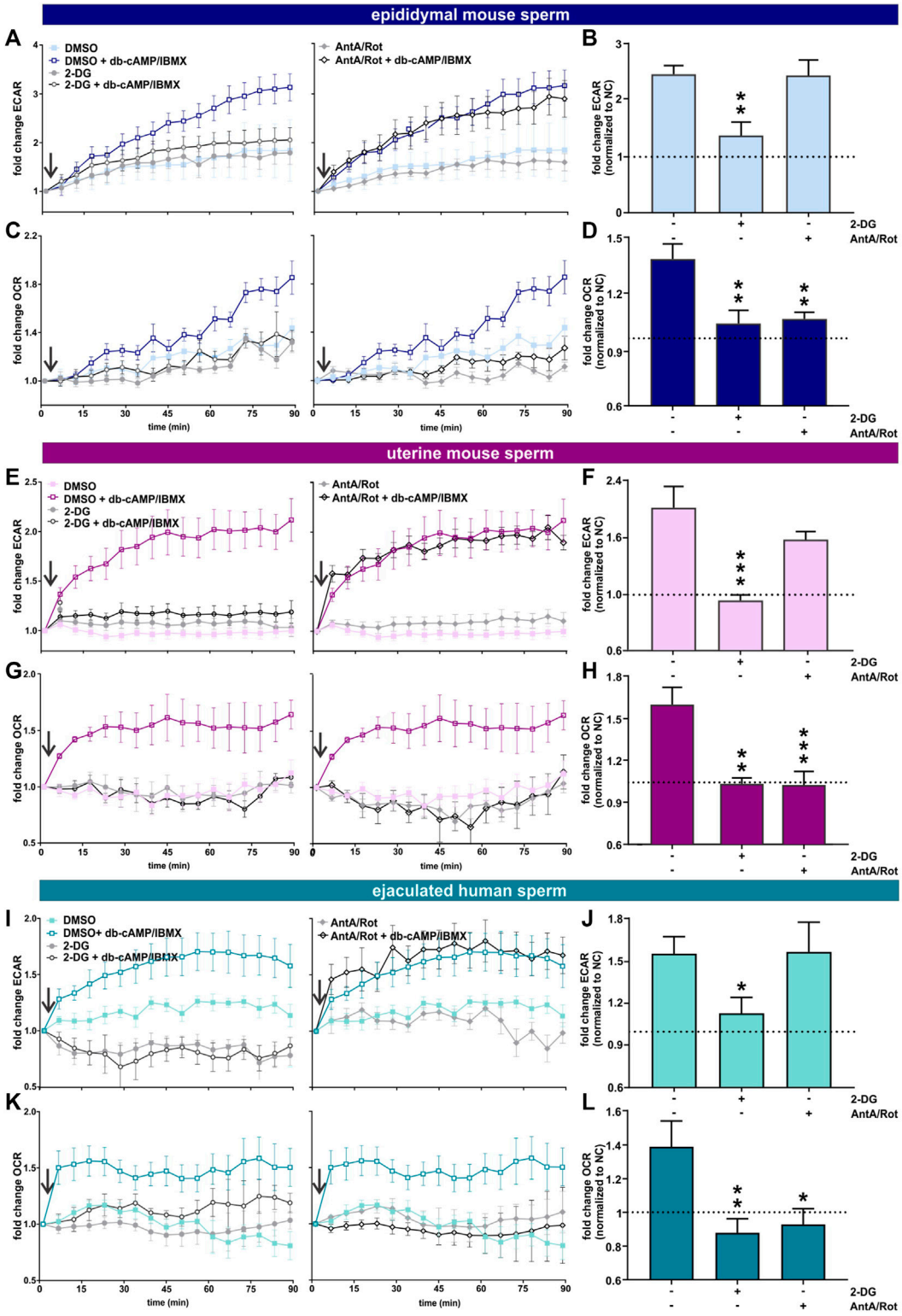

FIGURE 2
Capacitation of epididymal and ejaculated mouse and human sperm is accompanied by increased glycolysis and oxphos **(A, E, I)** Normalized ECAR of **(A)** epididymal mouse sperm, **(E)** uterine mouse sperm, or **(I)** ejaculated human sperm in non-capacitating or capacitating (db-cAMP + IBMX) media in the absence (DMSO) or presence of (left) 2-DG or (right) AntA/Rot; mean ± SEM (n ≥ 6). **(B,F, J)** Change in ECAR of **(B)** epididymal mouse sperm, **(F)** uterine mouse sperm, or **(J)** ejaculated human sperm in capacitating media relative to control in non-capacitating media in the absence or presence of 2-DG or AntA/Rot. The average of the last three data points was respectively used to calculate the fold change. **(C,G, K)** Normalized OCR of **(C)** epididymal mouse sperm, **(G)** uterine mouse sperm, or **(K)** ejaculated human sperm in non-capacitating or capacitating (db-cAMP + IBMX) media in the absence (DMSO) or presence of (left) 2-DG or (right) Rot/AntA; mean ± SEM (n ≥ 6) **(D, H, L)** Change in OCR of **(D)** epididymal mouse sperm, **(H)** uterine mouse

(*Continued*)

FIGURE 2 (Continued)
sperm, or **(L)** ejaculated human sperm in capacitating media relative to control in non-capacitating media in the absence or presence of 2-DG or AntA/Rot; mean +SEM ($n \geq 6$). The average of the last three data points was respectively used to calculate the fold change. Differences between conditions were analyzed using one-way ANOVA compared to the DMSO-treated capacitated control **(B, D, F, H, J, L)**,*$p < 0.05$, **$p < 0.01$, ***$p < 0.001$. The arrow indicates addition of 5 mM db-cAMP/500 μM IBMX.

coupled to export of glycolysis-generated lactate via proton-driven monocarboxylate transporters (Brauchi et al., 2005)' (Lee et al., 2014), to reflect changes in glycolysis. At the same time, it measures the oxygen consumption rate (OCR) to quantitate the uptake of O_2 used by oxphos (Balbach et al., 2020b). Because the system's sensitivity to pH changes prevents inducing capacitation via the physiological stimulant bicarbonate, we capacitated sperm by adding the cell-permeable cAMP analog db-cAMP together with the broad-specificity phosphodiesterase inhibitor IBMX. This combination initiates capacitation-induced changes, specifically the progesterone-induced acrosome reaction, as effectively as addition of HCO_3^- to both mouse (Balbach et al., 2020a) and human sperm (Supplementary Figure S1).

As shown previously (Tourmente et al., 2015; Balbach et al., 2020a), in exogenously-supplied glucose in non-capacitating conditions, epididymal mouse sperm exhibited a gradual increase in ECAR and OCR over time, possibly reflecting activation of their metabolic machinery. For uterine mouse sperm and ejaculated human sperm in non-capacitating conditions ECAR and OCR remained mostly stable over time. In all sperm samples, ECAR and OCR increased when capacitation was mimicked by exposure to cAMP (Figure 2), and the kinetics of the cAMP-induced changes differed depending upon the activation state of the sperm sample. Epididymal mouse sperm, which were never previously exposed to capacitating conditions, exhibited the strongest cAMP-induced stimulation in ECAR and OCR with a steady increase over time that did not saturate for the duration of the measurement (Figures 2A, C). In contrast, ECAR increased with a faster kinetic and saturated 60 min post injection of db-cAMP/IBMX in both uterine mouse sperm and ejaculated human sperm (Figures 2E, I). For OCR, in ejaculated sperm, we detected a strong initial increase post exposure to cAMP that saturated within 10 min (ejaculated human sperm) and 20 min (uterine mouse sperm) (Figures 2C, G, K). The faster ECAR and OCR kinetics suggest uterine mouse sperm and ejaculated human sperm start at a different metabolic state than epididymal mouse sperm when placed into the extracellular flux analyzer. Thus, while uterine mouse and ejaculated human sperm already had their metabolic pathways stimulated during ejaculation, epididymal mouse sperm start from a lower baseline of metabolic activity (Supplementary Table S1); hence, their activation kinetics is slower. Epididymal mouse sperm experience the largest capacitation-induced response presumably because these sperm were, until recently, stored in a dormant state with little metabolic activity.

In all sperm samples, the cAMP-induced changes in ECAR were prevented when glycolysis was blocked by 2-DG and unaffected by Rot/AntA (Figures 2A, B, E, F, I, J). Thus, the capacitation-induced changes in ECAR are driven by glycolysis with little contribution from oxphos. As expected, inclusion of Rot/AntA blocked changes in OCR in epididymal and uterine mouse sperm and ejaculated human sperm (Figures 2C, D, G, H, K, L), confirming that capacitation-induced increases in OCR are due to oxphos. In all three sperm samples, in the presence of a glycolytic energy source, changes in OCR were blocked by 2-DG, suggesting, as reported previously for epididymal mouse sperm (Balbach et al., 2020a), that the capacitation-induced increase in oxphos is fueled by glycolytic activity. This dependence establishes a functional link between these pathways in both human and mouse sperm before and after ejaculation. In summary, starting with ejaculation and continuing through capacitation, human and mouse sperm stimulate glycolytic activity leading to a concomitant increase in oxygen consumption. Depending upon the amount of uncoupling present in sperm mitochondria (Ferramosca et al., 2013; Carrageta et al., 2023), this increased oxygen consumption will translate into increased oxphos to support the greater energy demands of capacitating sperm.

Metabolite profiling confirms increased rates of glycolysis and oxphos during capacitation

To complement the real-time measurements via extracellular flux analysis, we utilized mass spectrometry and metabolic profiling to understand how individual endogenous metabolites change upon exposure to capacitating conditions. Unsupervised hierarchical clustering of metabolites extracted with methanol, analyzed via LC-MS/MS and confirmed using biochemical standards (all metabolites detected are listed in Tab. 1–6) revealed distinct patterns for epididymal and uterine mouse sperm and ejaculated human sperm incubated in non-capacitating and capacitating conditions for 90 min in the presence of glucose (Figures 3A–C).

Initially, we explored the levels of two intracellular metabolites predicted to change in capacitating sperm incubated in glucose and glucose/pyruvate. As expected, levels of intracellular cAMP, the earliest signaling pathway activated in capacitation (Wennemuth et al., 2003; Buffone et al., 2014; Balbach et al., 2018), were elevated in all sperm samples after exposure to capacitating conditions (Figures 3D–F, Supplementary Figures S2A, D, G). We previously showed that capacitating conditions stimulate ATP generation due to increased glucose uptake (Hidalgo et al., 2020) and utilization (Balbach et al., 2020a). However, ATP levels were lower in sperm incubated in capacitating conditions compared to the levels in sperm maintained in non-capacitating conditions (Figures 3D–F, Supplementary Figures S2A, D, G). We independently confirmed this change in ATP by directly measuring intracellular ATP over time. Consistent with metabolite profiling, ATP levels decreased in all sperm samples incubated in capacitating conditions, and as expected, ATP levels were dependent upon glycolytic activity; inhibiting glycolysis with 2-DG rapidly reduced ATP levels in both non-capacitating and capacitating conditions (Figures 4A–F). These data illustrate the important concept that metabolite levels measured by profiling, including cAMP and ATP, reflect a balance between production and consumption, and changes in metabolism during capacitation can result in increased or decreased metabolite levels. Thus, the reduced ATP levels in

10.3389/fcell.2023.1160154

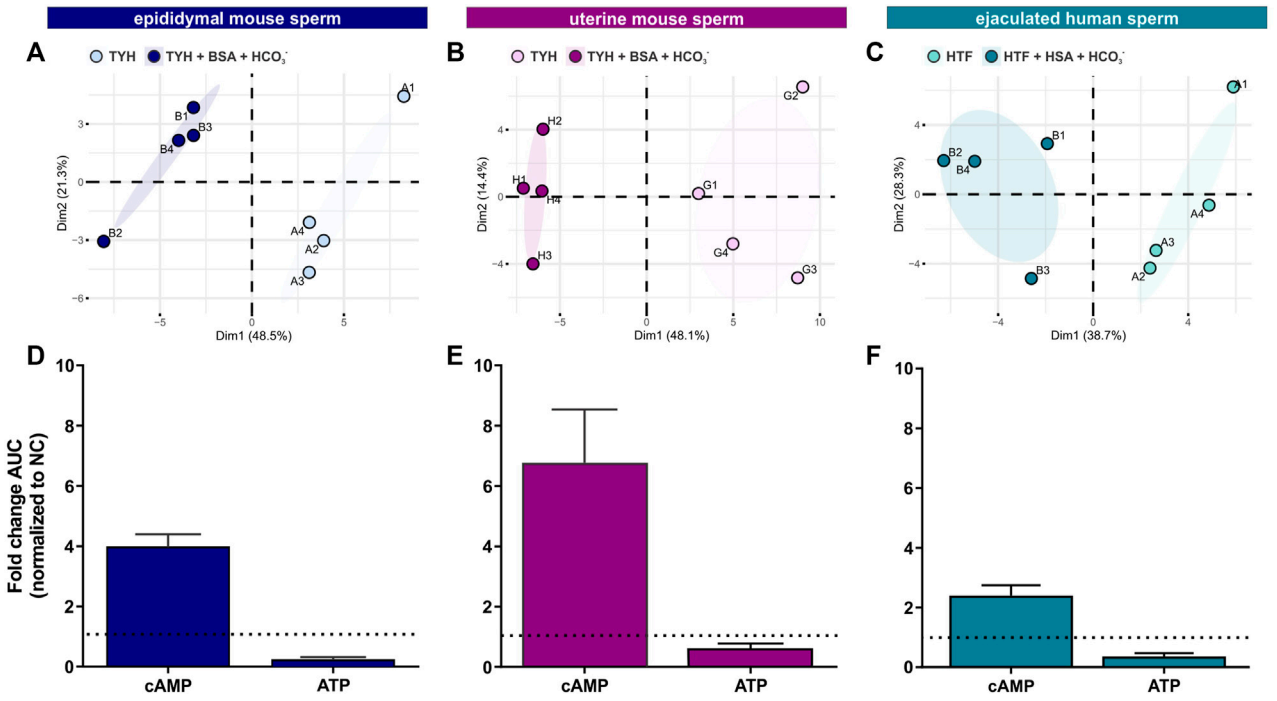

FIGURE 3
Sperm intracellular metabolite levels during capacitation are a product of production and consumption **(A–C)** Principal component analysis (PCA) plots of metabolites isolated from **(A)** epididymal mouse sperm (PC1 score p = ***, PC2 score p = n.s.), **(B)** uterine mouse sperm (PC1 score p = **, PC2 score p = n.s.), or **(C)** ejaculated human sperm (PC1 score p = **, PC2 score p = n.s.) incubated for 90 min in non-capacitating or capacitating media. To highlight the different cluster, sperm incubated in non-capacitating and capacitating conditions are surrounded by eclipses; representative plots are shown **(D–F)** Nucleotides detected in **(D)** epididymal mouse sperm, **(E)** uterine mouse sperm, or **(F)** ejaculated human sperm incubated for 90 min in capacitating conditions in glucose, fold change of integrated area under the peak (AUC) normalized to the non-capacitated control; mean +SEM (n = 3). Differences between conditions **(A–C)** were analyzed using two-tailed, paired *t*-test, $^{**}p < 0.01$, $^{***}p < 0.001$, n. s = not significant.

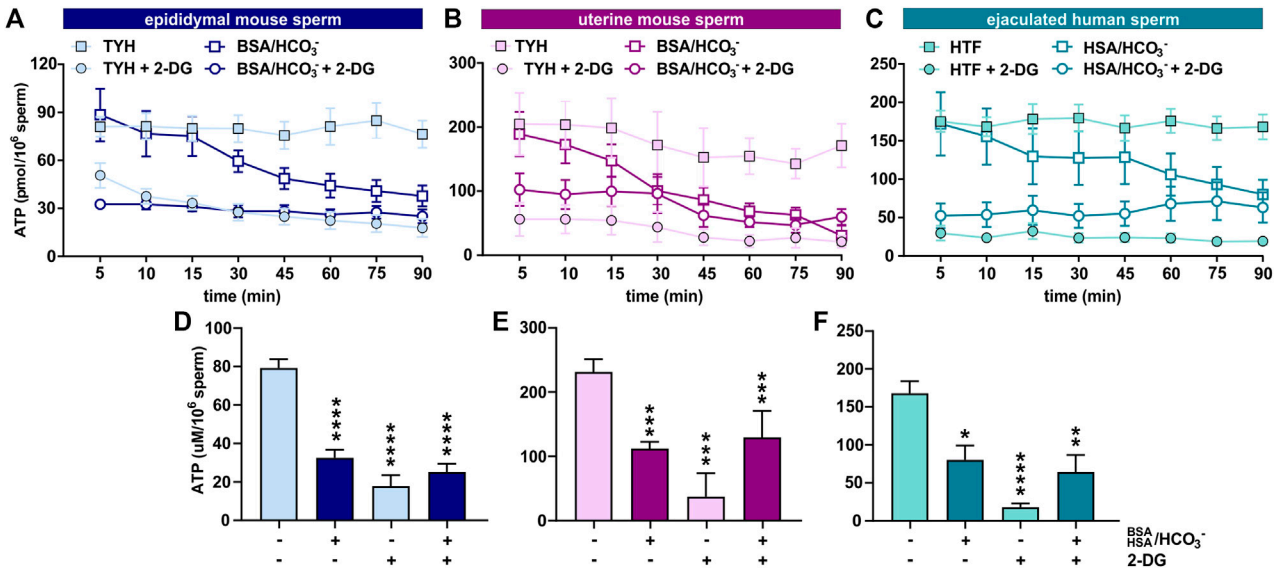

FIGURE 4
Sperm intracellular ATP levels decrease during capacitation **(A–C)** Intracellular ATP levels in **(A)** epididymal mouse sperm, **(B)** uterine mouse sperm, or **(C)** ejaculated human sperm at different time points during incubation in non-capacitating or capacitating media in the presence or absence of 2-DG; mean ± SEM (n ≥ 5) **(D–F)** Intracellular ATP levels in **(D)** epididymal mouse sperm, **(E)** uterine mouse sperm, or **(F)** ejaculated human sperm incubated in non-capacitating or capacitating media for 90 min in the presence or absence of 2-DG; mean ± SEM (n ≥ 5). Differences between conditions **(D–F)** were analyzed using one-way ANOVA compared to the non-capacitated control in DMSO, $^{*}p < 0.05$, $^{**}p < 0.01$, $^{***}p < 0.001$, $^{****}p < 0.0001$.

10.3389/fcell.2023.1160154

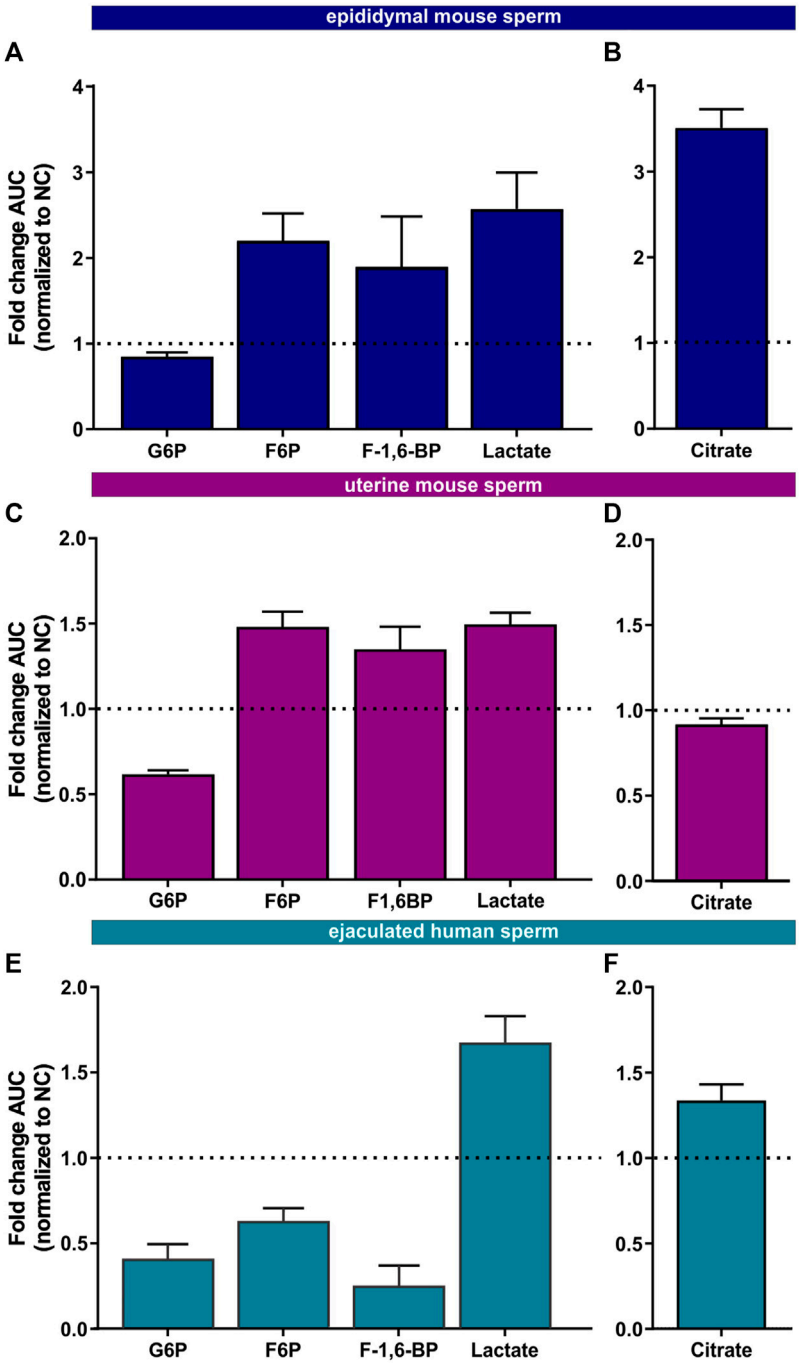

FIGURE 5
Metabolic profiling of mammalian sperm in non-capacitated and capacitating conditions **(A,C, E)** Glycolytic metabolites detected in **(A)** epididymal mouse sperm, **(C)** uterine mouse sperm, or **(E)** ejaculated human sperm incubated for 90 min in capacitating conditions in glucose, fold change AUC normalized to the non-capacitated control; mean +SEM (n = 3) **(B, D, F)** Citrate detected in **(B)** epididymal mouse sperm, **(D)** uterine mouse sperm, or **(F)** ejaculated human sperm incubated for 90 min in capacitating conditions, fold change AUC normalized to the non-capacitated control; mean +SEM (n = 3). G6P = glycerol-6-phosphate, F6P = fructose-6-phosphate, F-1,6-BP = fructose 1,6-bisphosphate.

capacitating sperm, despite increased production, reveal that the rate of ATP consumption during capacitation exceeds the stimulated production resulting in a lower ATP equilibrium. These data confirm that this metabolic profiling methodology is sufficiently stringent and sensitive to distinguish non-capacitating from capacitating sperm. To independently confirm the capacitation-induced changes in the rates of glycolysis and oxphos predicted by extracellular flux analysis, we focused on individual metabolites involved in glycolysis and the TCA cycle. Levels of the glycolytic intermediate glucose-6-phosphate in both glucose (Figures 5A, C, E) and glucose/pyruvate (Supplementary Figures S2B, E, H) were reduced following exposure to capacitating conditions in human

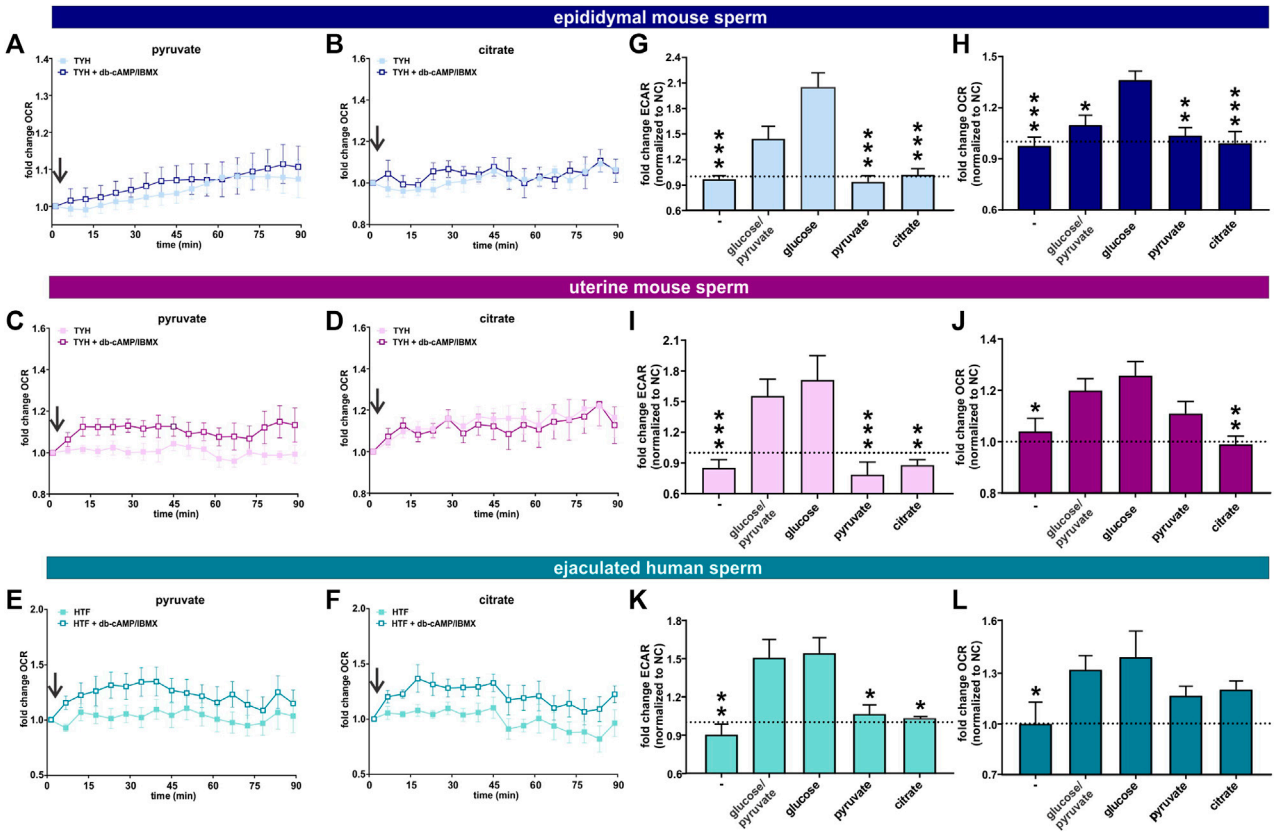

FIGURE 6
Post ejaculation, non-glycolytic substrates can support the capacitation-induced changes in metabolism **(A, B)** Normalized OCR of epididymal mouse sperm in non-capacitating or capacitating media with **(A)** pyruvate and **(B)** citrate; mean ± SEM (n ≥ 7) **(C, D)** Normalized OCR of uterine mouse sperm in non-capacitating or capacitating media with **(C)** pyruvate and **(D)** citrate; mean ± SEM (n ≥ 7) **(E, F)** Normalized OCR of ejaculated human sperm in non-capacitating or capacitating media with **(E)** pyruvate and **(F)** citrate; mean ± SEM (n ≥ 7). Arrow indicates addition of 5 mM db-cAMP/500 μM IBMX. **(G, I, K)** Change in ECAR of capacitated **(G)** epididymal mouse sperm, **(I)** uterine mouse sperm, or **(K)** ejaculated human sperm relative to non-capacitated control in the presence of no exogenous energy source (–), glucose/pyruvate, glucose, pyruvate, or citrate; mean +SEM (n ≥ 7) **(H, J, L)** Change in OCR of capacitated **(H)** epididymal mouse sperm **(J)** uterine mouse sperm, or **(L)** ejaculated human sperm relative to non-capacitated control in the presence of no exogenous energy source (–), glucose/pyruvate, glucose, pyruvate, or citrate; mean +SEM (n ≥ 7). The average of the last three data points was respectively used to calculate the fold change. Differences between conditions were analyzed using one-way ANOVA compared to sperm incubated in glucose **(G–L)**,*$p < 0.05$, **$p < 0.01$, ***$p < 0.001$. The arrow indicates addition of 5 mM db-cAMP/500 μM IBMX.

sperm and in mouse sperm before and after ejaculation. Similarly, and as previously reported in epididymal mouse sperm and in line with extracellular flux analysis (Calvert et al., 2019; Carrageta et al., 2020), all sperm samples incubated in capacitating conditions showed increased levels of lactate, the product of anaerobic glycolysis. Levels of other glycolytic intermediates also changed following capacitation, confirming that capacitation affects glycolytic rates, but there were potentially interesting species-specific differences. In human sperm, in both glucose and glucose/pyruvate fructose-6-phosphate and fructose-1,6-bisphosphate levels were decreased following capacitation, while these metabolites were elevated following capacitation in glucose in both epididymal and uterine mouse sperm. Interestingly, in glucose/pyruvate fructose-1,6-bisphosphate levels were decreased in epididymal and uterine mouse sperm. Investigating these potentially revealing species-specific differences and differences between glucose and glucose/pyruvate will require metabolic tracing studies monitoring flux of exogenously supplied glucose labeled with stable isotopes. Regarding lower glycolysis, capacitated epididymal and uterine mouse sperm had decreased levels of 2-phosphoglycerate and phosphoenolpyruvate (Supplementary Tables S1, S2, S4, S5). These metabolites were below the limit of detection in human sperm (Supplementary Tables S3, S6).

We also found changes in Krebs cycle metabolites in all three sperm samples in both glucose and glucose/pyruvate (Figures 5B, D, F, Supplementary Figures S2C, F, I) confirming the real-time observation that oxphos increases during capacitation. Human sperm accumulate citrate during capacitation. For mouse sperm, we identified a difference in Krebs cycle metabolism based upon activation state when incubated in glucose. While epididymal mouse sperm accumulate citrate during capacitation, citrate levels decreased following capacitation of uterine mouse sperm. However, when pyruvate was added to glucose, citrate accumulated in uterine sperm. These data suggest that the citrate equilibrium in uterine mouse sperm is altered when sperm additionally metabolize pyruvate.

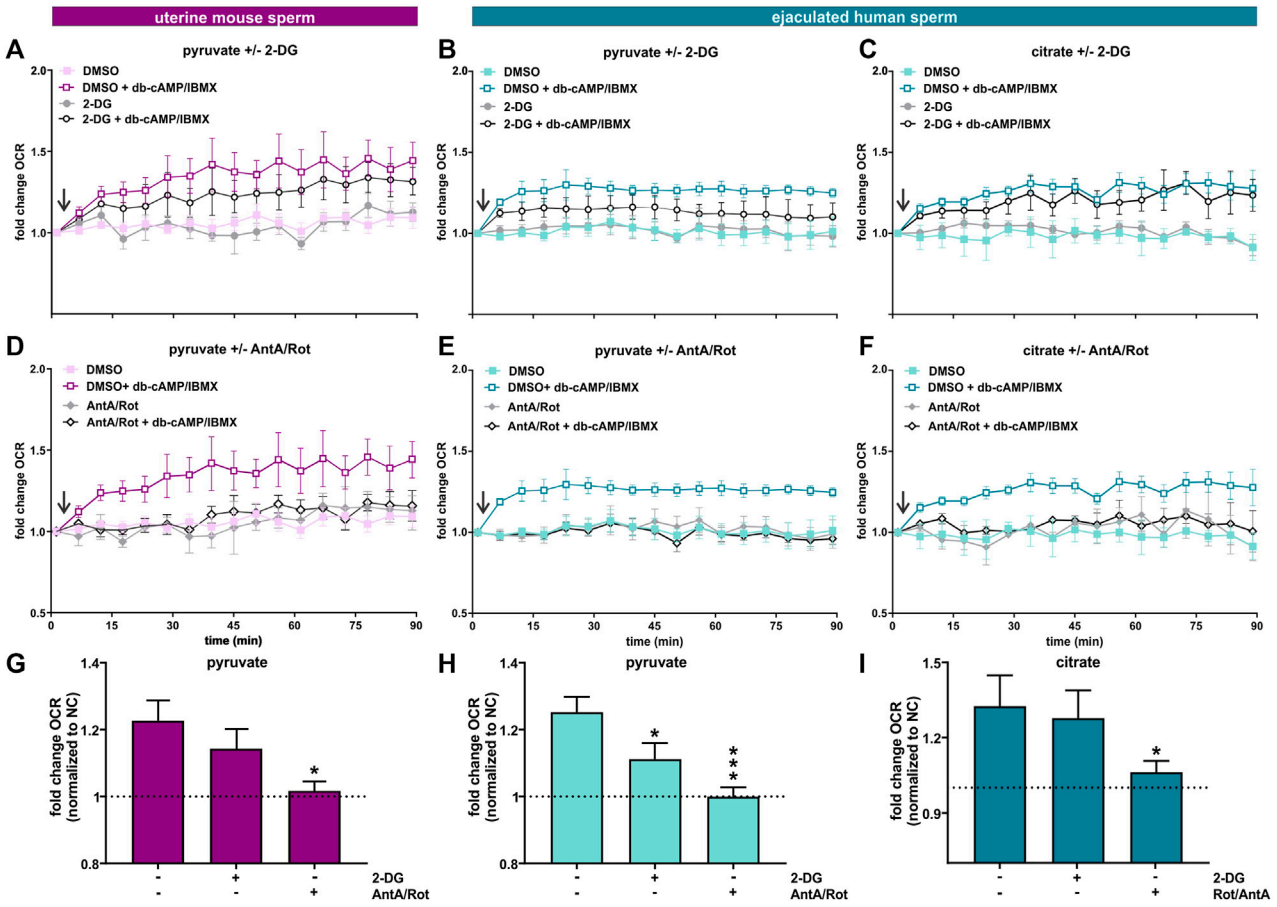

FIGURE 7
Capacitation induces an increase in oxphos independent from glycolysis **(A, D)** Normalized OCR of uterine mouse sperm in non-capacitating or capacitating media with pyruvate in the presence and absence of **(A)** 2-DG or **(D)** AntA/Rot; mean ± SEM (n ≥ 6). **(B, E)** Normalized OCR of ejaculated human sperm in non-capacitating or capacitating media with pyruvate in the presence and absence of **(B)** 2-DG or **(E)** AntA/Rot; mean ± SEM (n ≥ 6) **(C, F)** Normalized OCR of ejaculated human sperm in non-capacitating or capacitating media with citrate in the presence and absence of **(C)** 2-DG or **(F)** AntA/Rot; mean ± SEM (n ≥ 6). **(G)** Change in OCR of uterine mouse sperm in capacitating media containing pyruvate relative to control in non-capacitating media in the absence or presence of 2-DG or AntA/Rot **(H, I)** Change in OCR of ejaculated human sperm in capacitating media containing **(H)** pyruvate or **(I)** citrate relative to control in non-capacitating media in the absence or presence of 2-DG or AntA/Rot. The average of the last three data points was respectively used for normalization, mean +SEM (n ≥ 6). Differences between conditions were analyzed using one-way ANOVA compared to the DMSO-treated capacitated control **(G–I)**,*$p < 0.05$, ***$p < 0.001$. The arrow indicates addition of 5 mM db-cAMP/500 μM IBMX.

Post ejaculation, sperm can leverage exogenously supplied substrates which enter oxphos directly

In our previous studies focusing on epididymal mouse sperm, we demonstrated that the capacitation-induced increase in oxphos required substrates generated intrinsically from glycolysis: Fuels which bypass glycolysis and enter the Krebs cycle directly were unable to support the capacitation-induced increase in OCR (Balbach et al., 2020a). Here, we explore whether uterine mouse sperm and ejaculated human sperm, which have already encountered glycolytic substrates during ejaculation (Mann, 1965; Purvis et al., 1986; Owen and Katz, 2005), maintain a similar dependence. As anticipated, epididymal and uterine mouse sperm as well as ejaculated human sperm required exogenous nutrients to support the increase in glycolysis and oxphos elicited by the addition of db-cAMP/IBMX (Figures 6G–L) and including glucose in the extracellular flux analyzer media resulted in the strongest increase in both glycolysis and oxphos in all three sperm samples (Figures 6G–L, Supplementary Figure S3). As we previously showed, exogenous addition of pyruvate, which cannot, by itself, support an increase in glycolysis (Figures 6G, I, K), did not increase OCR in epididymal mouse sperm; they are dependent upon pyruvate generated intrinsically from glycolysis to support the capacitation-induced change in oxphos (Balbach et al., 2020a) (Figures 6A,H). Surprisingly, in both post-ejaculated human and uterine mouse sperm, OCR was stimulated upon addition of db-cAMP/IBMX in media containing pyruvate only (Figures 6C, E, J, L). This increase in OCR was prevented by Rot/AntA confirming it represents oxphos activity, and it was also partly diminished by the glycolysis inhibitor 2-DG (Figures 7A, B, D, E, G, H), supporting the existence of a functional link between glycolysis and oxphos. Also as we described previously (Balbach et al., 2020a), adding pyruvate to glucose diminished both ECAR and OCR responses relative to

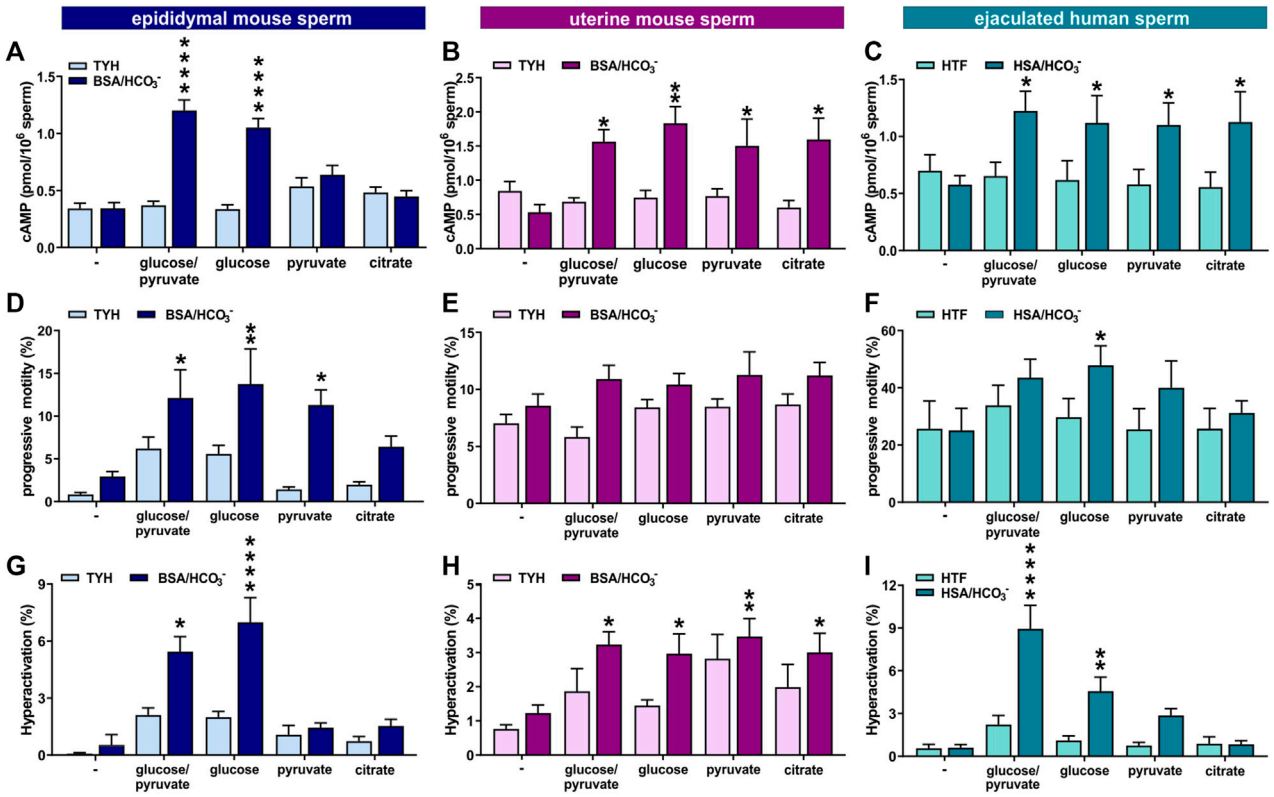

FIGURE 8
Ejaculation provides higher flexibility in the energy requirements for capacitation **(A–C)** Intracellular cAMP levels in **(A)** epididymal mouse sperm, **(B)** uterine mouse sperm, or **(C)** ejaculated human sperm incubated for 10 min (epididymal mouse sperm), 15 min (uterine mouse sperm), or 30 min (human sperm) in non-capacitating or capacitating media in the presence of no energy source (–), glucose/pyruvate, glucose, pyruvate, or citrate quantified by cAMP Elisa; mean +SEM (n ≥ 8) **(D–F)** Percentage of progressively motile **(D)** epididymal mouse sperm, **(E)** uterine mouse sperm, or **(F)** ejaculated human sperm incubated for 30 min (mouse) or 60 min (human) in non-capacitating or capacitating media in the presence of no energy source (–), glucose/pyruvate, glucose, pyruvate, or citrate; mean +SEM (n ≥ 7) **(G–I)** Percentage of hyperactivated **(G)** epididymal mouse sperm, **(H)** uterine mouse sperm, or **(I)** ejaculated human sperm incubated for 30 min (mouse) or 60 min (human) in non-capacitating or capacitating media in the presence of no energy source (–), glucose/pyruvate, glucose, pyruvate, or citrate; mean +SEM (n ≥ 7). Differences between conditions were analyzed using one-way ANOVA compared to the non-capacitated control in glucose,*$p < 0.05$, **$p < 0.01$, ****$p < 0.0001$.

glucose alone in epidydimal mouse sperm suggesting that pyruvate feeds back and partially inhibits glycolysis and oxphos. This effect was not seen in uterine mouse sperm and ejaculated human sperm; addition of pyruvate did not appreciably affect the capacitation-induced response (Figures 6I–K, L, Supplementary Figure S3). The ability of uterine mouse and ejaculated human sperm to increase OCR in the presence of exogenously supplied pyruvate reveals that the cAMP-dependent stimulation of oxphos does not simply reflect increased substrate availability (i.e., pyruvate) produced from the elevated glycolytic rate; there appears to be an independent, specific stimulation of oxphos activity in capacitating sperm post ejaculation.

The TCA cycle intermediate citrate presents a unique profile. Only human sperm were able to utilize citrate for the capacitation-induced increase in oxphos (Figures 6B, D, F, H , J, L). As expected, this increase in OCR was prevented by Rot/AntA and unaffected by 2-DG (Figures 7C, F, I). Despite being part of the Krebs cycle, citrate is not permeable to mitochondria, it first needs to be converted to malate. Human sperm appear to utilize citrate in unique ways relative to mouse sperm.

In summary, these data suggest ejaculation is accompanied by an increase in metabolic flexibility. To fuel the Krebs cycle, epididymal mouse sperm are dependent upon pyruvate generated intrinsically from glycolysis, while uterine mouse sperm and ejaculated human sperm are able to fuel the Krebs cycle with exogenously supplied pyruvate (and citrate for human sperm). In all sperm samples capacitation is accompanied by an increase in oxphos activity. In sperm supplied with glycolytic substrates, this increase may reflect more glycolytically derived pyruvate fueling the Krebs cycle. However, in post-ejaculated sperm, pyruvate alone can support the capacitation-induced stimulation of oxphos implying that the rate of oxphos is independently stimulated during capacitation.

Ejaculation provides higher flexibility in the carbon sources utilized for capacitation

Epididymal mouse sperm require glycolytic substrates to successfully undergo capacitation (Goodson et al., 2012; Balbach et al., 2020a), which may be at least partially due to their dependence on glycolytic substrates to support enhanced glycolysis and oxphos. Because uterine mouse sperm and ejaculated human sperm exhibit increased metabolic flexibility, we tested whether they are able to

complete the molecular and physiological changes associated with capacitation in non-glycolytic substrates. The first event in the signaling cascade of capacitation is the bicarbonate-induced increase in cAMP. We measured capacitation-induced changes in intracellular cAMP in media with different energy sources at the time point with the maximal response (Balbach et al., 2021). As shown previously, epididymal mouse sperm only evoked an increase in intracellular cAMP in capacitating media when glucose was present. In contrast, and consistent with their enhanced metabolic flexibility, uterine mouse sperm and ejaculated human sperm increased cAMP production in both glycolytic and non-glycolytic substrates (Figures 8A–C).

The increased flexibility in carbon source utilization of uterine mouse and ejaculated human sperm also impacted motility. In contrast to epididymal mouse sperm under non-capacitating conditions, which seemed to require glucose for progressive motility (Figure 8D), uterine mouse and ejaculated human sperm incubated in non-capacitating conditions displayed equivalent levels of progressively motile sperm in glycolytic and non-glycolytic energy substrates. Interestingly, uterine mouse and ejaculated human sperm were progressively motile even in the absence of any exogenous energy source (Figures 8E, F). When incubated in capacitation-inducing conditions, all sperm samples again required an exogenous nutrient to support the increased energy demands of progressive motility and hyperactivation (Figures 8D–I). Epididymal mouse sperm showed similar increases in progressive motility induced by capacitating conditions with either glucose alone, or glucose in the presence of pyruvate, and a partial increase in the presence of citrate (Figure 8D and as shown in (Goodson et al., 2012)), but the switch to hyperactivated motility induced by capacitation-inducing conditions was only observed in the presence of glucose (Figure 8G). In contrast, each of the tested exogenous nutrients, glucose, glucose/pyruvate, pyruvate, or citrate, were able to support high levels of progressive motility and the capacitation-induced increase in hyperactivation in uterine mouse sperm. Thus, it appears the enhanced metabolic flexibility of ejaculated mouse sperm is functionally relevant; it afforded them the ability to leverage non-glycolytic energy substrates for energy consuming pathways. For ejaculated human sperm the response was more nuanced; the capacitation-induced increase in hyperactivated motility was absent in citrate, and while the response was present in pyruvate, glucose was superior with the strongest increase seen when combining glucose with pyruvate (Figures 8F, I), as observed previously (Hereng et al., 2011).

Discussion

In mammals, the site of semen deposition is far from the site of fertilization, which means it is crucial for sperm to produce sufficient ATP to support their journey through the female genital tract. Mammalian sperm possess the molecular machinery to produce ATP via glycolysis and oxphos (Goldberg et al., 1977; Hess et al., 1993; Westhoff and Kamp, 1997; Narisawa et al., 2002; Miki et al., 2004; Nakamura et al., 2008; Danshina et al., 2010), and we now show that the activities of both pathways are stimulated during capacitation to meet the energy demands to successfully navigate the female reproductive tract. We find that human and mouse sperm depend upon both glycolysis and oxphos during capacitation to generate the additional energy required for progressive motility, which is only fully blocked when both pathways are inhibited. Additionally, our results indicate that for progressive and maximum hyperactivated motility, glycolysis and oxphos need to be simultaneously active.

Interestingly, ejaculated human sperm and post-ejaculated mouse sperm recovered from the uterus have the ability to leverage a variety of exogenous nutrients to fuel ATP generation which is different from mouse sperm isolated from the epididymis. Metabolic flexibility has been discussed previously as potentially beneficial for reproductive success (Travis et al., 2001; Miki, 2007; Storey, 2008; Tourmente et al., 2015; Tourmente et al., 2022a; Tourmente et al., 2022b). These data now suggest increased flexibility in carbon source utilization as a previously unappreciated change associated with sperm ejaculation.

Previous studies exploring the metabolism of mouse sperm started from dormant sperm isolated from the cauda epididymis, which were subsequently capacitated *in vitro*. In contrast, studies of human sperm used ejaculated sperm. Upon ejaculation, sperm are exposed to various energy substrates (Owen and Katz, 2005) and elevated levels of bicarbonate, which lead to changes in the sperm's metabolic environment and initiate capacitation. Therefore, comparisons between mouse and human sperm metabolism were confounded by having (at least) two distinctions; species differences as well as the changes that accompany ejaculation. Here, we attempted to disambiguate these differences by comparing a third population of sperm; ejaculated mouse sperm isolated from the female reproductive tract. Because they are already exposed to the environment of the female reproductive tract, using mouse sperm isolated from the uterus introduces a new variable. However, uterine sperm represent a readily accessible source of sufficiently abundant ejaculated mouse sperm for the metabolic profiling studies presented here.

We subjected these three sperm samples to two complementary methods for characterizing metabolism, extracellular flux analysis, and metabolic profiling. Extracellular flux analysis provides information about real-time changes in glycolysis and oxphos; these experiments inform how rates of these metabolic pathways change during the process of capacitation. Targeted metabolic profiling measures the levels of specific endogenous metabolites which allows comparison of their relative levels before and after incubation in capacitating conditions. As seen with cAMP, which increased during capacitation, and ATP, which decreased during capacitation, changes in metabolite levels in either direction can reflect capacitation-associated changes in the enzymatic activities producing and/or consuming metabolites.

When using these methods to compare ejaculated human sperm to uterine mouse sperm, we observed more similarities than differences between the two species. Measuring changes in glycolysis and oxphos in real-time revealed that the rate of both glycolysis and oxphos increase during mouse and human sperm capacitation. An increase in mitochondrial activity during capacitation of epididymal mouse sperm was independently observed using flow cytometry (Giaccagli et al., 2021) and high-resolution respirometry (Ferreira et al., 2021b). In contrast, a study by Tourmente *et al.* observed a shift in the usage ratio from oxphos

to glycolysis (Tourmente et al., 2022a) instead of an increase in the rate of oxphos and glycolysis. In their study, to overcome the limitation that bicarbonate cannot be included during incubations in the extracellular flux analyzer, Tourmente *et al.* pre-incubated epididymal mouse sperm in capacitating conditions in advance of the experiment and measured extracellular flux from sperm incubated in non-capacitating media. Since sperm capacitation is reversible (Cohen-Dayag et al., 1995; Navarrete et al., 2019), the absence of bicarbonate during the actual measurement makes the sperm maturation state unclear. Moreover, instead of monitoring physiologically induced changes in glycolysis and oxphos over time, in their study the authors extrapolate the contribution of glycolysis and oxphos from addition of pharmacological inhibitors of the two pathways. These differences between the experimental design of both studies make a direct comparison difficult.

The enhanced metabolic flexibility seen in sperm post ejaculation was observed under both non-capacitating as well as capacitating conditions. In contrast to epididymal mouse sperm, which required glycolytic substrates to support progressive motility, progressive motility in uterine mouse sperm under non-capacitating conditions was independent of exogenous nutrients. This suggests that uterine mouse sperm are able to leverage stored energy or secure sufficient nutrients from an initial exposure to energy substrates during ejaculation or in the female genital tract. In capacitating conditions, the bicarbonate-induced increase in progressive motility and hyperactivation demanded exogenous energy sources, and uterine mouse sperm, unlike epididymal sperm, were able to support hyperactivation using the non-glycolytic exogenous substrates pyruvate and citrate. Consistently, metabolic flux analysis revealed that uterine sperm can use pyruvate to support the capacitation-associated increase in the rate of oxphos. Because we observed similar tendencies in ejaculated human sperm, we posit that ejaculation equips sperm with enhanced metabolic flexibility. Importantly, this also suggests that the rate of oxphos is not just passively adapting to an increase in substrate availability generated by enhanced glycolytic activity. Instead, ejaculated sperm seem to actively increase the flux through oxphos during capacitation. Since sperm are transcriptionally silent and exist in a constantly changing environment with fluctuating O_2 tensions and energy substrate availability, bioenergetic adaptability would be beneficial for enabling sperm to achieve their ultimate function: fertilization of the oocyte.

Methods

Reagents

Reagents for media preparation were purchased from Sigma-Aldrich. 2-deoxyglucose (2-DG), 3-Isobutyl-1-methylxanthine (IBMX), antimycin A, BSA, concanavalin A (ConA), dibutyryl-cAMP (db-cAMP), progesterone, lectin from Pisum sativum FITC-conjugated (PSA-FITC) and lectin from *Arachis hypogaea* FITC-conjugated (PNA-FITC) were purchased from Sigma-Aldrich, rotenone (rot) from Cayman chemicals, HSA from Irvine Scientific and PBS buffer from Corning.

Mice

Adult 8–10 week old C57BL/6N (Stock #: 027) mice were purchased from Jackson Laboratory and allowed to acclimatize before use. Animal experiments were approved by Weill Cornell Medicine's and by the University of Massachusetts Institutional Animal Care and Use Committees (IACUC).

Sperm preparation

Epididymal mouse sperm were isolated by incision of the cauda epididymis in 500 µL modified TYH medium (in mM: 135 NaCl, 4.7 KCl, 1.7 $CaCl_2$, 1.2 KH_2PO_4, 1.2 $MgSO_4$, 10 HEPES, pH 7.4 adjusted at 37°C with NaOH) without energy source, prewarmed at 37°C. For Seahorse experiments, Seahorse TYH buffer with 1 mM HEPES was used for isolation. For assessment of ejaculated mouse sperm, single-housed male and female mice were acclimatized to a reverse light cycle (dark: 11 a.m. to 11 p.m.) for at least 2 weeks. On the day of the experiment at 11 a.m. individual males were paired with a female in estrus (identified by physical examination) and allowed to mate until a plug was discovered. Female mice were sacrificed, the uteri were isolated and both uterine horns opened in 1 mL TYH buffer without energy source. After 15 min swim-out at 37°C, sperm were counted using a hematocytometer and sperm cell numbers were adjusted to a concentration of 1×10^7 cells/mL. Sperm were washed twice with the TYH buffer with the respective energy source used for the experiment (glucose (5.6 mM), glucose (5.6 mM) and pyruvate (0.56 mM), pyruvate (0.56 mM), or citrate (0.56 mM)) by centrifugation at 700 x g for 5 min. For capacitation, sperm were incubated in TYH containing 3 mg/mL BSA and 25 mM $NaHCO_3$ in a 37°C incubator. For seahorse experiments, $NaHCO_3$ was replaced with 5 mM db-cAMP and 500 µM IBMX.

Samples of human semen were obtained from healthy volunteers with their prior written consent following a protocol approved by Weill Cornell Medicine's Institutional Review Board (IRB 21-03023495). Only samples that met the WHO 2010 criteria for normal semen parameters (ejaculated volume ≥1.5 mL, sperm concentration ≥15 million/mL, motility ≥40%, progressive motility ≥32%, normal morphology ≥4%) were included in this study. Semen was incubated for 30 min in a 37°C incubator to liquefy. Human sperm were purified by "swim-up" procedure in human tubular fluid (HTF) (in mM: 97.8 NaCl, 4.69 KCl, 0.2 $MgSO_4$, 0.37 KH_2PO_4, 2.04 $CaCl_2$, 20 HEPES, pH 7.4) with the respective energy source (glucose (2.8 mM), glucose (2.8 mM) and pyruvate (0.33 mM), pyruvate (0.33 mM), or citrate (0.33 mM)) used for the experiment. For Seahorse experiments, Seahorse HTF buffer with 1 mM HEPES was used. 0.5–1 mL of liquefied semen was layered in a 50 mL tube below 4 mL HTF. The tubes were incubated at a tilted angle of 45° at 37°C for 60 min. Motile sperm were allowed to swim up into the HTF layer; immotile sperm and other cells or tissue debris remain in the ejaculate fraction. Up to 3 mL of the HTF layer was transferred to a fresh tube and washed twice by centrifugation (700 × g, 20 min) with HTF buffer with the respective energy source. The purity and vitality of each sample was assessed via light microscopy. Sperm cell numbers were determined using a hemocytometer and adjusted to a concentration of 1×10^7 cells/mL. For capacitation, sperm were incubated in HTF with 72.8 mM NaCl containing 25 mM $NaHCO_3$ and 3 mg/mL human serum albumin (HSA) in a 37°C incubator. For

seahorse experiments, $NaHCO_3$ was replaced with 5 mM db-cAMP and 500 µM IBMX.

Sperm motility assays

Sperm motility as assessed using computer-assisted sperm analysis (CASA) via Hamilton–Thorne digital image analyzer (IVOS II, Hamilton Thorne Research, Beverly, MA) with the following parameters: 30 frames, frame rate: 60 Hz, cell size: 30–170 μm^2. Sperm movements of 5 fields of at least 200 sperm were examined. For mouse sperm analysis, following incubation for 30 min in non-capacitating or capacitating TYH buffer, 25 µL sperm suspension were loaded on a 100 µM Leja slide (Hamilton Thorne) and placed on a microscope stage at 37 °C. Mouse sperm were considered progressively motile when presenting STR ≥80% and VAP ≥50 µm/s and hyperactivated when presenting VCL ≥270 µm/s, LIN <50%, and ALH ≥7 µm. For human sperm analysis, following incubation for 60 min in non-capacitating or capacitating HTF buffer, 8 µL sperm suspension were loaded on a 20 µM Leja slide. Human sperm were considered progressively motile when presenting STR ≥80% and VAP ≥25 µm/s and hyperactivated when presenting VCL ≥150 µm/s, LIN <50%, and ALH ≥7 µm. Data is shown as percentage of the total cell number.

Acrosome reaction assay

For analysis of acrosomal exocytosis, 100 µL of 1 × 10^6 sperm/mL were capacitated for 90 min in TYH buffer supplemented with 3 mg/mL BSA and 25 mM $NaHCO_3$ or 3 mg/mL BSA, 5 mM db-cAMP and 500 µM IBMX (mouse sperm) or HTF buffer supplemented with 3 µL/mL HSA and 25 mM $NaHCO_3$ or 3 µL/mL HSA, 5 mM db-cAMP and 500 µM IBMX (human sperm). Acrosome reaction was induced by incubation with 10 µM progesterone for 15 min at 37 °C. The sperm suspensions were sedimented by centrifugation at 2,000xg for 5 min and the sedimented sperm were resuspended in 100 µL PBS buffer. Samples were air-dried on microscope slides and fixed for 30 min in 100% ethanol at room temperature. For acrosome staining, mouse and human sperm were incubated for 30 min in the dark with 5 µg/mL PNA-FITC or 5 µg/mL PSA-FITC, respectively, and counterstained with 2 µg/mL DAPI. After curing, slides were analyzed using a Zeiss LSM 880 Laser Scanning Confocal Microscope; images were captured with two photomultiplier and one Gallium Arsenide Phosphide detector using ZEN Imaging software. For each condition, at least 600 cells were analyzed using ImageJ 1.52.

Extracellular flux analysis

Extracellular flux analysis was performed as described in (Balbach et al., 2020a; Balbach et al., 2020b). In brief, 180 µL mouse and human sperm suspensions in Seahorse TYH/HTF buffer with 3 mg/mL BSA or HSA and the respective energy source were added to each well of a ConA-coated 96-well plate (8.3 × 10^5 sperm/well). To immobilize the sperm heads to the well bottom, the plate was centrifuged at 250 × g for 1 min, rotated by 180°, and centrifuged again. For experiments comparing different energy sources, after recording a baseline and a buffer injection with the respective buffer, db-cAMP/IBMX was injected into half of the wells to induce capacitation and changes in ECAR and OCR were monitored for 90 min. Alternatively, after the buffer injection, first 2-deoxyglucose (2-DG) or AntimycinA (AntA)/Rotenone (Rot) were injected followed, after 3 measurement cycles, by db-cAMP/IBMX to induce capacitation.

Data was analyzed as described in (Goodson et al., 2012) and is shown as fold change normalized to the data point before cAMP/IBMX injection. The fold change shown in the bar graphs was generated by normalizing the mean of the last three data points in capacitating conditions with the mean of the last three data points of non-capacitated sperm.

ATP quantification

Aliquots of 1 × 10^6 sperm were incubated for the indicated time points in non-capacitating or capacitating TYH buffer with glucose/pyruvate (mouse sperm) or non-capacitating or capacitating HTF buffer with glucose/pyruvate (human sperm) in the absence or presence of 2-DG. Sperm were sedimented by centrifugation at 2000 × g for 3 min and lysed in 250 µL lysis buffer (100 mM Tris, 4 mM EDTA, pH 7.75) at 95°C for 7 min. Sperm lysates were centrifuged at 10000xg for 3 min and the ATP in the supernatant was quantified using the ENLITEN ATP Assay Kit (Promega) according to the manufacturer's instructions.

Sample preparation for LC-MS/MS

Epididymal and uterine mouse sperm and ejaculated human sperm (5 × 10^6 sperm/mL) were isolated and incubated in non-capacitating and capacitating conditions for 90 min in quadruplicates in 500 µL TYH or HTF media with glucose or glucose/pyruvate. Following separation of the supernatant and sperm by centrifugation for 5 min at 700 × g, 450 µL of supernatant were transferred to a new vial and 450 µL ice-cold 90% MeOH were added to the sperm pellet resulting in a final concentration of 80% methanol (MeOH). For the supernatant samples, 100 µL were quenched with 400 µL 100% MeOH. Media without sperm was used as control and processed under the same conditions. After the addition of MeOH, samples were immediately vortexed and placed on dry ice. After 15 min, samples were moved to wet ice, vortexed again and incubated overnight at −80°C to aid protein precipitation. Sperm and supernatant samples were centrifuged at 20,000 × g for 20 min at 4°C and 450 µL of supernatant were transferred to a fresh tube, dried via speed-vac and stored at −80°C until analysis. Before LC-MS/MS analysis, the samples were resuspended in 30 µL of mobile phase A and incubated on wet ice for 20 min while being vortexed every 5 min. Samples were centrifuged at 20,000 × g for 20 min at 4°C and 25 µL of the supernatant was transferred into LC vials for injection.

LC-MS/MS analysis

Ion pair LC-MS/MS analysis was performed with LC separation on a Zorbax RRHD Extend-C18 column (150 mm × 2.1 mm, 1.8 µm particle size, Agilent Technologies), and using gradient of solvent A (10 mM tributylamine and 15 mM acetic acid in 97:3 water:

methanol) and solvent B (10 mM tributylamine and 15 mM acetic acid in methanol) according to the manufacturer's instructions (MassHunter Metabolomics dMRM Database and Method, Agilent Technologies).

cAMP quantification

Aliquots of 2×10^6 epididymal mouse sperm were incubated for 10 min in non-capacitating or capacitating TYH buffer with the respective energy source, aliquots of 2×10^6 uterine mouse or ejaculated human sperm were incubated for 15 or 30 min in non-capacitating or capacitating TYH or HTF buffer, respectively. Sperm were sedimented by centrifugation at 2000 × g for 3 min and lysed in 200 µL HCl for 10 min. Sperm lysates were centrifuged at 2000 × g for 3 min and the cAMP in the supernatant acetylated and quantified using the Direct cAMP ELISA Kit (Enzo) according to the manufacturer's instructions.

Statistical analysis

Statistical analyses were performed using GraphPad Prism 5 (Graph-Pad Software). All data are shown as the mean ± SEM. Statistical significance between two groups was determined using two-tailed, paired t-tests with Welch's correction, statistical significance between multiple groups was determined using one-way ANOVA with Dunnett's correction after confirming normal distribution via D'Agostino-Pearson and homoscedasticity (Breusch–Pagan test). Differences were considered to be significant if $^{*}p < 0.05$, $^{**}p < 0.01$, $^{***}p < 0.001$, and $^{****}p < 0.0001$.

Data availability statement

The original contributions presented in the study are included in the article/Supplementary Material, further inquiries can be directed to the corresponding author.

Ethics statement

The animal study was reviewed and approved by Weill Cornell Medicine's and by the University of Massachusetts Institutional Animal Care and Use Committees (IACUC).

Author contributions

Conceptualization: MB, LL, JB, and PV. Methodology: MB and SN. Investigation: MB, LG, and AK. Visualization: MB. Funding acquisition: LL, JB, and PV. Supervision: LL and JB. Writing—original draft: MB, LL, JB, JC, AR, and PV. All authors contributed to the article and approved the submitted version.

Funding

This study was supported by the Eunice Kennedy Shriver National Institute of Child Health and Human Development grants HD088571 (to JB, LL, and PV), and Male Contraceptive Initiative (to MB, JB, and LL).

Acknowledgments

The authors wish to thank Samuel Nidorf and Sylvia Ayoub for maintaining the mouse colony, Drs. Thomas Rosetti and Carla Ritagliati for a critical revision of the manuscript, and numerous anonymous sperm donors.

Conflict of interest

JB and LL have licensed commercialization of a panel of monoclonal antibodies directed against sAC to Millipore. LL and JB are co-founders of Sacyl Pharmaceuticals, Inc. established to develop sAC inhibitors into on-demand contraceptives.

The remaining authors declare that the research was conducted in the absence of any commercial or financial relationships that could be construed as a potential conflict of interest.

The handling editor RF declared a shared affiliation with the author(s) AR and PV at the time of review.

Publisher's note

Supplementary material

The Supplementary Material for this article can be found online at: https://www.frontiersin.org/articles/10.3389/fcell.2023.1160154/full#supplementary-material

References

Austin, C. R., and Bishop, M. W. (1958). Capacitation of mammalian spermatozoa. *Nature* 181, 851. doi:10.1038/181851a0

Balbach, M., Beckert, V., Hansen, J. N., and Wachten, D. (2018). Shedding light on the role of cAMP in mammalian sperm physiology. *Mol. Cell. Endocrinol.* 468, 111–120. doi:10.1016/j.mce.2017.11.008

Balbach, M., Gervasi, M. G., Hidalgo, D. M., Visconti, P. E., Levin, L. R., and Buck, J. (2020a). Metabolic changes in mouse sperm during capacitation. *Biol. Reprod.* 103, 791–801. doi:10.1093/biolre/ioaa114

Balbach, M., Buck, J., and Levin, L. R. (2020b). Using an extracellular flux analyzer to measure changes in glycolysis and oxidative phosphorylation during mouse sperm capacitation. *J. Vis. Exp.* 22. doi:10.3791/60815

Balbach, M., Ghanem, L., Rossetti, T., Kaur, N., Ritagliati, C., Ferreira, J., et al. (2021). Soluble adenylyl cyclase inhibition prevents human sperm functions essential for fertilization. *Mol. Hum. Reprod.* 27, gaab054. doi:10.1093/molehr/gaab054

Bohnensack, R., and Halangk, W. (1986). Control of respiration and of motility in ejaculated bull spermatozoa. *Biochim. Biophys. Acta* 850, 72–79. doi:10.1016/0005-2728(86)90010-1

Brauchi, S., Rauch, M. C., Alfaro, I. E., Cea, C., Concha, I. I., Benos, D. J., et al. (2005). Kinetics, molecular basis, and differentiation of L-lactate transport in spermatogenic cells. *Am. J. Physiol. Cell. Physiol.* 288, C523–C534. doi:10.1152/ajpcell.00448.2003

Buffone, M. G., Wertheimer, E. V., Visconti, P. E., and Krapf, D. (2014). Central role of soluble adenylyl cyclase and cAMP in sperm physiology. *Biochim. Biophys. Acta* 1842, 2610–2620. doi:10.1016/j.bbadis.2014.07.013

Calvert, S. J., Reynolds, S., Paley, M. N., Walters, S. J., and Pacey, A. A. (2019). Probing human sperm metabolism using 13C-magnetic resonance spectroscopy. *Mol. Hum. Reprod.* 25, 30–41. doi:10.1093/molehr/gay046

Carrageta, D. F., Guerra-Carvalho, B., Sousa, M., Barros, A., Oliveira, P. F., Monteiro, M. P., et al. (2020). Mitochondrial activation and reactive oxygen-species overproduction during sperm capacitation are independent of glucose stimuli. *Antioxidants (Basel)* 9, 750. doi:10.3390/antiox9080750

Carrageta, D. F., Freire-Brito, L., Guerra-Carvalho, B., Ribeiro, J. C., Monteiro, B. S., Barros, A., et al. (2023). Inhibition of mitochondrial uncoupling proteins arrests human spermatozoa motility without compromising viability. *Antioxidants (Basel)* 12, 409. doi:10.3390/antiox12020409

Chang, M. C. (1951). Fertilizing capacity of spermatozoa deposited into the fallopian tubes. *Nature* 168, 697–698. doi:10.1038/168697b0

Cohen-Dayag, A., Tur-Kaspa, I., Dor, J., Mashiach, S., and Eisenbach, M. (1995). Sperm capacitation in humans is transient and correlates with chemotactic responsiveness to follicular factors. *Proc. Natl. Acad. Sci. U. S. A.* 92, 11039–11043. doi:10.1073/pnas.92.24.11039

Danshina, P. V., Geyer, C. B., Dai, Q., Goulding, E. H., Willis, W. D., Kitto, G. B., et al. (2010). Phosphoglycerate kinase 2 (PGK2) is essential for sperm function and male fertility in mice. *Biol. Reprod.* 82, 136–145. doi:10.1095/biolreprod.109.079699

Dey, S., Brothag, C., and Vijayaraghavan, S. (2019). Signaling enzymes required for sperm maturation and fertilization in mammals. *Front. Cell. Dev. Biol.* 7, 341. doi:10.3389/fcell.2019.00341

du Plessis, S. S., Agarwal, A., Mohanty, G., and van der Linde, M. (2015). Oxidative phosphorylation versus glycolysis: What fuel do spermatozoa use? *Asian J. Androl.* 17, 230–235. doi:10.4103/1008-682X.135123

Fan, Y., Liu, Y., Xue, K., Gu, G., Fan, W., Xu, Y., et al. (2015). Diet-induced obesity in male C57BL/6 mice decreases fertility as a consequence of disrupted blood-testis barrier. *PLoS One* 10, e0120775. doi:10.1371/journal.pone.0120775

Ferramosca, A., Pinto Provenzano, S., Montagna, D. D., Coppola, L., and Zara, V. (2013). Oxidative stress negatively affects human sperm mitochondrial respiration. *Urology* 82, 78–83. doi:10.1016/j.urology.2013.03.058

Ferreira, J. J., Lybaert, P., Puga-Molina, L. C., and Santi, C. M. (2021a). Conserved mechanism of bicarbonate-induced sensitization of CatSper channels in human and mouse sperm. *Front. Cell. Dev. Biol.* 9, 733653. doi:10.3389/fcell.2021.733653

Ferreira, J. J., Cassina, A., Irigoyen, P., Ford, M., Pietroroia, S., Peramsetty, N., et al. (2021b). Increased mitochondrial activity upon CatSper channel activation is required for mouse sperm capacitation. *Redox Biol.* 48, 102176. doi:10.1016/j.redox.2021.102176

Ford, W. C., and Harrison, A. (1981). The role of oxidative phosphorylation in the generation of ATP in human spermatozoa. *J. Reprod. Fertil.* 63, 271–278. doi:10.1530/jrf.0.0630271

Fraser, L. R., and Quinn, P. J. (1981). A glycolytic product is obligatory for initiation of the sperm acrosome reaction and whiplash motility required for fertilization in the mouse. *J. Reprod. Fertil.* 61, 25–35. doi:10.1530/jrf.0.0610025

Gervasi, M. G., and Visconti, P. E. (2016). Chang's meaning of capacitation: A molecular perspective. *Mol. Reprod. Dev.* 83, 860–874. doi:10.1002/mrd.22663

Giaccagli, M. M., Gómez-Elías, M. D., Herzfeld, J. D., Marín-Briggiler, C. I., Cuasnicú, P. S., Cohen, D. J., et al. (2021). Capacitation-induced mitochondrial activity is required for sperm fertilizing ability in mice by modulating hyperactivation. *Front. Cell. Dev. Biol.* 9, 767161. doi:10.3389/fcell.2021.767161

Goldberg, E., Sberna, D., Wheat, T. E., Urbanski, G. J., and Margoliash, E. (1977). Cytochrome c: Immunofluorescent localization of the testis-specific form. *Science* 196, 1010–1012. doi:10.1126/science.193188

Goodson, S. G., Qiu, Y., Sutton, K. A., Xie, G., Jia, W., and O'Brien, D. A. (2012). Metabolic substrates exhibit differential effects on functional parameters of mouse sperm capacitation. *Biol. Reprod.* 87, 75. doi:10.1095/biolreprod.112.102673

Hereng, T. H., Elgstøen, K. B. P., Cederkvist, F. H., Eide, L., Jahnsen, T., Skålhegg, B. S., et al. (2011). Exogenous pyruvate accelerates glycolysis and promotes capacitation in human spermatozoa. *Hum. Reprod.* 26, 3249–3263. doi:10.1093/humrep/der317

Hess, R. A., Miller, L. A., Kirby, J. D., Margoliash, E., and Goldberg, E. (1993). Immunoelectron microscopic localization of testicular and somatic cytochromes c in the seminiferous epithelium of the rat. *Biol. Reprod.* 48, 1299–1308. doi:10.1095/biolreprod48.6.1299

Hidalgo, D. M., Romarowski, A., Gervasi, M. G., Navarrete, F., Balbach, M., Salicioni, A. M., et al. (2020). Capacitation increases glucose consumption in murine sperm. *Mol. Reprod. Dev.* 87, 1037–1047. doi:10.1002/mrd.23421

Ho, H. C., and Suarez, S. S. (2001). Hyperactivation of mammalian spermatozoa: Function and regulation. *Reproduction* 122, 519–526. doi:10.1530/rep.0.1220519

Hoppe, P. C. (1976). Glucose requirement for mouse sperm capacitation *in vitro*. *Biol. Reprod.* 15, 39–45. doi:10.1095/biolreprod15.1.39

Ishijima, S., Iwamoto, T., Nozawa, S., and Matsushita, K. (2002). Motor apparatus in human spermatozoa that lack central pair microtubules. *Mol. Reprod. Dev.* 63, 459–463. doi:10.1002/mrd.10197

King, W. W., St Amant, L. G., and Lee, W. R. (1994). Response to protocol review scenario: Add bryant to the protocol. *Lab. Anim. Sci.* 44, 295–296. doi:10.1038/laban.822

Lee, J., Lee, D. R., and Lee, S. (2014). The genetic variation in monocarboxylic acid transporter 2 (MCT2) has functional and clinical relevance with male infertility. *Asian J. Androl.* 16, 694–697. doi:10.4103/1008-682X.124561

Mann, T. (1965). *The biochemistry of semen and of the male reproductive tract*. Methuen and Co Ltd.

Marín-Briggiler, C. I., Luque, G. M., Gervasi, M. G., Oscoz-Susino, N., Sierra, J. M., Mondillo, C., et al. (2021). Human sperm remain motile after a temporary energy restriction but do not undergo capacitation-related events. *Front. Cell. Dev. Biol.* 9, 777086. doi:10.3389/fcell.2021.777086

Miki, K., Qu, W., Goulding, E. H., Willis, W. D., Bunch, D. O., Strader, L. F., et al. (2004). Glyceraldehyde 3-phosphate dehydrogenase-S, a sperm-specific glycolytic enzyme, is required for sperm motility and male fertility. *Proc. Natl. Acad. Sci. U. S. A.* 101, 16501–16506. doi:10.1073/pnas.0407708101

Miki, K. (2007). Energy metabolism and sperm function. *Soc. Reprod. Fertil. Suppl.* 65, 309–325.

Mukai, C., and Okuno, M. (2004). Glycolysis plays a major role for adenosine triphosphate supplementation in mouse sperm flagellar movement. *Biol. Reprod.* 71, 540–547. doi:10.1095/biolreprod.103.026054

Nakamura, N., Shibata, H., O'Brien, D. A., Mori, C., and Eddy, E. M. (2008). Spermatogenic cell-specific type 1 hexokinase is the predominant hexokinase in sperm. *Mol. Reprod. Dev.* 75, 632–640. doi:10.1002/mrd.20791

Narisawa, S., Hecht, N. B., Goldberg, E., Boatright, K. M., Reed, J. C., and Millán, J. L. (2002). Testis-specific cytochrome c-null mice produce functional sperm but undergo early testicular atrophy. *Mol. Cell. Biol.* 22, 5554–5562. doi:10.1128/mcb.22.15.5554-5562.2002

Navarrete, F. A., Aguila, L., Martin-Hidalgo, D., Tourzani, D. A., Luque, G. M., Ardestani, G., et al. (2019). Transient sperm starvation improves the outcome of assisted reproductive Technologies. *Front. Cell. Dev. Biol.* 7, 262. doi:10.3389/fcell.2019.00262

Odet, F., Duan, C., Willis, W. D., Goulding, E. H., Kung, A., Eddy, E. M., et al. (2008). Expression of the gene for mouse lactate dehydrogenase C (Ldhc) is required for male fertility. *Biol. Reprod.* 79, 26–34. doi:10.1095/biolreprod.108.068353

Owen, D. H., and Katz, D. F. (2005). A review of the physical and chemical properties of human semen and the formulation of a semen simulant. *J. Androl.* 26, 459–469. doi:10.2164/jandrol.04104

Park, S. K., Yoon, J., Wang, L., Shibata, T. K., Motamedchaboki, K., Shim, K. J., et al. (2012). Enhancement of mouse sperm motility by trophinin-binding peptide. *Reprod. Biol. Endocrinol.* 10, 101. doi:10.1186/1477-7827-10-101

Peterson, R. N., and Freund, M. (1970). ATP synthesis and oxidative metabolism in human spermatozoa. *Biol. Reprod.* 3, 47–54. doi:10.1093/biolreprod/3.1.47

Publicover, S., Harper, C. V., and Barratt, C. (2007). [Ca2+]i signalling in sperm-making the most of what you've got. *Nat. Cell. Biol.* 9, 235–242. doi:10.1038/ncb0307-235

Purvis, K., Magnus, O., Mørkås, L., Abyholm, T., and Rui, H. (1986). Ejaculate composition after masturbation and coitus in the human male. *Int. J. Androl.* 9, 401–406. doi:10.1111/j.1365-2605.1986.tb00902.x

Rogers, B. J., and Perreault, S. D. (1990). Importance of glycolysable substrates for *in vitro* capacitation of human spermatozoa. *Biol. Reprod.* 43, 1064–1069. doi:10.1095/biolreprod43.6.1064

Storey, B. T. (2008). Mammalian sperm metabolism: Oxygen and sugar, friend and foe. *Int. J. Dev. Biol.* 52, 427–437. doi:10.1387/ijdb.072522bs

Suarez, S. S. (2008). Control of hyperactivation in sperm. *Hum. Reprod. Update* 14, 647–657. doi:10.1093/humupd/dmn029

Suter, D., Chow, P. Y., and Martin, I. C. (1979). Maintenance of motility in human spermatozoa by energy derived through oxidative phosphorylation and addition of albumin. *Biol. Reprod.* 20, 505–510. doi:10.1095/biolreprod20.3.505

Tourmente, M., Villar-Moya, P., Rial, E., and Roldan, E. R. (2015). Differences in ATP generation via glycolysis and oxidative phosphorylation and relationships with sperm motility in mouse species. *J. Biol. Chem.* 290, 20613–20626. doi:10.1074/jbc.M115.664813

Tourmente, M., Sansegundo, E., Rial, E., and Roldan, E. R. S. (2022a). Capacitation promotes a shift in energy metabolism in murine sperm. *Front. Cell. Dev. Biol.* 10, 950979. doi:10.3389/fcell.2022.950979

Tourmente, M., Sansegundo, E., Rial, E., and Roldan, E. R. S. (2022b). Bioenergetic changes in response to sperm capacitation and two-way metabolic compensation in a new murine model. *Cell. Mol. Life Sci.* 80, 11. doi:10.1007/s00018-022-04652-0

Travis, A. J., Jorgez, C. J., Merdiushev, T., Jones, B. H., Dess, D. M., Diaz-Cueto, L., et al. (2001). Functional relationships between capacitation-dependent cell signaling and compartmentalized metabolic pathways in murine spermatozoa. *J. Biol. Chem.* 276, 7630–7636. doi:10.1074/jbc.M006217200

Visconti, P. E. (2012). Sperm bioenergetics in a nutshell. *Biol. Reprod.* 87, 72. doi:10.1095/biolreprod.112.104109

Wennemuth, G., Carlson, A. E., Harper, A. J., and Babcock, D. F. (2003). Bicarbonate actions on flagellar and Ca2+ -channel responses: Initial events in sperm activation. *Development* 130, 1317–1326. doi:10.1242/dev.00353

Westhoff, D., and Kamp, G. (1997). Glyceraldehyde 3-phosphate dehydrogenase is bound to the fibrous sheath of mammalian spermatozoa. *J. Cell. Sci.* 110, 1821–1829. doi:10.1242/jcs.110.15.1821

Whittingham, D. G. (1968). Fertilization of mouse eggs *in vitro*. *Nature* 220, 592–593. doi:10.1038/220592a0

Williams, A. C., and Ford, W. C. (2001). The role of glucose in supporting motility and capacitation in human spermatozoa. *J. Androl.* 22, 680–695.

Yanagimachi, R., and Chang, M. C. (1963). Fertilization of hamster eggs *in vitro*. *Nature* 200, 281–282. doi:10.1038/200281b0

Yanagimachi, R. (1970). The movement of golden hamster spermatozoa before and after capacitation. *J. Reprod. Fertil.* 23, 193–196. doi:10.1530/jrf.0.0230193

frontiers | Frontiers in Cell and Developmental Biology

TYPE Original Research
PUBLISHED 10 August 2023
DOI 10.3389/fcell.2023.1110681

OPEN ACCESS

EDITED BY
Shao-Chen Sun,
Nanjing Agricultural University, China

REVIEWED BY
Nicolas Brukman,
Technion Israel Institute of Technology, Israel
Yuhkoh Satouh,
Gunma University, Japan
Bart M. Gadella,
Utrecht University, Netherlands
Ken-Ichi Sato,
Kyoto Sangyo University, Japan

*CORRESPONDENCE
Katerina Komrskova,
katerina.komrskova@ibt.cas.cz

RECEIVED 29 November 2022
ACCEPTED 18 July 2023
PUBLISHED 10 August 2023

CITATION
Frolikova M, Sur VP, Novotny I, Blazikova M, Vondrakova J, Simonik O, Ded L, Valaskova E, Koptasikova L, Benda A, Postlerova P, Horvath O and Komrskova K (2023), Juno and CD9 protein network organization in oolemma of mouse oocyte.
Front. Cell Dev. Biol. 11:1110681.
doi: 10.3389/fcell.2023.1110681

Juno and CD9 protein network organization in oolemma of mouse oocyte

Michaela Frolikova[1], Vishma Pratap Sur[1], Ivan Novotny[2], Michaela Blazikova[2], Jana Vondrakova[1], Ondrej Simonik[1], Lukas Ded[1], Eliska Valaskova[1], Lenka Koptasikova[3], Ales Benda[3], Pavla Postlerova[1,4], Ondrej Horvath[2] and Katerina Komrskova[1,5]*

[1]Laboratory of Reproductive Biology, Institute of Biotechnology of the Czech Academy of Sciences, BIOCEV, Vestec, Czechia, [2]Light Microscopy Core Facility, Institute of Molecular Genetics of the Czech Academy of Sciences, Prague, Czechia, [3]Imaging Methods Core Facility at BIOCEV, Faculty of Science, Charles University, Vestec, Czechia, [4]Department of Veterinary Sciences, Faculty of Agrobiology, Food and Natural Resources, University of Life Sciences Prague, Prague, Czechia, [5]Department of Zoology, Faculty of Science, Charles University, Prague, Czechia

Juno and CD9 protein, expressed in oolemma, are known to be essential for sperm-oocyte binding and fusion. Although evidence exists that these two proteins cooperate, their interaction has not yet been demonstrated. Here in, we present Juno and CD9 mutual localization over the surface of mouse metaphase II oocytes captured using the 3D STED super-resolution technique. The precise localization of examined proteins was identified in different compartments of oolemma such as the microvillar membrane, planar membrane between individual *microvilli*, and the membrane of *microvilli*-free region. Observed variance in localization of Juno and CD9 was confirmed by analysis of transmission and scanning electron microscopy images, which showed a significant difference in the presence of proteins between selected membrane compartments. Colocalization analysis of super-resolution images based on Pearson's correlation coefficient supported evidence of Juno and CD9 mutual position in the oolemma, which was identified by proximity ligation assay. Importantly, the interaction between Juno and CD9 was detected by co-immunoprecipitation and mass spectrometry in HEK293T/17 transfected cell line. For better understanding of experimental data, mouse Juno and CD9 3D structure were prepared by comparative homology modelling and several protein-protein flexible sidechain dockings were performed using the ClusPro server. The dynamic state of the proteins was studied in real-time at atomic level by molecular dynamics (MD) simulation. Docking and MD simulation predicted Juno-CD9 interactions and stability also suggesting an interactive mechanism. Using the multiscale approach, we detected close proximity of Juno and CD9 within microvillar oolemma however, not in the planar membrane or *microvilli*-free region. Our findings show yet unidentified Juno and CD9 interaction within the mouse oolemma protein network prior to sperm attachment. These results suggest that a Juno and CD9 interactive network could assist in primary Juno binding to sperm Izumo1 as a prerequisite to subsequent gamete membrane fusion.

KEYWORDS

oocyte, Juno, CD9, oolemma compartments, protein interaction, STED, docking, MD simulation

1 Introduction

In mammals, fertilization is characterized by a cascade of protein-protein interactions between oocyte and sperm, however, the precise molecular mechanism of gamete binding and fusion has not yet been demonstrated. In oocyte, the glycophosphatidylinositol (GPI) anchored protein Juno (Bianchi et al., 2014) and tetraspanin family member CD9 (Kaji et al., 2000; Le Naour et al., 2000; Miyado et al., 2000) were identified to be essential for mammalian fertilization. In human, Juno was also reported to interact with sperm Izumo1 (Bianchi et al., 2014), and recently was proposed to be superseded during human gamete fusion by a newly identified human oocyte receptor FcRL3, named MAIA (Vondrakova et al., 2022). Nevertheless, the role of CD9 in the membrane protein network remains unclear. Despite the close proximity between Juno and CD9 proteins in oolemma, their interaction has not been shown. The initial contact between a sperm head plasma membrane and oolemma is probably facilitated by tetraspanin proteins (Bianchi and Wright, 2020) and mediated via mutual interaction between Juno (Bianchi et al., 2014) and its sperm receptor Izumo1 (Inoue et al., 2005). Tetraspanin proteins contribute to membrane compartment organization and via *cis* interaction the multimolecular web and protein clusters are formed (Jankovičová et al., 2020) that include integrins (Ziyyat et al., 2006) or EWI proteins (Sala-Valdés et al., 2006; Runge et al., 2007; Umeda et al., 2020). Importantly, CD9 deficiency resulted in severe fertility malfunction in female mice (Kaji et al., 2000; Le Naour et al., 2000; Miyado et al., 2000) reviewed in (Bianchi and Wright, 2016) and evidence was provided, that Juno localization is abnormal in $CD9^{-/-}$ oocytes (Inoue et al., 2020). Furthermore, distribution of CD9 is not uniform within oolemma and it is expressed only on *microvilli*, where CD9 is critical for influencing their number and shape (Runge et al., 2007; Benammar et al., 2017). The CD9 crystal structure revealed a molecule of highly asymmetric cone-like shape which is believed to be responsible for the generation of membrane curvature in the crystalline lipid layers (Umeda et al., 2020). Additionally, this could explain CD9 localization in membrane compartments with high curvature such as *microvilli*. The large extracellular loop of CD9 is most likely responsible for the critical role of CD9 in sperm-oocyte fusion (Zhu et al., 2002; Umeda et al., 2020). In mouse, the oocyte surface is not homogenous, and it is distinguished to a *microvilli*-free region covering the meiotic spindle and *microvilli*-rich region which facilitates sperm binding and fusion (Shalgi and Phillips, 1980; Yanagimachi, 1994). In addition to organizing *microvilli* formation, CD9 may participate in generating fusion competent sites (Jégou et al., 2011), which is supported by the accumulation of CD9 in the intercellular contact area after mutual binding of Izumo1 and Juno (Chalbi et al., 2014). This suggests the interaction of Juno and CD9 (Chalbi et al., 2014) and possible CD9 involvement in the organization of Juno localization within oolemma regions (Bianchi and Wright, 2016; Inoue et al., 2020). The role CD9 plays is supported by its participation in compartmentalization of oolemma and by the evidence that Juno is not well expressed in *microvilli*-free regions (Inoue et al., 2020). Importantly, CD9 is also included in molecular cargo carried by extracellular vesicles of unfertilized mouse oocytes (Miyado et al., 2008). Although, partial co-localization of Juno and CD9 was observed using Airy scan super-resolution imaging, precise Juno localization in the membrane compartments of *microvilli* rich regions is not known (Mori et al., 2021).

Protein structure and protein-protein interactive interfaces provide valuable information about the function of protein networks and presents a novel approach for microscopical data. It should be noted that, to obtain protein 3D structural prediction from amino acid sequences using experimental techniques like X-ray crystallography or NMR is challenging, time consuming, expensive, and not successful with certain proteins especially transmembrane proteins (Vyas et al., 2012). In the absence of experimental protein crystal structure, computationally derived structures can be generated using comparative modeling methods, or free modeling techniques. Currently, there is no crystal structure of mouse CD9 molecule available, therefore the computer program based comparative protein structural modelling software MODELLER was used for CD9 structure prediction (Webb and Sali, 2016). Protein-protein interactions trigger the molecular mechanism of most biological processes, their prediction is important for understanding various biological events and can be carried out using ClusPro (Kozakov et al., 2017); ZDOCK (Pierce et al., 2014); HADDOCK (de Vries et al., 2010) or HexServer (Macindoe et al., 2010). The experimental Juno-CD9 results were subsequently followed by protein 3D structural modelling to study individual protein structural and functional roles in biological systems, and their mutual interactions. To better understand the protein and protein-protein orientation within the membrane, a protein-membrane model structural prediction was performed followed by protein-protein side chains docking, to recognize the Juno-CD9 interacting pose and interacting residues in their dynamic state. To reveal Juno and CD9 motion, the protein-protein MD simulation was performed to identify the interaction stability, structural deviations, and real-time secondary structure alterations in the Juno-CD9 complex.

In this study, we aimed to clarify questions regarding the proximity of Juno and CD9 and their possible interaction within the same protein network in mouse oolemma. Using 3D STED super-resolution microscopy, electron microscopy and follow-up image analysis we detected and verified Juno and CD9 colocalization in the membrane of *microvilli*. Furthermore, proximity ligation assay (PLA) identified Juno and CD9 close proximity association and co-immunoprecipitation (co-IP) followed by mass spectrometry (MS) confirmed their interaction in HEK293T/17 transfected cell line. Molecular docking, protein-membrane structural prediction, and MD simulation was used to tract protein-protein interaction, their structural position in the biological membrane, and protein conformational changes at atomic level over time. Molecular docking and protein-membrane modeling indicated the most likely biologically relevant interaction mode and MD simulation confirmed Juno-CD9 mutual interactions and the stability of their complex. It also indicated an interactive mechanism and function with respect to Juno and CD9 motion.

2 Materials and methods

2.1 Animal source and ethics approval

Inbred C57BL/6J female mice were housed in a breeding colony of the Laboratory of Reproduction, IMG animal facilities, Institute of Molecular Genetics of Czech Academy of Science. Food and water

were supplied *ad libitum*. The female mice used for all experiments were healthy 23–26 days old with no signs of stress or discomfort. All the animal procedures and experimental protocols were approved by the Animal Welfare Committee of the Czech Academy of Sciences (Animal Ethics Number 66866/2015-MZE-17214, 18 December 2015).

2.2 Oocytes collection

Female mice were hormonally stimulated with 5UI PMSG, pregnant mare serum gonadotropine (Folligon®, Intervet International B.V., Netherlands), at 15:00 (eighth hour of light cycle) on the first day of protocol. 5UI of hCG, human Chorionic Gonadotropin (CG10, Sigma-Aldrich®, MI, USA), were applied to mice at 13:00 third day of protocol (46th hour after using PMSG). After 12 h, females started ovulating. At 09:00 on the fourth day of protocol, female mice were sacrificed by cervical dislocation and both ampullas of fallopian tube were isolated and placed in preheated M2 medium (M7167, Sigma-Aldrich®). Cumulus-oocytes complex (COC) was released into M2 medium by ampulla tearing. In the next step, for releasing cumulus cells, COC was transferred into fresh 100 mL drop of M2 medium with hyaluronidase (concentration 0.1 mg/mL) (Hyase, from bovine testes, H4272, Sigma-Aldrich®), covered with high viscous paraffin oil (P14501, Carl Roth, Germany) and left in the incubator (set on 37°C, 5% CO_2) for 10 min. Followed by washing, the cumulus-free oocytes were transfer into drop of Tyrode's solution (T1788, Sigma-Aldrich®) to remove *zona pellucida*.

2.3 STED microscopy

2.3.1 Oocyte preparation

The zona-free oocytes were fixed with 3.7% paraformaldehyde (P6184, Sigma-Aldrich®) for 20 min and washed 2 × in 1% bovine serum albumin (BSA) (A-1933-25G, Sigma-Aldrich®) in PBS (phosphate-buffered saline). The oocytes were incubated overnight in 4 °C in drop of primary antibodies rat anti-CD9 (KMC8.8) (sc18869, Santa Cruz Biotechnology, Inc., TX, USA) diluted 1:50 in 1% BSA and rabbit polyclonal anti Folate receptor 4 (Juno) (abx102438, Abbexa®, UK) diluted 1:50 in 1% BSA followed by secondary antibody anti-rat IgG Abberior STAR 635P (Abberior GmbH, Germany) and anti-rabbit IgG Abberior STAR 580 diluted 1:100 in 1% BSA were incubated for 1 h in room temperature (RT) and wash 2 × in 1% BSA in PBS. The finalization of the oocyte sample preparation was proceeded by a gentle alcohol-based dehydration of the specimen followed with gradual transfer into 2,2′-Thiodiethanol (TDE) based mounting medium AD-MOUNT C (ADM-009, ADVI, Czech Republic). To preserve the fragile oocyte structure, for the mounting between cover-glass and slide we applied 150 μm thick mounting spacers AD-SEAL (ADS-18-10150-20, ADVI).

2.3.2 Oocyte capturing

The STED super-resolution acquisition of oocytes was performed on a Leica TSC SP8 STED 3X microscope equipped with a pulse white light laser (WLL2) (Light Microscopy Core Facility, IMG CAS, Prague, Czech Republic) for the excitation and a pulse 775 nm laser for emission depletion. Images were acquired as *Z*-stacks in 3D STED imaging mode with settings: HC PL APO 100×/1.4 OIL STED WHITE CS2, oil n = 1.518, pinhole 0.6 AU according to the excitation wavelength 580 nm or 640 nm, pulsed 775 nm depletion laser with 60% 3D STED, detection was on HyD in photon counting mode, emission interval 587–617 nm or 647–728 nm respectively. Super-resolution images were finalized by deconvolution using the STED option module in Huygens Professional software (Scientific Volume Imaging, NL; version 20.10). For the analysis, top and bottom segments for each oocyte were acquired (see 2.5 Colocalization analysis). For the visualization, the entire oocyte was captured.

2.3.3 Colocalization analysis of STED images

The super-resolved images of mouse oolemma top and bottom segments were segmented according to CD9 labelling. 2D sections (XY) were processed separately. We used edge detection and morphological operations to define the oocyte border and to select the first 60 layers (in pixels) starting from the envelope reaching inside toward the geometrical center of each section. The layers represented a border of 2.4 μm in thickness. Pearson's correlation coefficient between CD9 and Juno labelling was calculated for each section in the selected layers and its average value along the *Z*-direction and standard deviation was computed. The average value of Pearson's correlation coefficient was measured for 8 oocytes (a top and bottom segment for seven oocytes and only bottom for one oocyte were analyzed).

Manders' correlation coefficients were evaluated using the same segmented areas for each oolemma top and bottom segment. The threshold was set up according to the automatic threshold algorithm (default, a variation of the IsoData algorithm) in Fiji (Schindelin et al., 2012). Coefficient M1 corresponds to the green channel (Juno) over red channel (CD9) overlap, while M2 to the red channel over green channel overlap. The values represent an average value along the *Z*-direction. The difference between the overall average value of M1 *versus* M2 was evaluated by *t*-test. Before testing, the normality of data was confirmed by Anderson–Darling test. The complete procedure was programmed in MATLAB (version 2019b, The MathWorks®, Natick, MA, USA).

Further quantification of Manders' correlation coefficients in separated regions of planar membrane and microvillar regions was evaluated using Fiji software (Schindelin et al., 2012). A macro was used for automated segmentation of 40 cropped 2D regions of the oocyte, with a minimum border length of 10 μm. The macro is based on the default thresholding, skeletonization, and morphological operations to select regions corresponding to planar membrane (PlnM) or *microvilli* (MvM), with exclusion of the questionable areas below the *microvilli*. Manders' coefficients M1 (green channel (Juno) over red channel (CD9) overlap and M2 (red channel over green channel overlap) were calculated separately for PlnM and MvM, using the same threshold for all cropped oocyte regions. The Mann–Whitney test (GraphPad Prism 9.3.1) was used to analyze the differences between the coefficients, with a p-value equal or lower than 0.05 considered significant ($p \leq 0.05$*; 0.01**; 0.001***).

2.4 Electron microscopy

2.4.1 Transmission electron microscopy (TEM)

The oocytes were prepared in the same way as described above until the primary antibodies were applied. The oocytes were then labelled for 1 h at RT with 6 nm or 12 nm gold-conjugated IgG secondary antibodies (Jackson ImmunoResearch, UK): 6 nm anti-rat (112-195-167, Jackson ImmunoResearch) diluted 1:30 in 1% BSA and 12 nm anti-rabbit (111-205-144, Jackson ImmunoResearch) diluted 1:30 in 1% BSA. After a brief wash, the oocytes were fixed with 3% glutaraldehyde (16220, Electron Microscopy Sciences, PA, USA) in 1% BSA in PBS pH 7.4 for 1 h at RT and for next at least 72 h at 4°C. The samples were cold-PBS washed 3 × 15 min at RT, post-fixed with 1% aqueous osmium tetroxide (#19152, Electron Microscopy Sciences) for 1 h at 4°C, washed with cold-PBS, embedded in 2% low-melting agarose type II (#17856, Thermo Fisher Scientific, MA, USA) and dehydrated with cold ethanol series on ice for 2–5 min. Final alcohol dehydration was done twice using acetone-anhydride for 5 min and samples were infiltrated using Epon EMbed-812 resin (#14120, Electron Microscopy Sciences) at ratios 1:2, 1:1, and 2:1 with acetone for 5–30 min. After final infiltration the samples were polymerized at +60°C for 72 h. Using ultramicrotome (Leica EM UC7, Leica Microsystems, Germany) the samples were cut to 80 nm thick sections, collected onto copper-grids (Electron Microscopy Sciences), post-contrasted with 4% aqueous uranyl acetate (#2400, Electron Microscopy Sciences) for 1 h at RT and carbon-coated. Prepared samples were imaged at 120 kV using transmission electron microscope Jeol JEM 2100-Plus by the TEM center imaging software (Imaging Methods Core Facility, BIOCEV, Vestec, Czech Republic).

2.4.2 Scanning electron microscopy (SEM)

For SEM, the samples were primarily fixed as described for TEM method. After three washing steps (15 min each) in buffer, the cells were fixed by buffered 1% osmium tetroxide for 1 h at 4°C and dehydrated with cold ethanol series (80–90–96%) for 2 min at RT each step. Ethanol was then replaced 1:1 with cold acetone for 5 min and finally, the anhydrous acetone was applied for 5 min before placing the samples into a Critical Point Dryer device (Leica EM CPD300). Samples were mounted on aluminum SEM stubs using carbon tape and sputter-coated in high-vacuum coater (Leica EM ACE600) with 4 nm of platinum. High-resolution images were obtained at accelerated voltage 1 kV and 0.1 nA using TLD detector operated in SE mode (FEI Helios NanoLab 660 G3 UC) (Imaging Methods Core Facility, BIOCEV, Vestec, Czech Republic).

2.4.3 Electron microscopy image analysis

Fiji software (Schindelin et al., 2012) was used for quantification of the gold particles number per length of planar and microvillar membrane from TEM images. The average value was manually calculated from 10 cropped images of immunolabelled oocyte, where number (n) of particles per microvillar/planar membrane length (L) measured in nm was counted. With exclusion of the questionable areas below the *microvilli*, differences in the (n) of particles per microvillar/planar membrane length were analyzed using Mann–Whitney test (GraphPad Prism 9.3.1). *p*-value equal or lower 0.05 was considered to be significant ($p \leq 0.05$*; 0.01**; 0.001***).

2.5 Proximity ligation assay

To detect the close proximity of proteins Juno and CD9, Proximity Ligation Assay (PLA)–Duolink *In Situ* Red Starter Kit, DUO92101 (Sigma-Aldrich®) was used as was described previously (Vondrakova et al., 2022). Fixed zona-free mouse mature oocytes (MII) were incubated overnight in 4°C with selected pair of primary antibodies: 1) experimental group: rat monoclonal anti CD9 (KMC8.8) (sc18869, Santa Cruz Biotechnology, Inc.) diluted 1:50 in 1% BSA and rabbit polyclonal anti Folate receptor 4 (Juno) (abx102438, Abbexa®, UK) diluted 1:50 in 1% BSA; 2) positive control–proteins with known interaction: mouse monoclonal anti-α tubulin diluted 1:1000 in 1% BSA (TU02) (sc8035, Santa Cruz Biotechnology) and rabbit polyclonal anti-β tubulin diluted 1:1000 in 1% BSA (ab15568, Abcam, UK); 3) negative control–protein with known absence of interaction: anti-α tubulin and rat monoclonal anti-CD9 (KMC8.8) diluted 1:50 in 1% BSA. Washed oocytes were incubated with PLUS and MINUS PLA probes and amplified following the manufacturer's protocol and transferred into 2 µL of VECTASHIELD Mounting Medium. Fluorescence was detected with a confocal microscope (Carl Zeiss LSM 880 NLO) (Imaging Methods Core Facility, BIOCEV, Vestec, Czech Republic).

2.6 Detection of Juno and CD9 protein complex in HEK293T/17 cell line

2.6.1 Co-transfection of HEK293T/17 cells

HEK293T/17 cells were seeded 24 h before transfection on cover slips placed in 60 mm-cultivation dishes. When cells reached 70–80% of confluence, they were co-transfected by 3 µg of mouse CD9-GFP plasmid DNA (MG226288, Origene, MD, USA) and 3 µg of mouse Juno plasmid DNA (MC207552, Origene) and left for 16 h in DMEM cultivation medium with 10% of FBS without antibiotics. Alternatively, HEK293T/17 cells were transfected only by 3 µg of mouse Juno plasmid DNA for control immunoprecipitation. The fluorescent signal of CD9-GFP transfected cells were visualized under the fluorescent microscope (Olympus CKX41, Olympus Corporation, Japan) using 20× objective. Cells were washed in ice-cold PBS buffer three times and lysed in non-reducing (2x) SDS (sodium dodecyl sulfate) lysis buffer for WB; and in lysis buffer, 1% CHAPS (Sigma-Aldrich®) in 30 mM Tris-HCl (pH 7.5) for co-immunoprecipitation. The sample without transfection (p−/−) was used as a negative control.

2.6.2 Co-immunoprecipitation and Western blotting (WB) for Juno detection

Co-transfected/Juno transfected cell lysates were centrifuged 15,000 × g for 15 min 4°C, supernatants were incubated with magnetic beads (Dynabeads Protein G Immunoprecipitation kit, 10003D, Invitrogen, MA, USA) conjugated with rabbit polyclonal anti-GFP primary antibody (ab290, Abcam) overnight at 4°C on a rocking platform. Precipitated protein complex was eluted from immunobeads by elution buffer of Dynabeads kit (Dynabeads Protein G Immunoprecipitation kit, 10003D, Invitrogen, MA, USA), and then incubated with the reducing sample buffer for 5 min at 70°C. Protein lysates for WB were quantified using a

NanoDrop 3000 spectrophotometer (Thermo Fisher Scientific, MA USA). Firstly, electrophoretic separation in 10% polyacrylamide gel was performed. Molecular mass was estimated with Prestained Precision Plus Protein Dual Color Standards (Bio-Rad, CA, USA). Tris-glycine buffer (pH 9.6) with 20% methanol was used for transfer of proteins onto a polyvinylidene difluoride (PVDF) membrane (Immobilon-P, Millipore, Germany). The electroblotting carried out for 1 h at 500 mA. PVDF membrane was blocked with 5% dry milk (Bio-Rad) in PBS-Tween. The targeted Juno protein from co-transfected (pJuno/pCD9-GFP) cell lysate, Juno transfected cells (pJuno/–), anti-GFP precipitate (pJuno/–) and precipitated Juno-CD9 complex (pJuno/pCD9-GFP) was detected by rabbit polyclonal anti-mFOLR4 (Juno) antibody (abx102438, Abbexa) diluted 1:500 in 5% low-fat milk. For control detection, rabbit polyclonal anti-GFP primary antibody in lysate from Juno transfected cells (pJuno/–) was used. After washing and incubation with secondary anti-rabbit IgG antibody conjugated with horseradish peroxidase (Bio-Rad) diluted 1:3000 in 5% milk, the protein signal was visualized using the SuperSignal Chemiluminescence Substrate (ThermoFisher Scientific) by the Azure c600 imaging system (Azure Biosystems, Inc., CA, USA).

2.6.3 Mass spectrometry (MS) analysis

Co-immunoprecipitates were digested on the beads by trypsin. After O/N digestion at 37°C, samples were analyzed using a liquid chromatography system Agilent 1200 (Agilent Technologies) connected to the timsToF Pro PASEF mass spectrometer equipped with Captive spray (Bruker Daltonics). Mass spectrometer was operated in a positive data-dependent mode. Five microliters of peptide mixture were injected by autosampler on the C18 trap column (UHPLC Fully Porous Polar C18 0.3 × 20 mm, Phenomenex). After 5 min of trapping at a flow rate of 20 µL/min, peptides were eluted from the trap column and separated on a C18 column (Luna Omega 3 µm Polar C18 100 Å, 150 × 0.3 mm, Phenomenex) by a linear 35 min water-acetonitrile gradient from 5% (v/v) to 35% (v/v) acetonitrile at a flow rate of 4 µL/min. The trap and analytical columns were both heated to 50°C. Parameters from the standard proteomics PASEF method were used to set timsTOF Pro. The target intensity per individual PASEF precursor was set to 6000, and the intensity threshold was set to 1500. The scan range was set between 0.6 and 1.6 V s/cm^2 with a ramp time of 100 ms. The number of PASEF MS/MS scans was 10. Precursor ions in the m/z range between 100 and 1700 with charge states ≥2+ and ≤6+ were selected for fragmentation. The active exclusion was enabled for 0.4 min.

The raw data were processed by PeaksStudio 10.0 software (Bioinformatics Solutions, Canada). The search parameters were set as follows: enzyme–trypsin (specific), carbamidomethylation as a fixed modification, oxidation of methionine and acetylation of protein N-terminus as variable modifications. The data were search against the *Mus musculus* database (Uniprot 12/2022).

2.7 CD9 structure prediction with homology modeling and structural comparison

Freely available MODELLER 9.25 software and python-based advanced scripting was used for generating the 3D structure of mouse CD9. Comparative structure prediction is divided into four steps. 1) Fold assignment for comparative modelling: one or more templates with a known sequence and 3D structure were identified for the modelling initiation. For known structure identification and assignment the BLASTp and Protein Data Bank curation was used. In the final stage of this fold assignment, a step profile was built by using build profile python scripting based on our query protein fasta sequence. 2) The sequence structure alignment: a target CD9 structure was aligned with the previously identified template structure with the help of another python script. This script reads the template PDB structures and the CD9 target sequence and performs the alignment; in the output, two different files ".ali" and ".pap" are generated. 3) Model python building: a script uses MODELLER's auto model class was used to generate models, and each model was assessed with the normalized discrete optimized protein energy (DOPE) assessment method. 4) Evaluation: based on energy profile with the best DOPE score generated models were evaluated by using energy profile python script (Webb and Sali, 2016). The generated structures side chain was corrected with the help of the WHAT IF server (Vriend, 1990) and the quality of the structure was assessed using the PROCHECK server (Laskowski et al., 1993). This work used FASTA sequence of mouse CD9 that was retrieved from the NCBI data bank with accession number AAH70474. The used protein templates for MODELLER were, 6K4J, 5TCX, 6RLR, 6Z1V. The predicted structure was compared with AlphaFold predicted CD9 structure (accession number P40240). Furthermore, the MODELLER predicted structure was compared with Human CD9 (PDB id 6K4J) structure to assess their probable structural and functional similarity.

2.8 Protein-membrane modeling, protein-protein docking, visualization, and analysis

The protein-membrane model was prepared using CHARMM-GUI Membrane Builder online module (Lee et al., 2019). The protein-protein docking for mouse CD9-Juno, mouse Izumo1-Juno protein-protein interaction pose prediction was carried out using the ClusPro server (Kozakov et al., 2017) and interaction site prediction, analysis, and visualisation was carried out in Chimera 1.16. In this study protein crystal structures were depicted from RCSB Protein Data Bank, for mouse Juno crystal structure ID number 5JYJ, for mouse Izumo1 crystal structure ID number 5B5K, human Izumo1-Juno complex crystal structure ID number 5F4E were used.

All structures were visualized and hydrogen bonding between protein-protein structures were analyzed using a graphical user interference (GUI) based Chimera program.

2.9 Molecular dynamics simulation

Molecular Dynamics Simulations were used to understand the conformational motion of protein over time at atomic level. Furthermore, MD simulation processes help to understand protein motion over the time as well as their conformational changes to help interpret protein function. The MD simulation process is divided into several steps followed by protein topology

formation, simulation box formation, and solvent addition (water in this case); ion addition for neutralizing the protein charge; energy minimization using energy minimization MD run in the steepest descent method; equilibration through position restraints and ensembles, and a final MD simulation run.

In this study MD simulations were performed at 300 K using the GROMACS 2020.1 software package in an Ubuntu Linux system by using an OPLS-All Atom force field. The whole system was packed in a cubic water box with a dimension of 10 Å by using the GROMACS gmx editconf module to set up the boundary conditions and GROMACS gmx solvate module for solvation.

Furthermore, the simulation systems were then packed in a simulation box using a SPC216 water model. For neutralizing the simulation system Na^+ and Cl^- ions were added in the system box and the physiological system was maintained (0.15 M) using the GROMACS gmx genion module. The steepest descents method was used for energy minimization. The maximum step size along a 0.01 nm gradient with a maximum of 50,000 steps. Furthermore, the simulation system was equilibrated at a constant temperature of 300 K (= ~27°C), by using an NVT and 100 ps NPT ensemble process. Firstly, a modified Berendsen thermostat with no pressure coupling was applied for NVT (constant number of particles, volume and temperature) canonical ensemble, and then the Parinello–Rahman method pressure of 1 bar (P) was applied the NPT ensemble (constant number of particles, pressure, and temperature). The final simulations were performed for each system for 10 ns where a leap-frog integrator was applied to the trajectories time evolution of the simulation trajectories (Sur et al., 2022). A series of simulation processes were performed for MODELLER predicted CD9, AlphaFold depicted CD9, Juno, and CD9-Juno.

3 Results

3.1 The interaction of Juno and CD9 within oolemma

To address the mutual relationship of Juno and CD9 in oolemma of mouse oocyte, we first employed 3D STED super-resolution microscopy followed by colocalization analysis. In order to use 3D STED microscopy for capturing the entire volume of the oocyte, the optimization of the standard labelling procedure was necessary (Frolikova et al., 2023). The advanced protocol enabled us to achieve maximal lateral resolution near 70 nm and distinguished individual *microvilli* on oocyte surface. The optimization of the protocol resulted in the ability to capture the entire oocyte surface (Figure 1A–C; Figures 2A, B; Supplementary Videos S1, S2) and study the proteins of interest in the context of different oolemma compartments (Figures 1D–I; Figures 2C–F), namely, *microvilli* and *microvilli*-free regions across the whole oocyte measuring 80 µm in diameter. Our results of the entire oocyte surface imaging indicated that both Juno and CD9 proteins are located in the same surface structures within the *microvilli*-rich region of the oocyte (Figures 1A–C, Figure 2A). Using our antibodies, we also detected a low protein expression of Juno within the *microvilli*-free region in comparison to CD9 which was absent (Figures 1A–F). We performed a control by imaging oocytes labeled with antibodies against individual proteins using 3D STED (Supplementary Figure S1), to ensure that the localization of detected proteins was not influenced by artifacts. The results confirmed that the dual immunofluorescence labelling did not modify detected protein localization. Also, in the absence of primary antibodies, there was no detected signal given by secondary antibodies (Supplementary Figure S2).

In order to analyze in detail Juno-CD9 protein localization within oolemma *microvilli* (Figures 2A, B), we captured two segments of 2.4 µm in thickness (Figure 2C) as described in (Frolikova et al., 2023). In our study, we employ the terminologies "top" and "bottom" for these segments, to designate distinct sides of the oocyte. Specifically, the term "bottom" denotes the region of the oocyte that is situated in closest proximity to the microscope objective and the coverslip, while the term "top" refers to the opposing side of the oocyte, which is farthest from the coverslip. It should be noted that these designations are exclusively employed to convey the orientation of the oocyte relative to the microscope objective, and do not pertain to any inherent characteristics of the oocyte. These 3D STED obtained data were used for follow-up image analysis. The algorithm in MATLAB software (see 2. Materials and Methods) was developed for the evaluation of Juno and CD9 mutual position and the average value of Pearson's correlation coefficient was measured for 8 oocytes (a top and bottom segment for 7 oocytes and only bottom for 1 oocyte were analyzed). The resulting average value of Pearson's correlation coefficient was 0.67 ± 0.06 indicating mutual colocalization of the proteins of our interest. Based on Pearson's correlation coefficient between Juno and CD9 labeling, the representative colocalization map was prepared using Imaris software (Figures 2C–F, F′; Supplementary Video S2). The results of this analysis provided evidence for the mutual proximity and potential existence of Juno and CD9 association.

Based on results of the colocalization analysis, the existence of Juno and CD9 association was subsequently investigated. PLA (Alam, 2018) was employed to detect association of Juno and CD9 in mouse oolemma (Figure 3). The PLA demonstrated a robust dotted signal in an experimental group of oocytes when primary antibodies against Juno and CD9 were used (Figure 3A; Supplementary Figures S3). As a positive control the interaction between α and β tubulin was used and the strongest signal was detected in the peri-chromosomal region. In contrast, hardly any signal was detected in a group considered as a negative control, when primary antibodies against α tubulin and CD9 were used, as these two proteins are not predicted to interact (Figure 3C). Given that PLA has been previously reported as a highly sensitive and specific powerful method for detecting protein-protein interactions *in situ* (Alam, 2018), and based on our results, we conclude to detect a potential interaction between Juno and CD9.

To further address Juno-CD9 interactions the HEK293T/17 cells were co-transfected by a mouse Juno plasmid and the CD9 plasmid with a GFP-tag for protein visualization (Figure 4A) and mouse Juno protein expression in transfected HEK293T/17 cells was confirmed by immunodetection with antibody in cell lysate (Figure 4B). The Juno-CD9 complex was precipitated via GFP-tag on CD9 using anti-GFP antibody. Although the Juno detection was partially masked by the light chain of the antibody used for immunoprecipitation, Juno antibody labeled the band of approximately 28 kDa, which was not visible in the non-transfected (p−/−) cell lysate (Figure 4C). For confirmation, the Juno-CD9 complex bound on the immunobeads

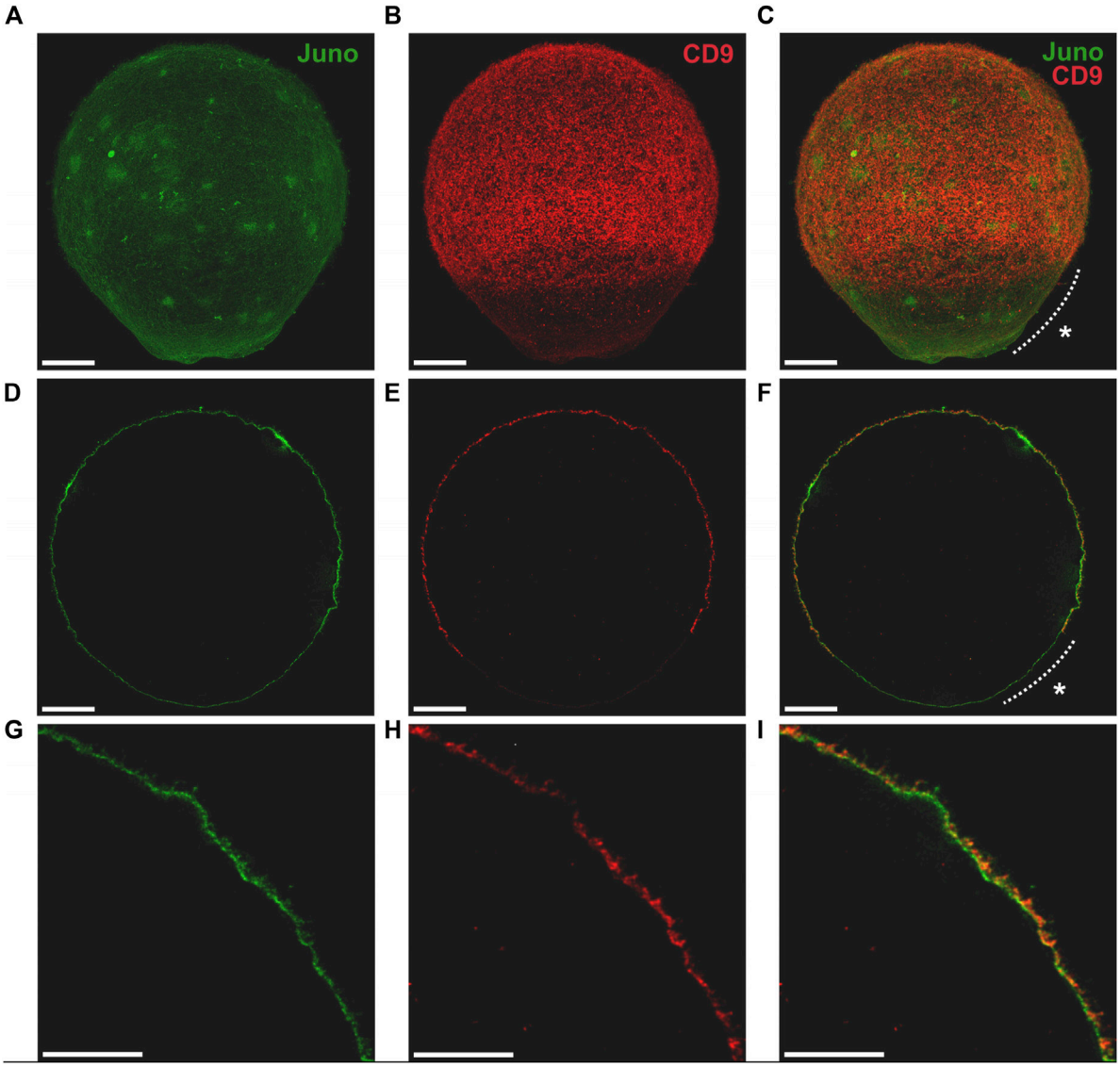

FIGURE 1
Visualization of Juno and CD9 localization in oolemma captured by 3D STED. Imaging of Juno (green) and CD9 (red) in oolemma **(A–C)** in whole oocyte surface visualized by maximal intensity projection, **(D–F)** in one plane and **(G–I)** in selected area of one plane. The asterisk (*) indicates *microvilli*-free region. Scale bar represents 10 μm **(A–F)**, 5 μm **(G–I)**. For more details see Supplementary Video S1.

was subjected to MS analysis (Figure 4D, raw data files Table 1 MS_IP; Table 2 MS_IP control; https://biobox.biocev.org/index.php/s/4NCxYE2ckAJ4eCP), which confirmed the presence of both proteins. GFP-tag immunoprecipitation specificity was confirmed by investigation of Juno protein in the anti-GFP immunoprecipitate and negative detection of Juno protein in Juno transfected (pJuno/–) cell lysate with GFP antibody (Figure 4E).

3.2 Nanoscale resolution of Juno and CD9 localization in *microvilli* rich compartments

Although Juno and CD9 was previously reported to be present in oolemma (Kaji et al., 2000; Le Naour et al., 2000; Miyado et al., 2000; Bianchi et al., 2014) the accurate localization of Juno in distinct compartments of the oolemma has not been identified. It is crucial to understand, that the membrane, which forms the *microvilli*-rich region consists of two distinct compartments, such as microvillar membrane (MvM) and planar membrane between individual *microvilli* (PlnM).

We combined indirect immunodetection captured by 3D STED super-resolution microscopy and electron microscopy (Figure 5) to determine mutual localization of Juno and CD9 in different *microvilli*-rich membrane compartments in nanoscale resolution. Firstly, 3D STED super-resolution microscopy for imaging of the whole oocyte surface enabled us to visualize the oolemma in such fine details (approximately 70 nm) that *microvilli* can be distinguished (Figure 5A) and is comparable to SEM (Figure 5B). While Juno-corresponding homogenous signal was localized in both

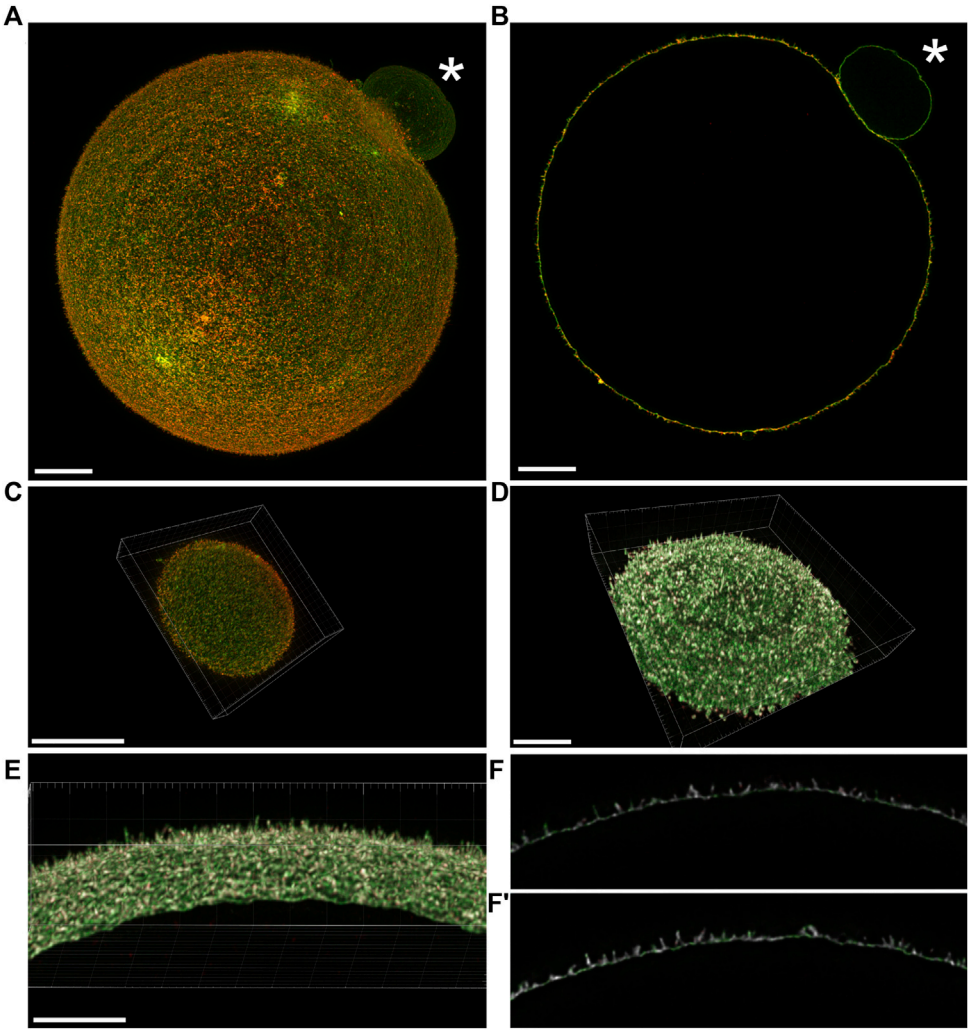

FIGURE 2
Visualization of the mutual position of Juno and CD9 in super-resolution images captured by 3D STED. **(A)** Imaging of Juno (green) and CD9 (red) in oolemma in whole oocyte surface visualized by maximal intensity projection and **(B)** in one plane. **(C)** A top and bottom segment of oocyte was captured for analysis of Juno and CD9 mutual localization within oolemma. **(D–F′)** The representative image analyzed by Imaris software shows the colocalization area (white) of the studied proteins in a top and bottom segment **(D)**, in selected area of oolemma **(E)** and in an individual plane **(F,F′)**. The asterisk (*) indicates polar body. Scale bar represents 10 μm **(A–D)**, 5 μm **(E)**. For details see Supplementary Videos S2, S3.

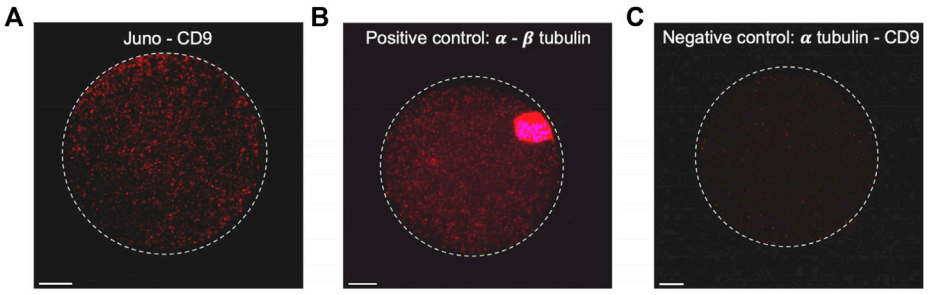

FIGURE 3
Study of close proximity of Juno and CD9 in mouse oocyte oolemma by PLA. **(A)** The presence of positive signal (red dots) on the sample stained by Juno and CD9 and visualized by maximal intensity projection, confirmed the existence of their close proximity, **(B)** α and β tubulin-stained sample was used as a positive control of the method. **(C)** Combination of α tubulin and CD9 staining was used as a negative control. Chromosomes are visualized with Dapi (blue). Scale bar represents 10 μm.

10.3389/fcell.2023.1110681

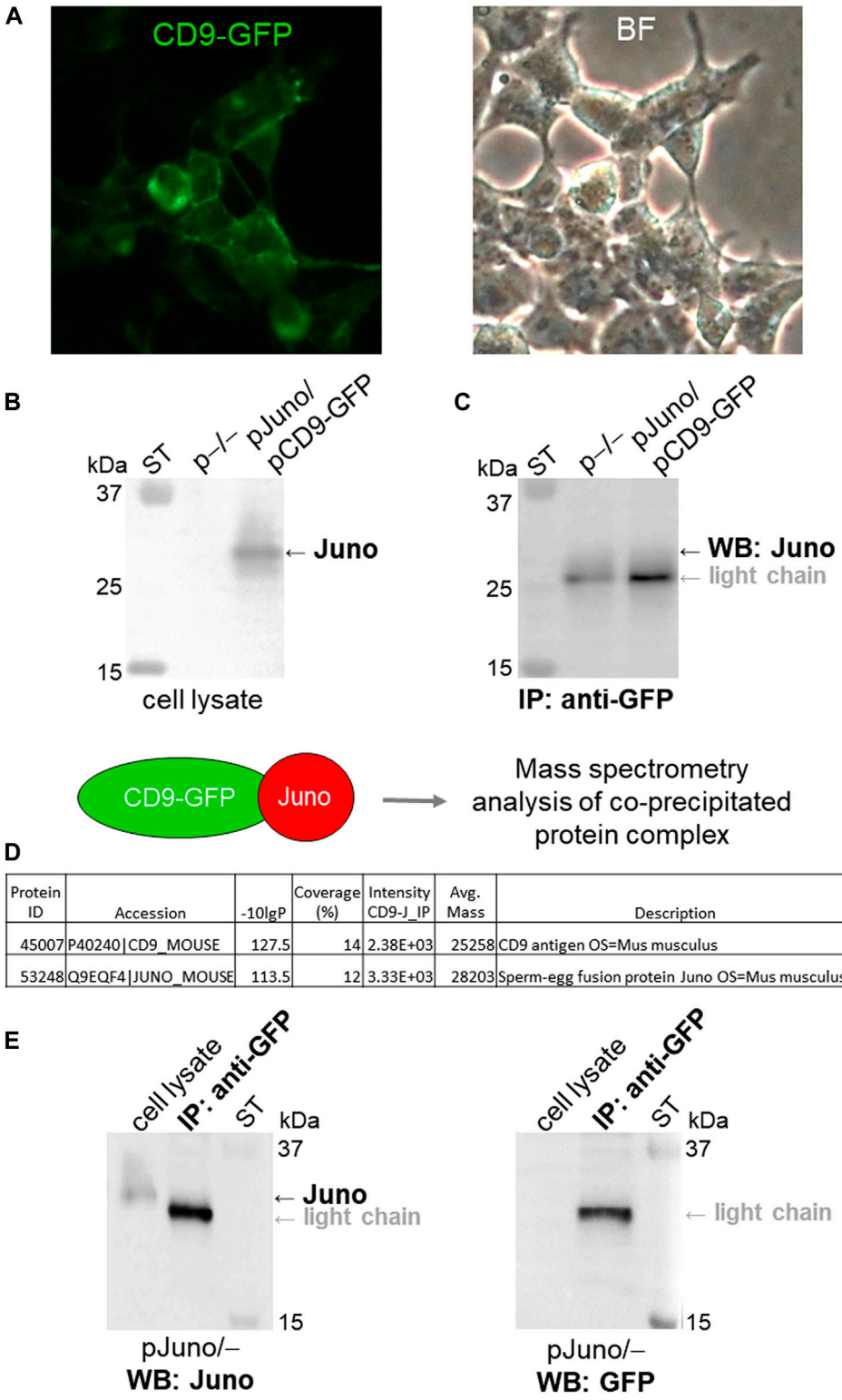

Protein ID	Accession	-10lgP	Coverage (%)	Intensity CD9-J_IP	Avg. Mass	Description
45007	P40240|CD9_MOUSE	127.5	14	2.38E+03	25258	CD9 antigen OS=Mus musculus
53248	Q9EQF4|JUNO_MOUSE	113.5	12	3.33E+03	28203	Sperm-egg fusion protein Juno OS=Mus musculus

FIGURE 4
Analysis of Juno-CD9 protein-protein interaction via co-immunoprecipitation and MS. **(A)** HEK293T/17 cells were co-transfected with Juno and CD9-GFP mouse plasmids (pJuno/pCD9-GFP). CD9 protein was visualized in the cell membrane immediately after transfection via fluorescent GFP-tag (green); BF (bright field). **(B)** Juno protein expression was confirmed by WB and visualized by anti-Juno antibody. **(C)** Juno-CD9 complex was precipitated via GFP-tag on CD9 using anti-GFP antibody. CD9-bound target protein Juno was detected by using WB analysis with anti-Juno antibody (~28 kDa); ST–molecular standards. **(D)** Schematic figure depicting MS analysis of the protein complex, which was bound to immunobeads. Database-search algorithms (bioinformatics) were used to identify specific proteins based on their mass spectra; see raw data files Table 1 MS_IP; Table 2 MS_IP control; https://biobox.biocev.org/index.php/s/4NCxYE2ckAJ4eCP). For both WB and MS the non-transfected HEK293T/17 cells were used as a negative control (p−/−), and neither CD9 nor Juno was detected and identified. **(E)** As a control for GFP-tag antibody specificity, the Juno and GFP antibody detection was performed in the anti-GFP immunoprecipitate (IP) and in Juno transfected cell lysate (pJuno/−), respectively; ST–molecular standards.

10.3389/fcell.2023.1110681

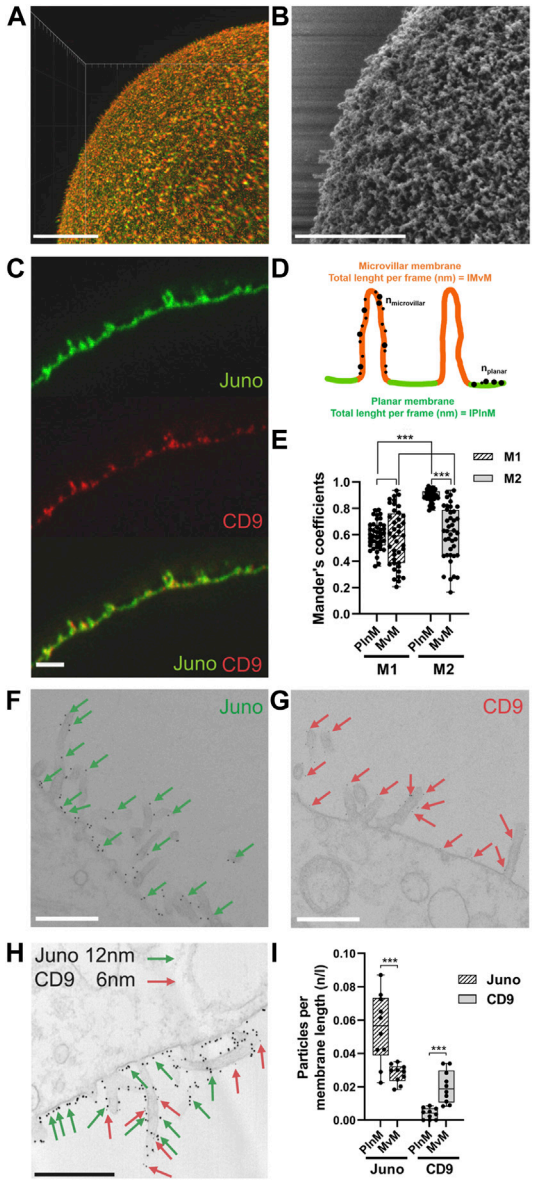

FIGURE 5
Localization of Juno and CD9 in MvM and PlnM compartments of *microvilli*-rich oolemma. **(A)** STED microscopy visualization of *microvilli* **(B)** SEM visualization of *microvilli*. **(C)** STED imaging revealed differences in Juno (green) and CD9 (red) localization within MvM and PlnM compartments of oolemma. **(D)** Scheme represents dividing the individual oolemma compartments for image analyzis of STED and TEM data. **(E)** Comparison of the localization of Juno and CD9 in MvM and PlnM separately in the segmented regions of oolemma shows significant difference between Meander's coefficient 1 (M1) and Meander's coefficient 2 (M2) in PlnM and significant difference in Meander's coefficient 2 (M2) between MvM and PlnM regions. **(F–H)** Juno and CD9 differences captured by TEM, Juno (green arrows) was present in both MvM and PlnM in contrast to CD9 (red arrows) which was mainly detected in MvM. **(I)** TEM image analysis confirmed significant differences in localization Juno and CD9 both between MvM and PlnM compartments. Scale bar represents 10 µm **(A)**, 1 µm **(C)** 500 nm **(B,F–H)**. *p*-value equal or lower 0.05 was considered to be significant ($p \leq 0.001$***). n–number of golden particles, l–total length per frame (nm), n/l–number of particles on total length per frame.

MvM and PlnM compartments, CD9 localization was concentrated mainly in MvM (Figure 5C). For evaluation and quantification of these differences in Juno and CD9 localization, image analysis based on Manders' correlation coefficients was used. The individual parts of the membrane used for analysis are illustrated in the scheme presented in Figure 5D. The average value of Manders' correlation coefficient was measured for 8 oocytes (a top and bottom segment for 7 oocytes and only bottom for 1 oocyte were analyzed). The resulting value for coefficient M1 corresponding to Juno signal over CD9 signal overlap was 0.68 ± 0.13, while the value for coefficient M2 corresponding to CD9 signal over Juno signal overlap was 0.82 ± 0.10. These results could be interpreted that CD9 has the same localization as Juno more frequently, than Juno with CD9 and indirectly confirmed the 3D STED imaging-based observation. To compare the localization of Juno and CD9 in MvM and PlnM separately, we analyzed the Manders' coefficients in the segmented regions of the oolemma sections. The differences in M1 and M2 in both regions were quantified (Figure 5E). There was no significant difference in M1 when comparing PlnM *versus* MvM, however, there was a significant difference ($p \leq 0.001$) in M2 between these two regions. Also, the resulting value of coefficient M1 showed a statistically significant difference from M2 in PlnM ($p \leq 0.001$), indicating that CD9 has the same localization as Juno more frequently than *vice versa*, while showing no significant difference between the coefficients in MvM.

These findings correspond with the results from transmission electron microscopy (TEM), where the data showed that Juno is localized in both oolemma compartments (MvM and PlnM), while CD9 is preferentially localized in MvM. Subsequently, the differences in microvillar membrane compartment localization of Juno and CD9, visualized by TEM (Figures 5F–H) were quantified (Figure 5I). The quantification showed statistically significant differences in expression of studied protein between MvM and PlnM. Data showed that higher expression of Juno was detected in PlnM compared to MvM ($p \leq 0.001$) and confirmed the higher expression of CD9 ($p \leq 0.001$) in MvM compared to PlnM.

The results suggest that although there exist differences in expression of Juno and CD9 between MvM and PlnM compartments, both proteins are expressed in the MvM part of oolemma. This finding suggests that Juno-CD9 could assist during primary sperm-oocyte binding in MvM prior to gamete membrane fusion.

3.3 CD9 structure prediction with homology modeling

The mouse Juno crystal structure was obtained from the RCSB protein data bank. Due to the unavailability of the mouse CD9 crystal structure, the CD9 structure was predicted using a python algorithm-based MODELLER. The primary amino acid sequence of mouse CD9 was used for BLASTp analysis and close PDB hit finding. The BLASTp PDB search showed that mouse CD9 has the highest sequence similarity with human CD9 protein (PDB id 6K4J), and human tetraspanin CD81 (PDB id 5TCX). The best matched PDB structures were selected as a template for mouse

10.3389/fcell.2023.1110681

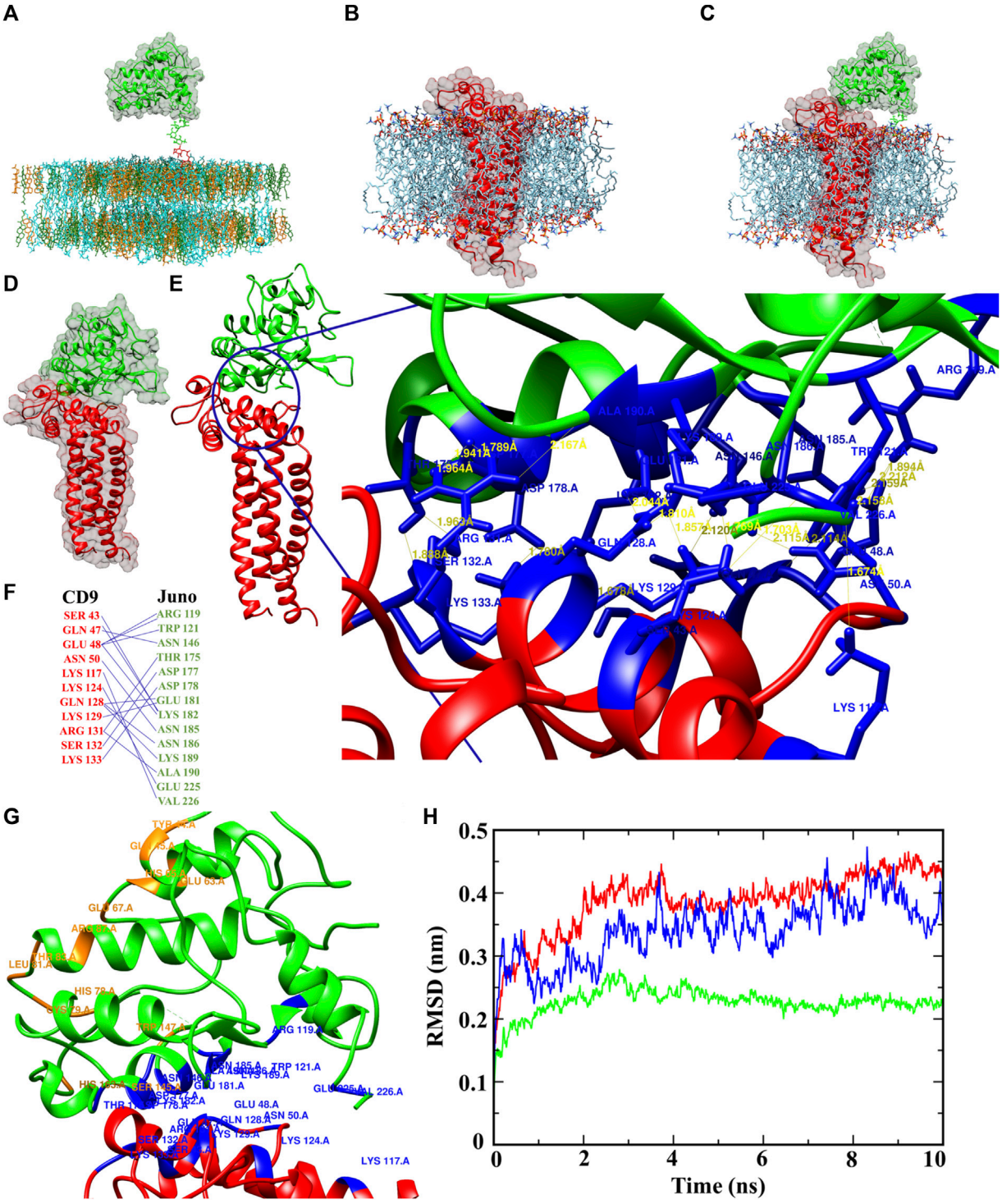

FIGURE 6
Juno-CD9 interactive model within the oocyte oolemma. **(A–C)** Biologically relevant position of Juno and CD9, shown by interacting pose in the membrane model for **(A)** Juno, **(B)** CD9, **(C)** Juno-CD9 prepared in CHARMM-GUI. **(D)** Energetically adequate and biologically most favorable and significant docked pose of Juno-CD9. **(E)** Interacting amino acids of Juno and CD9, where 26 hydrogen bonds were formed between Juno and CD9, and the distances between donor hydrogen and acceptor can be seen. **(F)** Responsible amino acids from Juno and CD9 responsible for hydrogen bonds formation and Juno-CD9 complex formations. **(G)** Juno-CD9 docked pose, where blue marked residues from Juno and CD9 are interacting for making the complex, whereas the orange residues were identified (either by docking or human Izumo1-Juno crystal analysis) for interacting with Izumo1. **(H)** RMSD plot for Juno (green), CD9 (red), and Juno and CD9 complex (blue). Based on RMSD analysis, Juno maintain the highest level of stability around 2.2 Å, CD9 showed highest deviation around 5.5 Å, whereas Juno and CD9 complex displayed deviation, 3.6 Å, in the middle between CD9 and Juno readings. The Juno-CD9 complex was reflected by highly stable conformation during the MD simulation which indicated a stable biological relevant structural conformation of Juno and CD9 complex.

CD9 3D structure prediction through homology modelling. Homology modelling with MODELLER was used to prepare several 3D models of mouse CD9. Based on their lowest DOPE score (−25904.08203) the best fit model was selected (Supplementary Figure S4). The model was additionally used for missing side chain building and quality assessment through the What If and PROCHECK servers. The PROCHECK server assessment allowed us to achieve an overall structural quality of 92%, and a Ramachandran plot (Supplementary Figure S5). The results of a comparison study between the predicted structures of CD9 by MODELLER and AlphaFold indicate a high degree of structural similarity, with a calculated similarity score of 98.17% (Supplementary Figure S6). The results of a comparison study between the structures of mouse CD9 and human CD9 (PDB id 6K4J) showed a high degree of sequence identity between these proteins, specifically 87.61% of their amino acid sequences are identical. Additionally, a Blast search revealed that mouse CD9 possesses 89.04% amino acid sequence identity with 100% query coverage (Supplementary Figures S7, S8).

3.4 Protein-membrane modeling, protein-protein docking, visualization and analysis

The protein-membrane model gives the relevant location of the protein in the membrane and position of the transmembrane regions. The protein-membrane model was prepared to visualize Juno and CD9 position within a membrane lipid bilayer (simulating oolemma) to recognize their possible interacting mode. GPI anchored Juno (Figure 6A), tetraspanin CD9 (Figure 6B), and Juno and CD9 potential interaction (Figure 6C) were predicted by a Dioleoyl phosphatidylcholine (DOPC) membrane model. The most favorable interaction complexes using the ClusPro server with a PIPER algorithm were ranked according to the lowest free energy and were grouped based on protein-protein interaction features. The scored best fit and biologically relevant structural position of Juno and CD9 docked model was visualized and analyzed by Chimera 1.16 (Figure 6D) where interaction of Juno in close proximity to CD9 was detected. Furthermore, the intramolecular hydrogen bonds between the protein molecules were analyzed. The docking analysis revealed 21 (Supplementary Table S1) specific hydrogen bond network formed between 14 amino acid residues of Juno and 11 amino acid residues of CD9 in the Juno-CD9 complexes. Intermolecular hydrogen bond analysis through the Chimera 1.16 platform revealed that most of the donor-acceptor distances were within the ideal distance parameters of 2.7–3.0 Å (Supplementary Table S1) (Harris and Mildvan, 1999). This indicated hydrogen bond formation and Juno-CD9 complex establishment. The bond distances (between a hydrogen donor and acceptor) indicated energetically favorable Juno and CD9 interacting mode (Figures 6E, F and Supplementary Table S1). Salt bridges could also play a role in proteins' complex formation, however, docking analysis did not reveal the presence of salt bridges between the proteins of interest. This could be interpreted as, salt bridges do not play a role in the Juno-CD9 complex formation. This study has suggested that the amino acid residues responsible for Juno interaction with Izumo1 may remain free to interact with Izumo1 even during the Juno-CD9 complex. To explore this possibility, two different sets of approaches were taken.

The first approach involved docking of mouse Izumo1-Juno complexes, showing the probability of Juno residues responsible for the interaction with CD9 in mouse marked in red; residues in yellow from mouse Juno are responsible for the interaction with mouse Izumo1; residues in magenta from mouse Izumo1 are responsible for interaction with mouse Juno (Supplementary Figure S9A and Supplementary Table S2). Our findings predicted that the amino acid residues of mouse Juno responsible for interaction with CD9 and Izumo1 were distinct and did not interfere with each other (Supplementary Figure S9A and Supplementary Tables S1, S2). These findings provide further support for the hypothesis that the amino acid residues involved in mouse Juno-Izumo1 interaction are likely to remain open during the mouse Juno-CD9 complex and available to bind Izumo1 protein. Mouse Izumo1-Juno docked complex was found to involve six residues of Juno interacting with eight residues of Izumo1, forming a robust network of 11 hydrogen bonds (Supplementary Figure S9B and Supplementary Table S2).

Further, the comparison of the previously published human Juno-Izumo co-crystal structure (PDB id 5F4E) revealed 11 amino acid residues that are involved in the interaction between Juno and Izumo1, as shown in Supplementary Figure S10A. Importantly, the result of our docking study showed that five of these residues in mouse Juno involved in Izumo1 interaction were identical with the amino acid residues involved in Juno-Izumo1 binding interface in the human crystal structure (Supplementary Figure S10B marked in yellow). These five residues were shown to remain empty during mouse Juno-CD9 interaction and could be predicted to remain available for mouse Juno-Izumo1 binding. These findings may suggest that specific amino acid residues in mouse Juno may play a critical role in binding to Izumo1 and provide further evidence to support the hypothesis that these residues are not involved in the Juno-CD9 interaction. Our data showed that all the amino acid residues in mouse Juno that could be involved in Izumo1 binding (based on either by docking or human Juno-Izumo1 interaction analysis, marked orange) did not overlap with the residues interacting with mouse CD9 (Supplementary Figure S10, marked red). These findings are supported by results showing that the amino acid residues responsible for the interaction of mouse Juno with Izumo1 are likely not involved in the mouse Juno-CD9 interaction (Figure 6G and Supplementary Table S1) and remain free. Specifically, docking and predicted interaction data suggest that mouse Juno-Izumo1 interacting interface contains residues (TYR 44, GLN 45, GLU 63, GLU 67, ARG 87, HIS 163, HIS 65, CYS 79, LEU 81, THR 83, SER 145, TRP 147) that are different from those of the Juno-CD9 interacting side (ARG 119, TRP 121, ASN 146, THR 175, ASP 178, ASP 177, GLU 181, LYS 182, ASN 185, ASN 186, LYS 189, GLU 225, VAL 226).

3.5 Molecular dynamics simulation

To analyze experimentally obtained data from the wet lab, we performed computational MD simulation to study the docked Juno-CD9 protein complex, the stability, compactness, and

various physicochemical parameters such as, flexibility, structural deviation, and energy level. Root mean square deviation (RMSD) of backbone atoms were calculated over the entire 10 ns simulation trajectories, where RMSD values for Juno, CD9, and Juno-CD9, are ~2.2 Å, ~4.3 Å, ~3.6 Å, respectively (Figure 6H), also on in reference the CD9 structure from AlphaFold showed same RMSD ~4.3 Å value (Supplementary Figure S11). All RMSD values indicated that all the protein structures including the predicted and docked Juno-CD9 interacting structure are in a stable biologically relevant condition which is in accordance with the obtained microscopical data. The structural stability data from MD simulation of Juno and CD9 also confirmed highly stable Juno and CD9 complex. Secondary structure analysis showed Juno contains 32% alpha helical structure, 6.1% beta strands, and 61.9% coiled structure with no turns found. Post MD analysis showed no changes in the secondary structure of Juno (Supplementary Figure S12). In the case of CD9, 77.4% alpha helical structure, 7.1% turns, and 15.5% coiled structure but no beta strands were found. After simulation CD9 protein showed a striking change in secondary structure with, 76.1% alpha helical structure and 23.9% coiled structure but interestingly, CD9 protein lost all the turns by that stage (Supplementary Figure S13). The complex of Juno-CD9 displayed 54.80% alpha helical structure, 4.3% beta strands, 10.2% turns, and 30.7% coiled, whereas post MD analysis showed 53.2% alpha helical structure, 3.3% beta strands, and 43.5% coiled and no turns were found (Supplementary Figure S14). It is clear that coil structure plays important roles in protein-protein interaction (Grigoryan and Keating, 2008). Therefore, our results support the Juno-CD9 complex formation, as both Juno and CD9 contain coil structures and extended coils are formed during the interaction. Further, during formation of Juno-CD9 complex there are larger numbers of coil structures which indicate their uninterrupted interaction over the 10 ns MD simulation time. As MD simulation represents a reflection of biological process, it could be predicted that in a biological system Juno and CD9 interact through their coil-coil structures, which is supported by presented microscopic data (Figure 3). Flexibility is an important phenomenon especially for protein-protein interaction (Grünberg et al., 2006). Based on our data, Juno did not change to any coils after the MD simulation run which could be interpreted as a non-flexible biological behavior of Juno. In contrast, when Juno is in interacting mode with CD9, the complex undergoes secondary structural changes indicating that structural flexibility is an important factor of protein-protein side chain interaction. The pre and post MD simulation data of secondary structure analysis clearly indicated that Juno-CD9 complex undergoes structural changes, which is in confirmation with the phenomenon of protein-protein interaction (Tobi and Bahar, 2005). With the knowledge that flexibility is also important for protein-protein interaction (Demirel and Keskin, 2005) the root mean square fluctuation (RMSF) technique was applied to evaluate protein flexibility (Sur et al., 2022). Atomic range RMSF analysis (Supplementary Figure S15) indicates that the Juno, CD9 and the complex of Juno-CD9 fluctuates in a stable range except the c-terminal atoms of the Juno-CD9 complex, where Juno showed rigid patterns in the atomic range. On the other hand, CD9 displayed a higher level of flexibility than Juno, and the Juno-CD9 complex mimicked the fluctuation pattern from both individual Juno and CD9 proteins. In the atomic range fluctuation study, it could be seen that Juno and CD9 exerted a fluctuation pattern mostly like CD9 with a higher flexibility. These results support the prediction of complex formation, where CD9 extends the side chains and contributes to the Juno-CD9 complex formation more than Juno, which agrees with the secondary structure data analysis (Supplementary Figures S12–S14). Along with other parameters, an electrostatic force which also plays a crucial role in protein-protein binding (Shashikala et al., 2019) was measured and an energy profile of Juno, CD9 and Juno-CD9 were obtained. Based on the results, in the case of Juno-CD9 complex formation, a short range electrostatic Coulombic energy seems to play a crucial role. Specifically, Coulombic energy for Juno was very low (88.3046 kg/mol) in contrast to the high energy for CD9 (−349.1170 kg/mol), with even higher readings for the Juno-CD9 complex (−727.8620 kg/mol). From the Coulombic energy profiling it could be deducted that the CD9 molecule contributes the highest energy towards the complex formation and the complex gains a higher electrostatic force during Juno-CD9 interaction resulting in a largely stable structure (Brock et al., 2007). There was no significant result found of short-range Lennard–Jones interaction (Supplementary Figure S16). Furthermore, the protein enthalpy plays an important role in protein-protein interactions, as it determines the overall energy change during the interaction. A favourable enthalpy change indicates that the interaction is energetically favourable and contributes to the stability of the complex. The protein enthalpy was measured as −188.69 kJ/mol (Juno), −410.06 kJ/mol (CD9), and −862.06 kJ/mol (Juno-CD9). The significantly more negative enthalpy for the Juno-CD9 complex suggests a stronger interaction between Juno and CD9 compared to their individual molecules and understanding the underlying mechanisms of protein-protein interactions (Bogan and Thorn, 1998) (Supplementary Figure S16). The Gibbs free energy for Juno (−2.06 kJ/mol), CD9 (−2.69 kJ/mol, and Juno-CD9 (−6.92 kJ/mol) further indicated the formation of a strong and stable condition for the thermodynamic reaction for Juno-CD9 complex formation (Supplementary Figure S17). Importantly, hydrogen bonds (H-bonds) are also crucial for protein stability, interaction, and protein folding (Erijman et al., 2014). Based on MD simulation H-bond analysis, it was predicted that during Juno-CD9 interaction possesses 278 sidechain H-bonds, in contrast to individual molecules of Juno (113 H-bonds) or CD9 (126 H-bonds). The H-bond numbers during the simulation period indicate that the Juno-CD9 complex gained 39 hydrogen bonds (Supplementary Figure S18). Based on protein-solvent interaction the Juno-CD9 complex possesses 808 H-bonds, in contrast to Juno (455 H-bonds) or CD9 (434 H-bonds). These H-bond numbers indicate that the Juno-CD9 complex loses 81 H-bonds towards the solution, and they could be possibly involved in Juno-CD9 complex. This interpretation most probably explains why these 81 H-bonds were not available for protein-solvent interaction and clearly indicates that the Juno-CD9 complex forms a higher hydrophobic core (Supplementary Figure S19). MD Simulation was captured as a movie file for better understanding of the dynamic state of Juno, CD9 Juno-CD9, and AlphaFold CD9 (Supplementary Videos S4–S7).

4 Discussion

Although, Juno and CD9 are the only oocyte surface presented proteins confirmed to be essential for mouse fertilization (Siu et al., 2021), their mutual relationship is unclear. Published data suggested the existence of Juno and CD9 cooperation within oolemma (Jégou et al., 2011; Inoue et al., 2020; Mori et al., 2021) strengthen by their protein expression in the same membrane compartments (Inoue et al., 2020; Mori et al., 2021). Using colocalization assay we detected Juno and CD9 colocalization in the *microvilli*-rich part of mouse oolemma which was absent in the *microvilli*-free region, which further supports previous findings (Runge et al., 2007; Inoue et al., 2020).

In relation to the detail of our study, we herein considered the existence of distinct compartments within mouse oolemma surface and possibility of spatially regulated structures (Mori et al., 2021), which are predicted to play a role in sperm-oocyte binding and could be determined by Juno and CD9 localization. The aspect of protein density, that could determine the Juno-CD9 close proximity and have an impact on oolemma microdomain function needed to be tested. Previously, STED microscopy was employed to analyze the microvillar region of the mouse oocyte (Wang and Kinsey, 2022). This study by Wang and Kinsey (2022) focused on imaging of the sperm-binding site, therefore, a relatively small area of oolemma was imaged. In contrast, using our newly developed strategy with a modified protocol for 3D STED super-resolution microscopy (Frolikova et al., 2023), we captured the entire oolemma with a high resolution of around 70 nm, which is unique for such large objects as oocytes, and it represents a significant improvement of previously used methods (Frolikova et al., 2023). This enabled us to distinguish two oolemma compartments within the *microvilli*-rich region. The findings that Juno protein expression is significantly elevated in planar membrane between individual *microvilli* while CD9 localization is confined to be mainly in microvillar membrane provides the evidence, that only certain parts of oolemma may likely serve as sperm binding regions. We could speculate that the existence of significant differences in Juno and CD9 distribution between planar and microvillar membrane regions has a functional reason, such as regulation of sperm attachment in terms of sperm number and consequential fusion of gamete membranes. The individual differences in Juno and CD9 oolemma location stress their different individual roles particularly for Juno in the blocking of polyspermy (Bianchi et al., 2014) and for CD9 in maintaining membrane curvature (Frolikova et al., 2018). Sperm fusion is likely facilitated in presence of CD9, which is localized in the membrane of extracellular vesicles (Miyado et al., 2008) as well as exclusion of Juno from *microvilli*-free region (Inoue et al., 2020) by RanGTP signaling, which may regulate localization of Juno through CD9 protein (Mori et al., 2021). However, their mutual localization and comparable protein amount in MvM points to the functional importance of Juno-CD9 complex formation for primary sperm-oocyte membrane recognition. This could be initiated by Juno-CD9 interface pocket in the microvillar part of oolemma surface supported by protein-membrane position modelling, with biologically relevant membrane orientation including Juno GPI anchor, and CD9 transmembrane domains (Umeda et al., 2020).

Furthermore, protein-protein flexible side chain docking depicted the most energetically and biologically relevant interacting formation reflected by an elevated number of hydrogen bonds that give stability to the Juno-CD9 complex. As proteins are dynamic structures within living biological systems, we addressed their activity by MD simulation followed by flexible side chain docking and discovered the most suitable interacting modes based on stability and fluctuation pattern. The docking pose and the higher stability of Juno-CD9 interacting modes and energy scale (mostly Gibbs free energy) supported experimentally derived Juno and CD9 complex. Mutual interaction of Juno with CD9 within the plasma membrane was confirmed by co-immunoprecipitation followed by MS identification of both proteins. Additionally, the GFP antibody used for co-IP did not react with Juno protein, indicating a specific pull-down of the Juno-CD9 complex via the GFP-tag from co-transfected cells.

Juno is shaded from oolemma in extracellular vesicles derived from the oolemma *microvilli*-rich part (Bianchi et al., 2014), and CD9 is present in the vesicles within the oocyte perivitelline space (Miyado et al., 2008). Based on these findings, we propose that the interaction between Juno and CD9 proteins in oolemma of MII oocyte, may precede or assist to Juno-Izumo1 binding during early stages of fertilization. This finding is supported by the knowledge that tetraspanins, such as CD9, are part of extracellular vesicles formation and their cargo (Andreu and Yáñez-Mó, 2014). The fact that both proteins are part of the extracellular vesicles released from the oocyte surface suggested their interaction not only before, but also after sperm-oocyte binding and membrane fusion including a formation and release of extracellular vesicles of oolemma origin that likely assist in block of polyspermy (Bianchi et al., 2014). The possible interaction between Juno and CD9 is further supported by the presented structural study, which revealed that CD9 protein possesses a high degree of sequence identity, with 87.61% structural similarity between mouse and human. Furthermore, a Blast search analysis revealed that Mouse CD9 shares 89.04% amino acid sequence identity with 100% query coverage. These findings support the theory that CD9 could play a similar role in fertilization in both mouse and human, and the structural features and functional properties of CD9 are conserved throughout evolution.

In summary, based on analysis of multiple disciplinary derived data, we propose the existence of Juno-CD9 complex in specific spatially defined compartments of microvillar regions of mouse oolemma with a distinct functional role in sperm-oocyte binding. Furthermore, these Juno-CD9 complexes may serve as competent microdomains for sperm-oocyte fusion.

Data availability statement

Source data files corresponding to individual panels in Figures 1–6 are deposited in as Source Data Archives 1-6. Link: https://biobox.biocev.org/index.php/s/4NCxYE2ckAJ4eCP.

Ethics statement

The animal study was reviewed and approved by Animal Welfare Committee of the Czech Academy of Sciences (Animal Ethics Number 66866/2015-MZE-17214, 18 December 2015).

Author contributions

MF design of the study, experimental work, 3D STED imaging, image analysis, writing of the manuscript; VS performed structural prediction, docking, MD simulations and data interpretation, contributed to writing of the manuscript; IN developed and optimized protocol for 3D STED imaging, performed the 3D STED acquisition settings and collaborated in 3D STED imaging and image processing, contributed to writing of the manuscript; MB image analysis of 3D STED data and contributed to manuscript writing; JV Co-IP assay and contributed to manuscript writing; EV and OS oocyte handling and experimental work; LD statistical analysis of EM data; LK TEM and SEM sample preparation, ultrathin sectioning, TEM imaging and contributed to manuscript writing; AB funding acquisition; PP design of the study and result interpretation; OH funding acquisition, KK design of the study, result interpretation, writing of the manuscript and funding acquisition. All authors contributed to the article and approved the submitted version.

Funding

This work was supported by the Grant Agency of the Czech Republic (GA 22-30494S); and by institutional support of from the Institute of Biotechnology of the Czech Academy of Sciences RVO (86652036); and by BIOCEV project (CZ.1.05/1.1.00/02.0109) from the ERDF. The work was supported from European Regional Development Fund, project "Modernization and support of research activities of the national infrastructure for biological and medical imaging Czech-BioImaging" (No. CZ.02.1.01/0.0/0.0/16_013/0001775). Light Microscopy Core Facility, IMG CAS, Prague, Czech Republic, was supported by MEYS (LM2018129, CZ.02.1.01/0.0/0.0/18_046/0016045) and RVO (68378050-KAV-NPUI), Imaging Methods Core Facility at BIOCEV, Vestec, Czech Republic was supported by the MEYS CR (Large RI Project LM 2023050 Czech-BioImaging). Structural mass spectrometry core facility of CIISB, Instruct-CZ Centre was supported by MEYS CR (LM2023042) and European Regional Development Fund-Project, "UP CIISB" (No. CZ.02.1.01/0.0/0.0/18_046/0015974) for MS data analysis and processing.

Acknowledgments

We thank Jiri Miksatko (Imaging Methods Core Facility at BIOCEV, Vestec, Czech Republic) for SEM data acquisition and we acknowledge Imaging Methods Core Facility at BIOCEV, for sample preparation and imaging of TEM data presented in this paper. We acknowledge Light Microscopy Core Facility, IMG CAS, Prague, Czech Republic for their support with the super-resolution imaging and image analysis presented herein, and Dr. Petr Pompach and Dr. Pavla Vankova from Structural mass spectrometry core facility of CIISB, Instruct-CZ Centre.

Conflict of interest

The authors declare that the research was conducted in the absence of any commercial or financial relationships that could be construed as a potential conflict of interest.

Publisher's note

All claims expressed in this article are solely those of the authors and do not necessarily represent those of their affiliated organizations, or those of the publisher, the editors and the reviewers. Any product that may be evaluated in this article, or claim that may be made by its manufacturer, is not guaranteed or endorsed by the publisher.

Supplementary material

The Supplementary Material for this article can be found online at: https://www.frontiersin.org/articles/10.3389/fcell.2023.1110681/full#supplementary-material

References

Alam, M. S. (2018). Proximity ligation assay (PLA). *Curr. Protoc. Immunol.* 123 (1), e58. doi:10.1002/cpim.58

Andreu, Z., and Yáñez-Mó, M. (2014). Tetraspanins in extracellular vesicle formation and function. *Front. Immunol.* 5, 442. doi:10.3389/fimmu.2014.00442

Benammar, A., Ziyyat, A., Lefèvre, B., and Wolf, J. P. (2017). Tetraspanins and mouse oocyte microvilli related to fertilizing ability. *Reprod. Sci.* 24 (7), 1062–1069. doi:10.1177/1933719116678688

Bianchi, E., and Wright, G. J. (2016). Sperm meets egg: the Genetics of mammalian fertilization. *Annu. Rev. Genet.* 50, 93–111. doi:10.1146/annurev-genet-121415-121834

Bianchi, E., and Wright, G. J. (2020). Find and fuse: unsolved mysteries in sperm–egg recognition. *PLOS Biol.* 18 (11), e3000953. doi:10.1371/journal.pbio.3000953

Bianchi, E., Doe, B., Goulding, D., and Wright, G. J. (2014). Juno is the egg Izumo receptor and is essential for mammalian fertilization. *Nature* 508 (7497), 483–487. doi:10.1038/nature13203

Bogan, A. A., and Thorn, K. S. (1998). Anatomy of hot spots in protein interfaces. *J. Mol. Biol.* 280 (1), 1–9. doi:10.1006/jmbi.1998.1843

Brock, K., Talley, K., Coley, K., Kundrotas, P., and Alexov, E. (2007). Optimization of electrostatic interactions in protein-protein complexes. *Biophys. J.* 93 (10), 3340–3352. doi:10.1529/biophysj.107.112367

Chalbi, M., Barraud-Lange, V., Ravaux, B., Howan, K., Rodriguez, N., Soule, P., et al. (2014). Binding of sperm protein Izumo1 and its egg receptor Juno drives Cd9 accumulation in the intercellular contact area prior to fusion during mammalian fertilization. *Development* 141 (19), 3732–3739. doi:10.1242/dev.111534

de Vries, S. J., van Dijk, M., and Bonvin, A. M. J. J. (2010). The HADDOCK web server for data-driven biomolecular docking. *Nat. Protoc.* 5 (5), 883–897. doi:10.1038/nprot.2010.32

Demirel, M. C., and Keskin, O. (2005). Protein interactions and fluctuations in a proteomic network using an elastic network model. *J. Biomol. Struct. Dyn.* 22 (4), 381–386. doi:10.1080/07391102.2005.10507010

Erijman, M., Rosenthal, E., and Shifman, J. M. (2014). How structure defines affinity in protein-protein interactions. *PLoS ONE* 9 (10), e110085. doi:10.1371/journal.pone.0110085

Frolikova, M., Manaskova-Postlerova, P., Cerny, J., Jankovicova, J., Simonik, O., Pohlova, A., et al. (2018). CD9 and CD81 interactions and their structural modelling in sperm prior to fertilization. *Int. J. Mol. Sci.* 19 (4), 1236. doi:10.3390/ijms19041236

Frolikova, M., Blazikova, M., Capek, M., Chmelova, H., Valecka, J., Kolackova, V., et al. (2023). A sample preparation procedure enables acquisition of 2-channel super-resolution 3D STED image of an entire oocyte. *bioRxiv*, 531472. doi:10.1101/2023.03.07.531472

Grigoryan, G., and Keating, A. E. (2008). Structural specificity in coiled-coil interactions. *Curr. Opin. Struct. Biol.* 18 (4), 477–483. doi:10.1016/j.sbi.2008.04.008

Grünberg, R., Nilges, M., and Leckner, J. (2006). Flexibility and conformational entropy in protein-protein binding. *Structure* 14 (4), 683–693. doi:10.1016/j.str.2006.01.014

Harris, T. K., and Mildvan, A. S. (1999). High-precision measurement of hydrogen bond lengths in proteins by nuclear magnetic resonance methods. *Proteins* 35 (3), 275–282. doi:10.1002/(sici)1097-0134(19990515)35:3<275::aid-prot1>3.0.co;2-v

Inoue, N., Ikawa, M., Isotani, A., and Okabe, M. (2005). The immunoglobulin superfamily protein Izumo is required for sperm to fuse with eggs. *Nature* 434 (7030), 234–238. doi:10.1038/nature03362

Inoue, N., Saito, T., and Wada, I. (2020). Unveiling a novel function of CD9 in surface compartmentalization of oocytes. *Development* 147 (15), dev189985. doi:10.1242/dev.189985

Jankovičová, J., Neuerová, Z., Sečová, P., Bartóková, M., Bubeníčková, F., Komrsková, K., et al. (2020). Tetraspanins in mammalian reproduction: spermatozoa, oocytes and embryos. *Med. Microbiol. Immunol.* 209 (4), 407–425. doi:10.1007/s00430-020-00676-0

Jégou, A., Ziyyat, A., Barraud-Lange, V., Perez, E., Wolf, J. P., Pincet, F., et al. (2011). CD9 tetraspanin generates fusion competent sites on the egg membrane for mammalian fertilization. *Proc. Natl. Acad. Sci. U. S. A.* 108 (27), 10946–10951. doi:10.1073/pnas.1017400108

Kaji, K., Oda, S., Shikano, T., Ohnuki, T., Uematsu, Y., Sakagami, J., et al. (2000). The gamete fusion process is defective in eggs of Cd9-deficient mice. *Nat. Genet.* 24 (3), 279–282. doi:10.1038/73502

Kozakov, D., Hall, D. R., Xia, B., Porter, K. A., Padhorny, D., Yueh, C., et al. (2017). The ClusPro web server for protein–protein docking. *Nat. Protoc.* 12 (2), 255–278. doi:10.1038/nprot.2016.169

Laskowski, R. A., Macarthur, M. W., Moss, D. S., and Thornton, J. M. (1993). Procheck - a program to check the stereochemical quality of protein structures. *J. Appl. Crystallogr.* 26, 283–291. doi:10.1107/S0021889892009944

Lee, J., Patel, D. S., Ståhle, J., Park, S. J., Kern, N. R., Kim, S., et al. (2019). CHARMM-GUI membrane builder for complex biological membrane simulations with glycolipids and lipoglycans. *J. Chem. Theory. Comput.* 15 (1), 775–786. doi:10.1021/acs.jctc.8b01066

Le Naour, F., Rubinstein, E., Jasmin, C., Prenant, M., and Boucheix, C. (2000). Severely reduced female fertility in CD9-deficient mice. *Science* 287 (5451), 319–321. doi:10.1126/science.287.5451.319

Macindoe, G., Mavridis, L., Venkatraman, V., Devignes, M.-D., and Ritchie, D. W. (2010). HexServer: an FFT-based protein docking server powered by graphics processors. *Nucleic Acids Res.* 38 (2), W445–W449. doi:10.1093/nar/gkq311

Miyado, K., Yamada, G., Yamada, S., Hasuwa, H., Nakamura, Y., Ryu, F., et al. (2000). Requirement of CD9 on the egg plasma membrane for fertilization. *Science* 287 (5451), 321–324. doi:10.1126/science.287.5451.321

Miyado, K., Yoshida, K., Yamagata, K., Sakakibara, K., Okabe, M., Wang, X., et al. (2008). The fusing ability of sperm is bestowed by CD9-containing vesicles released from eggs in mice. *Proc. Natl. Acad. Sci. U. S. A.* 105 (35), 12921–12926. doi:10.1073/pnas.0710608105

Mori, M., Yao, T., Mishina, T., Endoh, H., Tanaka, M., Yonezawa, N., et al. (2021). RanGTP and the actin cytoskeleton keep paternal and maternal chromosomes apart during fertilization. *J. Cell. Biol.* 220 (10), e202012001. doi:10.1083/jcb.202012001

Pierce, B. G., Wiehe, K., Hwang, H., Kim, B.-H., Vreven, T., and Weng, Z. (2014). ZDOCK server: interactive docking prediction of protein–protein complexes and symmetric multimers. *Bioinformatics* 30 (12), 1771–1773. doi:10.1093/bioinformatics/btu097

Runge, K. E., Evans, J. E., He, Z. Y., Gupta, S., McDonald, K. L., Stahlberg, H., et al. (2007). Oocyte CD9 is enriched on the microvillar membrane and required for normal microvillar shape and distribution. *Dev. Biol.* 304 (1), 317–325. doi:10.1016/j.ydbio.2006.12.041

Sala-Valdés, M., Ursa, A., Charrin, S., Rubinstein, E., Hemler, M. E., Sánchez-Madrid, F., et al. (2006). EWI-2 and EWI-F link the tetraspanin web to the actin cytoskeleton through their direct association with ezrin-radixin-moesin proteins. *J. Biol. Chem.* 281 (28), 19665–19675. doi:10.1074/jbc.M602116200

Schindelin, J., Arganda-Carreras, I., Frise, E., Kaynig, V., Longair, M., Pietzsch, T., et al. (2012). Fiji: an open-source platform for biological-image analysis. *Nat. Methods* 9 (7), 676–682. doi:10.1038/nmeth.2019

Shalgi, R., and Phillips, D. M. (1980). Mechanics of *in vitro* fertilization in the hamster. *Biol. Reprod.* 23 (2), 433–444. doi:10.1095/biolreprod23.2.433

Shashikala, H. B. M., Chakravorty, A., and Alexov, E. (2019). Modeling electrostatic force in protein-protein recognition. *Front. Mol. Biosci.* 6, 94. doi:10.3389/fmolb.2019.00094

Siu, K. K., Serrão, V. H. B., Ziyyat, A., and Lee, J. E. (2021). The cell biology of fertilization: gamete attachment and fusion. *J. Cell. Biol.* 220 (10), e202102146. doi:10.1083/jcb.202102146

Sur, V. P., Simonik, O., Novotna, M., Mazumdar, A., Liska, F., Vimberg, V., et al. (2022). Dynamic study of small toxic hydrophobic proteins PepA1 and PepG1 of *Staphylococcus aureus*. *Int. J. Biol. Macromol.* 219, 1360–1371. doi:10.1016/j.ijbiomac.2022.07.192

Tobi, D., and Bahar, I. (2005). Structural changes involved in protein binding correlate with intrinsic motions of proteins in the unbound state. *Proc. Natl. Acad. Sci.* 102 (52), 18908–18913. doi:10.1073/pnas.0507603102

Umeda, R., Satouh, Y., Takemoto, M., Nakada-Nakura, Y., Liu, K., Yokoyama, T., et al. (2020). Structural insights into tetraspanin CD9 function. *Nat. Commun.* 11 (1), 1606. doi:10.1038/s41467-020-15459-7

Vondrakova, J., Frolikova, M., Ded, L., Cerny, J., Postlerova, P., Palenikova, V., et al. (2022). MAIA, Fc receptor-like 3, supersedes JUNO as IZUMO1 receptor during human fertilization. *Sci. Adv.* 8 (36), eabn0047. doi:10.1126/sciadv.abn0047

Vriend, G. (1990). What if: a molecular modeling and drug design program. *J. Mol. Graph.* 8 (1), 52. doi:10.1016/0263-7855(90)80070-V

Vyas, V. K., Ukawala, R. D., Ghate, M., and Chintha, C. (2012). Homology modeling a fast tool for drug discovery: current perspectives. *Indian J. Pharm. Sci.* 74 (1), 1–17. doi:10.4103/0250-474x.102537

Wang, H., and Kinsey, W. H. (2022). Signaling proteins recruited to the sperm binding site: role of β-catenin and rho A. *Front. Cell. Dev. Biol.* 10, 886664. doi:10.3389/fcell.2022.886664

Webb, B., and Sali, A. (2016). Comparative protein structure modeling using MODELLER. *Curr. Protoc. Bioinforma.* 54 (1), 5.6.1–5.6.37. doi:10.1002/cpbi.3

Yanagimachi, R. (1994). "Mammalian fertilization," in *The physiology of reproduction*. Editors E. Knobil and J. Neill (New York: Raven Press).

Zhu, G. Z., Miller, B. J., Boucheix, C., Rubinstein, E., Liu, C. C., Hynes, R. O., et al. (2002). Residues SFQ (173-175) in the large extracellular loop of CD9 are required for gamete fusion. *Development* 129 (8), 1995–2002. doi:10.1242/dev.129.8.1995

Ziyyat, A., Rubinstein, E., Monier-Gavelle, F., Barraud, V., Kulski, O., Prenant, M., et al. (2006). CD9 controls the formation of clusters that contain tetraspanins and the integrin alpha 6 beta 1, which are involved in human and mouse gamete fusion. *J. Cell. Sci.* 119 (3), 416–424. doi:10.1242/jcs.02730

frontiers | Frontiers in Cell and Developmental Biology

TYPE Original Research
PUBLISHED 12 September 2023
DOI 10.3389/fcell.2023.1125096

OPEN ACCESS

EDITED BY
Shao-Chen Sun,
Nanjing Agricultural University, China

REVIEWED BY
Judit Castillo,
University of Barcelona, Spain
Jianqiang Bao,
University of Science and Technology of China, China
Yi Zheng,
Northwest A&F University, China
Brendan J. Houston,
The University of Melbourne, Australia

*CORRESPONDENCE
Maria Eugenia Teves,
maria.teves@vcuhealth.org

†These authors share first authorship

RECEIVED 15 December 2022
ACCEPTED 21 August 2023
PUBLISHED 12 September 2023

CITATION
Agudo-Rios C, Rogers A, King I, Bhagat V, Nguyen LMT, Córdova-Fletes C, Krapf D, Strauss JF III, Arévalo L, Merges GE, Schorle H, Roldan ERS and Teves ME (2023), SPAG17 mediates nuclear translocation of protamines during spermiogenesis. *Front. Cell Dev. Biol.* 11:1125096. doi: 10.3389/fcell.2023.1125096

SPAG17 mediates nuclear translocation of protamines during spermiogenesis

Clara Agudo-Rios[1,2†], Amber Rogers[1†], Isaiah King[1], Virali Bhagat[1], Le My Tu Nguyen[1], Carlos Córdova-Fletes[3], Diego Krapf[4], Jerome F. Strauss III[5], Lena Arévalo[6], Gina Esther Merges[6], Hubert Schorle[6], Eduardo R. S. Roldan[2] and Maria Eugenia Teves[1*]

[1]Department of Obstetrics and Gynecology, Virginia Commonwealth University, Richmond, VA, United States, [2]Department of Biodiversity and Evolutionary Biology, Museo Nacional de Ciencias Naturales, CSIC, Madrid, Spain, [3]Departamento de Bioquímica y Medicina Molecular, Facultad de Medicina, Universidad Autónoma de Nuevo León, Monterrey, Mexico, [4]Department of Electrical and Computer Engineering, Colorado State University, Fort Collins, CO, United States, [5]Department of Obstetrics and Gynecology, Perelman School of Medicine, University of Pennsylvania, Philadelphia, PA, United States, [6]Department of Developmental Pathology, Institute of Pathology, University Hospital Bonn, Bonn, Germany

Protamines (PRM1 and PRM2) are small, arginine-rich, nuclear proteins that replace histones in the final stages of spermiogenesis, ensuring chromatin compaction and nuclear remodeling. Defects in protamination lead to increased DNA fragmentation and reduced male fertility. Since efficient sperm production requires the translocation of protamines from the cytoplasm to the nucleus, we investigated whether SPAG17, a protein crucial for intracellular protein trafficking during spermiogenesis, participates in protamine transport. Initially, we assessed the protein-protein interaction between SPAG17 and protamines using proximity ligation assays, revealing a significant interaction originating in the cytoplasm and persisting within the nucleus. Subsequently, immunoprecipitation and mass spectrometry (IP/MS) assays validated this initial observation. Sperm and spermatids from *Spag17* knockout mice exhibited abnormal protamination, as revealed by chromomycin A3 staining, suggesting defects in protamine content. However, no differences were observed in the expression of *Prm1* and *Prm2* mRNA or in protein levels between testes of wild-type and *Spag17* knockout mice. Conversely, immunofluorescence studies conducted on isolated mouse spermatids unveiled reduced nuclear/cytoplasm ratios of protamines in *Spag17* knockout spermatids compared to wild-type controls, implying transport defects of protamines into the spermatid nucleus. In alignment with these findings, *in vitro* experiments involving somatic cells, including mouse embryonic fibroblasts, exhibited compromised nuclear translocation of PRM1 and PRM2 in the absence of SPAG17. Collectively, our results present compelling evidence that SPAG17 facilitates the transport of protamines from the cytoplasm to the nucleus.

KEYWORDS

protamine, SPAG17, spermatogenesis, nucleocytoplasmic transport, spermiogenesis

1 Introduction

Spermiogenesis, the last phase in the process of spermatogenesis, is a vital process for male germ cell differentiation, and encompasses a series of events crucial for sperm maturation and fertility. It involves various intricate steps such as sperm head elongation, nuclear remodeling, chromatin condensation, and flagellar development (Teves and Roldan, 2022). Notably, during the final stages of spermiogenesis, nuclear histones undergo replacement by two types of protamines, namely, PRM1 and PRM2. These protamines are proteins rich in arginine and cysteine residues, contributing to the structural and functional transformation of sperm chromatin (Teves and Roldan, 2022; Balhorn, 2007).

Protamines stand as the most prevalent nuclear proteins within sperm. These proteins, exclusive to male germ cells, play a pivotal role in packaging the paternal genome, gradually replacing histones during spermiogenesis (Oliva, 2006; Balhorn et al., 2018; Arévalo et al., 2022a). Numerous studies have shown that protamine-related changes can directly impact sperm DNA and the nucleus. Aberrations in DNA compaction by protamines can cause DNA fragmentation, alterations in seminal parameters, ultimately leading to reduced male fertility and the onset of genetic mutations in offsprings (Aitken et al., 2009; Andraszek et al., 2014; Ni et al., 2016). The significance of chromatin compaction facilitated by protamines has been highlighted by several studies on protamine deficient mice (Arévalo et al., 2022b; Moritz and Hammoud, 2022). Loss of both PRM1 alleles leads to infertility whereas loss of one PRM1 allele results in severe reduction of sperm motility and male subfertility (Merges et al., 2022). Sperm from *Prm1*$^{+/-}$ and *Prm1*$^{-/-}$ mice contained high levels of incompletely processed PRM2 which suggests that PRM1 is needed for PRM2 processing (Merges et al., 2022). Conversely, while *Prm2*$^{-/-}$ mice are infertile, the heterozygous loss of PRM2 does not lead to subfertility (Schneider et al., 2016). Unprocessed PRM2 seems to play a distinct role related to the elimination of intermediate DNA-bound proteins and the incorporation of both protamines into chromatin (Arévalo et al., 2022a). Hence, although both protamines are crucial for the production of functional sperm, they appear to perform distinct functions beyond simple DNA compaction (Arévalo et al., 2022b).

PRM1 is present in all mammals and is synthesized directly as a mature protein. In contrast, PRM2 is primarily found in rodents and primates and is synthesized as a precursor that is processed by sequential cleavage to its mature form (Balhorn et al., 2018; Arévalo et al., 2022b). These male germ cell specific proteins are responsible for DNA hyper-condensation and chromatin structural reorganization thus protecting DNA strands from possible breaks and preserving the integrity of the genome (Silva et al., 2021). This implies that any protamine-related changes can directly impact sperm DNA and nucleus, thus affecting sperm function (Andraszek et al., 2014).

Protamines are expressed in haploid male germ cells (Teves and Roldan, 2022). During spermiogenesis, protamine genes are expressed soon after completion of meiosis, in round spermatids (Hecht et al., 1986a; b). Subsequently, transcripts are stored as cytoplasmic ribonucleoprotein particles for several days until protein synthesis, which takes place in elongating spermatids (Kleene et al., 1984; Kleene, 1989). Most studies on protamines have focused on their interaction with nuclear chromatin and the relevance of chromatin reorganization and nuclear reshaping for sperm morphology and performance. However, very little is known regarding mechanisms of protamine transport from the cytoplasm to the nucleus.

Protein transport, including the trafficking of essential proteins such as protamines, plays a crucial role in spermiogenesis. During steps 8–14 of mouse spermiogenesis, a transient structure called the manchette, facilitates this transport process (Teves et al., 2020). The manchette comprises microtubules and actin filaments that act as tracks for intracellular protein trafficking through multi-subunit complexes, a mechanism known as intramanchette transport (IMT) (Kierszenbaum, 2002). Despite the significance of the manchette in protein trafficking, our understanding of its proteomics and its association with nucleocytoplasmic protein transport remains limited (Pleuger et al., 2020; Teves et al., 2020).

In a recent study by Kazarian et al. (2018), the Sperm-associated antigen 17 (SPAG17) was found to be expressed in testicular germ cells during the late stages of sperm development and was shown to localize to the manchette, contributing to protein trafficking. Notably, proteins known to be associated with the manchette and transported through it failed to properly localize to the manchette in *Spag17* knockout elongating spermatids, remaining in the cytoplasm instead. Additionally, electron microscopy evaluation of testicular preparations revealed multiple phenotypes, including defects in chromatin compaction and nuclear remodeling. These findings suggest a potential association between SPAG17 and the transport or dysfunction of protamines.

To further investigate the role of SPAG17 in protein transport during spermiogenesis, in the present study, we aimed to determine the interaction between SPAG17 and protamines, as well as its influence on the nuclear translocation of PRM1 and PRM2. By examining these protein interactions, we seek to gain insights into the role of SPAG17 in facilitating protamine transport and its impact on the process of spermiogenesis. This will contribute to a better understanding of the mechanisms underlying protein trafficking during spermiogenesis and shed light on the potential implications for male fertility.

2 Materials and methods

2.1 Animals

All animal studies were conducted in accordance with protocol AM10297 approved by the Virginia Commonwealth University Institutional Animal Care and Use Committee. Heterozygous *B6N(Cg)-Spag17 tm1b(KOMP)Wts1/J* (Stock No. 026485) mice from Jackson Laboratories were used to generate homozygous (*Spag17/Sox2-Cre*) mice with disrupted expression of the *Spag17* gene. The disruption in the gene was accomplished by the precise insertion of the L1L2_Bact_P cassette on Chromosome 3. This cassette comprised an array of genetic elements, including FRT sites, a lacZ sequence, and loxP sites. These loxP sites strategically flanked the critical exon, allowing for precise control and manipulation of gene expression. To generate the strain, the construct was introduced into JM8. N4 embryonic stem (ES) cells derived from the C57BL/6N lineage. After confirming the

correct targeting of the ES cells, they were injected into blastocysts obtained from *B6(Cg)-Tyrc-2J/J* mice (Stock No. 58). The resulting chimeric males were then bred to C57BL/6NJ females (Stock No. 005304), followed by mating with *B6N.Cg-Tg(Sox2-cre)1Amc/J* mice (Stock No. 014094) to excise the floxed neomycin cassette and critical exon sequences. This breeding strategy ensured the removal of unwanted transgenic elements and further refined the genetic background of the offspring. After a deletion in exon 5 a premature stop codon leads to absent SPAG17 expression. Male fertility phenotype and experiments validating the deletion of this gene were reported previously in Kazarian et al. (2018). The wild-type mice used as controls share the same genetic background as the *Spag17/Sox2-Cre* knockout (KO) mice. To ensure consistency and minimize genetic variations, we typically use mice from the same litter or mice derived from the same breeding line. The total number of animals used for these studies are wild-type n = 20 and knockout n = 22.

2.2 Mixed germ cells isolation

Testes from adult wild-type (n = 13) and *Spag17/Sox2-Cre* (n = 14) mouse line were de-capsulated and placed into isolation buffer containing 5 mL DMEM (Gibco, Life Technologies Corporation, Grand Island, NY, United States), 1 μg/mL DNase I (Sigma-Aldrich, St. Louis, MO, United States) and 0.5 mg/mL collagenase IV (Sigma-Aldrich, St. Louis, MO, United States), and then incubated for 30 min at 32°C to dissociate the tissue. The digested tissue was filtered through a 40 μm cell strainer to remove somatic cells. Then, the separated suspension containing mixed germ cells (from spermatogonia to elongated spermatids) was centrifuged for 5 min at 1,000 rpm and 4°C and washed twice with 5 mL PBS.

2.3 Proximity ligation assay (PLA)

Mixed germ cells isolated from adult wild-type (n = 3) and *Spag17/Sox2-Cre* knockout (n = 3) mice were fixed in 4% paraformaldehyde/PBS (containing 0.1 M sucrose) for 15 min at room temperature. After 3 washes with PBS, cells were resuspended in PBS, spread on SuperFrost/Plus slides (Fisher Scientific, Pittsburgh, PA, United States), and used for protein-protein interaction determination by Duolink® PLA (Sigma-Aldrich, St. Louis, MO, United States) following the manufacturer's instructions (Supplementary Figure S1). Anti-PRM1, anti-PRM2 and anti-SPAG17 were used as primary antibodies. Anti-α and anti-β tubulin antibodies were used as positive controls (Supplementary Table S1). Three independent PLAs experiments were performed for each protein-protein interaction.

2.4 Immunoprecipitation and mass spectrometry

Germ cells from adult wild-type (n = 3) and *Spag17/Sox2-Cre* knockout (n = 3) mice were isolated as described above and treated with NP40 lysis buffer (50 mM TRIS pH 7.4, 250 mM NaCl, 5 mM EDTA, 50 mM NaF, 1 mM Na_3VO_4, 1% NP40, 0.02% NaN_3 and protease inhibitor cocktail) for 30 min at 4°C. The cell lysate was then sonicated 10 times in 30 s intervals on ice and cleared by centrifugation. Protein concentration was determined using the Lowry assay protocol.

For each sample, a volume of 100 μL of Dynabeads M-280 sheep anti-rabbit IgG (Invitrogen) was pre-incubated with and without the previously validated anti-SPAG17 antibody (Zhang et al., 2005; Teves et al., 2015; Kazarian et al., 2018) at a dilution of 1/100 and rotated overnight at 4°C. The beads were subsequently washed seven times with DPBS (Gibco, Life Technologies Corporation, Grand Island, NY, United States). For immunoprecipitation (IP), 200 μg of total protein from each cell lysate was incubated with the pre-treated Dynabeads and left to incubate overnight at 4°C. The Dynabeads were then washed 14 times with DPBS at 4°C. The proteins were boiled in 4x Laemmli buffer for 10 min to separate them from the Dynabeads. The supernatant from each sample was loaded onto a respective 10% acrylamide gel well and electrophoretically separated at 80 V. As a control for peptides visualization gels were stained with Coomassie blue for 2 h (Supplementary Figure S2). Next, each well line was cut and submitted to liquid chromatography with tandem mass spectrometry (LC-MS/MS) using the Thermo Electron Q Exactive HF mass spectrometer system.

The gel pieces were transferred to a siliconized tube and washed in 200 μL 50% methanol. They were dehydrated in acetonitrile, rehydrated in 30 μL of 10 mM dithiolthreitol (DTT) in 0.1 M ammonium bicarbonate and reduced at room temperature for 0.5 h. The DTT solution was removed, and the sample alkylated in 30 μL 50 mM iodoacetamide in 0.1 M ammonium bicarbonate at room temperature for 0.5 h. The reagent was removed and the gel pieces dehydrated in 100 μL acetonitrile. The acetonitrile was removed and the gel pieces rehydrated in 100 μL 0.1 M ammonium bicarbonate and the pieces were let to dried by vacuum centrifugation. Rehydration was performed in 20 ng/μL trypsin in 50 mM ammonium bicarbonate on ice for 30 min. Any excess enzyme solution was removed, and 20 μL 50 mM ammonium bicarbonate was added. Next, samples were digested overnight at 37°C and the peptides formed were extracted from the polyacrylamide in a 100 μL aliquot of 50% acetonitrile/5% formic acid. The extract was evaporated to 100 μL for MS analysis. The LC-MS system consisted of a Thermo Electron Q Exactive HF mass spectrometer system with an Easy Spray ion source connected to a Thermo 75 μm × 15 cm C18 Easy Spray column (through pre-column). 0.8 μg equivalent of the original extract was injected and the peptides eluted from the column by an acetonitrile/0.1 M acetic acid gradient at a flow rate of 0.3 μL/min over 2 h. The nanospray ion source was operated at 1.9 kV. The digest was analyzed using the rapid switching capability of the instrument acquiring a full scan mass spectrum to determine peptide molecular weights followed by product ion spectra (Top10 HCD) to determine amino acid sequence in sequential scans. This mode of analysis produces approximately 30,000 MS/MS spectra of ions ranging in abundance over several orders of magnitude.

Data were analyzed by database searching using the Sequest search algorithm against Uniprot Mouse. For validation of MS/MS-based peptide and protein identifications, Scaffold 5 (Proteome Software Inc., Portland, OR) was used. Peptide identification was

accepted if it could be established at >95% probability by the Peptide Prophet algorithm with Scaffold delta-mass correction.

2.5 Sperm isolation

Sperm from adult wild-type (n = 3) and *Spag17/Sox2-Cre* knockout (n = 4) mice were collected from the caudae epididymides. Briefly, spermatozoa were collected by making several cuts into the cauda epididymis with surgical scissors in 1 mL of pre-warmed (35°C) PBS or Medium 199 (Gibco, Life Technologies Corporation, Grand Island, NY, United States) supplemented with 4 mg/mL BSA (Sigma, St. Louis, MO) and allowing the sperm to swim out from the tissue for 10 min. In the case of *Spag17/Sox2-Cre* knockout samples, additional gentle pipetting up and down of the suspension was performed to improve collection of sperm since lack of progressive movement is a phenotype present in these mice (Kazarian et al., 2018). As a control, aliquots of sperm suspension were used to assess % of sperm with progressive movement (WT = 70 ± 7.0%; KO = 0 ± 0.0%, Supplementary Movie S1, S2) and viability after trypan blue staining (Serafini et al., 2014) (No. T8154, Sigma, St. Louis, MO, WT = 87 ± 5.5%; KO = 70 ± 10.2%; Supplementary Figure S3) and observation using phase contrast or bright light microscopy, respectively.

2.6 Protamination assay

Assessments were performed in cells collected from adult wild-type (n = 3) and *Spag17/Sox2-Cre* knockout (n = 4) mice. The methodology used for the evaluation of protamine deficiency with chromomycin A3 (CMA3) was based on protocols used by Lolis et al. (1996) and Castro et al. (2018). Briefly, two smears, one for isolated sperm and one for isolated testicular germ cells, were prepared using 20 µL of sample and air-dried. Each slide was fixed in Carnoy's solution (ethanol:acetic acid, 3:1) for 5 min at 4°C and air-dried. For each slide 100 µL of 0.25 mg/mL CMA3 (Thermo Fisher Scientific Inc., Waltham, MA, United States) in McIlvain's buffer (7 mL citric acid 0.1M + 33 mL Na_2HPO_4 0.2 M, pH 7.0, containing 10 mM $MgCl_2$ and 1% DMSO to facilitate dissolution), was added and slides were incubated in the dark for 20 min at room temperature. Slides were rinsed in McIlvain's buffer and mounted with a drop of buffered glycerol (glycerol:phosphate buffer 0.2 M, pH 7.4, 1:1) for microscopic analysis. Images were captured by Zeiss LSM700 confocal microscope. Quantification of CMA3 positive cells was performed using the combination of bright and green fluorescent field. A total of 100–200 sperm or spermatids per slide were counted. Cells with correct protamination (negative green fluorescence) and abnormal protamination (positive bright green fluorescence) were identified and quantified.

2.7 Immunofluorescence staining

Isolated mixed germ cells from adult wild-type (n = 4) and *Spag17/Sox2-Cre* knockout (n = 4) mice were fixed in 4% paraformaldehyde/PBS (containing 0.1 M sucrose) for 15 min at room temperature. After 3 washes with PBS, cells were resuspended in PBS and spread on SuperFrost/Plus slides (Fisher Scientific, Pittsburgh, PA, United States) and used for immunofluorescence staining. Staining was conducted to examine the patterns of protein localization. Slides were blocked with blocking solution containing 10% goat serum (Vector Laboratories, Inc., Burlingame, CA, United States), 3% BSA (Sigma-Aldrich, St. Louis, MO, United States) and 0.2% Triton X-100 (Fisher Scientific, New Jersey, NY), and incubated at room temperature for 1 h. The respective primary antibodies (Supplementary Table S1) were diluted in the same blocking solution and incubated overnight at 4°C. Following incubation, samples were washed 3 times (10 min each) with PBS and incubated with secondary antibody (Alexa Fluor 594-conjugated anti mouse IgG; Supplementary Table S1) at room temperature (in the dark) for 1–2 h. After 3 washes with PBS, slides were mounted with VectaMount with DAPI mounting media (Vector laboratories, Inc., Burlingame, CA, United States) and sealed with a coverslip and nail polish. Images were captured with a Zeiss LSM700 confocal laser-scanning microscope and analyzed using ImageJ.

2.8 Cell culture and transfection

Mouse embryonic fibroblasts (MEFs) were isolated from wild-type (n = 4) and *Spag17/CMV-Cre* knockout (n = 4) E12.5 embryos as previously reported (Teves et al., 2015). They were then cultured in DMEM medium (Gibco, Life Technologies Corporation, Grand Island, NY, United States) supplemented with 1 mg/ml L-glutamine (Gibco, Life Technologies Corporation, Grand Island, NY, United States) and 10% FBS (R&D Systems, Minneapolis, MN, United States). At about 50%–60% confluency, cells were transfected with 1 µg mouse pPrm1-mCherry-N1 or mouse pPrm2-EGFP-N3 expressing vectors (Arévalo et al., 2022a) (Supplementary Figure S4) using Continuum (Gemini Bio-Products, West Sacramento, CA) to express PRM1 and PRM2, respectively. 1 µg of pmCherry-N1 or pEGFP-N3 were used as control vectors. After 6 h, transfection medium was replaced by culture medium for two time points 24 and 48 h. Then cells were fixed in 10% formalin (Sigma, St. Louis, MO, United States), mounted with VectaMount with DAPI mounting media (Vector laboratories, Inc., Burlingame, CA, United States) and sealed with a coverslip and nail polish. Four independent experiments were performed. *Spag17/CMV-Cre* KO MEFs were challenging to transfect, which led to a smaller number of transfected cells in this genotype than in the wild-type. For quantification, we analyzed approximately 60–80 transfected wild-type MEFs and 25–30 transfected knockout MEFs per treatment and experiment. Images were captured with a Zeiss LSM700 confocal laser-scanning microscope and analyzed using ImageJ.

2.9 Gene expression of protamines

RNA extraction, cDNA synthesis, quantitative PCR and analysis of expression data was carried out as described previously (Lüke et al., 2014). Briefly, RNA was extracted from adult wild-type (n = 4) and *Spag17/Sox2-Cre* knockout (n = 5) mouse testes using TRIzol (Invitrogen, Carlsbad, CA, United States), following the

manufacturer's recommendations. RNA concentration and purity were determined using a NanoDrop 1,000 spectrophotometer (Thermo Scientific, Washington, DE, United States). Total RNA was reverse-transcribed with RETROscript kit (Ambion, Austin, TX, United States) according to the manufacturer's instructions. Expression levels of *Prm1* and *Prm2* in wild-type and *Spag17* knockout mice was determined using a realplex mastercycler (Eppendorf, Hamburg, Germany). Primers used were those designed by Lüke et al. (2014) for mouse transcripts. qPCR reactions were run in 96-well plates with an end volume of 20 µL per sample containing 10 µL SiTaq universal SYBR green supermix (BIO-RAD, Hercules, CA, United States), 300 nM of each primer and 50 ng/mL of cDNA. The conditions of the thermocycler program consisted of an initial denaturation of 95°C for 2 min, 40 cycles of 95°C for 15 s and an annealing and elongation stage of 62°C for 1 min. Melt curve analysis was performed at the end of each run to check for multiple peaks, indicative of non-specific amplification. Cycle threshold data (CT) were normalized relative to 18SrRNA for each plate (ΔCT). Data were transformed by adding a constant based on the lowest ΔCT value. Expression ratios and percentages were calculated from transformed individual ΔCT values and median values were obtained for each group.

2.10 PRM1 and PRM2 protein expression in testes

Basic proteins were extracted from testes as described in Soler-Ventura et al. (2018) with slight modifications (n = 3 per genotype). Briefly, frozen testes were decapsulated, homogenized and washed in PBS. The pellet was resuspended in buffer containing 1 M Tris pH 8, 0.5 M $MgCl_2$ and 5 µL Triton X-100 and then treated with 1 mM PMSF in water inducing cell lysis. Subsequently the samples were treated with EDTA, DTT and GuHCl inducing DNA denaturation. The samples were then incubated at 37°C for 30 min in the presence of 1% vinylpyridine for mouse protamine separation on the subsequent protein gel. The amount of vinylpyridine used was slightly increased compared to the published protocol (0.8%), which improved the separation of the protamine bands. DNA was then precipitated by addition of ethanol and separated from the sample by centrifugation. Basic proteins were then dissolved in 0.5 M HCl and precipitated with TCA, followed by acetone washes and drying. The precipitated proteins were resuspended in sample buffer containing 5.5 M urea, 20% β-mercapto-ethanol and 5% acetic acid.

The samples were then run on a pre-electrophorized acid-urea polyacrylamide gel (AU-PAGE) (2.5 M urea, 0.9 M acetic acid, and 15% acrylamide/0.1% N,N′-Methylene bis-acrylamide, TEMED and APS). The extracted basic proteins migrate towards the negative pole at 110 V for 2 h and 10 min. The gels were stained with Coomassie Brilliant Blue (Sigma Aldrich, Taufkirchen, Germany) using standard procedures. The two main protamine bands can be observed in the bottom of the gel with mature-PRM2 corresponding to the upper and PRM1 the lower band (Ishibashi et al., 2010; Soler-Ventura et al., 2018; Arévalo et al., 2022). PRM2 precursor bands can be observed in the lower part of the gel above the mature-PRM2 band (Yu et al., 2000; Mateo et al., 2011; Arévalo et al., 2022). In the upper half of the gel, bands corresponding to other basic nuclear proteins, including histones can be found (see Soler-Ventura et al., 2018). The densities of Coomassie stained bands were analyzed using ImageJ (1.52k, Schneider et al., 2012). The protamine content was quantified relative to the whole lane for each individual to ensure comparability. The ratio between PRM1 and PRM2 was calculated using the respective band density in each lane.

2.11 Image analysis

In order to differentiate the stages of various spermatids within a heterogeneous population of germ cells, we examined the cellular topological morphology using microscopy to categorize each stage. This evaluation encompasses the analysis of nuclear positioning within the cytoplasm, the configuration of the acrosome, and the presence or absence of the manchette structure. The nuclear/cytoplasmic ratios for PRM1 and PRM2 were computed using ImageJ software to investigate protamine translocation across various spermiogenesis stages. Total cell area was established from bright field images. Immunofluorescence images with blue (nucleus) and red (PRMs) channels were separated. The blue channel determined the total nuclear area, while the red channel was used to quantify fluorescence intensity for PRMs. Fluorescence in the cytoplasmic region was derived by subtracting nuclear fluorescence from the fluorescence in the entire cell, then divided by the respective area to normalize. Subsequently, the nucleus's fluorescence intensity was divided by cytoplasmic fluorescence intensity (N/C ratio). The percentage of protamines in MEF nuclei was calculated by assessing fluorescence intensity as described. After adjusting for area effects, nuclear values were multiplied by 100 and divided by total cell fluorescence.

2.12 Statistical analysis

Statistical analysis was performed using GraphPad Prism 8 software (GraphPad Software, San Diego, CA). The data are presented as means ± standard error of the mean (SEM). To compare the means between two groups, Student's t-test was utilized. A significance level of $p < 0.05$ was considered to indicate statistically significant differences between the samples.

3 Results

3.1 Interaction of SPAG17 and protamines

The SPAG17 protein has recently been shown to play a role in protein transport via the manchette. Importantly, *Spag17* knockout mice have defects in chromatin compaction (Kazarian et al., 2018), suggesting influence of SPAG17 in protamines content or function. Thus, we investigated SPAG17-protamine interactions. By using proximity ligation assay (PLA), the protein-protein interactions between SPAG17 and PRM1 and PRM2 were assessed in elongating spermatids. An intense fluorescent signal was observed using anti-SPAG17 and anti-PRM1 or PRM2 antibodies in wild-type spermatids. Interaction starts in the cytoplasm (Supplementary Figure S5A, B) and

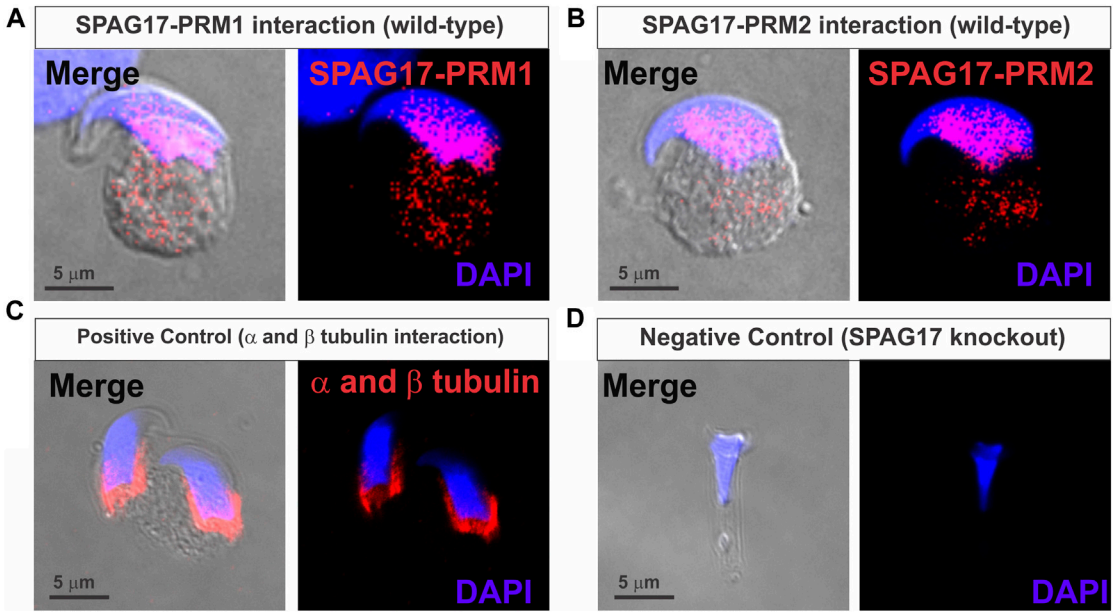

FIGURE 1
Proximity ligation assay (PLA) showing interaction of SPAG17 and protamines in mouse elongating spermatids. **(A)** Representative image showing interaction of SPAG17 and PRM1 in wild-type elongating spermatid step 12–13. **(B)** Representative images showing interaction of SPAG17 and PRM2 in wild-type elongating spermatid step 12–13. **(C)** Representative images showing positive control using anti-α and anti-β tubulin primary antibodies in wild-type elongating spermatids step 11. **(D)** Representative images showing lack of interaction in *Spag17* knockout elongating spermatid step 14, which lack SPAG17 protein, when anti-SPAG17 and anti-PRM2 antibodies were used. Images were collected from 3 independent PLAs experiments.

then moves to the nucleus following the nuclear translocation steps (Figures 1A,B). Positive controls using anti-α and β-tubulin antibodies also showed an intense fluorescent signal (Figure 1C), while anti-SPAG17 and anti-PRM1 or PRM2 antibodies did not show protein-protein interaction in *Spag17* knockout spermatids, as expected, due to lack of SPAG17 expression in these cells (negative control, Figure 1D; Supplementary Figure S5C).

Next, interaction of PRM1 and PRM2 with SPAG17 was confirmed by immunoprecipitation assay using anti-SPAG17 antibody and mass spectrometry. SPAG17, PRM1 and PRM2 were detected in germ cells collected from wild-type mice. In contrast, these proteins were not detected in samples from *Spag17* knockout mice. Table 1 shows the list of peptides found for the three proteins.

3.2 Sperm and spermatids from *Spag17* knockout mice display abnormal protamination

Because previous evidence indicated reduced chromatin condensation in *Spag17* knockout spermatids, we investigated the levels of protamination in spermatids from steps 8 to 16. For this purpose, chromomycin A3, a fluorochrome that binds to guanine- and cytosine-rich sites and competes with protamines for binding to the minor groove of DNA (Pourmasumi et al., 2019), was used as an indicator of protamine-deficient chromatin decondensation (Lolis et al., 1996; Bizzaro et al., 1998; Castro et al., 2018; Ribas-Maynou et al., 2021) (Figure 2A). Due to the occurrence of protamination during the late stages of spermiogenesis, a substantial proportion of

TABLE 1 List of peptides identified for SPAG17, PRM1 and PRM2. These peptides were discovered through immunoprecipitation using an anti-SPAG17 antibody, followed by proteomic analysis using LC-MS techniques. The results highlight the presence of multiple peptides associated with SPAG17, PRM1, and PRM2.

Proteins	Peptides
SPAG17	AVMPPLEQEASRVVTSQGTVIK
	SELSSLF
	VVTSQGTVIK
	ISSENYEPLQTHLAAVR
	TEEERGNAADLLK
	AVMPPLEQEASR
	VFTFESLKL
	QLTNIPAPILEGPK
	TQSYLMQIK
	SASQNEIEDLIK
PRM1	RRRRSYTIRCK
	RSYTIR
	RRSYTIR
PRM2	SPSEGPHQGPGQDHEREEQGQGQGLSPERVEDYGR
	EEQGQGQGLSPER
	EEQGQGQGLSPERVEDYGR

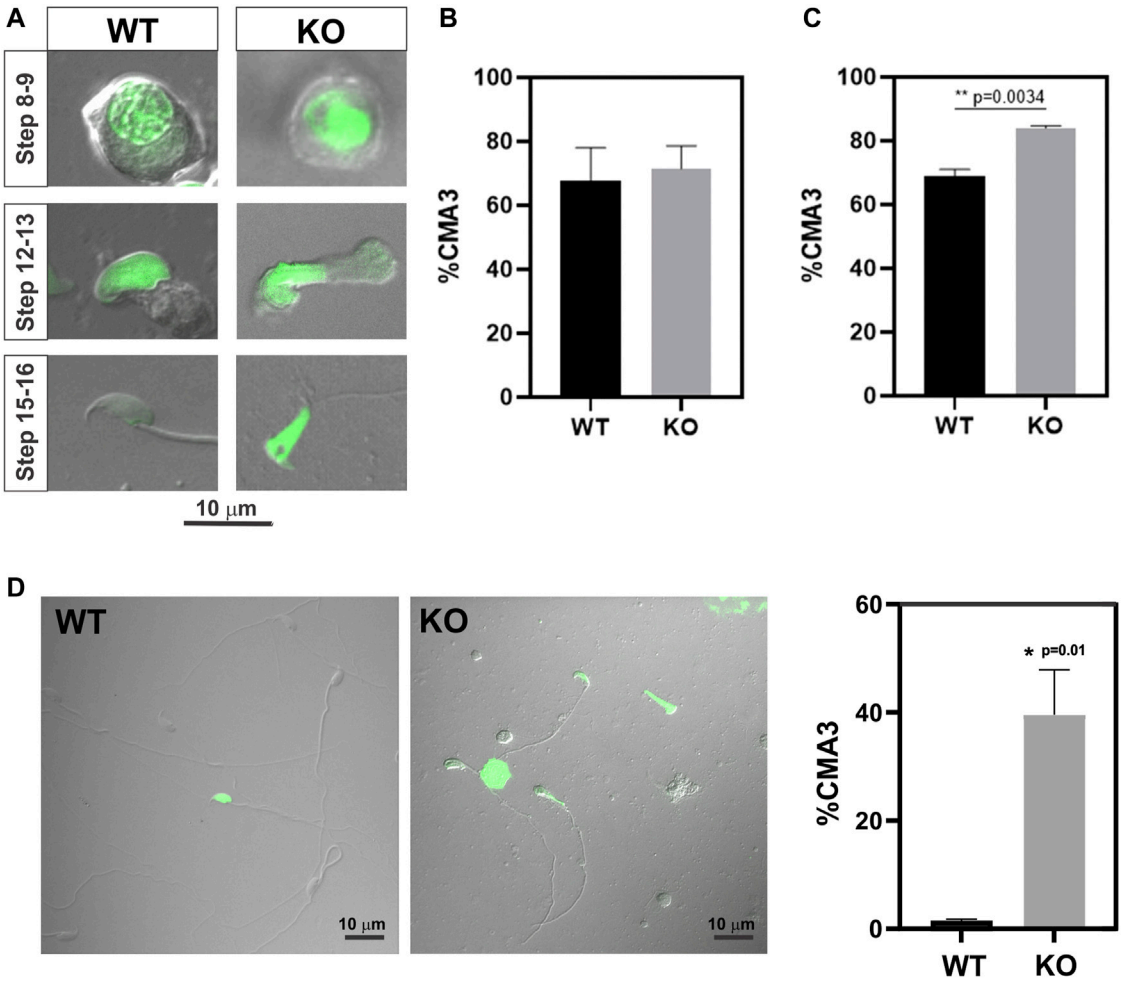

FIGURE 2
Abnormal protamination is observed in elongated spermatids and sperm from *Spag17* knockout mice. Spermatids and sperm were collected from the testes and cauda epididymis of wild-type (WT, n = 3) and *Spag17* knockout (KO, n = 4) mice, respectively, and stained with CMA3 to assess protamination. A total of 100–200 cells per sample were counted, and the percentage of CMA3-positive heads (green labeled) was calculated. **(A)** Representative images of spermatids at different steps. **(B)** Quantification of the percentage of CMA3-positive spermatids from step 8 to 16. **(C)** Quantification of the percentage of CMA3-positive spermatids from steps 15–16. **(D)** Representative images displaying CMA3-positive sperm and quantification of the percentage of CMA3-positive sperm. Results are means ± SEM. Significant differences were observed in comparison to WT, with * indicating $p = 0.01$ and ** indicating $p = 0.0034$.

spermatids exhibited positive staining for CMA3 when considering spermatids from steps 8 to 16 collectively. Notably, there was no significant difference in CMA3-positive cells between wild-type and *Spag17* knockout spermatids (67.6% ± 10.5%, n = 3 and 71.5% ± 7.2%, n = 4 respectively) (Figure 2B). However, upon analyzing spermatids at steps 15 and 16, a significant difference ($p = 0.0034$) was observed between genotypes (Figure 2C). To further explore this protamination defect, we examined mature sperm. The analysis of cauda epididymal sperm revealed a significant difference in the percentage of CMA3-positive spermatozoa between the wild-type and *Spag17* knockout groups (WT: 1.5% ± 0.3%, n = 3; KO: 39.6% ± 8.3%, n = 4, $p = 0.01$), indicating a grater protamine deficiency in the absence of SPAG17 (Figure 2D).

To determine if differences in protamination in *Spag17* knockout mice are related to gene expression levels, *Prm1* and *Prm2* mRNA expression was measured in wild-type and *Spag17* knockout testes by qPCR (Figure 3). No significant differences were found between the two groups for any of the protamines, nor for the ratio between them ($p = 0.17$ for *Prm1*, $p = 0.31$ for *Prm2* and $p = 0.96$ for *Prm1*/*Prm2* ratio), indicating that the loss of SPAG17 does not affect *Prm1* and *Prm2* expression at the mRNA level.

In order to explore the presence of defects at the protein expression level, we conducted an electrophoresis analysis of total proteins extracted from mouse testes, followed by relative quantification of protamine bands. The results indicated no significant difference in protamine content or PRM1/PRM2 ratio between the wild-type and knockout samples (Figure 4, Supplementary Figure S6). These findings suggest that the observed protamination defects are likely attributed to mechanisms other than protein expression levels.

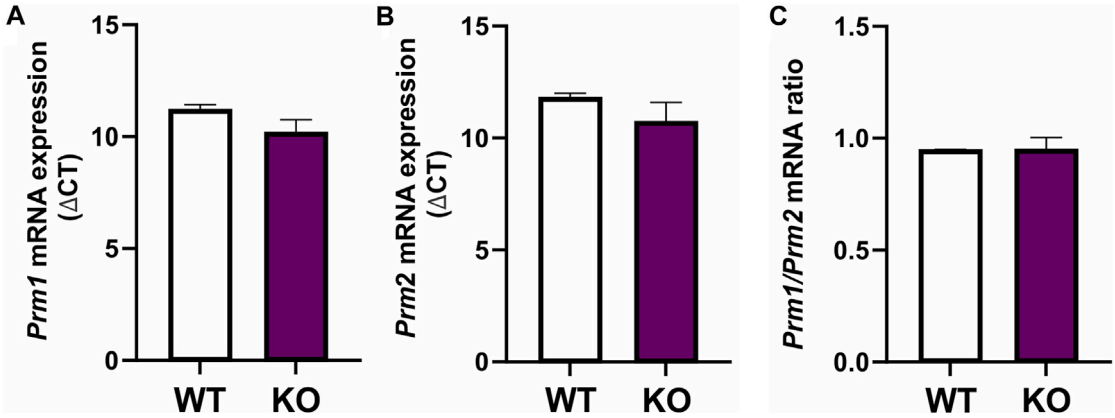

FIGURE 3
Expression of *Prm1* and *Prm2* mRNA is not different between testes from wild-type and *Spag17* knockout mice. Testes from adult wild-type (WT, n = 4) and *Spag17* knockout (KO, n = 5) mice were collected. Total RNA was extracted and used to determine *Prm1* and *Prm2* gene expression by qPCR using 18S rRNA as a housekeeping gene. **(A)** *Prm1* mRNA expression showed no differences between WT and KO testes; $p = 0.17$. **(B)** *Prm2* mRNA expression showed no differences between WT and KO testes; $p = 0.31$. **(C)** *Prm1/Prm2* mRNA ratio was not different between WT and KO testes. Results are means ± SEM, $p = 0.96$.

3.3 SPAG17 is important for nuclear translocation of protamines

To understand the association of SPAG17 with PRM1 and PRM2, we investigated whether SPAG17 is necessary for the transport of protamines. Thus, nuclear translocation of PRM1 and PRM2 was studied by immunofluorescence using anti-PRM1 and PRM2 antibodies in wild-type and *Spag17* knockout spermatids. Figures 5A,B show PRM1 and PRM2 nuclear localization in wild-type spermatids. In contrast, these proteins were mainly detected in the cytoplasm of *Spag17* knockout spermatids, indicating reduced nuclear translocation. Quantification of the nucleus/cytoplasm ratio of PRM1 and PRM2 in spermatids from steps 12 to 16 showed reduced ratio in *Spag17* knockout spermatids in comparison to wild-type (Figure 5C).

Building on this observation, we further explored the importance of SPAG17 in the transport of protamines using a fibroblast *in vitro* system. Mouse embryonic fibroblasts (MEFs) collected from wild-type and *Spag17* knockout embryos were transfected with mouse pPrm1-mCherry-N1 and mouse pPrm2-EGFP-N3 expressing vectors. pmCherry-N1 or pEGFP-N3 empty vectors were used as control vectors (Supplementary Figure S7). Figures 6A,B show that the localization of PRM1 and PRM2 is mostly in the nucleus of wild-type MEFs 24 h post-transfection. However, this does not occur in *Spag17* knockout MEFs, where protamines predominantly remain in the cytoplasm. Quantification of nuclear localization of PRM1 and PRM2 showed a significant difference ($p = 0.001$, for both PRM1 and PRM2, n = 4) between wild-type and *Spag17* knockout MEFs (Figure 6C). These results indicate that SPAG17 is required for transport of protamines from the cytoplasm to the nucleus. Due to the crucial role of protamines in DNA condensation, we conducted experiments to explore the subcellular localization of protamines within the nucleus. Interestingly, in our initial experiments, we did not observe noticeable areas enriched in protamines as markers for DNA condensation, as previously shown (Arévalo et al., 2022). To investigate further, we examined the time-dependent effect of protamines' subcellular localization after 48 h post-transfection. Remarkably, we observed a significant enrichment of protamines in distinct areas within the nucleus (Supplementary Figure S8), confirming that this phenomenon is indeed time-dependent in wild-type MEFs. Conversely, after 48 h, protamines remain predominantly localized in the cytoplasm in *Spag17* knockout MEFs.

4 Discussion

During spermiogenesis, spermatids undergo a dramatic transformation from a round morphology to an asymmetric and elongated shape which is accompanied by DNA compaction and nuclear remodeling. In order to undergo such "metamorphic" transformations, spermatids have a complex but well-articulated system that delivers proteins to specific subcellular domains. In this context, a transitory structure named the manchette is assembled and serves as a track for protein trafficking (Kierszenbaum, 2002). Several proteins have been shown to localize to the manchette (Pleuger et al., 2020; Teves et al., 2020) but the function of a good number of these proteins and their interactomes are mostly unknown. We have previously shown that SPAG17, a protein originally characterized as a central pair protein in the flagellar axoneme (Zhang et al., 2005), is also associated with the manchette and is important for protein trafficking (Kazarian et al., 2018). Because earlier observations by transmission electron microscopy showed disrupted chromatin condensation in *Spag17* knockout spermatids (Kazarian et al., 2018), we hypothesized that there could be interactions between SPAG17 and protamines and that SPAG17 may be important for protamine trafficking.

The results presented here revealed interactions between SPAG17 and PRM1 and PRM2 with PLA and IP/MS.

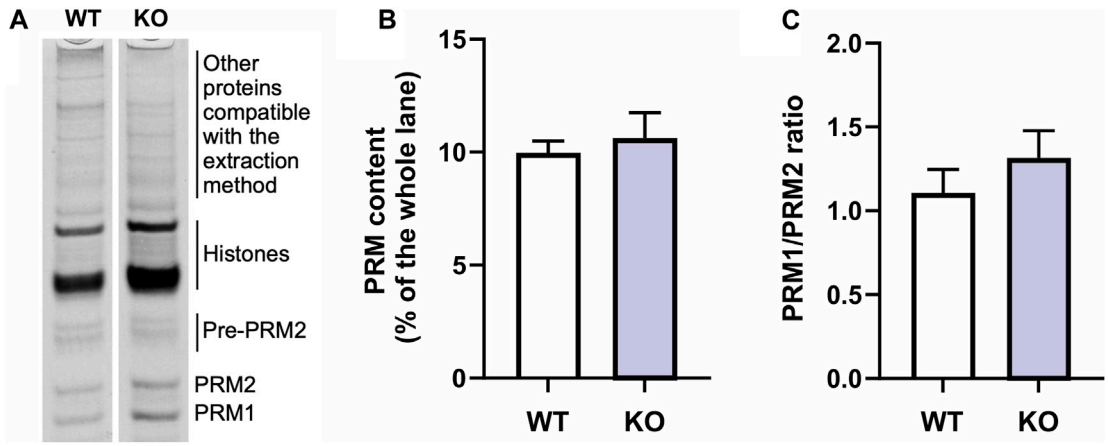

FIGURE 4
Comparison of protamine protein content between wild-type (WT) and *Spag17* knockout (KO). **(A)** Representative lanes of the acid-urea polyacrylamide gel indicating the bands corresponding to protamines (PRM1 and PRM2; pre-PRM2 = PRM2 precursor), histones and other extracted proteins. **(B)** Quantification showing protamine content as measured by protamine band density on a Coomassie blue stained acid-urea polyacrylamide gel as percent of the whole lane (p = 0.64). **(C)** Quantification of PRM1/PRM2 ratio (p = 0.38). Results are means ± SEM, n = 3 per genotype.

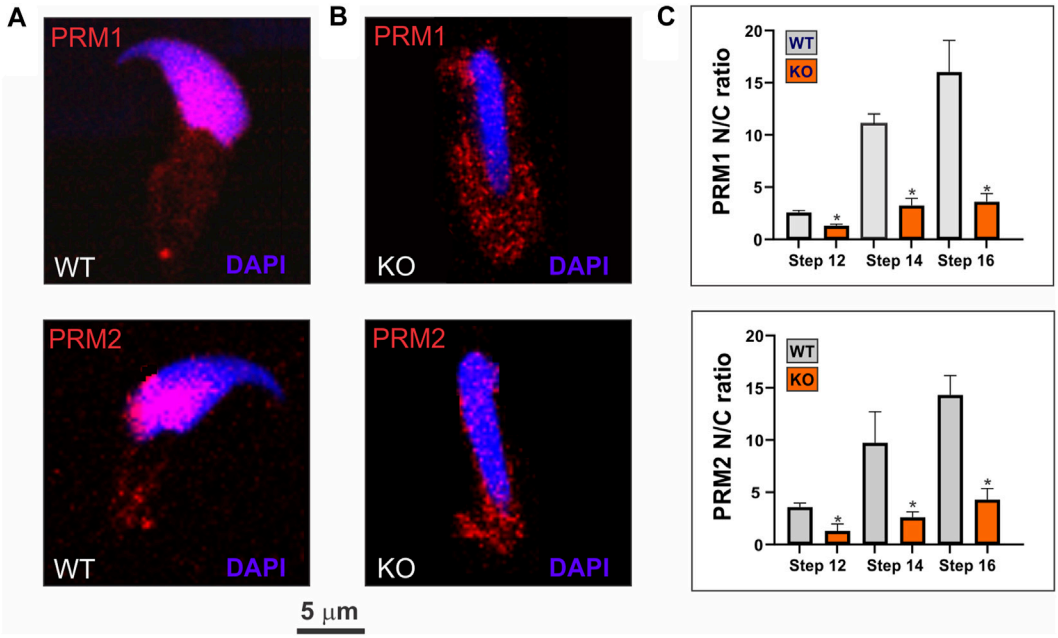

FIGURE 5
SPAG17 is important for nuclear translocation of protamines in spermatids. Spermatids were isolated from mouse testes and immunolabeled using anti-PRM1 and PRM2 antibodies. **(A)** Representative immunolabeling in wild-type (WT) spermatids showing nuclear localization of PRM1 and PRM2. **(B)** Representative immunolabeling in *Spag17* knockout (KO) spermatids revealed disrupted nuclear translocation of PRM1 and PRM2 **(C)** Quantification of nuclear/cytoplasmic (N/C) ratio of PRM1 and PRM2 localization in WT (n = 4) and KO (n = 4) spermatids at different steps during spermiogenesis. Results are means ± SEM. *Significant differences in comparison to WT; $p < 0.05$.

Remarkably, these proteins seem to interact in the cytoplasm and the nuclear area of elongating spermatids at the time when protamines are translocated into the nucleus.

Protamination was assessed in spermatids at different stages and in mature sperm as a measure of chromatin compaction promoted by protamines. It was anticipated that less compaction would translate into a higher proportion of cells staining with chromomycin A3 (Sakkas et al., 1995; Lolis et al., 1996). Our results indicated that protamination deficiency is significantly higher in the absence of SPAG17 in spermatids and in mature spermatozoa, similar to other knockout mouse models associated with defective DNA compaction (Yassine et al., 2014), and consistent with the original observations of disrupted

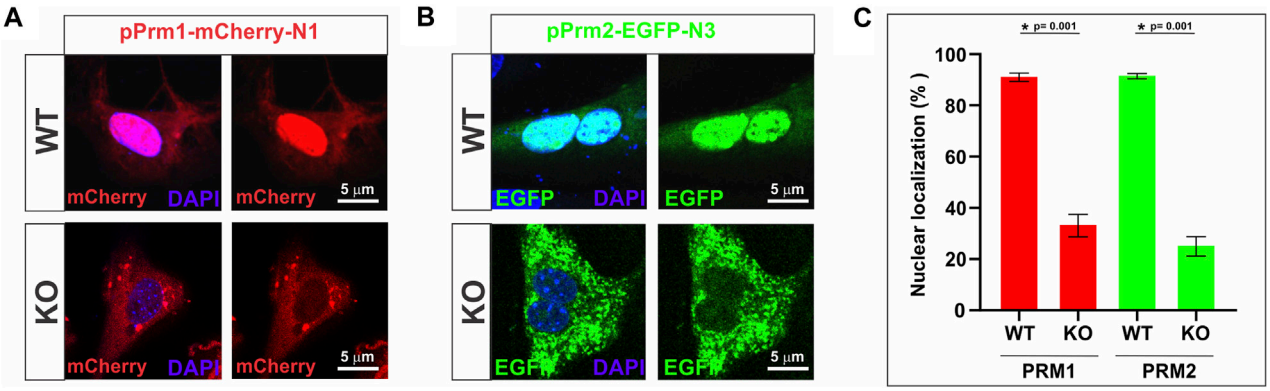

FIGURE 6
Transport of protamines into the nucleus is disrupted in the absence of SPAG17 in cultured fibroblasts. Mouse embryonic fibroblasts (MEFs) collected from wild-type (WT) and *Spag17* knockout (KO) embryos were transfected with mouse pPrm1-mCherry-N1 and mouse pPrm2-EGFP-N3 expressing vectors. **(A)** Representative images showing protamine localization in WT and KO MEFs after 24 h transfection with the PRM1 vector. **(B)** Representative images showing protamine localization in WT and KO MEFs after 24 h transfection with the PRM2 vector. **(C)** Quantification of nuclear localization of protamines. At 24 h post-transfection, the percentage of nuclear localization of PRM1 or PRM2 is significantly lower in *Spag17* knockout MEFs. Results are means ± SEM from four independent experiments. *Significant differences in comparison to WT; p = 0.001).

chromatin condensation in the *Spag17* knockout (Kazarian et al., 2018). Deficiency of protamination could be due to decreased levels of protamine synthesis, or it may relate to transport of these proteins into the nucleus. Our data showed that the decrease in protamination is not due to differences in available protamines based on the quantitation of mRNA expression levels. Lack of *Spag17* did not affect the expression of *Prm1* and *Prm2*, since no differences were observed in mRNA levels of both genes. In addition, the ratio of *Prm1/Prm2* mRNA was also not different. Moreover, no differences were detected at the protein level. These findings suggest that reduced protamines levels in the nucleus were not related to their expression patterns but, rather to altered translocation into the nucleus.

To further investigate the possibility of disruptions in the transport of PRM1 and PRM2 from the cytoplasm to the nucleus, the distribution of these proteins in spermatids at different stages of spermiogenesis was analyzed. In the absence of SPAG17, PRM1 and PRM2 distribution was more abundant in the cytoplasm of spermatids from steps 12 to 16 in comparison to wild-type mice. This suggests that SPAG17 may have an active role in the translocation of protamines from the cytoplasm to the nucleus.

Additional evidence for the influence of SPAG17 in protamine translocation was obtained from *in vitro* studies using fibroblasts transfected with PRM1 or PRM2. Previous studies have characterized this fibroblast model system to understand the mechanisms of nuclear remodeling and reprogramming (Iuso et al., 2015). In sheep or mouse fibroblasts, transfection with human or mouse PRM1 results in gene silencing, nuclear shape changes and chromatin compaction (Iuso et al., 2015; Czernik et al., 2016; Palazzese et al., 2018). These changes have biological relevance because they resembled reprogramming and nuclear reorganization taking place in spermatids during differentiation (Iuso et al., 2015; Czernik et al., 2016). Similar results were found with transfection of PRM2 into HEK293 cells, where PRM2 localized to the somatic cell nuclei and a few nuclei seemed to be fully condensed (Arevalo et al., 2022a).

Our results showed that mouse embryonic fibroblasts from wild-type mice transfected with either PRM1 or PRM2 exhibited a very high percentage of cells with protein localized to the nuclei, in agreement with earlier results (Iuso et al., 2015; Arévalo et al., 2022a). However, in fibroblasts from SPAG17 deficient mice, there was a diminished proportion of nuclei with protamine, with the majority of PRM1 or PRM2 remaining in the cytoplasm even after 48 h post transfection. This provides additional evidence for the protamine transport dependency of SPAG17. Other proteins have been shown to be important for protein trafficking during spermiogenesis (Pleuger et al., 2020). Knockout models for some of these proteins lead to deformities in the nucleus (Teves and Roldan, 2022). However, it is unknown whether there is also altered chromatin condensation or if there are any interactions between these proteins and protamines.

Classical transport of biomolecules to the nucleus is mediated via the nuclear pore complex (NPC). This process involves several proteins including importins, nucleoporins, and a gradient of the small GTPase Ran between the nucleus and the cytoplasm (Miyamoto et al., 2012). Importins are a group of proteins with the capacity to bind a cargo and translocate it through nuclear pores. Selective cargo transport is possible because individual importins preferentially bind specific cargoes (Nathaniel et al., 2022). Importantly, several importins have been shown to play a role during spermatogenesis (Arjomand et al., 2014; Miyamoto et al., 2020; Liu et al., 2021; Nathaniel et al., 2022). Two proteins, RanGTPase-activating protein 1 (RanGAP1), in the cytoplasm, and RCC1, in the nucleus, maintain a gradient between the nucleus and the cytoplasm in mammals (Teves et al., 2020), which facilitate the nuclear internalization of the importins and the cargo protein through the NPC. Remarkably, RanGap associates to the manchette before transporting the protein complex from the cytoplasm to the nucleus (Kierszenbaum et al., 2002). Then, high nuclear RanGTP levels dissociate the importin-cargo complex, and the cargo is thereby positioned to effect nuclear roles (Nathaniel et al., 2022). To date, it is unknown whether any of these proteins interact with PRM1 or PRM2.

In conclusion, we showed that the transport of protamines is dependent on SPAG17. The identification of other proteins that are

members of the interactome involved in this transport process requires further investigation. It is not known if SPAG17 is involved in the transport of other proteins into the nucleus including histones or transition nuclear proteins. The incomplete replacement of histones and/or aberrant PRM1 to PRM2 ratios, which are associated with sperm nuclear abnormalities, along with increased DNA fragmentation and decreased male fertility (Teves and Roldan, 2022), could arise from intricate interactions involved in the translocation of these proteins. Hence, understanding the mechanisms governing the nucleocytoplasmic transport of protamines holds significant importance for gaining a deeper insight into the underlying causes of male gamete dysfunction and infertility.

Data availability statement

The raw data supporting the conclusions of this article will be made available by the authors, without undue reservation.

Ethics statement

The animal study was approved by Virginia Commonwealth University Institutional Animal Care and Use Committee. The study was conducted in accordance with the local legislation and institutional requirements.

Author contributions

CA-R, AR, IK, VB and LN performed experiments; CC-F, DK, LA, JFS III, ERSR and MET analyzed data; GEM, LA and HS developed plasmids; JFS III provided key reagents, equipment and assisted in editing the manuscript, CA-R and AR drafted the manuscript; ERSR and MET designed the study and wrote the manuscript. ERSR and MET provided funding for this study. All authors contributed to the article and approved the submitted version.

Funding

Supported by the National Institutes of Health (grant R03HD101762) and the Spanish Agencia Estatal de Investigación (PID2019-108649GB-I00). CA-R is supported by a predoctoral studentship from the Spanish Agencia Estatal de Investigación, cofunded by the European Social Fund (PRE2020-095265).

Acknowledgments

Microscopy was performed at the VCU Microscopy Core, supported, in part, with funding from the NIH-NCI Cancer Center Support Grant P30 CA016059.

Conflict of interest

The authors declare that MET received research support unrelated to this work from Boehringer-Ingelheim.

The remaining authors declare that the research was conducted in the absence of any commercial or financial relationships that could be construed as a potential conflict of interest.

Publisher's note

Supplementary material

The Supplementary Material for this article can be found online at: https://www.frontiersin.org/articles/10.3389/fcell.2023.1125096/full#supplementary-material

References

Aitken, R. J., De Iuliis, G. N., and McLachlan, R. I. (2009). Biological and clinical significance of DNA damage in the male germ line. *Int. J. Androl.* 32, 46–56. doi:10.1111/j.1365-2605.2008.00943.x

Andraszek, K., Banaszewska, D., Czubaszek, M., Wójcik, E., and Szostek, M. (2014). Comparison of different chromatin staining techniques for bull sperm. *Arch. Anim. Breed.* 57, 1–15. doi:10.7482/0003-9438-57-013

Arévalo, L., Merges, G. E., Schneider, S., Oben, F. E., Neumann, I. S., and Schorle, H. (2022a). Loss of the cleaved-protamine 2 domain leads to incomplete histone-to-protamine exchange and infertility in mice. *PLoS Genet.* 18, e1010272. doi:10.1371/journal.pgen.1010272

Arévalo, L., Merges, G. E., Schneider, S., and Schorle, H. (2022b). Protamines: lessons learned from mouse models. *Reproduction* 164, R57–R74. doi:10.1530/REP-22-0107

Arjomand, A., Baker, M. A., Li, C., Buckle, A. M., Jans, D. A., Loveland, K. L., et al. (2014). The α-importome of mammalian germ cell maturation provides novel insights for importin biology. *FASEB J.* 8, 3480–3493. doi:10.1096/fj.13-244913

Balhorn, R. (2007). The protamine family of sperm nuclear proteins. *Genome. Biol.* 9, 227.

Balhorn, R. (2018). *Sperm chromatin: An overview. A clinician's guide to sperm DNA and chromatin damage*. Berlin, Germany: Springer Cham, 3–30. doi:10.1007/978-3-319-71815-6_1

Bizzaro, D., Manicardi, G. C., Bianchi, P. G., Bianchi, U., Mariethoz, E., and Sakkas, D. (1998). *In-situ* competition between protamine and fluorochromes for sperm DNA. *Mol. Hum. Reprod.* 4, 127–132. doi:10.1093/molehr/4.2.127

Castro, L. S., Siqueira, A. F. P., Hamilton, T. R. S., Mendes, C. M., Visintin, J. A., and Assumpção, M. E. O. A. (2018). Effect of bovine sperm chromatin integrity evaluated using three different methods on *in vitro* fertility. *Theriogenology* 107, 142–148. doi:10.1016/j.theriogenology.2017.11.006

Czernik, M., Iuso, D., Toschi, P., Khochbin, S., and Loi, P. (2016). Remodeling somatic nuclei via exogenous expression of protamine 1 to create spermatid-like structures for somatic nuclear transfer. *Nat. Protoc.* 11, 2170–2188. doi:10.1038/nprot.2016.130

Hecht, N. B., Bower, P. A., Waters, S. H., Yelick, P. C., and Distel, R. J. (1986a). Evidence for haploid expression of mouse testicular genes. *Exptl Cell Res.* 164, 183–190. doi:10.1016/0014-4827(86)90465-9

Hecht, N. B., Kleene, K. C., Yelick, P. C., Johnson, P. A., Pravtcheva, D. D., and Ruddle, F. H. (1986b). Mapping of haploid expressed genes: genes for both mouse protamines are located on chromosome 16. *Somat. Cell Mol. Genet.* 12, 203–208. doi:10.1007/BF01560667

Ishibashi, T., Li, A., Eirín-López, J. M., Zhao, M., Missiaen, K., Abbott, D. W., et al. (2010). H2A.Bbd: an X-chromosome-encoded histone involved in mammalian spermiogenesis. *Nucleic Acids Res.* 38, 1780–1789. doi:10.1093/nar/gkp1129

Iuso, D., Czernik, M., Toschi, P., Fidanza, A., Zacchini, F., Feil, R., et al. (2015). Exogenous expression of human protamine 1 (hPrm1) remodels fibroblast nuclei into spermatid-like structures. *Cell Rep.* 13, 1765–1771. doi:10.1016/j.celrep.2015.10.066

Kazarian, E., Son, H., Sapao, P., Li, W., Zhang, Z., Strauss, J. F., et al. (2018). SPAG17 is required for male germ cell differentiation and fertility. *Int. J. Mol. Sci.* 19, 1252. doi:10.3390/ijms19041252

Kierszenbaum, A. L. (2002). Intramanchette transport (IMT): managing the making of the spermatid head, centrosome, and tail. *Mol. Reprod. Dev.* 63, 1–4. doi:10.1002/mrd.10179

Kleene, K. C., Distel, R. J., and Hecht, N. B. (1984). Translational regulation and deadenylation of a protamine mRNA during spermiogenesis in the mouse. *Dev. Biol.* 105, 71–79. doi:10.1016/0012-1606(84)90262-8

Kleene, K. C. (1989). Poly(A) shortening accompanies the activation of translation of five mRNAs during spermiogenesis in the mouse. *Development* 106, 367–373. doi:10.1242/dev.106.2.367

Liu, N., Qadri, F., Busch, H., Huegel, S., Sihn, G., Chuykin, I., et al. (2021). Kpna6 deficiency causes infertility in male mice by disrupting spermatogenesis. *Development* 148, dev198374. doi:10.1242/dev.198374

Lolis, D., Georgiou, I., Syrrou, M., Zikopoulos, K., Konstantelli, M., and Messinis, I. (1996). Chromomycin A3-staining as an indicator of protamine deficiency and fertilization. *Int. J. Androl.* 19, 23–27. doi:10.1111/j.1365-2605.1996.tb00429.x

Lüke, L., Campbell, P., Varea Sánchez, M., Nachman, M. W., and Roldan, E. R. S. (2014). Sexual selection on protamine and transition nuclear protein expression in mouse species. *Proc. R. Soc. B* 281, 20133359. doi:10.1098/rspb.2013.3359

Mateo, S. d., Ramos, L., Boer, P. d., Meistrich, M., and Oliva, R. (2011). Protamine 2 precursors and processing. *Protein Pept. Lett.* 18, 778–785. doi:10.2174/092986611795713998

Merges, G. E., Meier, J., Schneider, S., Kruse, A., Fröbius, A. C., Kirfel, G., et al. (2022). Loss of Prm1 leads to defective chromatin protamination, impaired PRM2 processing, reduced sperm motility and subfertility in male mice. *Development* 149, dev200330. doi:10.1242/dev.200330

Miyamoto, Y., Boag, P. R., Hime, G. R., and Loveland, K. L. (2012). Regulated nucleocytoplasmic transport during gametogenesis. *Biochim. Biophys. Acta* 6, 616–630. doi:10.1016/j.bbagrm.2012.01.015

Miyamoto, Y., Sasaki, M., Miyata, H., Monobe, Y., Nagai, M., Otani, M., et al. (2020). Genetic loss of importin α4 causes abnormal sperm morphology and impacts on male fertility in mouse. *FASEB J.* 12, 16224–16242. doi:10.1096/fj.202000768RR

Moritz, L., and Hammoud, S. S. (2022). The art of packaging the sperm genome: molecular and structural basis of the histone-to-protamine exchange. *Front. Endocrinol. (Lausanne)* 13, 895502. doi:10.3389/fendo.2022.895502

Nathaniel, B., Whiley, P. A. F., Miyamoto, Y., and Loveland, K. L. (2022). Importins: diverse roles in male fertility. *Semin. Cell Dev. Biol.* 121, 82–98. doi:10.1016/j.semcdb.2021.08.002

Ni, K., Spiess, A. N., Schuppe, H. C., and Steger, K. (2016). The impact of sperm protamine deficiency and sperm DNA damage on human male fertility: A systematic review and meta-analysis. *Andrology* 4, 789–799. doi:10.1111/andr.12216

Oliva, R. (2006). Protamines and male infertility. *Hum. Reprod. Update.* 12, 417–435. doi:10.1093/humupd/dml009

Palazzese, L., Czernik, M., Iuso, D., Toschi, P., and Loi, P. (2018). Nuclear quiescence and histone hyper-acetylation jointly improve protamine-mediated nuclear remodeling in sheep fibroblasts. *PLoS One* 13, e0193954. doi:10.1371/journal.pone.0193954

Pleuger, C., Lehti, M. S., Dunleavy, J. E. M., Fietz, D., and O'Bryan, M. K. (2020). Haploid male germ cells-the Grand Central Station of protein transport. *Hum. Reprod. Update* 26, 474–500. doi:10.1093/humupd/dmaa004

Pourmasumi, S., Nazari, A., Fagheirelahee, N., and Sabeti, P. (2019). Cytochemical tests to investigate sperm DNA damage: assessment and review. *J. Fam. Med. Prim. Care.* 8 (5), 1533–1539. doi:10.4103/jfmpc.jfmpc_35_19

Ribas-Maynou, J., Garcia-Bonavila, E., Bonet, S., Catalán, J., Salas-Huetos, A., and Yeste, M. (2021). The TUNEL assay underestimates the incidence of DNA damage in pig sperm due to chromatin condensation. *Theriogenology* 174, 94–101. doi:10.1016/j.theriogenology.2021.08.024

Sakkas, D., Manicardi, G., Bianchi, P. G., Bizzaro, D., and Bianchi, U. (1995). Relationship between the presence of endogenous nicks and sperm chromatin packaging in maturing and fertilizing mouse spermatozoa. *Biol. Reprod.* 52, 1149–1155. doi:10.1095/biolreprod52.5.1149

Schneider, C. A., Rasband, W. S., and Eliceiri, K. W. (2012). NIH image to ImageJ: 25 years of image analysis. *Nat. Methods* 9, 671–675. doi:10.1038/nmeth.2089

Schneider, S., Balbach, M., Jikeli, J. F., Fietz, D., Nettersheim, D., Jostes, S., et al. (2016). Re-Visiting the protamine-2 locus: deletion, but not haploinsufficiency, renders male mice infertile. *Sci. Rep.* 11, 1–3. doi:10.1038/srep36764

Serafini, R., Longobardi, V., Spadetta, M., Neri, D., Ariota, B., Gasparrini, B., et al. (2014). Trypan blue/giemsa staining to assess sperm membrane integrity in salernitano stallions and its relationship to pregnancy rates. *Reprod. Domest. Anim.* 49, 41–47. doi:10.1111/rda.12221

Silva, T. V. G., Santana, P. D. P. B., Souza, E. B. de, Lima, A. J. M., Santos, C. D. A., Almeida, N. N. D. C., et al. (2021). Sperm chromatin protamination influences embryo development in unsexed and sexed bull semen. *Zygote* 29, 264–269. doi:10.1017/S0967199420000775

Soler-Ventura, A., Castillo, J., Iglesia, A. d. l., Jodar, M., Barrachina, F., Ballesca, J. L., et al. (2018). Mammalian sperm protamine extraction and analysis: A step-by-step detailed protocol and brief review of protamine alterations. *Protein Pept. Lett.* 25, 424–433. doi:10.2174/0929866525666180412155205

Teves, M. E., Roldan, E. R. S., Krapf, D., Strauss, J. F., Bhagat, V., and Sapao, P. (2020). Sperm differentiation: the role of trafficking of proteins. *Int. J. Mol. Sci.* 21, 3702. doi:10.3390/ijms21103702

Teves, M. E., and Roldan, E. R. S. (2022). Sperm bauplan and function and underlying processes of sperm formation and selection. *Physiol. Rev.* 102, 7–60. doi:10.1152/physrev.00009.2020

Teves, M. E., Sundaresan, G., Cohen, D. J., Hyzy, S. L., Kajan, I., Maczis, M., et al. (2015). Spag17 deficiency results in skeletal malformations and bone abnormalities. *PloS One* 5, e0125936. doi:10.1371/journal.pone.0125936

Yu, Y. E., Zhang, Y., Unni, E., Shirley, C. R., Deng, J. M., Russell, L. D., et al. (2000). Abnormal spermatogenesis and reduced fertility in transition nuclear protein 1-deficient mice. *Proc. Natl. Acad. Sci.* 97, 4683–4688. doi:10.1073/pnas.97.9.4683

Yassine, S., Escoffier, J., Martinez, G., Coutton, C., Karaouzène, T., Zouari, R., et al. (2015). Dpy19l2-deficient globozoospermic sperm display altered genome packaging and DNA damage that compromises the initiation of embryo development. *Mol. Hum. Reprod.* 21, 169–185. doi:10.1093/molehr/gau099

Zhang, Z., Jones, B., Tang, W., Moss, S. B., Wei, Z., Ho, C. K. M., et al. (2005). Dissecting the axoneme interactome: the mammalian orthologue of chlamydomonas PF6 interacts with sperm-associated antigen 6, the mammalian orthologue of chlamydomonas PF16. *Mol. Cell. Proteom.* 4, 914–923. doi:10.1074/mcp.M400177-MCP200

Frontiers in
Cell and Developmental Biology

Explores the fundamental biological processes of life, covering intracellular and extracellular dynamics.

The world's most cited developmental biology journal, advancing our understanding of the fundamental processes of life. It explores a wide spectrum of cell and developmental biology, covering intracellular and extracellular dynamics.

Discover the latest Research Topics

See more →

Frontiers

Avenue du Tribunal-Fédéral 34
1005 Lausanne, Switzerland
frontiersin.org

Contact us

+41 (0)21 510 17 00
frontiersin.org/about/contact